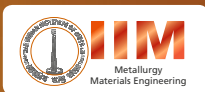


Indian Institute of Metals Series

N. Eswara Prasad
R. J. H. Wanhill
Editors

Aerospace Materials and Material Technologies

Volume 1:
Aerospace Materials



 Springer

Indian Institute of Metals Series

Editors-in-chief

Baldev Raj, National Institute of Advanced Studies, Bengaluru, Karnataka, India
U. Kamachi Mudali, Indira Gandhi Centre for Atomic Research, Kalpakkam,
Tamil Nadu, India

More information about this series at <http://www.springer.com/series/15453>

N. Eswara Prasad · R.J.H. Wanhill
Editors

Aerospace Materials and Material Technologies

Volume 1: Aerospace Materials

 Springer

Editors

N. Eswara Prasad
Defence Materials and Stores R&D
Establishment (DMSRDE)
Kanpur, Uttar Pradesh
India

R.J.H. Wanhill
Emmeloord, Flevoland
The Netherlands

ISSN 2509-6400

Indian Institute of Metals Series

ISBN 978-981-10-2133-6

DOI 10.1007/978-981-10-2134-3

ISSN 2509-6419 (electronic)

ISBN 978-981-10-2134-3 (eBook)

Library of Congress Control Number: 2016948239

© Springer Science+Business Media Singapore 2017

This work is subject to copyright. All rights are reserved by the Publisher, whether the whole or part of the material is concerned, specifically the rights of translation, reprinting, reuse of illustrations, recitation, broadcasting, reproduction on microfilms or in any other physical way, and transmission or information storage and retrieval, electronic adaptation, computer software, or by similar or dissimilar methodology now known or hereafter developed.

The use of general descriptive names, registered names, trademarks, service marks, etc. in this publication does not imply, even in the absence of a specific statement, that such names are exempt from the relevant protective laws and regulations and therefore free for general use.

The publisher, the authors and the editors are safe to assume that the advice and information in this book are believed to be true and accurate at the date of publication. Neither the publisher nor the authors or the editors give a warranty, express or implied, with respect to the material contained herein or for any errors or omissions that may have been made.

Printed on acid-free paper

This Springer imprint is published by Springer Nature

The registered company is Springer Nature Singapore Pte Ltd.

The registered company address is: 152 Beach Road, #22-06/08 Gateway East, Singapore 189721, Singapore

*To
our eminent teachers and close associates for
aerospace materials and material
technologies;*

and to

*our partners and families for their support,
notably during 2014–2016, the years in
which these books were prepared.*

N. Eswara Prasad and R.J.H. Wanhill

Foreword by Prof. Dipankar Banerjee



If the world has shrunk rapidly in recent centuries, this has been in no small measure due to the impact of materials on aerospace transport. The specific fuel consumption of commercial aircraft has, for example, decreased by an astonishing 70 % using the De Havilland Comet as baseline. The reliability of their propulsion systems allows long-haul flights that encircle the globe, travelling non-stop for 15–20 h. We have mastered space, with footsteps on the moon and images and analysis of the Martian terrain. The international space station has been continuously occupied since 2000. While it is hard to dissect and

break down contributions of any specific engineering discipline to these spectacular achievements, surely materials have played a significant enabling role, whether from the ‘fine-tuning’ of traditional metallic materials, or the development of newer composites and speciality materials including functional coatings. The integration of stealth materials into aerospace structures has added an extra dimension to military aerospace vehicles. The emergence of several high temperature monolithic and composite ceramic materials based on carbon and silicon carbide matrices and reinforcements has resulted in vastly improved material capabilities for high temperature aerospace applications. Several new refractory materials are finding ultrahigh temperature applications as 2000K+ materials, especially for reusable and re-entry hypersonic vehicles. Aviation accounts for about 3 % of global energy consumption, and the growth of energy use by the aviation sector exceeds that of other transportation sectors. Aircraft emissions, which are currently unregulated, are about 60 % in the upper troposphere and 20 % in the stratosphere. The industry will demand further materials-enabled improvements to address these challenges.

It is encouraging that the present volume on aerospace materials for the two-volume source book series of IIM/Springer Publication provides concise overviews of all the above. Development, physical metallurgy, processing,

properties and applications of each of nearly 26 categories of aerospace materials have been covered.

Dr. N. Eswara Prasad has been my close associate and colleague and has accumulated much experience and expertise with aerospace materials over the last 30 years. I am happy that he has accepted the major responsibility imposed on him by the Indian Institute of Metals (IIM), and the architect of its book series Dr. Baldev Raj, to co-author and co-edit with Dr. R.J.H. Wanhill (an international expert in the field of aerospace materials and technologies) the contents of these volumes. I am sure their readers will find them extremely useful, and the two-volume series will serve as a ready reference for engineering students, practicing engineers and aerospace structural designers.

I take this opportunity to congratulate all the authors and editors—Dr. N. Eswara Prasad, Dr. R.J.H. Wanhill and Dr. Baldev Raj, Editor-in-Chief, and Springer on the successful completion of this mammoth endeavour. This kind of international book project also serves as a road map for the future. We are reminded that materials development and translation into engineering practice is still a long and arduous task, with significant reliance on trial and error approaches. As a community we are now engaged in the task of redefining the processes of materials insertion into engineering products through integration of multiscale modelling, data analytics and materials informatics, uncertainty quantification and multi-objective optimisation into the materials design effort. I hope future volumes in this series will capture also these dramatic advances as the field matures.

Prof. Dipankar Banerjee
FASc, FNA, FNAE, FNASc
Former Director, Defence Metallurgical Research Laboratory
Hyderabad, India
Former Chief Controller R&D
(Aeronautics & Materials Science)
DRDO, New Delhi, India
Former President, Indian Institute of Metals (IIM)
Former President, Electron Microscopy Society (EMS) and
Presently Professor, Department of Materials Engineering
Indian Institute of Science, Bengaluru, 560 012, India

Foreword by Prof. Indranil Manna



Advancements in aerospace systems, materials and technologies in the last century are both voluminous and phenomenal. Several countries in both the developed and developing world have become principal players in developing aeronautical materials, thereby earning the credit for the advancement of aerospace systems including civil and military aircraft, helicopters, airborne surveillance systems, unmanned aerospace vehicles, guided missiles, supersonic re-entry vehicles and satellites. All these systems require advanced materials and cutting-edge material processing technologies. Hence synthesis,

processing, characterisation and testing of materials form the basis for the development and realization of aerospace components, sub-systems and systems. It is a well-recognized fact that aerospace engineering is principally responsible for developing several critical technologies that include (i) design and development of advanced materials, components and sub-systems; (ii) aeronautical material specifications and standards for materials and testing; (iii) characterisation and testing methodologies; and (iv) life estimations and predictions based on fatigue and fracture mechanics principles. In addition, aerospace engineering has advanced several other critical technologies such as propulsion, aeroengines, electronics, communication and guidance.

There are a number of text books and monographs on aerospace materials and related technologies. As well, several ASTM standards, metals handbooks and special volumes have compiled scientific and design data on various aerospace materials that are used by aerospace engineers for designing structures and systems. Such efforts have invariably brought out the latest information and also shown directions for future materials and systems developments. However, supplemental documentation on recent advances in core domain and interdisciplinary areas is always needed.

In this respect, the present two-volume book set is a carefully thought out compilation of overview articles on materials (both established and evolving) and material technologies that are important for aerospace systems. Volume 1 considers aerospace materials in three Parts. Part I covers Metallic Materials (Mg, Al, Al-Li, Ti, Aero steels, Ni, Intermetallics, Bronzes and Nb alloys); Part II deals with Composites (GLARE, PMCs, CMCs and Carbon based CMCs); and Part III considers Special Materials. This compilation has ensured that no important aerospace material system is ignored. Emphasis has been placed in each book chapter on the underlining scientific principles as well as basic and fundamental mechanisms leading to processing, characterisation/property evaluation and applications. Each chapter ends with a bibliography of several reference works, followed by standard sets of references appearing in the chapter. A considerable amount of materials data is compiled and presented in appendices at the end of each volume.

I sincerely wish that these volumes will serve as ready and useful references and source of relevant information for many aspects of aerospace materials, processing technologies, and component and structural designs.

Prof. Indranil Manna
FTWAS, FNA, FNAE, FASc., FNASc., FIIM, FIE
Professor, Department of Metallurgical and Materials Engineering
IIT, Kharagpur, India (On Lien)
Former Director, CSIR—Central Glass and Ceramic
Research Institute (CGCRI), Kolkata India
Vice-President, Indian Institute of Metals
and Indian National Academy of Engineering
Presently, Director, Indian Institute of Technology
Kanpur, India

Series Editors' Preface

The Indian Institute of Metals Series is an institutional partnership series focusing on metallurgy and materials sciences.

About the Indian Institute of Metals

The Indian Institute of Metals (IIM) is a premier professional body (since 1947) representing an eminent and dynamic group of metallurgists and materials scientists from R&D institutions, academia and industry mostly from India. It is a registered professional institute with the primary objective of promoting and advancing the study and practice of the science and technology of metals, alloys and novel materials. The institute is actively engaged in promoting academia–research and institute–industry interactions.

Genesis and History of the Series

The study of metallurgy and materials science is vital for developing advanced materials for diverse applications. In the last decade, the progress in this field has been rapid and extensive, giving us a new array of materials, with a wide range of applications and a variety of possibilities for processing and characterizing the materials. In order to make this growing volume of knowledge available, an initiative to publish a series of books in metallurgy and materials science was taken during the Diamond Jubilee year of the Indian Institute of Metals (IIM) in the year 2006. IIM entered into a partnership with Universities Press, Hyderabad, and as part of the IIM Book series, 11 books were published, and a number of these have been co-published by CRC Press, USA. The books were authored by eminent professionals in academia, industry and R&D with outstanding background in their

respective domains, thus generating unique resources of validated expertise of interest in metallurgy. The international character of the authors and editors has enabled the books to command national and global readership. This book series includes different categories of publications: textbooks to satisfy the requirements of undergraduates and beginners in the field, monographs on select topics by experts in the field and proceedings of select international conferences organized by IIM after a mandatory peer review. An eminent panel of international and national experts constitutes the advisory body in overseeing the selection of topics important areas to be covered in the books and the selection of contributing authors.

Current Series Information

To increase the readership and to ensure wide dissemination among global readers, this new chapter of the Series has been initiated with Springer. The goal is to continue publishing high-value content on metallurgy and materials science, focusing on current trends and applications. Readers interested in writing for the series may contact the undersigned series editor or the Springer publishing editor, Swati Meherishi.

About This Book

The current source book on “Aerospace Materials and Technologies—2 Volumes” with comprehensive coverage in aerospace, materials, technologies is the first and latest book to be published with Springer. This book comprises 2 volumes, with first volume dedicated to aerospace materials elaborately in three parts, a total of 26 chapters covering all types of materials including metallic, composites and special materials. The Volume 2, in 25 chapters, is fully dedicated to the recent and advanced material technologies, which have emerged in the aerospace industry. This volume consists of four parts covering processing technologies, characterization and testing, structural design and special technologies. As a whole, this source book on “Aerospace Materials and Technologies” fully covers the important aspects of the materials development and their technologies in aerospace industry and is an update and unique knowledge base. I am confident that the book would help the readers to develop the basic and advanced understanding of the materials and their recent developments which are essential to address significant growth in the aerospace industry. The authors and editors are of the conviction that the book would be a treasure to all those pursuing advanced materials and technologies in aerospace sectors. The students, young faculties, research scholars in academic and R&D institutions, in addition to a place in libraries and knowledge parks, are the

beneficiaries of the dedicated work and efforts put by Dr. N. Eswara Prasad and Dr. R.J.H. Wanhill, as editors, and a large number of eminent authors of the 2 volumes of this important book.

We wish you enrichment in knowledge and motivation. Also, we await your feedbacks for improving the book when it goes to second edition.

Baldev Raj
Editor-in-Chief, and
Director, National Institute of Advanced Studies, Bangalore

U. Kamachi Mudali
Co-Editor-in-Chief
Outstanding Scientist and Associate Director
Indira Gandhi Centre for Atomic Research, Kalppakam

Preface to Volume 1

The aerospace industry is at the forefront of materials and technologies developments. There are never-ending demands for high performance aerospace vehicles with lightweight, highly reliable and durable structures. Candidate materials are continually being developed and improved and their property envelopes expanded. Structural design and certification requirements, and inspection and monitoring techniques, also evolve to keep pace with these developments.

There are many excellent materials handbooks and source books available, most notably the ASM International series. These offer comprehensive multi-volume guides that belong in the libraries of every materials-oriented university and institute. However, they are less suitable, even in e-form, for regular ‘desktop’ consultation. This led us to the concept of a compact and affordable vade mecum that would serve as a ready reference for practicing engineers and a comprehensive introduction, at an advanced level, for students and faculty members.

It soon became evident that a two-volume series would be appropriate. These have the distinguishing titles ‘Aerospace Materials’ (Volume 1) and ‘Aerospace Material Technologies’ (Volume 2). These volumes are divided into the following main parts:

- Volume 1
 - Part I: Metallic Materials (Chaps. 1–12)
 - Part II: Composites (Chaps. 13–17)
 - Part III: Special Materials (Chaps. 18–26)
- Volume 2
 - Part I: Processing Technologies (Chaps. 1–5)
 - Part II: Characterization and Testing Technologies (Chaps. 6–11)
 - Part III: Structural Design (Chaps. 12–19)
 - Part IV: Special Technologies (Chaps. 20–25)

This Volume 1 contains chapters on (i) magnesium, aluminium, titanium, steel and nickel-base alloys, intermetallics, bronzes and refractory metals; (ii) 'GLARE' (glass-reinforced aluminium laminates), polymer-, carbon- and ceramic-matrix composites; (iii) ceramics, 'MAX' phases (carbides and nitrides), shape memory alloys, coatings, piezo-ceramics, stealth materials, paints, adhesives and elastomers.

Kanpur, India
Emmeloord, The Netherlands

N. Eswara Prasad
R.J.H. Wanhill

Acknowledgements

In 2012 the Indian Institute of Metals (IIM) invited me to prepare a monograph on Continuous Fibre-reinforced, Ceramic-matrix Composites (CFCCs) to publish in the IIM series. The outline of that monograph was prepared and a few chapters took preliminary shape. However, this project could not be completed because the subject was dealt with only in a very few institutions in India, and the processing details were mostly proprietary. In the meantime, several of my colleagues and well-wishers, who have worked with me for several years on a new generation of aluminium alloys, based on lithium additions, agreed to contribute comprehensive overview articles to a book on the Physical Metallurgy, Processing, Mechanical Behaviour and Applications of Aluminium-Lithium Alloys—a subject that I have been associated with for nearly 30 years. This book was published in 2014 by Butterworth-Heinemann—An Imprint of Elsevier, UK/USA.

But my quest to write on other aerospace materials (including the CFCCs) and their material technologies still was not quenched. This was the time, during one of the discussions with Dr. Baldev Raj, Editor-in-Chief, IIM Book series, that it was suggested to me that my recent experience on concurrent development and certification of aerospace materials should be used to prepare comprehensive book(s) on aerospace materials and technologies. I gratefully agreed to this suggestion of Dr. Baldev Raj and started almost immediately on an outline of such a compendium. I was most pleased when Dr. R.J.H. Wanhill of the NLR, the Netherlands (my co-editor for the Aluminium-Lithium Alloys Monograph and an internationally known materials scientist) agreed to co-edit this book series. Within months, by early 2015, the outline of the book series took a definite shape, in the form of a two-volume book series on Aerospace Materials and Technologies—Aerospace Materials (Vol. 1) and Aerospace Material Technologies (Vol. 2). I am profoundly grateful to both Dr. Baldev Raj and Dr. Wanhill for many in-depth subsequent discussions to shape these volumes.

I am very fortunate to have a long association with many outstanding aerospace materials scientists of India and abroad. Two of these most exemplary scientists,

Dr. Dipankar Banerjee and Dr. Indranil Manna have kindly consented to my request to provide the Foreword and Preface for Volume 1 of this book series, respectively.

The present book series comprises a number of overview articles on aerospace materials and aerospace material technologies. The authors of the book chapters have mostly been pooled from Indian aerospace materials institutions encompassing the Defence Research and Development Organisation (DRDO), Council of Scientific and Industrial Research (CSIR), Department of Atomic Energy (DAE), Defence Production, Govt India (particularly, Mishra Dhatu Nigam (MIDHANI) Limited, Hyderabad) and Hindustan Aeronautics Limited (HAL). My own colleagues at the Regional Centre for Military Airworthiness (RCMA (Materials)), CEMILAC and Defence Metallurgical Research Laboratory (DMRL) have contributed magnanimously to this book project. Some of the close associates of Dr. Wanhill have contributed also. Dr. Wanhill and I have also contributed considerable number of book chapters. I am grateful to each of these principal authors and their co-authors of the chapters for their valuable contributions to this book series.

Dr. Wanhill has further extended his help and guidance to shape the technical contents of these two book series by painstakingly reviewing all the book chapters. Although such an exercise is very arduous and difficult to accomplish, it has resulted in close uniformity in contents and style of the book chapters. I am most grateful and greatly indebted to him.

The book contents provided by the authors were typeset by my book secretariat which consisted of Mr. D.B.A. Sagar, Late Mrs. P. Varsha, Ms. S. Hima Bindu and Mr. Vishal Shreyas, who worked nearly full time on this project. They were also greatly aided by my colleagues Mrs. M. Swarna Bai, Shri P. Rambabu and Shri B. Saha. Shri B. Saha and my RCMA colleagues have been instrumental in finalising the data compilations for the appendices of the book volumes. I am very thankful to all these colleagues.

It is an honour for me that Springer has become the principal source of professional support by agreeing to publish these two book volumes. At this juncture I should acknowledge gratefully the initiative taken by the IIM, particularly Dr. Baldev Raj, to conduct a series of discussions with Springer thereby enabling publication of these volumes by Springer. I must mention here and express my gratitude for the help and support received by the Springer team, especially to Swati Meherishi, Senior Editor and Aparajita Singh, Editorial Assistant.

N. Eswara Prasad

Contents

Part I Metallic Materials

1	Magnesium Alloys	3
	T. Ram Prabhu, Srikanth Vedantam and Vijaya Singh	
2	Aluminium Alloys for Aerospace Applications	29
	P. Rambabu, N. Eswara Prasad, V.V. Kutumbarao and R.J.H. Wanhill	
3	Aluminium–Lithium Alloys	53
	N. Eswara Prasad, Amol A. Gokhale and R.J.H. Wanhill	
4	Titanium Sponge Production and Processing for Aerospace Applications	73
	Ch R.V.S. Nagesh, G.V.S. Brahmendra Kumar, B. Saha and Amol A. Gokhale	
5	Titanium Alloys: Part 1—Physical Metallurgy and Processing	91
	A. Bhattacharjee, B. Saha and J.C. Williams	
6	Titanium Alloys: Part 2—Alloy Development, Properties and Applications	117
	A. Bhattacharjee, B. Saha and J.C. Williams	
7	Aero Steels: Part 1—Low Alloy Steels	149
	K.P. Balan and A. Venugopal Reddy	
8	Aero Steels: Part 2—High Alloy Steels	173
	M. Srinivas and A. Venugopal Reddy	
9	Nickel-Based Superalloys	199
	D.V.V. Satyanarayana and N. Eswara Prasad	
10	Structural Intermetallics	229
	R. Mitra and R.J.H. Wanhill	

11	Bronzes for Aerospace Applications	247
	B. Saha, V. Nimbalkar, D.B. Anant Sagar, M. Sai Krishna Rao and V.P. Deshmukh	
12	Niobium and Other High Temperature Refractory Metals for Aerospace Applications	267
	V.V. Satya Prasad, R.G. Baligidad and Amol A. Gokhale	
Part II Composites		
13	GLARE®: A Versatile Fibre Metal Laminate (FML) Concept	291
	R.J.H. Wanhill	
14	Carbon Fibre Polymer Matrix Structural Composites	309
	R.J.H. Wanhill	
15	C/C and C/SiC Composites for Aerospace Applications	343
	Suresh Kumar, K. Chandra Shekar, B. Jana, L.M. Manocha and N. Eswara Prasad	
16	Ceramic Matrix Composites (CMCs) for Aerospace Applications	371
	N. Eswara Prasad, Anil Kumar and J. Subramanyam	
17	Nanocomposites Potential for Aero Applications	391
	Naveen K. Mahenderkar, T. Ram Prabhu and Anil Kumar	
Part III Special Materials		
18	Monolithic Ceramics for Aerospace Applications	415
	N. Eswara Prasad and S.B. Bhaduri	
19	Nano-enabled Multifunctional Materials for Aerospace Applications	439
	K. Balasubramanian, Manoj Tirumali, Yutika Badhe and Y.R. Mahajan	
20	MAX Phases: New Class of Carbides and Nitrides for Aerospace Structural Applications	455
	Sai Priya Munagala	
21	Shape Memory Alloys (SMAs) for Aerospace Applications	467
	R.J.H. Wanhill and B. Ashok	
22	Detonation Sprayed Coatings for Aerospace Applications	483
	D. Srinivasa Rao, L. Rama Krishna and G. Sundararajan	

23 Piezoceramic Materials and Devices for Aerospace Applications 501
P.K. Panda

24 Stealth Materials and Technology for Airborne Systems 519
N. Kumar and S.R. Vadera

25 Paints for Aerospace Applications 539
K. Shunmugapriya, Shirish S. Kale, G. Gouda, P. Jayapal
and K. Tamilmani

26 Elastomers and Adhesives for Aerospace Applications 563
C.M. Bhuvanewari, Shirish S. Kale, G. Gouda, P. Jayapal
and K. Tamilmani

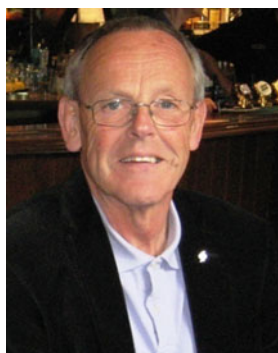
About the Editors



Dr. N. Eswara Prasad FIE, FAPAS, FIIM, a B.Tech. (1985) and a Ph.D. (1993) in Metallurgical Engineering from Indian Institute of Technology (BHU), Varanasi, India, is an innovative and creative researcher and technologist. He is currently serving as Director, Defense Materials and Stores Research and Development Establishment (DMSRDE), DRDO at Kanpur, India. He has made significant and outstanding contributions to the Indian Defense Research and Development Organization (DRDO) in the last 30 years in the fields of design, materials development and characterization, and airworthiness

certified production of many advanced aerospace, aeronautical and naval materials and components. The extensive research work conducted by him has resulted in the development and certified production of (i) Al and Al-Li alloys for LCA, LCH and Indian Space Programme, (ii) Aero Steels, including Maraging and PH Steels for Indian Missile Programmes, (iii) High strength and high temperature Ti Alloys, including β -Ti alloys for LCA's slat tracks and landing gear, (iv) Advanced Ultrahigh Temperature materials—Mo and Ti Intermetallics, Monolithic Ceramics (Structural Alumina, Graphite and SiC), Carbon, Silica and SiC based Continuous Fibre-reinforced, Ceramic-matrix Composites (CFCCs) for cutting-edge components, systems and technologies. Application of these materials in DRDO has been complemented by him by extensive fundamental research on tensile deformation, fatigue and fracture, correlations between chemical composition-processing-microstructure-texture-deformation, leading to first time scientific explanations on Property Anisotropy. In the last 6 years, Dr. Prasad has been instrumental in the concurrent development and production of several airworthiness certified materials and components of Aero and Naval steels, Al alloys, Ni-base Superalloys, Ti sponge and Special Ti alloys for Indian Defense, Indian Air Force, Indian Navy and ATVP—the Indian Submarine Program, which have resulted in realizing defense hardware worth more than Rs. 12 billion, out of which direct materials production

of nearly Rs. 6.2 Billions through 180 provisional clearances and 11 type approvals of CEMILAC. Dr. Prasad's prolific research resulted over 170 research articles in peer-reviewed national and international journals and conference proceedings, including 30 written/edited books and book chapters as well as 26 classified and unclassified, as also peer-reviewed technical reports and a highly acclaimed first International Monograph on Al-Li Alloys in 2014. He has also authored nearly 90 confidential reports and more than 260 certification documents for DRDO. In recognition of his original contributions in the fields of Metallurgy and Materials Engineering, Dr. Prasad had received several national and international awards. He has been the recipient of YOUNG SCIENTIST AWARD (ICSA, 1991), YOUNG METALLURGIST (Ministry of Steel, 1994), AvH's Humboldt Research Fellowship (1998-99), Max-Planck-Institute (Stuttgart)'s Visiting Scientist (1998-99), Binani Gold Medal (IIM, 2006), METALLURGIST OF THE YEAR (Ministry of Steel, 2010), AICTE-INAE Distinguished Visiting Professorship at Andhra University and Mahatma Gandhi Institute of Technology (INAE, 2012-Till Date), IIT-BHU(MET)'s Distinguished Alumnus Award (2013) and the prestigious Dr. V.M. Ghatge Award of AeSI (in 2014). Dr. Prasad is a Fellow of Institute of Engineers (India) [FIE], Indian Institute of Metals [FIIM] and AP Akademi of Sciences [FAPAS].



Dr. R.J.H. Wanhill is Emeritus Principal Research Scientist at the Netherlands Aerospace Centre, formerly the National Aerospace Laboratory NLR, in the Netherlands. He holds two Doctorates, one from the University of Manchester (1968) and the second from the Delft University of Technology (1994). He joined the NLR in 1970, and since then has investigated fatigue and fracture of all classes of aerospace alloys. He is co-author of the book 'Fracture Mechanics' (1984), which has run into a second edition; co-author with Simon Barter of the monograph 'Fatigue of Beta Processed and Beta Heat-treated

Titanium Alloys', published by Springer in 2012; and co-author and co-editor for the book 'Aluminium - Lithium Alloys: Processing, Properties and Applications', editors N. Eswara Prasad, Amol A. Gokhale and R.J.H. Wanhill, published in 2014. From 1978 to 1996 Dr. Wanhill was head of the Materials Department of the NLR, and in 1979-80 adjunct professor of materials at Delft University of Technology. From 1997 to 2008 he was a Principal Research Scientist in the Aerospace Vehicles Division of the NLR. From 2008 to 2015 he has been emeritus Principal Research Scientist at the NLR. In 2002 the Board of the Foundation NLR awarded Dr. Wanhill the first Dr. ir. B.M. Spee Prize for outstanding contributions on aerospace materials. In October 2014 he was awarded an Honour Diploma by the Netherlands Aerospace Fund for his long-term contributions to scientific research and knowledge at the NLR, and use of this knowledge for aircraft failure analyses. In recent

years Dr. Wanhill has worked on the analysis of fatigue cracking in GLARE panels from the Airbus 380 MegaLiner Barrel test (presented at ICAF 2009) and, in collaboration with Dr. Simon Barter (Defence Science and Technology Group, DSTG, Melbourne). From November 2009 to May 2010 Dr. Wanhill was a Visiting Academic at the DSTG. The work there included (i) a collaborative report, book chapter, and presentation for the Royal Australian Air Force (RAAF) on fatigue life assessment of combat aircraft; (ii) a book chapter on stress corrosion cracking (SCC) in aerospace; (iii) two seminar presentations, on service failures and the MegaLiner Barrel GLARE cracking (see above); and (iv) preparation of a course on failure analysis, held twice at Auckland Technical University at the beginning of May 2010. This course has been adopted by the RAAF as part of its instruction material. Since 1994 Dr. Wanhill has been investigating fracture phenomena in ancient silver and iron, and has published eight peer-reviewed papers on this topic. The most recent papers have been published in the *Journal of Failure Analysis and Prevention* (2011), *Metallography, Microstructure, and Analysis* (2012) and the leading archaeological scientific journal *Studies in Conservation* (2013). Dr. Wanhill also gives annual lectures on ancient silver for a Master's Degree course on conservation at the University of Amsterdam. Dr. Wanhill has been an author and speaker on several fatigue and fracture topics and also on fatigue-based design of aircraft structures. In 2012, Dr. Wanhill was a keynote speaker for the International Conference on Engineering Failure Analysis V, held in The Hague. He also had two additional contributions, with co-authors: "Validation of F-16 wing attachment fitting bolts" and "Five helicopter accidents with evidence of material and/or design deficiencies". All three presentations have been published as papers in *Engineering Failure Analysis* in 2013. In 2014 he was a keynote speaker at *Fatigue 2014*, held in Melbourne. In 2015 he gave a Public Lecture at *Materials Days 2015*, Rostock, with the title "Materials and structural integrity: Milestone aircraft case histories and continuing developments". This presentation has also been adopted by the RAAF as instruction material, and in written chapter form will be published in 'The Reference Module in Materials Science and Engineering'.

Contributors

B. Ashok Aeronautical Development Agency, Bangalore, India

Yutika Badhe Defence Institute of Advanced Technology (DU), DRDO, Ministry of Defence, Girinagar, Pune, India

K.P. Balan DMRL, Hyderabad, India

K. Balasubramanian Defence Institute of Advanced Technology (DU), DRDO, Ministry of Defence, Girinagar, Pune, India

R.G. Baligheid Defence Metallurgical Research Laboratory, Hyderabad, India

S.B. Bhaduri Department of MIME and Surgery, University of Toledo, Toledo, OH, USA

A. Bhattacharjee Materials Processing Division, Titanium Alloy Group, DMRL, Hyderabad, India

C.M. Bhuvanewari Regional Centre for Military Airworthiness (Foundry and Forge), CEMILAC, Bangalore, India

G.V.S. Brahmendra Kumar DMRL, Hyderabad, India

V.P. Deshmukh NMRL, DRDO, Ambarnath, India

N. Eswara Prasad DMSRDE, DRDO, Kanpur, India

Amol A. Gokhale Indian Institute of Technology Bombay, Mumbai, India

G. Gouda CEMILAC, DRDO, Bangalore, India

B. Jana RCMA, Hyderabad, India

P. Jayapal CEMILAC, DRDO, Bangalore, India

Shirish S. Kale Regional Centre for Military Airworthiness (Foundry & Forge), CEMILAC, Bangalore, India

- Anil Kumar** ASL, DRDO, Hyderabad, India
- N. Kumar** Defence Laboratory, Jodhpur, India
- Suresh Kumar** DMSRDE, DRDO, Kanpur, India
- V.V. Kutumbarao** DMRL, Hyderabad, India
- Y.R. Mahajan** Centre for Knowledge Management of Nanoscience and Technology (CKMNT), Secunderabad, AP, India
- Naveen K. Mahenderkar** Department of Materials Science and Engineering, Missouri University of Science and Technology, Rolla, MO, USA
- L.M. Manocha** DMSRDE, DRDO, Kanpur, India
- R. Mitra** IIT-Kharagpur, Kharagpur, India
- Sai Priya Munagala** Department of Materials Science, TU Darmstadt, Darmstadt, Germany
- Ch R.V.S. Nagesh** DMRL, Hyderabad, India
- V. Nimbalkar** NMRL, DRDO, Ambarnath, India
- P.K. Panda** Materials Science Division, CSIR-National Aerospace Laboratories, Kodihalli, Bangalore, India
- T. Ram Prabhu** RCMA (F&F), CEMILAC, Bangalore, India; RCMA (F&F-FOL), CEMILAC, Hyderabad, India
- L. Rama Krishna** International Advanced Research Centre for Powder Metallurgy and New Materials (ARCI), Hyderabad, India
- P. Rambabu** RCMA (Materials), CEMILAC, Hyderabad, India
- D. Srinivasa Rao** International Advanced Research Centre for Powder Metallurgy and New Materials (ARCI), Hyderabad, India
- M. Sai Krishna Rao** RCMA (Materials), CEMILAC, DRDO, Hyderabad, India
- A. Venugopal Reddy** ARCI, Hyderabad, India
- D.B. Anant Sagar** RCMA (Materials), CEMILAC, DRDO, Hyderabad, India
- B. Saha** RCMA (Materials), CEMILAC, DRDO, Hyderabad, India
- V.V. Satya Prasad** Defence Metallurgical Research Laboratory, Hyderabad, India
- D.V.V. Satyanarayana** DMRL, Hyderabad, India
- K. Chandra Shekar** VITS, Hyderabad, India
- K. Shunmugapriya** Regional Centre for Military Airworthiness (Foundry & Forge), CEMILAC, Bangalore, India

Vijaya Singh DMRL, Hyderabad, India

M. Srinivas DMRL, Hyderabad, India

J. Subramanyam DMRL, Hyderabad, India

G. Sundararajan International Advanced Research Centre for Powder Metallurgy and New Materials (ARCI), Hyderabad, India

K. Tamilmani Office of DG (AERO), DARE, DRDO, Bangalore, India

Manoj Tirumali Defence Institute of Advanced Technology (DU), DRDO, Ministry of Defence, Girinagar, Pune, India

S.R. Vadera Defence Laboratory, Jodhpur, India

Srikanth Vedantam IIT-Madras, Chennai, India

R.J.H. Wanhill Emmeloord, Flevoland, The Netherlands

J.C. Williams Department of Materials Science and Engineering, The Ohio State University, Columbus, USA

Part I
Metallic Materials

Chapter 1

Magnesium Alloys

T. Ram Prabhu, Srikanth Vedantam and Vijaya Singh

Abstract This chapter gives an overview of magnesium alloys with the emphasis on aerospace applications. The strengthening mechanisms, physical metallurgy principles, effects of alloying elements, conventional processing techniques, recent advancements in alloy development and processing are briefly discussed in the following sections. The mechanical properties, corrosion behaviour of aerospace castings and wrought alloys are presented and commented upon in detail. Recent trends in corrosion protection techniques and applications in national and international aerospace projects are presented at the end.

Keywords Magnesium · Alloys · Castings · Wrought products · Welding · Mechanical properties · Fatigue · Fracture · Corrosion · Applications

1.1 Introduction

Magnesium is known for its low density ($\rho \sim 1.738 \text{ g/cm}^3$), excellent damping capacity, good electromagnetic shielding, high recycling ability and machinability [1]. The potential weight savings in using magnesium make it highly attractive for aerospace and automobile structural applications.

Pure Mg has limited strength and is usually alloyed to improve the strength, as well as other properties. Mg alloys have the advantages of high strength: density ratios, high damping capacity and machinability compared to aluminium alloys, and

T. Ram Prabhu (✉)
RCMA (F&F), CEMILAC, Bangalore, India
e-mail: t.ramprabhu@cemilac.drdo.in; ramprabhu.t@gmail.com

S. Vedantam
IIT-Madras, Chennai, India
e-mail: srikanth@iitm.ac.in

V. Singh
DMRL, Hyderabad, India
e-mail: director@ceptam.drdo.in; uvsing@gmail.com

the added ability to be cast into intricate shapes. The major disadvantages, considerably mitigated over the past few decades, are poor corrosion resistance, cold formability and microstructural stability at elevated temperatures. In particular, galvanic corrosion is still an important problem.

1.2 Classification and Designation

Although there is no international system to classify Mg alloys, ASTM has developed a coding system [2]. In this system the two major alloying elements are identified with two code letters, followed by a two-digit number indicating the maximum weight percentages of these two alloying elements. The temper designation consists of a letter and one or a few digits added as suffixes to the alloy coding. The letter indicates one of the following conditions: as-fabricated (F), annealed (O), strain hardened (H), tempered (T) and solution heat treated (W). The digit(s) signify the type of heat treatment. The most commonly found digits in the aerospace grades are 4, 5, and 6, applying to the T4, T5 and T6 tempers, which represent solution treated (T4), direct cooling and artificially aged (T5), and solution treated and artificially aged (T6).

The most commonly used alloying elements in the aerospace grade Mg alloys are zinc, zirconium, aluminium, rare earth elements (RE), manganese, silver, silicon, thorium, copper, lithium and yttrium. These elements are coded as Z, K, A, E, M, Q, S, H, C, L and W respectively. Excepting Zr and Mn, which form peritectic alloy systems, the other elements form binary eutectic alloy systems [2].

1.3 Physical Metallurgy of Mg Alloys

Magnesium has a hexagonal-close-packed (hcp) crystal structure ($c/a = 1.623$, very close to the ideal hcp which has $c/a = 1.6333$). The hcp structure is retained up to the melting point at 650 °C. The metal is highly reactive and ignites and burns in an oxygen atmosphere, and can also be ignited in air.

Mg is readily alloyed with many elements to improve its mechanical and corrosion properties. In particular, additions of REs, Ag, Th, Li and Y make magnesium alloys amenable to precipitation hardening. However, the hcp structure limits the room temperature formability of Mg alloys.

1.3.1 Role of Different Alloying Elements

1.3.1.1 Zinc (Zn)

Zn is an effective solid solution strengthener in Mg alloys. Zn also negates the detrimental effects of Fe or Ni impurities on the corrosion resistance of Mg alloys. Zn is frequently added to Mg-RE-Zr or Mg-Th-Zr alloys to improve the age-hardening characteristics. Addition of Cu to Mg-Zn improves the strength and ductility of the alloy by increasing the eutectic temperature and changing the morphology of the eutectic phase from divorced to lamellar, both allowing better homogenization of the alloy during solution treatment.

1.3.1.2 Zirconium (Zr)

Zr is a very strong grain refiner in Mg alloys containing RE/Ag/Th combinations and Zn, although its maximum solubility at room temperature is less than 0.28 wt%. The effectiveness of Zr as a strong grain refiner in Mg is due to three requirements which it meets. First, there is a close match of the lattice parameters of α -Zr ($a = 0.323$ nm, $c = 0.514$ nm) and Mg ($a = 0.32$ nm, $c = 0.52$ nm). Second, a peritectic reaction occurs between Mg and the Zr-rich phase precipitating at 654 °C from the liquid containing 0.5 wt% Zr. Third, the growth restriction factor for Zr is highest amongst the elements which enhance grain refinement in Mg.

Enhanced grain refinement necessitates that Zr additions be more than 0.5 wt%, i.e. the maximum solubility of Zr in Mg at 654 °C. However, grain refinement in Mg has been observed with Zr additions below the solubility limit. This discrepancy has been attributed to the direct participation of fine, 0.5–2 μ m, faceted Zr particles (present in the grain refiners) to the nucleation process and resultant grain refinement.

Zr loses its grain refining ability in Mg alloys containing any one of the elements Al, Fe, Si, C and gases O₂, H₂, N₂, because it forms intermetallics with them. This significantly reduces the Zr in solid solution, making it unavailable for grain refinement.

1.3.1.3 Aluminium (Al)

Al in Mg alloys improves the strength and ductility by solid solution strengthening. The addition of 6 wt% Al provides the optimum strength and ductility. With Al being the primary alloying element, up to 10 wt% Al is used in both wrought and cast Mg alloys. Higher Al in Mg results in more eutectic phase, thus improving the castability of the alloy. The maximum solid solubility of Al in Mg is 12.7 wt% at 437 °C, reducing to 3 wt% at 93 °C. The decreasing solubility with decreasing temperature makes Mg-Al alloys age-hardenable.

1.3.1.4 Rare Earth (RE) Elements (Nd, Ce, La, Gd, Pr)

Rare earths are added to Mg alloys in the form of mischmetal (50 wt% Ce + 50 wt% (La + Nd)) or didymium (80–85 wt% Nd + 15–20 wt% Pr). These elements are the principle alloying elements in creep-resistant sand-casting alloys. The REs improve the creep strength of Mg alloys by forming stable grain boundary eutectics that pin the grain boundaries and restrict grain boundary sliding. Additions of REs also narrow the solidification range, and this helps in minimizing the micro-shrinkage porosities in castings, and cracking during welding.

1.3.1.5 Manganese (Mn)

Mn does not strengthen Mg alloys, but it is an effective scavenger in combining with detrimental heavy elements (e.g. Fe) to form harmless intermetallics in Mg–Al and Mg–Al–Zn alloys. Recent studies on Mg–Sc alloys have shown that Mn significantly improves the creep resistance by forming Mn_2Sc and other Mn_xSc_y phases [3].

1.3.1.6 Silver (Ag)

The addition of Ag improves the age-hardening characteristics of Mg alloys.

1.3.1.7 Silicon (Si)

Si helps in improving the fluidity of Mg alloys. Hence casting alloys invariably contain some Si.

1.3.1.8 Thorium (Th)

The maximum solubility of Th in Mg is 5 wt% at 582 °C. Thorium is one of the important alloying elements benefiting the creep strength, which is improved up to about 350 °C by the formation of $Mg_{23}Th_6$ precipitates. Also, the combination of Th and Zn in Mg alloys significantly improves the weldability. However, since Th is radioactive, its presence (about 2 wt%) in Mg alloys also makes them radioactive. This makes the processing and handling of the alloys more complex and costly.

1.3.1.9 Transition Elements (Copper (Cu), Iron (Fe), Nickel (Ni), Cobalt (Co))

Transition elements, even in trace amounts, are harmful in that they significantly reduce the corrosion resistance of Mg alloys. The maximum tolerance limits of Cu, Fe and Ni in Mg alloys are 0.05 wt% Cu and 0.005 wt% each of Fe and Ni.

1.3.1.10 Lithium (Li)

Li has a maximum solubility in Mg of 5.5 wt% at 588 °C. Alloying of Mg with Li improves the formability of wrought alloys besides reducing the density. Also, it helps in minimizing the difference between the tensile and compressive yield strengths of Mg alloys [4]. However, although Mg–Li alloys respond to age-hardening, they overage at about 60 °C, restricting Li's usefulness in this respect.

1.3.1.11 Yttrium (Y)

Y is another high-temperature-strengthening element in Mg alloys. Y is usually found with other RE elements in creep-resistant Mg alloys, e.g. the WE43 and WE53 grades, which have good creep strength up to about 300 °C.

1.3.1.12 Beryllium (Be)

Be has very limited solubility (0.001 wt%) in Mg. The beneficial effect of Be is that it reduces the tendency for surface oxidation of liquid Mg. However, the use of Be in Mg sand-casting alloys is usually not recommended because of the adverse effect of grain coarsening.

1.3.1.13 Calcium (Ca)

Similar to Be, Ca also helps in reducing the surface oxidation of liquid Mg. Also, Ca additions, particularly in wrought alloys, improve the sheet rolling and creep properties [5, 6]. However, Ca additions are restricted to below about 0.3 wt% to avoid cracking during post-forming processes such as welding.

1.3.2 Precipitation Reactions in Mg Alloys

The sequence of precipitation reactions for Mg alloys is as follows [2]:

Mg–Al alloys: SSSS (supersaturated solid solution) \rightarrow Mg₁₇Al₁₂ (incoherent equilibrium precipitates). This reaction does not improve the strength properties.

Mg–Zn alloys: SSSS \rightarrow coherent GP zones \rightarrow intermediate coherent (rod shape, hcp) and semi-coherent precipitates (disc shape, hcp) \rightarrow MgZn₂ (incoherent equilibrium precipitates, trigonal).

Mg–RE (Nd) alloys: SSSS \rightarrow coherent GP zones \rightarrow Mg₃Nd (hcp, fcc) (plate-like intermediate precipitates) \rightarrow Mg₁₂Nd (incoherent equilibrium precipitates, body-centred tetragonal, bct).

- The addition of Y to Mg–RE alloys changes the precipitate composition and structures. The sequence of the precipitation reaction is SSSS \rightarrow Mg₁₂NdY (coherent DO₁₉ superlattice hcp plates) \rightarrow Mg₁₂NdY (semi-coherent body-centred orthorhombic plates) \rightarrow Mg₁₁NdY₂ (incoherent).
- The addition of Ag to Mg–RE alloys gives two different precipitation reactions: (1) SSSS \rightarrow GP zones (rod, coherent) \rightarrow γ (hcp, plates), (2) SSSS \rightarrow GP zones (ellipsoidal, coherent) \rightarrow β (hcp equiaxed, semi-coherent) \rightarrow Mg₁₂Nd₂Ag (hcp laths, incoherent).

Mg–Th alloys: SSSS \rightarrow coherent GP zones \rightarrow β'' , Mg₃Th (hcp, intermediate semi-coherent rod shape precipitates) \rightarrow β , Mg₂₃Th₆ (fcc, incoherent equilibrium precipitates). In some cases it is also observed that intermediate semi-coherent Mg₂Th precipitates form before the equilibrium β . These are of two types: β'_1 (hcp) and β'_2 (fcc).

1.3.3 Strengthening in Mg Alloys

Mg alloys are strengthened by one or more of the following mechanisms: (1) solid solution strengthening, (2) grain refinement, (3) precipitation hardening and (4) work hardening. Most of the alloying elements contribute to solid solution strengthening of Mg alloys. Zr is the primary grain refiner in Mg alloys. Alloying with REs, Ag, Th, Al and Y makes Mg alloys *usefully* precipitation-hardenable. However, strengthening by work hardening during processing is usually not practiced because of the limited ductility of Mg alloys.

1.4 Aerospace Mg Alloys

Table 1.1 presents the compositions and physical and mechanical property data for some typical aerospace Mg alloys.

Table 1.1 Composition (in wt%) and mechanical properties of aerospace Mg alloys [7–14]

Alloys	Form and condition	Al	Zn	Mn	Zr	RE	Ag	Y	Th	Li	PS (MPa)	TS (MPa)	% EI	Fatigue strength (MPa) unnotched	Density	Young's modulus (GPa)	Fracture toughness, K_{Ic} (MPa \sqrt{m})	
<i>Alloys containing aluminium</i>																		
Elektron A8/BS 2L 122/GA 9/ML 5/3.5812/qq-M-56B	ST	8	0.5	0.3	–	–	–	–	–	–	100	230	6	75–90	1.81	–	–	
AZ 91C/BS 3L 125/GA 9Z1/ML 6/AMS 4437/3.5194/Air 3380 G-A9Z1	SC (T6)	8.7–9.5	0.5–0.7	0.1–0.3	–	–	–	–	–	–	195	275	6	80–95	1.81	45	11.43	
AZ80A/ASTM B91/QQ-M-40B/AMS 4360/3.5812/Air 9052 G-A7Z1	W (T5) Forgings	8.5	0.5	0.12	–	–	–	–	–	–	250	345	6	–	1.806	45	16.21	
ZM21	W (T6)	–	–	2	1	–	–	–	–	–	125	200	9	–	–	44	–	
<i>Alloys containing zirconium</i>																		
ZK 51A/BS 2L 127/Z 5Z/ML 12	T5	–	4.6	–	0.5	–	–	–	–	–	205	140	3.5	–	1.83	–	–	
ZE41A/BS 2L128/RZ05/ML 15/ASTM B80/AMS 4439/3.6104/	SC (T6)	–	4.2	–	–	1.2	–	–	–	–	145	210	3	90–105	1.84	45	15.49	
EZ33A/BS 2L126/ZR E1/ML 11	SC (T5)	–	2.7	–	0.6	3.3	–	–	–	–	110	160	2	–	1.8	44.8	–	
QE22A/DTD 5035/MSRB/AMS 4418/3.5164	SC (T6)	–	–	–	0.7	2.2 (ND)	2.5	–	–	–	195	260	3	100–110	1.82	45	13.18	

(continued)

Table 1.1 (continued)

Alloys	Form and condition	Al	Zn	Mn	Zr	RE	Ag	Y	Th	Li	PS (MPa)	TS (MPa)	% EI	Fatigue strength (MPa) unnotched	Density	Young's modulus (GPa)	Fracture toughness, K_{Ic} (MPa \sqrt{m})
WE54/ASTM B80/AMS 4426	SC/CC (T6)	-	-	-	0.5	3.5 (Nd)	5.25	-	-	-	185	255	2	95-100	1.85	-	11.43
	W (T6)	-	-	-	-	-	-	-	-	-	165	310	6	-	-	-	-
WE43/ASTM B80/AMS 4427	SC/CC (T6)	-	-	-	0.5	3 (Nd)	4	-	-	-	172	220	2	85	1.84	44.2	-
	W (T6)	-	-	-	-	-	-	-	-	-	155	285	6	-	-	-	-
Electron 21/AMS 4429	SC (T6)	-	0.3	-	0.6	2.7 (Nd), 1.3 (Gd)	-	-	-	-	145	248	2	115-120	1.82	-	-
	-	1.5	-	-	-	-	-	-	-	11-13	160	170	-	40	1.4	42	-
LA141A	-	0.75-1.75	-	-	-	-	-	-	-	13-15	137	154	10	-	1.35	42	-
	-	0.5-0.8	-	-	-	-	-	-	-	13-15	110	136	23	-	1.33	41	-
ZK600/AMS 4362	W (T5)	-	5.1-6	-	0.4-0.6	-	-	-	-	-	285	350	11	-	1.83	45	-
	Extrusions	-	-	-	-	-	-	-	-	-	-	-	-	-	-	-	-

SC Sand Cast, CC Chill Cast, W Wrought (measured in the direction of grain flow), ST Solution Treated, T5 Cooled from elevated temperature shaping process + artificially aged, T6 Solution treated + artificially aged; fatigue strength is based on a life of 5×10^7 cycles in rotating beam bend tests

1.4.1 Casting Alloys

Sand-permanent mould and die-casting processes are widely used for manufacturing intricate Mg alloy parts for aerospace applications. In fact, 90 % of Mg alloy components used in lightweight structural applications are made from casting alloys [15].

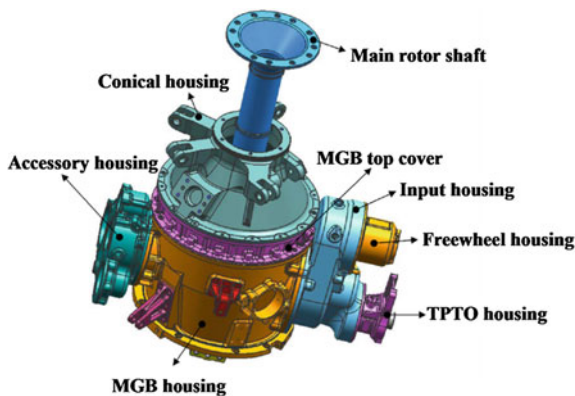
Most aerospace grade Mg alloy castings are thin-walled, geometrically complex castings with close dimensional tolerances. A typical example is the main gear box assembly (eight magnesium alloy castings, of which six are shown) in Fig. 1.1.

Sand castings are the preferred processing technique for complex castings with a minimum wall thickness of 4 mm. Die castings are mostly used for high volume production, small size and simple shape parts with a minimum wall thickness of 2 mm.

The high reactivity of liquid Mg with oxygen represents a fire hazard when melting and casting Mg alloys. Hence the melting of Mg alloys should be carried out with adequate precautions such as an inert gas atmosphere, dusting with sulphur and fluxes. Another problem is the low volumetric heat capacity of Mg castings. This requires faster mould filling, which gives the associated problems of turbulence and dross formation. Low density of magnesium necessitates larger risers to produce required hydrostatic pressure for feeding. In turn, these problems require an optimized gating system with many ingates and risers. These requirements severely affect the casting yields and increase the costs of the castings.

Cast Mg–Al alloys (AZ grades): These are seldom used for aerospace applications because of their poor creep strength above 100 °C [16]. This is due to the poor thermal stability of $Mg_{17}Al_{12}$ precipitates, self-diffusion of Mg, accelerated diffusion of Al in Mg at elevated temperatures, grain boundary sliding and diffusion-controlled dislocation climb [17–20]. Also, variable grain sizes in castings having thin and thick sections result in inconsistent properties. Another important problem in Mg–Al alloy castings is microporosity due to high solidification shrinkage (~5 %), which spoils the pressure tightness and toughness of the castings [19].

Fig. 1.1 Cast magnesium alloy main transmission gear box (MTGB) assembly for a helicopter. The gear box assembly has eight components: main gear box (MGB) housing, input housing, tail power take off (TPTO) housing, MGB top cover, freewheel housing, accessory housing, tail gear box housing and oil tank. (Courtesy HAL (F&F), India.)



Cast Mg-RE-Zn-Zr, Mg-Y-RE-Zn-Zr, Mg-Y-RE-Zr, Mg-RE-Zr grade alloys: These are more popular for aerospace applications because of their excellent creep strength up to 300 °C [21–24]. The grain refining effects of Zr and the grain boundary eutectic formed by REs eliminate the microporosity and reduce the variability in properties.

Neodymium (Nd) and Gadolinium (Gd) are the preferred REs. They significantly improve alloy castability when used in combination up to their solubility limits. Beyond these limits they form excess grain boundary eutectic, particularly in Nd-based alloys, and this impairs the short- and long-term properties [19].

The casting of these alloys by pressure die casting is not advisable because of the high cooling rate. This does not provide enough time for continuous grain boundary precipitation of Mg-RE compounds [25].

Since the 1970s magnesium foundries have been shifting to the use of SF₆ gas cover for very effective melt protection: this gas is nontoxic, nonflammable and noncorrosive. SF₆ has been used in dilution with other gases like CO₂, Ar, N₂ or air. These gas covers avoid the fire hazard due to oxidation, flux inclusion defects, and also improve the casting yields. However, SF₆ is a very potent and persistent greenhouse gas. This has led to worldwide research on alternative protection technologies.

1.4.2 Wrought Alloys

Wrought Mg alloys have high potential in *some* aerospace applications owing to excellent static and dynamic properties and pressure tightness in comparison to Mg casting alloys. Sheets and extruded shapes (bars, tubes and rods) are the main wrought products.

The cold deformability of Mg alloys is limited because of the lack of active slip or twin systems: basal plane slip {0001} <1120> and pyramidal plane twin systems {1012} <1011> are active up to 225 °C [24].

Sheet alloys: AZ-class alloys are used for sheet products and are usually formed above 200 °C at a low strain rate, typically less than 0.02 s⁻¹ [26]. Above 200 °C the flow stress is significantly reduced owing to dynamic recovery and activation of many slip systems, resulting in better sheet formability.

Forgings and extrusions: Mg alloys are forged at elevated temperatures in hydraulic presses. Even so, the high thermal conductivity of Mg results in quicker heat loss from the work piece, and this makes forging difficult. Thus precise temperature control of tools and the work piece is essential.

ZK, WE and ZM grade alloys are preferred to AZ grades for forgings and extrusions because of better hot formability. Aerospace grade Mg alloy forgings are usually produced by isothermal multi-axial forging or with tools and dies heated above 200 °C in order to avoid the heat loss. It is important to note that the forging

temperature should not be too high, since this can cause hot cracking owing to low melting point eutectics, and/or abnormal grain growth.

Mg forgings tend to show strong anisotropic behaviour, with higher tensile properties in the grain flow direction. Hence multi-axial forging is usually practiced in order to achieve isotropic properties. In this process the material is forged equally in all three directions.

Extrusion of Mg alloys is usually carried out using the direct extrusion process without lubricants [27]. The extrusion speed depends on the types and amounts of alloying elements: the extrusion speed decreases sharply with increasing amounts of alloying elements.

1.4.3 *Welding and Machining*

Gas welding of Mg alloys is not recommended because the joints have poor mechanical properties and corrosion resistance. Welding of cast or wrought Mg alloys is readily done by gas tungsten arc welding or gas metal arc welding.

Electron beam or laser beam welding enable higher welding speeds, thinner heat affected zones, less part distortion and superior weld joint quality with an efficiency of more than 90 %. However, the higher costs of these welding processes limits their use to specialized applications in the aerospace industries.

Dissimilar Mg alloys are welded using friction welding because (i) no liquid phase is involved, avoiding the formation of intermetallic phases or pores, (ii) the joining temperature is low and (iii) there are no filler rods or inert gas requirements [24].

Welding of Mg–Al alloys requires post-weld stress relief annealing in order to avoid stress corrosion cracking (SCC). Other types of Mg alloys (ZK, EZ, WE, Elektron grades) do not require post-weld annealing since they are not prone to SCC.

Machining (sawing, reaming, boring, milling, turning, drilling) of Mg alloys is very easy, since the chips are short, discontinuous and easily breakable. Therefore the cutting speed can be set high enough to finish the job quickly, resulting in low specific cutting power and an excellent surface finish.

1.4.4 *Recent Advancements in Mg Alloys*

Ultralight alloys: Lithium is an important alloying element for Mg alloys for two main reasons: (i) Li ($\rho \sim 0.534$ g/cc) is lighter than Mg ($\rho \sim 1.74$ g/cc); (ii) Li changes the crystal structure of Mg from hcp (α phase) to bcc (β phase) with just 10 wt% Li addition, and this enhances the formability of Mg–Li alloys. The decrease in density is favourable for lightweight structures.

These alloys have nearly the same elastic moduli as conventional Mg alloys. The ultralight characteristics of these alloys (75 % of the density of conventional Mg alloys) result in *specific* bending stiffnesses nearly twice that of conventional Al

alloys, and five times that of conventional Mg alloys [2]. The low density of Mg–Li alloys also provides excellent compression buckling resistance.

Mg–Li alloys are age-hardenable and usually supplied in the T7 (solution treated and stabilized) condition. The stabilization treatment is beneficial to the SCC resistance. Figure 1.2 gives a typical example of the microstructure of an Mg–10.7 wt% Li alloy showing β -MgLi (bcc) matrix grains.

Equal channel angular extrusion (ECAE): ECAE is an advanced forming technique in which fine-grained alloys are developed via severe plastic deformation. Fairly recently it has been reported that ECAE results in fine-grained Mg alloys with significantly improved room temperature formability [29–31].

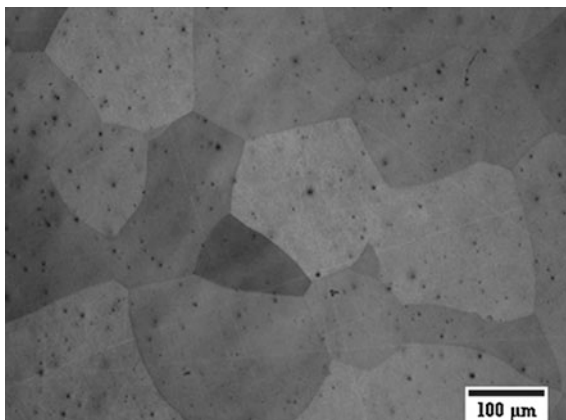
For example, ECAE-processed AZ31 and ZK60 alloys showed ductilities greater than 20 %. This improvement is due to dislocation cross-slip from basal to non-basal planes, dynamic recovery in both twinned and untwinned regions, and grain boundary sliding at room temperature [32].

The fine grain structure also makes ECAE Mg alloys amenable to superplastic forming. For instance, an ECAE-processed two-phase ($\alpha + \beta$) Mg–Li–Zn alloy exhibits high strain rate ($1 \times 10^{-3} \text{ s}^{-1}$) superplasticity with 391 % elongation at 150 °C [33]. And extrusion prior to ECAE improves the superplasticity by further grain refinement [34].

Rapid solidification and powder metallurgy processes (RS/PM): Currently, melt-spinning, gas sputtering and spray-forming are the main industrial RS technologies. In melt-spinning the molten metal drops are rapidly solidified by impacting on rotating water-cooled metal surfaces. In gas sputtering techniques the melt is sputtered with an inert gas at high velocities, resulting in rapid cooling of molten metal drops at high rates of the order of 10^6 K/s . On the other hand, in spray-forming the liquid droplets are atomized by spraying the molten metal through a nozzle in the presence of fast flowing inert gas (Ar). These droplets rapidly solidify when depositing on the substrate.

The extremely high RS cooling rates (10^5 – 10^6 K/s) can produce very fine grained (300 nm–1 μm) microstructures without macrosegregation. Also, the alloy

Fig. 1.2 Microstructure of Mg–Li alloy containing 10.7 wt% Li: grains of β -MgLi matrix (bcc), 25X. Section etched in 4 % HNO_3 and viewed with polarized light [28]



matrix becomes supersaturated with solutes and forms metastable and quasi-crystalline phases that improve the strength and ductility by solid solution strengthening and grain boundary strengthening. Another benefit is a significant improvement in corrosion resistance owing to more uniform dispersions of cathodic precipitate particles and extension of the solid solubility of the metallic elements that shifts the electrode potential to more noble metal regions [35].

Nanocrystalline powders produced by RS are used to make pellets which are subsequently extruded into bars. Since the pellets have nano-size grains, the extruded bars largely retain the same microstructure, resulting in much improved strengths. For instance, a nanocrystalline Mg-1 mol% Zn- 2 mol% Y alloy developed via the RS/PM extrusion technique had a yield strength of about 600 MPa (with 5 % ductility), compared to a yield strength of 250 MPa in a conventionally processed alloy [36, 37].

Alloys processed by RS have poor creep properties due to the coordinated grain boundary sliding of very fine grains. However, a benefit of the fine grain size is that they exhibit superplasticity at temperatures as low as 150° C. For example, the RS AZ91 alloy shows a superplastic strain of 1480 % when formed at a temperature and strain rate of 300 °C and $6.6 \times 10^{-3} \text{ s}^{-1}$ respectively. This is 7.4 times the forming strain of conventional cast and extruded AZ 91 alloy (200 %). The creep strength of this RS-processed alloy can be improved by adding Ca, which results in thermally stable Al_2Ca precipitates that pin the grain boundaries and hinder grain boundary sliding [38].

1.5 Mechanical Properties

1.5.1 Tensile Properties

The variations of yield and tensile properties of Mg alloys with temperature are presented in Figs. 1.3 and 1.4 respectively. These data are discussed with respect to alloy types in the next paragraphs.

Mg-Al alloys: Wrought alloys (AZ80A) possess higher tensile properties than the cast alloys (AZ91C). However, both alloys are unstable above 100 °C, and this is attributed to the softening of $\text{Mg}_{17}\text{Al}_{12}$ precipitates and activation of grain boundary sliding.

Mg-RE-Zn-Zr alloys: Cast alloys (EZ33A and ZE41A) have stable tensile properties up to 150 °C. This improvement over the AZ-class alloys is due to continuous networks of grain boundary eutectic Mg-R precipitates, the grain refining effects of Zr, and solid solution strengthening by the RE additions.

Mg-Zn-Zr alloys: For ZK51A (cast alloy) and ZK60A (wrought alloy) the room temperature strength is improved by solid solution strengthening (Zn) and grain refinement (Zr). However, grain boundary sliding and micro-shrinkages reduce the tensile properties dramatically with increasing temperature.

Fig. 1.3 Effects of temperature on the yield strengths of Mg alloys. (The superscripts (@ and \$) indicate wrought and cast alloys respectively.)

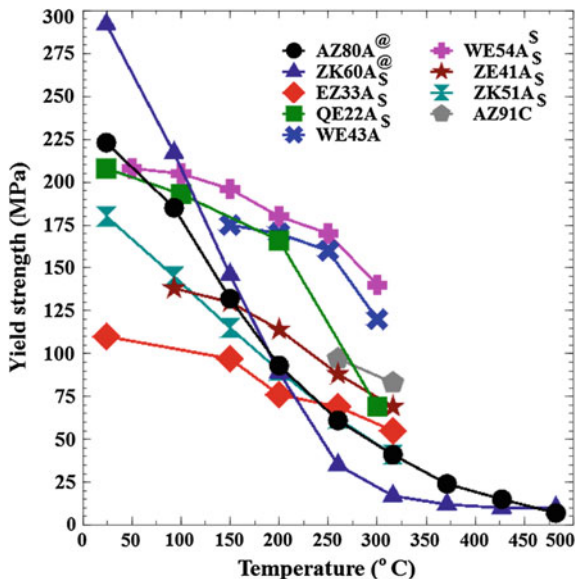
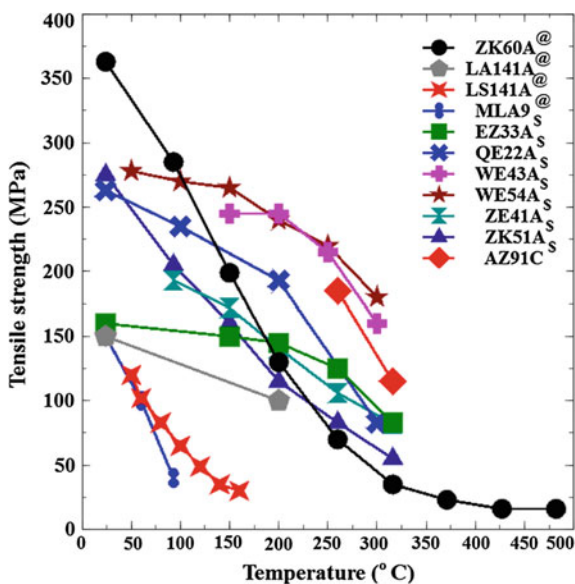


Fig. 1.4 Effects of temperature on the tensile strengths of Mg alloys. (The superscripts (@ and \$) indicate wrought and cast alloys respectively.)



Mg–Y–RE and Mg–Ag–RE alloys: Improved room and elevated temperature properties, up to 250 °C, are obtained from several sources. In both classes improvements are due to excellent solid solution strengthening (Y, Ag and REs) and less microporosity. Also, grain boundary sliding and dislocation-induced creep in Mg–Y–RE cast alloys (WE43A and WE54A) and Mg–Ag–RE cast alloys

(QE22A) are hindered by coherent fine plate precipitates (β' in Mg–Y–RE alloys; $\beta + \gamma$ in Mg–Ag–RE. alloys).

These alloys are widely used in aerospace applications up to 250 °C. Figures 1.3 and 1.4 show that WE54 has slightly better elevated temperature properties than WE43.

Mg–Li alloys: The ultralight wrought alloys LA141A, LS141A and MLA9 have moderate tensile strengths at room temperature, but lose strength dramatically at elevated temperatures because the strengthening metastable θ' precipitates transform to equilibrium θ . These alloys become unstable above 60 °C, restricting their use to secondary and noncritical applications at ambient temperatures.

1.5.2 Fatigue and Fracture Resistance

Fatigue: Fatigue data for Mg alloys in the literature are very limited. Figures 1.5 and 1.6 present a compilation of S–N curves obtained from rotating bending fatigue tests on smooth ($K_t = 1$) and notched ($K_t = 2$) specimens tested under reversed stressing, i.e. with a stress ratio $R = -1$.

Unlike steels, Mg alloys do not have a well-defined endurance limit. Also, the fatigue properties are influenced by many factors, including microporosity, precipitate size and coherency, grain size and crystallographic texture.

Microporosity in Mg–Al cast alloys (AZ91C) causes poor high cycle fatigue strength. The micropores in preferentially oriented grains enable slip-induced

Fig. 1.5 Fatigue S–N curves for unnotched ($K_t = 1$) specimens of Mg alloys at a stress ratio of $R = -1$. (The superscripts (@ and \$) indicate wrought and cast alloys respectively.)

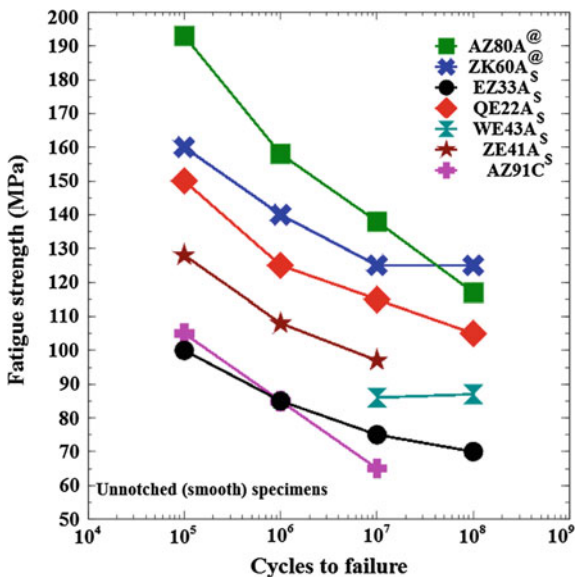
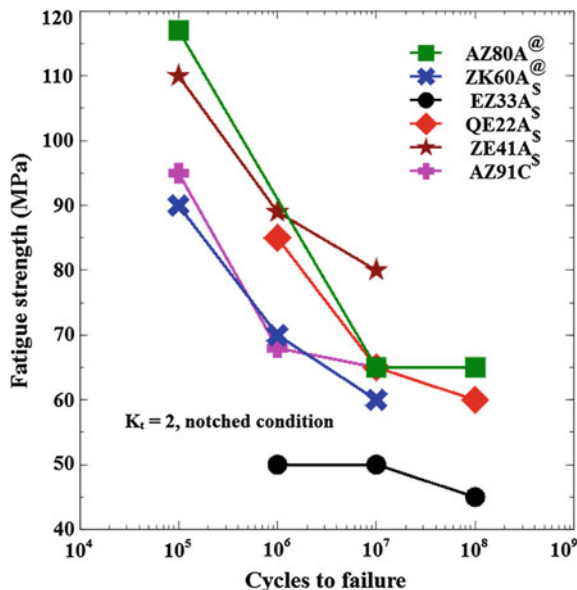


Fig. 1.6 Fatigue S-N curves for notched ($K_t = 2$) specimens of Mg alloys at a stress ratio of $R = -1$. (The superscripts (@ and \$) indicate wrought and cast alloys respectively.)



fatigue nucleation [39]. Fatigue cracks grow initially in a quasi-cleavage manner, due to the hcp crystal structure. The crack path later becomes non-crystallographically transgranular or intergranular, depending on the microstructure and environment.

Comparison of the fatigue limits of Mg alloys in Figs. 1.5 and 1.6 shows that they are highly notch sensitive. Therefore it is advisable to use cast or wrought parts in a machined condition, with added surface rolling or shot peening to generate surface residual compressive stresses and enhance the fatigue life.

Fracture toughness: Available fracture toughness data for Mg alloys are presented in Table 1.1. In the peak strength T6 conditions both wrought and cast alloys have K_{Ic} values between 11 and 16 $\text{MPa}\sqrt{\text{m}}$. These values are low in comparison to those for Al alloys and steels, and are attributed to a lack of ductility owing to the hcp crystal structure.

The low fracture toughness of Mg alloys makes them generally unsuitable for primary load-bearing structures in aerospace applications.

1.5.3 Creep and Oxidation Properties

Pure Mg creeps already at 80 °C. Three fundamental mechanisms (diffusion creep, dislocation creep and grain boundary sliding) are responsible for creep in metals and alloys. To reduce the creep rate, Mg alloys are usually strengthened by solid solution and precipitation strengthening. Solid solution strengthening reduces the

dislocation mobility and interdiffusion coefficient, and lowers the stacking fault energy and stabilizes stacking faults, thereby restricting dislocation creep, diffusion creep and grain boundary sliding. Intragranular and intergranular precipitation provide other ways of restricting dislocation motion and grain boundary sliding. To maximize the creep resistance the precipitates should be very fine, dense, strong and thermally stable; coherent with low interfacial energy and less diffusive into the matrix; and continuous if intergranular.

Figures 1.7 and 1.8 present compilations of available applied stress versus temperature data for Mg alloys tested for 1000 h to creep strains of 0.2 % and 0.5 %, respectively. These data are discussed with respect to alloy types in the next paragraphs.

Mg–Al alloys: In Mg–Al (AZ-class) alloys an increasing Al content increases the amount of interdendritic $Mg_{12}Al_{17}$ grain boundary precipitates. These non-coherent, equilibrium and low melting point (437 °C) precipitates soften and coarsen above 110 °C, reducing the resistance to thermally activated dislocation motion and grain boundary sliding. These effects result in significantly lower strength as well as creep properties [40]. For example, the AZ91 (cast) and AZ80A (wrought) alloys undergo creep strains of 1.2 and 0.5 %, respectively, at stresses of 45–50 MPa and a temperature of 150 °C. These poor creep properties are attributed to diffusion-controlled dislocation climb and grain boundary sliding [41].

Si is preferably added to improve the creep resistance because it replaces the $Mg_{17}Al_{12}$ precipitates with thermally stable Mg_2Si precipitates. Si also aids retention of Al in the Mg matrix, which helps in improving the strength by solid solution strengthening.

Fig. 1.7 Applied stress versus temperature plot for Mg alloys undergoing creep up to 0.2 % strain at 1000 h. (The superscripts (@ and \$) indicate wrought and cast alloys respectively.)

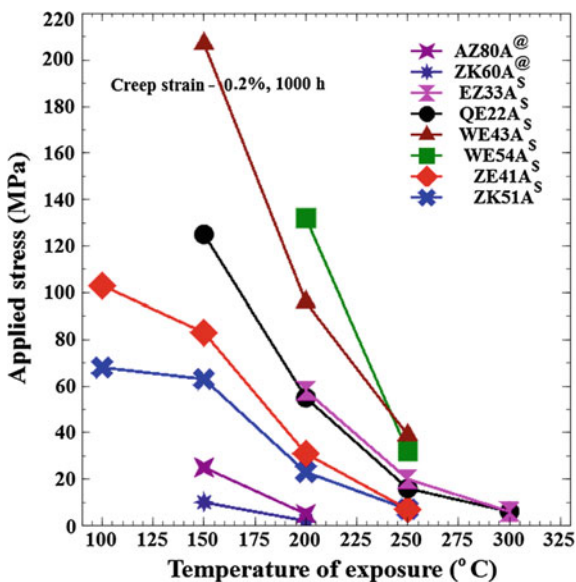
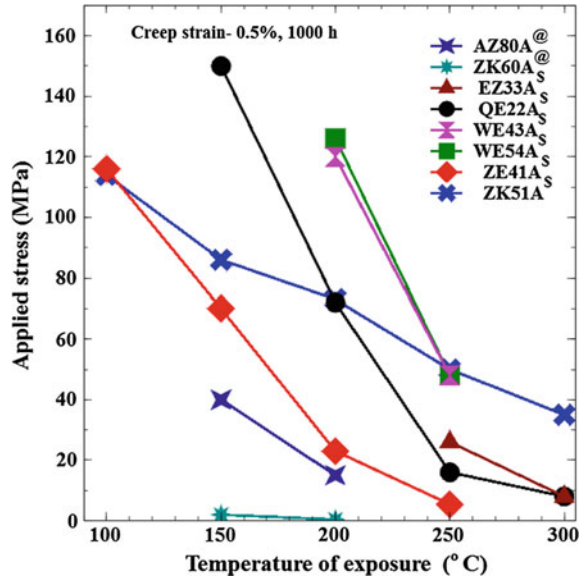


Fig. 1.8 Applied stress versus temperature plot for Mg alloys undergoing creep up to 0.5 % strain at 1000 h. (The superscripts (@ and \$) indicate wrought and cast alloys respectively.)



It is also reported that the addition of Sb and/or Bi helps in forming thermally stable precipitates such as Mg_3Bi_2 and Mg_3Sb_2 , which decrease the steady state creep rate to one order of magnitude less than that of Mg–Al alloys [40].

Mg–Zn alloys: These ZK-class alloys possess poor creep properties because the Mg_2Zn_3 precipitates do not help in strengthening or minimizing dislocation creep and grain boundary sliding. Minor additions of Ca are reported to form new precipitate phases ($Ca_2Mg_6Zn_3$, Mg_2Ca) that aid in improving creep properties [40].

Mg–RE–Zn–Zr (EZ) alloys: The addition of REs results in coherent and thermally stable precipitates with low diffusion coefficients, both inside the grains and along the grain boundaries. These precipitates enhance both the elevated temperature strength and creep strength. For instance, EZ33A (cast alloy) shows a 1000 h creep strain of 0.2 % for an applied stress of 70 MPa and a temperature of 200 °C.

Mg–Y (WE) alloys: Y improves the creep strength by serving as an effective solid solution hardener. Addition of a third element (Zn or an RE) to the binary alloy is beneficial because it increases the volume fraction of precipitates by reducing the solubility of Y in the Mg matrix. Comparison of the data for cast alloys WE43 and WE54 in Figs. 1.7 and 1.8 shows that the latter has better creep strength over the temperature ranges of the tests.

1.5.4 Corrosion Behaviour

1.5.4.1 General Corrosion

Mg oxidizes easily in normal air. However, the rate of oxidation is less than that of mild steel. Although Mg and its alloys form a thin oxide film in moist air, it leaves the surface unprotected because of its nonuniform, imperfect and porous structure [42]. Chlorides, sulphides and carbonates attack the unprotected Mg alloy by damaging the $\text{Mg}(\text{OH})_2$ passivating layer and causing pitting corrosion.

Alloying elements such as REs, Y, Zr and Th improve the salt water corrosion resistance of Mg alloys. Comparison of the corrosion rates of Mg–Y–RE (WE43, WE54) and Mg–RE (Elektron 21) alloys tested in 3.5 % aqueous NaCl at room temperature showed that the combination of Y and RE elements (WE43, WE54) is better than using only an RE (Elektron 21) [43].

1.5.4.2 Galvanic Corrosion

Mg (standard potential = -2.37 V) is situated near the top of the anodic region of the EMF series. Therefore, in the presence of an electrolyte Mg corrodes preferentially when in contact with most other conductive materials. Furthermore, even trace amounts of impurities such as Fe, Ni and Cu severely degrade the corrosion resistance. Hence it is recommended to keep these impurities as low as possible.

Galvanic corrosion is also facilitated by second phases, such as precipitates, that are cathodic to the Mg matrix. Fortunately, the cathodic nature of grain boundaries with respect to the grain interiors prevents intergranular attack.

Surface contamination by ferrous abrasives during shot blasting significantly enhances the corrosion rate of Mg alloys [44]. Acid pickling ($\text{H}_2\text{SO}_4/\text{HNO}_3/\text{CrO}_3$) or fluoride anodizing are generally used to remove the surface contaminants. Alternatively, glass beads or high purity alumina shot are used to avoid contamination.

In the aerospace industries Mg alloy components are usually protected by the process of degreasing, fluoride anodizing, chromate coating, and surface sealing with a polymer resin before finishing with primer painting.

1.5.4.3 Stress Corrosion Cracking (SCC)

Pure Mg is immune to stress corrosion cracking in air and aqueous environments even when loaded up to the yield strength [2]. On the other hand, the SCC resistances of Mg alloys can be categorized as follows:

- Mg alloys without Al or Zn (e.g. QE22, WE54, and WE43) have excellent SCC resistance.

- Mg alloys with REs and Zr or Zn have intermediate SCC resistance, e.g. ZK60, ZE41A [45].
- Mg–Al alloys have poor SCC resistance in air, distilled water and chloride solutions [46, 47], and Mg–Li–Al alloys are susceptible to SCC in humid air.

Mg–Al alloys: Increasing Al content reduces the SCC resistance, as does Zn in AZ-class alloys. For instance, AZ91 fractures by SCC at 50 % of the yield strength in distilled water. Hence it is recommended by designers to use this alloy only in applications undergoing loads and stresses less than 30 % of the yield strength. The heat treatment cycle (solutionising and ageing temperatures and times) does not appear to affect the SCC susceptibility of AZ alloys.

Mg–Li alloys: Additions of Zn, Si or Ag instead of Al improves the SCC resistance of Mg–Li alloys.

Cast and wrought alloy considerations: Cast alloys are more resistant to SCC at low stress levels, whereas the susceptibility is almost the same at high stress levels. The effects of crystallographic texture on wrought alloy SCC susceptibility are insignificant. However, low temperature stress relief annealing treatments are usually done to reduce the SCC susceptibility [2].

Environmental considerations: Not all environments induce SCC in Mg alloys. In air the SCC is promoted by a high relative humidity (85–90 %). Aqueous environments, including distilled water and solutions of NaCl, NaCl + K₂CrO₄, NaBr, and Na₂SO₄, also accelerate SCC. In fact, an NaCl + K₂CrO₄ solution is commonly used in accelerated SCC testing of Mg alloys.

Mg alloy SCC susceptibility generally increases with increasing temperature. However, in passivating solutions the increasing temperature is beneficial because of improved passivation kinetics.

1.5.4.4 Corrosion Fatigue

Corrosion fatigue occurs under the combined action of cyclic loading and a corrosive medium. The fatigue lives of Mg alloys are significantly reduced in corrosive media such as aqueous NaCl and CaCl₂. Compared with CaCl₂, the high Cl[−] concentration and low pH of an NaCl solution accelerate pit formation and crack growth, resulting in noticeable reductions in fatigue strength [48]. AZ-class alloys are highly susceptible to corrosion fatigue because of the presence of Mg₁₇Al₁₂ [48–51].

Mg alloys are widely used in engine gear box housings. The housings are dynamically loaded components with oil passages, and various types of oils are used for lubrication. Therefore it is important to understand the effects of various oil environments on the corrosion fatigue behaviour of Mg alloys. Studies have shown that mineral oil provides relatively better corrosion protection than gear oil under fatigue loading conditions [50, 51]. Mg alloys adsorb the mineral oil easily by physical or chemical adsorption, resulting in formation of a thick protective layer over the substrate. This layer helps in reducing the corrosion rate and improves the corrosion fatigue life of the component.

1.5.4.5 Advances in Corrosion Protection Techniques

An electroless chemical treatment using $\text{KMnO}_4 + \text{MnHPO}_4$ solutions forms a conversion layer that has been reported to have better passivating capability than conventional chromate conversion coatings [52].

Anodic spark deposition/discharge, micro-arc oxidation, electrical breakdown and plasma chemical oxidation techniques provide a protective high-hardness crystalline ceramic layer to protect against corrosion and wear [53, 54]. In addition to this beneficial effect, the ceramic nature of the coating provides excellent heat resistance.

Plasma deposition has been used with a hexamethyldisiloxane–oxygen mixture to deposit an organic film on an Mg–Y–RE alloy [55, 56]. The film is reported to provide significantly higher corrosion resistance to the Mg alloy.

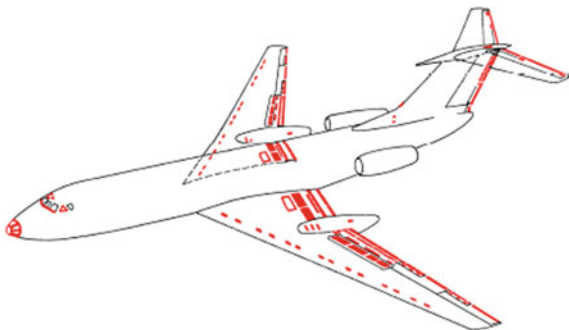
Other methods such as thermal spray coating, laser treatment, physical vapour deposition, ion implantation PVD, plasma oxidation, and galvanic deposition coatings have also been developed on a laboratory scale [57–60]. However, their practical applications have yet to be realized.

1.6 Global Scenario and Indian Programmes

Some aircraft built during the Second World War and the 1950s used significant amounts of Mg alloys in the primary structures. For example, the Lockheed F-80C Shooting Star was built primarily with Mg alloys, and the Convair B-36 used 8600 kg (5555 kg sheets + 700 kg forgings) of Mg components in the aircraft [61]. The Soviet Union Tupolev TU-134 had 1325 Mg secondary structure components (shown in Fig. 1.9) with a total weight of 780 kg [62].

More modern transport aircraft, e.g. the Boeing 727, use Mg alloy components for trailing edge flaps, control surfaces, door frames, wheels, engine gear boxes, accessory drives, thrust reversers, actuators, power generation components, etc.

Fig. 1.9 Locations of Mg secondary structure components in TU-134 aircraft (marked in Red) [62]



Indian helicopter projects such as the advanced light helicopter (ALH) and the light utility helicopter (LUH) use high strength, creep-resistant Mg alloy (EZ-class) sand castings in the main transmission gear box housings (MTGB), owing to significant weight savings. Excellent castability of EZ-class alloys allows the castings to be fabricated with intricate internal oil passages that cannot be made by any other forming or machining processes. A typical MTGB housing casting developed by HAL (F&F) has already been shown in Fig. 1.1. These castings are usually well sealed and corrosion protected by fluoride anodizing and a chromate conversion coating. They are also not considered to be damage tolerant (crack growth resistant) items, but instead are 'safe-life' items with large safety factors on the fatigue life. Other parts such as air intake cases for project engines and instrument panels are also manufactured from Mg alloys.

1.7 Summary

At present, most aerospace Mg alloy components are casting alloys for secondary structures. The use of wrought Mg alloys in aerospace applications is rather limited due to the poor workability of the alloys. Further, it is clear from the literature that the corrosion resistance (notably galvanic corrosion), ductility, elevated temperature strength, fatigue and toughness properties of conventional Mg alloys are still of concern.

There are promising advanced corrosion protection schemes (PVD, spray/deposition techniques, organic coatings) and innovative processing technologies (RSP, ECAE), that may make it possible to develop alloys with improved properties. Hence future goals should be to optimize these protection schemes and processes on an industrial scale, in order to exploit the full potential of Mg alloys in aerospace applications. Other important goals are the (further) development of innovative Mg alloys (Mg–Li and Mg–Sc alloys), and improved recycling methods to make these alloys cost-effective.

Acknowledgments The information and data in this chapter are taken mainly from the ASM Handbook: Magnesium and Magnesium alloys, edited by M.M. Avedesian and H.Baker, ASM International, 1999, USA; the Source Book: Mg Alloys Technology, edited by C.G.K. Nair, V. Gopalkrishna, and E.S.Dwarakadasa, and published by the Non-Ferrous Metals Division and IIM Bangalore Chapter, India; and Magnesium Alloys and Technology, edited by K.U.Kainer, Wiley VCH GmbH & Co, Germany.

One of the authors (T Ram Prabhu) would like to thank Dr. K Tamilmani, DG (Aero), DRDO and Shri P Jayapal, Chief Executive (A), CEMILAC, DRDO for their constant encouragement and kind support. The authors are grateful to the editors, Dr. N Eswara Prasad and Dr. RJH Wanhill for the opportunity to contribute this book chapter and also for their numerous valuable suggestions in finalizing its contents.

References

1. Edgar RL (2000) Magnesium alloys and their application. Kainer, K.U., Pub., France, p 3
2. Avedesian MM, Baker H (eds) (1999) Magnesium and magnesium alloys. ASM International (The Materials Information Society), Materials Park, OH, USA
3. Buch FV, Lietzau J, Mordike BL, Pisch A, Schmid-Fetzer R (1999) Development of Mg–Sc–Mn alloys. *Mater Sci Eng A* 263:1
4. Bach FW, Schaper M, Jaschik C (2003) Influence of lithium on hcp magnesium alloys. *Mater Sci Forum* 419–422:1037–1042
5. Bronfin B, Aghion E, Buch FV, Schumann S, Katzir M (2006) US Patent, No. 7041179
6. Hollrigl-Rosta F, Just E (1980) Magnesium in the volkswagen. In: *Light metals age*, vol 8, pp 22–29
7. Busk RS (1987) Magnesium products design. Marcel Dekker
8. Meredith PC (1969) QE22A-T6: a versatile magnesium alloy for high performance aerospace applications. Magnesium Elektron Ltd
9. Magnesium Casting Alloys, Datasheet: 440, Magnesium Elektron, Manchester, UK
10. Elektron Wrought Alloys, Datasheet: 441, Magnesium Elektron, Manchester, UK
11. Elektron Magnesium Alloys, Magnesium Elektron Ltd, 1983
12. Elektron EQ21A: Another casting alloy developed by magnesium electron Ltd. Bulletin 464, Magnesium Elektron Ltd., 1984
13. WE54, A new magnesium casting alloy for use up to 300 °C. Bulletin 466, Magnesium Elektron Ltd., 1985
14. Magnesium Elektron Ltd., Manchester, U.K., 1993
15. Yang Z, Li JP, Zhang JX, Lorimer GW, Robson J (2008) Review on research and development of magnesium alloys. *Acta Metall Sin (Engl Lett)* 21(5):313–328
16. Suman C (1991) Society of automotive engineers. SAE technical paper No. 910416. Warrendale, PA
17. Luo AA (2004) Magnesium technology 2004. TMS, Warrendale, PA, p 329
18. Lyon P, King JF, Nuttall (1996) In: Magnesium conference, proceedings 3rd International. Lorimer, G.W., Pub., London, p 99
19. Lyon P (2004) New magnesium alloy for aerospace and speciality applications. The Minerals, Metals & Materials Society, pp 311–315
20. Bronfin B, Aghion E (2001) Magnesium technology 2001. Hryn, J.N. Pub., Warrendale, p 127
21. Rokhlin LL (2003) Magnesium alloys containing rare earth metals-structure and properties. Taylor & Francis Pub., Moscow, p 197
22. Yang Z, Li JP, Guo YC, He F, Xia F, Liang MX (2008) Plastic deformation and dynamic recrystallization behaviors of Mg–5Gd–4Y–0.5Zn–0.5Zr alloy. *Mater Sci Eng, A* 485(1–2):487–491
23. Apps PJ, Karimzadeh H, King JF, Lorimer GW (2003) Phase compositions in magnesium-rare earth alloys containing yttrium, gadolinium or dysprosium. *Scr Mater* 48(5):475–481
24. Nie JF, Muddle BC (2000) Characterisation of strengthening precipitate phases in a Mg–Y–Nd alloy. *Acta Mater* 48:1691
25. Kainer KU (ed) (1999) Magnesium—alloys and technologies. Wiley-VCH GmBH & Co, KGaA, Weinheim
26. Doege E, Droder K (1997) Processing of Mg sheet metals by deep drawing and stretch forming. *Materiaux Tech* 7–8:19–23
27. Kittilsen B, Pinfield P (1992) Magnesium extrusion—recent developments. In: DGM-Tagung, proceedings, pp 85–92
28. Białobrzeski A, Saja K, Hubner K (2007) Ultralight magnesium-lithium alloys. *Arch Foundry Eng* 7:11–16

29. Slooff FA, Zhou J, Duszczyc J, Katgerman L (2007) Constitutive analysis of wrought magnesium alloy Mg–Al₄–Zn₁. *Scr Mater* 57(8):759–762
30. Wu L, Jain A, Brown DW, Stoica GM, Agnew SR, Clausen B, Fielden DE, Liaw PK (2008) Twinning–detwinning behavior during the strain-controlled low-cycle fatigue testing of a wrought magnesium alloy, ZK60A. *Acta Mater* 56(4):688–695
31. Riemelmoser FO, Kuhlein M, Kilian H, Kettner M, Hanzi AC, Uggowitzer PJ (2007) Micro-alloyed wrought magnesium for room-temperature forming. *Adv Eng Mater* 9(9):799–802
32. Kobayashi T, Koike J (2003) Anomalous activity of nonbasal dislocations in AZ31 Mg alloy at room temperature. *Mater Sci Forum* 419–422:231–236
33. Huang ZW, Yoshida Y (2003) Microstructures and tensile properties of wrought magnesium alloys processed by ECAE. *Mater Sci Forum* 419–422:243
34. Matsubara K, Miyahara Y, Makii K, Horita Z, Langdon TG (2003) Using extrusion and ECAP processing to achieve low temperature and high strain rate superplasticity. *Mater Sci Forum* 419:497
35. Munroe RA (1966) Magnesium-Lithium allot lightens electronic packaging. *Met. Prog.* 90 (1):89
36. Kawamura Y, Hayashi K, Masumoto T, Inoue A (2001) Rapidly solidified powder metallurgy Mg(97)Zn(1)Y(2) alloys with excellent tensile yield strength above 600 MPa. *Mater Trans* 42 (7):1172–1176
37. Inoue A, Kawamura Y, Matsushita M (2001) Novel hexagonal structure and ultrahigh strength of magnesium solid solution in the mg–zn–y system. *J Mater Res* 16:1894–1900
38. Gjestland H, Nussbaum G, Regazzoni G, Lohne O, Bauger O (1991) Stress-relaxation and creep behaviour of some rapidly solidified Mg alloys. *Mat Sci Eng A* 134:1197–1200
39. Stechens RI, Ogrevic VV (1990) Fatigue of magnesium alloys. *Annu Rev Mater Res* 20:141–177
40. Bamberger M, Dehm G (2008) Trends in the development of new Mg alloys. *Annu Rev Mater Sci* 38:505–533
41. Miller WK (1991) Creep of die cast AZ91 Mg at room temperature and low stress. *Met Trans A* 22A:873–877
42. Guo KW (2010) A review of magnesium/magnesium alloys corrosion and its protection. *Recent Pat Corros Sci* 2:13–21
43. Rzychoń T, Michalska J, Kielbus A (2007) Corrosion resistance of Mg–RE–Zr Alloys. *J Achievements Mater Manuf Eng* 21(1):51–54
44. Surface treatments for magnesium alloys in aerospace and defence, Datasheet: 256, Magnesium Elektron, Manchester, UK
45. Kannan MB, Dietzel W, Blawert C, Atrens A, Lyon P (2008) Stress corrosion cracking of rare-earth containing magnesium alloys ZE41, QE22 and Elektron 21 (EV31A) Compared with AZ80. *Mater Sci Eng A Struct Mater* 480:529–539
46. Winzer N, Atrens A, Dietzel W, Raja VS, Song GL, Kainer KU (2008) Characterisation of stress corrosion cracking (SCC) of Mg–Al Alloys. *Mater Sci Eng A Struct Mater* 488:339–351
47. Makar GL, Kruger J, Sieradzki K (1993) Stress corrosion cracking of rapidly solidified magnesium aluminum alloys. *Corr Sci* 34:1311–1323, 1325–1342
48. Bhuiyan MS, Mutoh Y, Murai T, Iwakami S (2008) Corrosion fatigue behavior of extruded magnesium alloy AZ61 under three different corrosive environments. *Int J Fatigue* 30:1756–1765
49. Nan ZY, Ishihara S, Goshima T (2008) Corrosion fatigue behavior of extruded magnesium alloy AZ31 in sodium chloride solution. *Int J Fatigue* 30:1181–1188
50. Eliezer A, Gutman EM, Abramov E, Unigovski Y (2001) Corrosion fatigue of die-cast and extruded magnesium alloys. *J Light Metals* 1:179–186
51. Eliezer A, Medlinsky O, Haddad J, Hamu GB (2008) Corrosion fatigue behavior of magnesium alloys under oil environments. *Mater Sci Eng A Struct Mater* 477:129–136
52. Chong KZ, Shih TS (2003) Conversion-coating treatment for magnesium alloys by a permanganate-phosphate solution. *Mater Chem Phys* 80:191–200

53. Ardelean H, Frateur I, Zanna S, Atrens A, Marcus P (2009) Corrosion protection of AZ91 magnesium alloy by anodizing in niobium and zirconium-containing electrolytes. *Corr Sci* 51:3030–3038
54. Shi ZM, Song GL, Atrens A (2006) Corrosion resistance of anodised single-phase Mg Alloys. *Surf Coat Technol* 201:492–503
55. Grundmeier G, Schmidt W, Stratmann M (2000) Corrosion protection by organic coatings: electrochemical mechanism and novel methods of investigation. *Electrochem Acta* 45:2515–2533
56. Fedrizzi L, Andreatta F, Paussa L, Deflorian F, Maschio S (2008) Heat exchangers corrosion protection by using organic coatings. *Prog Org Coat* 63:299–306
57. Liu ZM, Gao W (2006) The effect of substrate on the electroless nickel plating of Mg and Mg Alloys. *Surf Coat Technol* 200:3553–3560
58. Hollstein F, Wiedemann R, Scholz J (2003) Characteristics of PVD coatings on AZ31 magnesium alloys. *Surf Coat Technol* 162:261–268
59. Wan GJ, Maitz MF, Sun H, Li PP, Huang N (2007) Corrosion properties of oxygen plasma immersion ion implantation treated magnesium. *Surf Coat Technol* 201:8267–8272
60. Choi J, Nakao S, Kim J, Ikeyama M, Kato T (2007) Corrosion protection of DLC coatings on magnesium alloy. *Diam Relat Mater* 16:1361–1364
61. Ostrovsky I, Henn Y (2007) Present state and future of magnesium application in aerospace industry. In: International conference on new challenges in aeronautics. Moscow, 19–22 Aug 2007
62. Sadkov V, Laponov Y, Ageev V, Korovina N, Perspectives and conditions for Mg alloys application in “Tupolev” airplanes. In: Materials of the second international conference and exhibition, magnesium—broad horizons, conference CD: copies available from the chapter authors

Chapter 2

Aluminium Alloys for Aerospace Applications

P. Rambabu, N. Eswara Prasad, V.V. Kutumbarao and R.J.H. Wanhill

Abstract This chapter starts with a brief overview of the historical development of aerospace aluminium alloys. This is followed by a listing of a range of current alloys with a description of the alloy classification system and the wide range of tempers in which Al alloys are used. A description is given of the alloying and precipitation hardening behaviour, which is the principal strengthening mechanism for Al alloys. A survey of the mechanical properties, fatigue behaviour and corrosion resistance of Al alloys is followed by a listing of some of the typical aerospace applications of Al alloys. The Indian scenario with respect to production of primary aluminium and some aerospace alloys, and the Type Certification process of Al alloys for aerospace applications are described. Finally there is a critical review of some of the gaps in existing aerospace Al alloy technologies.

Keywords Aluminium · Alloys · Castings · Wrought products · Mechanical properties · Fatigue · Fracture · Corrosion · Applications

P. Rambabu
RCMA (Materials), CEMILAC, Hyderabad, India
e-mail: rambabu@cemilac.drdo.in; pothuri_rambabu@yahoo.co.in

N. Eswara Prasad (✉)
DMSRDE, DRDO, Kanpur, India
e-mail: nep@dmsrde.drdo.in; neswarap@rediffmail.com

V.V. Kutumbarao
DMRL, Hyderabad, India
e-mail: rao.vvk@gmail.com

R.J.H. Wanhill
Emmeloord, Flevoland, The Netherlands
e-mail: rjhwanhill@gmail.com

2.1 Introduction

Aluminium alloys have been the main airframe materials since they started replacing wood in the late 1920s. Even though the role of aluminium in future aircraft will probably be somewhat diminished by the increasing use of composite materials, high-strength aluminium alloys are, and will remain, important airframe materials.

The attractiveness of aluminium is that it is a relatively low cost, lightweight metal that can be heat treated to fairly high-strength levels; and it is one of the most easily fabricated of the high-performance materials, which usually correlates directly with lower costs. Disadvantages of aluminium alloys include a low modulus of elasticity, rather low elevated-temperature capability ($\leq 130\text{ }^\circ\text{C}$), and in high-strength alloys the susceptibility to corrosion [1].

Dramatic improvements in aluminium alloys have occurred since they were first introduced in the 1920s. These improvements, shown in Fig. 2.1, are a result of increasing understanding of chemical composition, impurity control and the effects of processing and heat treatment. The data in Fig. 2.1 pertain to established aerospace aluminium alloys; newer ones (such as AA7085) are under evaluation, as are the third-generation aluminium–lithium (Al–Li) alloys discussed in Chap. 3 of this Volume. The chemical compositions of some aerospace grade aluminium alloys [2] are given in Table 2.1.

One of the earliest aerospace Al alloys was Duralumin (AA2017) which had a yield strength of 280 MPa. Property improvements have come through development of new alloy systems, modifications to compositions within particular systems, and from the use of a range of multistage ageing treatments (tempers) [3].

Fig. 2.1 Yield strengths versus year of introduction of Al alloys [1]

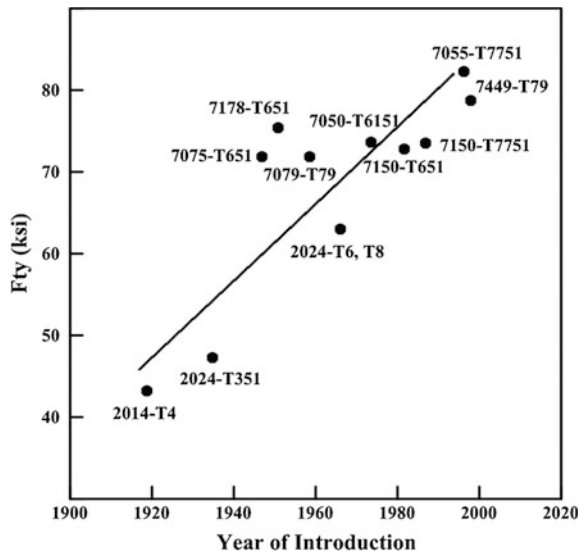


Table 2.1 Chemical compositions of some aerospace aluminium alloys [2]

Alloy	Cu	Mg	Zn	Mn	Si	Fe	Cr	Ti	Zr
AA2014	3.9–5.0	0.2–0.8	0.25 _{max}	0.4–1.2	0.5–1.2	0.7 _{max}	0.10 _{max}	0.15 _{max}	–
AA2017	3.5–4.5	0.4–0.8	0.25 _{max}	0.4–1.0	0.2–0.8	0.7 _{max}	0.10 _{max}	0.15 _{max}	–
AA2024	3.8–4.9	1.2–1.8	0.25 _{max}	0.3–0.9	0.50	0.50	0.10	0.15	–
AA2219	5.8–6.8	0.02 _{max}	0.10 _{max}	0.2–0.4	0.20 _{max}	0.30 _{max}	–	0.02–0.10	0.1–0.25
AA5083	0.10 _{max}	4.0–4.9	0.25 _{max}	0.4–1.0	0.40 _{max}	0.40 _{max}	0.05–0.25	0.15 _{max}	–
AA6061	0.15–0.4	0.8–1.2	0.25 _{max}	0.15 _{max}	0.4–0.8	0.7 _{max}	0.04–0.35	0.15 _{max}	–
AA7050	2.0–2.6	1.9–2.6	5.7–6.7	0.1 _{max}	0.12 _{max}	0.15 _{max}	0.04 _{max}	0.10 _{max}	0.08–0.15
AA7075	1.2–2.0	2.1–2.9	5.1–6.1	0.3 _{max}	0.4 _{max}	0.5 _{max}	–	0.10 _{max}	–
AA7150	1.9–2.5	2.0–2.7	5.9–6.9	0.10	0.12	0.15	0.04	0.08–0.15	0.06
AA7178	1.6–2.4	2.4–3.1	6.3–7.3	0.30	0.4	0.5	0.18–0.28	0.20	–
AA7475	1.2–1.9	1.9–2.6	5.2–6.2	0.06 _{max}	0.10 _{max}	0.12 _{max}	0.18–0.25	0.06 _{max}	–

Experiments with different levels of the alloying elements led to the Al–Cu–Mg alloy AA2014, which developed better properties than AA2017 after artificial (T6) ageing. Other experiments led to the development of AA2024-T3. This alloy attained a higher yield strength than AA2017-T4 by modest amounts of cold deformation followed by natural ageing, and has significantly higher ductility than AA2014-T6.

Several investigators found that aluminium alloys containing both zinc and magnesium developed substantially higher strengths than those containing either of the alloying elements added singly, and significantly higher strengths were obtained from these alloys. These findings led to the development of the Al–Zn–Mg–Cu alloy AA7075 in the early 1940s. A higher strength alloy, AA7178, was later developed [4], but low toughness led to alloys with much lower Fe and Si contents, e.g. AA7050 and AA7475.

As aircraft became larger it became necessary to use thicker-section airframe components. However, thick-section products of the high-strength 7XXX alloys like AA7075-T6 and particularly AA7079-T6 were found to be susceptible to stress corrosion cracking (SCC) in the short transverse direction. The overaged T73 and T76 tempers were developed in the early 1960s to make AA7075 more resistant to SCC and exfoliation corrosion.

Subsequently alloy 7475 was developed from 7075 to improve the fracture toughness. Then a new generation of alloys, including AA7050-T7351, was developed during the 1970s to fit the need for a material that would develop high strength in thick-section products, good resistance to SCC and exfoliation corrosion, and good fracture toughness and fatigue characteristics. These developments are continuing, with one of the latest alloys being AA7085.

Other developments include higher toughness 2XXX alloys and the third generation of Al–Li alloys, as already mentioned.

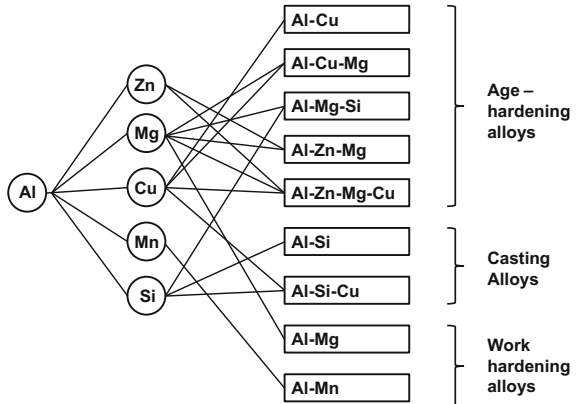
2.2 Classification and Designation

Aluminium alloys are classified as heat treatable or non-heat treatable, depending on whether or not they respond to precipitation hardening [2, 5]. The heat treatable alloys contain elements that decrease in solid solubility with decreasing temperature, and in concentrations that exceed their equilibrium solid solubility at room temperature and moderately higher temperatures. The most important alloying elements in this group include copper, lithium, magnesium and zinc [5].

A large number of other compositions rely instead on work hardening through mechanical reduction, usually in combination with various annealing procedures for property developments. These alloys are referred to as non-heat-treatable or work-hardening alloys.

Some casting alloys are essentially non-heat-treatable and are used as-cast or in thermally modified conditions uninfluenced by solutionizing or precipitation effects [2]. Figure 2.2 gives an overview of the principal types of aluminium alloys.

Fig. 2.2 The principal types of aluminium alloys [2]



2.2.1 Wrought Alloys

A four-digit numerical designation system is used to identify wrought aluminium and aluminium alloys. As shown below, the first digit of the four-digit designation indicates the group.

Aluminium, $\geq 99.00\%$ —1XXX. Aluminium alloys grouped by major alloying element(s); Copper—2XXX; Manganese—3XXX; Silicon—4XXX; Magnesium—5XXX; Magnesium and Silicon—6XXX; Zinc—7XXX; Other elements—8XXX; Unused series—9XXX.

2.2.2 Cast Alloys

A system of four-digit numerical designations incorporating a decimal point is used to identify aluminium and aluminium alloys in the form of castings and foundry ingots. The first digit indicates the alloy group.

Aluminium, $\geq 99.00\%$ —1XX.X. Aluminium alloys grouped by major alloying element(s); Copper—2XX.X; Silicon with added copper and/or magnesium—3XX.X; Silicon—4XX.X; Magnesium—5XX.X; Zinc—7XX.X; Tin—8XX.X; Other elements—9XX.X; Unused series—6XX.X

2.2.3 Temper Designations

The temper designation system is used for all product forms (both wrought and cast), with the exception of ingots. The system is based on the sequences of mechanical or thermal treatments, or both, used to produce the various tempers. The temper designation follows the alloy designation and is separated from it by a

hyphen. Basic temper designations consist of individual capital letters. Major subdivisions of basic tempers, where required, are indicated by one or more digits following the letter. These digits designate sequences of treatments that produce specific combinations of characteristics in the product. Variations in treatment conditions within major subdivisions are identified by additional digits.

T1—Cooled from an elevated-temperature shaping process and naturally aged to a substantially stable condition. This designation applies to products that are not cold-worked after an elevated-temperature shaping process such as casting or extrusion, and for which mechanical properties have been stabilized by room temperature ageing. This designation also applies to products that are flattened or straightened after cooling from the shaping process, whereby the cold-work effects imparted by flattening or straightening *are not* accounted for in the specified property limits.

T2—Cooled from an elevated-temperature shaping process, cold-worked, and naturally aged to a substantially stable condition. This designation refers to products that are cold-worked specifically to improve strength after cooling from a hot-working process such as rolling or extrusion, and for which the mechanical properties have been stabilized by room temperature ageing. This designation also applies to products in which the effects of cold-work, imparted by flattening or straightening, *are* accounted for in the specified property limits.

T3—Solution heat treated, cold-worked, and naturally aged to a substantially stable condition. T3 applies to products that are cold-worked specifically to improve strength after solution heat treatment and for which mechanical properties have been stabilized by room temperature ageing. This designation also applies to products in which the effects of cold work, imparted by flattening or straightening, *are* accounted for in the specified property limits.

T4—Solution heat treated and naturally aged to a substantially stable condition. This designation signifies products that are not cold-worked after solution heat treatment and for which mechanical properties have been stabilized by room temperature ageing. If the products are flattened or straightened, the effects of the cold-work imparted by flattening or straightening *are not* accounted for in the specified property limits.

T5—Cooled from an elevated-temperature shaping process and artificially aged. T5 includes products that are not cold-worked after an elevated-temperature shaping process such as casting or extrusion and for which the mechanical properties have been substantially improved by precipitation heat treatment. If the products are flattened or straightened after cooling from the shaping process, the effects of the cold-work imparted by flattening or straightening *are not* accounted for in the specified property limits.

T7—Solution heat treated and overaged or stabilized. T7 applies to wrought products that have been precipitation heat treated beyond the point of maximum strength to provide some special characteristics, such as enhanced resistance to stress corrosion cracking or exfoliation corrosion. This designation also applies to

cast products that are artificially aged after solution heat treatment to provide dimensional and strength stability.

T8—Solution heat treated, cold-worked, and artificially aged. This designation applies to products that are cold-worked specifically to improve strength after solution heat treatment and for which mechanical properties or dimensional stability, or both, have been substantially improved by precipitation heat treatment. The effects of cold work, including any cold work imparted by flattening or straightening, *are* accounted for in the specified property limits.

T9—Solution heat treated, artificially aged, and cold-worked. This group is comprised of products that are cold-worked specifically to improve strength after they have been precipitation heat treated.

T10—Cooled from an elevated-temperature shaping process, cold-worked, and artificially aged. T10 identifies products that are cold-worked specifically to improve strength after cooling from a hot-working process such as rolling or extrusion and for which the mechanical properties have been substantially improved by precipitation heat treatment. The effects of cold work, including any cold work imparted by flattening or straightening, *are* accounted for in the specified property limits.

2.3 Age-Hardenable Aluminium Alloys

Although most metals will alloy with aluminium, comparatively few have sufficient solid solubility to serve as major alloying additions, see Table 2.2. Some of the transition metals, e.g. chromium, manganese and zirconium, which have solid solubilities below 1 at.% confer important improvements to alloy properties by forming intermetallic compounds that control the grain structure. Apart from tin, which is sparingly soluble, the maximum solid solubilities in binary aluminium alloys occur at the eutectic and peritectic temperatures [6].

The heat treatment given to aluminium alloys to increase strength is age hardening. As stated at the beginning of Sect. 2.2, the basic requirement for an alloy to be amenable to age-hardening is a decrease in solid solubility of one or more of the alloying elements with decreasing temperature. Heat treatment normally involves the following stages:

1. Solution treatment at a relatively high temperature within the single-phase region.
2. Rapid cooling or quenching, usually to room temperature to obtain a supersaturated solid solution (SSSS) of the age-hardening elements in aluminium.
3. Controlled decomposition of the SSSS to form a finely dispersed precipitate, usually by ageing for convenient times at one and sometimes two intermediate temperatures.

Table 2.2 Solid solubility of elements in aluminium [6]

Element	Temperature for maximum solid solubility (°C)	Maximum solid solubility	
		(wt%)	(at.%)
Cadmium	649	0.4	0.09
Cobalt	657	< 0.02	< 0.01
Copper	548	5.65	2.40
Chromium	661	0.77	0.40
Germanium	424	7.2	2.7
Iron	655	0.05	0.025
Lithium	600	4.2	16.3
Magnesium	450	17.4	18.5
Manganese	658	1.82	0.90
Nickel	640	0.04	0.02
Silicon	577	1.65	1.59
Silver	566	55.6	23.8
Tin	228	~0.06	~0.01
Titanium	665	~1.3	~0.74
Vanadium	661	~0.4	~0.21
Zinc	443	82.8	66.4
Zirconium	660.5	0.28	0.08

The complete decomposition of an SSSS is usually a complex process which may involve several stages. Typically, Guinier–Preston (GP) zones and an intermediate precipitate may be formed in addition to the equilibrium phase.

Most aluminium alloys that respond to ageing will undergo some hardening at ambient temperatures. This is called ‘natural ageing’ and may continue almost indefinitely, although the rate of change becomes extremely slow after months or years. Ageing at sufficiently elevated temperature (artificial ageing) is characterized by a different behaviour in which the hardness usually increases to a maximum and then decreases. The highest value of hardness occurs at one particular temperature, which varies with each alloy.

Maximum hardening in commercial alloys normally occurs when a critical dispersion of GP zones, or an intermediate precipitate, or a combination of both, are present. In some alloys more than one intermediate precipitate may be formed.

The softening that occurs on prolonged artificial ageing is known as ‘overageing’. For commercial heat treatments an ageing schedule is usually selected to give the desired response to hardening (strengthening) within a convenient period of time.

Some alloys are cold-worked (e.g. stretching or compression, up to 5 %) after quenching and before ageing. The cold-work increases the dislocation density and provides more sites at which heterogeneous nucleation of intermediate precipitates may occur during ageing [6]. The result is an improvement in the strength properties.

2.4 Effects of Alloying Elements

The effect(s) of various alloying elements [2] are given below in alphabetical order. Some of the effects, particularly with respect to impurities, are not well documented and are specific to particular alloys or conditions.

Chromium: Is a common addition to many alloys of the aluminium–magnesium, aluminium–magnesium–silicon, and aluminium–magnesium–zinc groups, in which it is added in amounts generally not exceeding 0.35 wt%. Above this limit chromium tends to form very coarse constituents with other impurities or additions such as manganese and titanium.

Chromium has a low diffusion rate and forms a fine dispersed phase in wrought products. The dispersed phase inhibits nucleation and grain growth. Hence during hot working or heat treatment, chromium prevents grain growth in aluminium–magnesium alloys and recrystallization in aluminium–magnesium–silicon or aluminium–magnesium–zinc alloys.

The main drawback of chromium in heat treatable alloys is the increase in quench sensitivity when the hardening phase tends to precipitate on the preexisting chromium-phase particles.

Copper: Aluminium–copper alloys containing 2–10 wt% Cu, generally with other additions, form an important family of Al alloys. Both cast and wrought aluminium–copper alloys respond to solution heat treatment and subsequent ageing, with an increase in strength and hardness and a decrease in elongation. The strengthening is maximum between 4 and 6 wt% Cu, depending upon the influence of other constituents. N.B: the ageing characteristics of binary aluminium–copper alloys have been studied in greater detail than for any other system, but all commercial aerospace alloys contain other alloying elements.

Copper–Magnesium: The main benefit of adding magnesium to aluminium–copper alloys is the increased strength following solution heat treatment and quenching. In certain wrought alloys of this type, ageing at room temperature (natural ageing) causes an increase in strength accompanied by high ductility. Artificial ageing, at elevated temperatures, results in a further increase in strength, especially the yield strength, but at a substantial sacrifice in tensile elongation.

For both cast and wrought aluminium–copper alloys, as little as about 0.5 wt% Mg is effective in changing the ageing characteristics. In wrought products the effect of magnesium additions on strength can be maximized in artificially aged materials by cold-working prior to ageing. In naturally aged materials, however, the benefit to strength from magnesium additions can *decrease* with cold-working.

The effect of magnesium on the corrosion resistance of aluminium–copper alloys depends on the type of product and thermal treatment.

Copper–Magnesium plus Other Elements: Al–Cu–Mg alloys containing manganese are the most important and versatile class of commercial high-strength wrought aluminium–copper–magnesium alloys. In general, tensile strength increases with separate or simultaneous increases in magnesium and manganese, and the yield strength also increases, but to a lesser extent. Further increases in

tensile strength and particularly yield strength occur on cold-working after heat treatment.

Additions of manganese and magnesium decrease the fabrication characteristics of aluminium–copper alloys, and manganese also causes a loss in ductility. Hence the concentration of manganese does not exceed about 1 wt% in commercial alloys. Additions of cobalt, chromium, or molybdenum to the wrought Al-4 wt% Cu-0.5 wt% Mg type of alloy increase the tensile properties on heat treatment, but none offers a distinct advantage over manganese.

The cast aluminium–copper–magnesium alloys containing iron are characterized by dimensional stability and improved bearing characteristics, as well as high strength and hardness at elevated temperatures. However, in a wrought Al-4 wt% Cu-0.5 wt% Mg alloy, iron in concentrations as low as 0.5 wt% lowers the tensile properties in the heat-treated condition unless the silicon content is sufficient to sequester the iron as FeSi intermetallic particles. When sufficient silicon is present to combine with the iron, the strength properties are unaffected, although the FeSi particles are detrimental to fracture toughness, see Sect. 2.5.1.

However, if there is excess iron, it unites with copper to form the Cu_2FeAl_7 constituent, thereby reducing the amount of copper available for heat-treating effects. Silicon also combines with magnesium to form Mg_2Si precipitates that contribute to the age-hardening process, see below.

Silver substantially increases the strength of heat treated and aged aluminium–copper–magnesium alloys. Nickel improves the strength and hardness of cast and wrought aluminium–copper–magnesium alloys at elevated temperatures. However, addition of about 0.5 wt% Ni lowers the tensile properties of the heat-treated wrought Al-4 %Cu-0.5 %Mg alloy at room temperature.

Magnesium–Silicon: Wrought alloys of the 6XXX group contain up to 1.5 wt% each of magnesium and silicon in the approximate ratio to form Mg_2Si , i.e. 1.73:1. The maximum solubility of Mg_2Si in Al is 1.85 wt%, and this decreases with temperature. Precipitation upon age-hardening occurs by formation of Guinier–Preston zones and a very fine precipitate. Both confer an increase in strength to these alloys, though not as great as in the case of the 2XXX or the 7XXX alloys.

Al– Mg_2Si alloys can be divided into three groups. In the first group the total amount of magnesium and silicon does not exceed 1.5 wt%. These elements are in a nearly balanced ratio or with a slight excess of silicon. Typical of this group is AA6063, which nominally contains 1.1 wt% Mg_2Si and is widely used for extruded sections. Its solution heat-treating temperature of just over 500 °C and its low quench sensitivity are such that this alloy does not need a separate solution treatment after extrusion, but may be air quenched at the press and artificially aged to achieve moderate strength, good ductility, and excellent corrosion resistance.

The second group nominally contains 1.5 wt% or more of magnesium + silicon and other additions such as 0.3 wt% Cu, which increases strength in the T6 temper. Elements such as manganese, chromium, and zirconium are used for controlling grain structure. Alloys of this group, such as AA6061, achieve strengths about 70 MPa higher than in the first group in the T6 temper. However, this second group requires a higher solution treating temperature than the first and they are quench

sensitive. Therefore they generally require a separate solution treatment followed by rapid quenching and artificial ageing.

The third group contains an amount of Mg_2Si overlapping the first two but with substantial excess silicon. An excess of 0.2 wt% Si increases the strength of an alloy containing 0.8 wt% Mg_2Si by about 70 MPa. Larger amounts of excess silicon are less beneficial. Excess magnesium, however, is of benefit only at low Mg_2Si contents because magnesium lowers the solubility of Mg_2Si .

In excess silicon alloys, segregation of silicon to the grain boundaries causes grain-boundary fracture in recrystallized structures. Additions of manganese, chromium, or zirconium counteract the effect of silicon by preventing recrystallization during heat treatment. Common alloys of this group are AA6351 and the more recently introduced alloys AA6009 and AA6010. An addition of lead and bismuth to an alloy of this series (AA6262) improves machinability.

Silicon: In wrought alloys silicon is used with magnesium at levels up to 1.5 wt% to produce Mg_2Si in the 6XXX series of heat treatable alloys.

High-purity aluminium–silicon casting alloys exhibit hot shortness up to 3 wt% Si, the most critical range being 0.17–0.8 wt% Si. However, in aluminium–copper–magnesium alloys silicon additions (0.5–4.0 wt%) *reduce* the cracking tendency. Small amounts of magnesium added to any silicon-containing alloy will render it heat treatable, but the converse is not true, since excess magnesium over that required to form Mg_2Si sharply reduces the solid solubility of this compound.

Modification of the silicon morphology in casting alloys can be achieved through the addition of sodium in eutectic and hypoeutectic alloys and by phosphorus in hypereutectic alloys.

Titanium: Is used primarily as a grain refiner of aluminium alloy castings and ingots. When used alone, the effect of titanium decreases with time of holding in the molten state and with repeated remelting. The grain-refining effect is enhanced if boron is present in the melt or if it is added as a master alloy containing boron largely combined with titanium as TiB_2 .

Zinc–Magnesium: Addition of magnesium to aluminium–zinc alloys develops the strength potential of this alloy system, especially in the range of 3–7.5 wt% Zn. Magnesium and zinc form $MgZn_2$, which produces a far greater response to heat treatment than occurs in the binary aluminium–zinc system.

On the negative side, increasing additions of both zinc and magnesium decrease the overall corrosion resistance of aluminium, such that close control over the microstructure, heat treatment, and composition are often necessary to maintain adequate resistance to stress corrosion and exfoliation corrosion. For example, depending upon the alloy, stress corrosion is controlled by some or all of the following: overageing; cooling rate after solution treatment; maintaining an unrecrystallized structure via additions such as zirconium, copper or chromium (see zinc–magnesium–copper alloys); and adjusting the zinc–magnesium ratio closer to 3:1.

Zinc–Magnesium–Copper: Addition of copper to the aluminium–zinc–magnesium system, together with small but important amounts of chromium and manganese, results in the highest strength aluminium-base alloys (7XXX series) commercially available.

In this alloy system, zinc and magnesium control the ageing process. The effect of copper is to increase the ageing rate by increasing the degree of supersaturation and perhaps through nucleation of the CuMgAl_2 phase. Copper also increases the quench sensitivity upon heat treatment. In general, copper reduces the resistance to general corrosion of aluminium–zinc–magnesium alloys, but increases the resistance to stress corrosion. Minor alloy additions, such as chromium and zirconium, have a marked effect on mechanical properties and corrosion resistance.

Zirconium: Additions in the range 0.1–0.3 wt% are used to form a fine precipitate of intermetallic particles that inhibit recovery and recrystallization. An increasing number of alloys, particularly in the aluminium–zinc–magnesium family, use zirconium additions to increase the recrystallization temperature and to control the grain structure in wrought products. Zirconium additions render this family of alloys less quench sensitive compared to chromium additions.

Higher levels of zirconium are employed in some superplastic alloys to retain the required fine substructure during elevated temperature forming. Zirconium additions have been used to reduce the as-cast grain size, but the effect is less than that of titanium. In addition, zirconium tends to reduce the grain-refining effect of titanium plus boron additions so that it is necessary to use more titanium and boron to grain refine zirconium-containing alloys.

2.5 Mechanical Properties

2.5.1 *Strength and Fracture Toughness*

As previously mentioned, aluminium alloys may be divided into two groups depending upon whether or not they respond to precipitation hardening. For alloys that do not respond to ageing treatments, it is the finely dispersed precipitates that have the dominant effect in inhibiting dislocation motion and thereby raising yield and tensile strengths.

For the other group the grain size of cast alloys and the dislocation structures produced by cold-working in the case of wrought alloys are of prime importance. Some of the mechanical properties of wrought age-hardening aerospace aluminium alloys are given in Table 2.3.

Coarse intermetallic compounds have relatively little effect on yield or tensile strength but they can cause a marked loss of ductility in both cast and wrought products. The particles may crack at small plastic strains forming internal voids which, under the action of further plastic strain, coalesce leading to premature fracture.

Early work on the higher strength aluminium alloys was directed primarily at maximizing tensile properties in aerospace materials. Since the 1960s the emphasis in alloy development has shifted away from tensile strength as the primary consideration, and more attention is given to optimizing a combination of properties

Table 2.3 Typical mechanical properties of some standard and widely used aerospace aluminium alloys

Alloy	Temper	Density (g/cm^3)	Elastic modulus (GPa)	Tensile properties			HCF limit (MPa)	Fracture toughness ($\text{MPa}\sqrt{\text{m}}$)	References
				Yield (MPa)	Tensile (MPa)	% El			
AA2014	T6	2.80	72.4	415	485	13	125	26.4 (T651)	[2, 9, 10]
AA2219	T62	2.84	73.8	290	415	10	105	36.3 (T87)	[2, 9, 10]
AA2024	T4	2.77	72.4	325	470	20	140	22.0 (T851)	[2, 9, 10]
AA7050	T74	2.83	70.3	450	510	13	170	38.5 (T73651)	[2, 9, 10]
AA7075	T6	2.80	71.0	505	570	11	160	28.6 (T6)	[2, 9, 10]

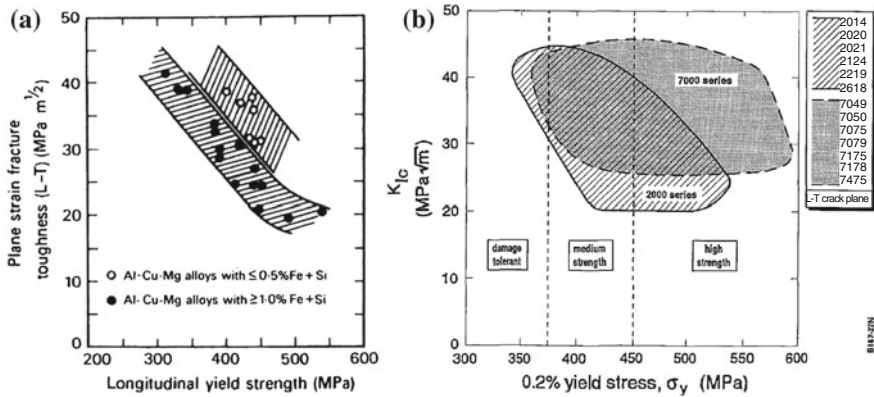


Fig. 2.3 Plane-strain fracture toughness of **a** Al-Cu-Mg alloys with differing levels of iron and silicon [3]; **b** 2XXX and 7XXX alloys covering three strength regimes [7]. Note the general inverse relationship between strength and fracture toughness

and the alloys' behaviour under a variety of service loadings and environmental conditions.

Yield strength is important for resisting deformation under service loads, but in the presence of cracks and other flaws it is the fracture toughness that generally becomes the more important parameter. Minimum fracture toughness requirements have become mandatory, and in the high-strength alloys the generally inverse relationship between strength and toughness, see Fig. 2.3, limits the level of yield strength that can be safely employed by the designer.

The major step in the development of aluminium alloys with greatly improved fracture toughness has come from controlling the levels of the impurity elements iron and silicon. This effect is shown in Fig. 2.3a for alloys based on the Al-Cu-Mg system: it can be seen that plane-strain fracture toughness values may be doubled by maintaining the combined levels of these elements below 0.5 wt% as compared with similar alloys in which this value exceeds 1.0 wt%. Consequently, some high-toughness versions of older alloy compositions are now commercially used with reduced impurity levels [3].

Figure 2.3b shows that in general the 7XXX series of alloys can attain superior combinations of strength and fracture toughness compared with 2XXX alloys.

2.5.2 Fatigue

Fatigue life and strength properties are always important design data for aircraft structures. The practical significance is, however, restricted to *notched* fatigue, since cracks start at stress concentrations, especially fastener holes [7].

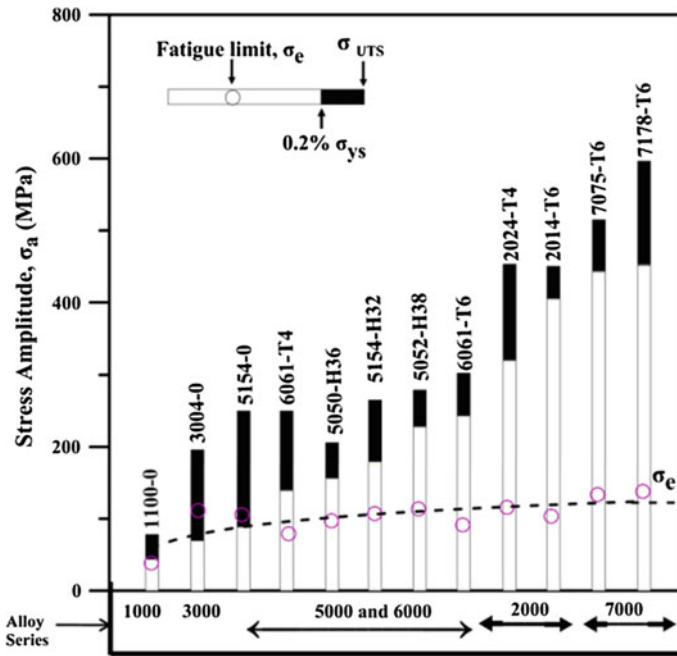


Fig. 2.4 Fatigue limits of conventional (non-lithium-containing) wrought aluminium alloys [11]

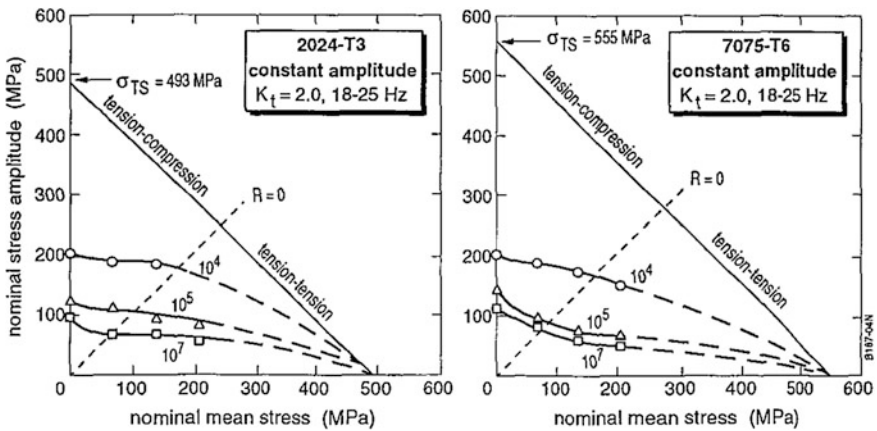


Fig. 2.5 Notched ($K_t = 2$) fatigue strengths of aircraft standard sheet alloys [7]

Unlike steels, the unnotched fatigue strengths of wrought aluminium alloys are not proportional to the static strengths, i.e. stronger alloys do not necessarily have a higher fatigue strength, see Fig. 2.4. This is even more marked for notched fatigue, and there is actually little difference in the high-cycle notched fatigue strengths of IM wrought alloys, for example Fig. 2.5.

2.5.3 Fatigue Crack Growth

Conventional (non-lithium-containing) 2XXX series alloys are generally superior to 7XXX series alloys under constant amplitude loading, for example Fig. 2.6, and gust spectrum loading (typical for transport aircraft), but not necessarily under manoeuvre spectrum loading representative for tactical (fighter) aircraft [8].

Also, for constant amplitude loading at low ΔK values, the alloy rankings depend strongly on the ageing treatment: naturally aged (T3X) and artificially aged (T8X) treatments for 2XXX series alloys, and artificially peak aged (T6X) and overaged (T7X) treatments for 7XXX series alloys [7].

Thus, summarising, fatigue crack growth testing, even at the basic materials level, when selecting candidate materials for further evaluation, should include realistic load histories and representative stress levels [8].

2.5.4 Corrosion Resistance

The corrosion resistance of any specific aluminium alloy depends on the environment as well as the alloy. Both chemical and physical environmental variables

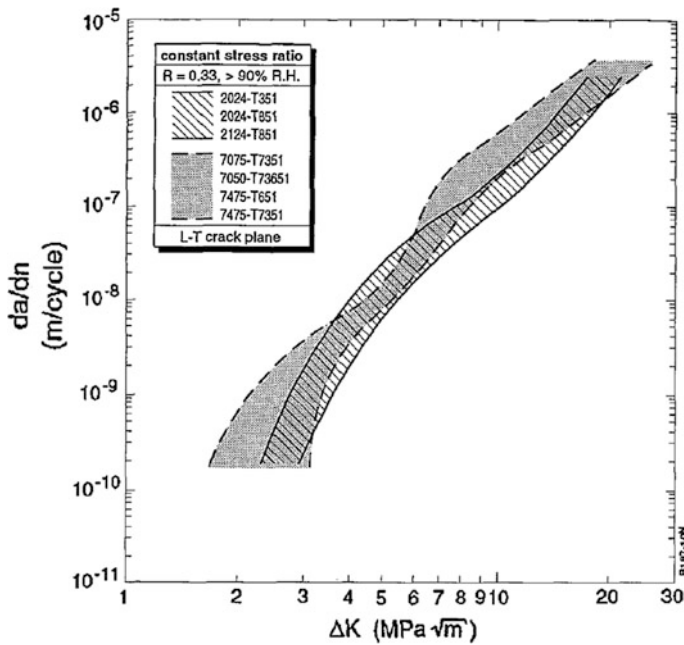


Fig. 2.6 Constant stress ratio fatigue crack growth rates for conventional 2XXX and 7XXX plate alloys [7]

affect corrosion. The influence of the environment depends on its composition and the presence of impurities, such as heavy metal ions. Physical variables are temperature, degree of movement and agitation, and pressure. Alloy variables that affect corrosion are composition and fabrication practice. These determine the microstructure, which controls whether localized corrosion occurs and the method of attack [9].

Conventional (non-lithium-containing) aerospace alloys always require some form of corrosion protection. This can be cladding with (nearly) pure aluminium and anodizing for sheet alloys; anodizing or ion vapour deposition for other types of products; and primer and paint systems.

Some aluminium alloys are susceptible to stress corrosion cracking (SCC), which occurs under the combined action of a continuous tensile stress and a specific corrosive environment. The most important aerospace aluminium alloys susceptible to SCC are the 2XXX-T8XX, 7XXX-T6XX and 7XXX-T7XX tempers [12]. Very rarely, SCC occurs in aluminium–magnesium–silicon alloys (6XXX).

The remedial measures against SCC include restricting the alloy strength levels, stress relief treatments, minimizing assembly stresses in built-up structures, and corrosion-resistant coatings, as above [12]. See also Chap. 19 in Volume 2 of these Source Books.

2.6 Typical Aerospace Applications of Aluminium Alloys

Even though the role of aluminium in future commercial aircraft will probably be ‘threatened’ by the increasing use of composite materials, the high-strength aluminium alloys are, and will remain, important airframe materials. Even in fighter aircraft, which already have composite material percentages in the range of 40–50 %, aluminium still plays a significant role [1]. The attractiveness of aluminium is that it is a relatively low cost, lightweight metal that can be heat treated to fairly high-strength levels, and it is one of the most easily fabricated high performance materials, i.e. the manufacturing costs are relatively low.

Improvements in aluminium manufacturing technology include high-speed machining and friction stir welding (FSR):

- Although higher metal removal rates are an immediate benefit of high-speed machining, an additional cost saving is the ability to machine extremely thin walls and webs. This allows the design of weight competitive high-speed machined assemblies, in which sheet metal parts that were formally assembled with mechanical fasteners can now be machined from a single or several blocks of aluminium plate.
- FSR is a solid state joining process that has the ability to weld the 2XXX and 7XXX alloys, which are not suited to conventional fusion welding. FSR also allows the design of weight competitive assemblies with a minimum number of mechanical fasteners.



Fig. 2.7 Engineering property requirements for main structural areas in a transport aircraft: *CYS* compressive yield strength; *E* elastic modulus; *TS* tensile strength; *DT* damage tolerance properties (fatigue, fatigue crack growth, fracture toughness)

More specifically, the alloy property requirements vary depending on the application. A generic example is given in Fig. 2.7, which illustrates the engineering property requirements for several of the main structural areas in a transport aircraft, namely (i) fuselage and pressure cabins, (ii) wings and (iii) empennage (horizontal and vertical stabilizers).

The engineering properties required for these structures are strength (*TS*, *CYS*), stiffness (*E*), damage tolerance (*DT*: fatigue, fatigue crack growth, fracture toughness), and corrosion (general and stress corrosion). The rankings of the requirements differ for different areas, but there is much commonality.

Table 2.4 presents a survey of the actual and proposed uses of conventional 2XXX and 7XXX aluminium alloys in airframe structures. Alloy producers develop basically similar alloys for different product forms and applications. The most important contribution to this flexibility is the development of a range of alloy tempers that allow optimizations and trade-offs of properties, and hence the ability to match the alloys to particular applications.

2.7 Indian Scenario

4 % of the global primary Al production of about 50 million tons is produced in India by three large manufacturers: NALCO, HINDALCO and the Vedanta Group. Comparable quantities are produced by recycling (using domestic as well as imported scrap, mostly by thousands of small units). About 80 % of the primary

Table 2.4 Actual and proposed uses of conventional aerospace aluminium alloys in airframe structures [13]

Product	Strength levels	Alloy/temper	Applications
Sheet	Damage tolerant	2024-T3, 2524-T3/351	Fuselage/pressure cabin skins
Plate	Damage tolerant	2024-T351, 2324-T39, 2624-T351, 2624-T39	Lower wing covers
	Medium strength	2024-T62	Tactical aircraft fuselage panels
	Medium strength	2124-T851	Tactical aircraft bulkheads
	Medium strength	7050-T7451, 7X75-T7XXX	Internal fuselage structures
	High strength	7150-T7751, 7055-T7751, 7055-T7951, 7255-T7951	Upper wing covers
	Medium strength	7050-T7451	Spars, ribs, other internal structures
Forgings	High strength	7175-T7351, 7050-T7452	Wing/fuselage attachments
Extrusions	Damage tolerant	2024-T3511, 2026-T3511, 2024-T4312, 6110-T6511	Lower wing stringers Fuselage/pressure cabin stringers
	Medium/high strength	7075-T73511, 7075-T79511, 7150-T6511, 7175-T79511, 7055-T77511, 7055-T79511	Fuselage stringers and frames, upper wing stringers, floor beams, seat rails

aluminium is consumed domestically, while the rest is exported, making India an Al-surplus country.

This deceptive surplus is essentially due to the very low per capita consumption of aluminium (under 1 kg) compared to the US and Europe (25–30 kg), and even China (3 kg). The domestic consumption pattern gives a clue to the reasons for this situation: the Power Industry (mainly overhead cables and other conductors) is the principal consumer of domestic aluminium (48 %). Other sectors lag far behind: Transport 15 %; Construction 13 %; Machinery and Equipment 7 %; Consumer Durables 7 %; Packaging: 4 %; Others 6 %.

From the foregoing list it is clear that only very small amounts of aluminium and its alloys made in India go into the aerospace industry, which itself is at an early stage of development, particularly in the private sector. The only primary aircraft manufacturer is the public sector Hindustan Aeronautics Limited (HAL), which produces military aircraft, either of its own design or under licence from a foreign

manufacturer. The other major aerospace organization is the Indian Space Research Organization (ISRO). This is a research establishment producing highly advanced Space Vehicles that serve as technology demonstrators. Nonetheless these have high commercial potential.

Several hundred ancillary units fabricate component parts for aerospace applications. Two examples are Hindalco-Almex Aerospace Ltd (HAAL), Aurangabad, and PMI Engineering Exports Pvt Ltd, Chennai. The aluminium alloys they state they are able to produce include AA2014, AA2618, AA5083, AA6061, AA7010, AA7020, AA7050, AA7075 and AA7175: in short, a considerable variety.

Besides industry, there is considerable aerospace R&D activity in other institutions in India, led by several prestigious DRDO laboratories. Missile development programs at several of these laboratories are supplemented by extensive work on manufacture and property studies for a range of Al alloys including Al-Li alloys (see Chap. 3 of this Volume) at the Defence Metallurgical Research Laboratory, Hyderabad.

Some CSIR labs like the National Aerospace Laboratory (NAL), Bengaluru, and the Regional Research Laboratory, Trivandrum, a few University Departments and Research Institutions like the celebrated Indian Institute of Science, Bengaluru, complete the R&D picture.

2.7.1 Gaps in Indian Aerospace Aluminium Technologies

A Delphi Expert Panel study on Vision 2019 for the Indian Aerospace Industry (published in EM India June/July 2010, p.38) has concluded that India is fast emerging as an international player in the aerospace industry owing to the low cost of labour, the growing manufacturing sector and the rising stock of its R&D capabilities.

Most experts seem to be expecting India to be a leading MRO (maintenance, repair and overhaul) hub in Asia, particularly for military aircraft. However, foreign organizations will continue to dominate the aerospace industry in India, since domestic companies will find it difficult to keep up, given the technological gaps between them and foreign companies. This situation could change if global players start their cutting edge R&D activities in India in association with Indian collaborators, subject to the Government enabling improved internet protocol (IP) protection.

The Indian aerospace sector has the potential to develop basic competencies in aircraft manufacture, at least in respect of development of small and medium aircraft. Demand for individual personalized flights is now increasing, so we could see a boom in private aircraft manufacturing in India. However, besides shortcomings in design, manufacturing and avionics capabilities, the availability of suitable materials is a serious problem limiting the growth of this sector.

Traditionally aluminium alloys have been the favoured materials for airframe structures. However, polymer matrix composites with high-specific strength and

modulus are serious challengers to the use of Al alloys, which inherently suffer from low stiffness. Significant improvements in specific elasticity cannot be achieved in conventional Al alloys. However, some publications have mentioned that a very light (density 2.1 g/cm^3) Al–Be alloy designated as AlBeMet AM162 can achieve a nearly four times higher specific modulus than the industry standard AA7075 alloy, with comparable strength and ductility but only half the fracture toughness and considerably increased toxicity (due to Be). Other possibilities for achieving high stiffnesses in Al alloys need to be explored.

Indian primary aluminium manufacture is beset with major technological challenges, particularly the high electricity consumption during reduction of alumina to aluminium by elevated-temperature electrolysis and large quantities of difficult to dispose of byproducts like “Red Mud” and extremely toxic “Spent Pot Lining (SPL)”.

An important issue is maintaining the high quality of products required for aerospace applications, while at the same time keeping the costs down to an acceptable level. Manufacturing units in the secondary sector are beset with the problem of variable quality and heterogeneity of the raw material—aluminium scrap—making it difficult to produce high quality end products.

2.7.2 Type Certification of Aluminium Alloys in India

Aluminium alloys type-certified for Indian aeronautical and missile applications by the Centre for Military Airworthiness and Certification (CEMILAC), Bengaluru, India are listed in Table 2.5. The significance of aero certification is that the design, production and qualification are established for all type-certified alloys. The large number of such alloys being type-approved denotes that aluminium alloy technologies and their production are maturing in India.

2.8 Summary and Conclusions

Because of the unique combination of light weight, high strength, and ease of fabrication, aluminium alloys have been the mainstay of the aerospace industry for nearly a century. Even though polymer-based composites have emerged in recent years as formidable competitors in this respect, the pre-eminence of Al alloys in civil transport aircraft remains hardly diminished, particularly in view of their near-infinite recyclability and flame-retarding properties, two issues that complicate and restrict the use of polymer-based materials.

However, serious consideration now needs to be paid to the well-known inadequacies of aluminium alloys, such as the high cost and environmental issues

Table 2.5 Aluminium alloys type-approved by CEMILAC, India

Sl. No.	Nomenclature	Issued to	RCMA [*]	TA No. ^{**}
1.	Al alloy AG5MC Sheets	M/s Hindustan Al Corp. U.P.	A/C	47
2.	Al alloy AL-5 for Castings	M/s HAL, Koraput	KPT	142
3.	Extruded bars AG5MC	Ordnance Factory, Nagpur	F&F	251
4.	Al Sheet Grade INDAL "IS"	M/s Indian Al Co., Kolkatta	NSK	347
5.	Rivet Wire Gr V-65	Indian Ordnance Factory, Nasik	NSK	348
6.	INDAL-B26SW	INDAL-B26SW	NSK	367
7.	INDAL-3S-0	M/s Indian Al Co., Kolkatta	NSK	371
8.	INDAL-M57S-0	M/s Indian Al Co., Kerala	NSK	396
9.	INDAL-24SWG	M/s Indian Al Co., Kerala	NSK	399
10.	Bars 5052 (ASM)	M/s Hindustan Al., U.P.	NSK	420
11.	AL-19 for Castings	M/s HAL, Koraput	KPT	444
12.	B51S	M/s Indian Al Co., Kolkatta	A/C	491
13.	Al Sheet '2S'	M/s Indian Al Co., Kolkatta	NSK	492
14.	Castings AL-9, T4, T5	M/s HAL, Koraput	KPT	517
15.	AK-6 Stampings	M/s HAL, Koraput	KPT	588
16.	HE-15A Extruded Bars	Ordnance Factory, Nagpur	F&F	617
17.	L-77 Extruded Bars	M/s Indian Al Co., Kerala	F&F	618
18.	AU4G1 Extruded Bars	M/s Indian Al Co., Kerala	F&F	668
19.	AU2GN Extruded Bars	M/s Indian Al Co., Kerala	F&F	669
20.	AMG-2	M/s Indian Al Co., Kerala	NSK	688
21.	AK-4-1	M/s Indian Al Co., Kerala	NSK	689
22.	Gr. BRAZHIMS 10-3-1.5	M/s Indoswe Engg. Ltd., Pune	NSK	690
23.	AK-8	M/s Indian Al Co., Kerala	NSK	691
24.	Gr BRZHN-10-4.4	M/s Indoswe Engg. Ltd., Pune	NSK	692
25.	HE 15A(ST)	Ordnance Factory, Nagpur	F&F	724
26.	HE 20A (Extruded Bars)	Ordnance Factory, Nagpur	F&F	736
27.	AG5MC Bars	Ordnance Factory, Nagpur	F&F	751
28.	Forgings of HE-15A	M/s HAL F&F Division, Bengaluru	F&F	950
29.	Extruded Bars 7010A ST	M/s Ordnance Factory, Nagpur	F&F	984
30.	AU4G1, Extruded flats	M/s Ordnance Factory, Nagpur	F&F	1327
31.	5086 Extruded Bars	M/s Ordnance Factory, Nagpur	F&F	1330
32.	Al-356 Investment Castings	M/s IPCL, Gujarat	MAT	1517
33.	HF 15, T652 Forgings	M/s DSPL, Hyderabad	MAT	1705
34.	HF 15, T652 Forged Flats	M/s DSPL, Hyderabad	MAT	1728
35.	AA2219-T8511	Ordnance Factory, Nagpur	F&F	1729
36.	HF 15, T652 Forgings	M/s MMBL, Hyderabad	MAT	1833

* Regional Centre for Military Airworthiness

** Type Approved

associated with their production. The most frustrating limitation is their inherently low elastic modulus, a problem that defies a satisfactory solution by the metallurgist's staple of microstructural modification. Novel thinking is required to address this problem.

Inadequate facilities in India for the production of high-quality components required by the aerospace industry are other issues that need to be urgently remedied by government and private initiatives.

Acknowledgments The authors wish to thank several colleagues from DRDO whose inputs have become part of this chapter. They particularly would like to thank Dr. Amol A. Gokhale, Dr. Ashim K. Mukhopadhyay, Mr. V.P. Deep Kumar, Dr. Shirish Kale and Mr. Sanjay Chawla. Two of the authors (PRB and NEP) are thankful to CEMILAC and DRDO for support and funding.

References

1. Campbell FC (2006) Manufacturing technology for aerospace structural materials. Butterworth-Heinemann Publication, An Imprint of Elsevier Publications, New York, NY, USA
2. Davis JR (1994) Aluminum and aluminum alloys. ASM Speciality Handbook, ASM International, Materials Park, OH, USA
3. Polmear IJ (2004) Aluminium alloys—a century of age hardening. In: Nie JF, Morton AJ, Muddle BC (eds) Materials forum, vol 28. Institute of Materials Engineering Australasia Limited, Melbourne, Australia
4. Starke EA Jr, Staley JT (1996) Application of modern aluminum alloys to aircraft. *Prog Aerospace Sci* 32:131–172
5. Vasudevan AK, Doherty RD (1989) Aluminum alloys—contemporary research and applications. Academic Press, Inc, Cambridge, MA, USA
6. Polmear IJ (2006) Light alloys. Butterworth-Heinemann Publication, An Imprint of Elsevier Publications, New York, NY, USA
7. Wanhill RJH (1994) Fatigue and fracture properties of aerospace aluminium alloys. In: Carpinteri (ed) Handbook of fatigue crack propagation in metallic structures. Elsevier Science Publishers, Amsterdam, The Netherlands, pp 247–279
8. Wanhill RJH (1994) Flight simulation fatigue crack growth testing of aluminium alloys. Specific issues and guidelines. *Int J Fatigue* 16(2):99–110
9. Hatch John E (1988) Aluminum—properties and physical metallurgy. American Society for Metals, Metals Park, OH, USA
10. NTIS (1973) Plane strain fracture toughness (KIC) data hand book for metals, USA
11. Wanhill RJH (1994a) Fatigue and fracture of aerospace aluminium alloys: a short course. National Aerospace Laboratory NLR Technical Publication 94034, Amsterdam, The Netherlands
12. Wanhill RJH, Byrnes RT, Smith CL (2011) Stress Corrosion cracking (SCC) in aerospace vehicles. In: Raja VS, Shoji T (eds) Stress corrosion cracking. Theory and practice. Woodhead Publishing Limited, Cambridge, UK, pp 608–650
13. Eswara Prasad N, Gokhale Amol A, Wanhill RJH (eds) (2014) Aluminum–Lithium alloys: processing, properties and applications. Elsevier Inc., Oxford, UK

Some Useful Data Handbooks

1. Metallic materials properties development and standardization (MMPDS), Battelle Memorial Inst. Columbus, OH, USA, 2003
2. Kaufman JG (1999) Properties of aluminum alloys—tensile, creep and fatigue data at high and low temperatures. ASM International, Materials Park, OH, USA
3. Aerospace structural metals handbook, mechanical properties data center. A DOD Materials Information Centre, Battelle Columbus Laboratories, OH, USA, vol 3, 198
4. Gupta Balram et al (1996) Aerospace materials, vol 3. S. Chand & Co Ltd., India
5. Source book on selection and fabrication of aluminum alloys. American Society for Metals, Metals Park, OH, USA, 1978
6. Davis JR (1994) Aluminum and aluminum alloys. ASM Speciality Handbook, ASM International, Materials Park, OH, USA

Chapter 3

Aluminium–Lithium Alloys

N. Eswara Prasad, Amol A. Gokhale and R.J.H. Wanhill

Abstract This chapter summarises the development and limitations of the first and second generation Al–Li alloys, and then discusses the recent developments leading to the third generation alloys. Emphasis is placed on the physical metallurgy of Al–Li alloys, progressive development of the three generations of these alloys, and finally the strategies for obtaining improved property combinations via various microstructural modifications closely linked to multistage processing. The way forward for Indian development of Al–Li alloys is also briefly discussed.

Keywords Aluminium–Lithium alloys · Mechanical properties · Fatigue · Fracture · Corrosion · Applications

3.1 History of Alloy Development

Interest in aluminium–lithium (Al–Li) alloys arises from the important consideration that as the lightest metal, lithium additions to Al reduce its density ($\sim 3\%$ decrease per every wt%) and increase the elastic modulus ($\sim 6\%$ increase per every wt%). The increases in *specific* strength (strength/density) and *specific* stiffness (E/density) combine with good fatigue and cryogenic properties to offer possibilities for the use of Al–Li alloys in aerospace structural applications, including fuel tanks in launch vehicles, like the external tank of the US Space Shuttle [1–3].

N. Eswara Prasad (✉)
DMSRDE, DRDO, Kanpur, India
e-mail: nep@dmsrde.drdo.in; neswarap@rediffmail.com

A.A. Gokhale
Indian Institute of Technology Bombay, Mumbai, India
e-mail: gokhale@iitb.ac.in; amol_gokhale@yahoo.in

R.J.H. Wanhill
Emmeloord, Flevoland, The Netherlands
e-mail: rjhwanhill@gmail.com

Developmental activities started from the 1920s, but the first commercial alloy AA2020 (Al–1.1Li–4.5Cu–0.5Mn–0.2Cd) was introduced only in 1958. This alloy was successfully used for the wing skins and tails of the Northrop RA-5C Vigilante aircraft, but concerns about its fracture toughness led to its withdrawal in the 1960s. In the same time period, research work in the former Soviet Union led to the development of VAD-23 with the nominal composition Al–1.1Li–5.3Cu–0.6Mn–0.17Cd and 1420 (Al–2.0Li–5.3 Mg–0.5Mn). All three alloys are customarily referred to as first generation alloys.

In the 1970s the potential threat of replacement of aluminium alloys by carbon fibre composites resulted in extensive research work on a new, second generation of Al–Li alloys. Development of these alloys has been largely unsuccessful owing to unacceptable degrees of property anisotropy, low short transverse properties and thermal instability. Work began in the late 1980s and early 1990s on a third generation of Al–Li alloys, and developments are ongoing. These newer alloys are candidates for widespread replacement of conventional aluminium alloys in aerospace structures. Table 3.1 lists typical compositions of some Al–Li alloys from all three generations [1].

3.2 Aircraft Structural Property Requirements

Figure 3.1 illustrates the engineering property requirements for several of the main structural areas in a transport aircraft, namely (i) Fuselage and Pressure Cabins, (ii) Wings and (iii) Empennage. The engineering properties required for these aircraft structures are strength (TS, CYS), stiffness (E), damage tolerance (DT: fatigue, fatigue crack growth, fracture toughness), and corrosion (general and stress corrosion). Also very important is the material density (ρ), reflected in weight savings per se and the specific strength and stiffness.

Figure 3.2 summarises calculations of aircraft structural weight savings due to property improvements [2], showing that a lower density is the most effective way of reducing the overall weight of an aircraft structure. Next are enhancements in strength and stiffness, which combine with reduced density to give improvements in specific strength and stiffness. Finally, improvements in damage tolerance (DT) properties have the least potential for saving weight, though even small amounts of weight savings can be important.

Additions of lithium to aluminium alloys decrease the density and increase the stiffness, thereby having a synergistic effect on the specific stiffness (E/ρ). Thus Al–Li alloy development may already be successful from an engineering property viewpoint—certainly with respect to equivalent conventional alloy products—if other properties are simply maintained. This is attractive to commercial alloy producers, since there is the possibility of obtaining families of Al–Li alloys to replace conventional alloys for a variety of applications.

Table 3.1 Compositions and densities of commercial Al–Li alloys [1]

Alloy	Composition (all elements in wt%)										Density, ρ (g/cm^3)	Introduction /Reference(s)	
	Li	Cu	Mg	Ag	Zr	Sc	Mn	Zn	Other elements				
<i>First generation</i>													
2020	1.2	4.5					0.5					2.71	Alcoa (1958)
1420	2.1		5.2		0.11							2.47	Soviet (1965)
1421	2.1		5.2		0.11	0.17						2.47	Soviet (1965)
<i>Second generation (Li \geq 2 %)</i>													
2090	2.1	2.7			0.11							2.59	Alcoa (1984)
2091	2.0	2.0	1.3		0.11							2.58	Pechiney (1985)
8090	2.4	1.2	0.8		0.11							2.54	EAA (1984)
1440	2.4	1.5	0.8		0.11							2.55	Soviet 1980s
1441	1.95	1.65	0.9		0.11							2.59	Soviet 1980s
1450	2.1	2.9			0.11							2.60	Soviet 1980s
1460	2.25	2.9			0.11	0.09						2.60	Soviet 1980s
<i>Third generation (Li < 2 %)</i>													
2195	1.0	4.0	0.4	0.4	0.11							2.71	LM/Reynolds (1992)
2196	1.75	2.9	0.5	0.4	0.11		0.35 max	0.35 max				2.63	LM/Reynolds/McCook Metals (2000)
2297	1.4	2.8	0.25 max		0.11		0.3	0.5 max				2.65	LM/Reynolds (1997)
2397	1.4	2.8	0.25 max		0.11		0.3	0.10				2.65	Alcoa (1993)
2098	1.05	3.5	0.53	0.43	0.11		0.35 max	0.35				2.70	McCook Metals (2000)
2198	1.0	3.2	0.5	0.4	0.11		0.5 max	0.35 max				2.69	Reynolds/McCook Metals/Alcan (2005)
2099	1.8	2.7	0.3		0.09		0.3	0.7				2.63	Alcoa (2003)

(continued)

Table 3.1 (continued)

Alloy	Composition (all elements in wt%)										Density, ρ (g/cm^3)	Introduction /Reference(s)
	Li	Cu	Mg	Ag	Zr	Sc	Mn	Zn	Other elements			
2199	1.6	2.6	0.2		0.09		0.3	0.6			2.64	Alcoa (2005)
2050	1.0	3.6	0.4	0.4	0.11		0.35	0.25 max			2.70	Pechiney/Alcan (2004)
2296	1.6	2.45	0.6	0.43	0.11		0.28	0.25 max			2.63	Constellium Alcan (2010)
2060	0.75	3.95	0.85	0.25	0.11		0.3	0.4			2.72	Alcoa (2011)
2055	1.15	3.7	0.4	0.4	0.11		0.3	0.5			2.70	Alcoa (2011)
2065	1.2	4.2	0.50	0.30	0.11		0.40	0.2			2.70	Constellium (2012)
2076	1.5	2.35	0.5	0.28	0.11		0.33	0.30 max			2.64	Constellium (2012)



Fig. 3.1 Engineering property requirements for a transport aircraft. See the text for the abbreviations [1]

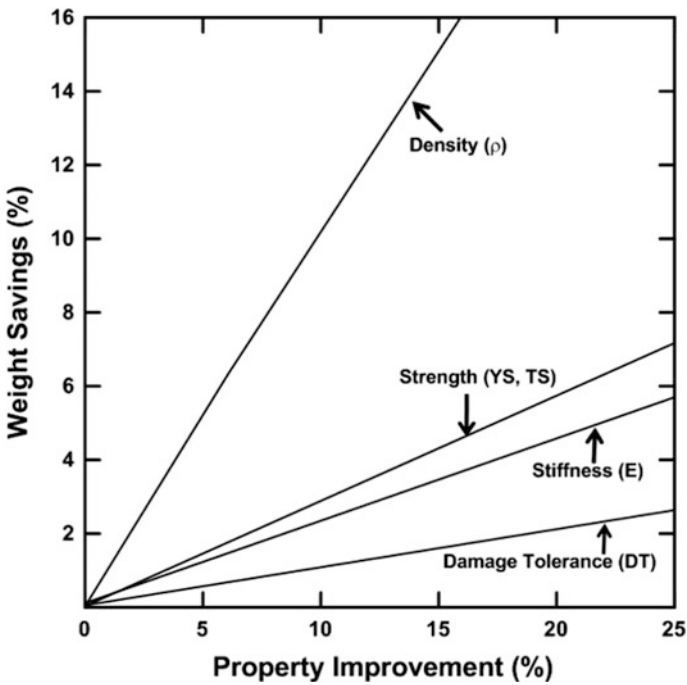


Fig. 3.2 Potential weight savings for aircraft structures owing to various property improvements [2]

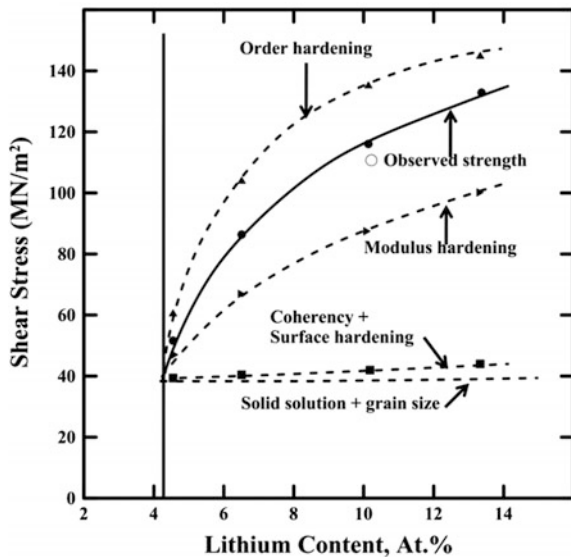
3.3 Physical Metallurgy of Al–Li Alloys

The presence of lithium atoms in an aluminium matrix gives only a small degree of solid solution strengthening, owing principally to atomic size differences. However, lithium substantially increases the elastic constants of the aluminium–lithium solid solution even though the values of its own constants are noticeably lower than those of aluminium [4, 5].

The general strength in Al–Li alloys is derived from the presence of large volume fractions of the coherent δ' (Al_3Li) phase. The δ' phase has a high intrinsic modulus due to its ordered nature, and this contributes to the high values of elastic modulus in these alloys. It should be noted that when lithium is in solid solution the elastic constants depend on both atomic interactions and interatomic potential. However, when lithium is present in a precipitated second phase the elastic constants depend on both the volume fraction and intrinsic modulus of the second phase [4]. Strength increases owing to the presence of δ' precipitates are obtained via several mechanisms. Figure 3.3 summarises the contributions of various mechanisms to the overall strength in terms of the shear stress for slip to occur. The net shear stress (reflected in the variation of observed strength in Fig. 3.3) is the weighted average of all the contributing strengthening mechanisms.

Order hardening and modulus hardening contribute the most, while coherency and surface hardening contribute relatively less. Order hardening makes a major contribution to strength owing to the creation of antiphase boundaries (APBs) [6, 7]. In order to eliminate the extra energy required to create the antiphase boundary (APB), the dislocations in Al–Li alloys move in pairs connected by a region of antiphase boundary such that passage of the second dislocation restores the disorder

Fig. 3.3 Contributions of various mechanisms to strengthening by δ' precipitates in Al–Li alloys [6, 7]



caused by the first [6, 7]. The critical resolved shear stress (τ_{CRSS}) for such a process was found to be [8]:

$$\tau_{\text{CRSS}} \propto (\gamma_{\text{APB}})^{3/2} \cdot r^{1/2} \cdot f^{1/2}. \quad (3.1)$$

In this expression γ_{APB} is the antiphase boundary energy of the δ' (Al_3Li) particles, r is the mean radius, and f is the volume fraction of the precipitate particles. Once sheared, the ordered precipitate particles would result in reduced contributions from order strengthening. This is essentially due to a reduction in cross-sectional area of the precipitate particles upon initial shearing. If \mathbf{n}_d dislocations, each having a Burger's vector \mathbf{b}_v , shear a given particle and we assume shearing to take place across the diameter of the precipitate particle, then τ_{CRSS} for continued shearing becomes

$$\tau_{\text{CRSS}} \propto (\gamma_{\text{APB}})^{3/2} \cdot f^{1/2} \left[(r - \mathbf{n}_d \mathbf{b}_v)^{1/2} \right]. \quad (3.2)$$

Thus a reduction in the critical resolved shear stress (τ_{CRSS}) becomes significant, making further slip on that particular plane conducive. Hence slip is favoured to become planar and the particular plane on which repeated slip occurs gradually becomes work-softened. Al–Li alloys that are artificially aged to the peak strength condition tend to exhibit such planar slip deformation behaviour [9–11], which is detrimental to some engineering properties, notably ductility and fracture toughness.

Besides order/APB strengthening, the contributions to modulus hardening were also found to be significant for Al–Li alloys [7] and can be estimated as [12]

$$\Delta\sigma = \frac{\Delta G}{2\pi^2} \left[\frac{3\Delta GI}{G_m b v} \right]^{1/2} \left[0.8 - 0.143 \ln \left[\frac{r}{b v} \right] \right]^{3/2} r^{1/2} f^{1/2} \quad (3.3)$$

where ΔG is the difference in the shear modulus values of the matrix (G_m) and the precipitate particles.

Apart from δ' (the major strengthening phase in second generation Al–Li alloys), other co-precipitates contribute to and control the strength, deformation and fracture of Al–Li alloys. They include θ' (Al_2Cu , the major strengthening phase in first generation Al–Li alloys); T_1 (Al_2CuLi), the major strengthening phase in third generation Al–Li alloys; and S/S' (Al_2CuMg), whose presence leads to significant slip homogenisation. There is also the β' (Al_3Zr) phase, which is the primary phase that pins the high angle grain boundaries and is therefore important in controlling and restricting recrystallisation and subsequent grain growth.

All other equilibrium phases are undesirable as they have been found to promote low energy intergranular fracture and result in low ductilities and inferior damage tolerant properties. Hence the following phases are kept to a minimum— δ (AlLi), T_2 (Al_6CuLi_3), T_B ($\text{Al}_{15}\text{Cu}_8\text{Li}_2$) and Ω (hexagonal thin plates in high Cu:Mg alloys).

For a summary of the various phases present in different Al–Li alloys see Figs. 3.4 and 3.5. It is evident that the microstructural situations can be complex for Al–Li–Cu–Mg–Zr alloys, including the Al–Li–low-Cu–high-Mg–Zr third generation alloys that are of most commercial interest. Thus it is no easy task for commercial processing to optimise the microstructures with respect to obtaining a good balance of engineering properties for these alloys.

3.4 Processing Technologies

Commercial and semi-commercial Al–Li alloys in different temper conditions are produced using the following process technologies:

1. Melting in fuel-fired reverberatory furnaces in air atmosphere (adding fluxes to the melt to reduce atmospheric oxidation), followed by melt degassing and filtration and Direct Chill (DC) casting into slabs and billets. These processes are much more challenging to carry out owing to high reactivity of lithium in the molten alloys [1, 13–19].
2. Thermomechanical working of the DC cast ingots and slabs by hot and cold working (mainly by rolling, forging and extrusion), employing workability/processing

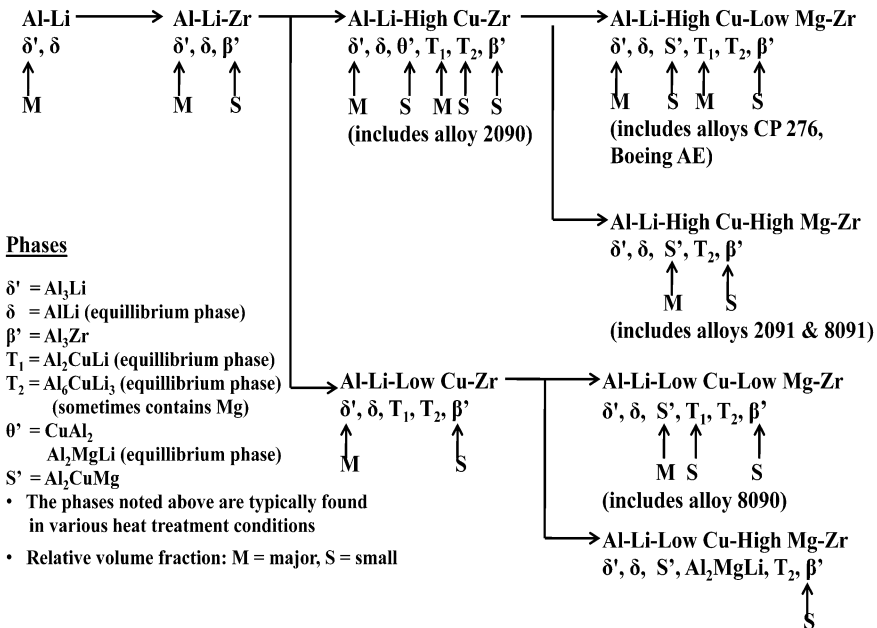


Fig. 3.4 Various precipitate phases that form in different Al–Li alloys depending on the concentrations of alloying elements [1]

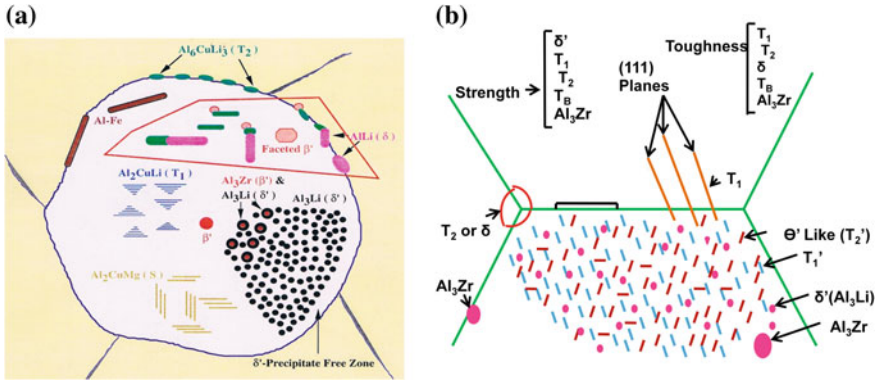


Fig. 3.5 Schematics of typical microstructural features in **a** second and **b** third generation Al–Li alloys [1]

maps [1, 20–26]. The thermomechanical processing consists of well-defined multiple steps [1] since, as mentioned in Sect. 3.3, it is no easy task to optimise the microstructures for a good balance of engineering properties.

3. Al–Li alloy products in near net shapes can be produced by superplastic forming [1, 27–30].
4. Various metal joining techniques can be used, including conventional gas tungsten arc (GTA) welding for the specially developed Weldalite™ family of Al–Li alloys and the third generation low-Li alloy 2195; laser beam welding (LBW), friction stir welding (FSW), and friction welding [1, 31–36].

3.5 Mechanical Properties

The mechanical properties of Al–Li alloys (overall strength, deformation (quasi-static, dynamic and cyclic) and fracture (in corrosive and noncorrosive environments)) are governed by metallurgical variables, including chemical composition; microstructure (strengthening precipitates, precipitate free zones (PFZs)) and grain boundary characteristics; the processing conditions, including thermal (ageing) and thermomechanical (ageing with cold work/stretch) treatments; and finally the shape, size and orientation of the product(s) [1, 37, 38]. Some of the salient features of the mechanical properties of Al–Li alloys are briefly discussed in the following sections.

3.5.1 Tensile Properties

The first generation Al–Li alloys suffered from low ductilities and the second generation from large degrees of anisotropy in yield and ultimate tensile strengths, especially very low yield strengths in the direction 45° from the rolling direction and severe delamination (low ductilities and work hardening exponents) in the through-thickness directions [37–40]. The development of third generation Al–Li alloys with lower lithium contents and novel processing techniques have made it possible for these alloys to possess tensile properties in both in-plane and through-thickness directions that are comparable to or even better than those of the traditionally used aluminium alloys [22].

3.5.2 Fatigue Properties

Low cycle fatigue (LCF)

The low cycle fatigue (LCF) behaviour of Al–Li alloys is primarily influenced by microstructural characteristics and to a lesser extent by crystallographic texture. Microstructural influences are the lithium content; volume fraction, size and distribution of the major strengthening precipitates; the degrees of ageing and recrystallisation; and incorporation of tensile stretching with or without natural ageing. The only available LCF data are for first and second generation alloys, see Table 3.2 and Fig. 3.6. These data indicate that the LCF properties of Al–Li alloys are generally inferior to those of conventional aluminium alloys [46, 47, 51].

High cycle fatigue (HCF)

The HCF resistance of Al–Li alloys is enhanced by solid solution strengthening and coarsening of δ' precipitates. Additional contributions come from thermomechanical treatments involving artificial ageing and tensile pre-straining, or cold work prior to artificial ageing. The available data for all three generations of Al–Li alloys show that their HCF properties are generally equivalent to, but not significantly better than those of conventional alloys. This is notably the case for notched fatigue behaviour, e.g. Fig. 3.7, and is of major importance for aerospace structures [48–51].

Fatigue crack growth (FCG)

Most of the available data for Al–Li FCG have been obtained for second generation alloys. These data showed that the Al–Li FCG rates were often lower than those of equivalent conventional alloys [52]. The main reason for this is ‘crack tip shielding’, i.e. the development of rough fracture surfaces causing high levels of crack closure in the wakes of the fatigue cracks and concomitant reductions in crack driving force. Unfortunately, this behaviour was associated with unacceptably high anisotropic mechanical properties.

Table 3.2 Some mechanical properties of Al–Li alloys

Alloy	Tensile properties at room temperature			Low cycle fatigue life power—law constants			Fracture toughness K_{Ic} (MPa m ^{1/2})	Ref(s).
	0.2 % YS (MPa)	UTS (MPa)	El. (%)	σ'_f (MPa)	ϵ'_f	–b		
Al (99.98 %)	–	–	–	–	0.87	–	0.62	[41]
Al–0.7 Li	45	65	26	–	0.42	–	0.6	[41]
Al–2.5Li	Underaged	67	157	33	>10 ^{3a}	–	2.38 ^a	[41]
	Peak aged	185	220	2.6	2.1 ^b	–	0.8 ^b	[41]
Al–3Li+Mn	Underaged	314	351	2.3	0.059	–	0.76	[42]
	Peak aged	342	373	1.4	0.146	–	0.96	[42]
First generation								
2020 plate	Underaged	333–500	–	15–17	–	–	27–19	[43]
	Peak aged	530	–	3–6	–	–	14	
	Overaged	460–420	–	6–9	–	–	16	
2020-T651	TMP (PR)	530	567	5	97 ^a	–	1.6 ^a	[44]
	TMP (UR)	462	509	12	0.038 ^a	–	0.451 ^b	
					250 ^a	–	1.56 ^a	
					0.058 ^b	–	0.448 ^b	

(continued)

Table 3.2 (continued)

Alloy	Tensile properties at room temperature			Low cycle fatigue life power—law constants			Fracture toughness K_{Ic} (MPa m ^{1/2})	Ref(s).	
	0.2 % YS (MPa)	UTS (MPa)	El. (%)	σ'_f (MPa)	ϵ'_f	-b			-c
Second generation (Li \geq 2 %)									
2091	300–350							[45]	
8090-T81 plate	300–340						25–30 (L-T, T-L); 12–16 (S-L, S-T)	[45]	
8090-T8E51 plate (12.5 mm)	L	485	555	5.4	887 ^a 575 ^b	5.5 ^a 0.06 ^b	0.093 0.035 ^b	1.15 ^a 0.46 ^b	[37,46, 47]
	L+45	393	478	11.5	662 ^a 501 ^b	2.7 ^a 0.012 ^b	0.67 ^a 0.037 ^b	1.02 ^a 0.56 ^b	
	LT	467	534	7	832 ^a 562 ^b	1.77 ^a 0.096 ^b	0.8 ^a 0.042 ^b	0.95 ^a 0.52 ^b	
8090 sheet	Underaged T3	350–360							[37]
	Peak aged T6	450–500							
	Damage tolerant T8	360–380							

(continued)

Table 3.2 (continued)

Alloy	Tensile properties at room temperature			Low cycle fatigue life power-law constants			Fracture toughness K_{Ic} (MPa m ^{1/2})	Ref(s).
	0.2 % YS (MPa)	UTS (MPa)	El. (%)	σ'_f (MPa)	ϵ'_f	-b		
Third generation (Li < 2 %)								
2198 sheet	L	324	442	13				[49]
	L+45	266	363	21				
	LT	300	416	15.4				
2050-T84 plate (51–76 mm)		420–460					28–30 (L-T, T-L) 22–24 (S-L, S-T)	[51, 54]
	2060-T8E33 plate (51–76 mm)	450–500					29–30 (L-T, T-L) 24 (S-L)	[22, 54]

^a Low strain amplitudes (Hypo-transition region)

^b High strain amplitudes (Hyper-transition region)

Fig. 3.6 Low cycle fatigue life as a function of plastic strain amplitude (Coffin-Manson Power law) for various Al-Li alloys. These data are compared with those of the conventional alloys AA2024-T4 and AA7075-T6 [46, 47, 51]

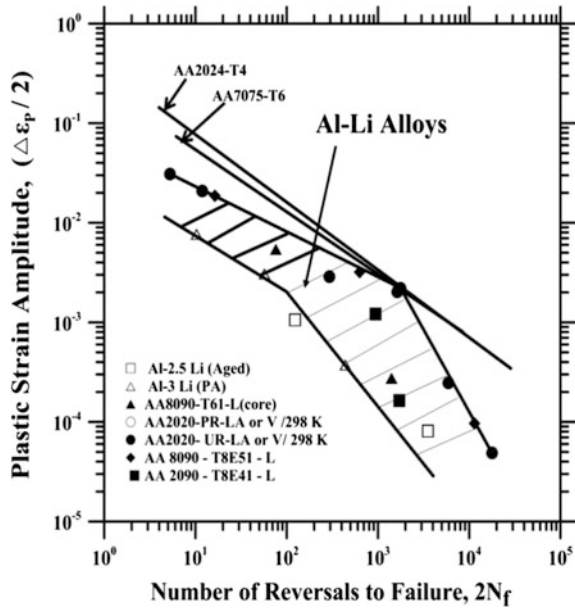
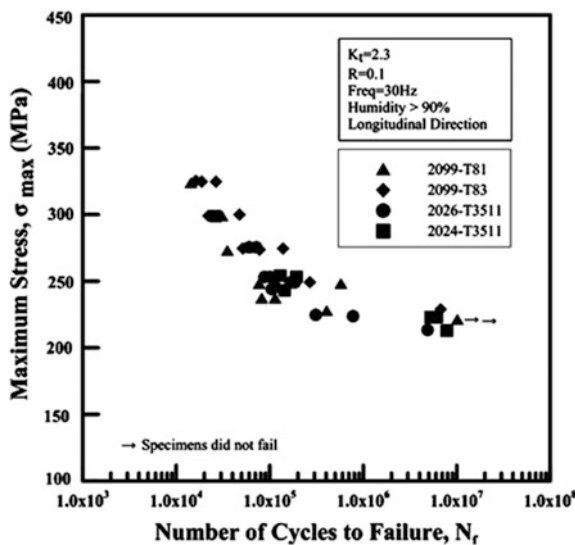


Fig. 3.7 High cycle fatigue life data as a function of maximum applied stress for various third generation Al-Li alloys compared with data for the conventional alloys AA2024-T3511 and AA2026-T3511 [50]



FCG data for third generation Al-Li alloys are becoming more available [52]. The anisotropy problems associated with second generation alloys have been eliminated or greatly alleviated in third generation alloys, resulting in much less rough FCG fracture surfaces. Nevertheless, third generation Al-Li alloys appear to have generally better FCG properties compared to those of the conventional Al alloys they are intended to replace, e.g. Fig. 3.8.

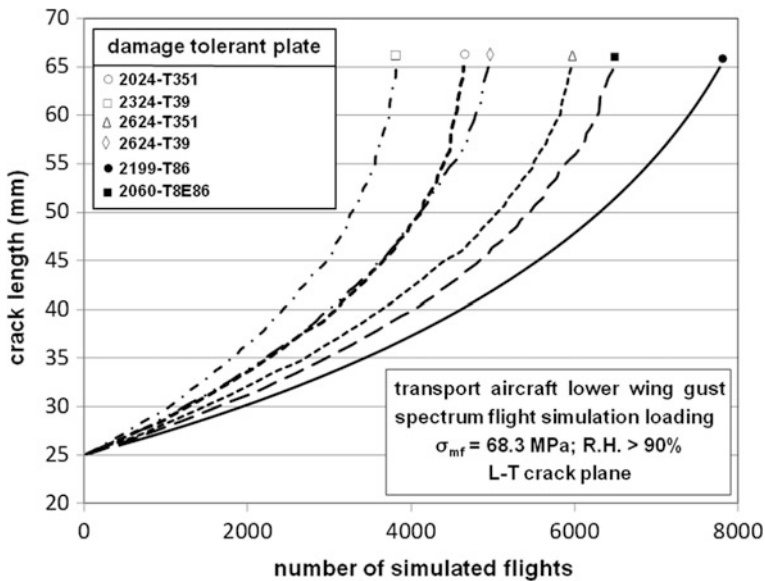


Fig. 3.8 Flight simulation FCG curves comparing the third generation damage tolerant AA2199 and AA2060 Al–Li alloys with equivalent conventional alloys: plate thickness 12 mm [52]

3.5.3 Fracture Toughness and R-curves

Fracture toughness is a critical property when selecting materials for aerospace applications, and has been a major limitation for the first and second generation Al–Li alloys. In particular, the short transverse (S–L and S–T) plane strain fracture toughness were too low, e.g. the values for AA 8090–T81 plate in Table 3.2. This problem has been solved for third generation plate alloys (see the data for AA2050 and AA2060 in Table 3.2).

Plane stress fracture toughness and R-curve data for third generation sheet and plate materials consistently show similar or better properties than those of equivalent conventional alloys at similar strength levels [53]. R-curve examples are given in Fig. 3.9: the third generation alloys AA2060 and AA2199 are superior to the conventional AA2X24 alloys. Also shown is the much inferior performance of the second generation Al–Li alloy AA 8090–T86, which was also in a damage tolerant temper.

3.6 Corrosion and Stress Corrosion Cracking

Corrosion

The first generation Al–Li alloys had adequate corrosion resistance, with no service problems. However, this changed for the second generation alloys, which were

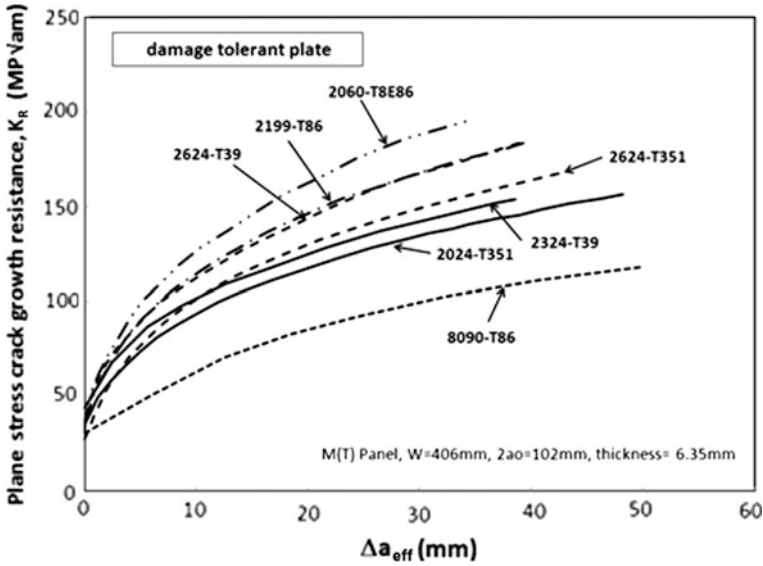


Fig. 3.9 Comparisons of R-curves for third generation AA2060 and AA2199 Al–Li damage tolerant plate alloys, conventional damage tolerant AA2X24 alloys and the second generation AA8090 Al–Li plate alloy [53]

found to be susceptible to intergranular corrosion (IGC), especially at higher Cu and Mg contents and with increased ageing: increasing susceptibility in the order: Underaged (UA) < Peak Aged (PA) < Overaged (OA) [54].

Available data on the third generation Al–Li alloys indicate that their IGC susceptibility can be significantly less than for the second generation alloys, particularly when ageing is done at lower temperatures [54]. The addition of Zn to these third generation Al–Li alloys, see Table 3.1, also improves the corrosion resistance [22]. Currently, it appears that optimum corrosion resistance, notably against exfoliation corrosion, is obtained from an intermediate regime of ageing, including peak aged tempers [54].

Stress corrosion cracking

Stress corrosion cracking (SCC) has also been a problem for the second generation Al–Li alloys, and unlike the IGC susceptibility the SCC resistance decreased with increased ageing: UA > PA > OA [54].

A similar trend has been found for third generation alloys, but these alloys benefit from a lower Li content and additions of Zn and Ag (see Table 3.1) such that in PA tempers they are capable of providing SCC resistances better than those of equivalent conventional Al alloys [54]. There is a caveat here: this conclusion is limited to product thicknesses up to about 30 mm. For thicker products it will likely be more difficult to apply the required thermomechanical processing and multistage ageing practices needed to optimise the grain boundary microstructures and hence the SCC resistances [54].

3.7 Current Indian Scenario

The Indian efforts in development of Al–Li products and components are summarised here

- (i) Extensive R&D at the Defence Metallurgical Research Laboratory, Hyderabad, during 1985–2000, establishing (a) Melting and casting technologies at 50 kg capacity, (b) Processing using process maps, (c) Microstructure /texture—processing—property relationships and (d) production of extrusions, forgings and clad sheets—all for the alloy 1440, equivalent to AA 8090. There has also been limited industrial level production of 1440 components for the Indian Light Combat Aircraft, using the large scale melting, casting and processing facilities of VIAM, Moscow.
- (ii) Concurrent R&D by IISc. and HAL (Foundry/Forge), Bangalore, with emphasis on optimization of thermal and thermomechanical treatments for improved corrosion and stress corrosion cracking resistances—again on alloys equivalent to AA 8090 and its products.
- (iii) Establishing welding technologies for Al–Li products.
- (iv) Detailed microstructural analyses, mechanical properties anisotropy, fatigue power law relationships, fracture toughness (including under mixed-mode loading) and fatigue crack growth (including Constant Amplitude, Random and Flight Spectrum Loading).
- (v) Most recently, there are initiatives to melt, cast and process third generation Al–Li alloy flat products at MIDHANI, Hyderabad, for the Indian Space Programme.

3.8 Conclusions

The third generation Al–Li alloys are actual and potential candidate materials for replacing the traditionally used Al alloys and competing with carbon fibre composites for applications in aerospace structures. Intense international scientific research, development and commercial production efforts have addressed the most outstanding problems associated with Al–Li alloy deployment in various aerostructural applications. This has meant establishing (i) production technologies for large-scale melting and casting Al–Li alloys with optimised chemistry, (ii) advanced processing based on process modelling, (iii) thermal and thermomechanical treatments to achieve the desired microstructures for optimum property combinations, and (iv) fabrication and joining technologies, including superplastic forming and innovative welding techniques.

Acknowledgments The authors wish to thank the many contributors to the monograph on Al–Li alloys (Ref. [1]) upon which the present chapter is based. In particular, they are most grateful to Professor Edgar A. Starke, Jr., Dr. Gary H. Bray and Michael Niedzinski for their expert advice and assistance that indeed enabled publication of the monograph, and hence the present chapter.

One of this chapter's authors (NEP) is most grateful to Dr. P. Rama Rao and Dr. Baldev Raj for their constant encouragement and valuable inputs to the present Source Book Volumes.

References

1. Eswara Prasad N, Gokhale AA, Wanhill RJH (eds) (2014) Aluminum–Lithium alloys: processing, properties and applications. Elsevier Inc., Oxford, UK
2. Ekvall JC, Rhodes JE, Wald GG (1982) Methodology for evaluating weight savings from basic material properties. In: Proceedings on design of fatigue and fracture resistant structures, ASTM STP 761. American Society for Testing and Materials, Philadelphia, USA, pp 328–341
3. Peel CJ, Evans B, Baker CA, Bennet DA, Gregson PJ, Flower HM (1983) The development and application of improved aluminum-lithium alloys. In: Sanders TH Jr, Starke EA Jr (eds) Proceedings 2nd international conference aluminum–lithium alloys II. The Metallurgical Society of AIME, Warrendale, USA, pp 363–392
4. Sankaran KK, Grant NJ (1980) The structure and properties of splat-quenched aluminium alloy 2024 containing Lithium additions. *Mater Sci Eng A* A44:213–227
5. Webster D (1986) Temperature dependence of toughness in various aluminium–lithium alloys. In: Baker C, Gregson PJ, Harris SJ, Peel CJ (eds) Proceedings on 3rd international conference aluminium–lithium alloys. The Institute of Metals, London, UK, pp 602–609
6. Vasudevan AK, Doherty RD (1987) Grain boundary ductile fracture in precipitation hardened aluminum alloys. *Acta Metall* 35:1193–1218
7. Noble B, Harris SJ, Dinsdale K (1982) Yield characteristics of aluminium-Lithium alloys. *Metal Sci J* 16:425–430
8. Palmer IG, Miller WS, Lloyd DJ, Bull MJ (1986) Effect of grain structure and texture on mechanical properties of Al-Li base alloys. In: Baker C, Gregson PJ, Harris SJ, Peel CJ (eds) Aluminium–lithium alloys III, Proceedings of 3rd international conference on aluminium–lithium alloys. The Institute of Metals, London, UK, pp 565–575
9. Sanders TH, Starke EA (1982) The effect of slip distribution on the monotonic and cyclic ductility of Al-Li binary alloys. *Acta Metall* 30:927–939
10. Gregson PJ, Flower HM (1984) δ' precipitation in Al-Li-Mg-Cu-Zr alloys. *J Mater Sci Lett* 3:829–834
11. Srivatsan TS, Coyne EJ, Starke EA (1986) Microstructural characterization of two lithium-containing Aluminium alloys. *J Mater Sci* 21:1553–1560
12. Dieter GE (1986) Mechanical metallurgy. McGraw-Hill Inc., London, UK
13. Birch MEJ (1986) Grain refining of aluminium-lithium based alloys with titanium boron aluminium. In: Baker C, Gregson PJ, Harris SJ, Peel CJ (eds) Aluminium–Lithium alloys III, Proceedings of 3rd international conference. The Institute of Metals, London, UK, pp 152–158
14. Starke EA Jr, Sanders TH Jr, Palmer IG (1981) New approaches to alloy development in the Al-Li system. *J Metals* 33:24–33
15. Divecha AP, Karmarkar SD (1981) Casting problems specific to aluminium–lithium alloys. In: Sanders TH Jr, Starke EA Jr (eds) Proceedings of 1st international conference on aluminium–lithium alloys. Metal Soc AIME, Warrendale, USA, pp 49–62
16. Fridlyander IN, Kolobnev NI, Berezina AL, Chuistov KV (1992) The effect of scandium on decomposition kinetics in aluminum-lithium alloys. In: Peters M, Winkler PJ (eds) Aluminium –lithium alloys VI, Deutsche Gesellschaft für Metallkunde, Frankfurt, Germany, pp 107–112
17. Singh V (1997) Preparation and characteristics of Al-Li-Cu-Mg-Zr based alloys. Doctoral thesis, Banaras Hindu University, Varanasi, India
18. Webster D, Haynes TG, Flemings RH (1988) Al-Li investment castings coming of age. *Adv Mater Process Inc Met Prog J* 133(6):25–30

19. Page FM, Chamberlain AT, Grimes R (1987) The safety of molten aluminium-lithium alloys in the presence of coolants. In: Champier G, Dubost B, Miannay D, Sabetay L (eds) Aluminium–Lithium alloys, Proceedings of 4th international conference, J de Physique, vol 48, pp C3.63–C3.73
20. Prasad YVRK, Sashidhara S (1997) Aluminum alloys. In: Prasad YVRK, Sashidhara S (eds) Hot working guide: a compendium of processing maps. ASM International, Materials Park, OH, USA, pp 160–177
21. Jagan Reddy G (2010) Study on high temperature flow properties of Al-Li alloy UL40 and development of processing maps. Doctoral Thesis, Indian Institute of Technology, Bombay, India
22. Rioja Roberto J, Liu John (2012) The evolution of Al-Li base products for aerospace and space applications. Metall Mater Trans A 43A:3325–3337
23. Mukhopadhyay AK, Flower HM, Sheppard T (1990) Development of microstructure in AA 8090 alloy produced by extrusion processing. Mater Sci Technol 6:461–468
24. Mukhopadhyay AK, Flower HM, Sheppard T (1990) Development of mechanical properties in AA 8090 alloy produced by extrusion processing. Mater Sci Technol 6:611–620
25. Skillingberg MH, Ashton RF (1987) Processing and performance of Al-Li-Cu-X extrusions. In: Champier G, Dubost B, Miannay D, Sabetay L (eds) Aluminium–Lithium alloys, Proceedings of 4th international conference, J de Physique, vol. 48, pp C3.179–C3.186
26. McNamara DK, Pickens JR, Heubaum FH (1992) Forgings of weldalite™ 049 alloys X2094 and x2095. In: Peters M, Winkler PJ (eds) Aluminium-Lithium alloys VI, vol 2. Deutsche Gesellschaft für Metallkunde, Frankfurt, Germany, pp 921–926
27. Mogucheva AA, Kaibyshev RO (2008) Ultrahigh superplastic elongations in an aluminium–lithium alloy. Physics 53:431–433
28. Gokhale AA, Singh V (2005) Effect of Zr content and mechanical working on the structure and tensile properties of AA8090 alloy plates. J Mater Process Technol 159:369–376
29. Pu HP, Liu FC, Huang JC (1995) Characterization and analysis of low-temperature superplasticity in 8090 Al-Li alloys. Metall Mater Trans A 34A:1153–1161
30. Islamgaliev RK, Yunusova NF, Nurislamova GV, Krasil'nikov NA, Valiev RZ, Ovid'ko IA (2009) Structure and mechanical properties of strips and shapes from ultrafine-grained aluminium alloy 1421. Met Sci Heat Treat 51:82–86
31. Pickens JR, Heubaum FH, Langan TJ, Kramer LS (1989) Al-(4.5–6.3) Cu-1.3 Li-0.4 Ag-0.4 Mg-0.14 Zr alloy weldalite 049. In: Sanders TH Jr, Starke EA Jr (eds) Aluminium–Lithium alloys, Proceedings of 5th international conference. Materials and Component Engineering Publications Ltd, Birmingham, UK, vol 3, pp 1397–1411
32. Kramer LS, Heubaum FH, Pickens JR (1989) The weldability of high strength Al-Cu-Li alloys. In: Sanders TH Jr, Starke EA Jr (eds) Aluminium–Lithium alloys, Proceedings of 5th international conference. Materials and Component Engineering Publications Ltd, Birmingham, UK, vol 3, pp 1415–1424
33. Madhusudhan Reddy G, Gokhale AA (1993) Gas Tungsten arc welding of 8090 Al-Li alloy. Trans Indian Inst Met 46:21–30
34. Madhusudhan Reddy G, Mohandas T, Sobhana Chalam P (2003) Metallurgical and mechanical properties of AA 8090 Al-Li alloy friction welds. International welding symposium (IWS 2k3) on Emerging Trends in Welding, Organized by Indian Welding Society, Hyderabad, India, pp 147–158
35. Cavaliere P, Cabibbo M, Panella F, Squillace A (2009) 2198 Al–Li plates joined by friction stir welding: mechanical and microstructural behavior. Mater Des 30:3622–3631
36. Niedzinski M, Thompson C (2010) Airware 2198 backbone of the Falcon family of SpaceX launchers. Light Met Age 68(6–7):55
37. Eswara Prasad N (1993) In-plane anisotropy in the fatigue and fracture properties of quaternary Al-Li-Cu-Mg alloys. Doctoral Thesis, Indian Institute of Technology (formerly Institute of Technology), Banaras Hindu University, Varanasi, India
38. Eswara Prasad N, Gokhale AA, Rama Rao P (2003) Mechanical behaviour of Al-Li alloys. Sadhana 28:209–246

39. Eswara Prasad N, Malakondaiah G (1992) Anisotropy in the mechanical properties of quaternary Al-Li-Cu-Mg alloys. *Bull Mater Sci* 15:297–310
40. Peters M, Eschweiler J, Welpmann K (1986) Strength profile in Al-Li plate material. *Scripta Metallurgica* 20:259–264
41. Dhers J, Driver J, Fourdeux A (1986) Cyclic deformation of binary Al-Li alloys. In: Baker C, Gregson PJ, Harris SJ, Peel CJ (eds) *Aluminium-Lithium alloys*, Proceedings of 3rd international conference. The Institute of Metals, London, UK, pp. 233–238
42. Coyne EJ, Sanders TH Jr, Starke EA Jr (1981) The effect of microstructure and moisture on the low cycle fatigue and fatigue crack propagation of two Al-Li-X alloys. In: Sanders TH Jr, Starke EA Jr (eds) *Aluminum-Lithium alloys*, Proceedings of 1st international conference. The Metallurgical Society of AIME, Warrendale, USA, pp 293–305
43. Rinker JG, Marek M, Sanders TH (1984) Microstructure, toughness and SCC behaviour of 2020. In: Sanders TH Jr, Starke EA Jr (eds) *Aluminum-Lithium alloys II*, Proceedings of 2nd international conference. The Metallurgical Society of AIME, Warrendale, USA, pp 597–626
44. Srivatsan TS, Yamaguchi K, Starke EA (1986) The effect of environment and temperature on the low cycle fatigue behavior of aluminum alloy 2020. *Mater Sci Eng* 83:87–107
45. Wanhill RJH (1994) Flight simulation fatigue crack growth testing of aluminium alloys. Specific issues and guidelines. *Int J Fatigue* 16:99–110
46. Eswara Prasad N, Malakondaiah G, Kutumbarao VV, Rama Rao P (1996) In-plane anisotropy in low cycle fatigue properties of and bilinearity in Coffin-Manson plots for quaternary Al-Li-Cu-Mg 8090 alloy plate. *Mater Sci Technol* 12:563–577
47. Eswara Prasad N, Rama Rao P (2000) Low cycle fatigue resistance in Al-Li alloys. *Mater Sci Technol* 16:408–426
48. De PS, Mishra RS, Baumann JA (2011) Characterization of high cycle fatigue behavior of a new generation aluminum lithium alloy. *Acta Mater* 59:5946–5960
49. Chen J, Mady Y, Morgeneyer TF, Besson J (2011) Plastic flow and ductile rupture of a 2198 Al-Cu-Li aluminium alloy. *Comput Mater Sci* 50:1365–1371
50. Alcoa Technical Fact Sheet (2008) Alcoa in-house data
51. Eswara Prasad N, Srivatsan TS, Wanhill RJH, Malakondaiah G, Kutumbarao VV (2014) Fatigue behaviour of Aluminum-Lithium alloys. In: Eswara Prasad N, Gokhale Amol A, Wanhill RJH (eds) *Aluminum-Lithium alloys: processing, properties and applications*. Butterworth-Heinemann Publication, An Imprint of Elsevier Publications, New York, USA, pp 341–379
52. Wanhill RJH, Bray GH (2014) Fatigue crack growth behaviour of Aluminum-Lithium alloys. In: Eswara Prasad N, Gokhale Amol A, Wanhill RJH (eds) *Aluminum-Lithium alloys: processing, properties and applications*. Butterworth-Heinemann Publication, An Imprint of Elsevier Publications, New York, USA, pp 381–413
53. Lynch SP, Wanhill RJH, Byrnes RT, Bray GH (2014) Fracture toughness and fracture modes of Aluminum-Lithium alloys. In: Eswara Prasad N, Gokhale Amol A, Wanhill RJH (eds) *Aluminum-Lithium alloys: processing, properties and applications*. Butterworth-Heinemann Publication, An Imprint of Elsevier Publications, New York, USA, pp 415–455
54. Holroyd NJH, Scamans GM, Newman RC, Vasudevan AK (2014) Corrosion and stress corrosion of Aluminum-Lithium alloys. In: Eswara Prasad N, Gokhale Amol A, Wanhill RJH (eds) *Aluminum-Lithium alloys: processing, properties and applications*. Butterworth-Heinemann Publication, An Imprint of Elsevier Publications, New York, USA, pp 457–500

Chapter 4

Titanium Sponge Production and Processing for Aerospace Applications

Ch R.V.S. Nagesh, G.V.S. Brahmendra Kumar, B. Saha
and Amol A. Gokhale

Abstract Titanium sponge is widely produced employing the Kroll process of high-temperature reduction of titanium tetrachloride by magnesium. The technological developments over the last few decades have focused on cost/energy savings in addition to introducing sophisticated systems in the manufacturing technology. This chapter concerns Indian efforts to develop ‘state-of-the-art’ Kroll technology for producing titanium sponge in industrial scale batches. While covering various features of the combined process technology developed at DMRL, the chapter also discusses advanced quality evaluation and sponge processing practice as developed at DMRL and implemented at the KMML sponge plant (which was established with the DMRL technology). Extensive measures that have been implemented to obtain high purity metal and assured quality of the product are discussed.

Keywords Titanium sponge · Extraction metallurgy · Chemical analysis

4.1 Introduction

Titanium and its alloys have excellent engineering properties, including low density (4.5 g/cm^3), good strength, and superior corrosion resistance. High-strength titanium alloys with lower density are attractive materials for aero engine components

C.R.V.S. Nagesh (✉) · G.V.S. Brahmendra Kumar
DMRL, Hyderabad, India
e-mail: nagesh@dmrl.drdo.in

G.V.S. Brahmendra Kumar
e-mail: gvskumar@dmrl.drdo.in

B. Saha
RCMA (Materials), CEMILAC, Hyderabad, India

A.A. Gokhale
IIT-B, Mumbai, India
e-mail: gokhale@iitb.ac.in; amol_gokhale@yahoo.in

at temperatures up to about 650 °C, and also airframe structural applications requiring higher load densities than aluminium alloys and also higher operating temperature capabilities.

Titanium metal is, however, reactive and poses several problems in high temperature processing operations. Ductility, workability, and other mechanical properties of titanium are highly sensitive to interstitial impurities such as oxygen, nitrogen, carbon, and hydrogen. The corrosion resistance of titanium is also impaired when iron is present beyond specified limits.

Because of the high chemical reactivity of titanium, there are no viable methods of purification for removing the impurity elements. Thus great care needs to be taken during the production of titanium sponge, which is the nascent form of titanium obtained from reduction of titanium tetrachloride by sodium or magnesium, see Sect. 4.2.

Titanium ore is available mostly in the form of the oxide minerals ilmenite (FeOTiO_2) and rutile (TiO_2). The titanium dioxide content of ilmenite usually lies in the range of 40–60 wt%, whereas rutile consists of up to 90 wt% TiO_2 , the remainder being mostly silica. By employing various physical and chemical methods of beneficiation, ilmenite is processed to increase the TiO_2 content, and this product is referred to as synthetic rutile. Indian reserves of ilmenite are estimated to be 593.5 million tons (12–15 % of world total) and the reserves of rutile are estimated at 31.3 million tons in terms of TiO_2 content [1].

Over 90 % of titanium minerals in the world are processed for the preparation of high purity (pigment grade) titanium dioxide (TiO_2), which has a wide range of applications in cement, textile, paints, pharmaceuticals, and plastics. Both the ‘sulphate route’ (in which titanium sulfate is the intermediate) and ‘chloride route’ (in which titanium tetrachloride is the intermediate) are widely used for manufacturing the high-purity TiO_2 .

4.2 Established Methods of Titanium Extraction

Early efforts by researchers to produce titanium by metallothermic (Al, Mg, and Ca) and carbothermic reduction of titanium dioxide failed to produce metal of the required purity. From these unsuccessful attempts it was learnt that to prepare pure titanium metal the starting material should be a non-oxygen-bearing compound. There have been several successful attempts:

- In 1910 Hunter succeeded in producing high-purity titanium by sodio-thermic reduction of titanium tetrachloride (TiCl_4) in a high-pressure steel vessel.
- In 1925 van Arkel and de Boer produced high purity titanium by dissociation of titanium iodide on a tungsten filament.
- In 1937 Kroll developed the method of magnesio-thermic reduction of TiCl_4 in an argon gas atmosphere.

- Fused salt electrolysis of $TiCl_4$ in alkali chloride mixtures was also extensively studied and reported to be a viable method of producing pure titanium metal.

Both the Hunter and Kroll processes were developed to produce titanium on an industrial scale by the late 1940s. While the Hunter process was extensively studied and developed by Imperial Chemical Industries, UK, the Kroll process was developed simultaneously by the US Bureau of Mines, and also in Japan and the former USSR.

Development of the fused salt electrolysis process was taken up by Dow Howmet, USA, and Electrochemica Marco Ginnatta, Italy. However, the process operated only on a pilot plant scale, and has not been implemented in commercial practice.

Historical developments in titanium extraction metallurgy are discussed in great detail in the literature [2–4]. Subsequent developments and new methods of titanium extraction are also summarized and made available in the literature [5–8].

Thus although there are three established methods of titanium extraction, see Fig. 4.1, only two, the Hunter and Kroll processes, are commercially implemented for large-scale production of titanium sponge. The Hunter process involves $TiCl_4$ reduction by sodium; the Kroll process involves $TiCl_4$ reduction by magnesium; and fused salt electrolysis uses $TiCl_4$ (which is obtained from high-temperature chlorination of oxide mineral concentrates) as starting material. In all cases an inert

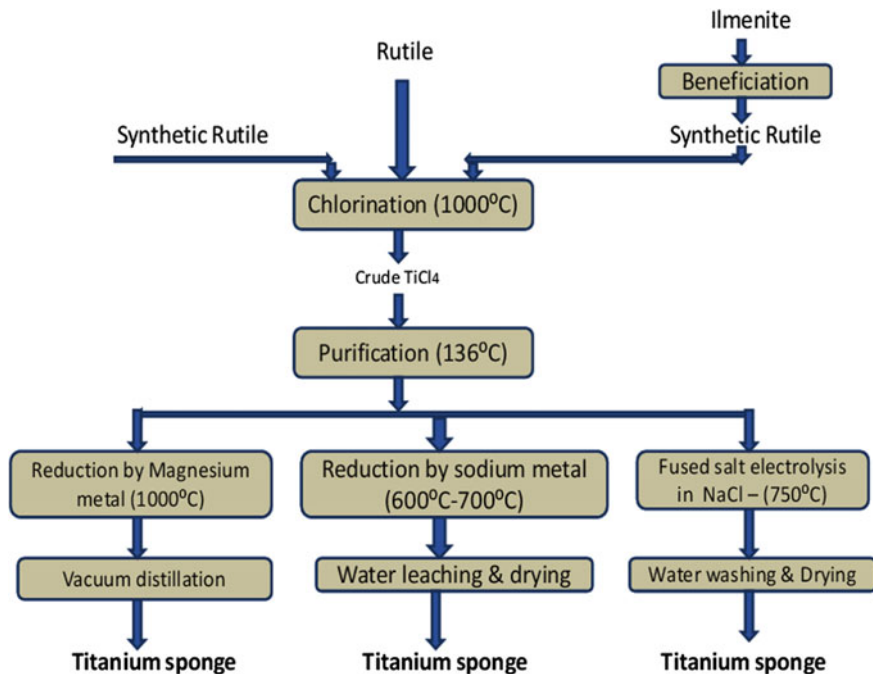


Fig. 4.1 Established methods of titanium sponge production

gas atmosphere is invariably used to protect the quality of the metal throughout the extraction process; and the titanium metal takes the form of a porous agglomerated powder particulate that is referred to as ‘titanium sponge.’

4.3 World Production of Titanium Sponge—Recent Developments

Major producers of titanium sponge have been Japan, the US, former USSR countries, the UK and China. Initially, most of the titanium production was for the aerospace industry, especially for military aircraft. The large dependency of titanium sponge production on military applications was mainly responsible for its cyclic demand in the Cold War era. However, subsequently there has been increased usage of titanium in non-aerospace sectors, especially in Japan and Russia.

Figure 4.2 shows that the world production capacity for titanium sponge has risen gradually from around 5000 metric tons (MT) in the beginning, to as high as 300,000 MT at present, although the actual production levels have fluctuated due to the above-mentioned reasons and also global economic recessions and booms in the civil aviation sector [9, 10].

Most of the sodium-based plants that were operating in the UK and Japan were closed in the early 1990s quoting techno-economical difficulties. Hence almost the entire world production is predominantly taking place via the Kroll process (with many engineering advancements and increased batch sizes). The current level of world production of sponge is much lower than the actual capacities (owing to

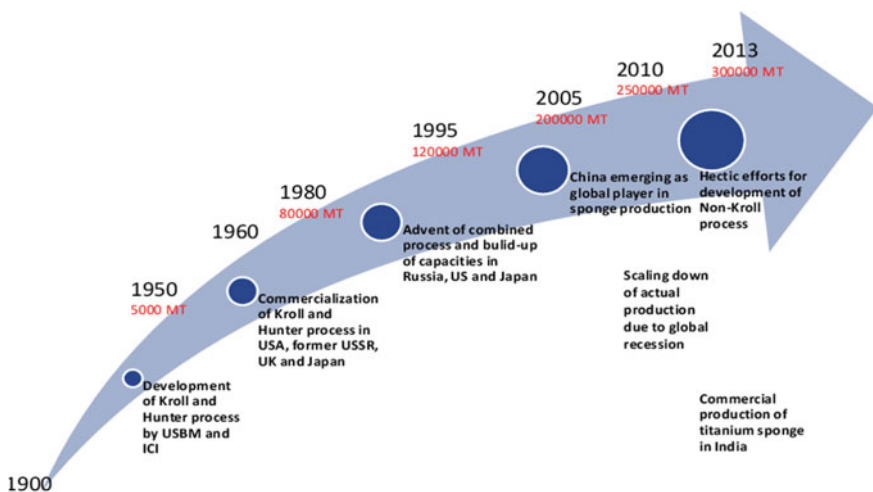


Fig. 4.2 Trends in world titanium sponge production. MT = metric tons

economic recession) and placed at about 160,000 MT per year, nearly half of it reportedly taking place in China [11].

There has been much effort to commercialize a non-Kroll process during the last decade or so. Salient among them include the Armstrong process of sodium reduction of TiCl_4 in the gas phase to produce titanium powder continuously [6], and electrochemical reduction of TiO_2 (FFC Cambridge process) [12]. It was also reported that a process for titanium hydride production by reduction of TiCl_4 by magnesium and hydrogen was tested on a pilot plant scale (ADMA pilot plant) [13].

However, the Kroll technology continues to be the globally most practiced method for the commercial production of titanium sponge. Based on several advancements in the Kroll technology, it has also become possible to produce titanium sponge of 5 N purity for selected electronic applications [14].

4.4 Indian Scenario on Titanium Sponge Production

In India basic research on the preparation of TiCl_4 by fluidized bed chlorination of mineral concentrates and production of titanium sponge by the Kroll and Hunter processes were carried out at Bhaba Atomic Research Centre (BARC), Mumbai, in the 1960s [15]. During the 1970s Nuclear Fuel Complex (NFC), Hyderabad, operated a Kroll/Hunter pilot plant facility where titanium sponge production in 100/60 kg batches was studied in detail. Based on this experience it was decided that the Kroll process was suitable for scaling up to industrial production [16].

4.4.1 *Development of Kroll Technology at DMRL, Hyderabad*

The main technological parameters to be standardized in the Kroll process are (i) control of reaction temperature, since the reduction process is exothermic, by selection of an appropriate TiCl_4 feed rate and admission scheme, (ii) tapping the magnesium chloride (MgCl_2) reaction by-product for effective utilization of reactor volume, (iii) heating rate, time, and temperature of vacuum distillation of reduced sponge to remove unreacted magnesium and trapped MgCl_2 , and (iv) grading and size reduction of titanium sponge cake to obtain high-purity sponge in the specified size range.

In the early 1980s the Defence Metallurgical Research Laboratory (DMRL) began industrial scale R&D for the Kroll process. A pilot plant was set up to investigate the sponge production process on a scaled up batch of 2000 kg, and to standardize the technical parameters for production of aeronautical grade sponge [17, 18]. The facilities established for this purpose included the following:

- (i) Fractional distillation system comprising a packed-bed distillation column and a stripper column to purify raw TiCl_4 and remove impurities such as dissolved gases, SnCl_4 , SiCl_4 , and oxy-chlorides.
- (ii) Reduction of TiCl_4 by magnesium in a stainless steel reactor placed in a multi-zone electrical resistance furnace. The bottom of the reactor has a plug and seat type valve to enable tapping hot MgCl_2 during the reduction process.
- (iii) A separate reactor assembly to carry out the pyro-vacuum distillation process of the reduced sponge, together with the reaction crucible. The reduced mass is heated to high temperature (950–975 °C) with the help of a resistance furnace, and the distillates are collected in a salt which can be placed below the reaction crucible. The assembly also consists of a water-cooled bottom retort connected to the vacuum pumping system.
- (iv) A custom-built horizontal hydraulic press for ejection of titanium sponge cake from the reaction crucible; and various size reduction operations to prepare titanium sponge pieces in the finished size range of 2–25 mm.

In a separate study the magnesiothermic reduction process was extensively studied and explored for improved understanding of the reaction mechanism and sponge formation scheme in the reduction reactor [19].

4.4.2 Development of Combined Process Technology at DMRL, Hyderabad

The quality of titanium sponge produced by the Kroll process depends on many factors such as purity of raw materials, cleanliness and leak tightness of the reactor; interruptions in process operations leading to exposure of reduced sponge to atmospheric air; reactor material; and care taken during handling of the sponge.

Aerospace grade sponge must meet stringent upper limit specifications with respect to O, N, C, Fe, Mg, and chloride. The *first phase* developmental work on 2000 kg batches at DMRL suffered from serious setbacks of (i) interruptions in process operations owing to problems in bottom tapping MgCl_2 via a valve, (ii) inevitable exposure of reduced sponge to atmospheric air while transferring it to the vacuum distillation assembly, (iii) jamming of connecting pipes with distillates during vacuum distillation, and (iv) unsatisfactory performance of sponge handling systems.

However, the engineering expertise gained from the developmental work immensely helped in understanding the technological requirements and designing improved systems for sponge production in the *second phase* of developmental work, i.e. development of a ‘Combined Process Technology’ in 3000–3500 kg batches. This combined process technology has the following advantages:

- (i) Low overall energy consumption.
- (ii) Highest achievable process efficiency and materials utilization.
- (iii) Significant reduction in process cycle time.
- (iv) Improved yield and purity of sponge.
- (v) Lower capital costs and reduced manpower requirement.
- (vi) Safe equipment and operating procedures.

Figure 4.3 shows details of the salient features of the ‘Combined Process Equipment’ developed at DMRL for sponge production in 3000–3500 kg batches. These features include the following:

- (i) Use of a single multi-zone electrical resistance furnace for reduction and vacuum distillation operations at a single station. This meets the requirements of heating in a controlled manner and removing exothermic heat from the reactor at selected sites.
- (ii) Two custom engineered identical clad stainless steel retorts (fabricated as per ASME pressure vessel code Section VIII) connected by a heated pipe. One of the two retorts is for sponge production, while the other receives the distillates in the condenser station. This results in improved materials utilization since the condenser retort is subsequently used for sponge production.

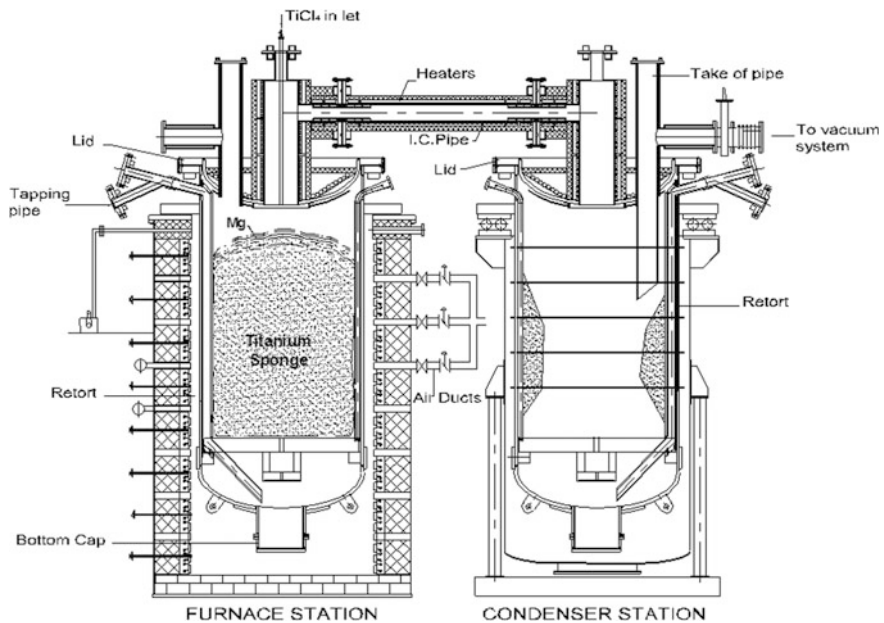


Fig. 4.3 Schematic of Combined Process Equipment developed at DMRL, Hyderabad, India

- (iii) A ‘valve-less’ pressure transfer system for tapping hot MgCl_2 periodically from the process reactor during the reduction process.
- (iv) A set of lightweight ceramic modules embedded with heaters wrapped over the interconnecting pipe to provide heating during the vacuum distillation process.
- (v) A high-vacuum pumping system with necessary interlocks for evacuating the reactor assembly.
- (vi) Custom-built equipment and tooling for ejection of sponge cake from the reactor and for size reduction operations to prepare homogeneous lots in the required finished sponge pieces of size 2–25 mm.
- (vii) A programmable logic controller (PLC) process control and data logging system.

Repeated experimentation and incorporation of several improvements gradually led to standardization [20–22] of all the parameters of the sponge manufacturing process, see Table 4.1, with the process becoming highly reproducible. A photograph of titanium sponge cake (weighing about 3.5 MT) produced at the DMRL technology demonstration plant is shown in Fig. 4.4.

Table 4.1 Standardized operating conditions for producing titanium sponge in 3–3.5 MT batches

TiCl ₄ purification	Parameters
<i>Column—1</i>	
(a) Top temperature	138 °C
(b) Bottom temperature	139 °C
(c) TiCl ₄ feed rate	157 kg/h
<i>Column—2</i>	
(a) Temperature	139 °C
(b) Feed rate	150 kg/h
Reduction	
(i) Excess magnesium	60 %
(ii) Reactor pressure	0.5–3.5 psig
(iii) TiCl ₄ feed rate	180–220 kg/h
(iv) Reaction zone temperature	800–810 °C
(v) Process time (including heating and cooling)	200 h
Vacuum distillation	
(i) Vacuum level	30 X 10 ⁻³ torr
(ii) Temperature	975–1000 °C
(iii) High temperature soak	64 h
(iv) Total cycle time	240 h

Fig. 4.4 Titanium sponge cake (weight about 3500 kg) produced at the DMRL technology demonstration plant



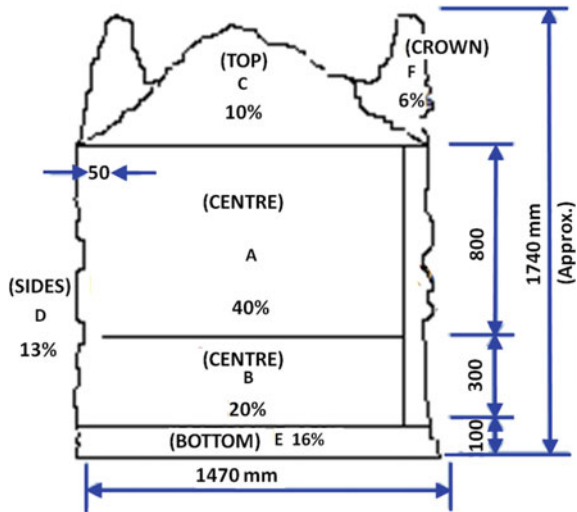
4.4.3 Quality Evaluation and Processing of Aerospace Grade Sponge

Titanium sponge obtained by the magnesium reduction and vacuum distillation process takes the shape of a cylindrical cake with loosely held deposits on the top and sides of the cake. The physical characteristics such as porosity and bulk density vary slightly from top to bottom of the cake, with material at the bottom usually being denser.

The quality of the sponge with respect to the impurities O, N, C, Fe, etc. also varies with position in the cake: impurities from the reactor steel wall and bottom contaminate the material at the sides and bottom of the cake, while the top surface material generally contains higher levels of oxygen, magnesium, and chlorides compared to the sponge from core fractions. Hence it becomes essential to isolate the high-purity core fraction from the rest of the material by meticulous sponge grading. At DMRL an elaborate sponge grading practice was evolved for this purpose [23], and cakes are divided into different fractions as shown in Fig. 4.5.

All the fractions are separately cut, crushed, and processed to prepare the finished size of material. The fractions A and B conform to the highest purity and

Fig. 4.5 Schematic of quality evaluation and grading of a typical titanium sponge block



meet all the technical requirements/stringent specifications of aerospace grade material.

Depending on the end-use specifications, separate lots of sponge are prepared and stored in argon-filled drums. A typical analysis of a finished sponge lot is presented in Table 4.2, showing that it compares very well with other grades, including ASTM grade MD 120 and the well-known Russian grade TG 90.

Table 4.2 Typical analyses (wt%) of aerospace grade sponge produced at DMRL and comparison with other standards^a

Element	Midhani specification	CIS TG-90	ASTM MD-120	Showa (japan) S-90	DMRL lot 1 L001/2 k
Fe	0.050	0.060	0.120	0.030	0.018
C	0.015	0.030	0.020	0.020	0.006
O	0.040	0.040	0.100	0.060	0.033
N	0.015	0.020	0.015	0.010	0.003
Mg	0.080	0.080	0.080	0.045	0.004
Chloride	0.100	0.080	0.120	0.080	0.005
Ni	0.050	NS	NS	NS	<0.005
Cr	NS	NS	NS	NS	0.009
H	NS	NS	0.01	0.002	0.0019
Ti (by difference)	99.6	99.6	99.6	99.8	>99.9
Hardness (BHN)	100	80–90	120	90	82

NS Not Specified

^aValues are upper limits for impurities and hardness

4.4.4 Commercial Production of Titanium Sponge at KMML, Chavara, India

Based on the technology developed at DMRL, a commercial titanium sponge plant with an installed capacity of 500 tons per year (expandable to 1000 tons per year) was established at Kerala Minerals & Metals Limited (KMML), Chavara, Kollam District. This was aided by funding from VSSC, Department of Space, the principal user of titanium and titanium alloys in the country.

Prior to the installation, technical personnel from KMML were given hands-on experience and training at the DMRL demonstration plant on all the activities of titanium sponge production.

The technology was successfully transferred to KMML: complete basic engineering was provided by DMRL, and the detailed engineering was done by DMRL in association with KMML, VSSC, and KITCO (Kerala Industrial & Technical Consultancy Organization), the engineering consultants.

The fully installed equipment was commissioned for (i) TiCl_4 purification to produce metal grade tetrachloride from the pigment grade TiCl_4 ; (ii) simultaneous operation of five reduction batches and five vacuum distillation processes on a scale of 3000–3500 kg/batch with related instrumentation; and (iii) ejection of sponge cake, its grading, and size reduction to prepare a generally acceptable finished size range of 2–25 mm. Provision is also made to prepare the finished sponge pieces in the range of 12–25 mm based on user requirements. The plant started production in June 2011 [24].

The first titanium sponge cake produced at the KMML plant is shown in Fig. 4.6. The sponge samples of the batch were analyzed and found to meet all the specifications for aerospace applications.

4.4.5 Quality Assurance Program at KMML Sponge Plant

After commissioning, regular production of titanium sponge has been taking place and efforts are being made to reach the rated production levels. DMRL has been consistently providing technical support, and in association with KMML and the Regional Centre for Military Airworthiness (RCMA, Materials) has drawn up a detailed quality assurance (QA) programme to ensure sponge purity requirements for aerospace/defence use.

The QA programme begins with visual inspection of the ejected sponge cake to remove discoloured material, if any, on the external surface of the cake.

The high-quality (aerospace) fraction of a given cake is then defined from extensive chemical analyses and hardness (BHN values) of buttons prepared from sponge samples. This high-quality fraction of a given cake is treated separately to prepare finished size sponge pieces (12–25 mm).

Fig. 4.6 First titanium sponge cake (weighing about 3 tons) produced in the KMML titanium sponge plant



Different fractions of sponge are also blended together for the preparation of a commercial purity sponge lot weighing about 1.75 MT. This was blended in a double-cone blender of 2 MT capacity.

Under an ongoing evaluation, three randomly chosen batches of sponge cakes have been sampled for an intensive QA programme, as indicated in the flowchart in Fig. 4.7. A typical analysis of one representative sample of a finished sponge lot is presented in Table 4.3. The material comfortably meets aerospace specifications in all respects.

4.4.6 Type Certification of Titanium Sponge—The Approach

Type certification (purity authentication) of titanium sponge is essential for its use in producing aerospace quality alloys. DMRL, RCMA (Materials), and KMML have jointly taken up this type certification of titanium sponge produced at KMML.

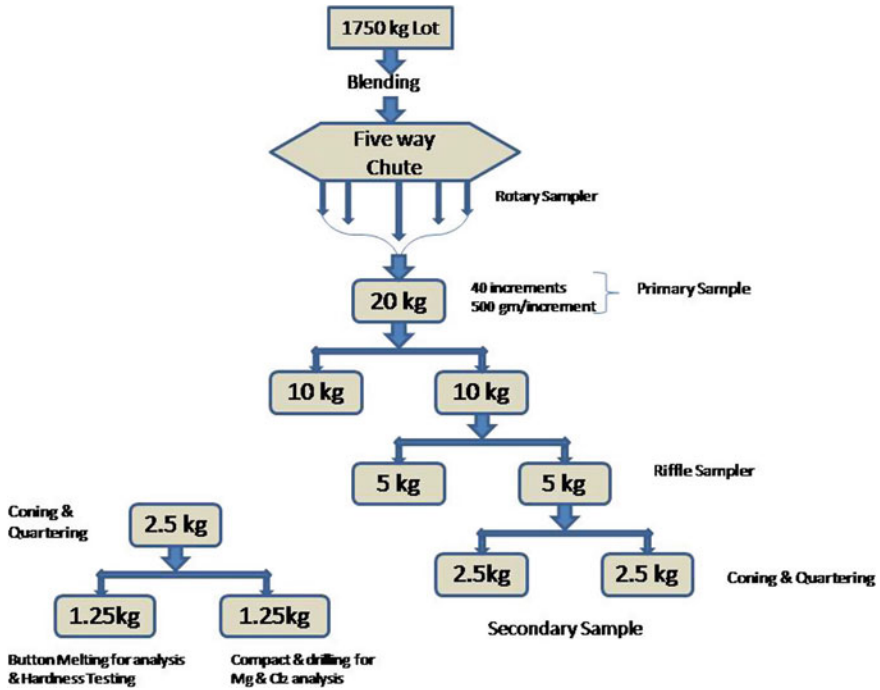


Fig. 4.7 Sampling procedure for the evaluation of finished titanium sponge

Table 4.3 Chemical analysis and hardness of a representative sample from a finished sponge lot of 1.75 MT: ND = detectable

Element	Content (wt%)
Iron (Fe)	0.0023
Oxygen (O)	0.0375
Silicon (Si)	ND
Nickel (Ni)	0.0063
Carbon (C)	0.0033
Chloride (Cl)	0.0243
Nitrogen (N)	<0.0020
Magnesium (Mg)	0.0122
Chromium (Cr)	0.0012
Hydrogen (H)	0.0019
Copper	0.0071
Tin (Sn)	ND
Manganese (Mn)	0.0009
Titanium (by difference)	99.901
Hardness (BHN)	78

As part of the sponge certification activity, the certification agency along with other partners ensured the following:

- (i) Capabilities of the firm for producing aeronautical quality sponge.
- (ii) Required quality norms followed by KMML in consistently producing a high-purity sponge.
- (iii) Availability of skilled and capable manpower with the firm.
- (iv) Availability of test facilities at the plant for quality evaluation.
- (v) Required procedures are adopted for the maintenance of process records, data logging, etc.
- (vi) Calibration of various equipments and instruments, etc., as per the requirement.

A threefold approach was evolved for carrying out the type certification process for titanium sponge, namely

- (a) quality checks at required stages of sponge production
- (b) implementation of suggested measures related to the quality assurance plan as listed in test schedules, and
- (c) sponge quality evaluation based on the stringent international norms.

4.5 Properties of Ti Sponge

During qualification, samples of titanium sponge are tested as per standards for various properties. The physical properties that are looked for include a uniform matte gray color and freedom from foreign particulates such as oxides, nitrides, and other contaminants, which give the sponge other colours/shades.

Also the other requirements to be met are as follows: The size of the finished sponge pieces shall be generally in the range of 12–25 mm. The bulk density of the sponge shall be not more than 1.53 g/cm³. The hardness of the buttons prepared by inert gas arc/vacuum arc melting of sponge, and tested according to ASTM E 10 (using a 10-mm ball and 1500 kgf load for 30 s) shall not exceed 90 BHN.

The chemical analysis of the sponge samples is carried out by the wet chemical method/spectroscopic method as agreed upon with the airworthiness agencies. The purity of the sponge is expected to meet the specifications as presented in Table 4.4.

Table 4.4 Chemical specification of titanium sponge (wt% basis)

Element	Minimum	Maximum
Titanium	99.74	–
Iron	–	0.05
Oxygen	–	0.04
Silicon	–	0.01
Nickel	–	0.04
Carbon	–	0.015
Chloride	–	0.08
Nitrogen	–	0.02
Magnesium	–	0.04
Chromium	–	0.06
Hydrogen	–	0.01
Water	–	0.02
All others	–	0.05

4.6 Concluding Remarks

Titanium sponge is of strategic importance owing to its usage in manufacturing titanium alloys for aerospace and defence applications. However, the extractive metallurgy of titanium, is complicated and cumbersome, resulting in high material costs and limitations on the use of titanium and its alloys.

Titanium sponge consumption in aerospace alloy manufacture has been increasing owing to growing demand. In view of its chemical reactivity and the sensitivity of titanium alloy properties to the presence of even small amounts of impurity elements, it is necessary to ensure that stringent quality specifications are met. In this chapter we have described successful efforts in the Indian context to develop high-purity titanium sponge for high-end aerospace applications.

Acknowledgments The authors are grateful to DRDO for constantly supporting the industrial scale R&D programme for development of the titanium sponge technology. They wish to express sincere thanks to Dr. G. Malakondaiah, former Distinguished Scientist and former Director, DMRL, for excellent guidance and support during the entire programme of technology transfer to KMML.

But for the vision of Dr. R.V. Tamhankar, Dr. V.S.Arunachalam, and Prof. P. Rama Rao and their pioneering initiatives and leadership, India would not have reached this stage of self-reliance with respect to titanium sponge. With deep sense of gratitude, the authors place on record the outstanding leadership provided by them.

The authors also gratefully acknowledge the key contributions of senior colleagues, Shri RB Subramanyam, Director (Projects)—retired, Late Dr. Ch. Sridhar Rao, Shri C.S. Ramachandran, and Dr. T.S. Sitaraman during various stages of titanium sponge technology development, demonstration and transfer to KMML.

The authors also wish to place on record the outstanding contributions and support by TSP, KMML during the entire programme of type certification of sponge.

References

1. Indian Minerals Year Book (2015) Indian Bureau of Mines
2. McQuillon AD, McQuillon MK (1956) Titanium. Butterworths Scientific Publications, London, UK
3. Garmata VA (1970) The metallurgy of titanium. Translation Division, Wright Patterson Air Force Base, Dayton, OH, USA
4. Bomberger HB, Froes FH, Morton PH (1985) Titanium—a historical perspective. Titanium technology—present status and future trends. Titanium Development Association, USA, pp 3–17
5. Nagesh ChRVS, Ramachandran CS (2005) Advancements in titanium extraction. *Miner Met Rev* 6(65):65–69
6. Kraft EH (2004) Summary of emerging titanium cost reduction technologies. Report by EHK Technologies, Vancouver, WA, USA
7. Froes FH et al (2007) Titanium—an update, innovations in titanium. In: Gungor MN, Iman MA, Froes FH (eds) *The Minerals, Metals and Materials Society*, Warrendale, PA, USA
8. Nagesh ChRVS, Ramachandran CS, Subramanyam RB (2008) Methods of titanium sponge production. *Trans Indian Inst of Met* 61(5):341–348
9. Mineral Commodities update USGS (2014), United States Geological Survey, VA, USA
10. McCoy D (2014) Titanium metal—a global perspective, Supply/demand and key industry driven threats and opportunities. 2014 ITA conference, 21–24 September 2014, Chicago, IL, USA
11. Benson Q (2014) Titanium sponge production in China. 2014 ITA Conference, 21–24 September 2014, Chicago, IL, USA
12. FFC Cambridge process from patent to production. 2012 ITA Conference, 4–7 October, 2012, Atlanta, GA, USA
13. Klevtsov A et al (2014) ADMA pilot plant for hydrogenated titanium powder production. 2014 ITA conference, 21–24 September 2014, Chicago, IL, USA
14. Hyado T, Ichihashi H (2004) Establishment of the manufacture of 5 N super purity titanium billets by Kroll process. In: Lutjering G, Albrecht J (eds) *Titanium'99 Science and Technology*. Wiley-VCH Verlag GmbH, Weinheim, Germany, pp 141–148
15. Ahluwalia HS et al (1973) Pilot plant studies in the production of ductile titanium sponge from pure titanium tetrachloride. BARC Report No.683
16. Kulkarni AP, Ahluwalia HS, Subramanyam RB, Rao NK, Mukherjee TK, Babu RS, Sridhar RCH (1980) Titanium-80: science and technology In: Kimura H, Izumi O (eds) *Proceedings of the fourth international conference on Titanium*, Kyoto, Japan, The Metallurgical Society of AIME, Warrendale, USA, pp 1927
17. Subramanyam RB, Sridhar CHR (1986) Extractive metallurgy of titanium in India. *Defence Sci J* 36(2):105–112
18. Nagesh ChRVS, Sitaraman TS, Ramachandran CS, Subramanyam RB (1994) Development of indigenous technology for production of titanium sponge by the Kroll process. *Bull Mat Sci* 17(6):1167
19. Nagesh ChRVS, Sridhar Rao CH, Ballal NB, Krishna Rao P (2004) Mechanism of titanium sponge formation in Kroll reduction reactor. *Metall Mater Trans B TMS* 35:65–74
20. Nagesh ChRVS et al (2006) Development of indigenous technology for commercial production of titanium sponge. *Met Mater Process* 18(3–4):239–248
21. Subramanyam RB, Sitaraman TS, Ramachandran CS, Nagesh ChRVS, Brahmendrakumar GVS (2009) Metals. *Mater Process* 1:27–44

22. Ramachandran CS, Sitaraman TS, Nagesh ChRVS, Kumar GVSB (2007) A method and apparatus for the production of aeronautical grade titanium sponge from titanium tetrachloride. Patent filed at the Indian Patent Office (2007)
23. Kirtania M, Nagesh ChRVS Ramachandran CS (2005) Development of equipment and practices for the processing of aeronautical grade titanium sponge. In: Proceedings of national conference on technological advancements in mechanical engineering, 3–4 December 2005, Sreenidhi Institute of Science & Technology, Ghatkesar, Hyderabad, India
24. Nagesh ChRVS, Brahmendrakumar GVS (2012) Commercial production of titanium sponge in India 2012 ITA Conference, 4–7 October 2012, Atlanta, GA, USA

Chapter 5

Titanium Alloys: Part 1—Physical Metallurgy and Processing

A. Bhattacharjee, B. Saha and J.C. Williams

Abstract Titanium alloys are the principal replacements, and in many cases also prime candidate materials to replace (i) aerospace special and advanced steels, owing to their higher specific strength properties, (ii) aluminium alloys, due to their better elevated temperature properties and (iii) nickel-base superalloys for high pressure compressors of modern engines, owing to their superior intermediate temperature (up to 600 °C) creep strength and excellent oxidation and corrosion resistance and good damage tolerant properties. This chapter summarily presents the chemical compositions, properties, aerospace applications and briefly covers (a) the physical metallurgy of titanium alloys, (b) Primary (Melting and Casting) and Secondary (Processing) processes and (c) alloy development (commercially pure Ti, α , near- α , $\alpha + \beta$ and β alloys). Towards the end, the Indian scenario is presented in terms of available production facilities and some of the indigenous alloys.

Keywords Titanium · Alloys · Physical metallurgy · Primary and secondary processing · Castings

5.1 Introduction

Titanium is present in the earth's crust at a level of about 0.6 % and is therefore the fourth most abundant structural metal after aluminium, iron and magnesium. The most important mineral sources for Ti are ilmenite (FeTiO_3) and rutile (TiO_2).

A. Bhattacharjee (✉)

Titanium Alloy Group, Materials Processing Division, DMRL, Hyderabad, India
e-mail: amitb@dmrl.drdo.in

B. Saha

RCMA (Materials), CEMILAC, Hyderabad, India
e-mail: bsaha@cemilac.drdo.in

J.C. Williams

Dept. of Materials Science & Engr., The Ohio State University, Columbus, Ohio, USA
e-mail: williams.1726@osu.edu

Table 5.1 Properties of titanium compared with those of the other widely used structural metals Fe, Ni and Al [1]

Attributes	Ti	Fe	Ni	Al
Melting point (°C)	1670	1538	1455	660
Allotropic transformation (°C)	882	912	–	–
Crystal structure	Bcc hex	Bcc hex	Fcc	Fcc
Room temperature E (GPa)	115	190	210	70
Yield stress (MPa)	1000	1000	1000	500
Density (g/cm ³)	4.5	7.9	8.9	2.7
Comparative corrosion resistance	Very high	Low	Medium	High
Comparative reactivity with oxygen	Very high	Low	Low	High
Comparative metal price	Very high	Low	High	Medium

High strength, low density and excellent corrosion resistance are the main properties that make titanium attractive for a variety of applications. Examples include aircraft (high strength in combination with low density), aeroengines (high strength, low density and good creep resistance up to about 600 °C), biomedical devices (corrosion resistance, low modulus compared to Co- and Fe-based alloys and high strength) and components in chemical processing equipment (corrosion resistance). The relatively high cost of titanium has hindered wider use, e.g. in automotive applications, although new fuel economy standards may change this.

Some of the basic characteristics of titanium are compared in Table 5.1 with those of the other major structural metals based on Fe, Ni and Al. Although titanium has the highest strength to density ratio, it is the material of choice only for certain applications because of its high cost, which is mainly due to the requirement of inert atmosphere or vacuum environments during production of titanium sponge from titanium tetrachloride, and also consolidation of the metal. Both processes require high energy consumption.

The high reactivity of titanium with oxygen leads to the immediate formation of a stable and adherent oxide surface layer when exposed to air, resulting in superior corrosion resistance in most aggressive environments, especially aqueous acid environments. However, this high reactivity with oxygen limits titanium alloy usage to about 600 °C. Above this temperature the diffusion of oxygen through the oxide surface layer becomes too fast, resulting in excessive growth of the oxide layer and embrittlement of the oxygen-enriched surface layer of the titanium alloy.

5.2 Physical Metallurgy of Titanium Alloys

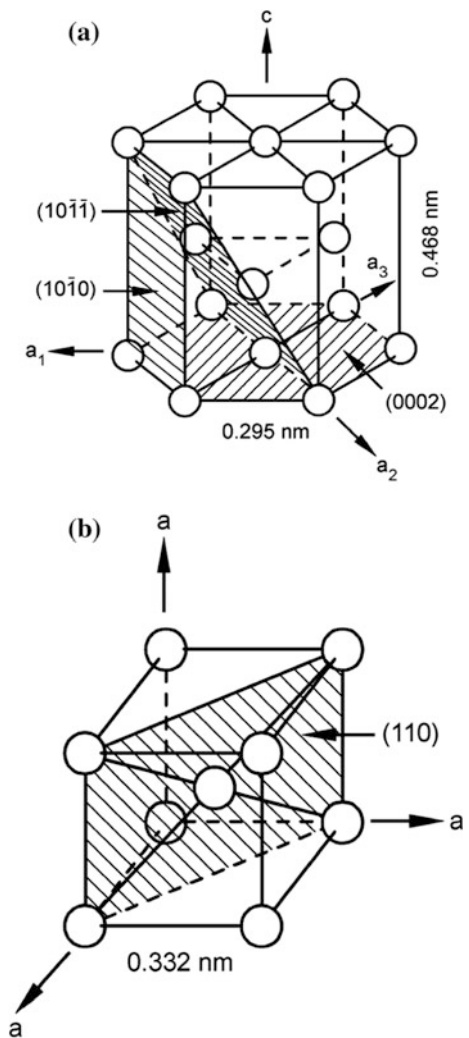
5.2.1 Crystal Structure

Pure titanium undergoes an allotropic phase transformation at 882 °C, changing from a body-centred cubic crystal structure (β phase) at higher temperatures to a hexagonal-close-packed crystal structure (α phase) at lower temperatures. The exact

transformation temperature is strongly influenced by interstitial and substitutional elements and therefore depends on the composition and purity of the metal.

The hexagonal structure cell of the α phase is shown in Fig. 5.1a, which also indicates the room temperature values of the lattice parameters ($a = 0.295$ nm and $c = 0.468$ nm). The resulting c/a ratio for pure α titanium is 1.587, less than the ideal ratio of 1.633 for the hexagonal-close-packed crystal structure. Also indicated in Fig. 5.1a are the three most densely packed lattice planes: the close-packed (0002) plane, also called basal plane; one of the three $\{10\bar{1}0\}$ prism planes; and one

Fig. 5.1 Unit cells of **a** hexagonal-close-packed (HCP) α titanium and **b** body-centred cubic (BCC) β titanium, showing different slip planes [1]



of the six $\{10\bar{1}1\}$ pyramidal planes. The three a_1 , a_2 and a_3 axes are the close-packed directions with the indices $\langle 11\bar{2}0 \rangle$.

The unit cell of the body-centred cubic (bcc) β phase is illustrated in Fig. 5.1b, also indicating one variant of the six most densely, but not close-packed $\{110\}$ lattice planes and the lattice parameter value of pure β titanium at 900 °C ($a = 0.332$ nm). The close-packed directions in the bcc structure are the six $\langle 111 \rangle$ directions.

5.2.2 Elastic Properties

The hexagonal crystal structure of the α phase is intrinsically anisotropic. This anisotropy has important consequences for the elastic and plastic properties of titanium and its alloys. Young's modulus varies with angle of declination from the 'c' axis. Young's modulus of elasticity, E , is about 145 GPa when the stress axis is parallel to the c -axis, and 100 GPa when the stress axis is perpendicular to the c -axis [2].

Similar strong directional variations are observed for the shear modulus, G , of single crystals: G varies between 46 and 34 GPa for shear stresses applied in $\langle 11\bar{2}0 \rangle$ directions and on (0002) or $\{10\bar{1}0\}$ planes, respectively. Less pronounced variations in elastic properties are observed in polycrystalline α titanium with crystallographic texture: a typical value for commercially pure (CP) titanium is 105 GPa.

In general, commercial β titanium alloys have lower E values than α and $\alpha + \beta$ alloys. Typical E values for commercial β alloys are 70–90 GPa in the as-quenched metastable β condition and 100–105 GPa for the annealed $\alpha + \beta$ condition. Average E values for the commercial $\alpha + \beta$ alloys are about 115 GPa [3] but depend on the Al content of each alloy.

5.2.3 Deformation Modes

The ductile behaviour of the hexagonal α -phase, especially at low temperatures, results from the activation of twinning deformation modes in addition to slip. These twinning modes are important for the deformation behaviour of CP titanium and for some α titanium alloys. However, twinning is suppressed nearly completely in two-phase $\alpha + \beta$ alloys by the fine microstructure (small phase dimensions), Al and oxygen content, and the presence of Ti_3Al precipitates. The $\alpha + \beta$ alloys are quite ductile at low temperatures owing to the fine microstructures and to the presence of the non-basal $\mathbf{c} + \mathbf{a}$ slip mode described later.

The bcc β phase also shows twinning in addition to slip, but the occurrence of twinning in β alloys is limited to the single-phase state and decreases with increasing solute content. In fully heat-treated β alloys, which are hardened by the

precipitation of α particles, twinning is completely suppressed. In these alloys twinning might occur during the forming operations prior to ageing. Some commercial β alloys also can form deformation-induced martensite, which further enhances their formability. Formation of this deformation-induced martensite is, however, very sensitive to alloy composition.

5.2.4 Slip Modes

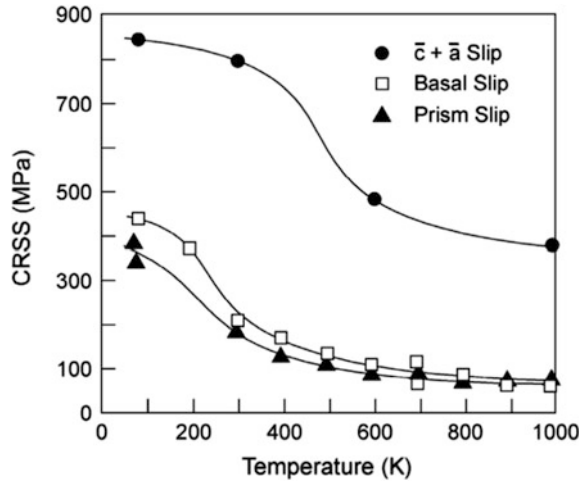
The various slip planes and slip directions for α titanium are indicated in the hexagonal structure cell in Fig. 5.1a. The main slip directions are the three close-packed directions of the type $\langle 11\bar{2}0 \rangle$. The slip planes containing this \bar{a} type of Burgers vector are the (0002) basal plane, the three $\{10\bar{1}0\}$ prism planes and the six $\{10\bar{1}\bar{1}\}$ pyramidal planes. Among these three different types of slip planes together with the possible slip directions there are a total of 12 slip systems, see Table 5.2 [4, 5], but these all have coplanar slip $\langle 11\bar{2}0 \rangle$ directions so do not satisfy the Taylor–Von Mises criterion for deformation of polycrystals. Therefore the $\mathbf{c} + \mathbf{a}$ slip mode is required.

Taking into account the large difference in critical resolved shear stress (CRSS) between $\mathbf{c} + \mathbf{a}$ slip and \mathbf{a} slip, which was measured for Ti–6.6Al single crystals (Fig. 5.2) [6], the percentage of grains deforming by $\mathbf{c} + \mathbf{a}$ slip will be quite low in α titanium polycrystals without crystallographic texture, because the activation of ‘a’ slip is easier even for an angle of about 10° between the stress axis and the c -axis. The absolute values of the CRSS are strongly dependent on alloy content and on test temperature (see Fig. 5.2). The small differences in CRSS at room temperature between the three types of slip systems with a basal (\bar{a} type) Burgers vector become even smaller with increasing temperature (Fig. 5.2). As shown for binary Ti–V alloys [7], the slip systems in bcc β titanium alloys are $\{110\}$, $\{112\}$ and $\{123\}$, all with the same $\langle 111 \rangle$ Burgers vector, in agreement with the generally observed slip modes in bcc metals.

Table 5.2 Slip systems in the hexagonal α phase [4, 5]

Slip system	Burgers vector	Slip directions	Slip planes	No. of slip systems	
				Total	Independent
1	\bar{a}	$\langle 11\bar{2}0 \rangle$	(0002)	3	2
2	\bar{a}	$\langle 11\bar{2}0 \rangle$	$\{10\bar{1}0\}$	3	2
$\bar{2}_3$	\bar{a}	$\langle 11\bar{2}0 \rangle$	$\{10\bar{1}\bar{1}\}$	6	4
4	$\bar{c} + \bar{a}$	$\langle 11\bar{2}\bar{3} \rangle$	$\{10\bar{2}\bar{2}\}$	6	5

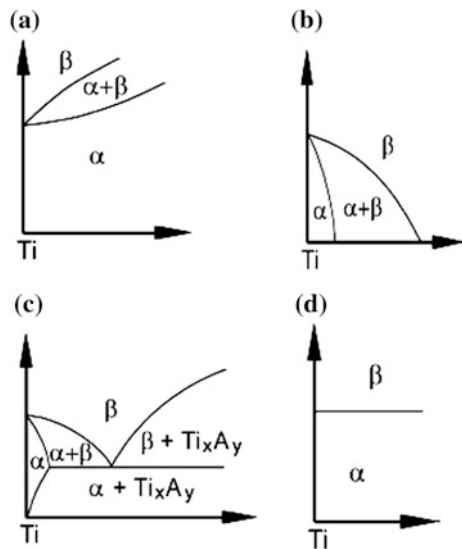
Fig. 5.2 Temperature dependence of CRSS for slip with \bar{a} and $\bar{c} + \bar{a}$ Burgers vectors in single crystals of Ti-6.6Al [6]



5.2.5 Alloying Additions

Alloying elements in titanium are usually classified into α - or β -stabilizing additions, depending on whether they increase or decrease the α/β transformation temperature of 882 °C of pure titanium. The substitutional element Al and the interstitial elements O, N and C are all strong α -stabilizers and increase the transformation temperature with increasing solute content, as can be seen from the schematic phase diagram in Fig. 5.3a.

Fig. 5.3 Schematics showing the effects of alloying elements on titanium alloy phase diagrams: **a** α stabilizers, **b** isomorphous β stabilizers, **c** eutectoid β stabilizers (A = Fe, Cr or Si) and **d** neutral



Aluminium is the most widely used alloying element in titanium alloys, because it is the only common metal that raises the transition temperature and has extensive solubility in both the α and β phases. Among the interstitial elements, oxygen can be considered as an alloying element when the oxygen content is used to obtain the desired strength level, as in different grades of CP titanium. Other α stabilizers include B, Ga, Ge and the rare earth elements, but their solid solubilities are much lower as compared to aluminium or oxygen and none of these elements is commonly used as an alloying element.

The β -stabilizing elements are divided into β -isomorphous elements and β -eutectoid-forming elements, depending on the details of the binary phase diagrams. These are shown schematically in Fig. 5.3b, c. The most frequently used β -isomorphous elements in titanium alloys are V, Mo and Nb. Sufficient concentrations of these elements make it possible to stabilize the β phase to room temperature by suppressing the martensitic reaction that can occur during the quenching of alloys with lower β stabilizer concentrations. Other elements belonging to this group that are rarely used, or not used at all because of density and melting point considerations, are Ta and Re.

Of the β -eutectoid-forming elements, Cr, Fe and Si are used in many titanium alloys (they can form compounds like Ti_xA_y as shown in Fig. 5.3c, where A is Cr, Fe or Si), whereas Ni, Cu, Mn, W, Pd and Bi have only very limited usage. Some of these latter elements are used only in one or two special purpose alloys. Other β -eutectoid-forming elements, such as Co, Ag, Au, Pt, Be, Pb and U, are not used in titanium alloys. **N.B:** It should be mentioned that hydrogen belongs to the β -eutectoid-forming elements. Hydrogen is undesirable in titanium alloys because it can cause embrittlement. Therefore the maximum hydrogen content in CP titanium and titanium alloys is strictly limited to about 125–150 ppm.

In addition, some elements (Zr, Hf and Sn) are considered neutral as shown in Fig. 5.3d, because they do not affect the α/β transformation (β transus) temperature, or lower it only slightly and then increase the transformation temperature again at higher concentrations. Zr and Hf are isomorphous with titanium and therefore they both undergo the same $\beta \rightarrow \alpha$ allotropic phase transformation. These elements have complete solubilities in the α and β phases of titanium. In contrast, Sn belongs to the β -eutectoid-forming elements, but has essentially no effect on the α/β transformation temperature.

Many commercial multi-component alloys contain Zr and Sn, but in these alloys both elements are considered as α -stabilizers. This is because of the chemical similarity of Zr to titanium and because Sn can replace or add to aluminium in the hexagonal-ordered Ti_3Al phase (α_2). When present with aluminium, Sn behaves as an α stabilizer. This example shows that the interactions between alloying elements make it difficult to understand titanium alloying behaviour on the basis of binary Ti-X systems. Rosenberg [8] attempted to express the effect of α -stabilizing elements in multi-component titanium alloys as an equivalent aluminium content by the following equation:

$$[Al]_{eq} = [Al] + \frac{[Zr]}{6} + \frac{[Sn]}{3} + 10[O + C + N] \tag{5.1}$$

Similarly, the potency of β -stabilizers is measured in terms of an equivalent molybdenum content by the following equation [9]:

$$[Mo]_{eq} = [Mo] + 0.67[V] + 0.44[W] + 0.28[Nb] + 0.22[Ta] + 1.6[Cr] + 1.25[Ni] + 1.7[Co] + 2.9[Fe] - 1.0[Al] \tag{5.2}$$

where $[X]$ indicates the wt% concentration of each element.

As already mentioned, aluminium is the most important α -stabilizer and is therefore present in most titanium alloys. The binary Ti–Al phase diagram, Fig. 5.4, shows that with increasing aluminium content the Ti_3Al (α_2) phase will be formed and that the two-phase region ($\alpha + Ti_3Al$) starts at about 6.5 wt% Al for a temperature of about 500 °C (indicated by the black arrow). This value also decreases with increasing oxygen content. To avoid any appreciable amount of Ti_3Al precipitates in the α phase, the aluminium content in most titanium alloys is limited to about 6 wt%. From Fig. 5.4 it can be seen that for 6 wt% aluminium the α/β transformation temperature is increased from 882 °C (0 % Al) to about 1000 °C for the narrow two-phase ($\alpha + \beta$) region.

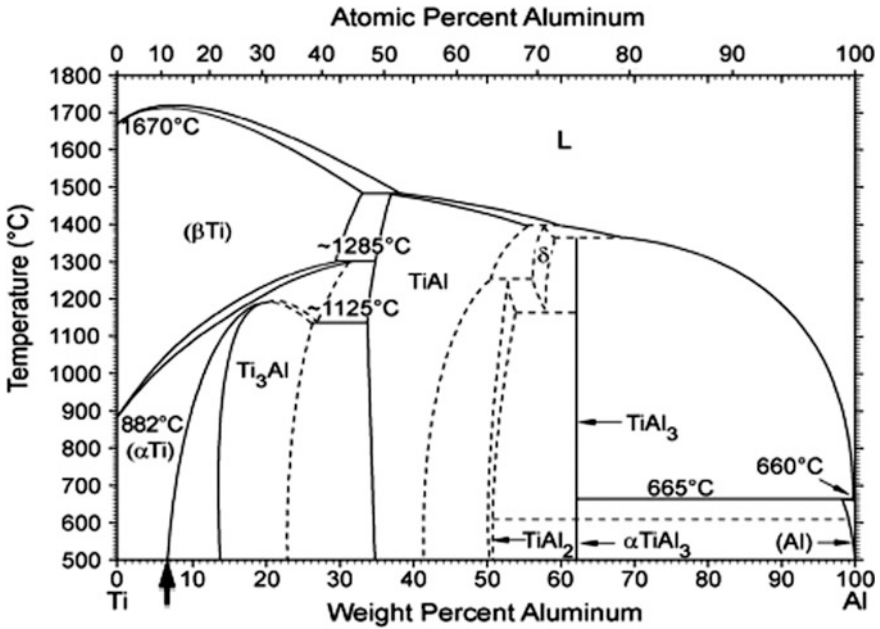


Fig. 5.4 Ti–Al phase diagram [10]; the black arrow points to an aluminium composition of 6 wt% Al, which is about the limit for aluminium additions to most titanium alloys

In addition to conventional titanium alloys, the Ti–Al phase diagram is also the basis for the so-called titanium aluminides, which are recently developed alloys based on the two intermetallic compounds based on Ti_3Al (Alpha-2 alloys), and a ternary orthorhombic variant based on Ti_2AlNb and $TiAl$ (Gamma alloys).

5.2.6 Phase Transformations

Titanium alloy systems include several types of phase transformations. Transformation of the bcc β phase to the hexagonal α phase in CP titanium and titanium alloys can occur martensitically, as mentioned earlier, or by a diffusion-controlled nucleation and growth process, depending on cooling rate and alloy composition. The crystallographic orientation relationship between α and β was first studied (*for zirconium*) by Burgers [11] and is therefore named the Burgers Orientation Relationship (BOR):

$$\begin{aligned} (110)_\beta \parallel (0002)_\alpha \\ [111]_\beta \parallel [11\bar{2}0]_\alpha \end{aligned}$$

The closest-packed bcc (110) plane maps onto the close-packed hcp (0002) plane, and the close-packed directions are congruent. This relationship was also confirmed for titanium [12].

According to the BOR, a bcc crystal can transform to 12 hexagonal variants that have different orientations with regard to the parent β crystal. The BOR is closely obeyed for both the conventional nucleation and growth process and for the martensitic transformation.

Martensitic transformation The martensite transformation in titanium alloys involves the cooperative movement of atoms by a shear-type process, resulting in a microscopically homogeneous transformation of the bcc crystal lattice into the hcp lattice over a given volume. The hexagonal martensite is designated α' and is observed in two morphologies: massive martensite (lath or packet martensite) and “acicular” martensite [13].

With increasing solute content the hexagonal structure of the martensite becomes distorted, losing its hexagonal symmetry and then is properly described as orthorhombic [13]. This orthorhombic martensite is designated α'' . This martensite can also be stress-induced, as may occur in certain alloys like Ti–10V–2Fe–3Al that are at the borderline of stability/metastability.

Titanium martensites are not as hard as steel martensites and cause only marginal strengthening, since there is no appreciable distortion of the lattice by the substitutional solutes such as Al or V.

Athermal and isothermal ω phase formation Although not relevant to any practical application of titanium alloys, it should be mentioned that in many alloys in

which the martensitic reaction is suppressed, the β phase decomposes athermally upon quenching to form the metastable athermal ω phase. This has been suggested to be a precursor to the martensitic reaction because the athermal transformation involves a shear displacement in the $\langle 111 \rangle$ direction of the bcc lattice [14], although this has not been proven. However, the ω particles may serve as nucleation sites for α phase precipitation.

The ω phase can also form isothermally during low temperature ageing of β alloys. However, ω phase formation is generally detrimental to the mechanical properties, and is usually avoided.

Nucleation and diffusion-controlled growth transformation When titanium alloys are cooled at sufficiently low rates from the β phase field into the $(\alpha + \beta)$ phase field, the α phase, which is incoherent with respect to the β phase, first nucleates preferentially at β grain boundaries, leading to a more or less continuous α layer along β grain boundaries. During continued cooling, α plates nucleate either at the interface of the continuous α layer or at the β grain boundary itself and grow into the β grain as parallel plates (so-called α colonies) [15]. They continue to grow into the β grain interior until they meet other α colonies nucleated at other grain boundary areas of the β grain. An example of such a microstructure is shown in Fig. 5.5a.

With increasing cooling rate the size of the α colonies as well as the thicknesses of the individual α plates become smaller. Colonies nucleated at β grain boundaries cannot fill the whole grain interior anymore, and colonies also start to nucleate on

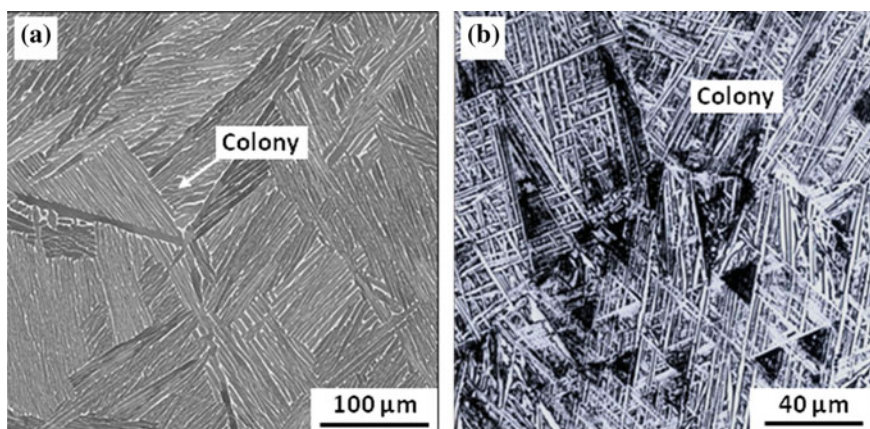


Fig. 5.5 Microstructures in alloy Ti-6Al-4V after cooling from the β phase field: **a** slow cooling resulting in a colony-type structure and α phase at prior β grain boundaries, and **b** faster cooling resulting in a basketweave/Widmanstätten structure

the boundaries of other colonies. To minimize the overall elastic strains the new α plates nucleating by “point” contact on the broad face of an existing α plate tend to grow nearly perpendicular to that plate. This selective nucleation and growth mechanism in combination with the smaller plates within the colonies leads to a characteristic “basketweave” or Widmanstätten microstructure, as shown in Fig. 5.5b.

5.3 Primary Processing: Melting and Consolidation

This section describes the procedures used to formulate titanium alloys and the melting technology used to produce ingots, which are the starting materials for both mill products and remelt stock for titanium castings. The solidification of the molten metal is the key to obtaining homogeneous, high-quality ingots for conversion to mill products. Melt-related defects must be minimized for titanium to perform at a level that justifies its cost and meets the intent of its use, especially in critical components like discs in aeroengines. This means that sophisticated and capital-intensive methods are used to melt titanium and produce sound, homogeneous ingots.

Molten titanium is very reactive, and special means are required to produce ingots of unalloyed titanium and titanium alloys. Titanium and its alloys are melted either in a vacuum arc remelting (VAR) furnace or in a cold hearth melting (CHM) furnace. In both cases melting is done in a manner that prevents molten titanium from contacting furnace refractories such as those used in vacuum induction melting (VIM) furnaces.

5.3.1 Vacuum Arc Remelting (VAR)

First melt electrode This consists of mechanically compacted blocks of titanium sponge and alloying elements that are welded together in an inert gas chamber. Each block has the desired nominal alloy composition from being mixed in a twin cone blender. Because titanium is expensive, there is a strong incentive to recycle and reuse titanium scrap (often called revert), including turnings and chips from machining. This reuse is accomplished for both unalloyed grades and alloys by welding appropriate-grade scrap to the electrode.

Scrap control and usage Revert is carefully controlled with regard to its origin and cleanliness. For example, scrap that has been flame-cut is generally not allowed. Experience has shown that the nitrogen- and carbon-enriched regions along the flame-cut edges are not always refined out during melting. This can leave interstitial-stabilized defects in the final product. Also, machine turnings from component manufacture are subject to special controls. The turnings must be

cleaned to remove any residual cutting fluids and X-rayed to ensure that they contain no WC cutting tool fragments or other high-density inclusions (HDIs) that can end up in the ingot.

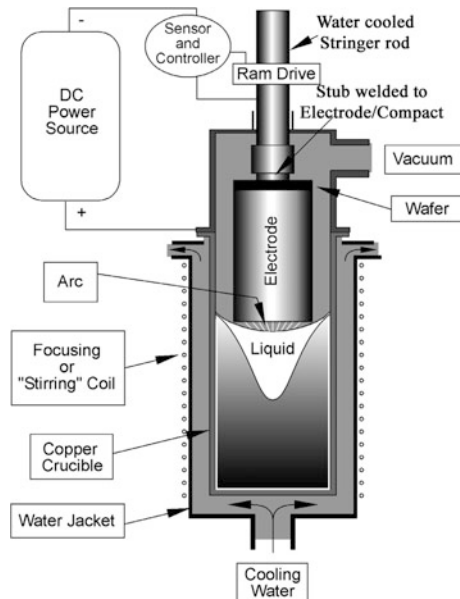
Master alloys Most of the β -stabilizing elements with higher densities and melting points, like Nb, Mo and V, are preferably added in the form of aluminium-based master alloys (Al–V, Al–Mo, Al–Nb, etc., in different ratios). These master alloys reduce the chance of alloy segregation.

VAR production of homogeneous, sound ingots of titanium alloys requires care and detailed attention to the melting procedure, which varies for particular alloys. Over the past several decades, dozens of improvements have been made to the process, some major and some minor. All have been directed towards reducing the possibility of defects and the extent of variation in the ingots. Figure 5.6 shows a schematic of the VAR process.

The VAR-melted ingots can be melted two or three times, depending on the intended end use of the material. There are a number of parameters that must be monitored and controlled to ensure homogeneity and soundness of the ingots:

- The furnace vacuum is continuously monitored to ensure that no air or small water leaks contaminate the melt with nitrogen or oxygen (major water leaks create an explosion hazard).
- The melt rate is continuously adjusted to control the size of the molten pool at the top of the ingot. In segregation-prone alloys, such as Ti–17 or Ti–10V–2Fe–3Al, it is common to melt smaller ingots, less than 75 cm in diameter, and melt at lower rates (5–6 kg/min instead of 8–10 kg/min). This modified melt practice

Fig. 5.6 Schematic of VAR furnace and ingot during a second melt: the electrode being remelted is at the *top*, and the new ingot is at the *bottom*



creates a smaller, shallower molten pool at the top of the ingot. The lower melt rates use correspondingly lower power settings (200–275 kVA instead of 400–500 kVA).

- At the top of the ingot mould most VAR furnaces have electrical coils to create an electromagnetic field to stir the molten metal and improve the ingot homogeneity.
- As the final part (25–35 %) of the ingot is approached, the melt rate is reduced by reducing the power in several steps. This procedure minimizes the extent of shrinkage pipe formation and other melt-related defects such as type II at the ingot top. (See Sect. 5.3.3 for discussion of melt-related type I and type II defects.)

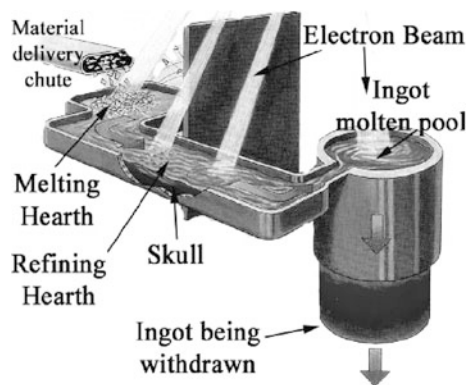
5.3.2 Cold Hearth Melting (CHM)

Cold hearth melting (CHM) is a relatively new melting method (see Fig. 5.7) that has several advantages over the VAR process and is now widely used for aero-engine disc grade alloys. This method uses a water-cooled copper vessel (the hearth), which contains the molten alloy. Melting is done using either a plasma arc or an electron beam as the heat source. In both cases the heat input is balanced against the rate of heat extraction from the water-cooled copper hearth. This maintains a thin layer of solid titanium alloy (called the “skull”) in contact with the hearth, so the molten titanium alloy only contacts the solid titanium alloy. This prevents any contamination by the hearth.

The potential advantages of CHM include the following:

- It permits the residence time of the titanium alloy in the molten state to be controlled independently of the volume of molten metal solidifying as an ingot. This enables refining by dissolution of any nitrogen- or oxygen-rich defects

Fig. 5.7 Schematic of a CHM furnace [1]



without incurring a large, deep molten metal pool (as in the VAR process) that can cause solute segregation.

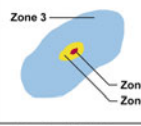



- It automatically introduces gravity separation of HDIs such as WC tool fragments or tungsten welding electrode tips that may be introduced along with the revert. This contrasts with the VAR process, where all of the material in the electrode ends up in the ingot.
- It allows direct casting of non-axis symmetric shapes, such as slabs or bars. These cast products are much better suited for conversion to flat mill products (plate, sheet and strip) than large round ingots. Consequently, the conversion losses are lower and products made this way can be more cost competitive. This capability has proved to be particularly attractive for making sheet and strip from alloys that are readily rolled into coils without reheating.
- In contrast to the physical environment in the VAR furnace chamber, the CHM furnace is more conducive to the use of online sensors, and hence is more amenable to real-time process controls and detection of process variations during melting.

5.3.3 *Melt-Related Defects*

Experience has shown that, once formed, melt-related defects are very difficult to eliminate and can have an extremely detrimental impact on material performance. Melt-related defects can be categorized as either intrinsic or extrinsic, depending on their origin. Extrinsic defects are caused by inadvertent introduction of impurities during preparation of the electrode or during the melt process. Intrinsic defects are those that can be present if ingot solidification occurs without proper control. The nature and origin of melt-related defects in VAR material are discussed in Ref. [16], and Fig. 5.8 shows a schematic of the types of defects.

Type I defects The reactivity of titanium creates the possibility of formation of interstitial-stabilized inclusions. These are known as Type I defects and are most frequently the nitrogen-rich compound TiN. The nitrogen-stabilized Type I inclusions are very hard and brittle and often called “hard alpha”. Consequently, they fracture at relatively low stresses leading to incipient cracks in the material. Type I inclusions also can have high concentrations of oxygen and/or carbon, but this is less common.

Because of the propensity to crack at low strains, a Type I inclusion can seriously decrease the fatigue capability of the material. Over the past 25 years, numerous restrictions have been placed on both input material and on melt practice with the goal of minimizing the presence of type I inclusions in titanium alloy products. Today, the frequency of Type I defects detected in aeroengine disc grade titanium alloys is less than one defect per every 500,000 kg of material melted.

Metallurgical observations (typical)	Type I Defects		Type II Defects	
	Category 1	Category 2	Category 3	Category 4
	<ul style="list-style-type: none"> Nitrogen stabilized hard alpha zone (zone 2) encasing large spongy-appearing void (zone 1) Alpha case surrounded by enlarged or blocky alpha grains or platelets (zone 3) 	<ul style="list-style-type: none"> Small or no voids (zone 1) No hard alpha zone Large area of nitrogen stabilized enlarged and elongated alpha grains or platelets (zone 3) 	<ul style="list-style-type: none"> Microvoids (zone 1) Low or no elevated nitrogen or oxygen concentration Large area of aluminium stabilized enlarged and elongated alpha grains or platelets (zone 3) 	<ul style="list-style-type: none"> Pure elemental segregation of Ti or Al (zone3) 
<ul style="list-style-type: none"> Zone 2 = RC 65-80 Zone 3 = RC 55-70 	RC 45-65	RC 35-45	RC 12	
Zone shape	All Zones Ellipsoid Shaped as Per the Direction of Work			
Most probable cause	Burnt titanium sponge (source material for ingot production)	Contaminated weldment or contaminated revert material entering ingot	Inclusion drop-in during ingot production	Improperly melted/homogenized alloy or a solidification pipe
Defects in 22 in-service discs	41%	41%	14%	4%
Increasing difficulty to detect by ultrasonic testing →				

* RC = Rockwell hardness °C scale

Fig. 5.8 Survey of possible VAR melt-related defects in titanium alloys [17]

However, since the aeroengine industry uses over 1,000,000 kg of titanium alloys each year, the detection and elimination of defects are still essential.

The most effective inspection method is ultrasonic inspection. The basis for detection is the void that usually accompanies the defect. A void occurs owing to the strain incompatibility between the matrix and the hard TiN inclusion. In principle the TiN should be detectable, because it has a modulus about 30 % higher than the average value of the titanium alloy matrix. In practice this modulus difference is about the same as the elastic anisotropy of α titanium. Thus any ultrasonic technique sensitive enough to detect such differences will also detect regions of texture or preferred orientation and lead to many false calls during ultrasonic inspection.

Type II defects These are Al-rich and usually the result of incorporation of Al-rich regions from the shrinkage pipe near the top of the ingot into the product. Type II defects are less detrimental to the alloy properties than Type I defects; but in high strength alloys such as Ti-17 these defects do not respond to heat treatment (ageing) in the same way as the surrounding matrix, and therefore remain softer. Consequently, they will deform preferentially in fatigue situations, leading to earlier crack nucleation. Type II defects are eliminated by proper melt practice and cropping the part of the ingot top that contains the shrinkage pipe. It is also possible to minimize them by ingot homogenization (see below).

Beta flecks These are due to alloy segregation. Alloys that contain β -eutectoid forming elements, in particular Fe and Cr, typically have depressed freezing temperatures, resulting in solidification over a significant temperature range. This

situation can lead to Fe or Cr segregation during ingot solidification. Alloys that contain only β -isomorphous alloying additions, such as Mo, V and Nb, do not have similarly depressed solidification temperatures, and these alloys are much less prone to freezing segregation.

Segregation of Fe or Cr during freezing results in regions that have a lower β transus temperature. These regions have a different microstructure compared to the surrounding material in the final product. These solute-rich regions sometimes become clearly visible in materials heat-treated below but near the nominal β transus, and are known generally as “beta flecks”. Figure 5.9 shows examples of beta flecks: note the large prior β grains and the lower volume fraction of α (the light-etching phase) in Fig. 5.9c. The segregated areas typically occur on a scale ranging from a few hundred micrometres to a few millimetres. These solidification-related defects *can* occur in any titanium alloy, but as mentioned earlier, alloys containing eutectoid-forming elements, such as Cr or Fe, are considerably more susceptible.

Like Type I and type II defects, beta flecks are detrimental to the fatigue strength. However, beta flecks more resemble Type II defects in their fatigue behaviour, since they are weaker than the matrix and deform preferentially, leading to early crack nucleation. Also, like Type II defects, beta flecks can be minimized by proper melt practice and by ingot homogenization.

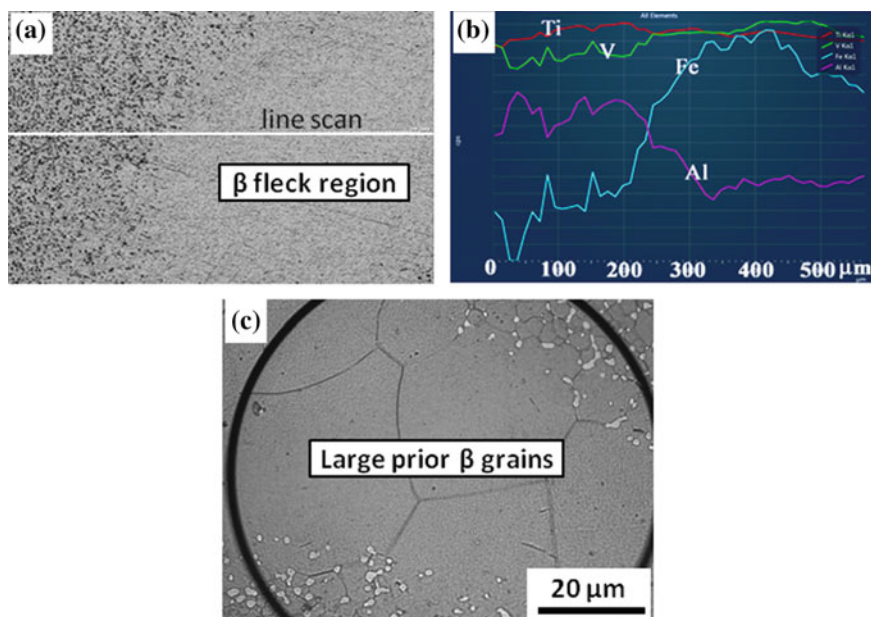


Fig. 5.9 Beta flecks in the alloy Ti-10V-2Fe-3Al **a** showing an SEM image of a beta fleck region; **b** EDAX line scanning of the image in (a); and **c** optical image of an etched beta fleck region

5.3.4 Conditioning and Homogenization

Irrespective of melt practice, after completion of the final melt process and before hot working the ingot undergoes conditioning. Conditioning creates a smoother ingot surface free from stress concentrations that could induce cracking during the ingot breakdown and conversion operations. This conditioning can be done by grinding or lathe turning of cylindrical ingots, or by grinding of slabs. Grinding is often done manually and care must be taken to control the surface temperature increase during grinding. If not done carefully, the temperature can get high enough to create interstitial-stabilized regions that can subsequently be retained in the final product.

Once the ingot is conditioned it is generally given a homogenization anneal in the β phase field prior to working. Not all titanium producers use a homogenization treatment, and not all producers do this for all alloys. When a homogenization treatment is used, the times and temperatures are alloy-dependent, but are typically 200–450 °C above the β transus for times of 20–30 h. It is important to emphasize that homogenization does not remove HDIs such as WC and Type I (hard alpha) defects.

5.4 Secondary Processing

5.4.1 Forging

Initial working (also called ingot breakdown) This is done on a forging press at a temperature of about 150 °C above the β transus. During this operation the initial round ingot is converted into a square or round-cornered square workpiece. The amount of initial strain before the first necessary reheat is typically 28–38 %, although it is somewhat alloy-dependent and also depends on whether the ingot has been homogenized.

The workpiece is fan-cooled after the initial working operation, and then is reheated to 35–50 °C below the β transus, i.e. within the ($\alpha + \beta$) phase field. It is then given a further reduction of about 30–40 % to recrystallize it and refine the structure in preparation for continued hot working. After this reduction the workpiece is air-cooled. The workpiece is then reheated to about 50 °C above the β transus and worked another 30–40 %, followed by a rapid cool (Ti–6Al–4V is water quenched, other alloys such as Ti-17 or Ti-10-2-3 are aggressively fan-cooled).

The basic intent of this initial heating, working, cooling, reheating, working and cooling is to improve the compositional homogeneity and thus the structural uniformity of the alloy workpiece. This improves its subsequent response to thermo-mechanical processing operations. The remaining hot working operations are typically done in the ($\alpha + \beta$) phase field. A minimum of 65 % additional reduction

is typically used to obtain uniform structures that will respond to forging or heat treatment and are more amenable to ultrasonic inspection.

N.B: In segregation-prone alloys, where the initial ingot size is smaller, an upsetting operation may be used to provide a large enough diameter workpiece that will yield a large diameter billet to enable maintaining the reductions mentioned above.

Secondary working steps These are mainly determined by the shape of the product form that the ingot is destined to become (billet, plate, sheet or bar). Before continuing, the workpiece is inspected for surface cracks or tears and any sharp discontinuities that could propagate during continued working. If present, these are blended out during a conditioning operation.

There are basically four types of titanium alloy mill products: billet, bar, flat-rolled product (plate and sheet) and casting electrode:

- Billet is typically round and is used as the input material for forgings and rolled rings.
- Bar can be round, square or shaped during rolling to meet a special need.
- Plate is a flat-rolled product thicker than about 25 mm.
- Sheet is a flat-rolled product up to a thickness of about 25 mm.
- Casting electrode is remelted by the casting producer and hence must have a billet-like shape, but it is shaped to the desired diameter and cut to length without regard for the need to create a particular microstructure, since it will be remelted.

Billet and Bar Billet and large diameter bar are made using a rotary general forging machine (GFM) or a forging press. Since billet is a semi-finished product used for making die forgings, the billet surface finish must be adequate to permit high sensitivity ultrasonic inspection. Depending on the alloy and the billet forging temperature, rough grinding or machining may be required.

Bar, on the other hand, is a finished product. Thus it always requires grinding or turning to impart an acceptable surface finish and uniform dimensions and shapes. A GFM gives a better surface finish and concentricity than a forging press, making the GFM product more economical. The other benefits from using GFMs are that they introduce uniform work into the product; they require fewer, if any reheats; and they are easy to control. Smaller diameter bar is finished in a rod mill that has a series of shaped rolls with successively smaller openings.

For both billet and bar the working temperature is normally in the ($\alpha + \beta$) phase field, typically 50–70 °C below the β transus. (Although there are exceptions when special properties are required from $\alpha + \beta$ alloys worked in the β phase field.)

N.B. Some important considerations:

1. Hot working requires close control. Titanium alloys have relatively poor thermal conductivity and relatively high flow stresses at all ($\alpha + \beta$) working temperatures. At high rates of deformation the thermal conductivity is too low to allow

heat dissipation, resulting in adiabatic heating. This can lead to localized flow softening in active shear bands, resulting in further strain localization and formation of intense shear bands. These result in non-uniform microstructures after recrystallization of the final product.

2. Under extreme circumstances the critical strain for ductile fracture is locally exceeded in the shear bands and small voids are formed. These voids are known as strain-induced porosity (SIP). (This SIP can also be created in plate, particularly if the working temperature is allowed to drop.)

Once SIP is created in forging billet, it is not always healed during subsequent forging operations. Consequently, it can be carried over into a finished component as a fatigue-nucleating defect. SIP is typically small and can be difficult to detect by ultrasonic inspection.

3. Alternatively, adiabatic heating can be beneficial if it is properly managed, since it can extend the working time and deformation extent between reheats.

An additional reason for careful control is that in alloys prone to beta fleck formation the adiabatic heating must not result in exceeding the local β transus in solute-rich regions of the workpiece, thereby perpetuating the microstructural inhomogeneity.

5.4.2 Rolling

Plate and sheet comprise 40 % of titanium mill products. Plate, sheet and small diameter bar (including rod) are all made in rolling mills with either flat or shaped rolls. Normally, a “four-high” rolling mill (each work roll is backed by a second roll) is used for hot rolling titanium alloy plate and sheet.

The starting material for plate and sheet is a forged bloom that is an intermediate product of the ingot conversion process. The bloom is hot-rolled into a slab, which then receives further hot reductions. The hot rolling operations may be done in either the β or the ($\alpha + \beta$) phase fields, depending on the alloy and on the end properties desired. For plate the final hot reduction stops at the desired thickness. The plate is then given an annealing treatment before it is surface conditioned by grinding and/or pickling.

Flat-rolled products require reheating more frequently because the plane strain imposed during rolling increases the incidence of edge cracking. The final annealing treatment is typically more of a stress relief than a true anneal. For example, Ti-6Al-4V is often shipped to users in the so-called mill-annealed condition.

Mill annealing means that the plate has been held at about 700 °C for times as short as 1 h or as long as 8 h. N.B: At higher annealing temperatures the yield stress can be lower than the initial residual stresses. This can cause relaxation of internal residual stresses by gross plastic deformation of the plate, causing it to lose flatness during the annealing treatment. Holding for longer times will result in flatness

recovery owing to creep flattening. Thus the flatness of the product after annealing is a function of the amount of work and the annealing time and temperature. Such plates are most frequently used for machining into aircraft parts.

Titanium alloy sheet is typically pack-rolled to avoid surface oxidation. In pack rolling, a group of sheet blanks are sealed in a steel retort and rolled as a group. The individual blanks have an inert “parting agent” between them to prevent bonding to one another during rolling. After hot rolling is completed the pack is cut open and the finished sheets are extracted, pickled and creep flattened or annealed in fixtures, depending upon the required flatness. Some final cold reduction also can be done to meet gauge and flatness requirements.

Sheet packs are often cross-rolled to widen the sheet. Cross-rolling also reduces the texture intensity (preferred crystallographic orientation) and the texture symmetry in the final product. Texture can be very important for the forming response of $\alpha + \beta$ alloy sheet, which tends to develop strong textures during hot working. This makes some properties (e.g. yield stress and modulus of elasticity) anisotropic, and this anisotropy must be taken into account during the design of structures and components made from sheet.

Strip is a sheet-like product, but typically narrower than sheet and very long. Strip is essentially unidirectionally rolled and coiled after the final rolling operation. The majority of strip is produced from one of the grades of CP titanium (usually Grade 2) or the alloy Ti–3Al–2.5V, both of which can be cold-rolled. The production of strip has enabled the economical production of welded CP titanium and Ti–3Al–2.5V tubing for aircraft heating and de-icing ducts. Beta 21S is a β titanium alloy which is also produced in strip form.

The early stages of strip production are identical to those for sheet and plate. However, at the slab stage the strip is hot-rolled, annealed, pickled, surface conditioned by grinding and coiled as hot band, which is the intermediate product used for cold rolling. It is then cold-rolled to gauge in a multi-stand mill such as a Steckel or Sendzimir mill. These mills use several rolls to back a pair of very small diameter work rolls, thereby ensuring the flatness of the thin, cold-rolled product. After cold rolling, the strip is annealed again and coiled for shipment. Because of the unidirectional working, strip always has a significant degree of texture, but because most strip is CP titanium, this is generally not a limitation.

5.5 Titanium Alloy Castings

The use of cast titanium components has grown over the past 10 to 15 years, owing to decreased costs and improvements in the casting process [18, 19]. The growth in the use of castings has resulted in fewer fabrication steps, by eliminating assembly from a number of parts. In some cases castings have replaced parts that were previously machined from forgings or heavy plate or billet. The substitution of castings for components made by other methods has been enabled by three factors:

- Improved net shape casting technology.
- Improved fatigue properties owing to the use of hot isostatic pressing (HIP) to heal internal porosity that can act as crack initiation sites.
- Decreased metal–mould reaction.

Casting of titanium alloys on a production scale is done using one of two methods: (i) conventional casting using rammed graphite moulds, and (ii) investment casting in ceramic shell moulds. Investment casting is more costly, but its shape-making capability makes the resulting castings economically attractive because they can displace very expensive forged and machined or fabricated parts.

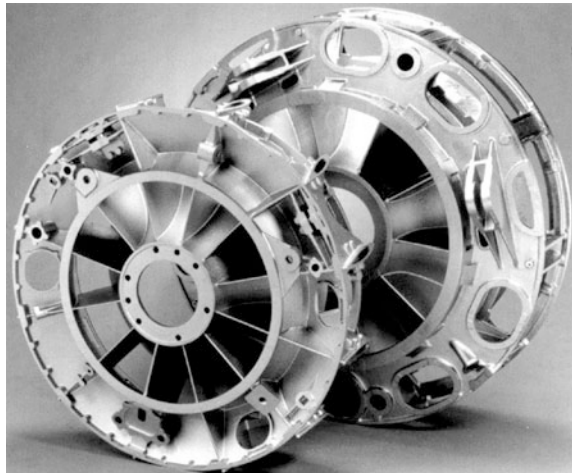
Furthermore, as Fig. 5.10 illustrates, the investment casting method is capable of producing highly intricate shapes with essentially a net shape. In this case, this single-piece casting replaced welded and mechanically fastened frames that contained more than 100 individual parts including the fasteners.

After casting, the following steps are taken:

- Hot isostatic pressing (HIP-ing) to close any internal voids.
- Chemical milling to remove any reaction zone resulting from contact between the mould and the molten titanium alloy.
- Weld repair, if necessary, to close surface-connected defects due to shrinkage, hot tearing or incomplete mould-filling.
- Stress relief heat treatment (if necessary).
- Final simple chemical milling.

Weld repair of high-value castings allows these parts to be used instead of being scrapped, but the weld repair is labour-intensive and therefore costly. Weld repair is typically done using tungsten inert gas (TIG) welding. Depending on the sizes of the casting defects, metal in the form of weld filler wire may be used to repair them. It is expensive to make weld wire from all the high-performance alloys, including Ti–6Al–4V. However, for alloys available as sheet, narrow strips can be cut and used as filler.

Fig. 5.10 Example of an investment cast aircraft engine frame [1]



Since weld repairs are costly, any improvements in casting technology would reduce the cost of titanium castings and could lead to an increased market share. An improved casting process currently under development is permanent mould casting. Permanent moulds have been used for casting lower melting point materials, e.g. Al and Mg and less reactive high melting point materials such as steel.

The challenge for permanent mould casting of titanium is to minimize the interaction of the molten metal with the mould while obtaining adequate superheating to permit good fill. Currently, castings of about 200 mm in maximum dimension represent the size limit that can be produced by titanium permanent mould casting. This limit is partly due to the sizes of available HIP pressure vessels.

5.6 Indian Scenario on Titanium Alloy Processing

The value of the titanium primary processing industry is well above US\$ 1 billion. If secondary processing and manufacturing is added, the world figure is likely to be well in excess of US\$ 2 billion.

In general, the issues for the titanium industry are mostly economical rather than technical, and have their origin in the too-close connection to the aerospace industry. This link has operated to the detriment of industrial developments that would otherwise give a wider market base and make titanium alloy production less dependent on aerospace demand cycles. The aerospace connection of titanium alloys has also resulted in production processes which are not suitable or too stringent for other industrial applications.

The present Indian scenario is very promising, specifically for aerospace grade titanium alloys. India is characterized by its vast reserves of rich ilmenite deposits all along its southern peninsular coasts. The reserves are estimated at 520 million tonnes (12–15 % of world total) and the reserves of rutile are estimated at 30 million tonnes in terms of TiO₂ content.

Mishra Dhatu Nigam Limited (MIDHANI), Hyderabad, is the only manufacturer in India having the capabilities for ingot melting and producing titanium mill products, starting from titanium sponge, which is imported at present. MIDHANI has been in operation since 1982 for the production of billets, plates, sheets, wire and seam-welded tubes for meeting indigenous demands. Also, the mineral separation unit of Kerala Minerals and Metals Ltd. (KMML), Sankaramangalam, has started producing aerospace quality titanium sponge for Indian applications: see Chap. 4 of this Volume of the Source Books.

The Indian Military Airworthiness regulatory body, i.e. the Centre for Military Airworthiness and Certification (CEMILAC), has approved MIDHANI for processing titanium alloys for aerospace and missile applications. There are many Indian programmes for indigenously produced and type-approved titanium alloys being produced at MIDHANI. Table 5.3 gives a detailed list of titanium alloys that are indigenously manufactured and provided with an airworthiness clearance.

Table 5.3 Type-approved and provisionally cleared indigenously produced titanium alloys

Alloy designation	Type	Form	Composition
BT 5-1	α Alloy	Forged and hot-rolled bars	Ti–5Al–2.5Sn
Titan 23A/OT4-1	Near- α alloy	Forged and hot-rolled bars	Ti–2Al–1.5Mn
		Cold-rolled sheets	
Titan 29A	Near- α alloy	Forged bars and HR bars	Ti–5.8Al–4Sn–3.5Zr–0.7Nb–0.5Mo–0.35Si–0.06C
Titan 26A (triple melted)	Near- α alloy	Forged bars	Ti–6Al–5Zr–0.5Mo–0.25Si
Titan 31A (triple melted)	$\alpha + \beta$ alloy	Forged and HR bars	Ti–6Al–4V
Titan 31A (double melted)		Forgings	Ti–6Al–4V
Titan 31 (Ti6Al4V ELI)		Forged and machined bars	Ti–6Al–4V (O < 1300 ppm)
BT 9-1	$\alpha + \beta$ alloy	Hot-rolled bars	Ti–6.5Al–3.3Mo–1.4Zr–0.25Si
BT 3-1	$\alpha + \beta$ alloy	Forged and HR bars	Ti–6.25Al–2Cr–2.5Mo–0.27Si–0.45Fe
<i>Provisionally cleared alloys</i>			
Titan 20A	CP Ti	Forged and HR Bars	Ti–0.4O
Titan 22A	α alloy	Hot-rolled/machined bars	Ti–8Al–1Mo–1V
Half alloy	$\alpha + \beta$ alloy	Forged and machined bars	Ti–3Al–2.5V
GTM 900	$\alpha + \beta$ alloy	Forged and hot-rolled bars and slabs	Ti–6.5Al–3.3Mo–1.4Zr–0.25Si
Titan 1023	Metastable β alloy	Forged and hot-rolled bars	Ti–10V–2Fe–3Al

5.7 Summary

In this chapter the basic crystallography and deformation modes of titanium alloys have been briefly considered. The different alloying elements of titanium and their use have been mentioned, and the melting techniques for industrial scale melting of titanium alloys have been described. The VAR process is generally more prevalent, but CHM is gaining popularity. In India VAR is the main industrial melting process, while the CHM electron beam melting process is becoming established. Common types of melt-related defects have also been discussed. Finally, ingot processing and casting techniques have been broadly described for wrought and cast products.

Acknowledgments The authors wish to place on record that Prof G. Lütjering would certainly have been included as an author but for his untimely demise. Nevertheless, the authors cannot thank him enough for the repository of knowledge that he has created in the second edition of the book on Titanium published by Springer publications. The authors would like to thank Dr. A.K. Gogia, Dr. TK Nandy and Mr. Dipak Kumar Gupta of DMRL; Mr. Ramesh Babu, Mr. GVR Murthy and Mr. U.V. Gururaja of Midhani; and Mr. VP Deep Kumar of ADA for many inputs and technical data. They profoundly thank the editors, Dr. N Esvara Prasad and Dr. RJH Wanhill for their help in reviewing the contents of the book chapter and also for their constructive comments. The authors (AB and BS) are greatly indebted to Prof D. Banerjee, Dr. K. Tamilmani, Dr. Amol A. Gokhale and Dr. Samir V. Kamat for their kind support and encouragement. Funding from DRDO is gratefully acknowledged.

References

1. Lütjering G, Williams JC (2007) Titanium: engineering materials and processes, 2nd edn. Springer, Berlin, Germany
2. Zarkades A, Larson FR (1970) Elasticity of titanium sheet alloys. The science, technology and application of titanium. Pergamon Press, Oxford, UK, pp 933–941
3. Boyer R, Welsch G, Collings EW (eds) (1994) Materials properties handbook: titanium alloys. ASM International, Materials Park, OH, USA
4. Partridge PG (1967) The crystallography and deformation modes of hexagonal close-packed metals. *Metall Rev* 12(1):169–194
5. Yoo HM (1981) Slip, twinning, and fracture in hexagonal-close packed metals. *Metall Trans A* 12A:409–418
6. Paton NE, Baggerly RG, Williams JC (1976) Deformation and solid solution strengthening of titanium-aluminum single crystals. Rockwell Report SC 526.7FR
7. Paton NE, Williams JC (1970) The deformation of body-centered-cubic titanium-vanadium single crystals. In: Proceedings of 'second international conference on the strength of metals and alloys'. ASM International, Materials Park, OH, USA, pp. 108–116
8. Rosenberg HW (1970) Titanium alloying in theory and practice. In: Jaffe RI, Promisel NE (eds) The Science, technology and application of titanium (The first international Conference on titanium, London). Pergamon Press, Oxford, UK, pp 851–859
9. Bania PJ (1993) Beta titanium alloys and their role in the titanium industry. In: Eylon D, Boyer RR, Koss DA (eds) Beta titanium alloys in the 1990's. TMMS, pp 3–14
10. Baker H (ed) (1992) Alloy phase diagrams, ASM handbook, vol 3. ASM International, Materials Park, OH, USA
11. Burgers WG (1934) On the process of transition of the cubic-body-centered modification into the hexagonal-close-packed modification of zirconium. *Physica* 1:561–586
12. Newkirk JB, Geisler AH (1953) Crystallographic aspects of the beta to alpha transformation in titanium. *Acta Metall* 1(3), pp. 370–371, 373–374
13. Williams JC (1973) Titanium science and technology. Plenum Press, New York, NY, USA, p 1433
14. Collings EW (1994) Materials properties handbook: titanium alloys. ASM, Materials Park, OH, USA, p 1
15. Peters M, Lütjering G, Ziegler G (1983) Control of microstructures of ($\alpha + \beta$)-titanium alloys. *Zeitschrift für Metallkunde* 74:274–282
16. Adams RT, Rosenberg HW (1982) Titanium and titanium alloys. Plenum Press, New York, NY, USA, p 127
17. Costa JG, Gonzalez RE, Guyotte RE, Salvano DP, Swift T, Koenig RJ (1990) Titanium rotating components review team report. United States of America Federal Aviation

Administration, Aircraft Certification Service, Engine and Propeller Directorate, Burlington, MA 01803, USA

18. Chen CC, Boyer RR (1979) Practical considerations for manufacturing high strength Ti–10V–2Fe–3Al alloy forgings. *J Met* 31(7):33–39
19. Boyer R, Welsch G, Collings EW (eds) (1994) Technical note 3: casting. In: *Materials properties handbook: titanium alloys*. ASM International, Materials Park, OH, USA, pp 1079–1082

Bibliography

1. Leyens C, Peters M (eds) (2003) *Titanium and titanium alloys: fundamentals and applications*. Wiley-VCH Verlag GmbH & Co. KGaA, Weinheim, Germany

Chapter 6

Titanium Alloys: Part 2—Alloy Development, Properties and Applications

A. Bhattacharjee, B. Saha and J.C. Williams

Abstract Titanium alloys are the principal replacements, and in many cases also prime candidate materials to replace (i) aerospace special and advanced steels, owing to their significantly higher usable specific strength properties, (ii) aluminium alloys due to their better elevated temperature properties and (iii) nickel-base superalloys for much of the high pressure compressors (HPCs) of modern engines, owing to their superior medium temperature (up to 550 °C) creep strength and acceptable oxidation and corrosion resistances. This chapter summarizes the chemical compositions, properties and applications of commercially pure α -titanium, near- α , $\alpha + \beta$ and β titanium alloys.

Keywords Titanium alloys · Secondary processing · Microstructures · Mechanical properties · Fatigue · Fracture · Applications

6.1 Introduction

Conventional titanium alloys consisting of α -titanium, near- α , $\alpha + \beta$ and β titanium alloys are used in various engineering sectors, but predominantly for aerospace because of cost. These alloys possess good corrosion resistance and a range of strengths starting from commercially pure titanium up to the high strength β titanium alloys, which can compete with steels on a density normalized basis. The near- α titanium alloys have the best combinations of strength and high temperature

A. Bhattacharjee (✉)
Materials Processing Division, DMRL, Hyderabad, India
e-mail: amitb@dmrl.drdo.in

B. Saha
RCMA (Materials), CEMILAC, Hyderabad, India
e-mail: bsaha@cemilac.drdo.in

J.C. Williams
Dept. of Materials Science & Engineering, The Ohio State University, Columbus, USA
e-mail: williams.1726@osu.edu

properties and are the natural choice for high temperature aerospace applications. The $\alpha + \beta$ titanium alloys have good strength and medium temperature capability.

In this chapter a review of each of these classes of titanium alloys will be given, and their generic processing, microstructure, mechanical properties and applications will be concisely discussed. The reader may obtain more details from the Bibliography.

6.2 Titanium Alloy Developments and Applications

There are numerous review articles and monographs that cover titanium alloy development as well as their production and applications aspects in detail [1–40]. In this section these aspects are dealt with briefly.

6.2.1 *Commercially Pure Titanium and α -Titanium Alloys*

All α -titanium alloys are based on the low temperature, hexagonal allotropic form of titanium. These alloys can contain substitutional alloying elements (Al or Sn) or interstitial elements (oxygen, carbon or nitrogen) that are soluble in the hexagonal α phase. These alloys also contain limited quantities of elements with limited solubility, such as Fe, V and Mo.

Specific alloys have been formulated to improve the environmental resistance of CP titanium and α -titanium alloys to provide comparable performance at reduced cost. Table 6.1 lists these alloys, their compositions and typical yield strengths.

All the alloys derive their characteristics from the hexagonal α phase, as mentioned earlier. The strengthening and processing aspects of these alloys can be obtained from Refs. [1, 25] and are summarized in Table 6.2 and Fig. 6.1, respectively. Referring to Fig. 6.1, stage II processing controls the preferred orientation (texture) intensity and α grain size; and the microstructure after stage III processing is controlled by the degree of deformation and the annealing temperature, which influences the α grain size with marginal effect on texture intensity.

Applications The excellent corrosion resistance of CP titanium, its good weldability and general fabricability have resulted in its use for aerospace tubing, e.g. in anti-icing ducts. However, the alloys Ti-2.5Cu and Ti-3-Al-2.5V offer higher strength alternatives with similar ease of fabrication (Ti-2.5 Cu in the annealed condition). Also, Ti-25Cu in the aged condition is used in engine bypass ducts owing to a higher temperature capability (up to 350 °C).

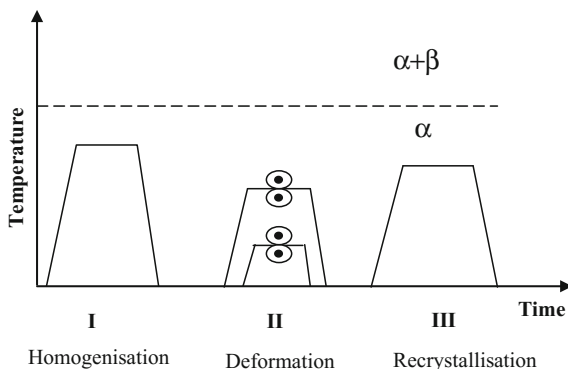
Table 6.1 Compositions and 0.2 % yield strengths of commercial CP titanium and α -titanium alloys [1]

Alloy		O (max) wt%	Fe (max) wt%	Other elements	0.2 % Yield strength (MPa)
<i>CP titanium</i>					
CP	Grade 1	0.18	0.20		170
	Grade 2	0.25	0.30		275
	Grade 3	0.35	0.30		380
	Grade 4	0.40	0.50		480
Ti–0.2Pd	Grade 7	0.25	0.30	0.12–0.25Pd	275
	Grade 11	0.18	0.20		170
Ti–0.05Pd	Grade 16	0.25	0.30	0.04–0.08Pd	275
	Grade 17	0.18	0.20		170
Ti–0.1Ru	Grade 26	0.25	0.30	0.08–0.14Ru	275
	Grade 27	0.18	0.20		170
<i>α-titanium alloys</i>					
Ti–0.3Mo–0.9Ni (Grade 12)		0.25	0.25	0.2–0.4Mo, 0.6–0.9Ni	345
Ti–2.5Cu		0.20	0.20	2.5Cu	600
Ti–3Al–2.5V (Grade 9)		0.15	0.25	2.5–3.5Al, 2.0–3.0V	485
Ti–3Al–2.5V–0.05Pd (Grade 18)		0.15	0.25	2.5–3.5Al, 2.0–3.0V, (+Pd)	485
Ti–3Al–2.5V–0.1Ru (Grade 28)		0.25	0.25	2.5–3.5Al, 2.0–3.0V, (+Ru)	485
Ti–5Al–2.5Sn (Grade 6)		0.20	0.20	4.0–6.0Al, 2.0–3.0Sn	795
Ti–5Al–2.5Sn ELI		0.15	0.25	4.75–5.75Al, 2.0–3.0Sn	725

Table 6.2 Strengthening mechanisms in CP titanium and α -titanium alloys [1]

Strengthening mechanism	Dependence	Examples/limitations
Grain size	$d^{-1/2}$	Fine grains limit twinning
Interstitial solid solution	$c^{1/2}$	Strain localization >2500 ppm oxygen
Substitutional solid solution	c	Strain localization >5 % Al equivalence
Texture	c -axis orientation	Max. strength when loaded along c -axis
Precipitation	$r^{1/2}, f^{1/2}$	Ti–2.5Cu; other alloys >5.5 % Al equivalence

Fig. 6.1 Schematic of processing for CP titanium and α -titanium alloys [1]



6.2.2 High Temperature Near- α Titanium Alloys

Alloy development For long-term applications at high temperatures the $\alpha + \beta$ titanium alloys, such as Ti-6Al-4V, are limited to about 350 °C. For higher temperatures near- α alloys such as Ti-6Al-2Sn-4Zr-2Mo + Si (Ti-6242) and Ti-5.8Al-4Sn-3.5Zr-0.5Mo-0.7Nb-0.35Si-0.06C (IMI 834) have been developed according to the following general principles:

- (1) The diffusion rates in the β phase are about two orders of magnitude faster than in the α phase. Therefore the volume fraction of β phase is reduced in these high temperature alloys as compared to Ti-6Al-4V.
- (2) The decrease in volume fraction of β phase in Ti-6242 and IMI 834 is achieved by reducing the total content of β stabilizing elements and by alloying with the α stabilizers Sn and Zr as well as about 6 wt% Al.
- (3) Furthermore, the β stabilizing element vanadium is replaced by Mo and Nb which are slower diffusing elements [37].
- (4) In addition, the contents of Fe and Ni, which are very strong β stabilizers and also lead to very fast diffusion rates in α titanium [38], are reduced especially in IMI 834 to the very low levels of about 150 ppm.
- (5) Owing to the reduction in volume fraction of β phase there is a potential problem: the thickness of the “ β lamellae” in a colony structure is reduced in many areas to zero, i.e. only low angle boundaries are left to separate parallel α lamellae. In this case, easy slip is possible over long distances with negative consequences, especially for fatigue strength (High Cycle Fatigue, HCF, and Low Cycle Fatigue, LCF).

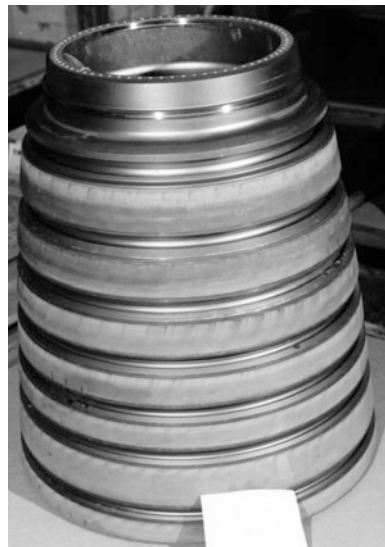
To create new obstacles to dislocation motion at the α/α lamellae boundaries, silicon is added to high temperature alloys (about 0.1–0.5 %). Silicon combines with titanium to form the intermetallic compound Ti_5Si_3 , or in the presence of zirconium the compound $(Ti,Zr)_5Si_3$. The silicides are incoherent with respect to β and α and precipitate at the α/β lamellae boundaries and at grain boundaries, providing effective barriers to slip transfer.

- (6) Since coherent precipitates are effective barriers for dislocation glide and climb, the volume fraction of Ti_3Al (α_2) particles is increased in high temperature titanium alloys, mainly owing to the addition of Sn, which adds to Al in promoting the formation of α_2 , which is then $\text{Ti}_3(\text{Al},\text{Sn})$. As an indication of their effectiveness, the solvus temperature for α_2 in Ti-6Al-4V is around 550–600 °C, in Ti-6242 around 650 °C and in IMI 834 around 750 °C.
- (7) In contrast to Ti-6Al-4V, the standard final heat treatment in Ti-6242 and IMI 834 is always an ageing treatment in the ($\alpha + \alpha_2$) phase region, i.e. 8 h 595 °C for Ti-6242 and 2 h 700 °C for IMI 834.

Processing The processing routes used to generate different microstructures, for example fully lamellar or bi-modal microstructures, in high temperature near- α titanium alloys (Ti-6242, IMI 834) are the same processing routes as those outlined in the next subsection for $\alpha + \beta$ titanium alloys. The only additional feature important for the processing route of high temperature near- α titanium alloys is the solvus temperature of the silicides in relation to the other temperatures in the processing route.

Applications The main applications of high temperature titanium alloys such as Ti-6242 and IMI 834 are blades and discs in the compressor sections of aero-engines, where the temperature exceeds 350 °C and Ti-6Al-4V cannot be used because of creep considerations. A good example is the CF6 HP compressor spool shown in Fig. 6.2, with five Ti-6Al-4V front stages followed by two Ti-6242 rear stages. Since the maximum temperature capability is about 500 °C for Ti-6242, the last stages in the HP compressors are made out of nickel-base superalloys.

Fig. 6.2 Compressor spool for GE CF6 class engine using inertia welding to connect the individual stages: front (smaller) five stages: Ti-6Al-4V; rear two stages: Ti-6242 [1]



A bi-modal microstructure is used for the Ti-6242 stages (as well as for the Ti-6Al-4V stages) because it gives the best LCF strength as well as adequate creep strength. The IMI 834 alloy can be used up to about 550 °C and is used for making blades and integrally bladed discs (blisks) in the EJ 200 aeroengine [39] and the Rolls-Royce TRENT 800 engine.

Another Ti-6242 application is the impeller shown in Fig. 6.3. Impellers are used as the last compressor stage in small (lower flow) aeroengines and in auxiliary power units (APUs).

Effect of Ni and Fe There can be considerable lot-to-lot variation in the creep strength of Ti-6242 as well as IMI-834. This variation is mainly due to variation in the concentration of Ni, which is a minor impurity that comes from vacuum distillation of Ti sponge (see Chap. 4 in this Volume) on stainless steel trays. Similar variations also appear to apply to other impurities such as Fe and Co, all at the trace impurity level. The effect of Fe has been recognized for some time, and the Fe concentration is deliberately and effectively managed by the material producers by selecting low-Fe sponge for alloy formulation.

In fact, Ni and Fe impurities are particularly troublesome in titanium production because of the use of stainless steel vessels in the Kroll reactors for making sponge, and for vacuum distillation of the sponge to remove residual $MgCl_2$ after reduction. Further, salt removal from the sponge is also done by vacuum distillation. Thus all sponge is exposed to Ni-bearing alloys during production, making trace concentrations of Ni unavoidable unless special precautions are taken.

Returning to the variation in creep behaviour, it has been shown that increasing the Ni impurity level from 0.005 to 0.035 % in Ti-6242 causes a large reduction in creep strength. This appears to be well understood in terms of Ni impurities affecting the rate-controlling creep mechanism, which is diffusion-controlled dislocation motion in the α phase [41–47]. Consistent improvement in the creep strength of high temperature alloys requires the use of materials with the lowest commercially feasible Ni and Fe levels.

Fig. 6.3 Impeller used in a small engine for regional jets, diameter 35 cm. The alloy is Ti-6242 with a bi-modal microstructure [1]



A special consideration for low temperature (up to about 150–200 °C) applications of near- α alloys in aeroengines is *dwell fatigue cracking*. This can occur when hold times at high load levels are part of the service fatigue history. Dwell cracking is a well-known and major concern for front-engine discs made from alloys such as Ti-6242, IMI 685, and IMI 834. It was first encountered in 1972 with two *in-service* fan disc failures [47]. Although not fully understood, the cracking involves creep (low temperature) as well as fatigue, and microtexture appears to play a major role. More details can be found in the specialist literature.

6.2.3 $\alpha + \beta$ Titanium Alloys

6.2.3.1 Processing and Microstructures of $\alpha + \beta$ Titanium Alloys

$\alpha + \beta$ alloys have at least two phases (α and β) and have good combinations of strength and high temperature properties. This is why these alloys have been so popular. Correct microstructures are essential, which is all the more important because titanium alloy microstructures are very sensitive to processing.

Three distinctly different types of microstructures can be obtained in $\alpha + \beta$ alloys by changing the thermomechanical processing route: so-called bi-modal (duplex) microstructures containing equiaxed primary α (α_p) in a lamellar $\alpha + \beta$ matrix; fully equiaxed structures; and fully lamellar structures. A common but less narrowly defined microstructure is the so-called mill-annealed condition.

Central to the processing of titanium alloys is the deformation and resulting morphology of the alpha/beta phase. An equiaxed α morphology is obtained by $\alpha + \beta$ processing and $\alpha + \beta$ solution treatment, whereas a fully lamellar α (transformed β) microstructure is obtained from heating and/ or processing in the β phase field.

Bi-modal microstructures The processing route for obtaining the bi-modal (duplex) microstructures is shown schematically in Fig. 6.4, where the process is divided into four different steps: homogenization in the β phase field (I), deformation in the ($\alpha + \beta$) phase field (II), α -phase recrystallization in the ($\alpha + \beta$) phase

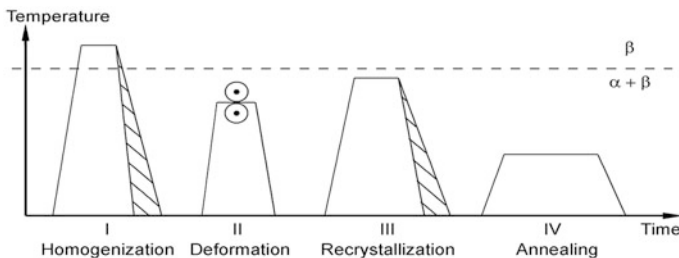


Fig. 6.4 Schematic processing route for bi-modal microstructures of $\alpha + \beta$ titanium alloys

field (III) and final ageing and/or stress relieving treatment (IV). Table 6.3 summarizes the important parameters of this processing route and the resulting microstructural features.

A critical parameter in the processing route is the cooling rate from the homogenization temperature in the β phase field (step I) because this cooling rate determines the width of the α lamellae. These are then deformed in step II and recrystallized in step III.

The relation between the prior α lamellae width resulting from step I and the equiaxed primary $\alpha + \beta$ size is illustrated in Fig. 6.5, where two bi-modal structures are compared. The faster the cooling rate, the finer are the α lamellae, the primary $\alpha(\alpha_p)$ grain size and the transformed β grain size.

Table 6.3 Important processing step parameters and resulting microstructural features for bi-modal microstructures

Step	Important parameters	Microstructural features
I	Cooling rate	Width of α lamellae ($\rightarrow \alpha_p$ size)
II	Deformation temperature Deformation degree Deformation mode	– Texture type – Texture intensity – Dislocation density – Texture symmetry
III	Annealing temperature Cooling rate	– Vol.% of α_p ($\rightarrow \beta$ grain size) – Alloy element partitioning Width of α lamellae
IV	Annealing temperature	– Ti_3Al in α – Secondary α in β

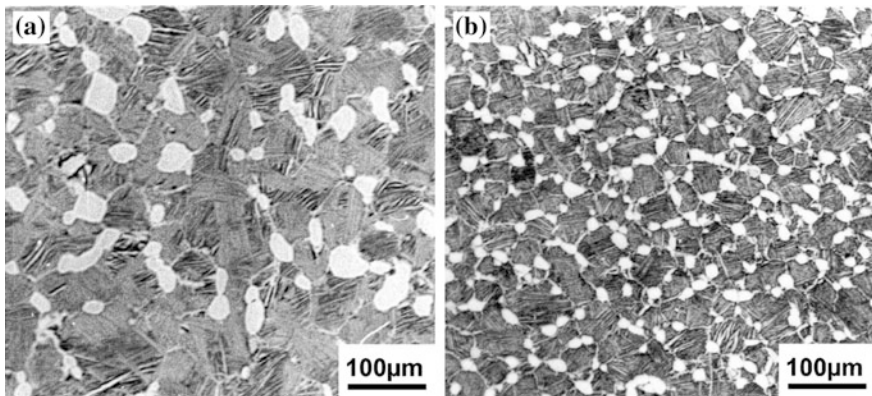


Fig. 6.5 Bi-modal microstructures (optical) of the IMI 834 alloy cooled differently from the β phase field in step I of the processing route: **a** bi-modal 1, slow cooling rate, **b** bi-modal 2, fast cooling rate

In bi-modal microstructures the cooling rate from the recrystallization annealing temperature in the ($\alpha + \beta$) phase field (step III in Fig. 6.4) mainly influences the width of the individual α lamellae (Table 6.3), whereas the α colony size and the length of the continuous α layers at β grain boundaries are largely determined by the β grain size. Within the normal range of commercial cooling rates of about 30–600 °C/min, the α colony size in bi-modal microstructures is about equal to the β grain size. Slower cooling rates increase both the size and volume fraction of α_p .

Fully equiaxed microstructures There are two possibilities to obtain a fully equiaxed microstructure. In the first case, the processing route is identical to the processing route for obtaining a bi-modal microstructure up to the recrystallization process in step III:

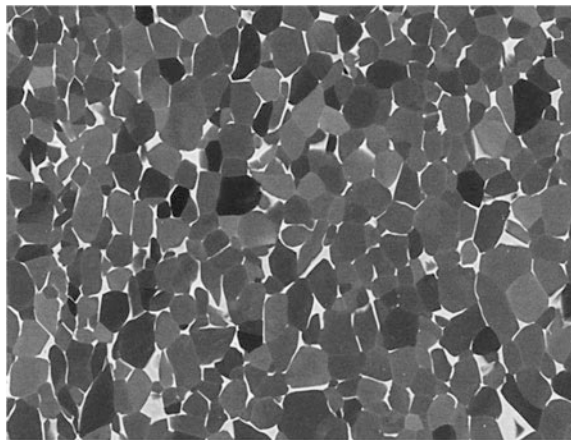
- (1) If the cooling rate from the recrystallization annealing temperature is sufficiently low, only the α_p grains will grow during the cooling process and no α lamellae are formed within the β grains, resulting in a fully equiaxed structure with the equilibrium volume fraction of β phase located at the “triple-points” of the α grains. In this case the α grain size will be fairly large and always larger than the α_p size of a bi-modal structure (which would have resulted from faster cooling).

An example for such a fully equiaxed microstructure is shown in Fig. 6.6.

- (2) The second possibility to obtain a fully equiaxed microstructure is to recrystallize in step III of the processing route (Fig. 6.4) at such a low temperature that the equilibrium volume fraction of α phase at that temperature is high enough to form the fully equiaxed microstructure directly from the deformed lamellar structure.

Using this second processing route with the (low) recrystallization annealing temperature (for example, for Ti–6Al–4V between 800–850 °C), smaller α grain

Fig. 6.6 Fully equiaxed microstructure obtained in Ti–6Al–4V



50 μm

sizes can be achieved provided a higher degree of deformation is used as compared to method (1). For example, for Ti–6Al–4V a recrystallization annealing temperature of 800 °C enables fully equiaxed microstructures with α grain sizes of about 2 μm or less [26] to be obtained.

N.B: Fully equiaxed microstructures can be changed to bi-modal microstructures by simply reheating the material to a temperature in the ($\alpha + \beta$) phase field that corresponds to the desired α_p volume fraction and subsequently cooling with a sufficiently high rate to form α lamellae within the β grains.

The mill-annealed condition mentioned earlier is obtained by omitting the recrystallization step III (see Fig. 6.4). Consequently, the details of the deformation procedure in step II (number of times it is reheated during deformation, soaking time, the amount of deformation and the cooling rate after deformation, etc.) determine the details of the resulting microstructure, especially the degree of recrystallization. Since the details of the deformation procedure are beyond the control of the customer or end-user, and these details will vary between producers or even between different lots, the mill-annealed condition is not a well-defined microstructural condition.

Fully lamellar microstructures Lamellar microstructures can be obtained fairly easily in the final steps of the processing route by an annealing treatment in the β phase field (β recrystallization). Hence this microstructure is often also called “ β annealed”. The processing steps are similar to those in Fig. 6.4, but the temperatures are different. The deformation process (step II) can be done by forging or rolling, either in the β phase field or in the ($\alpha + \beta$) phase field, as shown in Fig. 6.7, and the annealing step (shown as recrystallisation step III in Fig. 6.7) is carried out in the β phase field.

In industrial practice the material is usually first deformed in the β phase field to refine the coarse ingot microstructure, to homogenize the material, and because of the lower flow stress. The material is then deformed in the ($\alpha + \beta$) phase field to avoid large β grain sizes. Similarly, the recrystallization temperature in step III is usually kept within 30–50 °C above the β transus to maintain control of the β grain

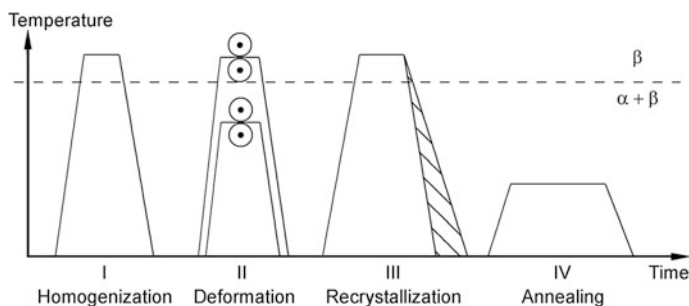


Fig. 6.7 Processing route to obtain fully lamellar microstructures in $\alpha + \beta$ alloys

size. As a result, the β grain size of fully lamellar microstructures is typically about 600 μm .

Another type of fully lamellar microstructure, namely a so-called β processed condition, is mentioned here, although for $\alpha + \beta$ alloys this condition is not used extensively in commercial applications. β processing (which is a very common processing route for β alloys) involves omitting β recrystallization, and the material remains therefore in an unrecrystallized condition.

6.2.3.2 Mechanical Properties of $\alpha + \beta$ Titanium Alloys

The mechanical properties emphasized in this section are tensile, fatigue and fracture toughness. A qualitative summary of the basic microstructure/property correlations is shown in Table 6.4.

The qualitative trends (+, 0, -) in Table 6.4 indicate the directions in which a specific mechanical property will change when a microstructural feature is changed according to the table footnotes. For the tensile properties the 0.2 % yield stress and fracture strain are used for the correlations. The HCF strength at 10^7 cycles is taken as a measure of the resistance to fatigue crack nucleation.

Bi-modal microstructures For the whole range of commercial cooling rates (30–600 $^{\circ}\text{C}/\text{min}$) the α colony size of bi-modal microstructures is about equal to the β grain size, and therefore much smaller than in fully lamellar microstructures.

Based on the effect of slip length on mechanical properties of fully lamellar structures, it can be postulated that if the slip length would be the only major parameter governing the mechanical properties of bi-modal microstructures, they should have a higher yield stress, a higher ductility and a higher HCF strength than fully lamellar microstructures, when compared for the same cooling rate.

In fact, Table 6.4 indicates that this is not so. The reason is that there is another important factor which complicates the situation. That is the alloy element partitioning effect, which increases with increasing volume fraction of α_p . The HCF strength (crack nucleation resistance) is usually reduced with increasing α_p volume

Table 6.4 Qualitative correlations between important microstructural parameters and mechanical properties for $\alpha + \beta$ titanium alloys [1]

Microstructural features	0.2 % YS	ϵ_F	HCF	K_{Ic}	Creep strength (0.2 %)
Small α colonies, α lamellae ^a	+	+	+	–	±
Bi-modal structure ^b	+	+	–	–	–
Small α grain size ^c	–	+	+	–	–
Ageing (α_2); oxygen	+	–	+	–	+
Secondary α in β	+	–	+	0	+

^aCompared to coarse lamellar structure

^bCompared to fully lamellar structure with same cooling rate

^cCompared to large α grain size of fully equiaxed microstructures

fraction. The fatigue cracks are nucleated in the lamellar grains of the bi-modal structure because the crack path is more irregular in this latter condition and these lamellar grains are softer than α_p as a consequence of the alloy element partitioning effect.

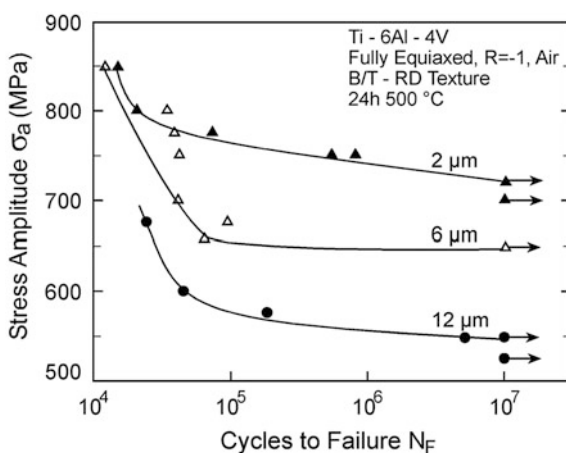
The fracture toughness of bi-modal microstructures of the Ti–6Al–4V alloy is only slightly higher than the fracture toughness of the fine lamellar microstructure, but much lower than the toughness of the coarse lamellar structure. A detailed discussion is beyond the scope of this chapter: the reader is referred to the Bibliography. Also, it is important to note that the creep properties of a lamellar structure are better than those of bi-modal structures: again see the Bibliography for a detailed discussion.

Fully equiaxed microstructures The mechanical properties of fully equiaxed microstructures of $\alpha + \beta$ titanium alloys are primarily influenced by the α grain size. It should also be emphasized that fully equiaxed microstructures of $\alpha + \beta$ titanium alloys are similar to the microstructures of CP titanium and other α titanium alloys. Therefore the general correlation between microstructure and mechanical properties is also similar.

The effect of α grain size on HCF strength of fully equiaxed microstructures is demonstrated in Fig. 6.8 for the Ti–6Al–4V alloy. It can be seen that high HCF strength values can be achieved with small α grain sizes. The corresponding yield stress values are 1120 MPa (2 μm grain size), 1065 MPa (6 μm grain size) and 1030 MPa (12 μm grain size), respectively. The tensile ductilities of these fully equiaxed microstructures are generally very high, i.e. equal to or higher than those of bi-modal microstructures on a strength-corrected basis.

The LCF strength is lower for fully equiaxed microstructures as compared to bi-modal microstructures. A similar evaluation of the effect of α grain size on LCF strength of fully equiaxed microstructures suggests that the LCF strength will

Fig. 6.8 Effect of α grain size on HCF strength of Ti–6Al–4V with fully equiaxed microstructures



increase with decreasing α grain size because of increased ductility: this follows from the Coffin-Manson Law prediction about LCF strength and ductility.

The effect of α grain size on fracture toughness of fully equiaxed microstructures has been investigated by comparing microstructures with 2 and 12 μm grain sizes. The fracture toughness values were 45 and 65 $\text{MPa}\sqrt{\text{m}}$, respectively. This result demonstrates the same tendency as found for lamellar microstructures (discussed next with respect to Fig. 6.8), namely, that the crack front roughness has a major influence on the fracture toughness.

Fully lamellar microstructures The most influential microstructural parameter for the mechanical properties of lamellar microstructures is the α colony size, which is the effective slip length and is controlled by the cooling rate from the β heat treatment temperature. With increasing cooling rate the α colony size decreases with a commensurate reduction in effective slip length and a corresponding increase in yield stress.

In the commercially feasible cooling rate regime (up to 1000 $^{\circ}\text{C}/\text{min}$), the effect on yield stress is only moderate (50–100 MPa), whereas a large increase in yield stress is observed when the colony structure is changed to a martensitic type of microstructure (slip length and “colony” size equal to the width of individual α plates).

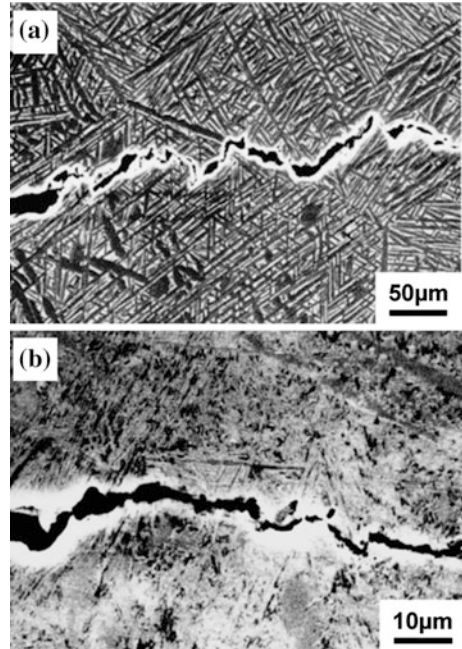
With increasing cooling rate the tensile ductility increases at first, consistent with the effect of decreased slip length. However, the ductility reaches a maximum and then declines. The ductility maximum corresponds to a change in fracture mode. For low cooling rates a ductile *transcrystalline* microvoid dimple type of fracture is observed, whereas at high cooling rates a ductile *intercrystalline* dimple type of fracture occurs along the continuous α layers at prior β grain boundaries. The effect of the continuous α layers on ductility is related to preferential plastic deformation in this lower strength region and concomitant early microvoid nucleation.

The magnitude of the ductility decline depends primarily on the strength difference between the continuous α layers and the matrix, and also the grain boundary length: a larger β grain size is detrimental.

The HCF strength depends primarily on the resistance to dislocation motion. Consequently, the HCF strength dependence on α colony size is qualitatively similar to that of the yield stress. It should be noted that for fully lamellar microstructures the absolute values for both the HCF strength and the yield stress depend, in addition to the cooling rate effect, on the details of the final annealing/ageing treatment (step IV in Fig. 6.7).

The fracture toughness of $\alpha + \beta$ titanium alloys usually increases with increasing α colony size owing to a rougher crack front profile. Figure 6.9 shows an example of the difference in crack path for a coarse lamellar microstructure (1 $^{\circ}\text{C}/\text{min}$ cooling rate) and a fine lamellar microstructure (8000 $^{\circ}\text{C}/\text{min}$ cooling rate) in Ti–6Al–4V. The corresponding fracture toughness values were 75 $\text{MPa}\sqrt{\text{m}}$ for the coarse structure and 50 $\text{MPa}\sqrt{\text{m}}$ for the fine structure. In other words, increasing crack front roughness increases the fracture toughness.

Fig. 6.9 SEM micrographs of crack paths in the centres of fracture toughness specimens of Ti-6Al-4V: **a** coarse lamellar (higher toughness), **b** fine lamellar (lower toughness). Note the difference in magnifications: the crack path in (a) is much rougher



Titanium alloy Ti6Al4V ELI grade Ti6Al4V ELI grade is similar to Ti6Al4V except that the ELI grade has reduced levels of oxygen, nitrogen, carbon and iron. ELI stands for “Extra Low Interstitials”, referring to oxygen, nitrogen and carbon.

The essential difference between Ti6Al4V ELI (grade 23) and Ti6Al4V (grade 5) is the reduction of oxygen content to 0.13 % (maximum) in grade 23. This confers improved ductility and fracture toughness, with some reduction in strength.

The improved properties, high specific strength (strength/density), good stress corrosion resistance and machinability are why Ti6Al4V ELI is extensively used for aerospace cryogenic applications (e.g. spacecraft pressure vessels and fuel tanks).

Ti6Al4V ELI has also been widely used in fracture critical airframe structures and for offshore tubulars. The mechanical properties for fracture critical applications can be enhanced, if necessary, by special processing and heat treatment.

6.2.3.3 Applications of $\alpha + \beta$ Titanium Alloys

This class of titanium alloys is the most used. Within this class the worldwide production of Ti-6Al-4V is the largest.

Airframe structures A major application area of $\alpha + \beta$ titanium alloys is in heavily loaded aircraft structural parts. For such applications, $\alpha + \beta$ titanium alloys can be

selected over other competing metallic materials, such as high strength aluminium alloys, because of higher yield strength and elastic modulus (and also higher specific strength and stiffness), fatigue strength, better corrosion resistance and higher temperature capability. Figures 6.10 and 6.11 show two heavy Ti-6Al-4V forgings for aircraft.

The most economically effective processing route for large forgings typically consists of forging in the ($\alpha + \beta$) phase field followed by mill-annealing. The mill-annealed microstructure gives generally faster fatigue crack propagation rates than a fully lamellar microstructure, which can be obtained by β annealing, however at increased cost. Although β annealing requires fixtures to support the part, the benefits of improved crack propagation resistance are in some cases sufficient to justify the added cost. This is sometimes done for fracture critical aircraft structural components such as bulkheads, cockpit window frames and attachment fittings for

Fig. 6.10 Large Ti-6Al-4V forging for Boeing 747 landing gear [1]

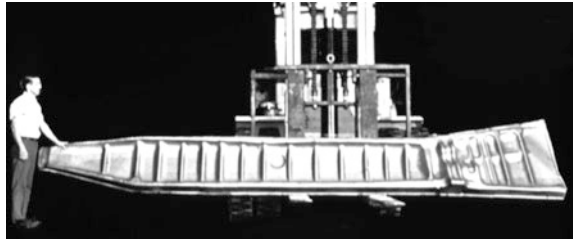
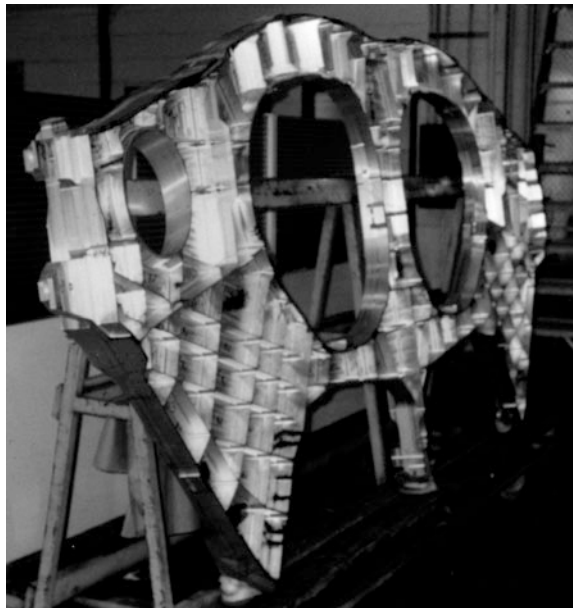


Fig. 6.11 Machined bulkhead forging for a twin engine military aircraft, [1]



the fin and horizontal stabilizers. β -annealed plate is used extensively for the Lockheed Martin F-35 Joint Strike Fighter (JSF).

Castings of Ti-6Al-4V already possess fully lamellar microstructures, but also have size limitations resulting from the casting furnace equipment and the hot isostatic press (HIP) facilities required for airworthiness certification of premium quality castings. Nevertheless, fairly large castings have been proposed for use in static property limited aircraft structural components. In such applications the large section sizes mean that the solidification rate will be quite slow. This results in a fairly coarse lamellar microstructure with excellent macrocrack fatigue crack growth resistance and high fracture toughness.

Aeroengines Another major application area of $\alpha + \beta$ titanium alloys is for rotating and non-rotating parts in aeroengines. The major limitation of Ti-6Al-4V is the maximum usage temperature of about 300 °C, which restricts this alloy to the fan stage (Fig. 6.12), the low pressure (LP) compressor section and the front stages in the high pressure compressor (HPC). Further back in the HPC the higher temperatures require creep-resistant high temperature titanium alloys (Ti-6242, Titan 29A and IMI 834), e.g. Figs. 6.13 and 6.14.

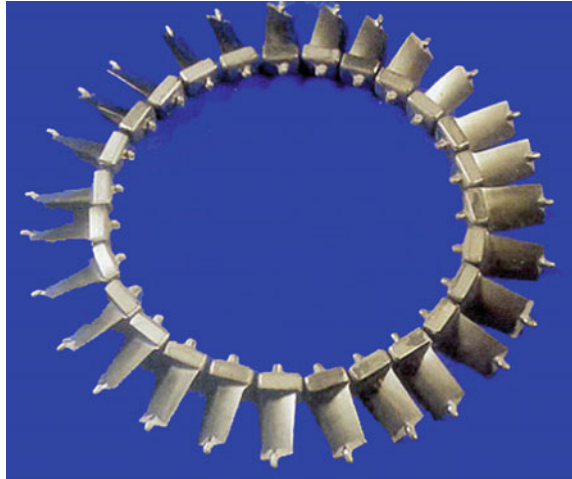
Fig. 6.12 Large fan blades (length of the larger blade about 1 m) of Ti-6Al-4V forged in the $(\alpha + \beta)$ phase field and recrystallized to a bi-modal microstructure [1]



Fig. 6.13 Aeroengine high pressure compressor rings made of Titan 29A



Fig. 6.14 Aeroengine high pressure compressor blades made of Titan 29A



Ti-6Al-4V is also used for the new technology of manufacturing integrally bladed rotors (IBR), either by direct attachment of the blades to the disc using solid-state linear friction welding, or by machining the rotor from a single-piece forging.

6.2.4 β Titanium Alloys

6.2.4.1 Introduction: General Characteristics

In contrast to $\alpha + \beta$ alloys, β alloys do not transform martensitically upon quenching to room temperature: instead they consist of metastable β . The α phase can be precipitated from the metastable β phase as very fine, undeformable particles (platelets) with a high volume fraction. Thus the main characteristic of β alloys is that they can be hardened to much higher yield stress levels than $\alpha + \beta$ alloys. Another advantage is that they can be processed at lower temperatures than $\alpha + \beta$ alloys, and some heavily stabilized β alloys are even cold deformable. Further, the corrosion resistance of β alloys is equal to or better than that of $\alpha + \beta$ alloys, and they are especially good in environments where hydrogen pickup is possible, because β has a higher hydrogen tolerance than α . In view of these advantages the usage of β alloys has been slowly but steadily increasing in recent years.

A distinction can be made between so-called “high strength” and “heavily stabilized” β alloys:

- (1) High strength alloys have chemical compositions close to the $\beta/\alpha + \beta$ phase boundary. In the aged condition they therefore contain a high volume fraction of α phase.

- (2) Heavily stabilized alloys are located more to the right in the pseudo-binary phase diagram. These alloys contain a much lower volume fraction of α phase and the maximum achievable strength is therefore lower.

Typical examples for the first group of alloys are Ti-6246, Ti-17, β -CEZ and Ti-10-2-3. Examples of the second group are Beta 21S, Ti-15-3 and Beta C. The main emphasis in this subsection is on the group of high-strength β alloys, and most examples are from this group, which are therefore simply referred to as “ β alloys”. Where heavily stabilized β alloys are discussed, this will be explicitly stated.

6.2.4.2 Processing and Microstructures

Beta-annealed microstructures The basic processing route for β -annealed microstructures is shown in Fig. 6.15. It can be seen that the β -annealed microstructure is obtained in a simple way, i.e. recrystallization in the β phase field (step III) and ageing in the ($\alpha + \beta$) phase field (step IV) to precipitate α as fine α platelets. Such a microstructure is shown in Fig. 6.16.

The main characteristic of all β alloys is that the α phase nucleates preferentially at β grain boundaries and forms a continuous α layer. Adjacent to this continuous α layer is a so-called PFZ (precipitate-free zone) which does not contain any α platelets, and which is therefore soft with respect to the age-hardened matrix.

The strength difference between the PFZs and the matrix (i.e. yield stress) and the slip length in the PFZs (i.e. β grain size) are important for the mechanical properties. Both of these parameters are influenced by alloy composition, such that the effect of the continuous α layers is large for high strength β alloys and smaller for heavily stabilized β alloys. This is the reason why high strength β alloys are not used in the β -annealed condition. On the other hand, heavily stabilized β alloys are commonly used in the β -annealed condition.

Table 6.5 summarizes the important processing parameters and resulting microstructural features of heavily stabilized β alloys. An important parameter of

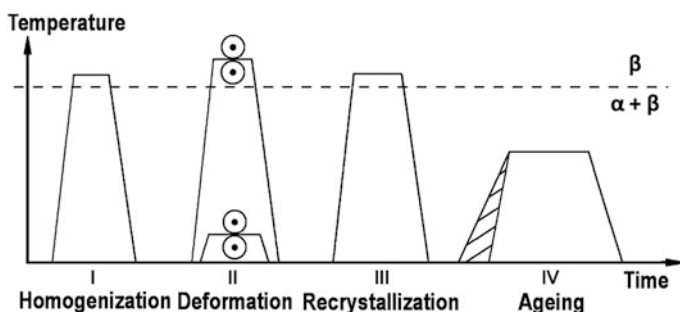


Fig. 6.15 Processing route for β -annealed microstructures of heavily stabilized β titanium alloys [1]

Fig. 6.16 β -annealed plus aged microstructure of a heavily stabilized β alloy, Beta 21S [1]: **a** optical and **b** TEM metallographs showing α precipitation within the grains and at the grain boundaries and narrow precipitate-free zones (PFZ) near the grain boundaries

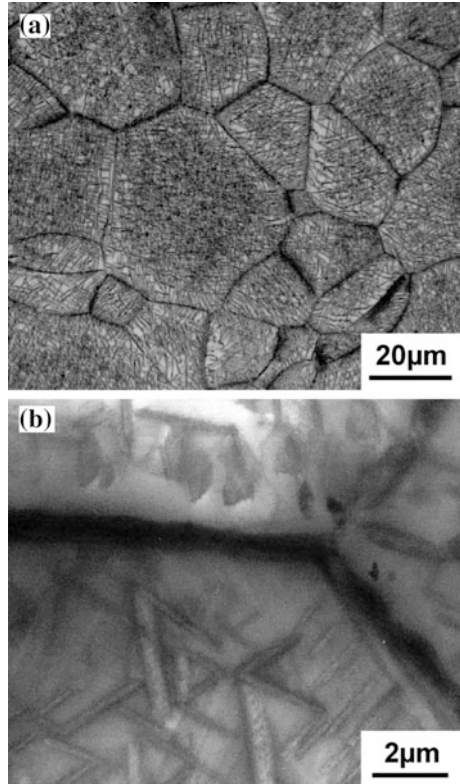


Table 6.5 Important processing parameters and resulting microstructural features for β -annealed microstructures of heavily stabilized β alloys [1]

Processing step (see Fig. 6.15)	Important parameters	Microstructural features
III	Recrystallization temperature	β grain size
IV	Heating rate	Distribution of α platelets
	Ageing temperature	Size and vol.% of α platelets GB α layer

the ageing treatment (step IV in Fig. 6.15) is the choice of the ageing temperature, because this determines the volume fraction of α platelets which influences the yield stress level. (Since the growth of the α platelets is diffusion controlled, the ageing *temperature* is much more important in step IV than the ageing *time*.) However, formation of the continuous α layers at β grain boundaries during the ageing treatment cannot be avoided.

It is sometimes difficult for heavily stabilized β alloys (especially for relatively high ageing temperatures) to obtain a homogeneous distribution of α platelets by

the normal one-stage ageing treatment shown in Fig. 6.15. This is because (i) the necessary formation of the ageing precursors (ω or β') can be too sluggish to occur during heating to the ageing temperature, and (ii) the ageing temperature is above the stability range for ω or β' . In this case a pre-ageing at lower temperatures can create a more homogeneous distribution of α platelets [48]. This means that there is a two-stage ageing step (step IV in Fig. 6.15).

After homogenization (step I), the deformation (step II) can be done either in the β phase field or in the $(\alpha + \beta)$ phase field, see Fig. 6.15. The latter has the advantage of creating smaller β grain sizes in the recrystallization step III. The grain size of β -annealed microstructures is somewhat smaller than the β grain size in fully lamellar microstructures of $\alpha + \beta$ alloys. A typical grain size of β alloys is about 400 μm as compared to about 600 μm for $\alpha + \beta$ alloys for equivalent processing histories and for a recrystallization temperature of 30–50 $^{\circ}\text{C}$ above the β transus. The smaller grain size of β alloys is a result of the lower β transus. The most important parameter in step III is the cooling rate from the recrystallization temperature because it controls the width and extent of the continuous α layers at β grain boundaries. **N.B.**: even for fast cooling rates in commercial practice (e.g. 600 $^{\circ}\text{C}/\text{min}$), formation of the continuous α layers cannot be avoided. Since the total volume fraction of α (coarse α plates plus fine α platelets and grain boundary α) is fixed by the alloy chemistry, the volume fraction of coarse α plates has a direct influence on the volume fraction and size of the fine α platelets and therefore on the resulting yield stress level of the material.

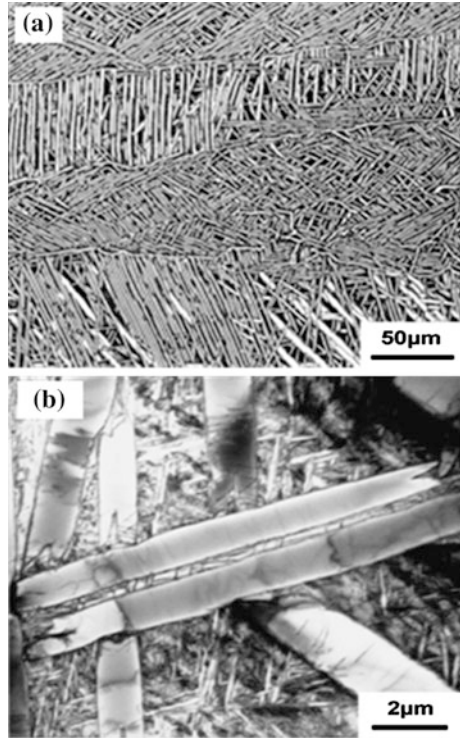
β processed microstructures To obtain β processed microstructures the recrystallization step III in Fig. 6.15 is omitted, with the intention of creating an unrecrystallized structure with highly deformed β grain boundaries. The α layers which form on the β grain boundaries during cooling from the β deformation temperature will then take on the local shape of the deformed grain boundaries. An example is given in Fig. 6.17a for the Ti-6246 alloy. This shows that the α layers are still fairly continuous but have a pronounced wavy shape. In other cases the α layers are broken up more into individual segments on most β grain boundaries with only a few long segments remaining on some boundaries. Irrespective of processing history, it is nearly impossible to completely avoid the α layers. This is because the β grain boundaries are strong heterogeneous nucleation sites for α formation.

Since the final deformation process must be a continuous operation without reheating, good control of the processing temperature and time is necessary. Critical parameters are the total time of the process, determined by deformation rate, amount of deformation and any holding times between deformation steps and after the deformation process.

The deformation mode determines the shape of the unrecrystallized β grains, for example ellipsoidal from unidirectional rolling, pancake-shaped from cross-rolling, or axisymmetric from upset forging. Consequently, the mechanical properties which are influenced by the α layers will be anisotropic.

Ageing results in small α platelets within the β grains and between the coarse α plates formed during cooling after the deformation step, see Fig. 6.17b.

Fig. 6.17 β processed microstructure of Ti-6246 alloy [1]: **a** optical image of deformed β grain boundaries outlined with α ; **b** TEM micrograph showing coarse primary α and fine secondary α within a grain



Through-transus processed microstructures Extensive development work on the through- β -transus processing route has been done for the β -CEZ alloy [49]. The intention of this processing route is to change the continuous α layers at β grain boundaries to individual globular α particles. In the through-transus processing route the deformation step II starts above the β transus and finishes below the beta transus. This process is otherwise identical to that for β processed materials, i.e. an unrecrystallized β grain structure is anticipated by omitting the recrystallization step III.

The control of deformation temperature and time in step II is even more critical for the through-transus processing route than for the β processing route [50]. The deformation time in the $(\alpha + \beta)$ phase region in step II should be long enough to cross the TTT boundary line for α precipitation at the deformed β grain boundaries, but the deformation process should be finished before crossing the TTT boundary line for α precipitation in the β matrix [50].

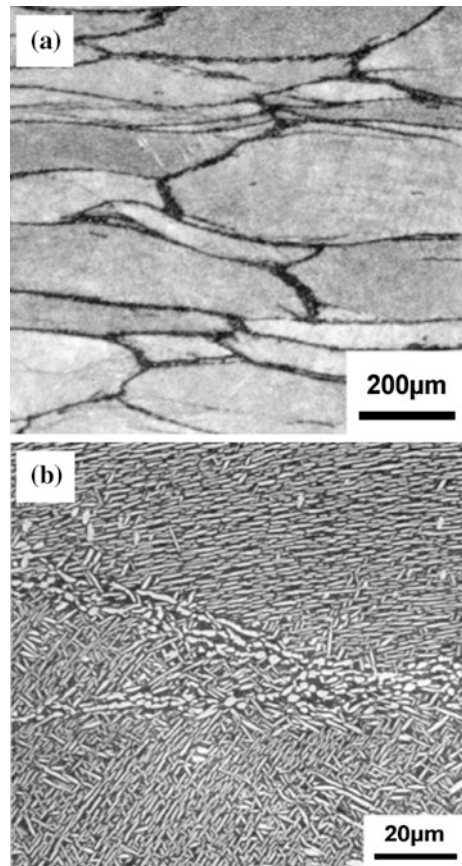
Another issue associated with through-transus processing is that the deformation time must be long enough to allow α precipitation to occur at β grain boundaries, but the time in the β phase field must be restricted to avoid recrystallization of the deformed β grains [50]. The only advantage in the through-transus processing route as compared to β processing is that the cooling rate after the deformation process is

less critical because the α phase is already precipitated at the β grain boundaries in the necklace microstructure (see next paragraph).

Examples of through-transus microstructures, obtained from Ti-6246 alloy, are given in Fig. 6.18. The as-deformed microstructure is shown in Fig. 6.18a. This kind of microstructure has been called a “necklace” microstructure by CEZUS for their β -CEZ alloy [51]. The higher magnification micrograph in Fig. 6.18b for the fully heat treated alloy shows globular α particles at the β grain boundaries and α plates within the grains.

Bi-modal microstructures The benefit of a bi-modal microstructure is to avoid the continuous α layers at the boundaries of large β grains by creating a small enough β grain size that any α layers that form have only a negligible effect on mechanical properties. The processing route for obtaining a bi-modal microstructure is shown schematically in Fig. 6.19. The important processing parameters and the resulting microstructural features are summarized in Table 6.6.

Fig. 6.18 Optical microstructure of a through-transus processed microstructure (“necklace” microstructure) of Ti-6246 alloy [1]: **a** as-deformed; **b** aged



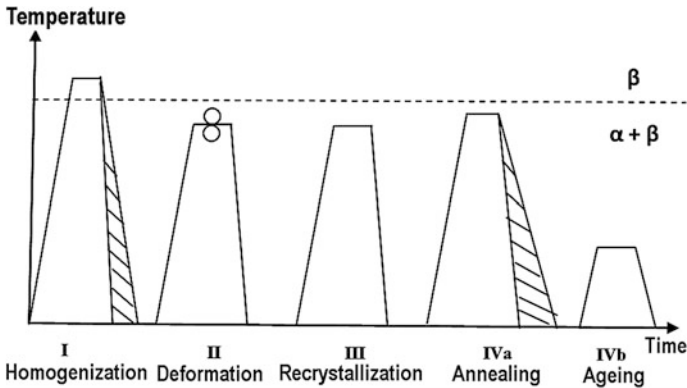


Fig. 6.19 Processing route for bi-modal microstructures of β alloys

Table 6.6 Important processing parameters and resulting microstructural features for bi-modal microstructures of β alloys

Processing step (see Fig. 6.19)	Important parameters	Microstructural features
I	Cooling rate	GB α layer
II	Deformation degree	Dislocation density
III	Annealing temperature	Vol.% of α_p (\rightarrow β grain size and vol.% of α plates in step IVa)
IVa	Annealing temperature and cooling rate	Size and vol.% of α plates (\rightarrow vol.% of α platelets in step IVb)
IVb	Ageing temperature	Size and vol.% of α platelets

When selecting the intermediate annealing temperature for bi-modal microstructures it should be realized that the volume fraction of coarse α plates is determined by the temperature difference between the recrystallization annealing temperature (formation of equiaxed primary α) and the intermediate annealing temperature.

6.2.4.3 Mechanical Properties of β Titanium Alloys

Microstructure and mechanical properties A qualitative summary of the microstructure/property correlations is shown in Table 6.7. The symbols (+, 0, -) indicate the direction in which the mechanical properties change when the microstructure is changed. This table compresses much comparative information as follows:

Table 6.7 Qualitative correlations between important microstructural parameters and mechanical properties for β titanium alloys (both high strength and heavily stabilized) [1]

Microstructural features	0.2 % YS	ϵ_F	HCF	K_{Ic}
GB α layers in β -annealed structure	0	–	–	+
Bi-modal structure ^a	0	+	+	–
“Necklace” ^a or β processed structure ^b (longitudinal direction)	0	+	+	+
	0	–	–	+
Decreasing age-hardening	–	+	–	+
Small β grain size in β -annealed structure ^c	0	+	+	–

^aCompared to β -annealed structure^bCompared to bi-modal structure^cOnly applies to heavily stabilized alloys

- (1) The first row gives the overall effects of continuous grain boundary (GB) α layers in ***β -annealed*** structures.
- (2) The second row compares the properties of ***bi-modal*** structures with those of ***β -annealed*** structures, both with continuous α layers.
- (3) The third row has two sub-rows (a and b) for comparing the effects of unrecrystallized microstructures with (a) ***β -annealed*** structures and (b) ***bi-modal*** structures.

This overall comparison of mechanical properties is discussed separately for strength, fatigue strength and fracture toughness in the following text; and on the basis of final ageing resulting in a constant yield stress level.

Tensile properties The mechanical properties of high-strength β alloys are dominated by the preferential plastic deformation along the continuous α layers at β grain boundaries. The unacceptably low ductility of high strength β alloys in the β -annealed condition can be drastically improved by $\alpha + \beta$ processing to a bi-modal microstructure with a small β grain size [52], see column “ ϵ_F ” in Table 6.7.

The β processed (unrecrystallized) condition shows high tensile anisotropy, with the lowest yield stress in the 45° test direction as compared to the other two directions: this is illustrated in Table 6.8. This yield stress anisotropy can be

Table 6.8 Tensile properties of β -CEZ alloy [1]

Processing and orientation		0.2 % YS (MPa)	UTS (MPa)	σ_F (MPa)	T.E. (%)	RA (%)
β annealed	L	1180	1280	1415	4	10
Bi-modal	L	1200	1275	1660	13	34
β -processed	L	1190	1275	1480	10	16
	45°	1145	1200	1220	2	2
	T	1185	1280	1410	6	10

explained from the crystallographic texture of the β matrix. Also the fracture properties are dominated by the angle of the tensile stress axis with the elongated β grain boundaries containing α layers.

Fatigue Properties Figures 6.20 and 6.21 give examples of the HCF properties of β -CEZ:

- (1) Figure 6.20 compares the fatigue properties of β processed β -CEZ for three test directions. The HCF strength for the ST test direction was higher than for the L direction, which is a remarkable result. On the other hand, the 45° test direction resulted in the lowest fatigue strength, and this correlates with the lowest yield stress (see Table 6.8).
- (2) Figure 6.21 compares the fatigue properties of β -CEZ for three different microstructures, with the added complication of a 45° test direction for the β processed material. The fine-grained bi-modal microstructure gave the highest fatigue strength; the coarse-grained β -annealed microstructure was intermediate; and the β processed material again gave the lowest fatigue strength when tested in the 45° direction.

Fig. 6.20 *S-N* curves of a β processed forged rectangular slab of β -CEZ [1]

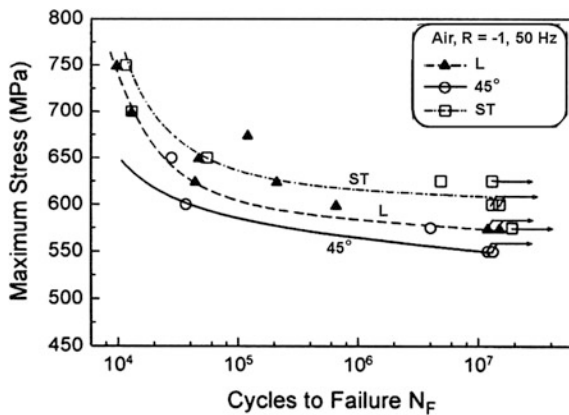


Fig. 6.21 *S-N* curves for different microstructures in β -CEZ [1]

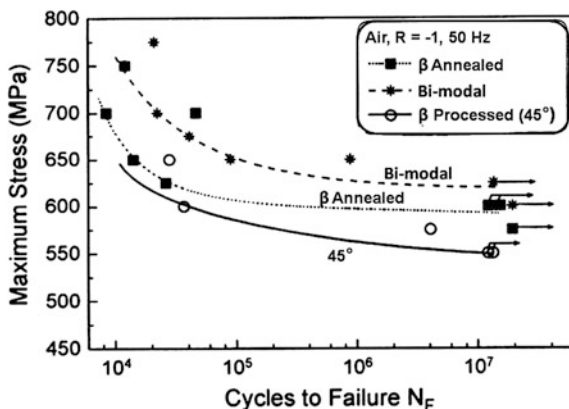
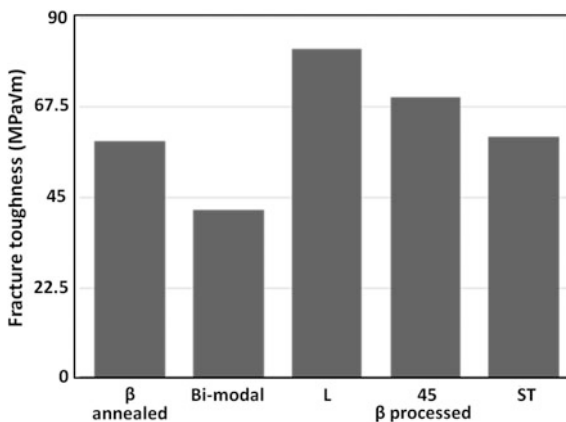


Fig. 6.22 Fracture toughness of Ti-6246 as a function of different processing and heat treatment conditions [1]



The HCF fatigue behaviour of Ti-6246 followed the same trends. A detailed explanation is beyond the scope of this chapter and is given in Refs. [1, 34].

Fracture Toughness The fracture toughness values of the β -annealed and bi-modal microstructures as well as those of the β processed condition for the three different testing directions (L, 45°, ST) are shown in Fig. 6.22 for Ti-6246.

As can be seen, the fracture toughness of the β -annealed condition is much higher than that of the bi-modal condition. This is because the crack tip plastic zone that forms during the onset of crack extension tends to follow β grain boundaries, more specifically along the α layers at β grain boundaries, and the resulting crack deflection contributes to the increased toughness. In contrast, the fine-grained bi-modal surface topography resulted in a much lower fracture toughness value [1].

In more detail, the data for β -annealed material in Fig. 6.22 and the fractographic observations [1] show that the influence of crack front profile (increased roughness lowers the *crack driving force*) is substantial and more than compensates for the easier crack path (lower *crack growth resistance*) within the weak PFZ zones along the β grain boundaries. This is why there is a (+) symbol for K_{Ic} in the first row of Table 6.7.

Returning to Fig. 6.22, the fracture toughness of the β processed material showed the highest value for the L test direction, followed by the 45° test direction and then the ST direction. This trend, notably the lowest toughness in the ST direction, is common for thick-section products of high-strength alloys.

6.2.4.4 Applications of β Titanium Alloys

Aerospace usage of β titanium alloys is increasing mainly at the expense of the widely used $\alpha + \beta$ Ti-6Al-4V alloy, and this is because higher strengths are achievable from β titanium alloys with retention of good ductility and acceptable fracture toughness.

Large and small forgings The Boeing 777 aircraft was the first commercial airplane for which the volume of β alloys exceeded the volume of Ti-6Al-4V. The main reason was use of the high strength β alloy Ti-10-2-3 in the landing gear structure, see Fig. 6.23a. Many parts in the landing gear structure are Ti-10-2-3, except for the outer and inner cylinders and the axles, all being steel. The biggest single item was the truck beam with a length of about 3 m and a diameter of about 0.34 m. The truck beam was initially fabricated by forging three pieces and joining them by electron beam welding. Later, the beam was made as a one-piece forging. The published forging practice for the Ti-10-2-3 alloy is β forging followed by $\alpha + \beta$ forging to plastic strains of about 15–25 % [35].

Smaller parts of Ti-10-2-3 alloy are easier to forge, and some examples of precision forgings are shown in Fig. 6.23b. These parts are used in the Boeing 777 cargo handling system. The cost advantage of Ti-10-2-3 over Ti-6Al-4V lies in the lower forging temperature and tooling costs [36]. Yet another application using relatively large Ti-10-2-3 forgings is the Super Lynx helicopter rotor head shown in Fig. 6.24.

Fig. 6.23 Boeing 777 landing gear and some small parts required in large numbers for an aircraft: all made using Ti-10-2-3 [1]

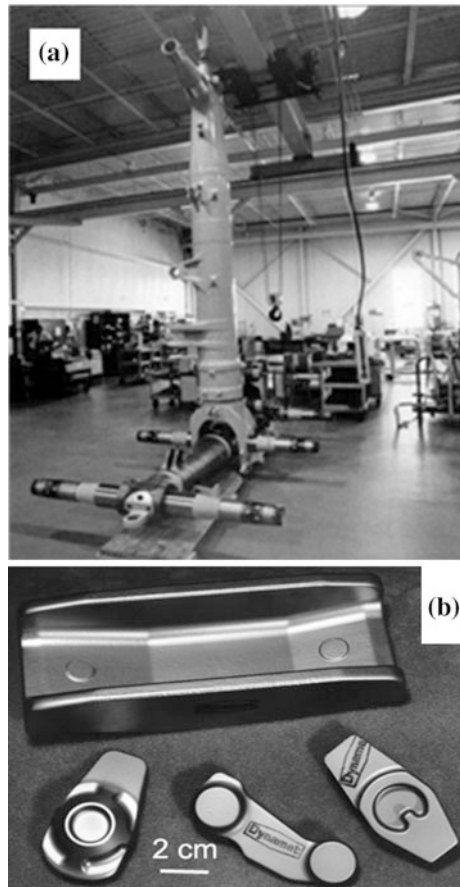
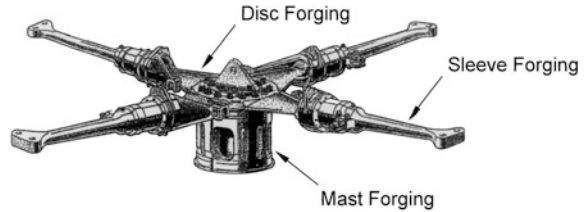


Fig. 6.24 Helicopter rotor using Ti-10-2-3 forgings [1]



Springs Springs made from heavily stabilized β titanium alloys are now commonly used in a large variety of shapes and sizes in airplanes. The prime reason is the low modulus of elasticity combined with the high yield stress. Titanium springs have two major advantages. First, they can save as much as 70 % in weight compared to steel springs; and second, they are immune to corrosion unlike steel springs. Details about the specific uses of the springs can be found in Ref. [13].

Flat springs are fabricated from strip, usually the alloy Ti-15-3. Springs made from round or square wire are commonly manufactured using the Beta C alloy. The processing route for the springs is the same as for β -annealed microstructures, which is normally used for heavily stabilized β alloys. If springs are required with a very low modulus of elasticity with reasonable strength, then the alloy is used without ageing. This is because ageing results in increasing the volume fraction of α phase, which in turn increases the modulus of elasticity.

Engine nacelles Another application worth mentioning is use of the heavily stabilized β alloy Beta 21S in the nacelle structure (exhaust plug, nozzle and aft cowl), e.g. Fig. 6.25, of the engines used for the Boeing 777 aircraft [13, 36].

Beta 21S sheets are used for this application because of the alloy's excellent oxidation resistance, which allows long-time operating temperatures in the range of 480–565 °C, with short-time periods up to 650 °C [53]. Beta 21S contains 15 %

Fig. 6.25 Use of Beta 21S as an engine tail plug (indicated by an arrow)



Mo and 2.7 % Nb, and was specially designed for high oxidation resistance. It also has excellent resistance to embrittlement when exposed to hydraulic fluid at elevated temperatures.

Beta 21S can be used for nacelle structures because the high temperature operational stresses are small. The Beta 21S sheets are basically used in the β -annealed condition, but two different final ageing treatments are used at Boeing [53]. These ageing treatments result in two different microstructures with quite different yield stress levels. Finally, it may be noted that a major European effort was initiated recently to use Beta 21S sheets in the exhaust structures of helicopter engines, in order to reduce the noise level of civil helicopters.

6.3 Summary

Conventional titanium alloys, especially near- α , $\alpha + \beta$ and the β alloys which have good strength and low densities, have a great future ahead. This is especially true in India, where many aircraft industries are being set up and the aerospace sector for repair and overhaul centres is growing. Because of this, the usage of titanium alloys can only grow, the only impediment being the cost.

Acknowledgments The authors wish to place on record that Prof G. Lütjering would certainly have been included as an author but for his untimely demise. Nevertheless, the authors cannot thank him enough for the repository of knowledge that he has created in the second edition of the book on Titanium, published by Springer publications. The authors would like to thank Dr. A.K. Gogia, Dr. T.K. Nandy and Mr. Dipak K. Gupta of DMRL; Mr. Ramesh Babu, Mr. G.V.R. Murthy and Mr. U.V. Gururaja of Midhani; and, Mr. V.P. Deep Kumar of ADA for many inputs and technical data. They profoundly thank the editors, Dr. N. Eswara Prasad and Dr. R.J.H. Wanhill for their help in reviewing the contents of the book chapter and also for their constructive comments. The authors (AB and BS) are greatly indebted to Prof D. Banerjee, Dr. K. Tamilmani, Dr. Samir V. Kamat and Dr. Amol A. Gokhale for their kind support and encouragement. Funding from DRDO is gratefully acknowledged.

References

1. Lütjering G, Williams JC (2007) Titanium: engineering materials and processes, 2nd edn. Springer, Berlin, Germany
2. Boyer R, Welsch G, Collings EW (eds) (1994) Materials properties handbook: titanium alloys. ASM International, Materials Park, OH, USA
3. Zarkades A, Larson FR (1970) Elasticity of titanium sheet alloys. In: Jaffee RI, Promisel NE (eds) The science, technology and application of titanium. Pergamon Press, Oxford, UK, pp 933–941
4. Conrad H, Doner M, de Meester B (1973) Deformation and fracture (controlling mechanisms for titanium plastic flow). In: Jaffee RI, Burte HM (eds) Titanium science and technology. Plenum Press, New York, USA, pp 969–1005

5. Partridge PG (1967) The crystallography and deformation modes of hexagonal close-packed metals. *Metall Rev* 12(1):169–194
6. Paton NE, Williams JC, Rauscher GP (1973) The deformation of alpha-phase titanium. In: Jaffe RI, Burte HM (eds) *Titanium science and technology*, Plenum Press, New York, USA, pp 1049–1069
7. Paton NE, Williams JC (1970) Second international conference on the strength of metals and alloys. ASM, Metals Park, OH, USA, p 108
8. Rosenberg HW, Jaffe RI (1970) The science, technology and application of titanium. In: Jaffe RI, Promisel NE (eds) *Proceedings of the 2nd international conference on titanium*, Pergamon Press, New York, USA, pp 851–859
9. Baker H (ed) (1992) *Alloy phase diagrams*, ASM handbook, vol 3. ASM, Materials Park, OH, USA
10. Newkirk JB, Geisler AH (1953) Crystallographic aspects of the beta to alpha transformation in titanium. *Acta Metall* 1(35):370, 373–371, 374
11. Williams JC (1973) Kinetics and phase transformations (in Ti alloys). In: *Titanium science and technology*, pp 1433–1494
12. Collings EW (1994) *Materials properties handbook: titanium alloys*. ASM, Materials Park, OH, USA
13. Boyer RR (1993) Applications of beta titanium alloys in airframes. In: Eylon D, Boyer RR, Koss Donald A (eds) *Beta Titanium Alloys in the 1990's*. The Minerals, Metal and Materials Society, Warrendale, PA, USA, pp 335–346
14. Buttrell WH, Shamblen CE (1999) Hearth melt plus vacuum arc remelt: production status. In: *Titanium'95, science and technology*, The Institute of Materials, London, UK, pp 1446–1453
15. Adams RT, Rosenberg HW (1982) Critical review a review of titanium ingot solidification. In: Williams JC, Belov AF (eds) *Titanium and titanium alloys: scientific and technological aspects*, 1st ed, Plenum Press, New York, USA, pp 127–135
16. Boyer R, Welsch G, Collings EW (eds) (1994) *Materials properties handbook: titanium alloys, technical note 3: casting*. ASM, Materials Park, OH, USA, pp 1079–1082
17. Eylon D, Froes FH, Gardiner RW (1983) Developments in titanium alloy casting technology. *JOM* 35(2):35–47
18. Schutz Ronald W, Thomas David E (1987) Corrosion of titanium and titanium alloys. In: *ASM Handbook Ninth Edition, Volume 13 Corrosion*, ASM, Metals Park, Ohio, USA, pp 669–706
19. Myers JR, Bomberger HB, Froes FH (1984) Corrosion behavior and use of titanium and its alloys. *JOM* 36(10):50–60
20. Schutz RW (1996) Development in Titanium alloy environmental behavior, titanium '95: science and technology. In: *Proceedings of the eighth world conference on titanium*. The Institute of Materials, London, UK, pp 1860–1870
21. Schutz RW (1994) *Metallurgy and technology of practical titanium alloys*. TMS, Warrendale, Pennsylvania, USA
22. Zwicker U (1974) *Titan und Titanlegierungen*. Springer-Verlag, Berlin, Germany, pp 102–107
23. Bania PJ, Parris WM (1990). Beta-21S: a high temperature metastable beta titanium alloy. In: *Proceedings of the international conference on titanium products and applications*, Titanium Development Association, vol 2, pp 784–793
24. Fleischer RL, Donald Peckner (1964) *The strengthening of metals*, vol 93. Reinhold, New York, USA
25. Okazaki K, Masuda I, Conrad H (1982) Mobile dislocation density during the plastic flow in Ti-interstitial alloys at low temperatures. In: Williams JC, Belov AF (eds) *Titanium and titanium alloys: scientific and technological aspects*, vol 1. Plenum Press, New York, USA, pp 497–505
26. Peters M, Lutjering G (1980) Control of microstructure and texture in Ti–6Al–4V. In: Jaffe RI, Kimura M, Izumi O (eds) *Titanium '80, science and technology*. AIME, Warrendale, PA, USA, pp 925–936

27. Lütjering G, Albrecht J, Ivasishin OM (1995) Influence of cooling rate and beta grain size on the tensile properties of (alpha + beta) Ti-alloys. In: Blenkinsop PA, Evans WJ, Flower HM (eds) Titanium '95: science and technology, vol 2. The Institute of Materials, London, UK, pp 1163–1170
28. Däubler MA, Helm D (1992) Surfaces and elevated temperature effects. In: Froes FH, Caplan IL (eds) Titanium '92: science and technology, vol 1. TMS, Warrendale, Pennsylvania, USA, pp 41–50
29. Ankem S, Seagle SR (1984) The detrimental effects of iron on creep of Ti-6242 S alloys. *Titanium Sci Technol* 4:2411–2418
30. Sinha V, Mills MJ, Williams JC (2001) Dwell-fatigue behavior of Ti-6Al-2Sn-4Zr-2Mo-0.1Si alloy. In: Jata K, Lee EW, Frazier W, Kim NJ (eds) Lightweight alloys for aerospace application. TMS, Warrendale, Pennsylvania, USA, pp 193–208
31. Woodfield AP, Gorman MD, Corderman RR, Sutliff JA, Yamrom B (1996) “Effect of microstructure on dwell fatigue behavior of Ti6242”, titanium'95: science and technology. The Institute of Materials, Birmingham, UK, pp 1116–1123
32. Albrecht J, Lütjering G (2000) Microstructure and mechanical properties of titanium alloys. In: Gorynin IV, Ushkov SS (eds) Titanium '99: science and technology, vol 1. Central Research Institute of Structural Materials, St. Petersburg, Russia, pp 363–374
33. Peters JO, Lütjering G, Koren M, Puschnik H, Boyer RR (1996) Processing, microstructure and properties of β -CEZ. In: Blenkinsop PA, Evans WJ, Flower HM (eds) Titanium'95: science and technology, vol 2. The Institute of Materials, London, UK, pp 1403–1410
34. Sauer C, Busongo F, Lütjering G (2002) Fatigue 2002. EMAS, Warley, UK, pp 2043–2050
35. Bania PJ (1994) Beta titanium alloys and their role in the titanium industry. In: Vassel A, Eylon D, Combres Y (eds) Beta titanium alloys (Société Française de Métallurgie et de Matériaux, Paris, France), pp 7–15
36. Boyer RR (1994) Beta titanium alloys. Société Française de Métallurgie et de Matériaux, Paris, pp 253–261
37. Peters M, Lütjering G, Ziegler G (1983) Control of microstructures of $\alpha + \beta$ titanium alloys. *Zeitschrift für Metallkunde* 74:274–282
38. Köppers M, Herzig C, Freisel M, Mishia Y (1997) Intrinsic self-diffusion and substitutional Al diffusion in α -Ti. *Acta Met* 45:4181–4191
39. Helm D (1999) Application of titanium alloys as compressor discs and blades. In: Boyer RR, Eylon D, Lütjering G (eds) Fatigue behavior of titanium alloys. The Minerals, Metals and Materials Society, Warrendale, PA, USA, pp 291–298
40. Lütjering G, Helm D, Daubler M (1993) Influence of microstructure on fatigue properties of the new titanium alloy IMI 834. In: Bailon J-P, Dickson JI (eds) Fatigue 93 – Proceedings of the 5th international conference on fatigue and fatigue thresholds, vol 1. EMAS Publishing, Warrington, UK, pp 165–170
41. Thiehsen KE, Kassner ME, Pollard J, Hiatt DR, Bristow BM (1993) The effect of nickel, chromium and primary alpha phase on the creep behavior of Ti6242Si. *Metall Trans* 24A:1819–1826
42. Russo PA, Wood JR, Brosius RN, Marcinko SW, Giangiordano SR (1995) Influence of Ni and Fe on the creep of beta annealed Ti6242S. In: Blenkinsop PA, Evans WJ, Flower HM (eds) Titanium'95: science and technology, vol 2. The Institute of Materials, London, UK, pp 1075–1082
43. Russo PA, Yu KO (1999) Effect of Ni, Fe and primary alpha on the creep of alpha-beta processed and annealed Ti-6Al-2Sn-4Zr-2Mo-0.9Si. In: Gorynin IV, Ushkov SS (eds) Titanium'99: science and technology, vol 1. Central Research Institute of Structural Materials, St. Petersburg, Russia, pp 596–603
44. Ankem S, Seagle SR (1984) Heat-treatment of metastable beta titanium alloys. In: Boyer RR, Rosenberg HW (eds) Beta titanium alloys in the 1980's. TMS, Warrendale, Pennsylvania, USA, pp 107–126

45. Hayes RW, Viswanathan GB, Mills MJ (2002) Creep behavior of Ti–6Al–2Sn–4Zr–2Mo: I. The effect of nickel on creep deformation and microstructure *Acta Mater*, vol 50, pp 4953–4963
46. Viswanathan GB, Karthikeyan S, Hayes RW, Mills MJ (2002) Creep behaviour of Ti–6Al–2Sn–4Zr–2Mo: II. Mechanisms of deformation *Acta Mater*, vol 50, pp 4965–4980
47. Jeal RH (1982) Defects and their effect on the behaviour of gas turbine discs. In: ‘Maintenance in service of high temperature parts’, AGARD conference proceedings no. 317. Advisory Group for Aerospace Research and Development, Neuilly sur Seine, France, pp 6.1–6.15
48. Wagner L, Gregory JK (1993) Improvement of mechanical behavior in Ti–3Al–8V–6Cr–4Mo–4Zr by duplex aging. In: Eylon D, Boyer RR, Koss DA (eds) *Beta titanium alloys in the 1990’s*. TMS, Warrendale, Pennsylvania, USA, pp 199–209
49. Prandi B, Wadier J-F, Schwartz F, Mosser P-E, Vassel A (1990) Titanium 1990, products and applications. Titanium Development Association (TDA) Dayton, Ohio, USA, pp 150–159
50. Peters JO, Lütjering G, Koren M, Puschnik H, Boyer RR (1996) Processing, microstructure, and properties of β -CEZ. *Mater Sci Eng A* 213(1):71–80
51. Combres Y, Champin B (1993) β -CEZ properties. In: Eylon D, Boyer RR, Koss Donald A (eds) *Beta titanium alloys in the 1990’s*. TMS, Warrendale, PA, USA, pp 477–484
52. Peters M, Lütjering G (1976) Influence of grain-size on tensile properties of a Ti–Mo alloy with precipitate-free zones. *Zeitschrift für Metallkunde* 67:811–814
53. Boyer RR (1996) An overview on the use of titanium in the aerospace industry. *Mater Sci Eng A* 213(1):103–114

Bibliography

1. Leyens C, Peters M (eds) (2003) *Titanium and titanium alloys: fundamentals and applications*. WILEY VCH Verlag GmbH & Co. KGaA, Weinheim, Germany

Chapter 7

Aero Steels: Part 1—Low Alloy Steels

K.P. Balan and A. Venugopal Reddy

Abstract This chapter demonstrates the objectives of adding alloying elements to steel through their effects on microstructure and consequent improvements in mechanical properties. Classifications and designations followed by different international standards are briefly outlined. The development of medium carbon low alloy steels used for aerospace applications is described, including their compositions and mechanical properties. Salient aspects of the physical metallurgy including heat treatment and surface hardening methods are brought out. The engineering properties of ultra high strength steels are briefly mentioned. The efforts towards indigenous development and manufacture of some aero steels are also presented.

Keywords Low alloy steels • Chemical compositions • Processing • Heat treatment • Fatigue • Fracture • Corrosion

7.1 Introduction

“Steel may lack the high-tech image that attaches to materials like titanium, carbon fibre reinforced composites and most recent nano materials, but make no mistake, its versatility, strength, toughness, low cost and wide availability are unmatched” [1].

The metallurgy of steels has grown far beyond the historical definition of ‘Steel is an alloy of iron and carbon’. Present-day steels are complex alloys of Fe and a host of major and minor alloying elements, whose concentrations are judiciously selected to achieve the desired mechanical properties for the intended applications.

K.P. Balan (✉)
DMRL, Hyderabad, India
e-mail: balankp4@gmail.com

A.V. Reddy
ARCI, Hyderabad, India
e-mail: aramadka@hotmail.com; aramadka@gmail.com

Modern computational and technological advances, coupled with the availability of tools for metallurgical characterization and non-destructive testing, have facilitated the production of clean steels with narrow compositional limits and property scatter. All these factors have contributed to the availability of inexpensive high strength–high toughness steels for aeronautical applications.

Over the years, because of the availability of high specific strength (strength/density) materials such as high strength aluminium alloys and titanium alloys, the usage of steels in aircraft structures and aeroengines has gradually decreased from 40 % to about 15 %. However, steels are the primary choices for applications like gears, bearings, undercarriages and high strength fasteners used in aeronautical engineering.

Steel is classified as carbon steel when the contents of the residual elements manganese and silicon are less than 0.5 wt% each. However, when deliberate additions of manganese and silicon beyond 0.5 wt% are made they become alloying additions in plain carbon steels. The principal elements contained in alloy steels are Mn, Si, Ni, Cr, Mo, V, W and Co, either singly or in combination. Alloy steels with total alloy content not exceeding 8 wt% are called low alloy steels [2].

The limitations of carbon steels are overcome by the addition of alloying elements in various combinations to derive the benefits of synergetic effects. The objectives of adding alloying elements to primary steel are to

- (a) improve the hardenability
- (b) increase resistance to softening on tempering
- (c) increase wear resistance
- (d) improve corrosion and oxidation resistance
- (e) improve machinability
- (f) improve mechanical properties both at room temperature and high temperatures
- (g) improve fabricability and weldability, and
- (h) produce fine grains that result in a good combination of strength and toughness.

As compared to plain carbon steels, alloy steels are expensive due to the ever-increasing costs of the alloying elements. Hence their use in the design of a steel should be made judiciously.

7.2 Classification and Designation

Alloy steels are generally classified based on *chemical composition* (Ni steels, Cr steels, Ni–Cr steels, etc.), *microstructure* (pearlitic, ferritic, martensitic, etc.), *functionality* (structural steels, tool steels, etc.) and *specific attributes* (magnetic steels, heat-resistant steels, corrosion-resistant steels, etc.). International standards have, however, classified steels mainly based on their composition, since this is deemed to be rational and convenient for both producers and users.

The designations followed by different international agencies are adopted for general engineering purposes. Aerospace steel standards are mostly derived from their corresponding general engineering standards, with narrower composition ranges, strict control on trace/deleterious elements and drastic reduction in inclusion sizes, shapes and populations.

In order to differentiate the aerospace grades from general engineering grades, every country/manufacturer has designated the standards with some alphanumeric feature. For example, the ASTM standard is replaced by aerospace materials standard (AMS). The aeronautical steels are also covered by defence standards like MIL Standard (American), DEFSTAN (British), etc. In addition, General Electric (GE), Rolls Royce (RR) and Pratt & Whitney (P&W) have their own internal standards.

The AMS grades are generally assigned based on their mill form, product description and supply condition. Hence, instead of reproducing the list, further information can be accessed on various steel grades and mill forms from the AMS designations (see Ref. [3]). For the sake of convenience and brevity the compositions of popular low alloy steels used in aerospace applications are listed in Table 7.1 as per their AISI/SAE designations [4]. Some of their major applications are listed in Table 7.2 [5, 6].

Table 7.1 Chemical compositions of UHSS low alloy aerospace steels (wt%) [4]

SAE	C	Mn	Si	Ni	Cr	Mo	V
4037	0.35–0.40	0.70–0.90	0.15–0.35	–	–	0.20–0.30	–
4130	0.28–0.33	0.40–0.60	0.20–0.35	–	0.80–1.10	0.15–0.25	–
4140	0.38–0.43	0.75–1.00	0.20–0.35	–	0.80–1.10	0.15–0.25	–
4340	0.38–0.43	0.60–0.80	0.20–0.35	1.65–2.00	0.70–0.90	0.20–0.30	–
6150	0.48–0.53	0.70–0.90	0.20–0.35	–	0.80–1.10	0.15–0.25	0.15 min
300M	0.40–0.46	0.65–0.90	1.45–1.80	1.65–2.00	0.70–0.95	0.30–0.45	0.05 min
D6ac	0.42–0.48	0.60–0.90	0.15–0.30	0.40–0.70	0.90–1.20	0.90–1.10	0.05–0.10
9260	0.56–0.64	0.75–1.00	1.80–2.20	–	–	–	–

N.B: The maximum limits of sulphur and phosphorus in all the grades are 0.02 and 0.025, respectively

Table 7.2 UHSS low alloy steels used in aerospace applications [5, 6]

SAE no. and type	Applications
4130 (Cr–Mo)	Sheet fittings, landing gear axles, turbine components (rotors, shafts and discs), highly stressed airframe components
4130 (Cr–Mo)	Axles, rotors, gears, perforators, high strength forged and machined parts, landing gear, highly stressed fuselage fittings, propeller hubs, snap rings, crankshafts
4140 (Cr–Mo)	
4340 (Ni–Cr–Mo)	
6150 (Cr–Mo–V)	Propeller cones and snap rings, springs, shafts, gears, pinions, axles, heavy duty pins, bolts
9260 (Mn–Si)	Springs
300M (Ni–Cr–Si–Mo)	Landing gear, airframe parts, fasteners
D6ac (Cr–Mo–Ni–V)	Landing gear, motor cases for solid fuel rockets, shafts, gears, springs

7.3 Compositions of Low Alloy Steels

Most of the aerospace low alloy steels are based on Cr–Mo–Si and Ni–Cr–Mo–Si combinations with varying carbon contents:

- Low Ni and low Cr steels contain a little over two parts of nickel to one part of chromium by weight. The combined effect of both elements results in increased hardenability and strength. The retardation of the austenite \rightarrow pearlite transformation during cooling from the austenite region avoids severe quenching problems. However, these steels are susceptible to temper embrittlement, which must be avoided.
- Low carbon Ni–Cr steels are used for case carburising since Cr is a carbide former for the case, and both Ni and Cr improve the toughness of the core.
- The susceptibility of Ni–Cr and Cr–Mn steels to temper embrittlement is reduced by the presence of 0.5 wt% Mo.
- Cr–Mo steels possess good machinability and mechanical properties.
- Ni–Cr–Mo steels possess the best combination of strength, ductility and toughness among low alloy steels.

As little as 0.1 wt% of vanadium in low alloy steels restricts grain coarsening during heat treatment. Vanadium forms finely dispersed carbides and nitrides that do not go into solution during austenitization. Vanadium also provides resistance to softening during tempering, and the finely dispersed vanadium carbides give a secondary hardening effect to steels.

Silicon up to 1.2 wt% is added to low alloy steels to retard softening during tempering. Modified Cr–Mo and Ni–Cr–Mo steels for aerospace applications are based on this concept. Finally, many nitriding grades contain Al and/or enhanced Cr levels.

Several variants of Cr–Mo–Ni steels have been developed especially for landing gear components like pistons, barrels and struts. These grades are 300M (or S155), 4330V, 4335V, 4340, D6ac, 35NCD16 (or S28). These steels are classified in the category of ultrahigh-strength steels.

7.3.1 Ultrahigh-Strength Steels (UHSS)

Structural steels with a minimum yield strength of 1380 MPa are referred to as ultrahigh-strength steels. Medium carbon low alloy steels that fall in this category are used for aerospace applications. The designations of these steels are AISI/SAE 4130, 4140, 4340, 300M (modified 4340), AMS 6434 and D6ac. The chemical compositions of these ultrahigh-strength steels (UHSS) are given in Table 7.1 and their aerospace applications are listed in Table 7.2.

AISI 4130 steel is amenable to intermediate hardening and is immune to temper embrittlement. Suitable hardening and tempering enables retention of good

mechanical properties like tensile, impact and fatigue up to 370 °C. However, the impact properties at cryogenic temperatures are poor. This steel is suitable for case hardening by nitriding.

AISI 4140 Steel has a higher carbon content than 4130 steel and therefore deeper hardenability and higher strength. Hardening and tempering gives good mechanical properties retained up to 480 °C. The steel is susceptible to hydrogen embrittlement at high strength levels. The steel is weldable and can also be nitrided for certain applications.

AISI 4340 steel is a deep hardenable Ni–Cr–Mo steel that is immune to temper embrittlement and gives a good combination of strength and toughness when suitably heat treated. It retains useful mechanical properties up to about 200 °C, as indicated in Fig. 7.1. This steel also has high impact toughness even at cryogenic temperatures [7]. However, it is prone to hydrogen embrittlement and stress corrosion cracking (SCC) at high strength levels (as are all the other low alloy steels: see Chap. 19 in Volume 2 of these Source Books).

300M Steel is a version of 4340 steel modified by the addition of 1.6 wt% Si. It contains slightly higher carbon as compared to 4340 steel and also vanadium. Addition of silicon to the steel provides deeper hardenability and resistance to softening when tempered at higher temperatures as compared to 4340 steel. The silicon content also shifts tempered martensite embrittlement (TME) to higher temperatures. At higher strength levels the steel is prone to hydrogen embrittlement and SCC. It is a weldable steel.

D6a and D6ac steel is a deep hardenable ultrahigh-strength steel that is immune to temper embrittlement and maintains a very high yield to tensile strength ratio up to 1930 MPa. Air-melted steel is designated by grade D6a, while air melted followed by vacuum arc remelting is designated by grade D6ac. Like other steels in its class it is susceptible to SCC.

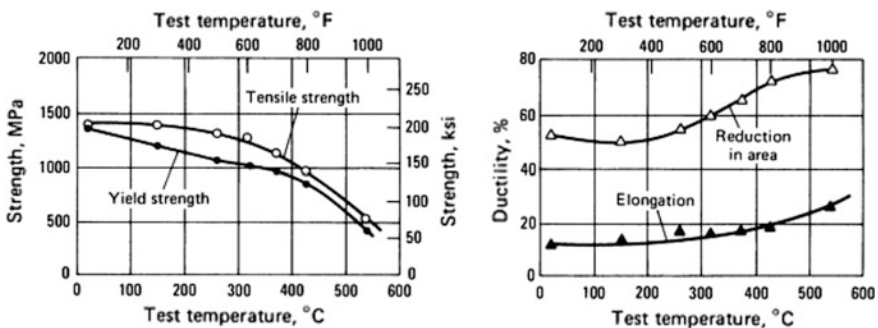


Fig. 7.1 Variation in tensile properties with test temperature for 4340 steel heat treated to a room temperature tensile strength of 1380 MPa [8]

7.3.2 *Bearing Steels*

The most popular bearing steel is AISI 52100 (1C–1.2Cr) grade, which can sustain service temperatures from -50 to $+150$ °C in a neutral environment.

In order to achieve a high rolling contact fatigue life, bearing steels are manufactured with high levels of cleanliness. Vacuum induction melting followed by vacuum arc remelting is found to give maximum freedom from non-metallic inclusions in bearing steels.

7.4 *Effects of Alloying Elements*

7.4.1 *Critical Transformation Temperatures*

The critical transformation temperatures are those that correspond to allotropic transformation when the steel is heated from ambient temperature to near its melting point. These are the A_1 , A_3 , and A_4 temperatures (A_2 , which occurs at 770 °C, corresponds to a magnetic change). The A_1 temperature is at 723 °C, and is called the lower critical temperature, where the ferrite \rightarrow austenite transformation starts. The A_3 temperature is at 910 °C, and is called the upper critical temperature, above which BCC (α) iron transforms to FCC (γ) iron. The A_4 temperature is at 1400 °C, above which FCC (γ) iron transforms to BCC (δ) iron.

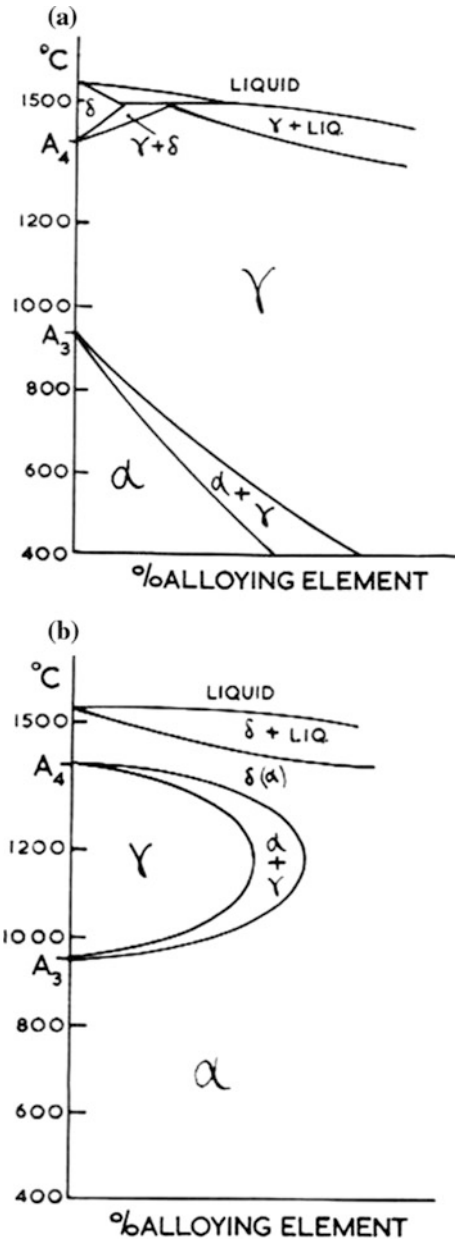
Ni, Mn, Co and Cu are some elements that raise the A_4 temperature and lower the A_3 temperature, thereby widening the γ phase field, see Fig. 7.2a. Cr, Mo, W, V, Al and Si have the reverse effect, since they raise the A_3 temperature and lower the A_4 temperature. This restricts the field over which austenite is stable, eventually forming what is commonly called a ‘ γ loop’ in more highly alloyed steels, see Fig. 7.2b. The former group of alloying elements is called ‘austenite stabilizers’ while the latter group is called ‘ferrite stabilizers’.

Most of the austenite (γ) stabilizing elements have an FCC crystal structure and easily dissolve in austenite. They also retard the precipitation of carbides in steels. The ferrite (α) stabilizers have a BCC crystal structure and therefore dissolve easily in ferrite.

7.4.2 *Formation and Stability of Carbides*

The elements which form stable carbides when added to steels are Cr, W, V, Mo, Ti and Nb. The formation of carbides increases the hardness of steels. The carbides are single, double or complex, containing one or more alloying elements and iron in them. Examples are M_3C , M_7C_3 and $M_{23}C_6$.

Fig. 7.2 Relative effects of additions of alloying elements on the polymorphic transformation temperatures A_3 and A_4 : **a** tending to stabilize γ , and **b** tending to stabilize α , resulting in a ‘ γ loop’



Mn is a weak carbide-forming element and increases the stability of other carbides present in steels. Elements like Ni, Co, Si and Al, which have no chemical affinity for carbon, tend to make iron carbides unstable by releasing free graphitic carbon. Hence these elements are added to very low carbon steels or together with carbide-forming elements to medium carbon steels. For example, most of the low alloy steels containing Ni also contain Cr for counterbalancing the graphitizing tendency of Ni.

When a steel containing carbon and any of the carbide-forming alloying elements is quench-hardened and tempered, alloy carbides are formed in the microstructure. The type and composition of such carbides depend on the chemical composition of the steel being tempered and the tempering parameters (temperature and time). At low tempering temperatures M_3C -type carbides are formed. With increase in tempering temperature this carbide is gradually replaced by M_7C_3 and finally $M_{23}C_6$ -type carbides.

The advantages of using an alloy steel that form alloy carbides are as follows:

- (a) Alloy carbides harder than cementite (Fe_3C at 840HV) impart greater wear resistance to steel, e.g. $M_{23}C_6$ which has hardness 1200HV.
- (b) For a given tempering parameter an alloy steel retains greater hardness compared to a plain carbon steel of similar carbon content.
- (c) Steels containing V, Mo and W exhibit a secondary hardening effect that raises the softening temperature of the quenched and tempered steel.

7.4.3 Grain Size

Coarse-grained structures result due to heating a steel to high temperature either during processing, heat treatment, or in service, causing a reduction in strength and toughness of the steel. Grain growth can be retarded by the addition of small amounts of V, Ti, Nb and Al. V is the most potent grain refiner: as little as 0.1 wt% forms finely dispersed carbides and nitrides that are relatively insoluble at high temperatures and act as barriers to grain growth. Ti and Nb additions have a similar effect. Aluminium added as deoxidiser in high-grade steel converts to Al_2O_3 that also acts as a grain refiner.

7.4.4 Eutectoid Point

Austenite stabilizers lower the eutectoid temperature whilst the ferrite stabilizers raise it (Fig. 7.3a). All alloying elements lower the eutectoid carbon content (Fig. 7.3b). This explains why low alloy steels can produce similar microstructures and properties as plain carbon steels with much less carbon content.

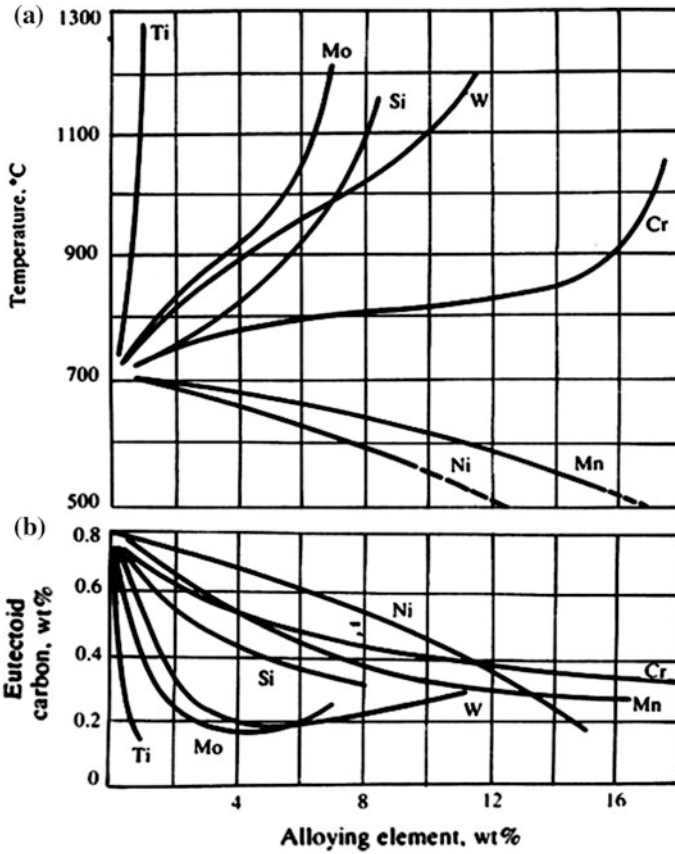


Fig. 7.3 Effects of alloying elements on a eutectoid temperature and b the eutectoid carbon content [9]

7.4.5 Hardenability

Hardenability of a steel is the relative ease with which a steel can be prevented from decomposition of austenite to ferrite and pearlite, thereby allowing the formation of martensite. The maximum cooling rate that will produce martensite in a steel is known as the critical cooling rate (CCR) of the steel. The CCR of carbon steels is high and hence their hardenability is low. Alloying with elements like Mn, Cr, Ni and Mo helps in increasing the hardenability of a steel.

For a particular strength level in a given composition of steel, there will be a maximum section size in which the desired transformation can be achieved. This is the *limiting ruling section (LRS)*, which is the largest diameter for a given steel that can achieve certain mechanical properties after a specified heat treatment.

Table 7.3 Improvements in tempered steel hardenability (increased LRS) by alloying [10]

Steel grade	C	Mn	Cr	Mo	Ni	LRS mm	UTS (MPa)	YS (MPa)	% El min	Impact CVN, J min
150 M40	0.36–0.44	1.30–1.70	–	–	–	13	850–1000	635	12	22
530 M40	0.36–0.44	0.60–0.90	0.90–1.20	–	–	29	850–1000	680	13	50
605 M36	0.32–0.40	1.30–1.70	–	0.22–0.32	–	63	850–1000	680	13	50
709 M40	0.36–0.44	0.70–1.00	0.90–1.20	0.25–0.35	–	100	850–1000	680	13	50
817 M40	0.36–0.44	0.45–0.70	1.00–1.40	0.20–0.35	1.30–1.70	150	850–1000	680	13	50

The benefits of alloying in order to achieve deep-hardening improvements in mechanical properties are illustrated in Table 7.3 [10]. Note that combinations of several alloying elements give the most improvement in LRS.

Besides improvements in LRS, one of the most important effects of alloying is that small additions of alloying elements allow much slower quenching rates to produce martensite, such that oil or air quenching can be resorted to instead of water quenching. This helps in avoiding distortion or cracking of components, see Sect. 7.4.6. A disadvantage is that all alloying elements, except cobalt, lower the martensitic start (M_s) and martensitic finish (M_f) temperatures. This results in retention of austenite in the as-quenched structure of alloy steels. The retained austenite content is kept below 2 % in UHSS by judicious heat treatment.

7.4.6 Volume Change

The austenite \rightarrow martensite transformation in steels is accompanied by an increase in volume. This effect can often lead to transformation stresses causing distortion and cracks in components. Judicious selection of alloying elements can reduce the risk of cracking of steel components during quenching, as mentioned in the last paragraph of Sect. 7.4.5.

7.4.7 Resistance to Softening While Tempering

Most low alloy steels soften rapidly with increase in tempering temperature. However, it is well known that silicon additions to steel improve the resistance of martensite to softening on tempering [11]. Such improved properties are of considerable importance in low alloy steels, since resistance to softening allows for

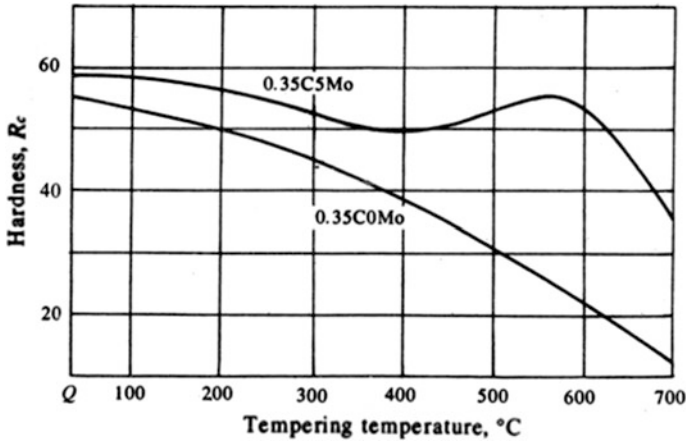


Fig. 7.4 Variation in hardness with tempering temperature for two different steels [12]

greater relief of thermal and transformation stresses on tempering. This leads to good combinations of strength and toughness.

Silicon additions also displace tempered martensite embrittlement (TME) to higher temperatures, as mentioned in Sect. 7.3.1, thus allowing tempering at elevated temperatures [13, 14]. The TME phenomenon in silicon-modified AISI 4340 (300M) steel was studied by Horn and Ritchie [15]. They suggested that displacement of TME to higher tempering temperatures is due to the Si enhancing the stability of carbides and retarding the formation and growth of cementite.

Carbide-forming elements like Cr, Mo and V at large concentrations are more effective in retarding softening of steel on tempering. These elements not only retard softening but also provide secondary hardening at higher temperatures of 500–550 °C, owing to fine alloy carbide precipitation. Alloy carbides resist softening up to around 550–600 °C. Above 600 °C there is a decrease in hardness, see Fig. 7.4, owing to carbide coarsening.

7.5 Strengthening Mechanisms

The strength of steels can be increased by (i) alloying, (ii) grain refinement, (iii) precipitation and dispersion of hard particles, (iv) martensitic and bainitic transformations, (v) retardation of softening during tempering and (vi) strain hardening.

Alloying: Designing steel compositions is a complex science. The choice of alloying elements depends on the desired microstructure to give the required mechanical properties. It is also essential to consider hot workability, heat treatment and joining. The general guidelines are as follows:

- Achieve the desired hardenability with Cr additions for martensitic transformation with the lowest quench rate to avoid distortion, warpage and quench cracks.
- Add Ni, Mn, W, etc. to increase the matrix strength.
- Increase temper embrittlement resistance.
- Induce secondary hardening during tempering with judicious additions of Si, Co, Al, V and Nb.
- Alter transformation characteristics to facilitate thermomechanical treatments like ausforming.
- Keep carbon as low as possible, i.e. deviate from the concept of increasing strength with increasing carbon.

Martensitic and Bainitic Transformations: Quite a few low and high alloy steels are strengthened by a martensitic transformation. The resultant martensite is strong but brittle. Tempering restores ductility by softening the matrix. If suitable alloy additions are made to retard softening during tempering, by decreasing the carbide growth rate, it is possible to temper at higher temperatures to achieve higher toughness without significantly sacrificing strength. Modified 4340 with addition of 1 wt% silicon (300M) is an outstanding example of this concept. An additional advantage is the elimination of tempered martensite embrittlement (TME), often encountered in steels tempered between 200 and 350 °C. This elimination of TME enables tempering above the susceptible temperature range without strength reduction.

Another form of embrittlement, temper embrittlement (TE), is observed in quenched and tempered steels when tempered between 500 and 600 °C. This can be avoided by the addition of about 0.5 wt% Mo.

Thermomechanical Treatments: Yet another, but less popular method, to increase the strength of low alloy steels is to design the composition in such a way that austenite can be deformed prior to martensite transformation (Ausforming) to introduce high dislocation densities. Ausforming results in high strength with good toughness. However, it is rarely employed in aerospace alloys.

7.6 Melting of Low Alloy Steels

Aerospace specifications stipulate stringent control of chemical composition and non-metallic inclusion limits to minimize scatter in the mechanical properties. Judicious combinations of primary (arc melting, induction melting or vacuum induction melting) and secondary (vacuum arc remelting or electro-slag remelting) techniques are usually employed to produce high-quality steels with close compositional tolerances. These modern melting practices help in reducing the contents of dissolved gases (hydrogen, oxygen and nitrogen) to very low levels. The non-metallic inclusion contents are reduced to <0.001 wt% by the combination of VIM + VAR, and ESR also helps in reducing the inclusion contents.

7.7 Fabrication of Low Alloy Steels

Large landing gears are usually press-forged at slow and controlled strain rates. Steel forgings are normalized to refine the as-forged grain size and minimize residual stresses before the forgings are hardened and tempered. Forged products possess the best combination of strength, ductility and toughness in low alloy steels.

Low alloy steel plates are welded by gas, arc and electron beam welding techniques. Welding rods of the same composition and of comparable strength are used. The plates are preheated and also subjected to inter-pass heating to avoid cracking. After welding, the welded plate structures are either stress relieved, followed by hardening and tempering; or hardened and tempered immediately after welding. These procedures depend on the complexity of the fabricated structure.

Welded structures of high strength low alloy steels are susceptible to hydrogen embrittlement and SCC [16]. Therefore absorption of hydrogen during welding should be minimized/avoided, and stress relieving should be carefully done to avoid SCC.

Post-fabrication electroplating should be preceded by a stress relief treatment to avoid hydrogen embrittlement during plating; and electroplating should be immediately followed by ‘baking’ to remove any galvanically absorbed hydrogen and minimize the risk of hydrogen embrittlement.

7.8 Heat Treatment

Heat treatment is employed in order to bring about changes in microstructure to obtain the desired properties. The heat treatment process consists of the following:

- (a) Heating the steel to a predetermined high temperature, the austenitizing temperature.
- (b) Soaking the steel at the austenitizing temperature for sufficient time to obtain a homogeneous austenite structure.
- (c) Cooling the steel to room temperature at a particular cooling rate to produce the correct microstructure.

Alloy steels require careful heating to prevent cracking from thermal shock. They require higher austenitizing temperatures and longer soaking times than plain carbon steels, owing to the lower rate of dissolution of alloying elements in the austenite. However, this carries the risk of grain growth (which should be avoided) during austenitizing. Cooling rates should also be carefully controlled in alloy steels. Some heat treatments normally employed for low alloy steels are described below.

Normalizing: This is carried out as a conditioning treatment before the final heat treatment. Medium carbon low alloy steel forgings are normalized before hardening to produce a finer grain structure and to minimize residual stresses. Normalizing at

815–930 °C, followed by tempering at 650–675 °C, produces a partially spheroidized structure that possesses adequate hardness suitable for machining.

Annealing: Depending upon the requirement, different annealing treatments, namely isothermal annealing, full annealing, process annealing and stress relief annealing, are employed.

Full annealing is carried out by heating to 730–870 °C, soaking for a suitable time period, and then slow furnace cooling. This treatment produces maximum softness in low alloy steels. Process annealing is carried out in wire drawing and cold rolling industries in order to remove the residual stresses of cold working processes. This process is *not* applicable to low alloy steels. Stress relieving treatment is used after fabrication processes like welding (Sect. 7.7), machining or cold working in order to relieve residual stresses.

Hardening: The steel is heated to the austenitizing temperature, held there for sufficient time for complete transformation to austenite and also to bring the carbides into solution, followed by quenching in a suitable medium (water, oil) to convert austenite into martensite.

Low alloy steels are heated to a temperature 50 °C above A_3 and soaked at that temperature for about 1 h per 25 mm section thickness. These steels are usually quenched in oil to avoid too-fast quenching problems, see subsection 7.4.5, but still fast enough to ensure complete transformation of austenite to martensite.

Tempering: Two important aspects that should be understood and considered while carrying out hardening and tempering of low alloy steels are (a) the effect of chemical composition on hardenability and (b) the effects of tempering temperature on variation in mechanical properties.

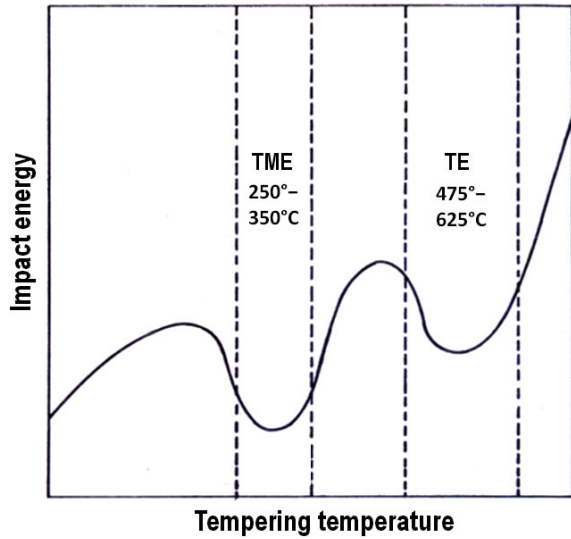
Although as-quenched steel is extremely hard and strong, it is also very brittle. Tempering is the treatment that is carried out on as-quenched steels in order to restore ductility and toughness at the cost of some loss of hardness and strength. During tempering of low alloy steels the as-quenched steel is re-heated to some intermediate temperature below the A_1 temperature, soaked for sufficient time (usually 2 h per 25 mm section), followed by air cooling to room temperature. In the case of steels prone to temper embrittlement, water quenching is done to avoid segregation of trace elements to prior austenite grain boundaries.

Embrittlement of Steels During Tempering: High strength martensitic steels are susceptible to embrittlement during tempering [17–19]. This embrittlement can result primarily from two types of thermal treatments, Fig. 7.5:

- Tempering as-quenched alloy steels in the range of 250–350 °C, resulting in tempered martensite embrittlement (TME).
- Tempering between 475 and 625 °C, causing temper embrittlement (TE).

The main characteristics of TME are (a) there is a minimum in fracture energy and (b) the fracture mode is usually transgranular owing to transformation of retained austenite at martensite lath boundaries. Sometimes intergranular fracture occurs, owing to impurities having segregated to prior austenite grain boundaries.

Fig. 7.5 Schematic illustration of TME and TE temperature ranges for low alloy steels



TE on the other hand is manifested by (a) a considerable increase in the ductile to brittle transition temperature, accompanied by a fall in the upper shelf energy in a notched bar test, and (b) intergranular fracture at prior austenite grain boundaries owing to co-segregation of impurities, namely As, Sb, Sn and P together with alloying elements like Ni and Cr.

TME is a rapid phenomenon that develops within the normal time of tempering and is irreversible. TE develops on prolonged heating or cooling through the susceptible temperature zone and is reversible: it can be eliminated by re-hardening the embrittled steel, tempering outside the susceptible temperature zone, and rapidly cooling through the susceptible temperature range.

7.9 Surface Hardening of Steels

Sometimes the service conditions of components like ball and roller bearings, gears, shafts, axles, cams, etc. require a hard, wear-resistant surface with a tough core. This kind of functional properties in a single component can be achieved only via surface hardening.

By employing a thermochemical treatment, carbon can be diffused to a regulated depth in a low carbon-alloy steel. Suitable hardening and tempering results in a hard wear-resistant case above a tough shock-resistant core. Similarly, nitrogen and boron can also be diffused to produce hardened surface cases. In all these treatments the solute elements C, N or B form hard phases that provide the wear resistance.

The popular surface hardening treatment methods are carburizing, cyaniding, carbonitriding, nitriding, boronizing and chromizing. These are described in detail in a recent ASM Handbook [20].

7.10 Engineering Properties

All the alloying elements dissolve in ferrite and result in solid solution strengthening. Chromium, tungsten, vanadium, molybdenum, titanium and niobium form stable carbides and therefore increase the hardness, retard softening on tempering, and also cause secondary hardening. Alloying elements that help in refining grain size result in improving the toughness of the steel. Thus the microstructural changes caused by alloying have remarkable influences in improving the mechanical properties of steels. The through-hardenable low alloy steels produce a wide range of mechanical strength, and so their mechanical properties are based on the tempering temperature employed, for example Table 7.4 [21].

Fatigue: The fatigue strengths of steels, including low alloy steels, are generally good. An engineering ‘rule of thumb’ is that the fatigue limit is approximately

Table 7.4 Mechanical properties of some aerospace low alloy steels [21]

SAE no. and heat treatment condition	YS (MPa)	UTS (MPa)	El (%)	Hardness (HB or HRC)
4130				HB
H + T 315 °C	1340	1570	13.0	425
H + T 370 °C	1250	1475	15.0	400
H + T 540 °C	1000	1170	20.0	325
H + T 650 °C	830	965	22.0	270
4140				HB
H + T 205 °C	1740	1965	11.0	578
H + T 315 °C	1570	1720	11.5	495
H + T 425 °C	1340	1450	15.0	429
H + T 650 °C	790	900	21.0	277
4340				HB
H + T 205 °C	1860	1980	11.0	520
H + T 315 °C	1620	1760	12.0	490
H + T 425 °C	1365	1500	14.0	440
H + T 650 °C	860	1020	20.0	290
6150				HB
H + T 205 °C	1810	2050	1.0	610
H + T 315 °C	1720	1950	7.0	540
H + T 425 °C	1490	1585	11.0	470
H + T 595 °C	1080	1150	16.0	350

(continued)

Table 7.4 (continued)

SAE no. and heat treatment condition	YS (MPa)	UTS (MPa)	El (%)	Hardness (HB or HRC)
300M				HRC
H + T 100 °C	1240	2340	6	56.0
H + T 200 °C	1650	2140	7	54.5
H + T 315 °C	1690	1990	9.5	53.0
H + T 370 °C	1620	1930	9.0	51.0
D6a				
H + T 205 °C	1620	2000	8.9	
H + T 315 °C	1700	1840	8.1	–
H + T 425 °C	1570	1630	9.6	
H + T 540 °C	1410	1450	13.0	

$0.5 \times \text{UTS}$. Since high strength and UHSS steels are not damage tolerant, see below, no fatigue cracking is permitted in aerospace components made from them. This means that fatigue design is on a *Safe-Life* basis, whereby service fatigue stresses should not cause cracking.

Fracture toughness: The fracture toughnesses of low alloy steels show a steep inverse relationship with yield strength. At yield strengths below 1500 MPa the fracture toughnesses are generally above $75 \text{ MPa} \sqrt{\text{m}}$, which is good. However, in the UHSS range, with yield strengths approaching 2000 MPa, the fracture toughnesses decrease to less than $30 \text{ MPa} \sqrt{\text{m}}$ [22]. From an engineering point of view this means as before that UHSS components must be designed as *Safe-Life* items.

In turn this also means that in-service cracking by fatigue (see above) and stress corrosion (see below) must be prevented; and also that UHSS components must be subjected to stringent quality control at all stages of the production process.

However, even in the lower strength range of good fracture toughness, low alloy steels are generally highly loaded to maximize their structural efficiency. Hence they cannot properly be regarded as damage tolerant. Other problems, e.g. stress corrosion, contribute to this limitation. Fatigue and fracture toughness data for some UHSS steels are presented in Table 7.5 [23].

Stress corrosion, hydrogen embrittlement and corrosion [24]: Low alloy steels such as 4330, 4330M, 4340, 300M, D6ac and H11 are all susceptible to SCC, and also hydrogen embrittlement at yield strengths above 1200 MPa; and they are *extremely susceptible* at yield strengths above 1400 MPa. This is why it is often advised to restrict the UTS to less than 1400 MPa. However, exceptions are made, notably for landing gear. K_{Isc} values for 4340 steel tempered to different hardnesses are given in Table 7.6 [23].

Low alloy steels also have poor corrosion resistance, and all UHSS must be protected against corrosion and the risk of SCC. Reliance is made in the first instance on high-quality cadmium, chromium and nickel plating, sometimes in combination with each other. Additional protection is provided by paint systems on external surfaces.

Table 7.5 Fracture toughness and fatigue limit of some VAR UHSS steels [23]

Grade	Equivalent tensile strength (MPa)	K_{Ic} (MPa \sqrt{m})	Fatigue limit (MPa)
4340			
Longitudinal	2035	60.4	965 ^a
Transverse	2015	61.5	715 ^a
		59.7 ^c	
Longitudinal	2005	44.5	–
Transverse	2000	45.8	–
		48.8 ^c	–
300M			
Longitudinal	2080	57.4	–
Transverse	2015	64.1	–
		61.4 ^c	–
D6ac			
T 575 °C	1434	110	–
	1520	–	780 ^b

^aAt 10⁷ cycles^bAt 10⁶ cycles^cWR orientation**Table 7.6** Fracture toughness and K_{Isc} for 4340 steel tempered to different hardnesses [23]

Hardness	Equivalent tensile strength (MPa)	K_{Ic} (MPa \sqrt{m})	K_{Isc} (MPa \sqrt{m})
550	2040	53	8
430	1520	75	30
380	1290	110	33

7.11 Indian Scenario

A number of aerospace low alloy steel grades have been developed in India by both private and public sector industries. Many of the steels are type-approved by the Regional Centre for Military Airworthiness (Materials) Hyderabad, India. Chemical composition, heat treatment schedules, physical properties, mechanical properties (both room temperature and high temperature), supply conditions, melting practices, etc. are available.

A list of through-hardenable steels, case hardening steels and spring steels detailing the grades, production agencies and applications is given in Table 7.7. The properties are given in the literature [25].

Table 7.7 Indigenous (Indian-manufactured) through-hardenable steels

Sl. no.	Alloy	Mill Form	Application	Production Agency
1.	Grade AISI 4130	Bars, Rods and Forgings	Engine mounting lugs, aircraft frame tubing for fuselage, jacks, shafts, fittings, bushings, gears, bolts, axles, structural plates	M/s. Mysore Iron and Steel Limited, Bhadravati, Shimoga Dist. Karnataka
2.	100C6	Forged Bars	Bearing races, balls and rollers bearing outer housing of aeroengine	M/s. Firth (India) Steel Co. Ltd, 40 MIDC, Hingana Road, Nagpur
3.	Grade 25CD4S	Bars	Rear and front flange of aeroengine	M/s. Firth (India) Steel Co. Ltd, 40 MIDC, Hingana Road, Nagpur
4.	Grade 35CDV4	Bars	Shafts, dowel bolts, studs and pins of aeroengine	M/s. Firth (India) Steel Co. Ltd, 40 MIDC, Hingana Road, Nagpur
5.	Grade 15CDV6	Bars	Turbine main shaft, junction wheel of aeroengine	M/s. Firth (India) Steel Co. Ltd, 40 MIDC, Hingana Road, Nagpur
6.	Grade 35NC6	Forged Bars	Nuts and washers of aeroengine	M/s. Firth (India) Steel Co. Ltd, 40 MIDC, Hingana Road, Nagpur
7.	BS S154, S98, S99	Forged Bars	Bolts, nuts, mounting pinions of aeroengine	M/s. Firth (India) Steel Co. Ltd, 40 MIDC, Hingana Road, Nagpur
8.	30NCD 16	Forged Bars	Axial compressor shaft of aeroengine	M/s. Firth (India) Steel Co. Ltd, 40 MIDC, Hingana Road, Nagpur
9.	BS S142	Forged Bars and Hot Rolled Bars	Aircraft frame tubing for fuselage, jacks, shafts, fittings, bushings, gears, shafting bolts, axles	M/s. Mishra Dhatu Nigam (MIDHANI) Kancharabagh, Hyderabad-58
10.	38XMUAW and 30XGC AW	Hot Rolled Bars	Aircraft	M/s. Mishra Dhatu Nigam (MIDHANI) Kancharabagh, Hyderabad-58
11.	MDN 127A	Plates and Strips	Stator plate, rotor segment, drive block	M/s. Mishra Dhatu Nigam (MIDHANI) Kancharabagh, Hyderabad-58
Russian Grades				
12.	20 G2	CD Wires	Aircraft fasteners	M/s. Firth (India) Steel Co. Ltd, 40 MIDC, Hingana Road, Nagpur
13.	38 Kh A	Hot Rolled Bars	Airframe and aeroengine parts	M/s. Firth (India) Steel Co. Ltd, 40 MIDC, Hingana Road, Nagpur

(continued)

Table 7.7 (continued)

Sl. no.	Alloy	Mill Form	Application	Production Agency
14.	40 Kh	Bars/Rods	Aircraft parts	M/s. Firth (India) Steel Co. Ltd, 40 MIDC, Hingana Road, Nagpur
15.	18KhSN	Filler Wire	Filler wire and flux coated electrodes	M/s. Firth (India) Steel Co. Ltd, 40 MIDC, Hingana Road, Nagpur
16.	16KhSN	Wire	Fasteners viz. rivets and bolts (by cold upsetting)	M/s. Firth (India) Steel Co. Ltd, 40 MIDC, Hingana Road, Nagpur
17.	MDN LA2	Cold Drawn Wire	Fasteners viz. rivets and bolts (by cold upsetting)	M/s. Mishra Dhatu Nigam (MIDHANI) Kanchanbagh, Hyderabad-58
18.	30XCA	Forging	Forgings of steel parts in R11F/R25 and R29B series of engines	M/s HAL, Koraput
19.	20Kh4GMA	Wires	Filler wire (electrode) for welding	M/s. Firth (India) Steel Co. Ltd, 40 MIDC, Hingana Road, Nagpur
20.	30KhGSA	Forging, HR Bars, CD Bars and CD Hexagonal Rods	Forgings of steel parts in R11F/R25 and R29B series of engines and aircraft structural components	M/s. Firth (India) Steel Co. Ltd, 40 MIDC, Hingana Road, Nagpur and M/s. Mishra Dhatu Nigam (MIDHANI) Kanchanbagh, Hyderabad-58
21.	30KhGSA-SSH	Wires	Aircraft fasteners	M/s. Firth (India) Steel Co. Ltd, 40 MIDC, Hingana Road, Nagpur
22.	30KhGSNA	Forgings	Aircraft machine components	M/s WG Forge and Allied Industries, PB 41, Thane, Mumbai
23.	30KhGSNA-SSH	CD Hexagonal, Rods, CD and HR Bars	Aircraft machine components	M/s. Firth (India) Steel Co. Ltd, 40 MIDC, Hingana Road, Nagpur
24.	30XGCN2A	All forms	Aircraft fasteners and transmission components	M/s. Mishra Dhatu Nigam (MIDHANI) Kanchanbagh, Hyderabad-58
Case Hardening Steels				
25.	12KhN3A	Rods	Gears, shafts, ball joint pins	M/s. Firth (India) Steel Co. Ltd, Thane, Mumbai 400 604
26.	MDN LA1	Hot Rolled Bars	Gears, shafts, ball joint pins	M/s. Mishra Dhatu Nigam Ltd. (MIDHANI), Kanchanbagh, Hyderabad-58

(continued)

Table 7.7 (continued)

Sl. no.	Alloy	Mill Form	Application	Production Agency
27.	12NC12	Forged Bars	Gear shaft, bearing housing gears, output shaft, lay shaft gears, bearing housing valves, drive shaft	M/s. Firth (India) Steel Co. Ltd, 40 MIDC, Hingana Road, Nagpur
28.	16NCD13	Forged Bars	Drive shaft, gear shaft, spiral gear, spur gear	M/s. Firth (India) Steel Co. Ltd, 40 MIDC, Hingana Road, Nagpur and M/s. Mishra Dhatu Nigam Ltd. (MIDHANI), Kanchanbagh, Hyderabad-58
29.	BS S82	Forged Bars	Gear driven, pinion driven, idler gear	M/s. Mishra Dhatu Nigam Ltd. (MIDHANI), Kanchanbagh, Hyderabad-58
30.	30 CD12	Forged Bars	Rear shaft, nose shaft, driving gear, bearing housing	M/s. Firth (India) Steel Co. Ltd, 40 MIDC, Hingana Road, Nagpur
31.	MDN 40A	Forged Bars	Quill shaft, mounting trunnions, bevel pinion, bearing housing, driving pump gear	M/s. Mishra Dhatu Nigam (MIDHANI) Kanchanbagh, Hyderabad-58
32.	MDN 132A	Forged Bars	Bush front mounting, bevel gear driver	M/s. Mishra Dhatu Nigam Ltd. (MIDHANI), Kanchanbagh, Hyderabad-58
33.	AE 712 BD	Forged Bars and Hot Rolled Bars	Gears	M/s. Mishra Dhatu Nigam Ltd. (MIDHANI), Kanchanbagh, Hyderabad-58
34.	AE 69	Forged Bars and Hot Rolled Bars	Pin (R/H diffuser) and plunger (starting system), casing starting system, valve hydraulic flap control (jet) and cam shaft etc.	M/s. Mishra Dhatu Nigam Ltd. (MIDHANI), Kanchanbagh, Hyderabad-58
Spring Steels				
35.	50KhFA	CD Wires	Aircraft springs	M/s. Firth (India) Steel Co. Ltd, Thane, Mumbai 400 604
36.	65S2VA-SH	CD Wires	Aircraft springs	M/s. Firth (India) Steel Co. Ltd, 40 MIDC, Hingana Road, Nagpur

7.12 Summary and Conclusions

Alloying elements added in small amounts, singly or in combination, to steel improve its fabricability, hardenability and mechanical properties. Most of the low alloy steels used for aerospace applications are based on the alloying addition combinations of Cr–Mo–Si and Ni–Cr–Mo–Si with varying carbon contents. Ultrahigh-strength steels are the most preferred for aerospace applications owing to their *high load density* capabilities, e.g. in landing gear. A combination of vacuum induction melting and vacuum arc remelting techniques is employed to produce high-quality steels. Low alloy steels are amenable to mechanical working, welding and heat treatment in order to make components with the desired dimensions and properties. A number of aerospace low alloy steel grades are presently developed and manufactured in India.

Acknowledgments The authors would like to thank Dr. R.J.H. Wanhill for his excellent review of this book chapter and also for his numerous inputs which have become integral parts of the text of this chapter. They are thankful to Dr. Amol Anant Gokhale, Distinguished Scientist and Director, Defence Metallurgical Research Laboratory Hyderabad, India, for his support and encouragement.

References

1. Ashby MF, Shercliff H, Cebon D (2007) *Materials: engineering, science, processing and design*. Elsevier (Butterworth-Heinemann), Oxford, UK
2. ASM Handbook (1993) Vol 1, 10th edn. ASM International, Metals Park, Ohio, USA, p 330
3. ASM Handbook (1993) Vol 1, 10th edn. ASM International, Metals Park, Ohio, USA, pp 362–406
4. ASM Handbook (1993) Vol 1, 10th edn. ASM International, Metals Park, Ohio, USA, p 1119
5. Gupta Balram et al (1996) *Aerospace materials, vol II*. S. Chand & Co., Ltd., New Delhi, India, pp 479–480
6. Krishnadas Nair CG (1993) *Handbook of aircraft materials*. Interline Publishing, Bangalore, India, p 59
7. ASM Handbook (1993) Vol 1, 10th edn. ASM International, Metals Park, Ohio, USA, p 1129
8. Brown Jr, WF (1989) *Aerospace structural metals handbook*. Code 1224, Metals and Ceramics Information Center, Battelle Columbus Laboratories, Columbus, Ohio, USA, pp 1–30
9. Higgins RA (1993) *Engineering metallurgy*. Part 1, Applied physical metallurgy, 6th edn. Edward Arnold, London, UK, p 287
10. Barnard SJ et al (1982) *Advances in physical metallurgy and application of steels*. The Metals Society, London, UK, pp 33–37
11. Singh V (2002) *Physical metallurgy*. Standard Publishers Distributors, New Delhi, India, p 614
12. Raghavan V (1998) *Physical metallurgy principles and practice*. Prentice-Hall of India Pvt. Ltd., New Delhi, India, p 99
13. Reisdorf BG (1963) *Trans TMS-AIME* 227:1334–1341
14. Gordine J, Codd I (1969) The influence of Si up to 1.5 wt% on the tempering of a spring steel. *J Iron Steel Inst* 207:461–467

15. Horn RM, Ritchie RO (1978) Mechanisms of tempered martensite embrittlement in low alloy steels. *Metall Trans A* 9A:1040–1053
16. Campbell FC (2006) Manufacturing technology for aerospace structural materials. Elsevier, London, UK, p 189
17. Low, JR Jr (1964) In: *Fracture of engineering materials*, ASM, Metals Park, Ohio, USA, pp 127–142
18. McMahon CJ Jr (1968) Temper brittleness—an interpretation review. In: *Temper embrittlement in steel*, ASTM STP 407, American Society for Testing and Materials, Philadelphia, Pennsylvania, USA, pp 127–167
19. Schulz BJ, McMahon CJ Jr (1972) Alloy effects in temper embrittlement. In: *Temper embrittlement of alloy steels*, ASTM STP 499, American Society for Testing and Materials, Philadelphia, Pennsylvania, USA, pp 104–135
20. *ASM Handbook* (1993) Vol 4, 10th edn. ASM International, Metals Park, Ohio, USA, pp 607–1029
21. *ASM Handbook* (1993) Vol 1, 10th edn, ASM International, Metals Park, Ohio, USA, p 1118
22. Wanhill RJH (1978) Microstructural influences on fatigue and fracture resistance in high strength structural materials. *Eng Fract Mech* 10:337–357
23. *ASM Handbook* (1993) Vol 1, 10th edn. ASM International, Metals Park, Ohio, USA, pp 1118–1145
24. Wanhill RJH, Byrnes RT, Smith CL (2001) Stress corrosion cracking (SCC) in aerospace vehicles. In: Raja VS, Shoji T (eds) *Stress corrosion cracking. theory and practice*. Woodhead Publishing Limited, Cambridge, UK, pp 608–650
25. Gupta Balram et al (1996) *Aerospace materials*, vol II. S. Chand & Co., Ltd., New Delhi, India, pp 482–566

Chapter 8

Aero Steels: Part 2—High Alloy Steels

M. Srinivas and A. Venugopal Reddy

Abstract Highly alloyed steels (total alloying element content more than 8 wt%) are generally classified as secondary hardening steels, maraging steels and precipitation hardening (stainless) steels. The effects of alloying elements on microstructure and mechanical properties are briefly described in this chapter. The manufacturing procedures and optimum processing parameters are discussed, and the heat treatment schedules and achievable properties are tabulated. Details on machining and weldability of these steels are also provided.

Keywords High alloy steels • Chemical compositions • Processing • Heat treatment • Mechanical properties

8.1 Introduction

High alloyed steels are defined as those having alloying element content more than 8 wt%. These steels are broadly categorized into three groups, namely Co + Mo secondary hardening steels, maraging steels, and precipitation hardening stainless steels. Some of these highly alloyed steels belong to the ultrahigh strength category where yield strengths are greater than 1380 MPa. Unlike low alloy steels, these ultrahigh strength high alloy steels do not have poor ductility, toughness and stress corrosion resistance.

M. Srinivas
DMRL, Hyderabad, India
e-mail: sameeramukthi@gmail.com

A.V. Reddy (✉)
ARCI, Hyderabad, India
e-mail: aramadaka@hotmail.com; aramadka@gmail.com

8.2 Secondary Hardening Steels

Secondary hardening steels belong to the quenched and tempered class of steels containing sufficient amount of carbide-forming elements (Cr, W, Mo, V). Tempering in the temperature range 500–600 °C forms fine dispersions of alloy carbides (Cr_7C_3 , W_2C , Mo_2C , VC_x) that replace the coarse cementite particles and are more stable. In the classical description of tempering, secondary hardening corresponds to the fourth stage of tempering. The replacement of coarse carbides by fine dispersions of alloy carbides occurs due to the enhanced diffusivity of carbide-forming substitutional solute atoms like Cr, Mo and V at higher tempering temperatures, and results in a hardening effect in contrast to the normal softening effect. Secondary hardening steels have a number of commercial applications such as tool steels and high strength structural applications due to their combination of ultrahigh strength and toughness.

The main alloying elements in this class of highly alloyed steels are carbon (0.2–0.5 wt%), molybdenum (0.2–2.0 wt%), chromium (0.2–1.0 wt%), cobalt (3.5–5 wt%) and nickel (7.0–10.0 wt%). International standards have classified them mainly based on their composition, which is considered to be both rational and convenient for the steel producers and users.

8.2.1 *Effects of Alloying Elements in Secondary Hardening Steels*

Increasing carbon content increases the peak hardness and strength in the secondary hardening regime, and this effect is directly related to increased volume fractions of alloy carbides [1]. An increase in strength with increasing carbon content results in a decrease in toughness. However, this effect is less marked for the high carbon grades. Increasing carbon content also decreases the ratio of notch tensile strength to yield strength, irrespective of strength level. Because of this, an optimum carbon content has to be chosen for a specific application.

Nickel increases the strength primarily by increasing the hardenability of the steel such that a lath martensite microstructure is formed. Nickel also lowers the ductile–brittle transition temperature and keeps the material ductile at room temperature even at high strength levels. The improvement of impact toughness with nickel addition is associated with enhancement of cross-slip at high strain rates and/or lower temperatures. Nickel also lowers the martensite start temperature, M_s , resulting in an increase in retained austenite. However, this increase in retained austenite content can be balanced by cobalt additions.

Cobalt addition increases the M_s temperature, refines the martensite structure and leads to retention of dislocation substructures at higher tempering temperatures, resulting in finer precipitation of dislocation-nucleated alloy carbides. Cobalt has several effects on the mechanical properties, depending on the baseline steel:

1. The effect of up to 8 wt% cobalt on tempering behaviour of carbon-free, 10 wt % Ni steel is to increase the hardness via a solid solution effect that is maintained throughout the tempering temperature range.
2. The influence of cobalt content on strength and impact toughness of a 5Ni–Cr–Mo–0.25C steel is shown in Fig. 8.1. It is seen that addition of 6 wt% Co increases the yield strength in the secondary hardening temperature range 425–540 °C. On the other hand, addition of 8 wt% Co increases the strength at all tempering temperatures, although the notch toughness decreases with increasing cobalt content particularly in the secondary hardening regime.
3. Cobalt additions to a 0.12C–10Ni steel increase the hardness and strength values at all tempering temperatures, see Fig. 8.2.

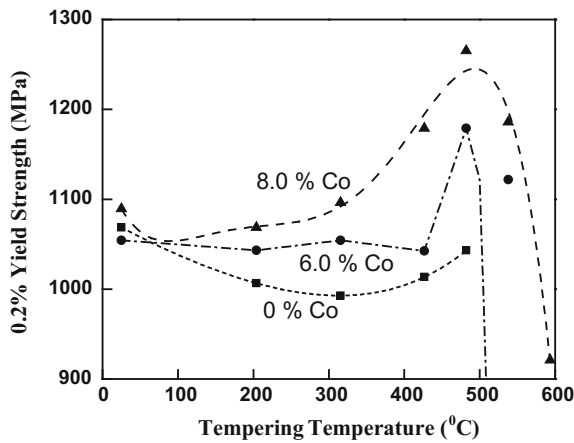


Fig. 8.1 Effect of cobalt content on tempering response of 5Ni–Cr–Mo steels [11]. Base composition: 0.25C, 0.75 Mn, 5Ni, 1.5 Cr, 0.5 Mo; austenitization: 815 °C-1 h; WQ; tempering time: 5 h

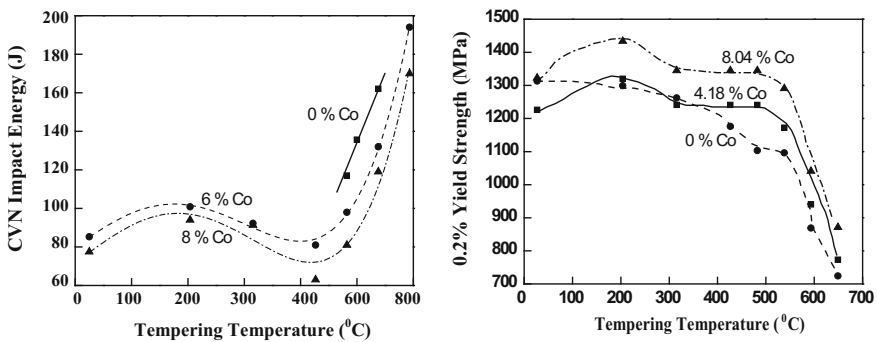


Fig. 8.2 Effect of cobalt content on the tempering response of 0.12C–10Ni–2Cr–1Mo steels [1, 11]. Austenitization: 815 °C-1 h; WQ; tempering time: 5 h

It is evident from Figs. 8.1 and 8.2 that the increased yield strength at the secondary hardening peak is higher in 10Ni–Co–Cr–Mo steels than in 5Ni–Cr–Mo steels. In addition, in 10Ni–Co–Cr–Mo steels the toughness is lower at lower tempering temperatures than those resulting in the peak yield strength. In other words, the toughness increases with increase in yield strength in the temperature range where the yield strength peak appears.

Manganese behaves in a similar manner to nickel. However, the manganese content is limited to 0.35 wt%, since further amounts do not contribute to the toughness.

Silicon additions increase the strength and decrease the toughness of the steels. In addition, silicon shifts the temper embrittlement regime from 260 °C to 425–480 °C. Hence special melting practices must be employed to keep silicon content as low as possible.

Effect of carbide-forming elements: Increasing the amount of carbide formers such as molybdenum and chromium also leads to higher peak hardness and strength [1]. The increase in hardness and strength can be attributed to the increase in alloy carbide content. Chromium in the presence of molybdenum goes into solution in the Mo_2C and results in a hardness increase. These carbide-forming elements are kept at minimum levels in medium carbon steels when high toughness is required. However, in low-carbon-containing steels these elements do not have a detrimental effect on toughness and hence they help in increased strength, weldability, temper resistance and elevated temperature properties [2].

Vanadium addition in low concentrations acts as a grain refiner and reduces the reaction rates of the pearlite and bainite transformations in HP 9-4-X steels.

Fracture in ultrahigh strength high-toughness steels occurs by microvoid nucleation, growth and coalescence. Therefore the well-known decrease in toughness with increased strength depends on factors that influence the microvoid coalescence. Microvoid nucleation occurs at inclusions and alloy carbides, with decohesion first occurring at large inclusions. The inclusion content can be minimized by adopting advanced melting practices. By increasing the size and spacing between inclusions for the same volume fraction, it is possible to achieve increased toughness. When the inclusion content is maintained constant, refining the size of the alloy carbides leads to a significant improvement in toughness. This is because more energy must be expended to nucleate microvoids at smaller carbides, such that they can then link up with the larger microvoids already nucleated at inclusions [1].

8.2.2 Processing and Thermal Treatments

Secondary hardening steels are produced by electric arc melting (EAM)/vacuum induction melting (VIM) followed by consumable-electrode vacuum arc remelting (VAR), depending on the stringency requirements. The optimum combinations of properties are obtained using vacuum arc remelting plus carbon deoxidation. The

hot working processes are similar to those used for AISI 4340 or similar medium carbon low alloy steels.

The maximum soaking temperature has been set at 1120 °C for carbon deoxidized material, to prevent grain coarsening in the absence of significant amounts of aluminium. Forging of VAR + carbon deoxidized steel ingots of HP 9-4-45 and HP 9-4-25 has to be carried out to 75 % of maximum reduction and a maximum finish temperature of 1040–1065 °C.

8.2.3 HP 9-4-X Steels

The chemical compositions of HP 9-4-X steels are given in Table 8.1. Heat treatments and mechanical properties given in Tables 8.2, 8.3, and 8.4 are discussed after these tables.

The HP 9-4-X steels, where X represents carbon contents over the approximate range 0.2–0.5C, can be through-thickness hardened up to diameters of 10–30 cm, respectively, using water quenching. The strongest grade HP 9-4-45 can give very high strength, but a refrigeration step should be included to transform retained austenite. Higher toughness is obtained from a bainitic treatment, which results in slightly lower yield strength. For the HP 9-4-30, HP 9-4-25 and HP 9-4-20 grades only a martensitic treatment is recommended.

HP 9-4-30: This steel is widely used because of an optimum combination of strength and fracture toughness: HP 9-4-25 has lower strength and HP 9-4-45 has poor fracture toughness. HP 9-4-30 steel is usually melted in an electric arc furnace followed by VAR. Forging temperatures should not exceed 1120 °C. This steel has good hardenability and a fully martensitic structure can be obtained in section thicknesses up to 150 mm.

The heat treatment requirements are as follows:

1. **Normalizing.** Austenitize between 870 and 925 °C and hold for 1 h per 25 mm of thickness, and air cool.
2. **Annealing.** Heat to 620 °C, soak for 24 h and furnace cool.

Table 8.1 Chemical compositions (wt%) of HP 9-4-X steels

Steels	C	Mn	Si	P	S	Ni	Co	Mo	Cr	V	Al
HP 9-4-45	0.42–0.48	0.10–0.25	0.10 max	0.01 max	0.01 max	7.0–8.5	3.5–4.5	0.2–0.35	0.2–0.35	0.06–0.12	–
HP 9-4-30	0.29–0.34	0.10–0.35	0.10 max	0.01 max	0.01 max	7.0–8.0	4.25–4.75	0.9–1.1	0.9–1.1	0.06–0.12	–
HP 9-4-25	0.24–0.30	0.10–0.35	0.10 max	0.01 max	0.01 max	7.5–9.0	3.5–4.5	0.35–0.55	0.35–0.55	0.06–0.12	–
HP 9-4-20	0.16–0.23	0.10–0.35	0.20 max	0.01 max	0.01 max	8.5–9.5	4.25–4.75	0.9–1.1	0.65–0.85	0.06–0.12	–

Table 8.2 Standard thermal treatments for HP 9-4-X steels

Steels	Normalizing temperature (°C)	Austenitizing temperature (°C)	Quenching media	Cryogenic treatment	Tempering temperature (°C), and microstructure
HP 9-4-45	870–900	790–815	Oil	Refrigerate at -73°C	205 for 2 + 2 h <i>tempered martensite</i>
	870–900	790–815	Molten salt at 240–245 °C	–	240–245 for 4–8 h <i>AC bainite</i>
HP 9-4-30	900–930	830–855	Oil	Refrigerate at -73°C	540 for 2 + 2 h <i>tempered martensite</i>
	900–930	830–855	Molten salt at 445–455 °C for 6–8 h	–	445–455 for 6–8 h <i>bainite</i>
HP 9-4-25	900–930	830–855	Oil or water	–	540 for 2 h <i>tempered martensite</i>
HP 9-4-20	885–915	800–830	Water	–	540–565 for 4–8 h <i>tempered martensite</i>

AC Air cooled

Table 8.3 Mechanical properties of HP 9-4-X steels

Materials and conditions	UTS (MPa)	0.2 % YS (MPa)	Elongation on 50 mm (%)	RA (%)	CVN impact (J)	K_{Ic} (MPa $\sqrt{\text{m}}$)	Hardness (R _c)
HP 9-4-45 (martensitic)	1930–2070	1680–1790	6–10	20–35	14–16	55–77	51
HP 9-4-45 (bainitic)	1790–1930	1520–1620	12–14	40–50	27–41	71–104	51
HP 9-4-30 (martensitic)	1520–1660	1310–1380	12–16	50–60	27–34	110–132	44
HP 9-4-30 (bainitic)	1520–1660	1310–1389	12–16	50–60	34–41	132–148	44
HP 9-4-25 (martensitic)	1345–1450	1225–1325	15–18	55–65	43–54	>154	42
HP 9-4-20 (martensitic)	1310–1480	1240–1345	14–20	61–71	68–98	170–192	41

- Hardening.** Austenitize at 830–860 °C and soak for 1 h per 25 mm of thickness (1 h minimum); quench in water or oil. Cryogenic treatment of at least 1 h at -87 to -60°C is applied to convert retained austenite into martensite.
- Tempering.** Heat to 200–600 °C, depending on the desired strength and toughness. Double tempering is preferred: the most widely used tempering

Table 8.4 Room temperature mechanical properties of HP 9-4-30 steel

Heat treatment	UTS (MPa)	0.2 % YS (MPa)	Elongation in 4D (%)	RA (%)	CVN impact (J)	K_{Ic} (MPa \sqrt{m})	Hardness (R _C)
845 °C OQ + -73 ° C + double temper at 205 °C	1650–1790	1380–1450	8–12	25–35	20–27	66–99	49–53
845 °C OQ + -73 ° C + double temper at 550 °C	1520–1650	1310–1380	12–16	35–50	24–34	99–115	44–48

treatment is heating to between 540 and 580 °C and soaking for 2 h, and air cool, followed by 2 h more at the same elevated temperature.

5. Stress relief after welding restrained systems. Heat to 540 °C and hold for 24 h; air cool to ambient temperature.

HP 9-4-30 can be formed by bending and rolling, and is weldable in the heat-treated condition. Tungsten inert gas welding is recommended, and after welding the components have to be stress relieved at 540 °C for 24 h. This steel is available as billet, bar, rod, plate, sheet and strip. It is extensively used in pressure vessels, rotor shafts, drop hammer rods, aircraft structural components and high strength shock absorbing automotive parts.

8.2.4 AF1410 Steel

This steel is resistant to stress corrosion cracking and can be used in advanced submarine hulls and aircraft components. The chemical composition and mechanical properties of AF1410 steel are given in Tables 8.5 and 8.6. Processing and heat treatments are discussed in the following paragraphs.

The preferred melting route for AF1410 is VIM followed by VAR. However, melting may be carried out employing VIM followed by VAR/electroslag remelting (ESR). Melting practice requires that trace and impurity elements be kept very low to achieve high fracture toughness. AF1410 is forgeable to 1120 °C, and a minimum of 40 % reduction should be given below 900 °C to attain optimum properties. This steel is air hardenable up to 75-mm-thick sections and is easily weldable, with continuous-wave gas tungsten arc welding preferred.

Table 8.5 Chemical composition (wt%) of AF1410 steel

Steel	C	Mn	Si	P	S	Ni	Co	Mo	Cr	V	Al	Fe
AF1410	0.13–0.17	0.10 max	0.10 max	0.01 max	0.01 max	9.5–10.5	13.5–14.5	0.9–1.1	1.8–2.2	–	–	Balance

Table 8.6 Effect of quench media on mechanical properties of AF1410 steel

Quench medium	UTS (MPa)	0.2 % YS (MPa)	Elongation in 4D (%)	RA (%)	CVN impact (J)	K_{Ic} (MPa \sqrt{m})
Air	1680	1475	16	69	69	174
Oil	1750	1545	16	69	65	154
Water	1710	1570	16	70	65	160

The microstructure after quenching from the austenitizing temperature consists of highly dislocated Fe–Ni lath martensite. The choice of ageing and tempering schedules is very important, as may be inferred from the following reactions:

- Ageing/tempering at 425 °C gives rise to Fe₃C, while tempering at 455 °C results in precipitation of (Fe–Cr–Mo)-containing M₂C carbides.
- Ageing/tempering at 480 °C converts the (Fe–Cr–Mo)-containing M₂C carbides into (Mo–Cr)-containing M₂C carbides.
- Increasing the temperature to 510 °C results in M₂C beginning to coarsen; and at 540 °C M₆C starts replacing M₂C.

AF1410 steel attains maximum strength when aged for 5 h at 480 °C, the peak secondary hardening temperature. The toughness is very dependent on ageing temperature: minimum impact toughness results from ageing at 425 °C; over the range 425–540 °C, the impact energy attains a maximum value when aged at 508 °C. Ageing above 540 °C reduces both strength and toughness.

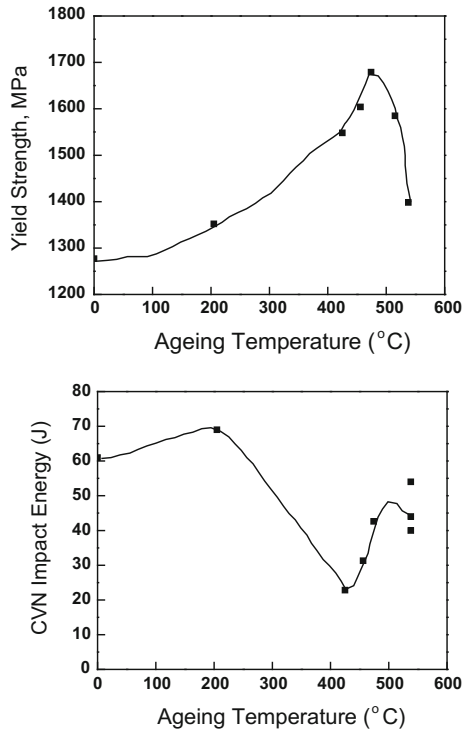
The heat treatment requirements are as follows:

1. Normalizing and overageing. Austenitize between 880 and 900 °C and hold for 1 h per 25 mm of thickness, and air cool and overage at 675 °C for 5 h minimum. This treatment is best suited to achieve good machinability.
2. Stress relief. After normalizing and overageing a stress relief treatment at 675 °C may be applied.
3. Hardening. Double austenitize at 870–900 °C and soak for 1 h per 25 mm of thickness (1 h minimum); quench either in water, oil or air; a cryogenic treatment for 1 h at –87 to –60 °C is optional.
4. Tempering/ageing. The most widely used tempering treatment is heating to 480–510 °C for 5–8 h followed by air cooling. The effects of ageing temperature on the strength and impact energy are shown in Fig. 8.3.

8.2.5 AerMet Steels

AerMet steels are another group of Ni–Co–Cr–Mo secondary hardening steels used for many critical aerospace applications. Based on the attainable strength levels, AerMet steels are designated as AerMet 100, AerMet 310 and AerMet 340.

Fig. 8.3 Variations of strength and impact toughness with ageing temperature for AF1410 steel [12]



- AerMet 100 steel provides high hardness and strength coupled with extraordinary fracture toughness and stress corrosion resistance. This steel is used up to about 425 °C for landing gear components, jet engine shafts, drive shafts, structural tubing, fasteners, actuators, armour and ordnance.
- AerMet 310 alloy possesses higher strength than AerMet 100 and may be used in similar applications for components requiring ultrahigh strength, high fracture toughness and exceptional stress corrosion cracking resistance.
- AerMet 340 possesses the highest strength and may be considered for applications like structural tubing, drive shafts, springs, connecting rods and crank shafts.

The chemical compositions and mechanical properties of AerMet steels are given in Tables 8.7 and 8.8. Processing and heat treatments are discussed in the following paragraphs.

Table 8.7 Chemical compositions (wt%) of AerMet steels

Steels	C	Ni	Co	Mo	Cr	Ti	Al	Fe
AerMet 100	0.23	11.1	13.4	1.2	3.1	0.05 max	–	Balance
AerMet 310	0.25	11.0	15.0	1.4	2.4	0.05 max	–	Balance
AerMet 340	0.33	12.0	15.60	1.85	2.25	–	–	Balance

Table 8.8 Mechanical properties of AerMet steels after ageing at 485 °C

Steels	UTS (MPa)	0.2 %YS (MPa)	Elongation in 4D (%)	RA (%)	CVN impact (J)	K_{Ic} (MPa \sqrt{m})	Hardness (R_C)
AerMet 100	1980	1697	16	67	45.6	132	53.0–54.0
AerMet 310	2170	1900	14.5	63	27.1	71.5	55
AerMet 340	2379	2068	11	53	15	37	56.5

The AerMet steels are manufactured using VIM + VAR melting. Forging for primary breakdown should be done at a maximum starting temperature of 1230 °C. Finish forging should be done from 980 °C, with a finishing temperature less than 900 °C. Forged parts should be air cooled to ambient temperature followed by annealing. After annealing, the forgings should be normalized to restore the properties of the dead zones.

Machining of AerMet steels is more difficult than for normal medium carbon low alloy steels (Rockwell hardness R_C38), and requires carbide-tipped tools. After rough machining, a stress relief treatment may be given at 425 °C for 1–3 h, as desired. AerMet 100 is weldable and requires no pre-heating or post-heating. All three steels are available in the form of billet, plate, round bars, sheets, tubes, strip and wire, including welding wire.

The heat treatment requirements are as follows:

1. Normalizing.

- AerMet 100: Austenitize between 900 and 925 °C and hold for 1 h per 25 mm of thickness, and air cool. Optimum softening for machining is obtained by normalizing at 900 °C followed by overage annealing at 675 °C for 16 h.
 - AerMet 310: Austenitize at 970 °C and hold for 1 h per 25 mm of thickness, and air cool. Optimum softening for machining is obtained by normalizing at 970 °C followed by overage annealing at 675 °C for 16 h.
 - AerMet340: Austenitize at 968 °C and hold for 1 h per 25 mm of thickness, and air cool. Optimum softening for machining is obtained by normalizing at 968 °C followed by overage annealing at 675 °C for 16 h.
2. Stress relief. After normalizing and overageing a stress relief treatment at 675 °C may be applied.
 3. Annealing. Heat to 677 °C, soak for 16 h, and air cool. The maximum annealed hardness is R_C 40.
 4. Hardening. Austenitize at 870–900 °C for AerMet 100; 900–925 °C for AerMet 310; and 955–988 °C for AerMet340. Soak for 1 h per 25 mm of thickness (1 h minimum). The alloys should be cooled from the austenitizing temperature to 65 °C in 1–2 h to obtain optimum properties. Water quenching is not recommended. However, sections larger than 50 mm diameter or 25 mm thickness

must be quenched with oil in order to reach 65 °C in 1–2 h. Individual sections up to 50 mm diameter or 25-mm-thick plates should be air cooled to 65 °C in 1–2 h. Cryogenic treatment is then to be given for 1 h at –75 °C, followed by warming to room temperature.

5. Tempering/ageing. The standard ageing treatment is to hold at a temperature between 475 and 488 °C for 5 h. AerMet steels should never be aged below 468 °C, since this results in very low toughness.
6. Straightening. Though AerMet steels show minimum distortion during heat treatment, some parts may require mechanical straightening. Prior to straightening a low temperature stress relief treatment at 175/205 °C for 5 h has to be given after cryogenic treatment.
7. Decarburization. Similar to other carbon-containing high strength steels, AerMet alloys undergo decarburization during hardening. Heat treatment should be done in a neutral atmosphere furnace, salt bath or under vacuum. The depth of decarburization should be determined by microhardness measurements of a small test sample and should never exceed 10 % of the thickness/diameter.

8.2.6 Ferrium Steels

Ferrium C61 and C64 steels are carburizing steels that provide higher core strength and corrosion resistance, high fracture toughness, high temperature resistance and high surface hardenability as compared to medium carbon low alloy steels intended for similar applications, e.g. AISI 9310 and AISI 8620. Ferrium C61 develops a surface hardness of R_C 60–62, and Ferrium C64 develops a surface hardness of R_C 62–64. These Ferrium alloys attain these superior properties due to nano-size M_2C carbide dispersions in a Ni–Co lath martensitic matrix.

The chemical compositions and mechanical properties of Ferrium C61 and C64 are given in Tables 8.9 and 8.10. These alloys are generally double vacuum melted (VIM + VIM/VAR). They can be used as gears, shafts, actuators and other power transmission components. They have the advantages of compactness, weight savings, high temperature resistance and durability compared to other regularly used steels for similar applications.

Table 8.9 Chemical compositions (wt%) of Ferrium steels

Steels	C	Ni	Co	Mo	Cr	W	Fe
Ferrium C61	0.15	9.5	18.00	1.10	3.5	–	Balance
Ferrium C64	0.11	7.50	16.30	1.75	3.50	0.20	Balance

Table 8.10 Mechanical properties of Ferritic steels

Steels	UTS (MPa)	0.2 % YS (MPa)	Elongation in 4D (%)	RA (%)	Achievable surface hardness (R_C)	Core hardness (R_C)	K_{Ic} (MPa \sqrt{m})	Tempering temperature ($^{\circ}C$)
Ferritic C61	1656	1552	16	70	60–62	48–50	143	482
Ferritic C64	1580	1373	18	75	62–64	48–50	93.5	496

8.3 Maraging Steels

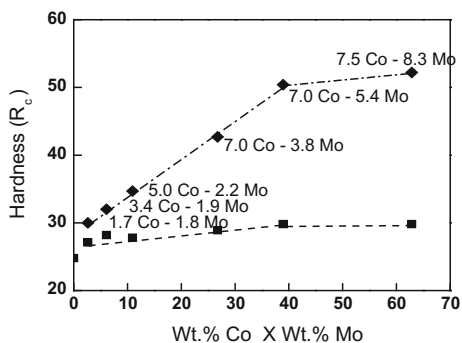
The maraging steels are a group of interstitial-free Ni–Co–Mo–Ti high alloy steels. Maraging steels belong to a class of ultrahigh strength steels where the strengthening mechanism is different from the classical mechanism associated with carbon martensite, bainite or precipitation of carbides during tempering. Maraging steels have very low carbon content, replacing this with elements like Mo and Ti that produce age hardening in Fe–Ni martensite. These steels attain ultrahigh strength from precipitation of intermetallic compounds during ageing of martensite, hence the name *maraging*.

Maraging steels have a wide range of aerospace applications such as missile casings, aircraft forgings, cannon recoil springs, Belleville springs, bearings, transmission shafts, fan shafts in commercial jet engines, couplings, hydraulic hoses and bolts.

The development of maraging steels was started in the late 1950s by the International Nickel Company [3]. Initial work started with 20 and 25 wt% nickel steel [4]. However, the 20 and 25 % nickel-containing steels were not pursued further as they were very brittle at ultrahigh strength levels [5].

The most common maraging steels are based on the 18Ni–Co–Mo type: the effects of cobalt and molybdenum on hardening of Fe–Ni martensite were studied in detail in the 1960s. Figure 8.4 shows the synergistic effect of cobalt and molybdenum on the age hardenability of Fe-18 % Ni alloys [6].

Fig. 8.4 Effects of Co \times Mo contents on maximum hardness of Fe-18.5–20.1 wt % Ni alloys [6]: *filled diamonds* maraged 3–10 h at 425–480 $^{\circ}C$; *filled squares* annealed 1 h at 870 $^{\circ}C$, air cooled



The Fe-18 % Ni binary was chosen as base since higher nickel contents result in excessive retained austenite. Generally, the heat treatment of maraging steels consists of solutionizing at 815–820 °C, followed by air cooling to room temperature, which results in complete transformation to martensite. In these steels complete hardenability is achieved irrespective of cooling rate, since the carbon content is low and the nickel content is high. In the annealed condition the hardness is around R_C 30 and the steels can be readily machined or fabricated. Ultrahigh strength is achieved by maraging, namely ageing at 485 °C for 3–6 h. Maraging steels can be welded without preheat in both the annealed and aged conditions.

8.3.1 Effects of Alloying Elements in Maraging Steels

The main alloying elements in maraging steels are Ni, Co, Mo and Ti (in addition to iron):

Nickel: Ni ensures a lath martensite structure, lowers the resistance of the crystal lattice to dislocation movements, and reduces the energy of interaction of dislocations with interstitial atoms [7]. Nickel promotes stress relaxation and reduces susceptibility to brittle fracture.

Cobalt: Co lowers the lattice resistance to dislocation movements and reduces the energy of interaction between dislocations and interstitial atoms. In addition, cobalt raises the M_s temperature and allows increased amounts of alloying elements that induce hardening during ageing without leading to retained austenite. Further, cobalt increases the amount of age hardening by reducing the solubility of the hardening elements Ti and Mo in α -iron, thereby increasing the volume fraction of the precipitates. Figure 8.5 shows (somewhat indirectly) the effect of cobalt and titanium on the UTS for all the specific grades (grades 200 through 500) of maraging steels.

Molybdenum: Mo lowers the diffusion coefficients of a number of elements in the grain boundaries and thereby reduces the preferential precipitation of second phase particles during ageing. This helps in increasing the ductility and plasticity in the aged condition.

Titanium: Ti acts as a hardening element as well as refining element by binding residual carbon.

Aluminium: At concentrations above 0.2–0.3 wt% aluminium lowers the ductility. The addition of aluminium also leads to limited hardening of the martensite.

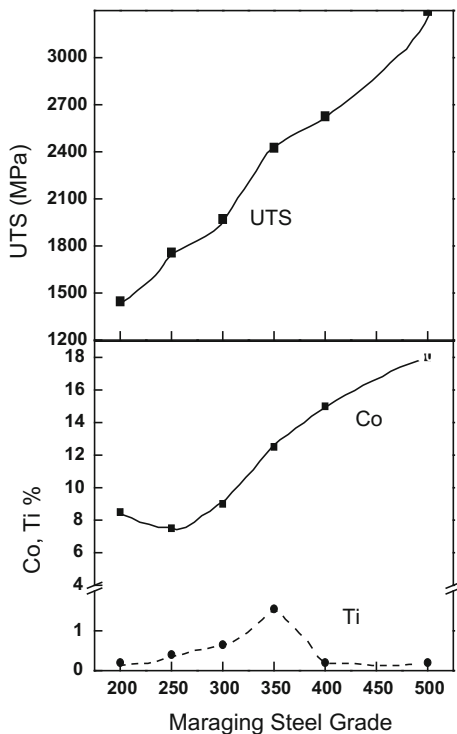
Manganese: Mn leads to the formation of martensite at low nickel contents, and reduces the ductility after ageing.

Chromium: Cr additions increase the corrosion resistance and increase the strain hardening coefficient of the martensite.

Silicon: Silicon above 0.1 wt% reduces the ductility.

Microstructure: The microstructure of maraging steels consists of soft Fe–Ni lath martensite. The martensite hardens during ageing owing to the following two mechanisms:

Fig. 8.5 UTS and cobalt and titanium contents plotted against the maraging steel grades [13]



1. Fine uniform precipitation of intermetallic precipitates or austenite.
2. An ordering reaction in the cobalt-containing solid solution.

The generally observed intermetallic precipitates are Ni_3Mo and Ni_3Ti .

The chemical compositions and mechanical properties for several maraging steels are given in Tables 8.11 and 8.12. Processing and heat treatments are discussed in Sect. 8.3.2.

Table 8.11 Chemical compositions (wt%) of maraging steels

Steels	C	Ni	Co	Mo	Ti	Al	Fe
18 Ni 200	<0.03	18	8.5	3.3	0.2	0.1	Balance
18 Ni 250	<0.03	18	8.5	5.0	0.4	0.1	Balance
18 Ni 300	<0.03	18	9.0	5.0	0.7	0.1	Balance
18 Ni 350	<0.03	18	12.5	4.2	1.6	0.1	Balance
18 Ni Cast	<0.03	17	10.0	4.6	0.3	0.1	Balance

Table 8.12 Mechanical properties and fracture toughness data for maraging steels

Steels	UTS (MPa)	0.2 %YS (MPa)	Elongation on 50 mm (%)	RA (%)	CVN impact (J)	K_{Ic} (MPa \sqrt{m})	Hardness (R _C)
18 Ni 200	1500	1400	10	60	35–68	155–240	44–48
18 Ni 250	1800	1700	8	55	24–45	99–165	48–50
18 Ni 300	2050	2000	7	40	16–26	88–143	51–55
18 Ni 350	2450	2400	6	25	–	35–50	–
18 Ni Cast	1750	1650	8	35	20	105	–

8.3.2 Processing and Heat Treatments of Maraging Steels

Maraging steels can be manufactured using either air or vacuum induction melting. For steels with higher titanium contents vacuum melting is desirable. VAR improves cleanliness and results in superior properties. Hence the general melting practice for aerospace quality is VIM followed by VAR.

Cast grade maraging steel can be melted and cast in air, since the steel has sufficient castability and fluidity [8]. For investment castings to have a good surface finish, vacuum melting is recommended [9, 10].

The wrought maraging steel grades are easily workable by means of forging, rolling, drawing and extrusion. Homogenizing of ingots at 1260 °C is recommended. Hot working may be carried out at temperatures between 1260 °C and 815 °C. To minimize scale formation the hot working may be started in the temperature range 1150–1049 °C. Finishing at low temperatures is desirable to obtain a fine grain size and optimum properties.

Precipitation of TiC films should be avoided. These films form during slow cooling after hot working in the temperature range 650–1095 °C. It is also important to note that long dwell times in this temperature range should be avoided. However, it is safe to heat the steel into this temperature range, since stable carbides will already have precipitated.

Maraging steels can be cold-worked in the solution-annealed condition. They have a very low work-hardening rate and hence can be subjected to heavy reductions.

The heat treatment requirements for wrought maraging steels are as follows:

1. Solutionizing. Solutionize at 820 °C for 1 h for each 25 mm of thickness, and air cool.
2. Ageing. Ageing is carried out for most grades at 480 °C for 3 h. In the case of 18Ni350, the ageing time is extended to 12 h.

For the 18Ni cast grade solutionizing is done at 1150 °C for 1 h for each 25 mm thickness. Primary ageing is at 595 °C for 1 h. This is followed by another solutionizing treatment at 820 °C for 1 h, and subsequent ageing at 480 °C for 3 h.

8.4 Precipitation Hardening (PH) Steels

Precipitation hardening (PH) stainless steels are a family of corrosion resistant alloys that achieve high strengths from the precipitation of alloy carbides and solid solution strengthening. These steels contain a minimum of 12 wt% chromium to obtain stainless properties. Many 12 % Cr steels have been developed to attain high strengths via the addition of carbide-forming elements such as tungsten, molybdenum and vanadium; several others derive their strength from precipitation of intermetallic compounds.

The family of PH stainless steels may be divided into three main types:

1. **Low-carbon martensitic.** Typical examples and chemical compositions of these steels are given in Table 8.13.
2. **Semi-austenitic.** These have a microstructure of single-phase austenite in the annealed condition, but transform to fully martensitic after ageing, or refrigeration, or deformation. Typical examples and chemical compositions of these steels are given in Table 8.14.

Table 8.13 Chemical compositions (wt%) of low carbon martensitic PH stainless steels

Steels	C	Cr	Ni	Cu	Mo	Ti	Al	Others	Fe
17-4 PH	0.07 max	15– 17.5	3–5	3–5	–	–	–	0.15–0.45 (Cb + Ta) 0.4 Mn	Balance
AM 363	0.05 max	11	4.0	–	–	1.0	–	–	Balance
PH 13-8Mo	0.05 max	12.25– 13.25	7.5– 8.5	–	2.0– 2.5	–	0.90– 1.35	–	Balance
Custom 450	0.05 max	14.0– 16.0	5.0– 7.0	1.25– 1.75	0.5– 1.0	–	–	8 × C min Nb	Balance

Table 8.14 Chemical compositions (wt%) of semi-austenitic PH stainless steels

Steels	C	Cr	Ni	Cu	Mo	Ti	Al	Others	Fe
15-7Mo PH	0.07	15.1	7.1	–	2.2	–	1.1	0.70 Mn	Balance
17-7 PH	0.07	17.0	7.1	–	–	–	1.1	0.70 Mn	Balance
AM 350 PH	0.08	16.5	4.3	–	2.8	–	–	0.1 N	Balance
AM 355 PH	0.13	15.5	4.3	–	2.8	–	–	0.1 N	Balance
PH 14–8Mo	0.04	14.4	8.2	–	2.2	–	1.1	–	Balance

Table 8.15 Chemical compositions (wt%) of fully austenitic PH stainless steels

Steels	C	Cr	Ni	Cu	Mo	Ti	Al	Others	Fe
17-10P PH	0.07	17.2	10.8	–	–	–	–	0.28 P, 0.75 Mn	Balance
(A286 Specification) AISI 600	0.04	15.25	26.0	–	1.25	2.15	0.15	0.25 V, 0.007 B	Balance

3. Fully austenitic. Fully austenitic grades are stable down to room temperature. The chemical compositions of fully austenitic steels are given in Table 8.15. Fully austenitic steels are the least widely used of the three classes of PH steels.

8.4.1 Mechanical Properties of Typical PH Stainless Steels

Mechanical properties for different heat treatment conditions of some of the steels listed in Tables 8.13, 8.14 and 8.15 are given in Table 8.16.

Table 8.16 Mechanical properties of different PH steels solution treated at 1038 ± 15 °C, followed by air cooling and ageing at different ageing temperatures

Steels	Conditions	UTS (MPa)	0.2 %YS (MPa)	Elongation in 4D (%)	Hardness
17-4 PH	H900	1448	1379	7	R _C 45
	H925	1379	1345	8	R _C 43
	H1025	1276	1172	8	R _C 38
	H1075	1207	1148	8	R _C 37
	H1150	1103	1034	11	R _C 35
17-7 PH	Austenite conditioning	896	276	35	R _B 85
	TH1050	1379	1276	9	R _C 43
	RH950	1620	1517	6	R _C 48
	Cold reduction to condition C	1517	1310	5	R _C 43
	CH900	1827	1793	2	R _C 49
15-7Mo PH	Austenite conditioning	896	372	35	R _B 88
	TH1050	1448	1379	7	R _C 44
	RH950	1655	1552	6	R _C 48
	Cold reduction to condition C	1517	1310	5	R _C 45
	CH900	1828	1793	2	R _C 50
AM 355 PH	H850	1489	1255	19	R _C 48
	H1000	1276	1179	15	R _C 40

(continued)

Table 8.16 (continued)

Steels	Conditions	UTS (MPa)	0.2 %YS (MPa)	Elongation in 4D (%)	Hardness
AM 350 PH	H850	1275 min	1000 min	8 min	R _C 38
	H1000	1140 min	1035 min	8 min	R _C 37
Custom 450	Annealed	979	814	13	R _C 28
	H900	1351	1296	14	R _C 42.5
	H950	1289	1269	16	R _C 41.5
	H1000	1193	1165	17	R _C 30
	H1050	1103	1048	20	R _C 37
	H1150	979	634	23	R _C 28
PH 13-8Mo	RH950	1620	1482	12	R _C 48
	H950	1551	1449	12	R _C 47
	H1000	1482	1413	13	R _C 45
	H1050	1310	1241	15	R _C 43
	H1100	1103	1034	18	R _C 35
	H1150	1100	724	20	R _C 33
	H1150 M	896	586	22	R _C 32
17-10P PH	Annealed	613	255	70	R _B 82
	H700	985	675	20	R _C 32

8.4.2 Processing and Heat Treatments of PH Stainless Steels

The heat treatment requirements for PH stainless steels involve precipitation strengthening, which is generally done in three steps: solution treatment, quenching and precipitation or ageing:

1. **Solutionizing.** This treatment is done at a temperature where the pre-existing precipitates dissolve and alloying elements go into supersaturated solid solution. Typical solution treatment temperatures are in the range of 980–1065 °C.
2. **Quenching or cooling.** This can be done in air or oil or water, but must be fast to retain a supersaturated solid solution.

The low-carbon martensitic steels transform to martensite at relatively low temperatures, e.g. 250 °C for 17-4 PH.

The semi-austenitic steels are supplied in the metastable austenite condition. They may also contain up to 20 % of delta ferrite in equilibrium with austenite at the solution temperature. The martensite finish temperature of these steels is well below room temperature, and hence a conditioning treatment at ~750 °C should be carried out to achieve an austenite to martensite transformation after a forming operation. A cryogenic treatment is required if the conditioning temperature used is above 930 °C.

Fully austenitic steels have very low martensite start temperatures and hence cannot be transformed to martensite.

3. Precipitation and age hardening

Martensitic PH steels, for example 17-4 PH steels, are aged in the temperature range between 480 and 620 °C to achieve the required strength. Precipitation of hardening in this class of steels is achieved by precipitation of intermetallic phases such as Ni₂Al, Ni₃Ti, Ni₃(TiAl), Ni₃Al, Ni₃Nb, Ni₃Cu and carbides.

For the semi-austenitic steels the ageing temperatures are within the range 500–600 °C. Hardening occurs by precipitation of intermetallic compounds and carbides, resulting in room temperature yield strengths up to 1400 MPa.

In the case of fully austenitic grades, improvements in strength can be obtained from ageing between 500 and 750 °C, resulting in precipitation of a very fine coherent intermetallic Ni₃Ti phase. The precipitation reaction is very sluggish in this class of steels. Fully austenitic steels possess good toughness and may be used at cryogenic temperatures.

8.4.3 *Weldability of PH Stainless Steels*

Martensitic PH steels: These can be welded by most of the conventional arc welding (GTAW) processes in the solution-treated condition: Tungsten inert gas (TIG) welding results in the best GTAW toughness, since it produces clean weld metal. However, electron beam (EB) and laser welding give still better toughnesses.

Pre-heating of the weld joints is generally not required, since the low-carbon martensite is soft. However, for welds over 25 mm thickness pre-heating around 100 °C is suggested to prevent the risk of cracking. An interpass maximum temperature of 200 °C is recommended because these steels transform to martensite at relatively low temperatures. If the weld joint is highly restrained a post-weld heat treatment has to be carried out to avoid cracking of the weld. Matching filler materials are available for all the martensitic grades.

Semi-austenitic PH steels: Common arc and resistance welding processes can be used with stainless steel grade 17-7PH. However, during fusion welding inert gas shielding should be used to prevent oxidation of aluminium during the process.

Austenitic PH steels: Fully austenitic alloys have to be welded in the solution-treated condition. These steels are solutionized at 980 °C. To develop strength in welded joints an ageing treatment has to be carried out for 15 h at 720 °C. Pre-heating of welds is not necessary for these steels.

8.5 Illustration of Martensitic PH Steels Diversity: Custom 455, 465 and 475

The Carpenter Technology Corporation has developed many specialty steels, including Custom 450 (see Tables 8.13 and 8.16) and Custom 455, 465 and 475. Typical aerospace uses are for landing gear components, slat components, torque tubes and pneumatic cylinders.

Custom 455 is relatively soft and formable in the annealed condition. This steel can be used at temperatures close to 595 °C and shows excellent oxidation resistance. It has generally high corrosion resistance comparable to that of 17 % Cr ferritic (non-hardenable) steels (Type AISI 430).

Custom 465 is a premium melted steel designed to have excellent fracture toughness and notch tensile strength in the aged condition H950. In the H1000 condition this steel has a superior combination of strength, toughness and stress corrosion cracking resistance compared with Custom 455 and PH 13-8Mo. Its corrosion resistance is high and comparable to that of the fully austenitic steels like AISI 304.

Custom 475 is also a premium melted steel, capable of high strength up to 2000 MPa, good toughness and ductility, and high corrosion resistance similar to that of Custom 455.

The nominal chemical compositions of Custom 455, 465 and 475 and their mechanical properties are given in Tables 8.17 and 8.18.

8.5.1 Processing and Heat Treatments of Custom 455, 465 and 475 Stainless Steels

Hot working: Custom 455 is forgeable in the temperature range 900–1260 °C. Optimum properties can be achieved by heating the material uniformly to 1035–1150 °C and soaking for 1 h. The forging finishing temperature should be between 815 and 925 °C to achieve optimum grain size and properties after heat treatment. The forgings are cooled to room temperature and annealed.

Custom 465 is forgeable in the temperature range 1010–1095 °C. The forgings are cooled to room temperature and solution treated prior to age hardening.

Cold Working: All three steels can be cold-worked easily. Cold working prior to ageing results in much higher strengths.

Machinability: All three steels are easily machinable, and the machining practices are similar to those used for other high strength alloys.

Availability: Custom 455 and 465 are available in the form of round bars, square bars, flat bars, billet, strip and wire. Custom 475 is available in the form of strip and wire.

Table 8.17 Nominal chemical compositions of Custom steels 455, 465 and 475

Steels	C	Cr	Ni	Cu	Mo	Ti	Nb	Nb + Ti	Mn	S	P	Si	Ta	Fe
Custom 455	0.05 max	11.0–12.5	7.5–9.5	1.5–2.5	0.5 max	0.8–1.4	0.5 max	0.1–0.5	0.5 max	0.03 max	0.04 max	0.5 max	0.5 max	Balance
Custom 465	0.02 max	11.0–12.5	10.75–11.25	1.5–2.5	0.75–1.25	1.5–1.8	0.5 max	0.1–0.5	0.25 max	0.01 max	0.015 max	0.25 max	0.5 max	Balance
Steel	C	Cr	Ni		Mo	Co	Al	Mn		S	P	Si		Fe
Custom 475	0.02 max	10.5–11.5	7.5–8.5	7.5–8.5	4.5–5.5	8.0–9.0	1.0–1.5	0.50 max	0.01 max	0.015 max	0.015 max	0.50 max	0.50 max	Balance

Table 8.18 Mechanical properties of Custom 455, 465 and 475 steels after ageing at different temperatures

Steels	Conditions	UTS (MPa)	0.2 % YS (MPa)	Elongation in 4D (%)	RA (%)	CVN impact (J)	Hardness (R _C)	K _{Ic} (MPa√m)
Custom 455	H900	1724	1689	10	45	12	49	~ 40
	H950	1620	1551	12	50	19	48.0	~ 55
	H1000	1448	1379	14	55	27	45.0	85
	H1050	1310	1207	15	55	48	40.0	~ 100
Custom 465	H950	1765	1669	13	62	30	49.5	104.5
	H975	1703	1620	13	61	36	48.0	120.0
	H1000	1593	1510	15	63	55	47.5	142.0
	H1050	1482	1386	17	66	70	45.5	152.9
Custom 475	H950	1765	1669	13	62	30	49.5	104.5
	H975	1703	1620	13	61	36	48.0	120.0
	H1000	1593	1510	15	63	55	47.5	142.0
	H1050	1482	1386	17	66	70	45.5	152.9

The heat treatment requirements for these steels are as follows:

1. Solution treated or annealed.

- Custom 455: Heat to 815–845 °C and cool rapidly. Water quenching is recommended for small sections.
- Custom 465: Heat to 980 ± 10 °C, hold for 1 h and cool rapidly. Sections above 300 mm should be subjected to rapid air cooling, while sections below 300 mm should be quenched in a suitable coolant. Cryogenic treatment at –70 °C for 8 h after solutionizing and prior to ageing results in an optimum ageing response.
- Custom 475: Heat to 925–935 °C, hold for 1 h and cool rapidly. Cryogenic treatment at –70 °C for 8 h after solutionizing and prior to ageing results in optimum ageing response. This cryogenic treatment should be given within 24 h of solution treatment.

2. Ageing:

- Custom 455, conditions H900, H950, H1000 and H1050: ageing between 480 and 565 °C for 4 h, followed by air cooling. The ageing temperature depends on the property requirements.
- Custom 465, conditions H900, H950, H1000, H1050 and H1100: ageing between 480 and 565 °C for 4 h, followed by water or oil quenching for optimum properties. The ageing temperature depends on the property requirements.
- Custom 475: conditions H975, H1000, H1025, H1050 and H1100: ageing between 525 and 595 °C for 4 h, followed by water or oil quenching for optimum properties. The ageing temperature depends on the property requirements.

8.5.2 Weldability of Custom 455, 465 and 475 Stainless Steels

Shielded fusion welding and resistance welding processes can be used for Custom 455, 465 and 475 stainless steels. Oxy-acetylene welding is not recommended since the carbon content increases in the welds.

Welding in the solution-annealed condition and subsequent ageing is recommended for optimum strength, ductility and corrosion resistance. If high residual stresses are likely, then welding in the overaged condition is advised. The component or part has then to be resolutionized and aged to achieve optimum properties.

8.6 Indian Scenario

In India Mishra Dhatu Nigam Ltd (MIDHANI), Hyderabad, manufactures some PH steels. Their chemical compositions and mechanical properties are given in Tables 8.19 and 8.20.

MIDHANI also manufactures considerable amounts of maraging steel 18 Ni 250, in all product forms; and this and other maraging steels are widely used in India for aerospace applications.

The other classes of high-alloyed steels like the Ni–Co–Cr–Mo secondary hardening steels (e.g. AF1410 and the AerMet family) are yet to enter the Indian market. It is to be noted that the AerMet class of alloys is patented by Carpenter Steel Corporation USA.

Table 8.19 Chemical compositions of PH stainless steels manufactured at MIDHANI, Hyderabad, India

Steels	C	Cr	Ni	Cu	Mo	Ti	Si	Mn	Others	Fe
MDN15-5 PHA	0.07	15.0	5.0	3.5	–	–	1.0	1.0	0.4Cb	Balance
MDN174A	0.07	17.0	4.0	4.0	–	–	1.0	1.0	0.4 (Cb + Ti)	Balance
MDN13-8Mo PHA	0.05	13.0	8.0	–	2.0	–	–	–	1 Al	Balance
MDN465A	0.02	11.5	11.0	–	1.0	1.6	–	–	–	Balance
MDN11-10T PH	0.03	10.0– 11.3	9.0– 10.3	0.3	1.8– 2.3	1.0– 1.4	0.15	0.10	0.15Nb	Balance

Table 8.20 Mechanical properties of PH stainless steels manufactured at MIDHANI, Hyderabad, India

Steels	Conditions	UTS (MPa)	0.2 % YS (MPa)	Elongation in 4D (%)	RA (%)	Hardness	K_{Ic} (MPa \sqrt{m})
MDN15-5 PHA	H1025	1069 min	1000 min	12 min	45 min	331–401 BHN	–
	H1150	931 min	724 min	16 min	50 min	277–352 BHN	–
MDN174A	H1025	1069 min	1000 min	12 min	45 min	331–401 BHN	–
	H1150	931 min	724 min	16 min	50 min	277–352 BHN	–
MDN13-8Mo PHA	H1000	1413	1310	10	60	43.0 min R _C	–
MDN465A	H950	1655	1515	10	45	47 R _C	77 min
	H1000	1515	1380	10	50	45.0 R _C	104 min
MDN11-10T PH	Hot Rolled/ST	880	785	6	–	306 BHN	–
	ST 800–820 °C/1 h/AC + Age 510–530 °C/3 h/AC	1420	1325	5	–	470–525 BHN	–

8.7 Summary

High-alloyed steels are capable of developing ultrahigh strengths coupled with high fracture toughness and stress corrosion resistance. These highly alloyed steels may be divided into three categories: secondary hardening steels, maraging steels and precipitation hardening stainless steels.

Secondary hardening steels must be fabricated in the soft-annealed condition. They have to be quenched and tempered to obtain ultrahigh strengths, which are due to precipitation of nano-size M_2C carbides in a nickel lath martensite. The tempering takes place in the range of 455–525 °C, and this results in high fracture toughness and high stress corrosion resistance at ultrahigh strength levels. Secondary hardening steels are useful for aerospace applications such as structural tubing, drive shafts, springs, connecting rods, fasteners, landing gear and crank shafts.

Maraging steels, on the other hand, do not require quenching. They can be air cooled from the solutionizing temperature and aged in the temperature range of 485–510 °C to achieve ultrahigh strength and excellent toughness. This strength and toughness is due to a fine precipitation of Ni_3Mo and Ni_3Ti intermetallic precipitates. Maraging steels can be fabricated in the solutionized condition, which is a major advantage. They have a wide range of aerospace applications such as missile casings, aircraft forgings, cannon recoil springs, Belleville springs, bearings, transmission shafts, fan shafts in commercial jet engines, couplings, hydraulic hoses and bolts.

Precipitation hardening (PH) stainless steels are classified into three categories: martensitic stainless steels, semi-austenitic stainless steels and fully austenitic stainless steels. These steels achieve ultrahigh strength due to precipitation of intermetallic phases or carbides, or by both, depending on the category of steel. PH stainless steels are used in aerospace applications such as landing gear components, slat components, torque tubes, pneumatic cylinders and many other parts.

References

1. Speich GR, Dabkowski DS, Porter LF (1973) Strength and toughness of Fe-Ni alloy containing C, Co, Mo and Cr. *Metall Trans* 4:303–315
2. Pascover JS, Matas SJ (1960) Relationships between structure and properties in the 9Ni-4Co alloy system. In: *Structure and Properties of Ultrahigh-Strength Steels*, ASTM Special Technical Publication STP 370 (American Society for Testing and Materials, Philadelphia, PA, USA), pp 30–46
3. Bieber CG (1960) Progress with 25 % nickel steels for high strength applications. *Met Prog* 78 (5):99–100
4. Bieber CG (1962) 20 and 25 % nickel maraging steels. Seminar on maraging steels, The International Nickel Company, Inc., New York, USA
5. Hall AM (1964) Review of maraging steel developments. *Cobalt* 24:138
6. Decker RF, Eash JT, Goldman AJ (1962) 18% nickel-maraging steel. *ASM Trans Q* 55:58–76

7. Perkas MD (1970) Structure and properties of high strength maraging steels. *Met Sci Heat Treat Met* 12:558–571
8. Leger MT, Aymard JP (1971) Contribution to the metallurgical investigation of a cast maraging type steel. *Les Mémoires Scientifiques de la Revue de Métallurgie* 68:783
9. Hulit GW (1964) Maraging steel: a new casting alloy. *Modern Castings* 46:508
10. Koppi WA, Sadowski EP (1967) 17% nickel cast maraging steel accepted by industry. *Modern Castings* 52(3):122
11. Porter LF, Manganello SJ, Dabkowski DS, Gross JH (1966) Ultra service steels with yield strengths of 130 to 200 ksi. *Met Eng Q* 6(3):17–32
12. Brown Jr, WF (1989) *Aerospace structural metals handbook*. Code 1224, Metals and Ceramics Information Center, Battelle Columbus Laboratories, Columbus, OH 43201, USA, pp 1–30
13. Magnée A, Viatour P, Drapier JM, Coutsouradis D, Habraken L (1973) Microstructure, strength and toughness of 13Ni(400) Maraging steel. *Cobalt* 1:3–10

Bibliography

1. Magnée A, Drapier JM, Dumont J, Coutsouradis D, Habraken L (1974) Cobalt monograph series: ‘cobalt-containing high strength steels’. Centre D’Information Du Cobalt, Brussels, Belgium
2. Pickering FB (ed) (1992) Constitution and properties of steels. In: Cahn RW, Haasen P, Kramer EJ (eds) Volume 7 of the series materials science and technology. VCH Verlagsgesellschaft mbH, Weinheim, Germany
3. ASM Handbook, Volume 1: Properties and Selection: Irons, Steels and High-Performance alloys, ASM International, Materials Park, OH 44071-0002, USA

Chapter 9

Nickel-Based Superalloys

D.V.V. Satyanarayana and N. Eswara Prasad

Abstract Nickel-based superalloys are an exceptional class of structural materials for high temperature applications, particularly in the challenging environment of the turbine sections of aircraft engines. Continued improvements in the properties of these materials have been possible through close control of chemistry and microstructure as well as the introduction of advanced processing technologies. Surface modification by application of coating technology concurrent with the introduction of directional structures and then single crystals, has extended the useful temperature range of superalloys. Further improvements are likely with the development and implementation of tools for alloy design, microstructure-process evolution, and mechanical-property modelling. To date, six generations of single crystal (SC) nickel-based superalloys have been developed with improved creep properties and phase stability. Therefore it appears that the evolution of advanced nickel-based superalloys is a never ending process, and their replacement in turbine engine applications seems to be impossible at least for a few more decades. The present chapter is a brief review of various aspects pertaining to chemical composition, heat treatment, microstructure, properties and applications of both cast, and wrought alloys as well as the evolution of advanced cast nickel-based superalloys.

Keywords Nickel • Superalloys • Chemical compositions • Physical metallurgy • Processing • Heat treatment • Castings • Wrought products • Mechanical properties • Fatigue • Creep

D.V.V. Satyanarayana (✉)
DMRL, Hyderabad, India
e-mail: dvvsn@rediffmail.com; dvvsnarayana@dmrl.drdo.in; dvvsn25@gmail.com

N. Eswara Prasad
DMSRDE, DRDO, Kanpur, India
e-mail: nep@dmsrde.drdo.in; neswarap@rediffmail.com

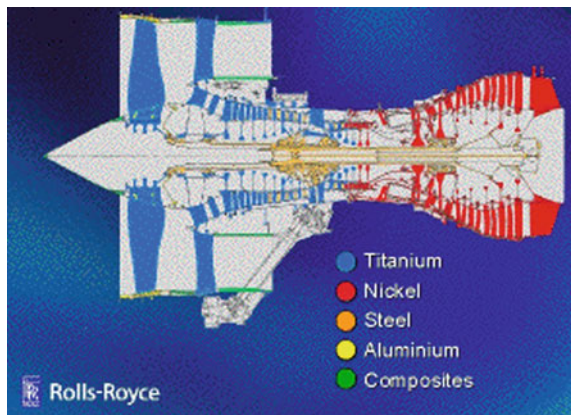
9.1 Introduction

“Superalloys” belong to a group of alloys developed after World War II for use in turbo-superchargers and aircraft gas turbine engines that required high performance at elevated temperatures. The use of these alloys has subsequently expanded to many other areas, including land-based gas turbines, rocket engines, chemical, and petroleum plants. These materials are particularly well suited for these demanding applications because of their ability to retain most of their strength even after long exposure times above 650 °C. Their versatility stems from the fact that they combine high strength with good low-temperature ductility and excellent surface stability. Several books [1–5] as well as numerous papers and reports [6–26] giving detailed account of various aspects of superalloys are already available in the open literature. Nevertheless, an attempt has been made in the chapter of this book is not only to briefly present the physical metallurgical aspects and mechanical properties of nickel-based superalloys, but also include details on the evolution of advanced cast nickel-based superalloys so as to prepare a brief up-to-date compilation of information on this class of alloys. Indian efforts in producing type-certified superalloy primary and secondary products as well as select components are surveyed in Chap. 24 in Volume 2 of these Source Books.

9.2 Classification of Nickel-Based Superalloys

Superalloys are the major materials used for the turbine sections of aircraft. Nickel-based superalloys along with iron-based/ iron-nickel-based and cobalt-based superalloys are used in wrought, cast, powder metallurgy, and cast-single crystal forms to meet the demands imposed by efficient high-temperature use. Figure 9.1 illustrates the use of nickel-based superalloys and other alloys for various sections

Fig. 9.1 Sectional view of an advanced aircraft gas turbine engine (Source Michael Cervenka, Rolls-Royce) [5]



of an aircraft gas turbine engine, where it is seen that superalloys are employed in the combustion chamber and turbine sections.

The superalloys are based on Group VIII B elements of the Periodic Table, and usually consist of various combinations of Fe, Ni, Co, and Cr, as well as lesser amounts of W, Mo, Ta, Nb, Ti, and Al. The three major classes of superalloys are nickel-, iron-iron-nickel-, and cobalt-based alloys. In all cases, the crystal structure is face centered cubic (fcc) at all temperatures, owing to stabilization of this structure by the alloying elements, particularly nickel. A large number of superalloys have been invented and studied, and many have been patented. However, only a few are extensively used. The present chapter considers only nickel-based superalloys.

All superalloys products can be classified into three main categories [3–5]: (i) cast, (ii) wrought, and (3) powder metallurgy (PM). Examples of alloys in these categories are listed in Tables 9.1 and 9.2. Wrought alloys are generally more homogeneous with more uniform microstructures than cast alloys, which usually have segregation caused by the solidification process. As a consequence, wrought alloys are considered more ductile and exhibit more consistent mechanical properties.

Early in the history of superalloys, the development of new alloy compositions was successful only if melt processing techniques were advanced enough to produce commercial-size quantities. As higher strength and more highly alloyed materials were produced, melt processes were developed which reduced ingot

Table 9.1 Chemical compositions of wrought nickel-based superalloys

Alloy	Cr	Al	Co	Mo	W	Nb	Ti	B	Fe	C	Others	Ni
<i>Combustor applications</i>												
Hastelloy X	22	–	1.5	9	0.7	–	–	0.005	1.9	0.07	–	Bal
Nimonic C-263	20	0.4	20	6	–	–	2.1	–	0.4	0.06	–	Bal
IN617	22	1.2	12.5	8.5	–	–	–	–	–	0.05	–	Bal
IN 230	22	0.35	5	2	14	–	–	0.015	3	0.1	–	Bal
<i>Disc applications (aircraft engines and industrial gas turbines)</i>												
IN 706	16	–	–	–	–	2.9	1.8	–	37	0.03	–	Bal
IN 718	19	0.5	–	3	–	5.1	0.9	–	18.5	0.03	–	Bal
Udimet 720	18	2.5	14.8	3	1.25	–	5	0.033	–	0.035	0.03 Zr	Bal
Udimet 720 LI	16	2.5	15	3	1.25	–	5	0.018	–	0.025	0.03 Zr	Bal
IN 100 ^a	10	5.5	15	3	–	–	4.7	0.015	–	0.15	0.06 Zr; 1 V	Bal
Rene 88 DT ^a	16	2.1	13	4	4	0.7	3.7	0.015	–	0.03	0.03 Zr	Bal

^aProcessed by powder metallurgy(PM) route

Table 9.2 Chemical compositions of cast nickel-based superalloys

Alloy	Cr	Al	Co	Mo	W	Nb	Ti	B	Fe	C	Others	Ni
IN 713	12.5	6.1	–	4.2	–	2	0.8	0.01	–	0.12	0.1 Zr	Bal.
IN 100	10	5.5	15	3	–	–	4.7	0.01	–	0.18	0.06 Zr	Bal.
Mar-M200	9	5.5	15	–	12.5	1.8	2	0.015	–	0.14	0.05 Zr	Bal.
Mar-M246	9	5.5	10	2.5	10	–	1.5	0.015	–	0.14	0.05 Zr; 1.5 Ta	Bal.
Mar-M246 +Hf	8	5.5	10	2.5	10	–	1.5	0.015	–	0.15	0.05 Zr; 1.5 Ta, 1.5 Hf	Bal.
Rene 80 + Hf	14	3	9.5	4	4	–	4.7	0.015	–	0.15	0.01 Zr; 0.8 Hf	Bal.
IN 738	16	3.4	8.5	1.75	2.6	0.9	3.4	0.01	–	0.11	0.04 Zr; 1.75 Ta	Bal.

segregation and allowed sufficient ingot sizes such that subsequent thermomechanical processing was adequate to homogenize the macrostructures and microstructures.

The development of PM superalloys arose when conventional melt processing methods were inadequate for highly alloyed compositions. Ingots cast from these advanced compositions would either self-destruct due to thermal stress, or show severe dendritic segregation, which would be impractical to homogenize.

9.3 Physical Metallurgy

9.3.1 Chemical Composition

Nickel-based alloys can be either solid solution or precipitation strengthened. Solid solution strengthened alloys, such as Hastelloy X, are used in applications requiring only modest strength, e.g., combustion chamber walls. For the most demanding applications, such as high pressure turbine blades and vanes, precipitation strengthened alloys are required.

Most nickel-based alloys contain 10–20 % Cr, up to 8 % Al and Ti, 5–10 % Co, and small amounts of B, Zr, and C. Other common additions are Mo, W, Ta, Hf, and Nb. The elemental additions in Ni-based superalloys can be categorized as (i) γ formers (elements that tend to partition to the matrix), i.e. solid solution strengtheners, (ii) γ' formers (elements that partition to the γ' precipitate), (iii) carbide formers, and (iv) finally, the elements that segregate to the grain boundaries. The roles of alloying elements in the formation of various phases are described in Table 9.3 as well as in Fig. 9.2.

Elements which are considered γ formers are Group V, VI, and VII elements of the Periodic Table such as Co, Cr, Mo, W, and Fe. γ' formers come from group III,

Table 9.3 Alloying elements in nickel-based superalloys and their role

Elements	Effects
Ni	Stabilizes fcc matrix, forms γ' ($\text{Ni}_3(\text{Al,Ti})$), and inhibits formation of deleterious phases
Cr	Imparts oxidation and sulphidation resistance as well as solid solution strengthening, and forms grain boundary carbides
Co	Raises solvus temperature of γ' and lowers stacking fault energy (thereby making cross-slip of screw dislocations more difficult)
Mo, Ta and W	solid solution strengthening and formation of MC-type carbides
Ti	Forms γ' ($\text{Ni}_3(\text{Al,Ti})$) and MC-type carbides
Al	Forms γ' ($\text{Ni}_3(\text{Al,Ti})$) and improves oxidation resistance
B and Zr	Improve stress rupture properties and retard grain boundary Ni_3Ti formation
La and Y	Improve oxidation resistance
C	Formation of carbides (MC, M_{23}C_6 etc., type)
Nb and Ta	Form γ'' (Ni_3Nb) and MC-type carbides

IV, and V elements and include Al, Ti, Nb, Ta, Hf. Furthermore, Co, Fe, Cr, Nb, Ta, Mo, W, V, Ti, and Al are solid solution strengtheners in both γ and γ' . There are, therefore, limits to the concentrations of these elements that can be added without inducing precipitation.

It is particularly important to avoid certain embrittling phases such as Laves and Sigma. There are no simple rules governing the critical concentrations. A major concern in the design of new alloys, and in defining specification limits for the acceptable range of individual alloying elements, is the avoidance of a class of phases known as topologically closed packed phases (TCPs). These phases are typically rich in refractory alloying elements and possess complex crystal structures characterized by closed-packed layers of atoms (atomic coordination number >12).

Examples of TCPs include the orthorhombic P phase, the tetragonal σ phase, and the rhombohedral R and μ phases [27–31]. TCP phases are detrimental because they not only deplete strengthening elements from the microstructure but also serve as crack-initiation sites during cyclic loading [4, 27–29]. However, precipitation kinetics for these phases is often very sluggish, resulting in precipitation only after extended times in service.

The main carbide formers are C, Cr, Mo, W, C, Nb, Ta, Ti, and Hf. The carbides tend to precipitate at grain boundaries and hence reduce the tendency for grain boundary sliding, thereby improving the creep resistance. Also, polycrystalline superalloys contain grain boundary strengthening elements such as boron and zirconium (and also carbon, already mentioned above). The resulting increase in grain boundary cohesive strength improves creep rupture strength and ductility.

Chromium and aluminium are essential for oxidation resistance, and small quantities of yttrium help the service-induced oxide scale to cohere to the substrate.

New alloy design tools based on the Calphad method [32–35] are increasingly used in the design of new alloys and to establish or modify specification ranges for

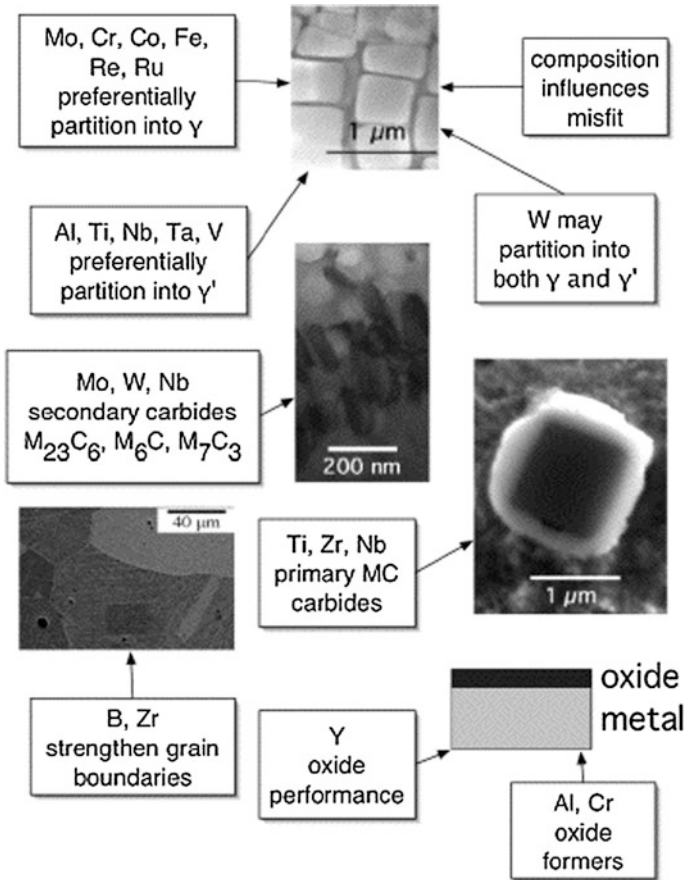


Fig. 9.2 Role of alloying elements in nickel-based superalloys

existing alloys to avoid deleterious phases. The ability to predict phase compositions and their ranges of stability depends on the development of thermodynamic models for the complex intermetallic phases and on the availability of databases to validate the modelling.

9.3.2 Microstructural Constituents

The major phases present in most nickel-based superalloys are as follows [1–5, 11, 12]:

Gamma (γ): The continuous matrix (called gamma) is an fcc nickel-based austenitic phase that usually contains a high percentage of solid solution elements such as Co, Cr, Mo, and W.

Gamma Prime (γ'): The primary strengthening phase in nickel-based superalloys is $\text{Ni}_3(\text{Al,Ti})$, and is called gamma prime (γ'). Aluminium and titanium are the major alloying elements in γ' , and are added in amounts and mutual proportions to precipitate a high volume fraction of γ' in the matrix. In some modern alloys the volume fraction of γ' is around 70 %.

γ' is a coherently precipitating phase (i.e. the crystal planes of the precipitate are in registry with the gamma matrix) with an ordered L12 (fcc) crystal structure. The close match in matrix/precipitate lattice parameter ($\sim 0\text{--}1\%$) combined with the chemical compatibility allows γ' to precipitate homogeneously throughout the matrix and have long-time stability. In addition, γ' is quite ductile and thus imparts strength to the matrix without lowering the fracture toughness of the alloy.

There are many factors that contribute to the hardening imparted by the γ' and include γ' fault energy, γ' strength, coherency strains, volume fraction of γ' , and γ' particle size.

Extremely small γ' precipitates always occur as spheres, owing to the dominance of minimizing the surface energy. For larger coherent precipitates it becomes more important to minimize the interfacial energy, and this result in γ' forming cubes, thereby allowing the crystallographic planes of the cubic matrix and precipitate to remain continuous. Thus as the γ' volume fraction increases, the morphology changes from spheres to cubes, or plates. However, coherency can be lost by overageing, and this is evidenced by directional coarsening (change in aspect ratio) and rounding of the cube edges.

Carbides: Carbon, added at levels of 0.05–0.2 %, combines with reactive and refractory elements such as titanium, tantalum, and hafnium to form carbides (e.g. TiC, TaC, or HfC). During heat treatment and service, these begin to decompose and form lower carbides such as M_{23}C_6 and M_6C , which tend to form on the grain boundaries [3, 4, 12]. These common carbides all have an fcc crystal structure. In general, carbides are considered to be beneficial by increasing the creep rupture strength at high temperatures.

TCP phases: These are generally undesirable brittle phases that can form during heat treatment or service. TCPs (σ , μ , Laves, etc.) usually form as plates (which appear as needles in 2-D micrographs). The plate-like structure adversely affects the ductility and creep rupture strength. Sigma appears to be the most deleterious, while strength retention has been observed in some alloys containing μ and Lave phases.

TCPs are potentially damaging for two main reasons: they sequester γ and γ' strengthening elements in a non-useful form, thus reducing the overall creep strength, and they can act as crack initiators because of their brittle nature [3, 4, 11, 12].

9.3.3 Heat Treatment

To optimize properties (often of an alloy/coating system), solution-treated nickel-based superalloys are aged at two different temperatures within the γ/γ'

phase field. The higher temperature heat treatment precipitates coarser particles of γ' . The lower temperature heat treatment leads to a finer, secondary dispersion of γ' . The net result is a bimodal distribution of γ' . Typical microstructures of wrought and cast nickel-based superalloys are illustrated in Figs. 9.3, 9.4 and 9.5.

The solution heat treatment temperature determines not only the amount of γ' that dissolves, but also the γ grain size. This coarsens if all the γ' is dissolved, since the grain boundaries are no longer pinned by precipitates. Typical heat treatment cycles (combinations of solution and ageing treatments) for wrought and cast superalloys are given in Table 9.4.

Fig. 9.3 Wrought alloy microstructures: **a** equiaxed annealed grain structure, **b** coarse MC-type (TiC) carbides within grains and $M_{23}C_6$ -type ($Cr_{23}C_6$) carbides along grain boundaries, and **c** spherical γ' precipitates

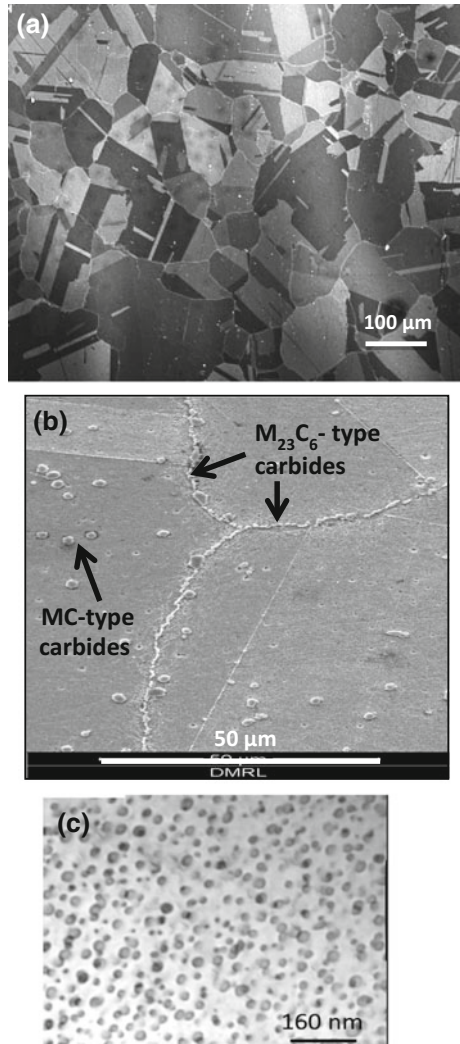
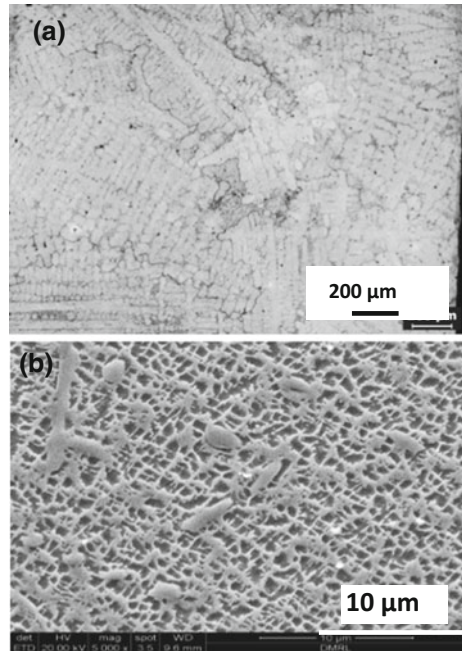


Fig. 9.4 Cast alloy microstructures: **a** dendrites within coarse equiaxed grain structure **b** coarse MC-type (TiC) carbides and near cuboidal γ' precipitates within grains



9.3.4 Strengthening Mechanisms

Nickel-based superalloys consist of matrix γ containing a dispersion of ordered intermetallic precipitates of the type Ni_3Al (γ'). To increase the strength of initial simple Ni–Cr–Al–Ti alloys, the approach has been to strengthen the matrix by adding other elements that can be taken into substitutional solid solution and to increase the volume fraction of γ' .

The grain boundaries are reinforced by carbide precipitation and by the use of minor additions of boron and zirconium to increase grain boundary cohesion. This strengthening method obviously does not apply for SCs.

Because of its electronic structure, the fcc nickel lattice enables a larger solubility for many other elements [3–5]. Solid solution strengthening is partly caused by lattice distortion and therefore increases with increase in atomic size difference up to a maximum of about 10 %. High melting point elements provide strong lattice cohesion and reduce diffusion, particularly at high temperatures. Mo and W are particularly effective for both these reasons.

Atomic clustering or short range order can also strengthen the matrix. This is an electronic effect and is observed with Mo, W, Cr, and Al. These elements therefore produce greater hardening than Fe, Ti, Co, or V. However, strengthening due to short range order diminishes rapidly above about $0.6 T_m$ owing to increased diffusion.

Fig. 9.5 **a** Scanning electron micrograph of a typical single crystal microstructure, cuboidal γ' -precipitates surrounded by γ -matrix, **b** fcc gamma structure and, **c** L12-ordered crystal structure of γ' -phase

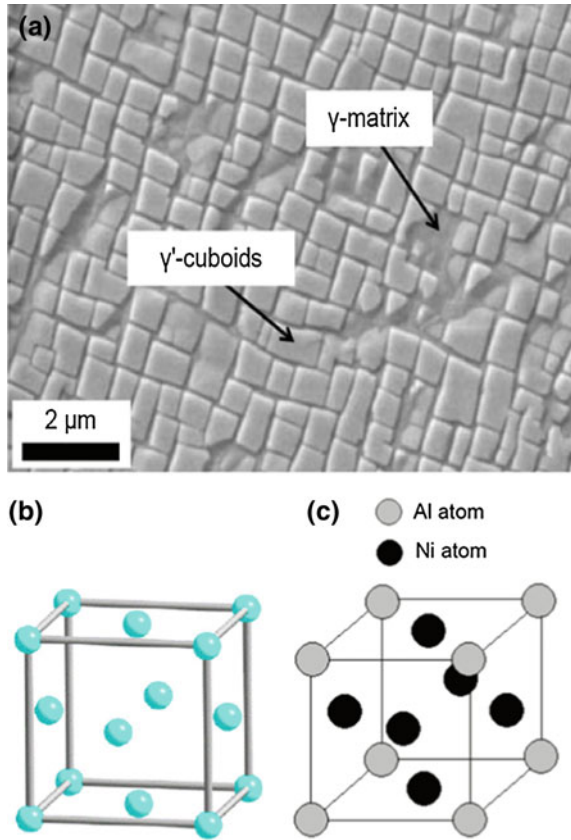


Table 9.4 Typical heat treatment cycles for various types of nickel-based superalloys

Alloy	Alloy type	Heat treatment cycle
IN718	Wrought	980 °C/1 h/AC-720 °C/8 h-FC-620 °C/8 h/AC
Udimet 720		1113 °C/2 h/AC-1079 °C/4 h/OQ-649 °C/24 h-760 °C/8 h
Mar-M-200	Cast: equiaxed grain structure	1230 °C/1 h-1260 °C/0.5 h-1080 °C/8 h-870 °C/15 h
DS CM 247	Cast: directionally solidified	1230 °C/1 h-1260 °C/3 h/Argon quench-1080 °C/4 h/Argon quench-870 °C/20 h/AC
AM1	Cast: single crystal	1300 °C/3 h/Argon quench-1100 °C/9 h/Argon quench-870 °C/20 h

AC air cooled; FC furnace cooled; OQ oil quenched

The origin of precipitation hardening is complex. The size and spacing of the precipitates and therefore their volume fraction are important factors [3–5]. Generally, the hardening increases with increased amounts of precipitate, and it also increases, up to a peak value, with increasing precipitate size:

- Before the age-hardening peak is reached, the operative strengthening mechanism involves cutting of γ' particles by dislocations, and the strength increases with increasing γ' size as shown in Fig. 9.6.
- After the age-hardening peak, the strength decreases with continuing particle growth, because dislocations no longer cut the γ' particles but bypass them. This effect can be demonstrated for tensile or hardness behaviour in low-volume fraction γ' alloys (A-286, Incoloy 901, Waspaloy), but may not be as readily apparent in high-volume fraction γ' alloys such as MAR-M-247 and IN-100 [4]

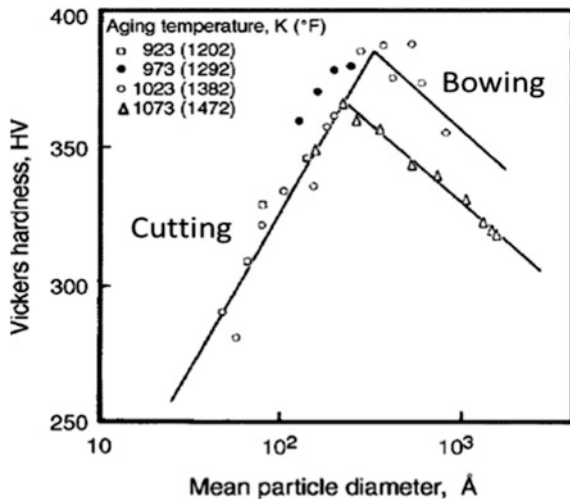
For creep rupture the effects of ageing are less well defined than for short-time properties such as tensile strength. Uniform fine to moderate γ' sizes (0.25–0.5 μm) are preferred to coarse or hyperfine γ' for optimal creep properties. The reasons for this are related to the interactions of dislocations with matrix/precipitate interfaces and the precipitates themselves [3–5, 11, 12].

9.4 Manufacturing Processes

Superalloy ingots are subsequently used for one of three major processing routes, see Fig. 9.7. These are (1) remelting and subsequent investment casting, (2) remelting followed by wrought processing, or (3) remelting to form superalloy powder that is subsequently consolidated and subjected to wrought processing operations.

Ingots are fabricated by vacuum induction melting (VIM) in a refractory crucible to form a base alloy. Although selected alloys can be melted in air/slag environments using electric arc furnaces, VIM melting of superalloys is much more effective in the removal of low melting point trace contaminants [2–4, 11]. The

Fig. 9.6 Strength (hardness) versus particle diameter [4]. Smaller particles are cut by dislocations, but they have to bypass larger particles by bowing out between them. The result is a strength increase. Note that lower ageing temperatures increase the strength as well



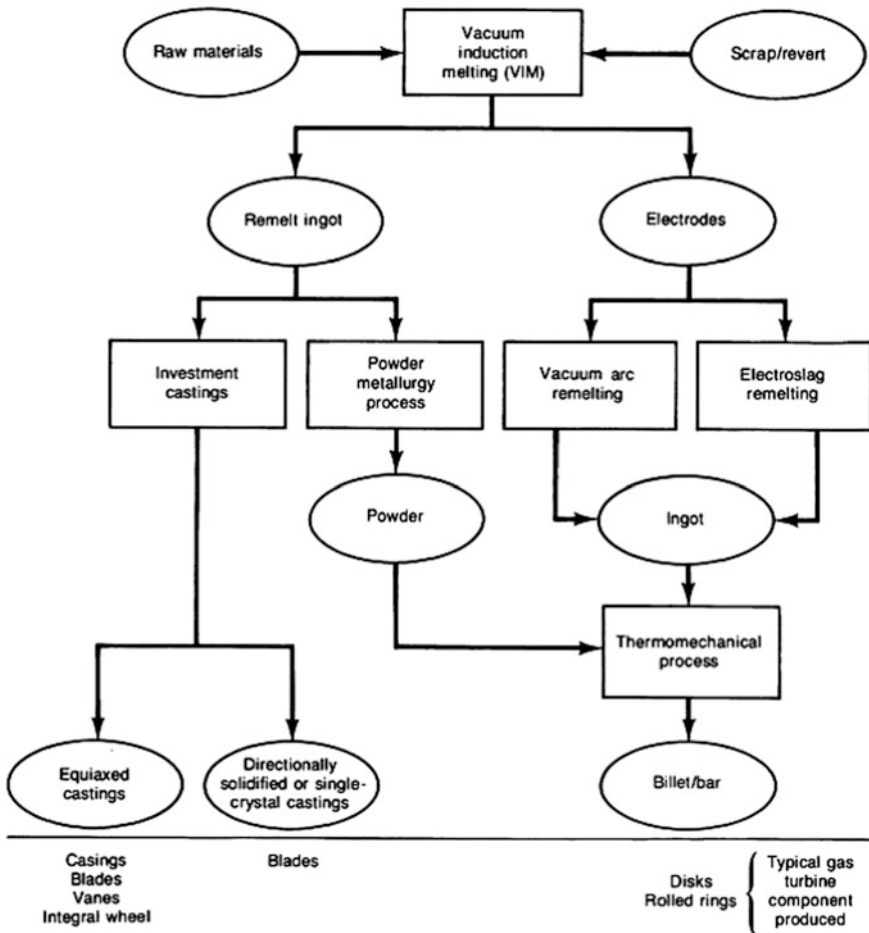


Fig. 9.7 Process flow chart illustrating manufacturing routes for superalloy products and components

alloy ingots are subsequently subjected to additional melting or consolidation processes that depend upon the final application of the material.

9.4.1 Wrought Alloys

Wrought alloys are typically fabricated by remelting of VIM ingots to form secondary ingots for subsequent deformation processing. A secondary melting process is necessary for wrought alloys because the high temperature structural properties of nickel-based superalloys are very sensitive to microstructural variations, chemical

inhomogeneities, and inclusions. As ingot sizes increase, VIM melting often results in macrosegregation or the formation of large shrinkage cavities during solidification. The formation of these solidification defects is caused by large-scale solute segregation associated with dendritic solidification under low thermal gradients. Because heat transfer during solidification of VIM ingots is limited by the low intrinsic thermal conductivity of the solidifying mass, large ingots are very prone to the formation of these defects [4, 8, 11]. Thus other secondary melting processes are utilized, including vacuum arc remelting (VAR), electro-slag remelting (ESR), and electron beam cold hearth refining (EBCHR) [4, 8, 11].

For the production of critical rotating components, such as turbine discs, VAR is used to refine the ingot and eliminate macrosegregation. Consumable electrodes (30–50 cm in diameter) cast by VIM are remelted into a water cooled copper crucible. Unlike the VIM process, in which the entire quantity of the alloy is molten and allowed to solidify, VAR involves only localized melting of the electrode tip. Melt rates of VAR are on the order of 0.5–1 kg/s. Defect features, such as macrosegregation and shrinkage, are effectively minimized since high thermal gradients are maintained during solidification of the comparatively smaller melt pool [4, 8, 11]. The remelted ingots are subsequently subjected to thermomechanical processing such as forging, hot rolling, extrusion, etc., to obtain the final products including billets, slabs, rods, plates, and sheets.

Combustor components are fabricated out of sheet nickel-based superalloys. Hastelloy X was used from the 1960–1980s. Nimonic 263 was subsequently introduced and has higher creep strength [36]. As combustion temperatures have further increased in newer gas turbines, HA-188, a cobalt-based superalloy has been recently introduced for some combustion system components for improved creep rupture strength [36].

IN 718 has been used for the manufacture of discs in aircraft engines for more than 25 years [36]. This alloy has been produced through the conventional ingot metallurgy route. IN 718 is the most frequently used superalloy for aircraft gas turbines, but because of its segregation tendency it could not be produced with ingot diameters more than 500 mm until the beginning of the twenty-first century. Remelting developments and very close control of chemical composition have enabled production of ingots as large as 750 mm in diameter. This has resulted in the ability to process IN 718 to the large disc sizes needed in modern industrial gas turbines (IGTs). A considerable amount of R&D on IN 718 has been reported at several international conferences [37–42].

Udimet 720 [43] has also evolved as an advanced wrought alloy for land-based gas turbines. Reductions in Cr content to prevent sigma phase formation and in carbon and boron levels to reduce stringers and clusters of carbides, borides, or carbonitrides, have led to the development of Udimet 720 LI. Both alloys have also been incorporated in some aircraft gas turbines [43]. The chemical compositions of Udimet 720 and 720 LI alloys may be compared from Table 9.1.

9.4.2 Cast Superalloys

The compositions of wrought alloys are restricted by the hot workability requirements, and this has led to the development of cast alloys. The main advantage of cast alloys is that their compositions can be tailored for good high-temperature strength, since there is no forgeability requirement. Further, cast components are intrinsically stronger than forgings at high temperatures, owing to their coarse grain size. A recent review has covered the advances made in cast nickel-based superalloys [44].

Cast IN 713 was among the early grades established as materials for airfoils in the most demanding gas turbine applications. Efforts to increase the γ' volume fraction to realize higher creep strength led to the development of alloys like IN 100 and Rene 100. Increased amount of refractory solid solution strengtheners such as W and Mo were added to some of the grades developed later, and this led to the availability of grades like MAR-M200, MAR-M246, IN 792, and M22. Subsequent addition of 2 wt% Hf improved ductility, and a new series of alloys became available, such as MAR-M200 + Hf, MAR-M246 + Hf, and Rene 125 + Hf.

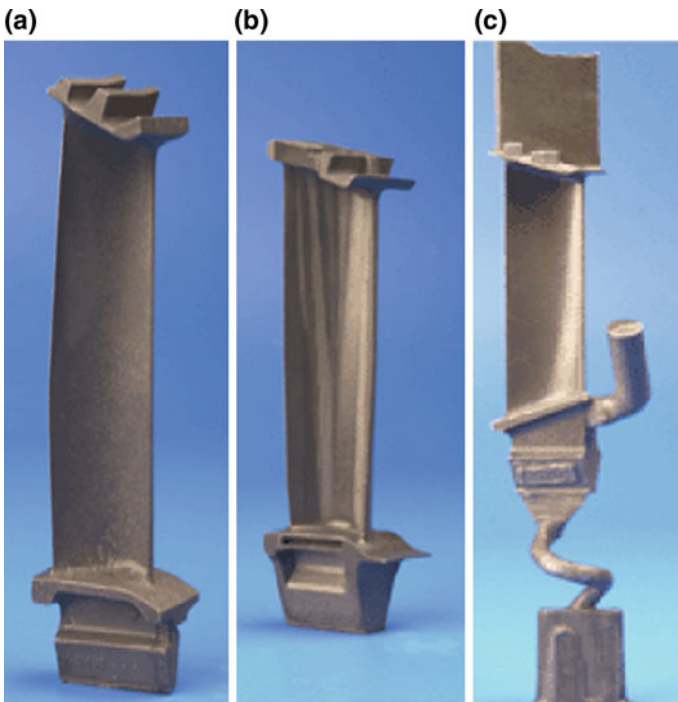


Fig. 9.8 Turbine blades: **a** equiaxed polycrystalline, **b** DS polycrystalline, and **c** single crystal, showing the as-cast component

General Electric pursued its own alloy development with Rene 41, Rene 77, Rene 80, and Rene 80 + Hf having relatively high Cr content for improved corrosion resistance at the cost of some high-temperature strength. Similar alloys with high Cr content are IN738C, IN738LC, Udimet 700, and Udimet 710. The chemical compositions of all these cast alloys are included in Table 9.2.

Investment casting [2–4, 11] is the primary casting process for fabrication of superalloy components with complex shapes, including blades and vanes. Ceramic moulds containing alumina, silica, and/or zirconia are utilized in this process. The moulds are fabricated by progressive buildup of ceramic layers around a wax pattern of the cast component. Ceramic cores can be embedded in the wax to obtain complex internal cooling structures.

A thermal cycle removes the wax, and the mould is filled with remelted superalloy in a preheated vacuum chamber to obtain a shaped casting. Castings thus obtained may be equiaxed, directionally solidified (DS) columnar grained, or single crystal (SC) (Fig. 9.8). Equiaxed castings solidify fairly uniformly throughout their volume, whereas columnar and SC castings are withdrawn from a hot zone in the furnace to a cold zone at a controlled rate. A schematic is shown in Fig. 9.9.

Following initial solidification, castings are subjected to a series of heat treatment cycles that serve to reduce segregation, establish one or more size populations of γ' precipitates, modify the structure of grain boundary phases (particularly carbides), and/or assist in the application of coatings.

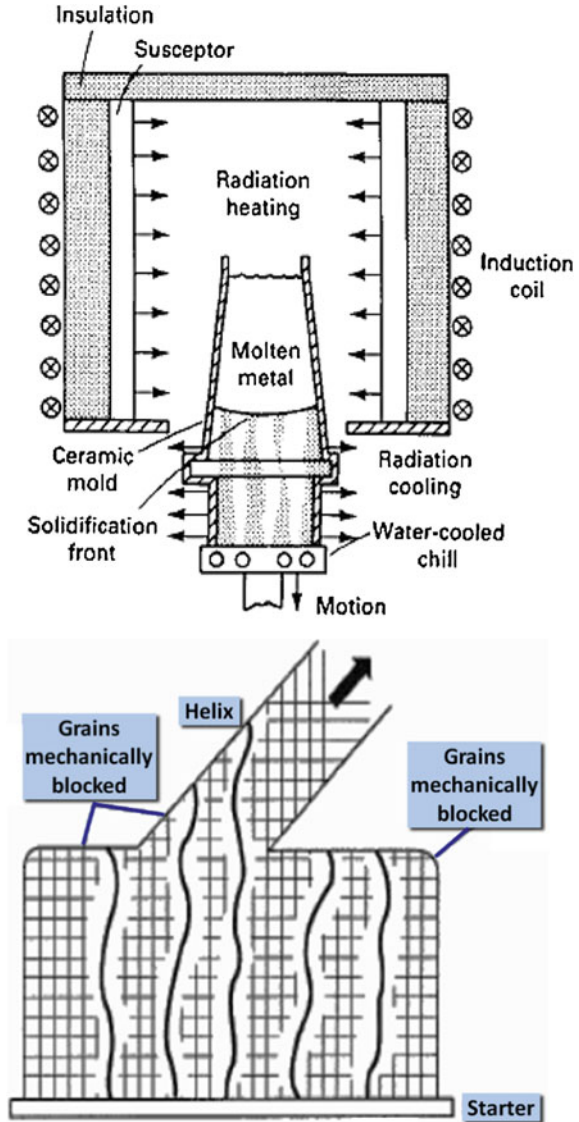
DS-induced grain defects: DS processing can result in several types of chemistry sensitive grain defects [46]. The two most common defects are freckle chains and misoriented grains (Fig. 9.10).

Freckle-type defects [45–52] occur because of convective instabilities in the mushy zone. The instabilities develop as a result of density inversions created by progressive segregation of individual alloying elements during solidification. The fluid flow within “channels” that develop because of these instabilities [53, 54] results in fragmentation of dendrite arms, producing a small chain of equiaxed grains aligned approximately parallel to the solidification direction. The freckles are enriched in elements that segregate to the interdendritic region during solidification and thus differ in composition from the base alloy [46]. Freckle formation is promoted by low cooling rates, (low thermal gradients) and corresponding large dendrite arm spacings [47].

Misoriented grains differ from freckles in that they have the same nominal composition as the base alloy, but are typically larger and elongated along the solidification direction.

The occurrence of these defects can be avoided by reducing the *density gradient* in the mushy zone, which is accomplished by increasing the thermal gradient in the process [46–49]. There has recently been greater effort aimed at increasing the thermal gradients. A new approach involves the use of liquid-metal coolants (LMCs) during solidification [53]. A modified Bridgman system using liquid tin as a cooling medium has been developed. Substantial increases in cooling rate and elimination of freckle defects have recently been demonstrated by this method [54].

Fig. 9.9 Schematics of typical DS process (*top*) and the beginning of the single crystal DS process (*bottom*), whereby a helical mould section prevents all but one grain from growing into the main casting



9.5 Properties of Superalloys

Superalloys constitute a large fraction of the structural materials in turbine engines because of their unique combination of physical and mechanical properties. Table 9.5 lists some typical physical properties of superalloys. In aircraft engines, it is typical to consider density normalized properties, especially in rotating

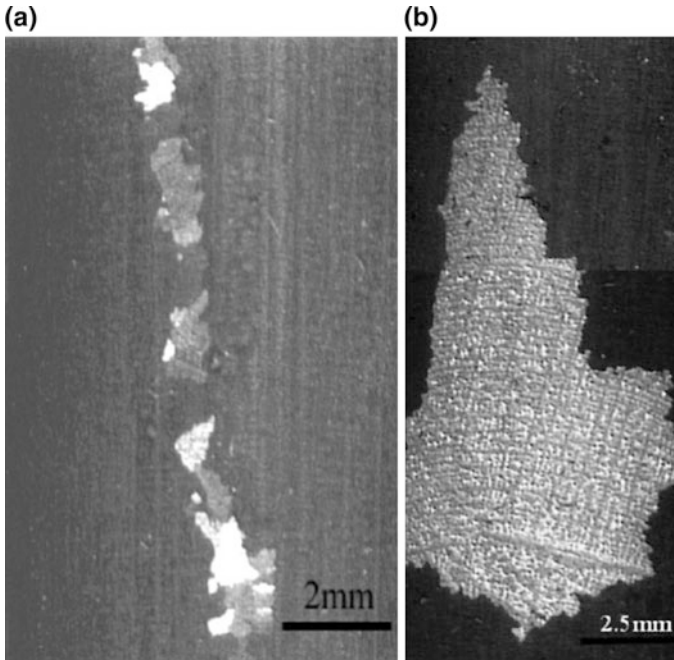


Fig. 9.10 Macroscopic chemistry-sensitive grain defects present on the surfaces of single crystal nickel-based superalloy castings: **a** freckles and **b** a misoriented grain

components. Thus alloy densities, which are typically in the range of 7.7–9.0 g/cm³, are of particular interest.

Optimization of mechanical properties is of paramount importance and depends on a high level of control and understanding of the processes mentioned in Sect. 9.4. Mechanical properties of primary interest include tensile properties, creep, fatigue, and cyclic crack growth. Depending on the details of component design, any one of these four properties may be life-limiting.

9.5.1 Tensile Properties

Nickel-based superalloys have relatively high yield and ultimate tensile strengths, often in the respective ranges of 900–1300 MPa and 1200–1600 MPa at room temperature. Figure 9.11 shows the temperature dependence of the yield strength of an SC alloy and a PM-processed disc alloy [11, 55, 56]. The blade alloy tensile properties do not substantially decay until temperatures above 850 °C. However, disc alloys are typically developed to have higher strengths at temperatures below 800 °C, with some design margin in strength to protect against disc burst in the event of an engine overspeed.

Table 9.5 Physical properties of nickel-based superalloys

Properties	Typical ranges and values
Density	7.7–9.1 g/cm ³
Melting point	1320–1450 °C
Elastic modulus	RT: 210 MPa 800 °C: 160 MPa
Thermal expansion coefficient	8–18 × 10 ⁻⁶ /°C
Thermal conductivity	RT: 11 W/m.K 800 °C: 22 W/m.K

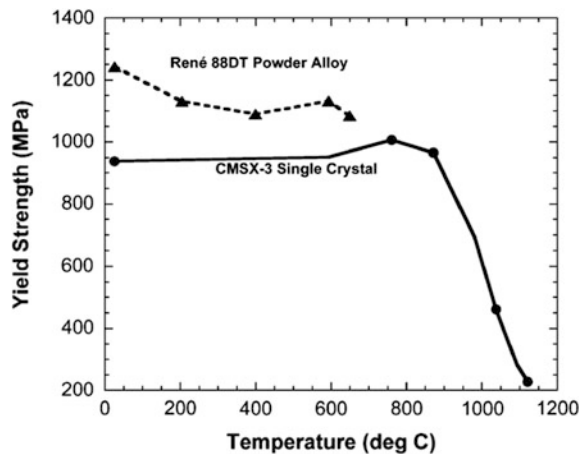
Figure 9.11 also shows that the yield strengths increase slightly at intermediate temperatures. This unusual behaviour is due to the complicated dislocation movements required to shear the γ' precipitates in this temperature range [5, 57–59]. Note also from Fig. 9.12 that a two-phase superalloy is much stronger than either the matrix or precipitate materials in their bulk form.

9.5.2 Creep Resistance

Gas turbine components experience stresses at high temperature for extended periods. Hence a high resistance to creep deformation is essential. This is very important for cast blade alloys, because they are exposed to temperatures up to 1100 °C, whereas disc alloys are typically limited to less than 700 °C.

For a fixed stress and temperature precipitate-strengthened superalloys have much higher creep resistance than their single-phase counterparts. It has been reported that the strength peaks when the precipitate volume fractions are in the range of 0.6–0.7, and many advanced alloys contain precipitates in this range [60].

Fig. 9.11 Temperature dependence of yield strength for a single crystal turbine blade alloy and a PM polycrystalline disc alloy



Alloy chemistry is also important to creep properties. Because the rate-controlling processes in creep are diffusion-controlled, elements that have low interdiffusion coefficients with nickel are generally beneficial. Elements most effective at slowing diffusion include Ir, Re, Ru, Pt, W, Rh, and Mo [61, 62]. Advanced creep-resistant alloys benefit from substantial additions of Re, W, and Mo (Tables 9.2, 9.6, 9.7, 9.8 and 9.9).

A combination of increasing additions of refractory elements and advances in processing has resulted in substantial increases in the maximum temperature capability of superalloys since the 1950s (Fig. 9.13). For a creep rupture life of 1000 h at a stress of 137 MPa, the most recently developed single crystal superalloys [63, 64] have a temperature capability of approximately 1100 °C, whereas conventionally cast equiaxed alloys had a temperature capability of 900–950 °C. In fact, the temperature capabilities of advanced superalloys have now reached 85–90 % of the melting point, which is truly remarkable.

9.5.3 Fatigue

Turbine components also experience significant fluctuations in stress and temperature during their repeated start—flight operation—shutdown cycles. These cycles can result in localized small plastic strains. Thus low cycle fatigue is of interest to engine design and operation; and engine vibrations and gas/airflow fluctuations between turbine stages can also result in high cycle fatigue, with rapid cycle accumulation in airfoils at frequencies in the kHz range.

Figure 9.14 shows the conventional smooth-specimen S-N fatigue properties of the PM disc alloy Rene 88 DT at room temperature and 593 °C [65]. In the low cycle fatigue regime (typically up to about 20,000 cycles) such disc alloys exhibit

Fig. 9.12 Temperature dependence of flow stress for an as-cast and heat treated nickel-based superalloy, and the individual phases [60]

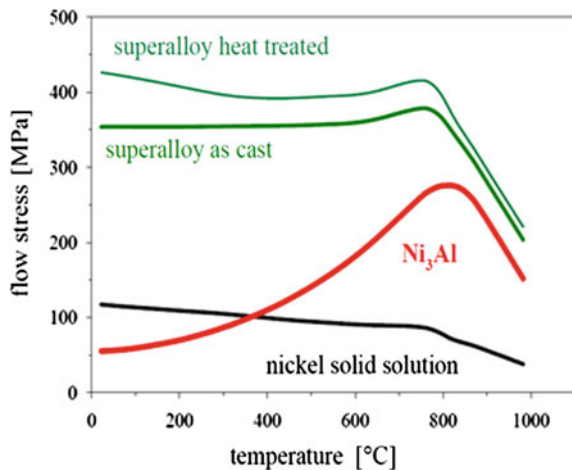


Table 9.6 Chemical compositions (wt%) of first generation single crystal nickel-based superalloys

Alloy	Cr	Co	Mo	W	Al	Ti	Ta	Nb	V	Hf	Density (g/cm ³)
CMSX-2	8	4.6	0.6	8	5.6	1	6	–	–	–	8.6
PWA 1480	10	5	–	4	5	1.5	12	–	–	–	8.7
SRR 99	10	5	–	10	5.5	2.2	3	–	–	–	8.56
Rene N4	9	8	2	6	3.7	4.2	4	0.5	–	–	8.56
AM1	7.8	6.5	2	5.7	5.2	1.1	7.9	–	–	–	8.6

Table 9.7 Chemical compositions (wt%) of second generation single crystal nickel-based superalloys

Alloy	Cr	Co	Mo	Re	W	Al	Ti	Ta	Nb	Hf	Density (g/cm ³)
CMSX-4	6.5	9	0.6	3	6	5.6	1	6.5	–	0.1	8.7
PWA 1484	5	10	2	3	6	5.6	–	8.7	–	0.1	8.95
Rene N5	7	8	2	3	5	6.2	–	7	–	0.2	8.7
MC2	8	5	2	–	8	5	1.5	6	–	–	8.63

Table 9.8 Chemical compositions (wt%) of third generation single crystal nickel-based superalloys

Alloy	Cr	Co	Mo	Re	W	Al	Ti	Ta	Nb	Hf	Others	Density (g/cm ³)
CMSX-10	2	3	0.4	6	5	5.7	0.2	8	0.1	0.03	–	9.05
Rene 6	4.2	12.5	1.4	5.4	6	5.75	–	7.2	–	0.15	0.05 C; 0.004 B 0.01 Y	8.97
TMS-75	3	12	2	5	6	6	–	6	–	0.1	–	–

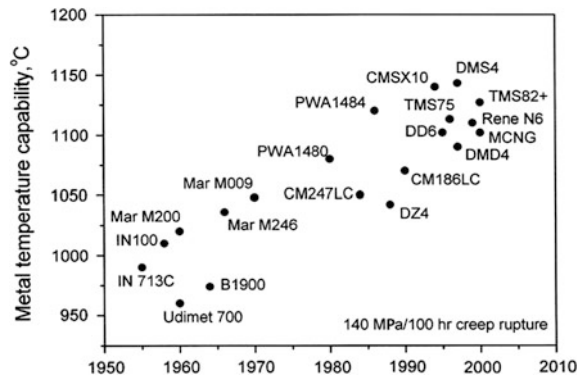
outstanding fatigue properties, with fatigue strengths that are a high fraction of the monotonic yield strength.

The variability (scatter) in fatigue lives increases at lower stresses and longer lives. This is also shown in Fig. 9.14, where fatigue lives at 593 °C vary between approximately 10⁶ cycles and 10⁹ cycles. The scatter is probably caused by differences in the fatigue crack initiation lives. In turn, these differences can be due to intrinsic variations in microstructure [65–69] and/or the infrequent presence of PM-induced discontinuities (defects). In cast alloys fatigue cracks may also initiate at porosity, carbides, or eutectic.

Table 9.9 Chemical compositions (wt%) of fourth, fifth, and sixth generation single crystal nickel-based superalloys

Alloy	Cr	Co	Mo	Re	W	Al	Ru	Ta	Hf	Others	Density (g/cm ³)	Alloy Generations
EPM-102	2	16.5	2	5.95	6.0	5.6	3.0	8.25	0.15	0.03 C	9.2	Fourth
										0.004 B		
										0.001 Y		
TMS-138	3.2	5.8	2.9	5	5.9	5.8	2.0	5.6	0.1	–	8.95	Fourth
Tms-138A	3.2	5.8	2.9	5.8	5.6	5.7	3.6	5.6	0.1	–	9.01	
TMS-162	3.0	5.8	3.9	4.9	5.8	5.8	6.0	5.6	0.1	–	9.04	Fifth
TMS-173	3.0	5.6	2.8	6.9	5.6	5.6	5.0	5.6	0.1	–	9.11	
TMS-196	4.6	5.6	2.4	6.4	5.0	5.6	5.0	5.6	0.1	–	9.01	
TMS-238	4.6	6.5	1.1	6.4	4.0	5.9	5.0	7.6	0.1	–		Sixth

Fig. 9.13 Illustration of the enhancement of creep performance of nickel-based superalloys from the 1950s to the present, owing to casting technology developments



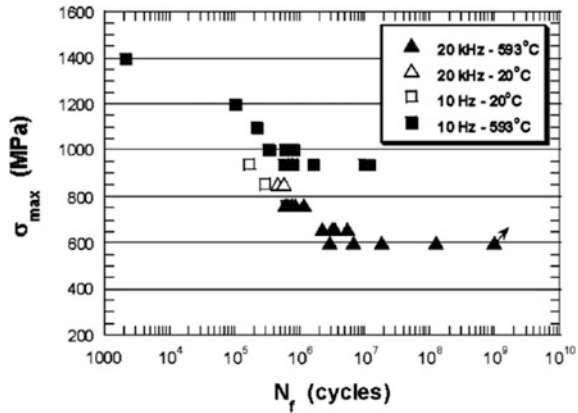
9.5.4 Fatigue Crack Growth

Fatigue crack propagation is also an important aspect of superalloy behaviour, particularly for turbine disc materials. So-called ‘Paris Law’ crack growth behaviour is displayed over a wide range of stress intensity factor ranges (ΔK) for most superalloys [66, 67, 69]. The fatigue crack growth threshold ΔK values (ΔK_{th}) [70] are relatively high and often above $8 \text{ MPa}\cdot\text{m}^{1/2}$.

The crack growth rates are sensitive to microstructural features, including grain sizes, precipitate sizes, and volume fractions of precipitates [70]. At temperatures above about $500 \text{ }^\circ\text{C}$ environmental and cycle frequency effects become significant factors, with higher crack growth rates in air than *in vacuo* or in inert environments [4].

In single crystal superalloys, cracks may grow crystallographically along $\{111\}$ planes, particularly in the early stages of growth (stage I) [7, 70]. Depending on

Fig. 9.14 Fatigue (S-N) behaviour of PM Rene 88 DT at 20 and 593 °C at a load ratio of 0.05 and frequencies of 10 Hz and 20 kHz. The arrow shows a specimen runout beyond 10^9 cycles



testing conditions, as cracks grow longer (stage II) there is a greater tendency toward mode I behaviour [68, 71].

Because fatigue and fatigue crack growth are often limiting properties, comprehensive models for life prediction that account for complex loading, crack initiation and crack growth, as well as microstructural and environmental effects, continue to be developed. The integration of physics-based models with advanced sensors that can diagnose the current “damage state” is a promising approach for life prediction [72].

9.6 Evolution of Advanced Nickel-Based Superalloys

In the case of cast superalloys, the introduction of directionally solidified (DS) columnar grained blades led to considerable increases in creep strength owing to the elimination of transverse grain boundaries. SC castings were developed during the 1970s and were a spin-off from the technological advances made in the DS casting processes. SC castings are produced in a similar fashion to DS by selecting a single grain via a grain selector, see Figs. 9.8 and 9.9. During solidification, this single grain grows to encompass the entire part.

Even more spectacular improvements in creep strength became possible for SC castings, since besides the total elimination of grain boundaries, the chemistries could be altered (rebalanced) to increase the solidus temperature beyond the γ' solvus. This avoided the formation of eutectic nodules and made it possible to use high temperature homogenization, with complete solutionizing of the γ' and subsequent formation of a uniform distribution of fine precipitates.

In slightly more detail, the exceptional properties of DS and SC alloys are due to [4, 11, 15]:

1. The alignment or elimination of any weak grain boundaries oriented transverse to the loading direction.
2. The low modulus associated with aligning the $\langle 100 \rangle$ crystallographic directions parallel to the blade or vane spans enhances the thermomechanical fatigue resistance in areas of constrained thermal expansion, particularly for turbine vanes.

In general, the lack of transverse grain boundaries coupled with the lower modulus can result in 3–5 times improvement in creep rupture life.

As should be evident from subsection 9.4.2, the manufacture of advanced SC blades is a high-precision casting process. Many of the early DS blades produced from the late 1960s were hollow, with air cooling channels about half a millimetre in diameter [3–5]. Today's SC blades often contain even more intricate cooling circuits, and the wall thickness can be as small as a few tenths of a millimetre. These developments have resulted in progressively higher operating temperatures, as was already shown in Fig. 9.13.

The SC superalloys are often classified into first, second, third, fourth, and fifth generation alloys. The evolution of these alloys is summarized in Sects. 9.6.1–9.6.6. Also, Tables 9.5, 9.6, 9.7, and 9.8 give the chemical compositions and densities of a few SC alloys from each generation.

9.6.1 First Generation Superalloys

These alloys were derived from wrought superalloys to take advantage of vacuum melting and casting introduced in the early 1950s. All these cast superalloys can be grouped into conventionally cast (CC), DS and SC superalloys.

Important aspects of alloy development toward improving the strength of the alloys include introduction of higher γ' contents, elimination of formation of deleterious phases such as σ and Laves phases using phase computation (PHACOMP [73] and Calphad [32–35]), improved castability through additions of Ta, increased additions of refractory solid solution strengtheners (such as W and Mo) to impart higher temperature capability, and addition of Hf (~ 2 wt%) to improve stress rupture ductility and minimize porosity via increased amounts of low melting point eutectic.

Subsequently, elimination of transverse grain boundaries by direct solidification (DS) of blades and vanes led to a further improvement in temperature capability. Although transverse grain boundary elimination was the original motivation for DS, it was the favoured $\langle 100 \rangle$ growth directions and improved heat treatment characteristics from which most benefits occurred. Alignment of a $\langle 100 \rangle$ direction along the blade span not only provided intrinsically high creep resistance, but also greatly improved the thermal fatigue life, since this is a low Young's modulus direction [4, 7, 9].

DS turbine blades and vanes began appearing in military and commercial aeroengines in the 1960s. A logical extension of eliminating transverse grain boundaries in DS technology was to remove grain boundaries altogether to produce SC blades and vanes.

9.6.2 *Second Generation Superalloys*

The development of second generation SC alloys [10–16], which are essentially rhenium (Re)-modified (~ 3 wt%, see Table 9.7), was marked by increased additions of refractory alloying elements, while maintaining a γ' volume fraction above 60 %.

Re is known to partition mainly to the γ -matrix, to retard γ' coarsening, and to increase the γ'/γ misfit. It is argued that some of the enhanced resistance to creep comes from the promotion of γ' 'rafting' by Re [14–16]. It is also claimed that Re reduces the overall diffusion rate in nickel-based superalloys [10–16].

In summary, the second generation SC alloys provide about a 30 °C metal operating temperature improvement, together with adequate resistance to oxidation, thermal fatigue and deleterious phase formation relative to the first generation SC alloys.

9.6.3 *Third Generation Superalloys*

The development of third generation superalloys [17–19] was marked by yet higher additions of Re (~ 6 wt%, see Table 9.8) due to its dual role of improving creep strength as well as environmental resistance in spite of a low Cr level. Development of these alloys has led to yet another 30 °C improvement in metal operating temperature capability, this time relative to the second generation superalloys. Some examples follow:

1. Cannon Muskegon Corporation, USA, optimized their third generation SC alloy CMSX10 employing total refractory elements of about 20 wt%, with 6 wt% Re after tailoring the Cr, Co, and W levels to 2, 3, and 5 wt%, respectively [17, 18].
2. GE designed an SC superalloy, Rene 6, with optimized composition to have a good balance between stress rupture strength and microstructural stability [19]. This overcame the problem of TCP formation in CMSX10 during long-term exposure at higher temperature.
3. An SC superalloy DMS4 [74] was developed at DMRL, India, by pushing the total refractory element content to 22 wt%, with about 6.5 wt% Re and removing Mo and Ti completely. This alloy exhibits superior strength together with good castability, alloy phase stability, and environmental resistance.

4. Further, a columnar grained superalloy DMD4 [74] was derived from the DMS4 alloy for cost competitive production of complex turbine airfoils, which are difficult to cast in SC form. The alloy composition has been tailored by replacing some of the Ta with Hf and incorporating C and B for grain boundary strengthening. The alloy also had good phase stability, environmental resistance, and creep rupture properties close to those of the *second generation SC* superalloy CMSX-4.

9.6.4 Fourth Generation Superalloys

The fourth generation superalloys, Table 9.9, were developed by the additions of platinum group metals (PGMs), especially ruthenium (Ru), to third generation superalloys to further improve the phase stability in the presence of higher refractory element contents, thereby improving the strength [20–23]. Further, the higher negative γ/γ' misfit resulted in γ' rafting perpendicular to the applied stress, thereby acting as a barrier to deformation under high temperature and low stress conditions.

9.6.5 Fifth Generation Superalloys

The fifth generation superalloys [24, 25] was developed with yet higher Ru contents (≥ 6 wt%). TMS-162 and TMS-172 are the first two fifth generation SC superalloys (Table 9.9) developed by the National Institute of Materials Science (NIMS) [25] and have excellent creep resistance.

Higher Ru contents (≥ 5 wt%) allow higher Mo and Re additions in TMS-162 and TMS-173, respectively. Higher lattice misfit and further solid solution strengthening by Mo and Re as well as Ru, and improved phase stability by Ru can all contribute to superior creep resistance over the previous generations. However, the lower Cr content of these two alloys has resulted in poorer oxidation resistance at elevated temperatures, owing to vaporization of Ru and Re oxides [25].

On the other hand, another fifth generation superalloy, TMS-196, with a moderate amount of Cr, exhibits acceptable oxidation resistance similar to that of Rene N5. Also, TMS-196 possesses better microstructural stability and shows significant improvements in creep resistance and thermal fatigue properties over the current commercial superalloys such as CMSX-4, CMSX-10, PWA1484, and Rene N5 [25].

9.6.6 Sixth Generation Superalloys

As can be seen from Table 9.9, the fifth generation SC superalloy TMS-196 has higher contents of Re and Ru as compared to the fourth generation superalloy TMS-138A. These changes were made in order to obtain better mechanical properties [26]. TMS-196 also has better oxidation properties due to its higher Cr content.

Continuing the developments, NIMS have recently developed yet another advanced alloy, TMS-238, with mechanical properties similar to those of TMS-196 but with improved oxidation and hot corrosion resistance.

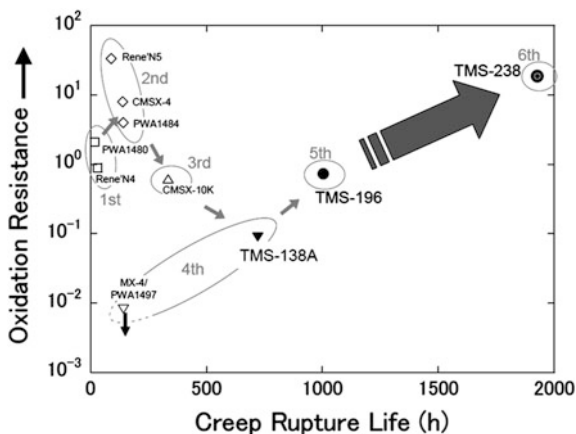
For TMS-238 the Mo and W contents were reduced and the Co and Ta contents were increased, as can be seen in Table 9.9. The tensile properties of this sixth generation superalloy are given in Table 9.10, and it is claimed that these properties are superior to those of all other generations of superalloys.

The creep rupture properties of TMS-238 at 800, 900, and 1000 °C are comparable to those of TMS-138A and TMS-196, but at 1100 °C TMS-238 is superior, see Fig. 9.15. TMS-238 alloy also has superior oxidation properties, and thus an unmatched combination of mechanical and environmental properties [26].

Table 9.10 Tensile properties of various generations of single crystal nickel-based superalloys

Alloy and generation	400 °C		750 °C	
	0.2 % yield strength (MPa)	UTS (MPa)	0.2 % yield strength (MPa)	UTS (MPa)
CMSX-4: II	860	950	950	1150
TMS-138A: IV	830	906	868	1241
TMS-196: V	879	1214	845	1308
TMS-238: VI	925	1373	1041	1348

Fig. 9.15 Comparison among different generations of nickel-based superalloys in terms of 1100 °C/137 MPa creep and 1100 °C oxidation resistance [26]



9.7 Concluding Remarks

The ordered gamma prime (γ'), which is the main source of strengthening, endows nickel-based superalloys with exceptional performance and renders them superior to most of the other high temperature structural alloys. This is because γ' is stable up to temperatures of 1000 °C and can directionally coarsen under service conditions for enhanced creep resistance.

The performances of the superalloys have progressively improved by controlling chemistry and microstructure, and by innovative processing technologies. Surface modification by application of coating technology concurrent with the introduction of directionally solidified (DS) structures and then single crystals (SCs), has extended the useful temperature range of superalloys. In spite of considerable recent efforts toward developing other materials such as intermetallics, ceramics, and their composites for engine applications, nickel-based superalloys continue to be the most reliable materials for hot sections of turbines.

Six generations of SC nickel-based superalloys with improved creep properties and phase stability have already been developed. Therefore it appears that the evolution of advanced nickel-based superalloys is a never-ending process, and their replacement in turbine engine applications seems to be impossible at least for the next few decades.

Acknowledgments The authors acknowledge Dr. R. J. H. Wanhill for many useful and critical comments. They are thankful to the Director, DMRL, for his permission to publish this present work, and DRDO for financial support.

References

1. Betteridge W (1974) The Nimonic alloys, and other Nickel-base high temperature alloys. In: Betteridge W, Heslop J (eds) Edward Arnold, London, UK
2. Sims CT, Stoloff NS, Hagel WC (1987) Superalloys II. Wiley, Hoboken, NJ, USA
3. Meetham GW, Van de Voorde MH (2000) Materials for high temperature engineering applications. Springer-Verlag, Berlin, Germany
4. Donachie MJ, Donachie SJ (2002) Superalloys: a technical guide, 2nd edn. ASM International. Materials Park, OH, USA
5. Reed RC (2006) The superalloys: fundamentals and applications. Cambridge University Press, Cambridge, UK
6. Mukhtinalapati NR (2011) Materials for gas turbines—an overview, advances in gas turbine technology. Benini E (ed). Intech Open Source Publisher: book.department@intechopen.com, pp 293–314
7. MacKay A, Gabb TP, Smialek JL, Nathal MV (2009) Alloy design challenge: development of low density superalloys for turbine blade applications. Rebecca Glenn Research Center, Cleveland, Ohio 44135, NASA/TM—2009-215819
8. Caron P, Khan T, Evolution of Ni-based superalloys for single crystal gas turbine blade applications. *Aerosp Sci Technol* 3(8):513–523
9. Khan T (1986) High temperature alloys for gas turbines and other applications. In: Betz W et al (eds) D. Reidel Publishing Company, Dordrecht, Holland, p 21

10. Cetel AD, Duhl DN (1992) Second generation columnar grain Nickel-base superalloy. In: Antolo SD, Stusrud RW, MacKay RA, Anton L, Khan T, Kissinger RD, Klarstrom L (eds) *Superalloys 1992*, TMS, Warrendale, PA, USA, pp 287–296
11. Pollock TM, Tin S (2006) *Propulsion and power*, vol 22, 2, p 361
12. Diego Colombo (2006–2007) Nickel-based superalloys and their application in the aircraft industry. Anno accademico, Università Deglistudi Di Trento, Italy
13. Caron P, Lavigne O (2011) Recent studies at onera on superalloys for single crystal turbine blades. *J Aerosp Lab* 3, pp 1–14
14. Second Generation single crystal superalloy(Developed under NIMS1/Toshiba2 collaboration), High Temperature Materials Group, Materials Engineering Laboratory (MEL), National Institute for Materials Science(NIMS), Japan, August, 2004
15. Li JR, Zhong ZG, Tang DZ, Liu SZ, Wei P, Wei PY, Wu ZT, Huang D, Han M (2000) A Low-cost second generation single crystal superalloy DD6. In: Pollock TM, Kissinger RD, Bowman RR, Green KA, McLean S, Olson, Schina JJ (eds) *Superalloys 2000*, TMS, Warrendale, PA, USA, pp 777–783
16. Cetel AD, Duhl DN (1988) Second generation nickel base single crystal superalloy. In: Reichman S, Ihhl DN, Maurer G, Antolovich, S, Lund C (eds) *Superalloys 1988*, TMS, Warrendale, PA, USA, pp 235–244
17. Ericson Gary L, JOM BS (2006) A new third generation, single crystal, casting superalloy 47 (5):36–39
18. Walston S, O'Hara, KS, Ross EW, Pollock TM, Murphy WH (1996) RENE N6: third generation single crystal superalloy. In: Kissinger RD, Deye DJ, Anton DL, C&I AD, Nathal MV, Pollo TM, Woodford DA (eds) *Superalloys 1996*, TMS, Warrendale, PA, USA, pp 27–34
19. Caron P, Khan T (1996) Evolution of Ni-based superalloys for single crystal gas turbine blade applications. Office National d'Etudeset de Recherches Aérospatiales (ONERA), BP72 - 92322, Châtillon Cedex, France
20. Zietara M, Ceteland A, Czyska-Filemonowicz A (2011), Microstructure stability of 4th generation single crystal superalloy, pwa 1497, during high temperature creep deformation. *Materials Transactions*, vol 52, no 3, pp 336–339
21. Walston S, Cetel A, MacKay R, O'Hara K, Duhl D, Dreshfield R (2004) Joint development of a fourth generation single crystal superalloy. In : 10th international symposium on superalloys cosponsored by the seven springs international symposium committee. The Minerals, Metals, and Materials Society (TMS), the TMS High Temperature Alloys Committee, and ASM International Champion, PA, USA, pp 19–23
22. Kawagishi Kyoko, Harada Hiroshi, Sato Akihiro, Kobayashi Toshiharu (2006) *JOM* 58 (1):43–46
23. Sato A, Yeh AC, Kobayashi T, Yokokawa T, Harada H, Murakumo T, Zhang JX (2007) *Energy materials* 2(1):19–25
24. Sato A, Harada H, Yeh A-C, Kawagishi K, Kobayashi T, Koizumi Y, Tadaharu Y, Zhang J-X (2008) A 5th generation SC superalloy with balanced high temperature properties and processability. In: Reed RC, Green KA, Caron P, Gabb, Fahrman MG, Huron ES, Wodard SA (eds) *Superalloys 2008*, TMS, Warrendale, PA, USA, pp 131–138
25. Nickel base single crystal superalloys, TMS-196, July, 2008, High temperature materials center, National Institute for Materials Science, Japan
26. Kawagishi K, Yeh A-C, Yokokawa T, Kobayashi T, Koizumi Y, Harada H (2012) Development of an oxidation resistant high strength sixth generation SC superalloy. In: 12th international symposium on superalloys. In: Huron ES, Reed RC, Hardy MC, Mills MJ, Montero RE, Portella PD, Telesman J (eds) TMS, Warrendale, PA, USA, pp 189–195
27. Ross EW (1967) Rene 100-a sigma-free turbine blade alloy. *J Met* 19(12):12–14
28. Nystrom JD, Nystrom TM, Murphy WH, Garg A (1997) Discontinuous cellular precipitation in a high-refractory nickel-base superalloy. *Metall Mater Trans* 28A:2443–2452
29. Wlodek ST (1964) The structure of IN100. *Trans ASM* 57:110–119

30. Rae CMF, Reed RC (2001) The precipitation of topologically close-packed phases in rhenium-containing superalloys. *Acta Mater* 49(10):4113–4125
31. Darolia R, Lahrman DF, Field RD (1988) Formation of topologically closed packed phases in nickel base single crystal superalloys. TMS, Warrendale, PA, USA, pp 255–264
32. Agren J (1996) Calculation of phase diagrams: Calphad. *Curr Opin Solid State Mater Sci* 1:355–360
33. Kattner UR (1997) Thermodynamic modeling of multicomponent phase equilibria. *J Met* 49(12):14–19
34. Saunders N, Fahrman M, Small CJ (2000) The application of CALPHAD calculations to Ni-Based superalloys. *Superalloys 2000*. TMS, Warrendale, PA, USA, pp 803–811
35. Wu K, Chang YA, Wang Y (2004) Simulating interdiffusion microstructures in Ni–Al–Cr diffusion couples: a phase field approach coupled with calphad database. *Scripta Materialia* 50:1145–1150
36. Schilke PW (2004) Advanced gas turbine materials and coatings. Available at www.Gepower.com/prod-serv/products/tech-docs/en/downloads/ger3569.pdf
37. Loria ED (1989) Proceedings of conference on superalloy 718—metallurgy and applications, TMS, Warrendale, PA, USA
38. Loria ED (1991) Proceedings of conference on superalloy 718, 625 and various derivatives. TMS, Warrendale, PA, USA
39. Loria ED (1994) Superalloys 718, 625, and various derivatives. The Minerals, Metals & Materials Society, Warrendale, PA, USA
40. Loria ED (1997) Superalloys 718, 625, 706 and various derivatives. The Minerals, Metals & Materials Society. Warrendale, PA, USA
41. Loria ED (2001) Proceedings of the fifth international conference on superalloys 718, 625, 706 and various derivatives. TMS, Warrendale, PA, USA
42. Loria ED (2005) Proceedings of sixth international symposium on superalloys 718, 625, 706 and derivatives. TMS, Warrendale, PA, USA
43. Furrer D, Fecht H (1999) *JOM*, vol 51, 1, pp 14–17
44. Das N, *Trans. IIM*, vol 63, 210, pp 265–274
45. Tien JK, Caulfield T (1988) *Superalloys, supercomposites and superceramics*. Academic Press, New York, USA
46. Tin S, Pollock TM, Murphy W (2001) Stabilization of thermosolutal convective instabilities in Ni-based single crystal superalloys: carbon additions and freckle formation. *Metall Mater Trans* 32A(7):1743–1753
47. Tin S, Pollock TM (2004) Predicting freckle formation in single crystal Ni-base superalloys. *J Mater Sci* 39(24):7199–7205
48. Beckermann C, Gu JP, Boettinger WJ (2000) Development of a freckle predictor via rayleigh number method for single-crystal superalloy castings. *Metall Mater Trans* 31A(10):2545–2557
49. Wang W, Lee PD, McLean M (2003) A model of solidification microstructures in Nickel-Based superalloys: Predicting primary dendrite spacing selection. *Acta Mater* 51(10):2971–2987
50. Pollock TM, Murphy WH (1996) The breakdown of solidification in high refractory nickel-base superalloys. *Metall Mater Trans* 27A(4):1081–1094
51. Giamei AF, Kear BH (1970) Nature of freckles in nickel-base superalloys. *Metall Trans A* 1:2185–2192
52. Copley SM, Giamei AF, Johnson SM, Hornbecker MF (1970) Origin of freckles in unidirectionally solidified castings. *Metall Trans A* 1(8):2193–2204
53. Giamei AF, Tschinkel JG (1976) Liquid metal cooling—a new solidification technique. *Metall Trans A* 7A:1427–1434
54. Elliott AJ, Tin S, King WT, Huang SC, Gigliotti MFX, Pollock TM (2004) Directional solidification of large superalloy castings with radiation and liquid-metal cooling: a comparative assessment. *Metall Mater Trans A* 35A(10):3221–3231
55. Huron ES (1992) Serrated yielding in a nickel-base superalloy. TMS, Warrendale, PA, USA, pp 675–684

56. Pollock TM, Field RD (2002) Dislocations and high temperature plastic deformation of superalloy single crystals. In: Nabarro FRN, Duesbery MS (eds) *Dislocations in solids*, vol 11. Elsevier, Amsterdam, pp 549–618
57. Yoo MH (1986) *Scripta Metallurgica* 20:915–920
58. Kear BH, Wilsdorf HGF (1962) *Trans Metall Soc AIME* 224:382–386
59. Copley SM, Kear BH (1967) *Trans AIME* 239:984–992
60. Murakumo T, Kobayashi T, Koizumi Y, Harada H (2004) Creep of Ni-base single-crystal superalloys with various gamma volume fraction. *Acta Mater* 52(12):3737–3744
61. Karunarante MSA, Reed RC (2003) Interdiffusion of platinum-group metals in nickel at elevated temperatures. *Acta Mater* 51(10):2905–2914
62. Reed RC, Karunarantne MSA (2000) Interdiffusion in the face-centered cubic Phase of Ni–Re, Ni–Ta and Ni–W systems between 900 °C and 1300 °C. *Mater Sci Eng A* 281(1–2):229–233
63. Walston WS, Cetel A, MacKay R, O’Hara K, Duhl D, Dreshfield R, Joint development of a fourth generation single crystal superalloy. TMS, Warrendale, PA, USA, pp 15–24
64. Tanaka R (2000) Research and development of ultra-high temperature materials in Japan. *Mater High Temp* 17(4):457–464
65. Shyam A, Torbet CJ, Jha SK, Larsen JM, Caton MJ, Szczepanski CJ, Pollock TM, Jones JW (2004) Development of ultrasonic fatigue for rapid, high temperature fatigue studies in turbine engine materials. TMS, Warrendale, PA, USA, pp 259–267
66. Miner RV, Gayada J, Maier RD (1982) Fatigue and creep fatigue deformation of several nickel-base superalloys at 650 °C. *Metall Trans A* 13A(10):1755–1765
67. Clavel M, Pineau A (1982) Fatigue behavior of two nickel-base alloys: Experimental results on low cycle fatigue, fatigue crack propagation and substructures. *Mater Sci Eng* 55(2):157–171
68. Chan KS, Hack JE, Leverant GR (1987) Fatigue crack growth in mar-m200 single crystals. *Metall Trans* 18A(4):581–591
69. Antolovich SD, Lerch B (1989) Cyclic deformation, fatigue and fatigue crack propagation in Ni-base alloys. In: Tien JK, Caulfield T (eds) *Superalloys, supercomposites and superceramic*. Academic Press, New York, USA, pp 363–412
70. Wright PK, Jain M, Cameron D (2004) High cycle fatigue in a single crystal superalloy: time dependence at elevated temperature. TMS, Warrendale, PA, pp 657–666
71. Crompton JS, Martin JW (1984) Crack growth in a single crystal superalloy at elevated temperature. *Metall Trans A* 15A:1711–1718
72. Larsen JM, Christodoulou (2004) Using materials prognosis to maximize the utilization of complex mechanical systems. *J Met* 56(3):15–28
73. Saunders N (1995) *Phil Trans R Soc Lond A* 351:543–561
74. Das N (2008) Unpublished work, DMRL, Hyderabad, India

Chapter 10

Structural Intermetallics

R. Mitra and R.J.H. Wanhill

Abstract Development of materials for structural applications at elevated temperatures in aeroengines has encouraged research on intermetallic alloys. A select group of aluminides and silicides has shown significant promise for high temperature structural applications owing to their high melting temperatures, as well as their ability to retain strength and oxidation resistance at elevated temperatures. In recent years the focus is on multiphase multicomponent intermetallic alloys with significant volume fractions of ductile constituents to achieve an optimum combination of toughness and elevated temperature strength. The engineering properties and actual or potential aerospace applications of the currently most important structural intermetallics, the nickel, iron, and titanium aluminides, are concisely discussed.

Keywords Intermetallics · Nickel aluminides · Titanium aluminides · Iron aluminides · Molybdenum silicides · Niobium silicides · Processing · Properties · Applications

10.1 Introduction

Intermetallics with high melting points are of interest for structural applications in aeroengine and automotive components, and also nuclear and power generation equipment requiring strength retention at elevated temperatures. Intermetallics are either compounds with fixed stoichiometric ratios between the metals, or phases having an extended range of compositions that may vary with temperature.

Stoichiometric intermetallics consist of strictly periodic arrangements of atoms. The formation and evolution of intermetallic phases in the microstructure depends

R. Mitra (✉)
IIT-Kharagpur, Kharagpur, India
e-mail: rahul@metal.iitkgp.ernet.in

R.J.H. Wanhill
Emmeloord, Flevoland, The Netherlands

on their thermodynamic stability. However, metastable phases with inhomogeneous compositions are often formed during solidification, and the equilibrium phases are subsequently obtained by a suitable heat treatment.

Much research has concentrated on development of intermetallics for various structural and functional applications. The properties of interest for high temperature aerospace applications are high melting point, strength retention, ductility, and resistance to environmental degradation.

This chapter provides a concise overview of the structural intermetallics based on aluminides and silicides. These have received the most attention over the past three decades owing to their promise for elevated temperature use.

For overviews and details of the fundamentals regarding phase equilibria, processing, structure, and properties of intermetallics as well as development of selected intermetallic types, the reader is referred to Refs. [1–7].

10.2 Crystal Structures and Compositions of Selected Intermetallics

The typical crystal structures, space-groups, and lattice constants of some of the structural intermetallics are shown in Table 10.1 [6].

Table 10.1 Nominal compositions and crystal structures of selected intermetallics [6]

Composition	Crystal structure	Structure symbol and space group	Lattice constants (nm)
NiAl	Body-centered cubic	B2 (cP2), Pm-3m	0.2887
Ni ₃ Al	Face-centered cubic	L1 ₂ (cP4)	$a = 0.356$
Al ₃ Ti	Tetragonal	D0 ₂₂ (tI8), I4/mmm	$a = 0.3809$; $c = 0.847$
TiAl	Face-centered tetragonal	L1 ₀ (tP4), P4/mmm	$a = 0.3997$; $c = 0.4081$
Ti ₃ Al	Hexagonal	D0 ₁₉ (hP8), P6 ₃ /mmc	$a = 0.5729$; $c = 0.4574$
Fe ₃ Al	Face-centered cubic	D0 ₃ (cF16), Fm3m	0.5655
FeAl	Body-centered cubic	B2 (cP2), Pm-3m	0.291
MoSi ₂	Body-centered tetragonal	C11 _b (tI6), I4/mmm	$a = 0.3202$; $c = 0.7845$
Mo ₅ Si ₃	Body-centered tetragonal	D8 _m (tI32), I4/mcm	$a = 0.959$; $c = 0.487$
Mo ₃ Si	Cubic	A15 (cP8), Pm3n	0.4892
Mo ₅ SiB ₂	Body-centered tetragonal	D8 ₁ (tI32), I4/mcm	$a = 0.6013$; $c = 1.103$
Mo(Si,Al) ₂	Hexagonal	C40 (hP9), P6 ₂ 22	$a = 4.644$; $c = 6.548$
NbSi ₂	Hexagonal	C40 (hP9), P6 ₂ 22	$a = 4.7971$; $c = 6.592$
Nb ₅ Si ₃	Body-centered tetragonal	α : D8 ₁ (tI32) β : D8 _m , I4/mcm	$a = 0.656$; $b = 1.187$ $a = 1.0$; $b = 0.507$

10.2.1 Nickel Aluminides

The Ni–Al binary system contains the following intermetallic phases starting from the Al-rich side: Al_3Ni , Al_3Ni_2 , AlNi (or NiAl), Al_3Ni_5 , and AlNi_3 (or Ni_3Al) [7, 8], see Fig. 10.1. NiAl and Ni_3Al are the most important, owing to their high melting/liquidus temperatures:

- NiAl has a wide temperature-dependent homogeneous phase field ranging from 40–69 at.% Ni, with the highest congruent melting point (1638 °C) at the stoichiometric composition (50:50 at.%).
- Ni_3Al has a homogeneity range of ≈ 4.5 at.% around its stoichiometric composition, and a melting point of 1395 °C at the stoichiometric composition.

Table 10.1 shows that NiAl has an ordered body-centered structure (B2, cP2), whereas Ni_3Al has an ordered face-centered cubic (fcc) structure (L1_2 , cP4). The ordered structure in NiAl remains stable even above $0.65T_M$ (melting point temperature in K). This is attributed to strong covalent bonding along $\langle 111 \rangle$ directions between the nearest neighbour Ni–Al atom pairs [9]. This bonding is accompanied by weak ionic repulsion between second nearest neighbour atoms along $\langle 100 \rangle$.

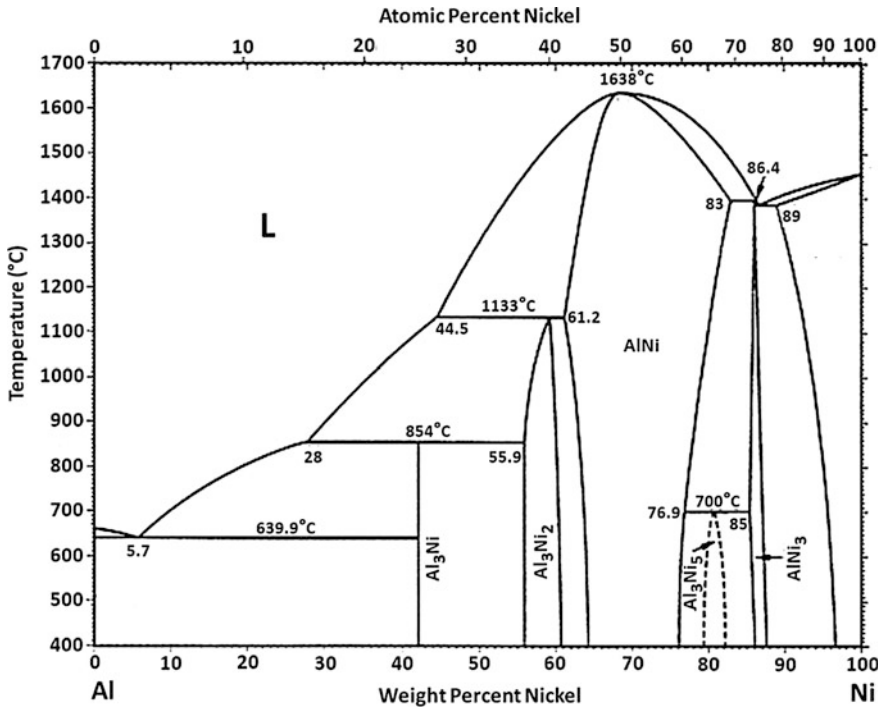


Fig. 10.1 Ni–Al phase diagram: after [7]

Both types of directional bonds are superimposed upon the nondirectional metallic bonds between unlike and similar metallic atoms and are responsible for the elastic anisotropy of NiAl.

10.2.2 Titanium Aluminides

The Ti–Al binary system contains three intermetallic phases, Al_3Ti , TiAl , and Ti_3Al [10], with a posited Ti_2Al phase at 66 at.% Al, see Fig. 10.2. Only TiAl (γ TiAl alloys) and Ti_3Al (α -2 alloys) are of engineering importance.

Ti–Al: The binary intermetallic exists over a wide range (49–66 at.% Al) of temperature-dependent stability, and apparently remains ordered up to its melting point of about 1450 °C [7].

The γ alloys of engineering importance contain about 45–48 at.% Al and 1–10 at.% M, where $M = \text{V}$, Cr , Mn , Nb , Ta , or W , or combinations of some of these elements. These γ alloys may be divided into two categories: single-phase (γ) and two-phase ($\gamma + \alpha$ -2).

The single-phase alloys contain additional alloying elements such as Nb or Ta to improve strength and oxidation resistance. Two-phase alloys have additions of V , Cr , and Mn to increase ductility; Nb and Ta for increased oxidation resistance; or combinations of these elements to improve both ductility and oxidation resistance [7]. The maximum temperature capability, above which protective coatings must be used, is about 750–800 °C, depending on long- or short-term applications, e.g. in gas turbines or missile fins [7].

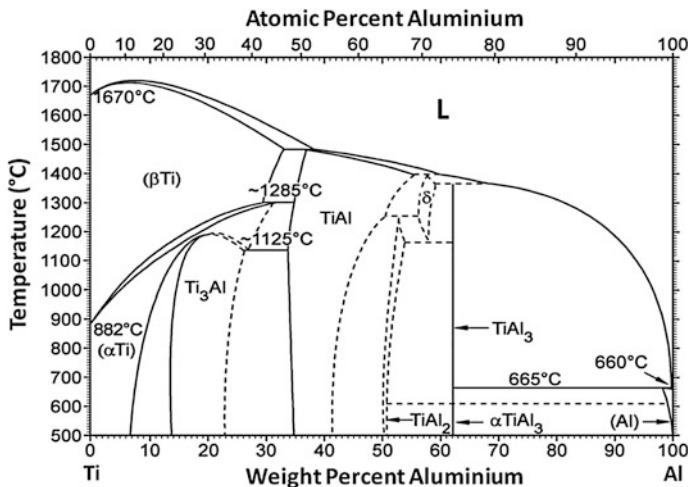


Fig. 10.2 Ti–Al phase diagram: after [7]

Ti₃Al: As shown in Fig. 10.2, the α -2 alloy has a wide range (22–39 at.%) of compositional stability. The stoichiometric composition (Ti-25 at.% Al) is stable up to about 1090 °C [7], while the limit of ordering in any composition is about 1180 °C [11].

The hexagonal crystal structure (see Table 10.1) is retained when small amounts of alloying additions (Nb, V, Mo) are made to improve creep resistance while retaining an Al content \approx 25 at.% [7]. However, additions of Nb above about 10 at.% result in a change to an ordered orthorhombic structure based on the O phase (Ti₂AlNb).

The incentives for higher alloying and changing the crystal structure are significant improvements in strength and ductility over a wide range of temperatures, though at the expense of maximum temperature capability (about 650 °C) [7].

These Ti–Al–Nb alloys have been studied for several decades and can be classified according to the amount of β -stabilizers (Nb, Mo, Ta and V) [11] as:

- (1) 10–12 at.% Nb. These alloys have two-phase microstructures consisting of α -2 and β or B2 (disordered or ordered bcc phase).
- (2) 14–17 at.% Nb. These alloys contain three phases: α -2, β (or B2), and O.
- (3) 25–30 at.% β -stabilizers. These alloys are reported to have two-phase microstructures consisting of β (or B2) and O.

10.2.3 Iron Aluminides

The Fe–Al binary system contains the following intermetallic phases starting from the Fe-rich side: Fe₃Al, FeAl, FeAl₂, Fe₂Al₃, Fe₂Al₅, and FeAl₃. [7, 12], see Fig. 10.3. Only Fe₃Al and FeAl are of interest for structural applications, since the rest are very brittle.

Fe₃Al: This intermetallic has an ordered fcc D0₃ structure up to 540 °C, and then an ordered body-centered cubic B2 structure up to 760 °C [7]. Above this temperature the B2 structure becomes disordered.

The D0₃ \rightarrow B2 transition temperature decreases with increasing Al content above 25 at.%, and only the B2 structure is stable at Al contents above 36 at.% [7]. The most commonly used composition is Fe-28 at.% Al.

FeAl: This ordered B2 phase has a wide range of compositional stability, approximately 30–50 at.% Al, as may be seen from Fig. 10.3. The most commonly used composition is Fe-40 at.% Al.

10.2.4 Molybdenum Silicides

The Mo–Si binary phase diagram shows the presence of two stoichiometric compounds with compositions Mo₃Si and MoSi₂; and the compound Mo₅Si₃, which has

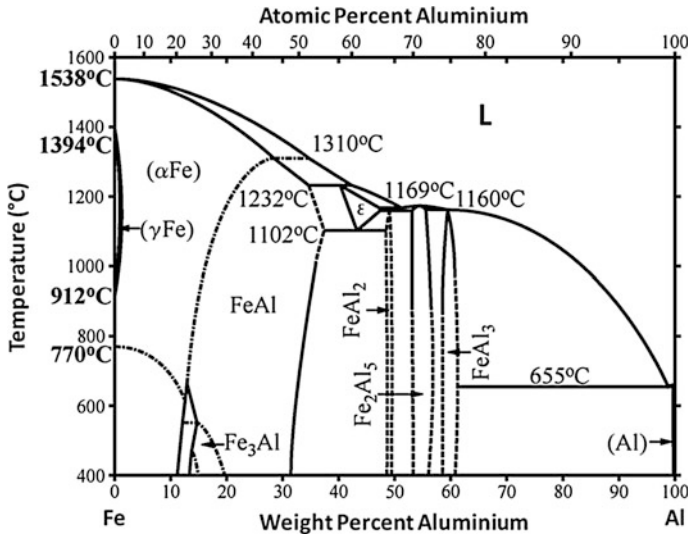


Fig. 10.3 Fe–Al phase diagram: after [7]

a homogeneity range of 3 at.% Si [13], see Fig. 10.4. Most interest for practical applications has been directed to MoSi₂ itself and Mo–Si–B alloys containing Mo, Mo₃Si, and Mo₅SiB₂.

MoSi₂: This has an ordered body-centered tetragonal structure up to 1900 °C. It is attractive because of its high temperature capabilities, but is very hard and brittle at ambient temperatures.

R&D on this compound for structural applications has been directed toward rather exotic high temperature composite materials with MoSi₂ as matrix, and ceramic or refractory metal reinforcements [7].

Mo–Si–B alloys: These have potential for advanced gas turbine engines with turbine entry temperatures (TET) beyond the capabilities of nickel-base superalloys [14].

As an example, Fig. 10.5 shows the Mo-rich section of the ternary isothermal phase diagram [14] of the Mo–Si–B system at 1600 °C, indicating the various phases. The ternary alloys can be designed to have the optimum volume fractions of Mo_{ss} (Mo-solid solution), Mo₃Si, and Mo₅SiB₂ phases. All three phases have nearly fixed composition with limited solubility for other elements, and they therefore provide microstructural stability at high temperatures.

10.2.5 Niobium Silicides

The Nb–Si binary phase diagram shows the presence of two intermetallic compounds with compositions Nb₅Si₃ and NbSi₂, see Fig. 10.6. Nb₅Si₃ has a very

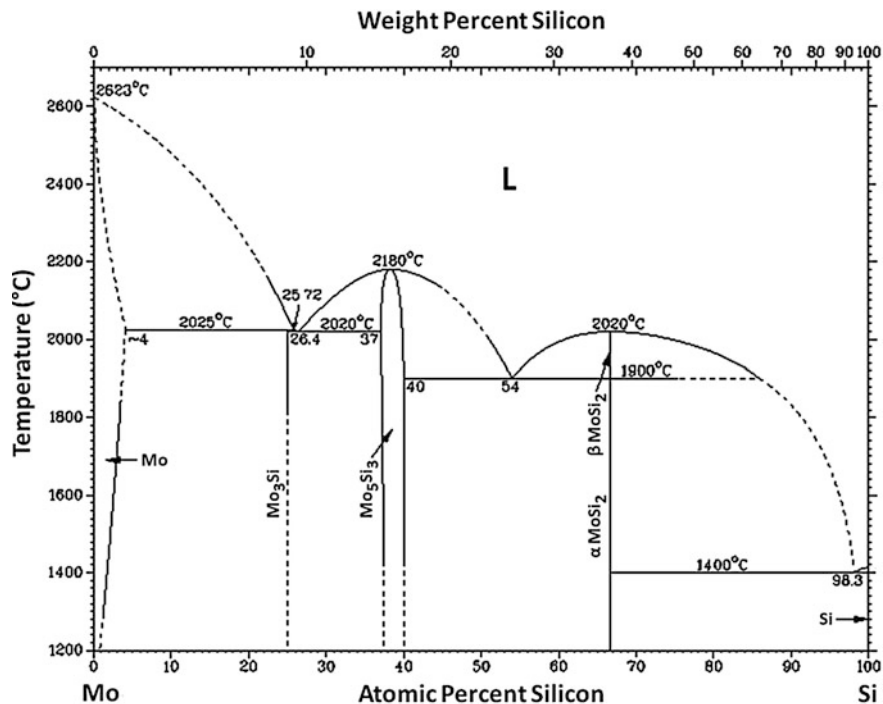
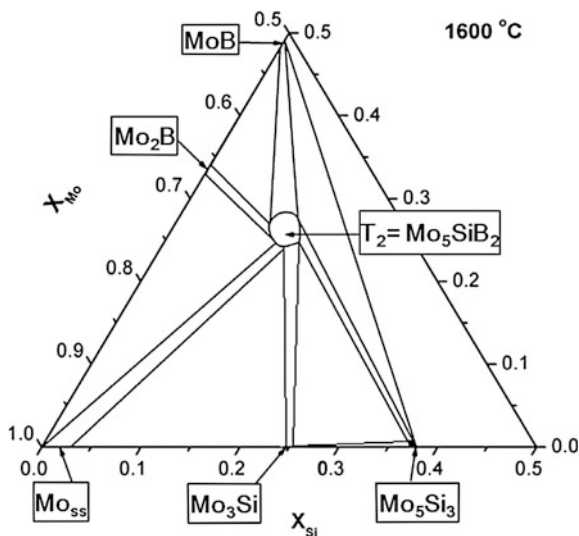


Fig. 10.4 Mo-Si phase diagram: after [13]

Fig. 10.5 Mo-Si-B isothermal section for Mo-rich compositions for Mo-rich compositions at 1600 °C [14]



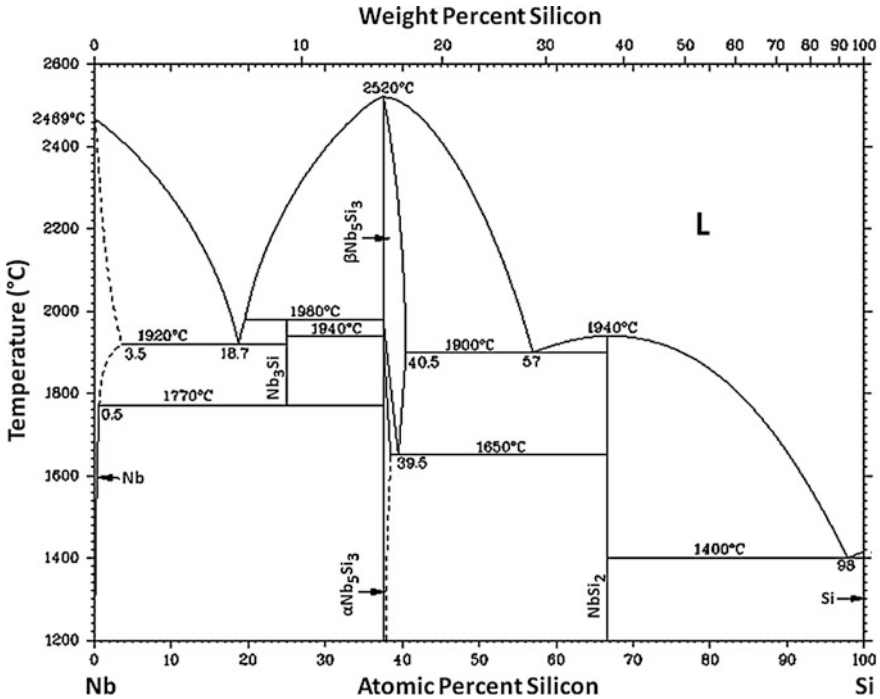


Fig. 10.6 Nb–Si phase diagram: after [15]

small homogeneity range at lower temperatures ($\alpha\text{Nb}_5\text{Si}_3$) and a homogeneity range of about 3 at.% Si when changed to $\beta\text{Nb}_5\text{Si}_3$. A eutectoid reaction at around 1770 °C leads to decomposition of the Nb_3Si phase into Nb solid solution (Nb_{ss}) and Nb_5Si_3 .

As in the case of molybdenum silicide alloys, the niobium silicide alloys have potential to replace nickel-base superalloys in advanced gas turbines. Since the monolithic phase Nb_5Si_3 is very brittle at ambient temperatures, multiphase composites are envisaged based on Nb_5Si_3 alloyed with other elements (e.g. Ti) and employing a ductile niobium solid solution (Nb_{ss}) as the matrix [16]. This is ongoing R&D, with actual applications still in the future.

10.3 Processing

General information: Bulk intermetallics can be processed by conventional ingot metallurgy (IM) and powder metallurgy (PM) routes, as well as by rapid solidification processing (RSP). Coatings are prepared by various methods including electron beam physical vapour deposition (EB-PVD), which has become

increasingly favoured for aerospace-quality coatings on gas turbine and other components. The coatings are generally of the NiCoCrAlY (oxidation resistant) or CoCrAlY (hot corrosion resistant) types.

The purity of raw materials and the processing route control the final impurity content, and also influence the microstructural evolution, thereby influencing the properties. Special methods of processing have been developed to control the impurity levels, the grain sizes, and the sizes of dispersed phases, all of which affect the mechanical properties

IM processing: The ingot metallurgy processing methods include arc-melting [17], induction skull melting [18], single crystal growth [19], directional solidification [20], and investment casting [21].

There are also several special techniques to produce in situ composites [22]. These are not limited to intermetallics and are currently more in the developmental stage than ready for actual production.

PM processing: The powder metallurgy processing methods involve consolidation of the powders to form densified intermetallic alloys of a specified composition. The powders can have either the specified composition of the intermetallic alloy, or be synthesized reactively from elemental precursors.

For some intermetallic alloys reactive synthesis of elemental powders is combined with uniaxial hot pressing or hot isostatic pressing (HIP). A reaction is started by applying heat in the form of a laser pulse or electric discharge to one surface of the elemental powder compact [23]. The reactions during synthesis are exothermic and release sufficient heat to drive them to completion. If the reaction initiation temperature is higher than the melting point of one of the reactant elements, then the presence of a transient liquid phase enhances the reaction kinetics and the process of densification, as occurs for nickel aluminides.

RSP methods: These include both the formation of powders for PM processing and thermal spray deposition on a substrate. Thermal spray deposition has some applications for bulk products and coatings, e.g. the ‘Osprey’ process [24], but the quality is insufficient for aerospace bulk products and also coatings on critical components such as high pressure turbine blades and vanes.

Secondary fabrication: Nickel, iron, and titanium aluminides can be fabricated by IM and PM, and also as castings [7, 25]. Iron and titanium aluminide ingots can be conventionally hot-rolled, but nickel aluminide ingots must be isothermally forged since there is only a narrow temperature window before the ingot surfaces cool to become brittle and crack [7]. However, conventional (secondary) hot forging is feasible for fine-grained nickel aluminides [7].

PM consolidation can be done, e.g. by steel-canning and hot forging or extrusion, and also by HIP followed by forging or extrusion.

10.4 Properties of Ni-, Fe-, and Ti-Based Aluminides

Nickel, iron, and titanium aluminides are currently the most likely intermetallics to (partly) replace nickel-base superalloys in high-performance aeroengines. The main obstacles to their use have been, and continue to be, brittleness and low ductility at ambient temperatures [7].

Much R&D has been directed to enhance the low temperature ductility, and also improving the high temperature properties. This includes the development of in situ composites, mentioned in Sect. 10.3.

The properties of interest for high temperature aerospace applications are high specific strength and stiffness (favoured by low densities), high melting points, strength retention and creep resistance, ductility, and resistance to environmental degradation.

10.4.1 Property Surveys

Mechanical properties: Table 10.2 lists some generic properties and characteristics of nickel, iron, and titanium aluminides. Table 10.3 compares the properties of titanium aluminides with those of titanium alloys and nickel-base superalloys. Table 10.4 lists the mechanical properties of molybdenum and niobium silicides. From these tables the following points can be made:

1. The titanium aluminides offer large advantages in density compared to nickel-base superalloys, and are also less dense than conventional titanium alloys. TiAl is especially attractive because of its high elastic modulus (and hence high specific stiffness), and high creep and oxidation resistance.

Table 10.2 Some properties and characteristics of nickel, iron, and titanium aluminides [7]

Alloy	Melting point (°C)	Density (g/cm ³)	R.T. E (GPa)	Maximum use (°C)		Alloy characteristics
				Strength	Corrosion	
Ni ₃ Al	1390	7.50	179	1000	1150	Oxidation resistance; high temperature strength
NiAl	1640	5.86	294	1200	1400	Oxidation resistance; high melting point
Fe ₃ Al	1540	6.72	141	600	1100	Oxidation and sulphidation resistance
FeAl	1250	5.56	261	800	1200	Oxidation and sulphidation resistance
Ti ₃ Al	1600	4.2	145	760	650	Low density; good specific strength
TiAl	1460	3.91	176	1000	900	Low density; good specific strength
MoSi ₂	2020	6.24	440			

Table 10.3 Properties of titanium aluminides, titanium alloys, and nickel-base superalloys [7]

Alloys	Density (g/cm ³)	R.T. E (GPa)	R.T. Y.S. (MPa)	R.T. UTS (MPa)	Creep limit (°C)	Oxidation limit (°C)	Ductility (%)	
							R.T.	H.T.
Ti-alloys	4.5	96–100	380–1150	480–1200	600 ^a	600	20	High
Ti₃Al	4.1–4.7	100–145	700–990	800–1140	760	650	2–10	10–20
TiAl	3.7–3.9	160–176	400–650	450–800	1000	900^b	1–4	10–60
Ni-alloys	8.3	206	–	–	1090 ^a	1090 ^a	3–5	10–20

^a1995 data; ^bNeeds coating above 750–800 °C, see Sect. 10.2.2

Table 10.4 Properties of Mo-silicide and Nb-silicide based binary and multicomponent intermetallic alloys [5, 6]

Alloys	Melting point (°C)	Density (g/cm ³)	R.T. E (GPa)	R.T. Flexural strength (MPa)	R.T. Fracture toughness (MPa√m)	Creep limit (°C)	Oxidation limit (°C)
MoSi ₂	2020	6.24	440	140–160	2.5–5.0	1300	1700
Mo ₃ Si	2025	8.9	295	–	3.0	1300	1000
Mo ₅ SiB ₂	2160–2200	8.8	383	–	2.0	1500	1400
Mo-Si-B (Mo ₈₈ -Mo ₃ Si-Mo ₅ SiB ₂)	2025	8–9	310–325	400–600	5.0–20.0	1400	1300
Nb ₈₈ -Nb ₅ Si ₃	≥1915	7–7.5	170	500–1450	6–24	1200	1200
Nb-Si multicomponent alloys	≥1800	6.6–7.2	165	800–950	18.2–23.3	1200	1300

2. The nickel aluminides have lower densities than nickel-base superalloys, notably NiAl, which also has a much higher elastic modulus.
3. The iron aluminides also have lower densities than nickel-base superalloys and are resistant to high temperature oxidation and corrosion. However, the maximum strength capability of the iron aluminides is relatively low.
4. The silicides and multicomponent silicide-based alloys have much higher melting points and higher temperature capabilities compared to aluminides, but have higher densities. Furthermore, these materials are brittle at ambient temperatures in polycrystalline form, with the brittle-to-ductile temperature being very high, at about 1100 °C.

While useful, Tables 10.2, 10.3, and 10.4 are *generic*. They cannot provide the whole story, since (i) they do not fully cover the ambient and elevated temperature properties, and (ii) they do not account for the large amount of R&D on alloy processing and development over the past three decades. Both of these topics are beyond the necessarily limited scope of the present chapter. The reader is therefore referred, as mentioned earlier, to Refs. [1–7].

Nevertheless, it is important to note that the characteristic low ductility or brittleness of these intermetallics at ambient temperatures is (or has been) a major disadvantage with respect to (i) alloy processing and component manufacture, and (ii) service performance.

The first problem has been the focus of much fundamental and applied research to improve the ductility and toughness through alloying additions and process-based microstructural control. For example, Ref. [7] lists some 13 compositional variations and 19 processing methods for TiAluminides. An analogous, though less extensive, situation exists for Ni₃Al [7], whose commercial alloys contain small additions of boron (B) to enhance the ambient temperature ductility [7, 26]; and varying amounts of Cr, Fe, Mo, and Zr [7].

There has also been much R&D directed to improving the high temperature properties, particularly the creep resistance of nickel aluminides to enable them to compete with advanced superalloys. However, although detailed comparisons are not available, the latest generations of nickel-base superalloys (discussed in Chap. 9 of this Volume of the Source Books) would appear to have high temperature properties beyond the capabilities of nickel aluminides, which have a temperature limit ≈ 1100 °C [27].

Oxidation: The nickel aluminides have an inherently high oxidation resistance, especially NiAl, which is why this alloy is used in bondcoats for thermal barrier coatings (TBCs). The high oxidation resistance is due to the formation of a protective Al₂O₃ scale.

The oxidation behaviour of the iron aluminides is determined by the nature and composition of the oxide scale. The minimum concentration of Al to enable a continuous and protective Al₂O₃ scale is reported to be about 15 at.% Al in a binary Fe-Al alloy [28]. Addition of Cr accelerates the formation of this protective scale [29].

The titanium aluminides TiAl and Ti₃Al do not form a protective scale. However, certain alloying additions (Mo, Nb, Si) improve the oxidation resistance by enabling the formation of a continuous Al₂O₃ scale [30].

Much more information on the oxidation characteristics of all these aluminides (and the silicides) is available in the literature, e.g. Ref. [2].

10.5 Aerospace Applications

10.5.1 Silicides

Earlier in this chapter it was stated that molybdenum and niobium silicides are potential replacements for nickel-base superalloys in advanced gas turbines. When this major change will occur, if it occurs, is unknown. For example, a decade ago, in 2006, General Electric (GE) suggested that niobium silicide low-pressure turbine (LPT) blades could be in use by 2012, with high pressure turbine (HPT) blades

following by 2015 [31]. This suggestion has been overtaken by events (continued superalloy improvements), but it does show the direction of thinking by a major engine manufacturer.

10.5.2 *Aluminides*

Nickel and iron aluminides: The prospects for using nickel and iron aluminides in aerospace gas turbines are uncertain. As mentioned in subsection 10.4.1, nickel aluminides may not be competitive with the latest generation of superalloys, even though NiAl has a significantly lower density (compare the data in Tables 10.2 and 10.3). In 1996 Darolia et al. [32] summarized the problems thus:

1. Nickel-base superalloys have properties that are extremely difficult to surpass.
2. Any intermetallics intended to replace superalloys will probably retain vestiges of one or more of the following generic problems:
 - Low ductility and toughness, especially at low temperatures.
 - Obtaining a balance of sufficient creep strength, ductility, and toughness.
 - Environmental stability.

Darolia et al. [32] concluded that the use of intermetallics will be very selective and gradual, and it is unlikely that superalloys will be rapidly and widely displaced. This conclusion is reinforced by superalloy developments and improvements in the subsequent two decades, see Chap. 9 of this Volume of the Source Books.

Furthermore, there seems no reason why iron aluminides should show any benefits in the relatively non-corrosive environments pertaining in aeroengine gas turbines.

Titanium aluminides: TiAl alloys are the first aluminides to have reached operational status in aeroengines, as 6th and 7th stage cast blades for the LPTs of the General Electric GENx-1B and GENx-2B engines, see Figs. 10.7 and 10.8. Similar components will be used in the GE9x engine, which is currently (early 2016) still under development.

The GENx engines entered service in late 2011 with the Boeing 787 *Dreamliner* (GENx-1B), and the Boeing 747-8F (GENx-2B). Testing had already demonstrated that TiAl blades with redesigned (thicker) leading edges should survive relatively large impacts from foreign object ingestion [33]: this is important for *all* engine blades.

Nevertheless, it is noteworthy that this first application of TiAl blades is in the last stages of the engines. Thus any service failures would cause minimal damage. As service experience with TiAl LPT blades accumulates, it may be possible to consider aluminide blades for replacing conventional titanium alloys in some of the last stages of the high pressure compressor (HPC).

Other, potential, aeroengine applications of titanium aluminides include compressor casings and blade dampers; and critical components for the exhaust nozzle



Fig. 10.7 TiAl LPT turbine blade for the GENx aeroengine. *Source* GE

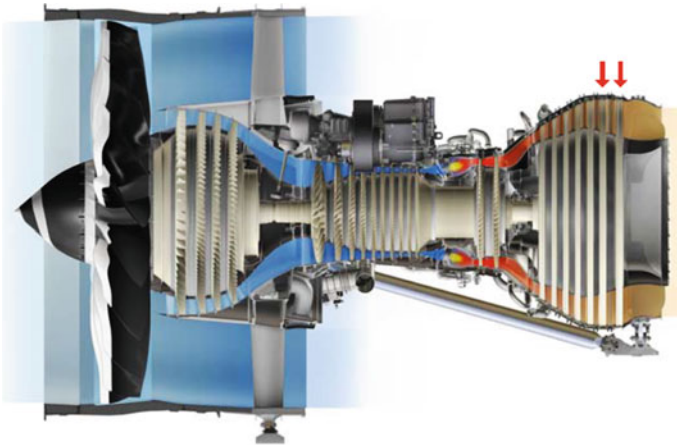


Fig. 10.8 LPT turbine blade locations (*arrowed*) in the GENx aeroengine: modified Boeing illustration

of an (eventual) future high speed civil transport (HSCT) [34]. However, it should be noted that ceramic matrix composites (CMCs) could be serious contenders [31].

10.5.3 Indian Scenario

Hindustan Aeronautics Limited (HAL) in Bengaluru has developed the precision forging of Ti₃Al aluminide compressor blades, the alloy supplier being Mishra Dhatu Nigam (MIDHANI) in Hyderabad. Also, the Defense Metallurgical Research Laboratory in Hyderabad has demonstrated isothermal forging of in-house developed TiAl alloys [35].

These activities were carried out as part of the indigenous Kaveri engine program, which, however, was discontinued in 2015. Some information on the *structural* design of the Kaveri engine is given in Chap. 24 of Volume 2 of these Source Books.

10.6 Summary

Intermetallics are a class of materials that have been studied extensively, motivated by a variety of potential structural applications in the aerospace, automotive, and power generation industries. The materials discussed in this chapter are (i) nickel, iron, and titanium aluminides, and (ii) molybdenum and niobium silicides. These have been, or are, candidates for applications in aerospace gas turbines.

Only one intermetallic, TiAl and its alloying variants, has attained service use in aircraft engines. It is uncertain or unlikely that nickel and iron aluminides will do so. The main reason is that conventional nickel-base superalloys already have outstanding combinations of properties and are continuously being improved.

Molybdenum and niobium silicide composites are potential candidates for advanced engines with turbine entry temperatures beyond the capabilities of superalloys. However, they will have to compete with other materials such as ceramic matrix composites.

References

1. Gottstein G (2004) Chapter 4, section 4.4. In: Physical foundations of materials science. Springer, Berlin, Germany
2. Westbrook JH, Fleischer RL (eds) (1994) Intermetallic compounds: principles and practice, vol 2. John Wiley & Sons Inc., Chichester, UK
3. Sauthoff G (1995) Intermetallics. VCH Verlagsgesellschaft, Weinheim, Germany
4. Stoloff NS, Sikka VK (eds) (1996) Physical metallurgy and processing of intermetallic compounds. Springer, New York, NY 10036, USA

5. Mitra R (2015) Structural intermetallics and intermetallic matrix composites. IIT Kharagpur Research Monograph Series, CRC Press, Taylor & Francis Group, Boca Raton, FL 561, USA
6. Mitra R (2006) Mechanical behavior and oxidation resistance of structural silicides. *Int Mater Rev* 51(1):13–64
7. Davis JR (ed) (1997) ASM Specialty Handbook, Heat-resistant materials. ASM International, Materials Park, OH 44073-0002, USA, pp 389–414
8. Nash P, Singleton MF, Murray JL (1991) Al-Ni (aluminum-nickel). In: Nash P (ed) Phase Diagrams of Binary Nickel Alloys, ASM International, Materials Park, OH 44073-0002, pp 3–11
9. Lui SC, Davenport JW, Plummer EW, Zehner DM, Fernando GW (1990) Electronic-structure of NiAl. *Phys Rev B*, 42(3):1582–1597
10. Murray JL (1988) Calculation of the titanium–aluminum phase diagram. *Metall Trans A* 19A:243–247
11. Banerjee D (1994) Ti₃Al and its alloys. In: Westbrook JH, Fleischer RL (eds) Intermetallic compounds: principles and practice, vol 1. John Wiley & Sons Inc., Chichester, UK, pp 91–131
12. Vedula K, Stephens JR (1987) B2 aluminides for high temperature applications. In: Stoloff NS, Koch CC, Liu CT, Izumi O (eds) Proceedings of High Temperature Ordered Intermetallics II, Materials Research Society Symposium, vol 81. Materials Research Society, Warrendale, PA 15086, USA, pp 381–392
13. Gokhale AB, Abbaschian GJ (1991) The Mo–Si (molybdenum-silicon) system. *J Phase Equilib* 12(4):493–498
14. Sakidja R, Perepezko JH, Kim S, Sekido H (2008) Phase stability and structural defects in high-temperature Mo–Si–B alloys. *Acta Mater* 56:5223–5244
15. Schlesinger ME, Okamoto H, Gokhale AB, Abbaschian R (1993) The Nb–Si (niobium-silicon) system. *J Phase Equilib* 14(4):502–509
16. Mao W, Guo X (2012) Effects of alloying and high-temperature heat treatment on the microstructure of Nb–Ti–Si based ultrahigh temperature alloys. *Prog Nat Sci: Mater Int* 22(2):139–145
17. Schneibel JH, Liu CT, Heatherly L, Kramer MJ (1998) Assessment of processing routes and strength of a 3-phase molybdenum boron silicide (Mo₅Si₃–Mo₅SiB₂–Mo₅Si). *Scripta Mater* 38:1169–1176
18. Breig PG, Scott SW (1989) Induction skull melting of titanium aluminides. *Mater Manuf Process* 4:73–83
19. Bewlay BP, Jackson MR, Lipsitt HA (1996) The balance of mechanical and environmental properties of a multielement niobium-niobium silicide-based in situ composite. *Metall Mater Trans A* 27A:3801–3808
20. Bewlay BP, Jackson MR, Subramanian PR (1999) Processing high-temperature refractory-metal silicide in-situ composites. *J Metals* 51(4):32–36
21. Aguilar J, Schievenbusch A, Kättlitz O (2011) Investment casting technology for production of TiAl low pressure turbine blades—process engineering and parameter analysis. *Intermetallics* 19(6):757–761
22. Aikin RM Jr (1997) The mechanical properties of in-situ composites. *J Met* 49(8):35–59
23. Morsi K (2001) Review: reaction synthesis processing of Ni–Al intermetallic materials. *Mater Sci Eng, A* 299:1–15
24. Sandvik Osprey Ltd, Neath, West Glamorgan, UK
25. Sikka VK, Wilkening D, Liebetrau J, Mackey B (1998) Melting and casting of FeAl-based cast alloy. *Mater Sci Eng A* 258:229–235
26. Aoki K, Izumi O (1979) Improvement in room temperature ductility of the intermetallic compound Ni₃Al by ternary element addition. *J Jpn Inst Met* 43:358–359
27. Jozwik P, Polkowski W, Bojar Z (2015) Applications of Ni₃Al based intermetallic alloys –current stage and potential perceptivities. *Materials* 8(5):2537–2568. doi:[10.3390/ma8052537](https://doi.org/10.3390/ma8052537)

28. Vedula K (1994) FeAl and Fe₃Al. In: Westbrook JH, Fleischer RL (eds) *Intermetallic compounds: principles and practice*, vol 2. John Wiley & Sons Inc., Chichester, UK, pp 199–209
29. Tortorelli PF, DeVan JH (1992) Behavior of iron aluminides in oxidizing and oxidizing/sulfidizing environments. *Mat Sci Eng A*, 153:573–577
30. Kim BG, Kim GM, Kim CJ (1995) Oxidation behavior of TiAl-X (X = Cr, V, Si, Mo or Nb) intermetallics at elevated temperature. *Scr Metall Mater* 33(7):1117–1125
31. Norris G (2006) Power house. Flightglobal.com, 13 June 2006
32. Darolia R, Walston WS, Nathal MV (1996) NiAl alloys for turbine airfoils. In: Kissinger RD, Deye DJ, Anton DL, Cetel AD, Nathal MV, Pollock TM, Woodford DA (eds) *Superalloys 1996*, The Minerals, Metals & Materials Society, Warrendale, PA 15095, USA, pp 561–570
33. Nathal M, Veris SJ (2008) Glenn takes a bow for impact on GENx engine, http://www.nasa.gov/centers/glenn/news/AF/2008/July08_GENx.html
34. Bartolotta PA, Krause DL (1999) Titanium aluminide applications in the high speed civil transport. National Aeronautics and Space Administration Technical Memorandum NASA/TM–1999-209071, Glenn Research Center at Lewis Field, Cleveland, OH 44135-3191: available from the NASA Center for Aerospace Information, Hanover, MD 21076-1320, USA
35. Banerjee D (2003) Titanium, its alloys and intermetallics. In: Chidambaram R, Banerjee S (eds) *Materials research: current scenario and future projections*. Allied Publishers Pvt. Limited, New Delhi, India, pp 215–237

Chapter 11

Bronzes for Aerospace Applications

**B. Saha, V. Nimbalkar, D.B. Anant Sagar, M. Sai Krishna Rao
and V.P. Deshmukh**

Abstract This chapter provides an overview of various bronzes with special attention to aerospace applications. Bronzes consist of several families of alloys but only those with specific properties applicable to the aircraft industries are discussed here. Bronze alloys like tin bronzes (C5100–C54400), beryllium bronzes, manganese bronzes, high leaded tin bronzes, oil impregnated bronzes, aluminium bronzes and silicon bronzes are some of the bronzes which have found their place in aircraft applications. This chapter briefly discusses these bronzes, highlighting their physical metallurgy, processing and properties. A specific part of this chapter has been dedicated to discussing the indigenous development of two types of bronzes, Al-bronzes and Si-bronzes, mainly for aerospace applications. These two bronze types have been specifically developed for fabrication of anti-friction bearing cages for aircraft and have to undergo rigorous quality assurance during production type certification.

Keywords Bronzes · Alloys · Processing · Heat treatment · Applications

B. Saha (✉) · D.B.A. Sagar · M.S.K. Rao
RCMA (Materials), CEMILAC, DRDO, Hyderabad, India
e-mail: bsaha898@yahoo.co.in

D.B.A. Sagar
e-mail: anantnani15@gmail.com

M.S.K. Rao
e-mail: munjuluri@rediffmail.com

V. Nimbalkar · V.P. Deshmukh
NMRL, DRDO, Ambernath, India
e-mail: vijayn@nmrl.drdo.in

V.P. Deshmukh
e-mail: vinay@nmrl.drdo.in

11.1 Introduction

The word ‘bronze’ is derived from the Italian word ‘*bronzo*’ meaning ‘bell metal’. Bronzes are copper alloys consisting of several families based on the principal solid solution alloying elements. For example, the familiar tin bronzes (C50100–C54400); the aluminium bronze alloys containing 2–15 % Al (C60800–C64200); and the silicon bronzes (C64700–C66100). Because of their specific properties, bronze alloys are considered for aerospace applications such as bearings and bushings in landing gears, cargo doors, wheel and brake components, etc.

11.2 Bronzes

The tin bronze series (C50100–C54400) comprise a set of good work-hardening solid solution alloys having around 0.8 % Sn (C50100) to 11 % Sn (C52400), with small additions of phosphorus mainly for its effective deoxidation abilities. Tin bronzes possess an excellent combination of formability, softening resistance, strength, corrosion resistance and electrical conductivity.

Another commercially important series are aluminium bronzes, containing around 2–15 % Al and belonging to the series C60800–C64200. The addition of aluminium imparts good solid solution strengthening and also work hardening in addition to improved corrosion resistance. Iron is an important addition in aluminium bronze alloys, usually of the order of 2–5 % Fe, mainly providing elemental dispersions to promote dispersion strengthening of the alloys, and also grain size control for better uniform properties.

The other bronzes suitable for aerospace are silicon bronzes of the series C64700–C66100. These bronzes provide good strength via solid solution hardening and work hardening, as well as excellent resistance to stress corrosion and general corrosion. Tables 11.1, 11.2, 11.3, 11.4, 11.5, 11.6 and 11.7 show the chemical compositions of several types of commercial bronzes, including phosphor bronzes [1].

11.2.1 *Effects of Alloying Elements*

Solid solution strengthening of copper is a common procedure and much used for bronzes. The classic bronzes are essentially binary Cu–Sn alloys. These are not used as such in aerospace applications, since other elements are also added. Solid solution strengthening is also achieved by additions of aluminium, manganese, nickel and zinc.

Table 11.1 Chemical compositions of commercial aluminium bronzes

Aluminium bronzes									
Alloys	Chemical composition (wt%)								
	Pb	Fe	Sn	Zn	Al	Mn	Si	Ni	Cu
C60800	0.10	0.10	–	–	5.0–6.5	–	–	–	Bal.
C61000	0.02	0.50	–	0.20	6.0–8.5	–	0.10	–	Bal.
C61300	0.01	2.0–3.0	0.20–0.50	0.10	6.0–7.5	0.20	0.10	0.15	Bal.
C61400	0.01	1.5–3.5	–	0.20	6.0–8.0	1.0	–	–	Bal.
C61500	0.015	–	–	–	7.7–8.3	–	–	1.8–2.2	Bal.
C61550	0.05	0.20	0.05	0.8	5.5–6.5	1.0	–	1.5–2.5	Bal.
C61800	0.02	0.50–1.5	–	0.02	8.5–11.0	–	0.10	–	Bal.
C61900	0.02	3.0–4.5	0.6	0.8	8.5–10.0	–	–	–	Bal.
C62200	0.02	3.0–4.2	–	0.02	11.0–12.0	–	0.10	–	Bal.
C62300	–	2.0–4.0	0.6	–	8.5–10.0	0.50	0.25	1.0	Bal.
C62400	–	2.0–4.5	0.20	–	10.0–11.5	0.30	0.25	–	Bal.
C62500	–	3.5–5.5	–	–	12.5–13.5	2.0	–	–	Bal.
C62580	0.02	3.0–5.0	–	0.02	12.0–13.0	–	0.04	–	Bal.
C62581	0.02	3.0–5.0	–	0.02	13.0–14.0	–	0.04	–	Bal.
C62582	0.2	3.0–5.0	–	0.02	14.0–15.0	–	0.04	–	Bal.
C63000	–	2.0–4.0	0.20	0.30	9.0–11.0	1.5	0.25	4.0–5.5	Bal.
C63010	–	2.0–3.5	0.20	0.30	9.7–10.9	1.5	–	4.5–5.5	78.0 Min
C63020	0.03	4.0–5.5	0.25	0.30	10.0–11.0	1.5	–	4.2–6.0	74.5 Min
C63200	0.02	3.5–4.3	–	–	8.7–9.5	1.2–2.0	0.10	4.0–4.8	Bal.
C63280	0.02	3.0–5.0	–	–	8.5–9.5	0.6–3.5	–	4.0–5.5	Bal.
C63380	0.02	2.0–4.0	–	0.15	7.0–8.5	11.0–14.0	0.10	1.5–3.0	Bal.
C63400	0.05	0.15	0.20	0.50	2.6–3.2	–	0.25–0.45	0.15	Bal.
C63600	0.05	0.15	0.20	0.50	3.0–4.0	–	0.7–1.3	0.15	Bal.
C63800	0.05	0.20	–	0.8	2.5–3.1	0.10	1.5–2.1	0.20	Bal.
C64200	0.05	0.30	0.20	0.50	6.3–7.6	0.10	1.5–2.2	0.25	Bal.
C64210	0.05	0.30	0.20	0.50	6.3–7.0	0.10	1.5–2.0	0.25	Bal.

Another copper strengthening method is precipitation hardening. This process is often used for copper alloys containing beryllium, chromium or zirconium. Precipitation hardening offers distinct advantages. Fabrication is relatively easy using the soft solution-annealed form of the quenched metal. The subsequent ageing process of the fabricated part can be performed using relatively inexpensive furnaces. Often the heat treatment can be performed in air, at moderate furnace temperatures and with little or no controlled cooling. Many combinations of ductility, impact resistance, hardness and strength can be obtained by varying the heat treatment times and temperatures.

Table 11.2 Chemical compositions of silicon bronzes

Silicon bronzes								
Alloys	Chemical composition (wt%)							
	Pb	Fe	Sn	Zn	Mn	Si	Ni	Cu
C64700	0.10	0.10	–	0.50	–	0.40–0.8	1.6–2.2	Bal.
C64710	–	–	–	0.20–0.50	0.10	0.50–0.9	2.9–3.5	95.0 Min
C64730	–	–	1.0–1.5	0.20–0.50	0.10	0.50–0.9	2.9–3.5	93.5 Min
C64900	0.05	0.10	1.2–1.6	0.20	–	0.8–1.2	0.10	Bal.
C65100	0.05	0.8	–	1.5	0.7	0.8–2.0	–	Bal.
C65400	0.05	–	1.2–1.9	0.50	–	2.7–3.4	–	Bal.
C65500	0.05	0.8	–	1.5	0.50–1.3	2.8–3.8	0.6	Bal.
C65600	0.02	0.50	1.5	1.5	1.5	2.8–4.0	–	Bal.
C66100	0.20–0.8	0.25	–	1.5	1.5	2.8–3.5	–	Bal.

Table 11.3 Chemical compositions of phosphor bronzes

Phosphor bronzes						
Alloys	Chemical composition (wt%)					
	Pb	Fe	Sn	Zn	P	Cu
C50100	0.05	0.05	0.50–0.8	–	0.01–0.05	Bal.
C50200	0.05	0.10	1.0–1.5	–	0.04	Bal.
C50500	0.05	0.10	1.0–1.7	0.30	0.03–0.035	Bal.
C50700	0.05	0.10	1.5–2.0	–	0.30	Bal.
C50710	–	–	1.7–2.3	–	0.15	Bal.
C50715	0.02	0.05–0.15	1.7–2.3	–	0.025–0.04	Bal.
C50900	0.05	0.10	2.5–3.8	0.30	0.03–0.30	Bal.
C51000	0.05	0.10	4.2–5.8	0.30	0.03–0.35	Bal.
C51100	0.05	0.10	3.5–4.9	0.30	0.03–0.035	Bal.
C51800	0.02	–	4.0–6.0	–	0.10–0.35	Bal.
C51900	0.05	0.10	5.0–7.0	0.30	0.03–0.35	Bal.
C52100	0.05	0.10	7.0–9.0	0.20	0.03–0.35	Bal.
C52400	0.05	0.10	9.0–11.0	0.20	0.03–0.35	Bal.

Table 11.4 Chemical compositions of leaded phosphor bronzes

Leaded phosphor bronzes						
Alloys	Chemical composition (wt%)					
	Pb	Fe	Sn	Zn	P	Cu
C53400	0.8–1.2	0.10	3.5–5.8	0.30	0.03–0.35	Bal.
C54400	3.5–4.5	0.10	3.5–4.5	1.5–4.5	0.01–0.50	Bal.

Table 11.5 Chemical compositions of wrought and cast beryllium bronzes

Wrought and cast beryllium bronzes								
Alloys	Chemical composition (wt%)							
UNS No.	Be	Co	Ni	Co + Ni	Co + Ni + Fe	Si	Pb	Cu
<i>Wrought alloys</i>								
C17200	1.8–2.0	–	–	0.2 min	0.6 max	–	–	Bal.
C17300	1.8–2.0	–	–	0.2 min	0.6 max	–	0.2–0.6	Bal.
C17000	1.6–1.79	–	–	0.2 min	0.6 max	–	–	Bal.
C17510	0.2–0.6	–	1.4–2.2	–	–	–	–	Bal.
C17500	0.4–0.7	2.4–2.7	–	–	–	–	–	Bal.
C17410	0.15–0.5	0.35–0.6	–	–	–	–	–	Bal.
<i>Cast alloys</i>								
C82000	0.45–0.8	–	–	2.4–2.7	–	–	–	Bal.
C82200	0.35–0.8	–	1.0–2.0	–	–	–	–	Bal.
C82400	1.6–1.85	–	–	0.2–0.65	–	–	–	Bal.
C82500	1.9–2.25	–	–	1.0–2.0	–	0.2–0.35	–	Bal.
C82510	1.9–2.15	–	–	–	–	0.2–0.35	–	Bal.
C82600	2.25–2.55	–	–	–	–	0.2–0.35	–	Bal.
C82800	2.5–2.85	–	–	–	–	0.2–0.35	–	Bal.

Table 11.6 Chemical compositions of manganese bronzes

Chemical composition (wt%)								
Element	Cu	Al	Fe	Pb	Mn	Ni	Sn	Zn
Min-Max	60–66	5.0–7.5	2–4	0.20	2.5–5.0	1.0	0.20	22–28

Table 11.7 Chemical compositions of leaded tin bronzes

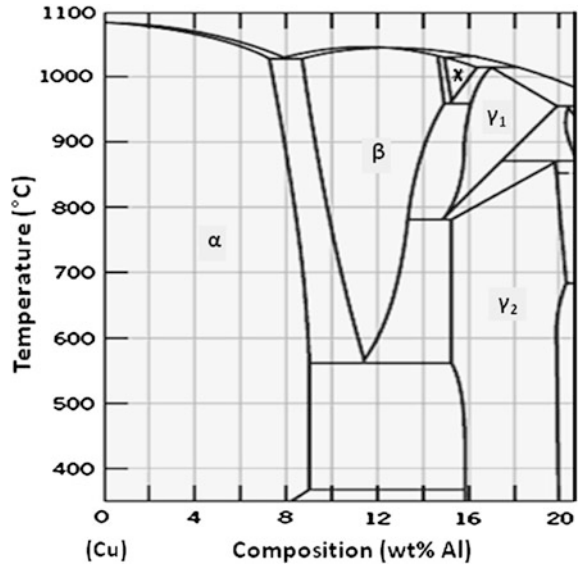
Chemical composition (wt%)								
Element	Cu	Pb	Sn	Fe	Ni	Zn	P	Sb
Min-Max	78–82	8–11	9–11	0.70	0.5	0.8	0.1	0.5

11.2.2 Aluminium Bronzes

Aluminium bronzes are the alloys with the best chemical resistance, and have high strength. They are standardised as wrought materials in UNS numbers C60600–C64499 and DIN 17665, and as cast materials in UNS numbers C95200–C95900 and DIN 1714.

Al-bronze alloys contain 2–15 wt% Al, which increases their resistance against seawater, sulphuric acid, and salt solutions, as well providing good wear properties and oxidation resistance. Their strengths, and in many respects their corrosion resistance, are better than those of many stainless steels, especially in aggressive

Fig. 11.1 Copper–aluminium phase diagram (Cu-rich side)



marine environments. They are readily weldable for fabrication of large components. The excellent natural corrosion resistance of all copper alloys is enhanced by the protective film of aluminium oxide formed very rapidly under normal operating conditions. If damaged, this film is self-healing, such that the alloys can be used in service conditions where abrasion and wear can be expected.

Most aluminium bronzes have aluminium contents below 10 wt%, see Table 11.1. This is because alloys with more than 10 % Al cannot be cold-worked, since the α solid solution phase boundary is then exceeded, see Fig. 11.1. Other alloying elements are iron (grain refining, magnetic permeability), manganese (deoxidation), nickel (excellent corrosion resistance), arsenic (resistance against salt solutions) and silicon (elevated strength, better machinability) [2–4].

Wrought aluminium bronzes: There are six compositions of Al-bronze covered by British standards, three of which have an α structure and are therefore ductile and amenable to cold-working [5]. The presence of β phase in the higher aluminium alloys makes them more difficult to form at normal temperatures but they are readily fabricated at temperatures ranging from 665 to 1000 °C, with adequate control to avoid grain growth.

The alpha alloys are generally used in the soft and lightly worked conditions for applications requiring maximum corrosion resistance. They are available as sheet, tubes, sections and wire. The duplex $\alpha + \beta$ alloys are hot rolled, extruded and forged. As the aluminium content increases above 10 wt%, the wear resistance increases but the ductility and toughness decrease.

The alloys can be joined by welding using the inert gas arc processes and friction welding. They are readily machined and can be finished to good surfaces of typical gold shades.

The indigenous Indian development of Al-bronze alloys equivalent to C63000 and AMS 4640 is discussed in detail in Sect. 11.4.

Cast aluminium bronzes: There are two basic aluminium bronze alloys in BS 1400. Alloys AB1 and AB2 each have nominally 9.55 wt% aluminium, with AB2 having higher contents of iron (3.5–5.5 wt%) and nickel (4.3–5 wt%) and each giving $\alpha + \beta$ structures with properties depending on the detailed composition and method of casting [3]. The alloys can be sand- or die-cast, and their short freezing range makes their properties almost independent of section thickness, which is a great advantage. These aluminium bronzes require expert handling in the foundry, particularly to avoid oxide inclusions, and with close attention to the rate of cooling. Heat treatment is sometimes applied to increase the strength or wear resistance, but there is a risk of distortion. A stress relief anneal is desirable to minimise distortion on machining, and also after welding to homogenise the properties across the heat affected zone.

Applications: Owing to their good (high-temperature) strength in the hot-worked and cast conditions, Al-bronze alloys are used in steam fittings, guides and valves. Their high corrosion resistance enables their application in the food, chemical and petrochemical industries, ship construction, desalination plants, the electrical industry, power plants, etc.

Typical products are pumps, turbines, propellers, valves, tees, branches and other water fittings, pressure vessels, heavy duty journal and flat bearings, gearbox components and masonry fixings [6]. Nickel aluminium bronzes containing around 10 wt% aluminium, with additions of iron and manganese to increase strength and toughness still further, are widely specified for aircraft applications.

11.2.3 Aluminium-Silicon Bronzes

Alloys having silicon contents ranging up to about 2 wt% and aluminium to about 6 wt% are known as aluminium-silicon bronzes. Silicon improves machinability and also has a deoxidising effect and increases the strength and corrosion resistance. These alloys are stronger than unmodified single-phase aluminium bronzes and can be cast and hot-worked more readily. Like other aluminium bronzes, they have a low magnetic permeability and excellent resistance to shock loading. The alloys are available in wrought and cast forms. They are used particularly in refrigeration related applications, in heat exchangers, armatures, chemically resistant castings, etc. [6].

11.2.4 Silicon Bronzes

Silicon bronze is a low-lead brass alloy that is generally composed of 96 % copper. The remainder can be silicon and a variety of other elements such as manganese,

tin, iron or zinc. Silicon bronze is known for its easy pouring ability, appealing surface finish and superior corrosion resistant properties, even when submerged in liquids and chemicals. Silicon bronze was originally developed for the chemical industry, but later became more widely used owing to its good casting characteristics.

AMS 4616(C65620) is a special high strength silicon bronze that is easily machined into ball-bearing cage assemblies. The additional iron content in this alloy provides added strength for easy machinability. Silicon bronze offers added strength in conjunction with the self-lubricity of silicon for excellent bearing cages, raceways and spacers for the aerospace industry.

11.2.5 Phosphor Bronzes

Phosphor bronze or tin bronze, is a mixture of copper, tin and phosphorus. Phosphor bronze alloys are primarily used for electrical products because they have excellent spring qualities, high fatigue resistance, excellent formability and high corrosion resistance. The phosphorus increases the wear resistance and stiffness of the alloy.

Phosphor bronze C 544 was one of the first bearing alloys available, and can be supplied as sheet, strip, wire, rod and bar. Other uses include corrosion resistant bellows, diaphragms, spring washers, bushings, bearings, shafts, gears, thrust washers and valve parts. This material has found use in aircraft components.

11.2.6 Beryllium Bronzes

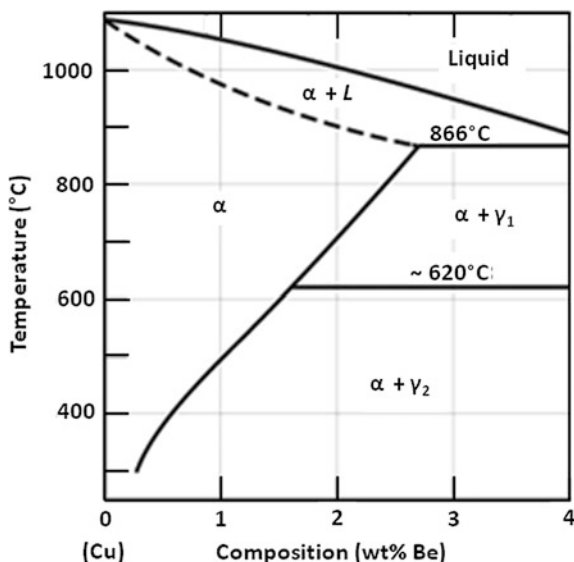
Beryllium bronzes are some of the most successful of the copper-base alloys. Their compositions are given in Table 11.5. Wrought Be-bronze alloys contain 0.2–2.0 wt% Be and up to 2.7 wt% Co (or up to 2.2 wt% Ni). Be-bronzes used for castings are generally slightly richer in Be content, with up to 2.85 wt%.

The beryllium content can be reduced by replacement with alloying elements such as Zr, Co, Si or Ag. Normally some nickel (0.5 wt% Ni) or cobalt is added to reduce grain growth, silver to prevent surface oxidation and to increase the conductivity, and lead to improve the machinability.

The most significant feature of these alloys is that the addition of beryllium enables precipitation hardening and strengthening by Cu_2Be . The tensile strength can be raised from 480 MPa in the annealed state to 1380 MPa in the fully heat treated state [7]. High strength is achievable while retaining effective and useful levels of electrical and thermal conductivity.

Physical metallurgy: Fig. 11.2 shows the copper-rich side of the Cu–Be binary phase diagram. The solid solubility of beryllium in the α copper matrix decreases

Fig. 11.2 Copper–beryllium phase diagram (Cu-rich side)



sharply as the temperature is lowered, and hence Be-bronzes are precipitation hardenable. For these alloys, solution annealing followed by precipitation treatment/age hardening is the general heat treatment. Be-bronzes can be cold-worked between annealing and age hardening to improve the age hardening response.

Actually, a third element, either cobalt (Co) or nickel (Ni), is usually added to Be-bronzes, see Table 11.5. The main function of these additions is to restrict grain growth during the annealing process by ensuring a good dispersion of precipitates in the matrix. The other advantage of these additions is to improve the age hardening response and avoid the tendency to overage or soften at prolonged ageing times and at higher ageing temperatures.

Solution annealing: The alloy is heated to a temperature just below the solidus so that a maximum amount of beryllium is dissolved, followed by rapid quenching to room temperature to retain the beryllium in a supersaturated solid solution. For high strength Be-bronzes the annealing temperature range is around 760–800 °C, and for high conductivity the annealing temperature range is from 900 to 955 °C. The lower and upper temperature limits (760 and 955 °C) are set to ensure complete recrystallisation and avoid excessive grain growth (or even incipient melting), respectively. The heating period during solution annealing is usually estimated at 1/2 to 1 h per inch of thickness.

Age hardening: After quenching, the solution-annealed material is reheated to a temperature below the equilibrium solvus line for a period sufficient to nucleate and grow the beryllium-rich precipitates responsible for hardening. The age hardening temperatures are within a range of around 260–400 °C for 0.1–4 h for high strength alloys, and 425–565 °C for 0.5–8 h for high conductivity alloys. The wrought

alloys are cold-worked between solution annealing and age hardening to increase the rate and magnitude of the age hardening response [8, 9]. The increased age hardening response is beneficial to both strength and electrical conductivity: when the alloys are in the solution annealed condition, the electrical conductivity is at its lowest mainly due to the presence of beryllium dissolved in the copper matrix; during age hardening the electrical conductivity increases as dissolved beryllium precipitates from the solid solution. The ageing time and temperature increase the conductivity, but ageing temperature has a more pronounced effect.

Applications: The commercial mill forms for Be-bronzes are mostly ingot, cast billets, rods, bars, tubes, strips and plates. The alloys can be easily formed conventionally and they respond adequately during plating and joining processes. Depending on the temper (age-hardening) conditions, the wrought Be-bronzes can be stamped, cold-formed and machined. Be-bronzes can be soldered with standard fluxes and also be joined by normal brazing and many fusion welding processes.

The resistance of Be-bronzes to fatigue and wear makes them suitable for diaphragms, precision bearings and bushings, ball cages and spring washers. Certain specific applications of beryllium bronzes are electrical contact springs, miniaturised electronics parts in space applications, automotive electronic connectors and as parts of electronic devices for interference grounding, mechanical springs and electrical switches for aerospace applications [10, 11].

11.2.7 Manganese Bronzes

Manganese bronzes have exceptionally high strength, toughness and corrosion resistance. The alloys contain aluminium, manganese, iron and occasionally nickel or tin. The chemical composition ranges are shown at Table 11.6. Equivalent specifications for these bronzes are C86300, SAE 430 B, CDA 863 and ASTM B 505 (continuous cast). Typical minimum tensile properties are shown in Table 11.8.

These alloys can be formed, extruded, drawn or rolled to any desired shapes. They are used for slow speed heavy duty load bearings, gears, cams and hydraulic

Table 11.8 Minimum tensile properties of a typical manganese bronze

UTS (MPa) Min	YS (MPa) Min	% El (Min)	Hardness (BHN)
760	415	14	225

Table 11.9 Minimum tensile properties of typical leaded tin bronzes

Sample type	UTS (MPa) Min	YS (MPa) Min	% El (Min)
Centrifugally cast	207	83	15
Continuously cast	241	138	6
Sand cast	207	83	15

cylinder parts. Certain marine applications are rudders, clamps, boat parts, etc. Specific aircraft and aerospace applications are heavy-load bearings and bushings, screw-down nuts and hydraulic cylinder parts.

11.2.8 High Leaded Tin Bronzes

High leaded tin bronzes (C93700) have excellent machining properties, medium strength and good corrosion resistance. They can withstand mild acids as found in mineral waters. The chemical composition ranges are shown in Table 11.7. Typical minimum tensile properties are shown in Table 11.9.

These bronzes can be used where lubrication is less than adequate. For example, bearings manufactured from C93700 alloy provide low friction and have excellent wear resistance under conditions of high speed, heavy pressure and vibration. This alloy may be joined by brazing and soldering, but welding is not recommended.

11.2.9 Sintered Bronzes (Oil Impregnated Bronzes)

These tin bronzes are made via powder metallurgy rather than standard ingot metallurgy. The chemical composition ranges are given in Table 11.10.

A controlled powder blending and sintering process results in a uniform grain structure and spheroidised interconnected porosity, which should be a minimum of 19 %. This enables oil impregnated components to provide a uniform oil coating of contact surfaces. Typical room temperature tensile properties of these sintered bronzes are given in Table 11.11.

During operation the oil impregnated bronze SAE 841 has a proven record of excellent wear resistance and long life where normal lubrication is difficult or

Table 11.10 Chemical composition ranges of typical sintered bronzes

Chemical composition (wt%)				
Element	C	Cu	Sn	Fe
Min-Max	1.75	87.5–90.5	9.5–10.5	1.0

Table 11.11 Typical tensile properties of sintered bronzes

UTS (MPa)	YS (MPa)	% El
97	75	1.0

Table 11.12 Chemical composition of aircraft bronze UZ19A16

Chemical composition (wt%)					
Element	Al	Zn	Mn	Fe	Cu
Min-Max	6.5–7.0	18–21	4.5–5.5	3.5	Balance

Table 11.13 Minimum tensile properties at room temperature for aircraft bronze UZ19A16

UTS (MPa) Min	YS (MPa) Min	% El (Min)
135	90	10

impossible to provide. The equivalent and related specifications for this alloy are ASTM B 438 (Grade 1, Type 2), AMS 4805, SAE 841 and Military Standard MIL-B-5687D. This alloy is used for manufacturing various aerospace components.

11.2.10 Aircraft Bronze (French Bronze)

The aircraft bronzes known as French bronze (UZ19 AL60 and UZ19A16) are used extensively for aircraft landing gear components. UZ19A16 is a high strength bronze with good brush and excellent wear resistance. Its chemical composition and tensile properties are given in Tables 11.12 and 11.13.

This alloy is especially resistant to friction under high loads. Its fretting properties and resistance to oxidation are comparable to those of many other bronzes. Some of the equivalent specifications for this alloy are NFL 14707, DIN 1709 (Bars) [12]. Finally, it should be noted that aircraft bronzes are not recommended for joining by brazing and welding.

11.2.11 Nickel-Silicon Bronzes

The nickel-silicon alloy Super Bronze contains 2–3.5 wt% Ni and 0.4–0.8 wt% Si, and is age hardenable. The alloy possesses high strength and good ductility combined with high electrical and thermal conductivity. The resistance to corrosion in marine and industrial environments is excellent and the alloy has good antifrictional and bearing properties.

The versatility of this type of alloy is demonstrated by widespread use in diverse industry sectors: applications include valve guides and end bushes in high performance internal combustion engines, aeroengine bearing cages, aircraft landing gear components, splined motor shafts in helicopters, slipper pistons in fuel pumps, gears and bushes, resistance welding electrodes, electrical contacts, piston crowns, clutch plates in marine engines and nonmagnetic naval vessel winches [13].

11.3 Processing of Bronzes

11.3.1 Melting Practices

During melting, bronzes are particularly susceptible to gas reactions with hydrogen, oxygen, sulphur dioxide and carbon monoxide. Sulphur must be absent from the fuel used, and the risk of reaction between the liquid metal and water vapour in the air must be minimised. Electric furnaces are therefore favoured and rapid melting is essential (for example, 200 kg in less than an hour). A charcoal cover is usual, but a slightly oxidising atmosphere (5–6 % oxygen) is required to avoid hydrogen or carbon monoxide pick up.

Degassing is carried out by means of an oxidising slag or by adding proprietary tablets, or by gas scavenging with nitrogen or air. This is followed by deoxidation usually with phosphor copper (15 wt% phosphorus), but since excess phosphorus reduces the mechanical properties, lithium (as 10 wt% lithium copper) may be used.

Control tests are normally made for melt quality of gunmetal castings and particular attention is necessary to prevent metal—mould reactions when sand castings are produced. For aerospace applications special care is taken during melting, and generally addition of scrap material is not allowed when the alloy is used for fabrication of critical components.

Impurities: Impurities have effects on copper-rich materials including bronzes. Lead, antimony and bismuth derived from the ores are especially harmful since they segregate to grain boundaries and cause embrittlement. Their limits are given in Table 11.14.

Antimony and bismuth in aluminium bronzes are detrimental to the mechanical properties owing to forming brittle films at grain boundaries. The tin bronzes are adversely affected by antimony, bismuth, arsenic and aluminium: as little as 0.005 wt% aluminium can be harmful, as also can 0.3 wt% arsenic or antimony.

Aluminium causes difficulties in many alloys owing to the ease with which alumina is formed. This gives unsoundness and films at grain boundaries. It is not easy to exclude aluminium when scrap copper alloys are remelted—hence the need for care in handling and storing scrap material.

Aluminium bronze: Cathode copper is preferred for this group of alloys, but high purity tough pitch metal is also used; and process scrap of known composition is also suitable. Aluminium is added directly or as 50/50 master alloy. Other alloying elements dissolve best as master alloys, such as 60 wt% copper, 30 wt% manganese and 10 wt% iron or nickel.

Table 11.14 Impurity limits for lead, antimony and bismuth in copper-rich bronzes

Element	wt%
Lead	0.02
Antimony	0.01
Bismuth	0.003

Melting should take place as quickly as possible under a dried charcoal cover. Deoxidation with manganese may be required before adding the aluminium, which is a powerful deoxidant but could result in oxide inclusions. Carbon monoxide, carbon dioxide and nitrogen are insoluble in the melt, hence hydrogen is the only gas likely to cause porosity. For large melts in reverberatory furnaces a flux cover may be used to minimise oxidation, but this may attack the refractory lining and the metal may require degassing with nitrogen.

11.3.2 Casting Practices

Aluminium bronzes: The casting characteristics of aluminium bronzes require special techniques, particularly to avoid entrapment of oxide and gross shrinkage porosity. The short freezing range, coupled with the liquid-to-solid contraction, can cause cavities and piping unless solidification is controlled by the use of large feeder heads.

The major difficulty arises from rapid oxidation of the aluminium content to give alumina, which forms instantly whenever the surface of the molten metal is exposed to air. The alumina is inert, insoluble and melts at a temperature in excess of 2200 °C; and its density is low, such that any stirring or turbulence traps it in the melt to give films and inclusions which reduce the mechanical properties and machinability, as well as impairing pressure tightness and surface finish. It is therefore essential to cast aluminium bronze ingots and billets without breaking the aluminium oxide film, and this is done by tilting both the ladle and mould so that the molten alloy remains enclosed in its alumina 'bag'. The method most commonly used was patented in 1919 by Durville and latter modified as the semi-Durville process.

The moulds are cast iron or copper, and normally no dressing is used, although a light refractory coating may be necessary.

Continuous and semi-continuous casting of aluminium bronze billets has been adopted and is very successful provided that the metal is poured slowly and quietly into the water-cooled mould at a rate equal to the rate of withdrawal of the solid billet. Centrifugal casting has also proved very suitable [14].

Of the two basic alloys AB1 and AB2 (see Sect. 11.2.2.), AB1 is preferred for die castings made in weights ranging from 50 g to 20 kg with thicknesses of 2–20 mm. This is because the higher alloy content of AB2 makes it less fluid and increases the difficulty of economical die casting.

The copper-manganese-aluminium alloys, e.g. C63380 in Table 11.1, are normally classified as aluminium bronzes, although they contain about 12 wt% manganese in addition to approximately 8.5 wt% aluminium.

Tin bronzes: Water-cooled copper or iron moulds are used, copper moulds being preferred as they give better surfaces and have a longer life than cast iron. Slow pouring of degassed alloy is recommended at temperatures not exceeding 1200 °C, and top pouring is common. The long freezing range of these alloys demands

effective feeding, and pressure methods may be used. Mould dressings are usually of alumina or 10 % aluminium powder in synthetic resin.

Tin bronzes and gunmetal are cast by semi-continuous processes, resulting in very sound bars and tube shells with optimum properties. Sections from about 12–120 mm diameter (or equivalent) are commonly cast vertically using a graphite die cooled by a water jacket. Alternatively, dies of chromium-copper are used, and for hollow billets the mandrel may also be of chromium-copper.

Centrifugal casting is widely used for bronzes and gunmetal with either cast iron or sand-lined moulds, which are generally horizontal but may also be vertical or inclined. In general, vertical moulds are used for castings when the length/diameter ratio is more than 1.5, otherwise the bore tends to taper and more inclusions may be found.

11.3.3 Hot-Working

Deformation of copper and its alloys above their recrystallisation temperatures (i.e. hot working) is widely practised as the initial step in the production of finished shapes and semi-fabricated forms. Hot-working results in no work hardening, and the phase changes that occur tend to improve the microstructural homogeneity. The operations used include rolling, extrusion and piercing, forging, and pressing, over a range of temperatures. Extrusion causes less cracking than hot rolling, bending or piercing operations, which impose tensile stresses on the hot metal.

Large slabs for rolling are scalped, and billets may require machining to remove surface defects which would otherwise persist in the finished product. Preheating is usually undertaken in gas- or oil-fired furnaces or in electric muffle furnaces, using a controlled atmosphere that is neutral or slightly reduced to prevent excessive oxidation. Induction heating is suitable for billets for extrusion or forging.

The duplex binary alloys are most readily hot-worked with preheating temperatures up to 850–900 °C: otherwise grain growth may be excessive. Lower temperatures can be used as the aluminium content increases, with finishing temperatures down to 650 °C. Higher temperatures are necessary for alloys containing iron and nickel: for example, 950 °C for alloys with 4–6 wt% iron or nickel (iron above 1.5 wt% inhibits grain growth). Any type of preheating furnace can be used, since scaling is minimal; and induction heating of extrusion billets has advantages, particularly in minimising the risk of grain growth at high temperatures.

Extrusion presses up to 3000 tons capacity are used, and air cooling is preferred for the best combination of strength and ductility. This is because quenching gives too much β in the microstructure, while slow cooling favours eutectoid formation: both phenomena reduce the ductility. Die wear is likely to be high due to the high temperatures and alumina in the surface films. Hence the need for high grade tool steels for the dies, which should be water-cooled if possible [14].

Descaling: All hot-worked copper-base materials require descaling. This is conventionally done by pickling in an acid bath containing 5–10 % sulphuric acid at about 80 °C. For removal of alumina-containing films 1–2 % nitric or hydrochloric acid may be added, or strong hydrochloric acid is used. Washing is essential, and metal recovery from descaling operations is standard practice.

11.3.4 Cold-Working and Annealing

The rate of work hardening, which governs the amount of cold-working undertaken between successive process anneals, varies proportionally to the initial annealed strength of the metal and is indicated by the slopes of the tensile strength and hardness curves. Thus pure copper work hardens least rapidly and aluminium bronzes the most (with the exception of copper-nickel alloys, which work-harden at a lower rate than brasses).

Continuous or batch rolling is undertaken, and modern cold mills permit high production rates. Cold rolling operations include single pass mills, tandem mills for continuous production of coiled strip, Sendzimir multi-roll plants, the pendulum (Sachs-type) mill and foil mills.

Cold rolling of rods is practiced at the break-down stage, particularly for phosphor bronzes and beryllium copper. Cold drawing of hot rolled or extruded rods is undertaken as a final operation to give the required temper, size and finish, and cold drawing of sections from strip is commonly used.

Bronze tubes can be fabricated by welding formed strip, but by far the greater proportion is made as seamless tubing from extruded or hot pierced shells. The main problems are avoidance of eccentricity and the provision of a smooth, clean inner surface. The tube shells are drawn through successive dies on draw benches at speeds from 3 to 100 m/min. While copper permits severe reductions and several drawing operations before annealing is required, alloys may need to be softened between successive draws. It is essential that all traces of lubricant are removed from the metal before annealing; otherwise any carbonaceous residue is likely to cause pitting corrosion when the tube is used for water services or to convey more corrosive media.

Annealing is undertaken in electric or gas-fired furnaces which may be continuous or batch type (for example, bell furnaces). Suitable atmospheres enable bright or clean annealing. Sulphur must be absent from furnace atmospheres and lubricants from rolling or drawing must be removed by prior degreasing.

Alloys with readily oxidisable elements, such as aluminium bronze and beryllium bronze, are bright annealed in hydrogen or in a cracked ammonia atmosphere free from water vapour. Partially burnt hydrocarbons can also be used if mild oxidation is acceptable.

The rate of cooling is not important, except for the precipitation hardening alloys, and quenching in water is often practised after annealing in air. This removes scale and facilitates pickling, as well as preventing further oxidation during cooling.

11.4 Indigenous Development of Aluminium and Silicon Bronzes for Aerospace

An indigenous development programme has been undertaken for two aerospace grades of aluminium bronze and silicon bronze. The programme specifically targeted the development of an Al-bronze equivalent to AMS 4640F (UNS C63000) and an Si-bronze equivalent to AMS 4616F (UNS C65620), mainly for extruded tubes and rods used in fabricating anti-friction bearing cages. These bearing cages are required for various military aircraft being flown in India [15, 16]. It was decided that the development of these two bronzes would be done with an industrial partner having the requisite facilities and expertise for copper-base extruded products.

The finally developed bronze products will have to undergo airworthiness qualification procedures to ensure that they meet all the requirements for flight clearance. The development activities therefore involve airworthiness agencies in addition to the development agency, the designer, user and manufacturer. The type certification methodology mandated by the airworthiness agencies ensures that the vendor is fully qualified to manufacture airworthy products. The airworthiness

Table 11.15 Required dimensions of aluminium and silicon bronze tubes and rods

Alloy	Sizes (in mm)
Al-bronze AMS 4640F	OD 45 × 1D 28 OD 63 × 1D 32
Si-bronze AMS 4616F	Tubes OD 80 × 1D 32 Rod

Table 11.16 Chemical compositions of aluminium and silicon bronzes as per AMS specifications

Chemical composition (wt%)									
Alloys	Al	Ni	Si	P	Fe	Mn	Zn	Sn	Cu
Al-Bronze AMS4640F (UNS C63000)	9.0– 11.0	4.0– 5.5	0.25 max.	–	2.0– 4.0	1.5 max.	0.30 max.	0.20 max.	Bal.
Si-Bronze AMS 4616F (UNS C65620)	–	–	2.40– 4.00	0.10 max.	1.00– 2.00	1.00 max.	1.50– 4.00	–	Bal.

Table 11.17 Mechanical properties of the aluminium and silicon bronzes at room temperature

Alloys	Mechanical properties			
	YS (MPa) min	UTS (MPa) min	% El (min)	Hardness (HB)
Al-Bronze AMS4640F (UNS C63000)	345	655	10	183–241
Si-BronzeAMS 4616F (UNS C65620)	138	386	30	> 90

agencies qualify the products based on Development/Type Test Schedules (DTS/ TTS) and other relevant aerospace specifications such as AMS and MIL specifications. The complete type certification methodology followed by airworthiness agencies is discussed in Chap. 24 of Volume 2 of these Source Books.

The product sizes required by the user for fabrication of the bearing cages using these Al- and Si-bronze alloys are given in Table 11.15. The chemical compositions and the room temperature mechanical properties are given in Tables 11.16 and 11.17, respectively.

During the actual development phase, two firms were shortlisted based on their technical competence to process the bronzes in the tube size 63 OD \times 32 ID mm \times 1500 mm length. The alloys were processed using either an oil-fired furnace route

Table 11.18 Qualification tests as per development test schedules (DTS)

S. no.	Tests and checks
1	Chemical composition
2	Dimension checks
3	Visual inspection
4	Surface cleanliness
5	NDT: ultrasonic, eddy current, hydrostatic, pneumatic
6	Metallography: microstructure, macro etch test
7	Mechanical properties: hardness, tensile properties (RT, -50 , 150 °C), shear strength (RT), impact (RT and -50 °C), fatigue
8	Embrittlement: hydrogen embrittlement, mercurous nitrate
9	Wear resistance
10	Corrosion resistance
11	Stress corrosion cracking (SCC)
12	Physical properties: density, elastic modulus, Poisson's ratio, coefficient of thermal expansion, coefficient of thermal conductivity

Table 11.19 Chemical compositions of oil-fire (A) and induction melted (B) aluminium bronze 4640 F

Chemical composition (wt%)									
Aluminium bronze 4640F (UNS C 63000)									
Elements		Al	Ni	Fe	Mn	Zn	Si	Sn	Cu
Specified (AMS 4640F)	Min	9.0	4.0	2.0	–	–	–	–	Balance
	Max	11.0	5.5	4.0	1.50	0.3	0.25	0.20	
Al-Bronze route (A)	Obtained	9.54	5.06	3.24	0.84	0.04	0.07	–	80.17
Al-Bronze route (B)	Obtained	9.41	4.20	3.80	0.54	0.30	0.10	0.02	80.60
Al-Bronze imported	Obtained	10.33	4.37	3.74	0.66	0.045	0.045	0.033	80.22

Table 11.20 Chemical compositions of oil-fire (A) and induction melted (B) Silicon bronze 4616F

Chemical composition (wt%)							
Silicon bronze 4616F (UNSC 65620)							
Elements		Fe	Mn	Zn	Si	P	Cu
Specified AMS 4616F	Min	1.0	–	1.50	2.4	–	Balance
	Max	2.0	1.0	4.0	4.0	0.10	
Si-Bronze Route (A)	Obtained	1.32	0.38	3.05	2.86	–	92.59
Si-Bronze Route (B)	Obtained	1.23	0.001	2.31	2.40	–	93.71

Table 11.21 Mechanical properties of oil-fire (A) and induction melted (B) aluminium bronze 4640F

Properties	UTS (MPa)	YS 0.5 % Ext. (MPa)	%El (4D)	Hardness (HB)
Specified Al-Bronze (AMS 4640F)	655 (min)	345 (min)	10 (min)	187–241
Al-Bronze Route (A)	689	370	11.35	200
Al-Bronze Route (B)	744	429	10.40	194
Imported Al-Bronze	742	430	10.38	219

Table 11.22 Mechanical properties of oil-fire (A) and induction melted (B) Silicon bronze 4616F

Properties	UTS (MPa)	YS at 0.5 % Ext. (MPa)	%El (4D)	Hardness (HB)	Grain size (mm)
Specified Si-Bronze (AMS4616F)	386 (min)	138 (min)	30 (min)	> 90	< 0.20
Si-Bronze Route (A)	422	202	44	110	0.045
Si-Bronze Route (B)	431	258	51	116	0.015
Imported Si-Bronze	435	204	58	120	–

(A) or an induction melting furnace route (B), followed by hot extrusion to arrive at the required development size. The tube products were then evaluated and characterised using the DTS tests and checks listed in Table 11.18.

Summaries of the chemical composition and mechanical property test results are presented in Tables 11.19, 11.20, 11.21 and 11.22, together with the AMS specifications and data for imported material, which was tested with the indigenous materials wherever possible.

Based on the results in Tables 11.19, 11.20, 11.21 and 11.22 and other detailed characterisations it was decided to follow the induction melting route (B) for subsequent certification activities. The final extruded tube products (63 OD × 32 ID mm × 1500 mm length) for both alloys met all the DTS requirements issued by the airworthiness agencies. Hence it was concluded that the development activity was successful, and these alloy products can now be brought into regular production in India.

11.5 Summary and Conclusions

Several of the bronzes discussed in this chapter offer specific properties required for aircraft components. The manufacturers of these necessarily high quality alloys must fulfil stringent quality assurance (QA) requirements. Two bronze alloys, an Al-bronze and an Si-bronze, were developed indigenously for Indian aircraft applications, and are intended to achieve the necessary quality for passing through a rigorous quality assurance check during production and requirements type certification.

Acknowledgments The authors would like to thank several colleagues from NMRL, CVRDE and CEMILAC. They particularly would like to thank Dr. K. Tamilmani, DS and Director General (Aero systems), Shri P. Jayapal, Chief Executive (A), CEMILAC, Dr. P. Siva kumar, Director, CVRDE and Sri R.S. Hastak, Director, NMRL. They also wish to thank Dr. R.J.H. Wanhill for his comprehensive review.

References

1. Tyler DE, Black WT (1990) Introduction to copper and copper alloys. In: American Society for metals, 'Properties and selection: nonferrous alloys and special purpose materials'. ASM Handbook, vol 2, 10th edn. ASM International, Materials Park, OH, USA
2. Aluminium bronze alloys: Corrosion resistance guide. Copper development association. Publication No. 80, Aug 2010, Copper Development Association Inc, New York, USA
3. Aluminium Bronze alloys for Industries, Publication No. 83: Copper Development Association, 2005, Copper Development Association Inc, New York, USA
4. Aluminium bronze alloys Technical Data, Copper development association, Publication No. 82, Aug 2010, Copper Development Association Inc, New York, USA
5. Aluminium bronze-Essential for industry: Copper development association. CDA publication No. 86, 1989, Copper Development Association Inc, New York, USA
6. Vijayaram TR (2012) The role of copper and copper alloys in engineering industries: metallurgical perspectives. The Monthly Bulletin of the Institution of Engineers, IEM, Dimension Publishing, Puchong, Selangor, Malaysia
7. Sriram P, Rao V (2006) Recent developments in cast non-ferrous bearing materials. 54th Indian Foundry Congress (IFC), 20–22 January, Pune, India
8. Davis JR (1998) Copper and copper alloys. In: Metals Handbook, Desk edition (2nd), pp 506–558
9. Brooks CR (1982) Copper-base alloys in heat treatment, structure and properties of non-ferrous alloys. American Society for Metals, Metals Park, OH, USA, pp 275–327
10. IBC Advanced alloys: alloy selection for the aerospace industry. IBC Advanced alloys Corporation, Vancouver, Canada
11. Glaeser W (1983) Wear properties of heavy loaded copper base bearing alloys. J Metals
12. West EG (1982) Copper and its alloys. Ellis Horwood Ltd, Hemel Hempstead, UK
13. Bendall KC (1997) Selection of copper alloys for aircraft engineering. In: Aircraft engineering and aerospace technology, vol 69, pp 328–331
14. Maken PJ, Smith AA (1966) The aluminium bronzes: properties and production processes. CDA publication No. 31, Copper Development Association Inc, New York, USA
15. AMS 4640 F: Aluminium bronze bars, rods, shapes, tubes and forgings (81.5Cu-10.0Al-4.8Ni-3.0Fe) stress relieved
16. AMS 4616 D: Silicon bronze bars, forgings and tubings. (92Cu-3.2Si2.8Zn-1.5Fe) stress relieved

Chapter 12

Niobium and Other High Temperature Refractory Metals for Aerospace Applications

V.V. Satya Prasad, R.G. Baligheid and Amol A. Gokhale

Abstract Refractory metal alloys based on Nb, Mo, Ta, W, and Re find applications in the aerospace industries because of their high melting points and high temperature strengths. They are generally produced by powder metallurgy technique due to their very high melting points. However, when refining is desired, melting under high vacuum becomes necessary, for which nuggets or powder based electrodes are employed. Niobium is the lightest refractory metal with density close to that of nickel, and exhibits good thermal conductivity. Niobium can be alloyed to improve high temperature strength and oxidation resistance. Applications in nuclear, aerospace, and defence sectors have been reported. The goal of current research in Nb alloys is to simultaneously achieve high strength and workability, and provide protection from oxidation for long-term operation. There is strong research interest in intermetallics also. This chapter will discuss the salient features of refractory metals and alloys in general, and Nb-based alloys in particular.

Keywords Niobium · Refractory alloys · Processing · Mechanical properties · Creep · Applications

12.1 Introduction

Future aerospace applications such as advanced turbojet and scramjet engines to be used in subsonic, supersonic, and hypersonic flights will require materials with ever increasing temperature- and load-bearing capabilities for improved performance

V.V. Satya Prasad (✉) · R.G. Baligheid
Defence Metallurgical Research Laboratory, Hyderabad 500058, India
e-mail: vvsatya2004@yahoo.co.in

R.G. Baligheid
e-mail: rbaligheid@yahoo.co.in

A.A. Gokhale
Indian Institute of Technology Bombay, Powai, Mumbai 400 076, India
e-mail: amol_gokhale@yahoo.in

under extreme environmental conditions. The state-of-the-art superalloys can be utilized to a maximum temperature of 1077 °C, and the need for viable materials with higher (1127–2027 °C) temperature capabilities has long been felt. Hence work is being pursued in different directions to develop materials with very high temperature capability [1, 2].

One such area is the development of ceramics and composite materials which have very good high temperature capability. However, designers frequently find that these newer materials cannot be easily fabricated into the shapes required. In other instances, users of high temperature materials are rediscovering that the applicability of advanced nonmetallic and composite materials may be limited by their relatively low thermal conductivity: alloys with good thermal conductivity require less intense air cooling in applications such as turbine hot sections.

Although there are a number of metals that can be considered as refractory by virtue of their high melting points, tungsten, molybdenum, tantalum, and niobium are the promising ones, all of which have body centered cubic (bcc) structures. Rhenium, a hexagonal close packed metal, is also often considered to be a member of this group. The common characteristic of these metals, as shown in Table 12.1 [3], is a high melting point ranging from 2468 °C (Nb) to 3410 °C (W). It would seem natural that these elements would form the bases for high temperature structural materials. Their high temperature strength and Young's modulus are shown in Figs. 12.1 and 12.2 [3].

Unfortunately, all four of the traditional refractory metals have little or no resistance to oxidation in the service temperature range. Niobium and tantalum are the most versatile refractory metals due to their relative ease of fabrication (because of excellent room temperature ductility and low ductile-to-brittle transition temperature, DBTT) and corrosion resistance. The corrosion resistance of niobium is provided by the formation of a very dense and adhesive oxide layer. With the exception of hydrofluoric acid, concentrated hot sulphuric acid and hot alkaline solutions, niobium shows good resistance to aqueous solutions.

In comparison to tantalum the corrosion resistance of niobium is less, but still much better than that of stainless steels or nickel-base alloys used in chemical industries.

Although tungsten finds applications as ballast and nozzle material in rocket systems, its main use has been as core material in antitank penetrators owing to its very high density. All refractory metals find use as alloying elements in nickel-base superalloys since they are beneficial to the creep resistance.

Table 12.1 Properties of common refractory metals

Metal	M.P. (°C)	V.P. (torr) at 2327 °C	DBTT (°C)	Density (g/cm ³)
Nb	2468	4×10^{-5}	< -126	8.75
Mo	2617	6×10^{-4}	27	10.2
Ta	2996	8×10^{-7}	< -248	16.7
Re	3179	1.3×10^{-6}	–	21.0
W	3410	7×10^{-8}	302	19.3

M.P. melting point, *V.P.* vapour pressure, *DBTT* ductile to brittle transition temperature

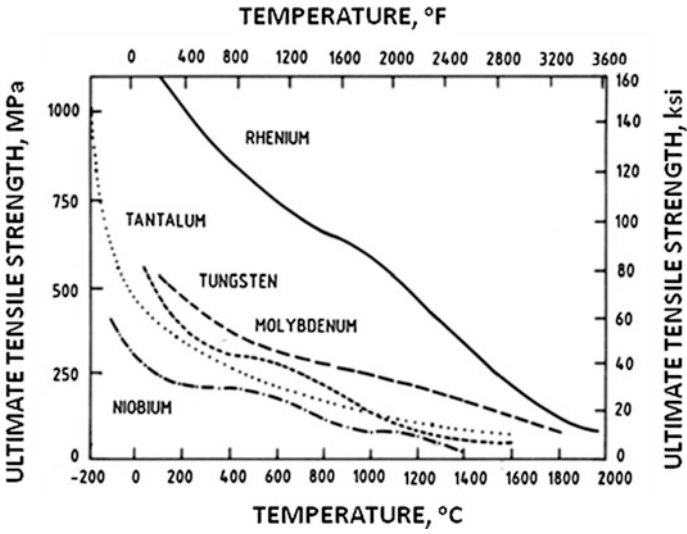


Fig. 12.1 Tensile strength of refractory metals versus test temperature

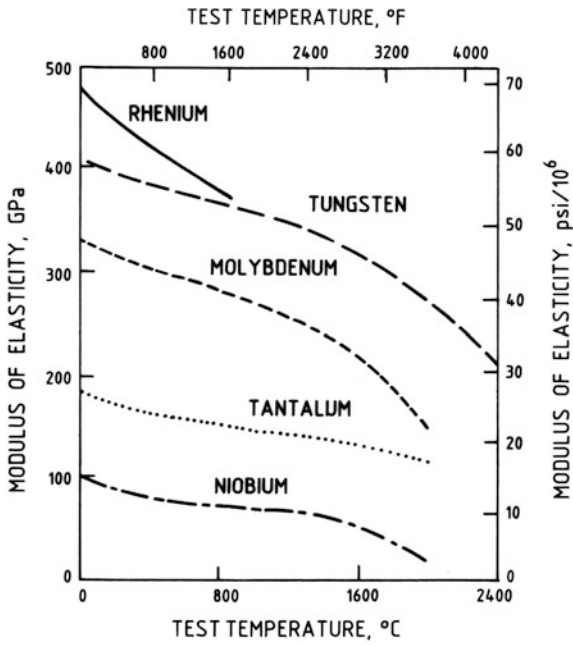


Fig. 12.2 Variation of the modulus of elasticity of refractory metals with temperature

In view of the excellent potential of niobium as an advanced candidate material for aerospace applications, this chapter deals extensively with melting, processing, properties, and applications of Nb alloys and also describes important characteristics of other refractory alloys.

12.2 Niobium Alloys

12.2.1 Nb Alloys and Their Properties

Niobium is a tough, shiny, silver-gray, soft, ductile metal that somewhat resembles stainless steel in appearance. The metal was discovered in 1801 in an ore shipped from Connecticut, more than 100 years earlier, by the English scientist Charles Hatchett, who named it Columbium. The name niobium was adopted by IUPAC in 1950. The important physical properties of niobium metal are listed in Table 12.2. Currently about 1000 tons of niobium is produced per year, of which 95 % is used as additions to steel and nickel-base alloys for increasing strength, while the balance is used either as pure Nb or its alloys.

Niobium is also the lightest refractory metal, with density close to that of nickel, and has good thermal conductivity (65.3 W/mK at 600 °C). Its bcc structure enables a higher solubility of alloying elements, and the metal has excellent formability and weldability, and is not susceptible to low temperature notch sensitivity. However, although niobium is attractive in terms of melting temperatures and room temperature ductility, its applications have been limited because of its poor high temperature strength and oxidation resistance.

Niobium is easily oxidized at about 250 °C. The oxidation takes place rapidly above 500 °C. Its high temperature oxidation resistance and high temperature strength have to be improved for long-term very high temperature structural applications [2]. Nevertheless, it is noteworthy that this metal possesses qualities that cannot be offered by any other type of material. Hence considerable effort has been made to compensate for its disadvantages via engineering design of the components.

Table 12.2 Physical properties of niobium

Properties	
Density at 20 °C (g/cm ³)	8.75
Crystal structure, lattice parameter	Body centered cubic, $a = 3.3 \times 10^{-10}$ m
Melting point (°C)	2468
Boiling point (°C)	4927
Linear coefficient of thermal expansion (K ⁻¹)	6.892×10^{-4}
Specific heat (kJ kg ⁻¹ K ⁻¹)	0.26
Latent heat of fusion (kJ/kg)	290
Latent heat of vaporization (kJ/kg)	7479
Thermal conductivity at 0 °C (W cm ⁻¹ K ⁻¹)	0.533
Electrical resistivity (μΩ cm)	15.22

Niobium can be alloyed to improve the oxidation resistance and also the high temperature strength. The problem is that it is not always possible to achieve the desired combination of improvement through alloying without sacrificing some of the other desirable properties. For example, a higher strength, oxidation resistance, and good room temperature ductility combination has not yet been found. Nor has anyone yet achieved the excellent high temperature strength from alloying without sacrificing something in fabricability and weldability.

In searching for ways to increase high temperature strength and creep resistance with satisfactory workability, as well as methods of protection against oxidation at operating temperatures exceeding 1027 °C, significant Nb alloy development activities were undertaken in the 1960s and early 1970s. Several potential alloys were developed [4–6] that may be conveniently divided into low, medium-, and high-strength alloys that have been used for long-term operation at 1000–1200 °C and for short-term operation at 1200–1700 °C.

These alloys were extensively investigated as candidate materials for nuclear applications and structural components in aircraft, space vehicles, rockets, etc.; and are also used for electronic, high energy physics, and chemical process industries. Even in these areas, their applications have been limited by their susceptibility to high temperature oxidation and long-term creep [7]. Efforts to improve the resistance to high temperature oxidation through modification of alloy chemistry have not been successful.

Although protective coating systems were developed to permit the use of Nb alloys in high temperature oxidizing aerospace applications [8], the goal of simultaneously achieving high strength and workability, and providing safe protection for long-term operation remained unsolved. Hence the interest in refractory metallic systems based on Nb declined.

However, the more recent need, since the 1980s, for (very) high temperature materials in aerospace and power engineering has rejuvenated the interest in refractory metallic systems, particularly Nb-based alloys. Two problem areas were identified:

1. In the temperature range 600–900 °C wrought titanium alloys are unsuitable, while nickel-base alloys do not meet specific (i.e. density compensated) strength requirements.
2. In the temperature range 1100–1500 °C wrought nickel-base alloys are unsuitable, whereas alloys based on intermetallics and heat-resistant ceramics, considered as prospective structural materials, do not provide the required strength, ductility or fracture toughness.

Commercial Nb alloys are relatively low in strength and extremely ductile, and can be cold-worked by over 70 % before annealing becomes necessary. Alloying elements such as Mo and W, which are group VIA elements and which go into solid solution with Nb, are the most effective in imparting high temperature strength. However, when added in sufficient quantity to give appreciable strengthening effect, these elements raise the temperature to achieve 10 % reduction in area, see Fig. 12.3, and adversely affect the fabricability and weldability.

Another potent strengthening mechanism characteristic of most of the high strength alloys is the interaction between one of the reactive elements Zr or Hf and

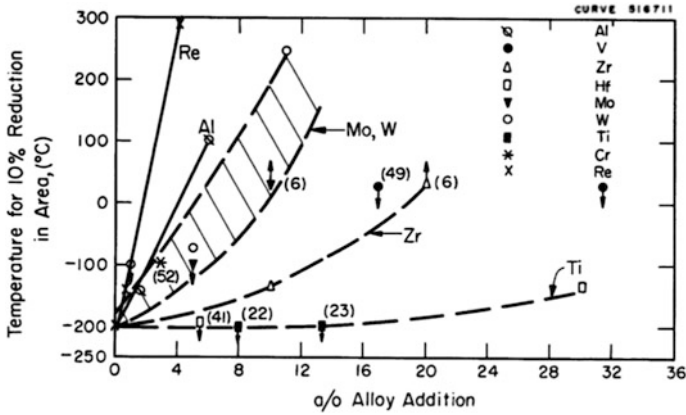


Fig. 12.3 Effect of alloying addition on ductility transition temperature of niobium

C, O, or N to form precipitates. The precipitates are very effective for high temperature strengthening and maintaining ductility after welding. The most common high temperature niobium alloys are listed in Table 12.3 [9, 10]. All are hardened by solid solution strengthening; however, small amounts of second phase particles such as oxides, nitrides, and carbides are present. The size and distribution of second phase precipitate particles can often have a strong influence on mechanical properties and recrystallization behaviour. Typical room temperature mechanical properties of unalloyed niobium and the most common Nb alloys are given in Tables 12.4 and 12.5 [9, 10], respectively.

The WC-3009 alloy listed in Tables 12.3 and 12.5 contains ~0.10 wt% oxygen, which is about five times more than in other niobium alloys. This high level of oxygen is the result of powder processing. It is not deleterious to mechanical properties because oxygen combines with hafnium in the alloy to form stable hafnium oxide precipitates. WC-3009 is unique in that it exhibits an oxidation rate less than one tenth that of most other niobium alloys. When WC-3009 was developed, it was speculated that such an alloy could survive a short supersonic mission even in the event of a protective coating failure.

Table 12.3 Commercial niobium alloys

Nominal composition (wt%)	Commercial nomenclature
Nb-1Zr	Nb-1Zr
Nb-1Zr-0.1C	PWC-11
Nb-28Ta-10W-1Zr	FS-85
Nb-10W-2.5Zr	Cb-752
Nb-10Hf-1Ti	C-103
Nb-10W-10Hf-0.1Y	C-129Y
Nb-30Hf-9W	WC-3009
Nb-46.5Ti	–
Nb-55Ti	–

Table 12.4 Mechanical properties of niobium

Mechanical properties	
<i>Annealed condition</i>	
Ultimate tensile strength	195 MPa
Yield strength	105 MPa
Elongation	30 %+
Reduction in area	80 %+
Hardness	60HV
Poisson's ratio	0.38
Strain hardening exponent	0.24
Elastic modulus	103 GPa
DBTT	-126 °C
Recrystallization temperature	800–1000 °C
<i>Cold-worked condition</i>	
Ultimate tensile strength	585 MPa
Elongation	5 %
Hardness	150HV

Table 12.5 Room temperature tensile properties of commercial niobium alloys

Commercial name of alloy	Alloy composition (wt %)	YS (MPa)	UTS (MPa)	EL (%)
Nb-1Zr	Nb-1Zr	150	275	40
PWC-11	Nb-1Zr-0.1C	175	320	26
FS-85	Nb-28 Ta-10W-1Zr	462	570	3
Cb-752	Nb-10W-2.5Zr	400	540	20
C-103	Nb-10Hf-1Ti	296	420	26
C-129Y	Nb-10W-1Hf-0.1Y	515	620	25
C-3009	Nb-30Hf-9W	752	862	24

All the alloys (except FS-85) are quite ductile at room temperature. The highest tensile strength at room temperature is exhibited by C-3009 (Nb-30Hf-9W), while the highest ductility is shown by Nb-1Zr. The high temperature tensile and creep properties of common Nb alloys are shown in Fig. 12.4. Even though WC-3009 clearly exhibits the highest tensile strength over the entire temperature range, FS-85 has superior creep strength. Its high creep strength is due to its higher melting point, which is due to its high concentration of Ta and W.

Niobium alloys are much less tolerant to impurity pick-up than other reactive metals such as titanium and zirconium. Alloys containing second phase particles that form a continuous boundary between grains can show drastically reduced room temperature tensile elongation. This condition is usually caused by contamination (omit) or improper heat treatment.

The total permissible interstitial oxygen, hydrogen, carbon, and nitrogen contents of niobium alloys are typically one-fifth to one-tenth of those for titanium or zirconium alloys.

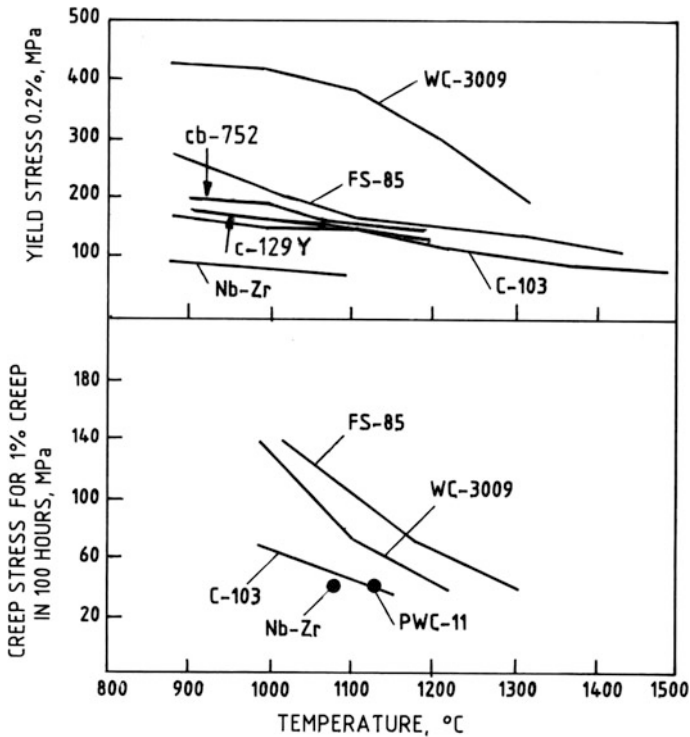


Fig. 12.4 Strength and creep properties of common Nb alloys

Elastic modulus, thermal conductivity, and total hemispherical emissivity are listed in Tables 12.6, 12.7, and 12.8. Generally, smooth and non-oxidized surfaces have much lower emissivity than their oxidized counterparts. Also shown in Table 12.8 is an emissivity value of 0.7–0.82 for silicide coated C-103. This value is for a common Si-20 %Fe-20 %Cr coating applied by the slurry coat and diffusion method.

12.2.2 Production Methods for Niobium

Niobium metal was originally produced by powder metallurgy methods that involved high temperature vacuum sintering and carbon reduction. However, aluminothermic reduction and electron beam (EB) purification became the standard practices since the early 1960s [11, 12].

In aluminothermic reduction, Nb_2O_5 and aluminium powders are first blended together and then reacted exothermically to form crude niobium metal and Al_2O_3 slag. The crude niobium metal typically contains several percent impurities,

Table 12.6 Elastic moduli of commercial niobium alloys

Alloy	Elastic modulus (GPa)	
	20 °C	1200 °C
Nb-1Zr	80	28
FS-85	140	110
C-103	90	64
C-3009	123	–
Cb-752	110	–

Table 12.7 Thermal conductivity of commercial niobium alloys

Alloy	800 °C (W/mK)	1200 °C (W/mK)
Nb-1Zr	59.0	63.1
C-103	37.4	42.4
FS-85	52.8	56.7
Cb-752		

Table 12.8 Total hemispherical emissivity of commercial niobium alloys

Alloy	800 °C	1200 °C
Nb-1Zr	0.14	0.18
C-103	0.28	0.4
C-103 (silicide coated)	0.70	0.82

including aluminium and oxygen. At elevated temperatures many of these impurities have a much higher vapour pressure than niobium metal, because of which they can be purified commercially by EB melting; while the low vapour pressure impurities such as tantalum and tungsten are more difficult to remove. The real impetus to niobium and niobium alloy metallurgy came with the commercialization of the EB Melting Process.

12.2.3 *Melting and Refining of Niobium and Preparation of Nb-Based Alloys*

It is well established that the properties of wrought refractory metal products depend to a large extent on the purity of the raw material, particularly the interstitial impurity contents [13, 14], which tend to embrittle the alloys. Therefore raw material production methods which result in lower impurity contents are preferred. As such, although Nb-based alloys can be prepared by powder metallurgy (PM) methods, the more common and economic way of preparing the starting material is the ingot metallurgy (IM) route, since it results in lower impurity contents.

Conventional melting and casting techniques are unsuitable for refractory metals and alloys production, since the melting temperatures of these metals are above the working temperatures of common refractories. Vacuum arc remelting (VAR) and

EB melting furnaces are widely used for melting niobium and its alloys. Powders of Nb and other alloying elements are premixed, compacted, and vacuum sintered to produce consumable electrodes for these processes. VAR is suitable for preparation of Nb-based alloys containing alloying elements with high vapour pressure. However, it is necessary to start with high purity Nb, since no refining is possible during VAR. High purity Nb is produced by multiple melting in EB furnaces. Recently, it has been demonstrated that it is possible to produce high purity niobium ingots in one single step of melting by operating the EB melting process under optimum process parameters. Nb-based alloys containing alloying elements with low vapour pressure can be directly EB melted to produce alloys.

The most common alloy additions to Nb are zirconium, titanium, and hafnium. Higher melting temperature elements such as tungsten or tantalum can be added during EB melting. Even though VAR (commonly used for alloy steels, nickel, and titanium alloys) can also be used for niobium, it should be noted that the high melting temperature of niobium requires much higher power levels. It is not unusual to melt 200 mm diameter ingots using 15,000–20,000 amperes of current. Some alloys such as Nb-1Zr are prone to arcing against the crucibles and causing burning of the water jacket. Therefore intensive water cooling is required to minimize this risk.

12.2.4 Processing of Niobium

Niobium can be worked by most metal working processes. However, compared to other more common materials like steel or titanium alloys, niobium alloys have higher flow stresses at hot working temperatures. Processing temperatures of Nb and its alloys are given in Table 12.9 [15].

Breakdown of the generally large-grained ingots by mechanical working is a challenging problem from the cracking point of view, particularly for high strength alloys. Recently, extrusion has become an attractive alternative for alloys with low workability, because of improved glass lubricating and die coating techniques. These reduce frictional stresses and the resultant cracking tendency.

Forging is done for primary breakdown of alloys, although intermediate extrusion is necessary for low workability alloys. Both hammer and press forging techniques are used to produce flat slabs or round billets. Hot forging temperatures for typical commercial alloys range between 650 and 1400 °C.

Heating to the above-mentioned temperatures causes excessive oxidation, and oxygen, nitrogen, and hydrogen can be picked-up, occupying interstitial positions. Thus the alloys are heated using protective coatings or in inert gas atmospheres. Coating protects the alloys during both heating as well as forging, but a certain amount of material must be sacrificed in subsequent grinding or pickling.

Most niobium alloys are either cold rolled or warm rolled (200–370 °C) to produce plates, wires, rods, etc. Cold die forging, spinning, hydroforming, and welding techniques are employed to produce complex shapes.

Table 12.9 Mill processing temperature for niobium and its alloys

Commercial name of alloy	Forging temp. (°C)	Forging total thickness reduction (%)	Extrusion temp. (°C)	Extrusion area reduction ratio	Rolling temp. (°C)	Rolling total reduction in thickness between anneals (%)
Nb	980–650	50–80	1095–650	10:1	315–205; 20	50 breakdown; 90 finish
Nb-1Zr	1205–980	50–80	1205–980	10:1	315–205; 20	50 breakdown; 80 finish
FS-85	1315–980	50	1315–980	4:1	370–205; 20	40 breakdown; 50 finish
Cb-752	1205–980	30	1315–980	4:1	370–260; 20	50 breakdown; 60 finish
C-103	1315–980	50	1315–980	8:1	205; 20	50 breakdown; 60 finish
C-129Y	1315–980	50	1315–980	4:1	425; 20	50 breakdown; 60 finish

During the early 1980s there were several programmes aimed at producing niobium alloy parts by more cost-effective methods. Several attempts were made to manufacture niobium alloy net shape parts by investment casting. This method presented some special challenges with respect to extensive metal–mould reaction, and to get enough superheating into the metal to avoid cold laps. While it was demonstrated that casting is possible even for niobium alloys with melting temperatures over 2400 °C, the “as-cast” microstructure is typically less ductile than normal wrought microstructures.

The economic aspects of producing niobium alloy castings were also severely hindered by the loss of metal in the form of gates, skull, and risers. Unlike titanium and nickel alloys, the gates and other casting scrap are not remeltable for niobium alloy production, owing to the metal’s low tolerance for interstitial impurities. An investment cast C-103 alloy turbine engine stator is shown in Fig. 12.5. At this time no niobium alloy parts are actually produced by this method.

12.2.5 Applications of Niobium and its Alloys

The largest amount of niobium production is as FeNb in the steel industry, where niobium is used as an alloying element for improvement of the high temperature strength and for providing non-scaling properties during hot working. A special property of niobium is its superconductivity, which was discovered in 1911. For practical use of superconductivity ultrapure niobium is required.

Since niobium is relatively low in density and can maintain its strength at high temperatures, niobium and its alloys are finding high temperature applications. The

Fig. 12.5 Investment cast C-103 stator ring produced by precision casting



most common application of the alloys is in sodium vapour lamps: the Nb-1Zr alloy demonstrates excellent formability, weldability, and long life in a sodium vapour environment. The small tubular shapes of Nb-1Zr in these lamps are made from seamless tubing, which in turn is made by deep drawing sheet metal. Today, the primary application for high temperature niobium alloys is for rocket thrusters and nozzles.

The alloy with the most promising combination of elevated temperature strength and fabrication characteristics is the C-103 alloy. For aerospace applications at 1100–1500 °C, alloy C-103 has been the workhorse of the niobium industry because of its higher strength. Excellent cold forming and welding characteristics enable manufacturers to construct very complex shapes such as thrust cones and high temperature valves. Closed die forgings are also easily produced.

Most of the components in propulsion systems are exposed for relatively short times to temperatures between 1200 °C and 1400 °C. The service environments for propulsion systems are often less oxidizing than the normal atmosphere. However, because C-103 has virtually no oxidation resistance, components are extensively coated with silicides. The coatings contain elements such as chromium, hafnium, iron and nickel in addition to silicon. After the element-mixed coating is applied by spraying or dipping, it is diffused into the alloy at high temperature.

C-103 has also been considered for thrust augmentor (afterburner) flaps in aircraft engines. These flaps are placed at the tail end of the engine to form a high temperature liner in the afterburner section, typically reaching 1200–1300 °C and lasting for ~100 h of afterburner time.

Niobium alloys have also been evaluated for various high temperature components of the (cancelled) US National Aerospace Plane. Hypersonic leading edges and nose cones were fabricated to function as heat pipe thermal management systems. The heat pipe concept was designed to transport extreme heat away from hot spots, such as hypersonic leading edges, to cooler areas, where heat could be

expelled by radiation. A typical 500 g niobium heat pipe can dissipate over 10 kW of heat and operate isothermally at 1250–1350 °C.

In addition to these applications, niobium and its alloys are used in more common applications, for example in chemical engineering for heat exchangers, in high temperature furnace construction for heating, and for shielding elements.

12.3 Niobium-Silicide Based Composites

Niobium-silicide based composites are promising candidates for high temperature applications in the next generation advanced jet engines [16–19]. The suction casting method with large cooling rates has been used to produce alloys with refined and large volume fraction eutectic structures [20]. There have been several reviews of development of Nb-silicide based composites [21, 22]. Simple Nb-silicide composites are based on binary Nb-Si alloys; more complex systems are alloyed with Ti, Hf, Cr, and Al.

Alloying strategies have been developed to achieve an excellent balance of room temperature toughness, high temperature strength, and oxidation resistance. The melting point of the Nb-silicide based composites is in excess of 1750 °C. The density is in the range of 6.6–7.2 g/cm³. The room temperature fracture toughness of the Nb-silicide based composite system has been reported to be >20 MPa/m.

Many of the research programme have focussed on developing a fundamental understanding of the solidification paths, mechanical behaviour, and oxidation resistance of the Nb-silicide based system.

The reactivity of the Nb alloy melts excludes the use of ceramic-based melting crucibles. However, Nb-silicide based composites have been fabricated using a range of processes including arc melting, ingot casting plus thermomechanical processing [21], directional solidification [22], vapour deposition, and powder metallurgy processing [21]. These techniques have successfully produced laboratory scale materials for alloy development and property studies. Directional solidification, investment casting, and hot extrusion have been used successfully to produce Nb-silicide composites. Recent investment mould developments have shown excellent potential for thin wall airfoils, although these techniques are not well developed with regard to the production of net-shaped airfoils.

The oxidation resistance of the Nb-silicides is sufficient to qualify for near term engine testing applications, but further improvements are required to satisfy the long-term design requirements. Additional work is required to generate an understanding of the mechanisms controlling properties such as fracture toughness, fatigue crack growth, and creep performance before these alloy systems can be considered for service. Process developments are required to manufacture actual components of Nb-silicide composites.

12.4 Other Refractory Metals

12.4.1 Tantalum and its Alloys

Tantalum provides a unique combination of properties among refractory metals. Its high melting point (2996 °C), reasonable modulus of elasticity, excellent room temperature ductility, low DBTT, and relatively high solid solubility for other refractory and reactive metals make it an alternative base material for high temperature structural applications.

The most common tantalum alloys are listed in Table 12.10 [15]. Ta-10W is primarily being considered for aerospace applications, while Ta-2.5W is used in heat exchangers and other welded-tube applications where high formability is needed. Other elements that can be added to modify tantalum properties include zirconium, hafnium, molybdenum, niobium, rhenium, and vanadium. The typical tensile strengths of tantalum and tantalum alloys from room temperature to 1800 °C are shown in Fig. 12.6 [15].

High purity Ta is produced by multiple melting in an electron beam melting (EBM) furnace. EBM can also be used for melting Ta-based alloys containing alloying elements with low vapour pressure. Vacuum arc remelting (VAR) is suitable for preparation of Ta-based alloys containing alloying elements with high vapour pressure.

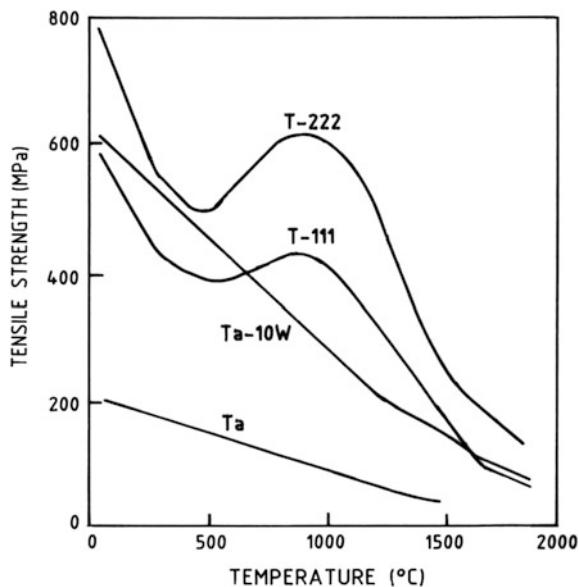
Both hammer and press forging techniques are used to produce flat slabs or round billets. Hot forging temperatures for typical commercial alloys range between 815 °C and 1260 °C. However, heating to temperatures within this range causes excessive oxidation. Therefore these alloys are heated using protective coatings or an inert gas atmosphere. Most tantalum alloys are either cold-rolled or warm-rolled (260–370 °C) to produce plates, wires, rods, etc. Cold die forging, spinning, hydroforming, and welding techniques are employed to produce complex shapes.

It has been reported that the largest (66 %) quantity of tantalum is used in the electronic industry in the form of powder, wire, and furnace hardware for the production of solid electrolyte capacitors. About 22 % tantalum finds applications in cutting tool industries, and only about 2 % is used for nuclear industries and defence applications. Primarily because of its unique combination of ductility and

Table 12.10 Commercial tantalum alloys

Alloy name	Composition (wt%)
	Ta-2.5W
	Ta-7.5W
	Ta-10W
T-111	Ta-8W-2Hf
T-222	Ta-10W-2.5Hf
ASTAR-811C	Ta-8W-1Re-1Hf-0.025C
	Ta-20Ti
	Ta-40Nb

Fig. 12.6 Tensile strengths versus temperature for pure tantalum and typical tantalum alloys



high density, tantalum has become the material of choice for several advanced anti-armour weapon systems. However, because of its very high density, initial efforts to use Ta and its alloys for aerospace applications have not been successful.

12.4.2 Molybdenum and Its Alloys

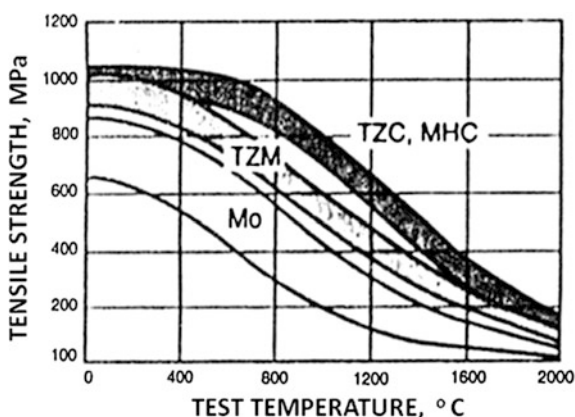
Molybdenum combines a high melting point with strength retention at high temperatures. Molybdenum also has a high specific elastic modulus, which makes it attractive for applications that require both high stiffness and low weight. The high thermal conductivity, low coefficient of thermal expansion, and low specific heat of this metal provide resistance to thermal shock and fatigue. These properties are also important for electronic applications.

Carbide-strengthened alloys were the first molybdenum alloys to be commercialized, see Table 12.11 [23]. Mo-0.5Ti, the initial alloy, is no longer commercially available. Its high temperature strength and recrystallization resistance were improved by adding about 0.08 % zirconium, resulting in the alloy known as TZM. A higher alloy-content modification of TZM, called TZC, has improved properties and responds to an age-hardening heat treatment. However, TZC has not replaced TZM as the commercial alloy of choice, primarily due to economic considerations.

More recently, alloys strengthened with hafnium carbide (MHC) and combinations of reactive metals carbides (ZHM) have been marketed. Figure 12.7 [23] compares the elevated temperature tensile properties of carbide-strengthened Mo

Table 12.11 Commercial molybdenum alloys

Alloy name	Composition (wt%)
TZM	Mo-0.5Ti-0.08Zr-0.01C
TZC	Mo-1.2Ti-0.3Zr-0.1C
MHC	Mo-1.2Hf-0.05C
ZHM	Mo-0.5-1.5Hf-0.2C

Fig. 12.7 Elevated temperature properties of carbide-strengthened molybdenum alloys

alloys. N.B: Both TZM and MHC are used as tooling materials in the isothermal forging of nickel-base superalloy parts for aircraft gas turbine engines.

Primary consolidation of molybdenum and its alloys can be done by either VAC or powder metallurgy (P/M) techniques. Both mechanical pressing and cold isostatic pressing (CIP) are used to consolidate P/M billets, although most P/M mill products originate as CIP'ed billets.

P/M billets are typically sintered in hydrogen because hydrogen reduces molybdenum oxides and further purifies the material. Vacuum sintering is used by some manufacturers.

Unalloyed molybdenum and TZM can be readily forged with a variety of tools including steam hammers, drop hammers, and hydraulic forging presses using either open or closed dies. Unalloyed molybdenum and TZM are typically forged in the 870–1260 °C temperature range. Billet heating is conducted in commercial gas or oil-fired furnaces. Billets and work pieces will lose weight from volatilization of the oxide at temperatures above 650 °C, but there is no scale formation: weight losses of 1–5 % can be anticipated.

Molybdenum and its alloys are readily extruded to form a variety of shapes including tubes, round to round bars, round to square bars, and round to rectangular bars. Pure molybdenum is typically extruded in the temperature range 1065–1090 °C, and TZM is extruded in the temperature range 1120–1150 °C. Large tubes and rings are fabricated from back-extruded solid billets. Additional ring-forming operations are undertaken via ring rolling. Molybdenum and its alloys can be

fabricated in sheet form by conventional rolling and cross-rolling processes, and molybdenum and TZM sheet are typically supplied in the annealed condition.

Molybdenum is important in the missile industry, where it is used for high temperature structural parts such as nozzles, leading edges of control surfaces, support vanes, struts, re-entry cones, heat-radiation shields, heat sinks, turbine wheels and pumps. Alloy Mo-0.5Ti has been used for some aerospace applications, but TZM is preferred where higher hot strength is needed. The service temperatures for molybdenum alloys in structural applications are limited to a maximum of about 1650 °C.

12.4.3 Tungsten and Its Alloys

Tungsten has the highest melting point of any metal (3410 °C) and also the highest density (19.26 g/cm³). It also has an unusually high elastic modulus (414 GPa) and is the only elastically isotropic metal. The high melting temperature and low vapour pressure of tungsten, along with its ability to be drawn into fine wire, were responsible for its initial commercial application in lamp filaments at the beginning of the twentieth century.

Tungsten has high tensile strength and good creep resistance. At temperatures above 2205 °C, tungsten has twice the tensile strength of the strongest tantalum alloys and is only 10 % denser. However, its high density, poor low temperature ductility, and strong reactivity in air limit its usefulness. Maximum service temperatures for tungsten range from 1925–2480 °C, but surface protection is required for use in air at these temperatures.

Tungsten heavy alloys usually contain Ni and Cu or Ni and Fe. The mechanical properties of tungsten heavy alloys are closely linked to W content, sintering variables, and the amount of post-sintering mechanical working. These alloys are mainly used in counterweights and anti-armor kinetic-energy penetrators. They are also considered for radiation shielding.

Three types of tungsten alloys are produced commercially: W-ThO₂, W-Mo, and W-Re alloys (Table 12.12) [24]. The W-ThO₂ alloy is a dispersed-second-phase alloy containing 1–2 % thorium oxide (thoria). The thoria dispersion enhances thermionic electron emission, which improves the starting characteristics of gas tungsten arc weld (GTAW) welding electrodes. Thoria also imparts creep strength to wire at temperatures above one-half of the absolute melting point of tungsten.

The W-Mo alloys are solid solution alloys. These alloys are used mostly for improved machinability, where strength requirements are somewhat lower than those of W and the W-ThO₂ alloy. W-Re alloys are also solid solution alloys. The W-1.5Re and W-3Re alloys are used to improve the resistance to cold fracture in lamp filaments, especially for lamps subjected to vibrations. These alloys also contain the AKS (alumina, silica, and potassium) dopants to improve the creep

Table 12.12 Commercial tungsten alloys

Alloy name	Composition (wt%)
W-ThO ₂	W-1ThO ₂
	W-2ThO ₂
W-Mo	W-2Mo
	W-15Mo
W-Re	W-1.5Re
	W-3Re
	W-25Re
AKS doped	0.0015 Al, 0.009 K, 0.005 Si and 0.0035 O

strength in filament wire: undoped W-1.5Re and W-3Re alloys are used in thermocouple applications where strength is not the primary concern.

Tungsten is consolidated to full density by three principal methods, two of which are P/M processes. These methods are (i) solid-state sintering and mechanical working (wrought P/M tungsten), (ii) liquid-phase sintering of powders, and (iii) chemical vapour deposition (CVD). Tungsten and tungsten alloys may also be produced by arc casting or EBM, but these methods are not of significant commercial interest. Although tungsten produced by the melting route can have higher purity than P/M or CVD products, the slight improvement in mechanical and physical properties does not justify the added expense and engineering challenge of melting tungsten.

A cold isostatically pressed (CIP'ed) tungsten powder bar is self-resistance heated to around 2500 °C and sintered to 90 % of the theoretical density. The bar is then swaged and drawn into wire; or alternatively the sintered tungsten bar may be forged or rolled into bar or sheet products. Initial hot working is done at temperatures above 1500 °C, since the as-sintered bar is brittle at low temperature because it is fully recrystallized and not fully dense. However, there are more considerations about hot working: the DBTT of fully dense unalloyed tungsten is approximately 3000 °C and the recrystallization temperature is 1700 °C, and so the common thermomechanical processing scheme is to deform the metal at temperatures between the DBTT and the recrystallization temperature. As the amount of deformation increases, both the DBTT and the recrystallization temperature decrease. Hence at room temperature hot-worked tungsten bar is brittle, but heavily worked tungsten wire exhibits significant ductility.

Tungsten and tungsten alloys are used in mill products, as an alloying element in tool steels and superalloys, in tungsten carbide cutting tools, and in a variety of tungsten-based chemicals. In terms of refractory metal consumption, tungsten ranks second to molybdenum, with more than 8500 metric tons consumed annually. Cutting tools account for 59 % of the total; mill products, 26 %; alloying, 9 %; and chemicals and miscellaneous applications, 6 %.

12.4.4 Rhenium and Its Alloys

Rhenium has a very high modulus of elasticity and does not have a DBTT, since it retains its ductility from subzero to high temperatures. Its hardness increases sharply after a small amount of deformation: the work hardening rate is higher than that of any other pure metal. Rhenium products withstand many heating–cooling cycles without losing their strength. Rhenium also has superior tensile and creep rupture strength over a wide range of temperatures [25]: for example, rhenium shows longer rupture life compared to tungsten up to 1800 °C. In addition, rhenium has been found to survive more than 1,000,000 thermal fatigue cycles from room temperature to over 2500 °C without any evidence of failure [25, 26].

Rhenium powder can be produced by the reduction of pure ammonium perrhenate in a stream of hydrogen. The desired properties of the metal powder, such as grain size and surface area, can be achieved by adjustment of the reduction parameters. The rhenium metal powder with added compaction agents is compressed into pellets and then sintered (1000–1500 °C) under an atmosphere of hydrogen. Large workpieces are produced by compressing rhenium metal powders isostatically and then sintering. EBM and zone refining are the methods used to produce rhenium with 99.995 % or more purity [27].

Rhenium has very poor oxidation resistance and therefore cannot be hot-worked when exposed to air. Hence hot working has to be done under vacuum or in a protective atmosphere, or by adopting an encapsulation technique. Because of its very good ductility, rhenium can be cold-worked into wire, rod, sheet, plate, and tubing. Frequent intermittent annealing may have to be performed since, as mentioned above, rhenium work hardens very quickly. Electrical discharge machining, centreless grinding, and welding are manufacturing techniques commonly used for rhenium components.

Platinum-rhenium reforming catalysts are the major rhenium end-use products and account for a significant proportion of rhenium consumption. The higher electrical resistivity coupled with low vapour pressure makes it ideally suited for filament applications. One of the largest applications for rhenium is for mass spectrometer filaments. These are generally available in commercial (99.99 %) and zone-refined (99.995 %) purities.

Besides its intrinsic properties, rhenium is a beneficial alloying addition to other refractory metals and alloys, greatly enhancing their strength. This capability is maintained even when heating above the recrystallization temperature. For example, all aeroengine turbine blades made of second and subsequent generations of nickel-base superalloys contain 3–6 % Re, which significantly improves the creep properties [28]. Rhenium alloys are used in nuclear reactors, semiconductors, electronic tube components, thermocouples, gyroscopes, miniature rockets, electrical contacts, thermionic converters, and other commercial and aerospace applications. Tungsten-rhenium alloys, obtained by vapour deposition, are used to coat the surfaces of molybdenum targets in X-ray tubes. Other rhenium alloys (with tungsten or molybdenum) are used for filaments, grid heaters, cathode cups, and

igniter wires in photoflash bulbs. Rhenium has been used as a heat exchanger material for a solar rocket, nozzles for rocket thrusters, and in high temperature thermocouples. Also, rhenium is unique among refractory metals in that it does not form a stable carbide. For this reason, rhenium-coated carbon has been evaluated for rocket nozzles.

The use of rhenium has been restricted by its high density and high cost. For example, the addition of 3 % rhenium to tungsten wire doubles the cost of the wire.

12.5 Indian Scenario

In India a number of organizations have been focussing efforts to develop different refractory metals and their alloys for a variety of applications. Nuclear Fuel Complex, Hyderabad, has been engaged in the production of aluminothermically reduced niobium from the ore, which is refined by multiple EB drip melting to produce reactor grade Nb. This is used to manufacture coolant tubes of Zr-2.5Nb alloy for heavy water nuclear reactors.

Recently M/s MIDHANI, Hyderabad, has produced sheets of C-103 (Nb-10Hf-1Ti) alloy for satellite applications, starting from imported sheets of high purity raw material. Two EBM furnaces of 150 and 300 kW have been recently established at MIDHANI to develop alloys based on refractory metals. BARC, Mumbai, is actively pursuing development of Nb-1Zr-0.1C alloy for nuclear applications. DMRL is involved in developing an Nb-based (Nb-W-Zr) alloy for aerospace applications.

DMRL has pioneered the development and application of tungsten for penetrator applications. An industrial plant (Ordnance factory) is in operation at HAPP, Trichy, producing W-based penetrators based on the DMRL technology. C-Met, Hyderabad, has perfected the technology of producing high purity tantalum for capacitor applications.

12.6 Summary

Future high temperature materials will depend on developments in refractory metals and alloys in view of their high melting temperatures and good high temperature mechanical properties. Refractory metals, with their unique properties, can perform in situations where no other materials can meet the required properties. The future developments in this area include developing alloys with the desired combinations of strength, ductility, and oxidation resistance. Niobium is particularly attractive for aerospace applications because of its lower density among refractory metals, which is comparable to that of nickel-base superalloys.

An effort has been made in this chapter to discuss the important features of refractory metals and their alloys in general, and niobium and niobium-based alloys in particular.

References

1. Stephen JJ (1990) Recent advances in high-temperature niobium alloys. *JOM* 42(8):22–23
2. Wittenauer J (1990) Refractory metals 1990: old challenges, new opportunities. *JOM* 42(8):07–10
3. Lambert JB (1990) Refractory metals and alloys. In: *ASM handbook volume 2: properties and selection: nonferrous alloys and special-purpose materials*. ASM International, Materials Park, OH, USA, pp 557–585
4. Frank RG (1968) Recent advances on columbium alloys. In: Machlin I, Begley RT, Weisert ED (eds) *Refractory metal alloys metallurgy and technology*. Plenum Press, New York, USA, pp 325–372
5. Comie JA (1971) Development of precipitation strengthened columbium base alloys. AFML technical report AFML-TR-71-51, Air Force Materials Laboratory, Wright-Patterson Air Force Base, Dayton, OH, USA
6. Roche TK, Graham DL (1970) Development of oxidation-resistant high strength columbium alloys. AFML technical report AFML-TR-69-344, Air Force Materials Laboratory, Wright-Patterson Air Force Base, Dayton, OH, USA
7. Craigwojck C (1991) High temperature niobium alloys. In: Stephens JJ, Ahmad I (eds) *High temperature niobium alloys*. The Minerals, Metals & Materials Society (TMS), Warrendale, PA, USA, pp 1–12
8. Sankar MV, Satya Prasad VV, Baligidad RG, Alam MdZ, Das DK, Gokhale AA (2015) Microstructure, oxidation resistance and tensile properties of silicide coated Nb-alloy C-103. *Mater Sci Eng, A* 645:339–346
9. Eckert J (1997) Refractory metals. In: Habashi F (ed) *Handbook of extractive metallurgy, vol III'*. Wiley-VCH, Weinheim, Germany, pp 1403–1416
10. Wojcik CC (1998) High temperature niobium alloys. *Adv Mater Processes* 154(6):27–30
11. Katsutoshi O, Kim YH (1992) Electron beam melting and refining of niobium. *ISIJ Int* 32(5):650–655
12. Choudhary A, Hengsberger E (1992) Electron beam melting and refining of metals and alloys. *ISIJ Int* 32(5):673–681
13. Loomis BA, Greber B (1970) The yield-stress of niobium and niobium-oxygen solid solutions. *Scr Metall* 4(11):921–924
14. Sankar M, Baligidad RG, Gokhale AA (2013) Effect of oxygen on microstructure and mechanical properties of niobium. *Mater Sci Eng, A* 569:132–136
15. Buckman RW (2000) New applications for tantalum and tantalum alloys. *JOM* 52(3):40–41
16. Mendiratta MG, Lewandowski JJ, Dimiduk DM (1991) Strength and ductile-phase toughening in the two-phase Nb/Nb₅Si₃ alloys. *Metall Trans A* 22A:1573–1581
17. Mendirattaa MG, Dimiduk DM (1993) Strength and toughness of a Nb/Nb₅Si₃ composite. *Metall Trans A* 24A(2):501–504
18. Bewlay BP, Jackson MR, Lipsitt HA (1996) The balance of mechanical and environmental properties of a multielement niobium-niobium silicide-based in-situ composite. *Metall Mater Trans A* 27A(12):3801–3808
19. Bewlay BP, Jackson MR, Subramanian PR (1999) Processing of high-temperature refractory metal silicide in-situ composites. *JOM* 51(4):32–36
20. Kashyap C, Tiwary CS, Chattopadhyay K (2013) Microstructural and mechanical behaviour study of suction cast Nb-Si binary alloys. *Mater Sci Eng, A* 583:188–198

21. Subramanian PR, Mendiratta MG, Dimiduk DM, Stucke MA (1997) Advanced intermetallic alloys—beyond gamma titanium aluminides. *Mater Sci Eng, A* 239–240:1–13
22. Bewlay BP, Jackson MR, Gigliotti MF (2002) Niobium silicide high temperature in situ composites, Chap 26. In: Westbrook JH, Fleischer RL (eds) *Intermetallic compounds—principles and practice—Volume 3: progress*, 3rd edn. Wiley, Hoboken, NJ, USA, pp 541–560
23. Shields JA (1992) Molybdenum and its alloys. *Adv Mater Processes* 142(3):28–36
24. Wittenaure JP, Nieh TG, Wadsworth J (1992) Tungsten and its alloys. *Adv Mater Processes* 142(3):28–37
25. Carlen JC, Bryskin BD (1994) Rhenium—a unique rare metal. *Mater Manuf Processes* 9(6):1087–1104
26. Sherman AJ, Tuffias RH, Kaplan RB (1991) The properties and applications of rhenium produced by CVD. *JOM* 7(7):20–23
27. Bryskin BD (1992) Rhenium and its alloys. *Adv Mater Processes* 142(3):22–27
28. Reed RC (2008) *The superalloys: fundamentals and applications*. Cambridge University Press, New York, NJ, USA, pp 170–187

Part II

Composites

Chapter 13

GLARE[®]: A Versatile Fibre Metal Laminate (FML) Concept

R.J.H. Wanhill

Abstract This chapter surveys the applications and properties of the fibre metal laminate (FML) concept GLARE. This concept includes a family of FMLs that can be tailored to specific requirements for aerospace applications, including resistance to fatigue crack growth, fracture, impact and fire and blast damage.

Keywords Fibre metal laminates · GLARE · Properties · Fatigue · Fracture · Corrosion · Applications

13.1 Introduction

Fibre metal laminates (FMLs) intended for aerospace structures have a long history, going back at least to the 1970s [1]. Their development has not been easy, and some initially promising candidates have proven non-viable as property and cost-effective alternatives to all-metal structures.

GLARE (GLASS REinforced aluminium laminates) have, however, succeeded in reaching production and service deployment, notably in the Airbus A380 civil transport aircraft, but also for other applications, as will be mentioned. This success has been made possible by a huge and well-documented R&D effort [2].

The first point of contact concerning GLARE and other FMLs is the Fibre Metal Laminates Centre of Competence (FMLC), founded in 2001 and based at the Delft University of Technology in the Netherlands. GLARE production currently takes place at Fokker Papendrecht (Netherlands) and Premium Aerotec Nordenhamm (Germany).

R.J.H. Wanhill (✉)
Emmeloord, Flevoland, The Netherlands
e-mail: rjhwahill@gmail.com

13.2 GLARE: A Family of Materials

GLARE is a member of the family of FMLs. A GLARE laminate consists of alternating layers of aluminium alloy sheets and unidirectional (UD) prepregs of S-glass fibres. The number and orientation of the UD prepreg layers between the aluminium alloy sheets can be varied to ‘tailor’ the engineering properties to the required application, see Table 13.1, which shows that there are currently six different standard grades of GLARE. Within each grade there can be many variations, depending upon the thicknesses of the aluminium alloy layers and the numbers of interleaved aluminium and prepreg layers. These variations are captured in a standard classification system, examples of which are shown in Fig. 13.1.

Figure 13.2 illustrates the build-up of a GLARE 3 laminate with a 3/2 lay-up, see Table 13.1 also.

Table 13.1 Standard types of GLARE: (1) each prepreg layer is 0.127 mm thick; (2) RD-Al is the rolling direction for the aluminium alloy sheet, defined as 0° for all the GLARE laminates

GLARE type	Prepreg lay-up between each alloy layer	Alloy and sheet thickness (mm)	Main beneficial characteristics	Typical applications
GLARE 1	0°/0°	AA7475-T761 0.3–0.4 mm	Fatigue, strength, yield stress	UD-loaded parts, RD-Al in loading direction (stiffeners)
GLARE 2A	0°/0°	AA2024-T3 0.2–0.5 mm	Fatigue, strength	UD-loaded parts, RD-Al in loading direction (stiffeners)
GLARE 2B	90°/90°		Fatigue, strength	UD-loaded parts, RD-Al perpendicular to loading direction (butt straps)
GLARE 3	0°/90°		Fatigue, impact	Biaxially loaded parts with principal stress ratio 1:1 (fuselage skins, bulkheads)
GLARE 4A	0°/90°/0°		Fatigue, strength in 0° direction	Biaxially loaded parts with principal stress ratio 2:1 and RD-Al in main loading direction (fuselage skins)
GLARE 4B	90°/0°/90°		Fatigue, strength in 90° direction	Biaxially loaded parts with principal stress ratio 2:1 and RD-Al perpendicular to main loading direction (fuselage skins)
GLARE 5	0°/90°/90°/0°		Impact	Floors and cargo liners, leading edges
GLARE 6A GLARE 6B	+45°/–45° –45°/+45°		Shear, off-axis properties	Blast-resistant luggage containers

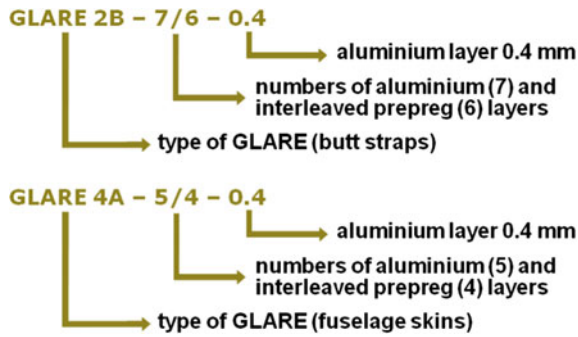


Fig. 13.1 GLARE standard notation examples

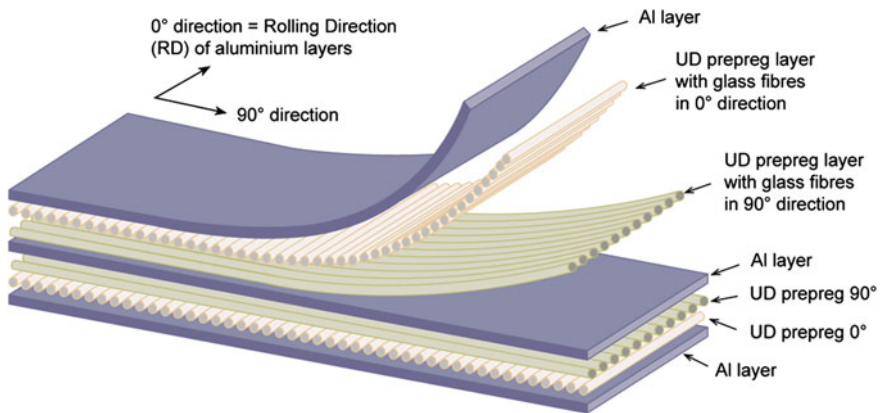


Fig. 13.2 Illustration of the build-up of a GLARE 3 laminate with a 3/2 lay-up: see Table 13.1 also

13.3 GLARE Applications

The most notable success of GLARE in airframe structures is its use in the Airbus A380, Fig. 13.3. Four grades of GLARE have been used: grade 2A for stringers, grade 2B for butt straps, grades 3 and 4A for fuselage skins [3, 4] and grade 5 for the horizontal and vertical stabiliser leading edges [5].

It should also be noted that the A380 airframe employs several classes of materials. These include conventional aluminium alloys, aluminium-lithium (Al-Li) alloys, GLARE and carbon fibre reinforced plastics (CFRPs) [6]. This reflects the modern trend of designing and using hybrid structures for optimum efficiency, in both civil and military aircraft and especially helicopters and VTOL configurations.



Fig. 13.3 GLARE deployment in the Airbus A380 [3–5]

Other applications of GLARE include [7, 8]:

- cargo bay floor replacements for civil transport aircraft (GLARE 5)
- radome front bulkhead for Learjet 45 (GLARE 5)
- blast-resistant cargo containers (GLARE 5 and 6)
- bonded patch repairs on Lockheed C-5A fuselage crowns (GLARE 2A/B).

Besides these actual uses, there are more possibilities. The following have been suggested: upper and lower wing skins, fuselage frames, passenger floors, flat or curved fuselage bulkheads, firewalls and cargo barriers [9].

Notwithstanding these possibilities, GLARE must generally compete with several other candidates, especially in primary structures. This is discussed in Sect. 13.5.

13.4 GLARE Properties

The main incentive for developing GLARE and other FMLs has been the quest for improved Damage Tolerance (DT) properties combined with high structural efficiency (strength and stiffness). Vogelesang [1] describes the history of FML developments in the Netherlands that led to GLARE, pointing out that fatigue damage dominates during the service life of an aircraft. Other sources amply support this [10, 11].

This section will focus on the DT properties of GLARE. Other properties that will be (briefly) considered are impact, flame and corrosion resistance; and

inspection and repair, both with respect to repair of GLARE itself and the use of GLARE patches to repair other structures. Much more information is in the modestly titled book *Fibre Metal Laminates: An Introduction* [2].

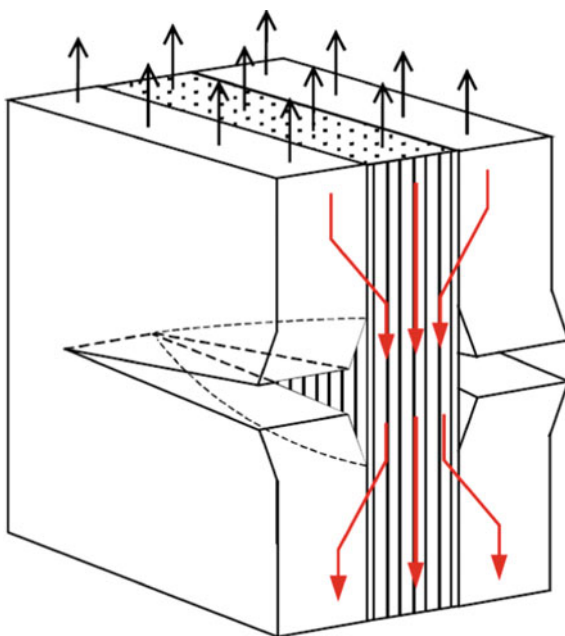
13.4.1 Damage Tolerance (DT): GLARE Basics

GLARE is produced by elevated temperature curing of the assembly of aluminium alloy and prepreg layers. Thermal expansion differences between the aluminium alloy and prepreg layers result in residual tensile stresses in the aluminium layers [12]. Although these stresses are minimised by careful design and production, they nevertheless adversely affect the resistance to fatigue crack initiation in the aluminium layers.

On the other hand, GLARE has a very high resistance to fatigue crack growth. The reason is ‘crack bridging’, see Fig. 13.4. Intact fibres in the aluminium alloy crack wake restrain the crack opening and reduce the crack driving force owing to load transfer into the fibre layers. Some delamination does, however, occur between the aluminium and fibre layers along the crack flanks.

The residual strength of GLARE is more complicated to evaluate [13]. This is because there are two different possible scenarios: (i) cracks with completely or mainly intact fibre layers, typically resulting from fatigue, and (ii) cracks through all

Fig. 13.4 Aluminium alloy crack bridged by unbroken fibres in the crack wake [12]: original diagram by J. Schijve



the layers owing to severe Foreign Object Damage (FOD) e.g. an uncontained engine failure due to rotor burst.

13.4.2 Fatigue Evaluation: The MLB Test

Many laboratory tests have determined the fatigue and fatigue crack growth properties of GLARE, but probably the most definitive test is the Airbus MegaLiner Barrel (MLB) full-scale fatigue test. This test was done by Airbus Deutschland in Hamburg, Germany.

Figure 13.5 shows (i) the MLB; (ii) the types of applied loads, namely fuselage pressurisation (ΔP) and bending (MY , MZ) and ground loads QZ and (iii) the number of simulated flights applied during testing. This is slightly more than twice the nominal Design Service Goal (DSG) of 20,000 flights.

After the test there were teardowns of three key GLARE areas and details [4]:

- stringer coupling (GLARE 2A, stiffener; 2B, butt strap; 4A, skin)
- passenger window area (GLARE 3)
- passenger door beam (GLARE 3).

Cracks at fastener holes were detected by eddy current non-destructive inspection (NDI) after removal of the fasteners. Selected cracked holes from the windows

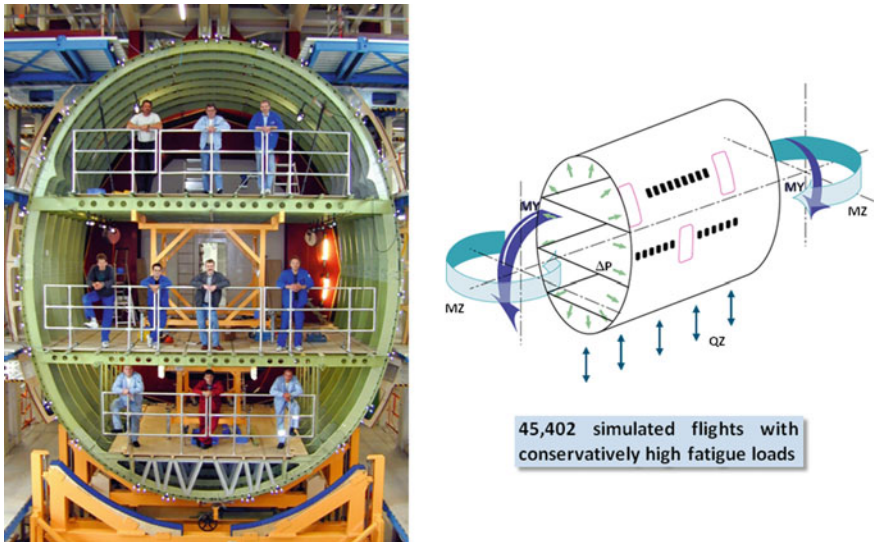


Fig. 13.5 Airbus A380 MegaLiner Barrel (MLB) full-scale fatigue test 'specimen', the general loading conditions, and the number of simulated flights applied during testing [4]

and door beam were broken open for Quantitative Fractography (QF). The results are summarised here:

Stringer couplings: Figure 13.6 classifies the NDI-indicated crack lengths for the GLARE coupling assembly and two AA7349-T7651 stringers. There were many crack indications for the GLARE components, but all were less than 4.5 mm. However, two crack indications for the aluminium alloy stringers were longer: 6.3 and 7 mm.

Windows and door beam: Figure 13.7 compares the fatigue crack growth behaviours of the largest cracks from these areas, which had differing local load levels and histories. However, the GLARE window skin and AA7175-T73 window frame were directly comparable. There are two main points to note:

1. The fatigue crack growth rates in the GLARE window skin were much lower than those in the AA7175-T73 window frame and tended to decrease.
2. The door beam crack had a nearly constant growth rate up to its end point (6.54 mm).

In a broader context, Figs. 13.6 and 13.7 show that fatigue cracks readily initiate in GLARE but do not accelerate. They also grow more slowly than in monolithic aluminium alloys. This agrees with small-scale test results, e.g. Ref. [1], crack growth modelling for GLARE [4], and the following contract report available from the first author and the author of this chapter:

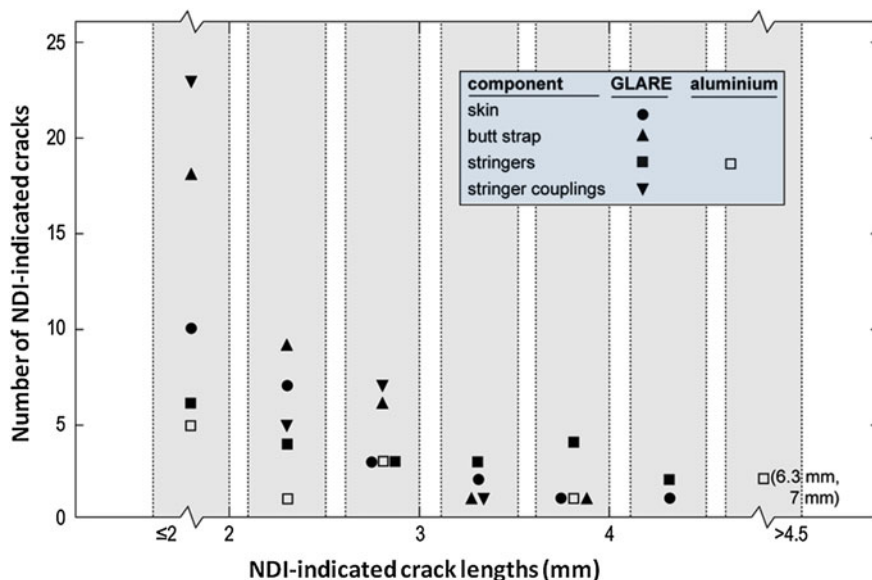


Fig. 13.6 Classification of NDI-indicated cracks for the MLB GLARE stringer coupling assembly and two AA7349-T7651 stringers [4]

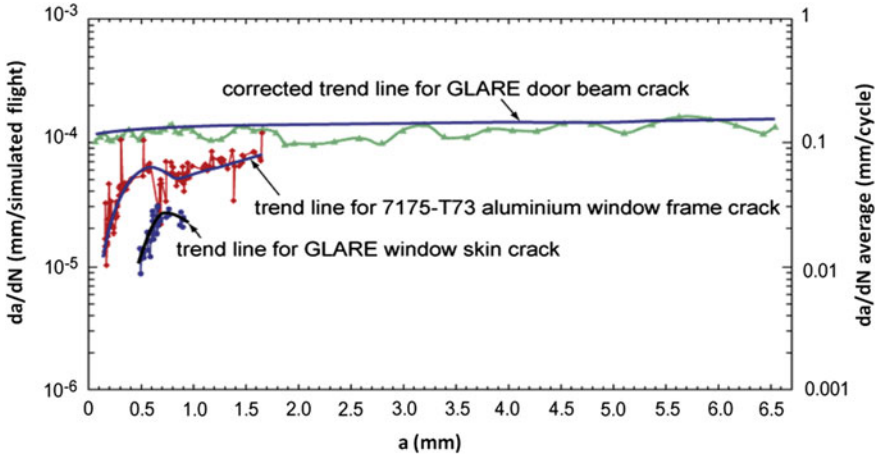


Fig. 13.7 Comparisons of fatigue crack growth rates for the longest cracks in the MLB passenger window area and passenger door beam [4]. The corrected trend line for the door beam crack is explained in the original paper [4]

- Schijve, J., Wiltink, F.J. and Bodegom, V.J.W., 1994, “Flight-simulation fatigue tests on notched specimens of fiber-metal laminates”, Report LRV-10, Faculty of Aerospace Engineering, Delft University of Technology, Delft, the Netherlands.

However, the MLB results are more significant because they represent full-scale fatigue testing of GLARE to more than twice the DSG. Also the load levels were set conservatively high [14]. Thus the fact that no GLARE fatigue crack exceeded 6.54 mm in length (the largest detected crack in the door beam) indicates the high DT capability of GLARE under realistic service-related conditions.

13.4.3 Residual Strength

As stated in Sect. 13.4.1, there are two different scenarios to evaluate the effectiveness of GLARE: (i) cracks with completely or mainly intact fibre layers, typically resulting from fatigue, and (ii) cracks through all the layers owing to severe FOD:

1. Figure 13.8 shows that the residual strength of GLARE with cracked aluminium alloy layers is much better than that of through-cracked GLARE, as would be expected.
2. Figure 13.9 shows crack growth resistance (K_R) curves for several through-cracked GLARE types together with K_R curves for the standard damage tolerant alloy AA2024-T3 and the improved modern alloy AA2524-T351.

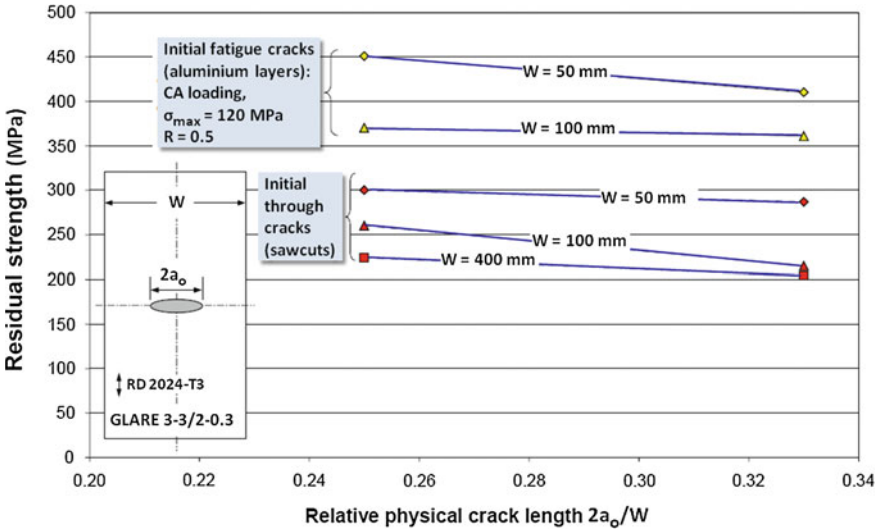


Fig. 13.8 Residual strength of partially (aluminium layers) and completely through-thickness cracked GLARE 3-3/2-0.3 laminates [13]

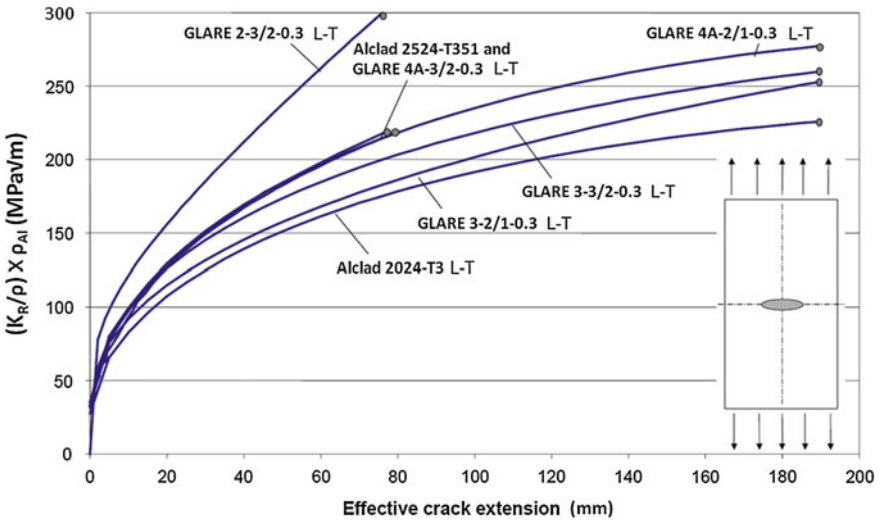


Fig. 13.9 Comparison of crack growth resistance (K_R) curves for through-thickness cracked GLARE laminates and the AA2024-T3 and AA 2524-T351 damage tolerant aluminium alloys [13]. The results have been adjusted to account for the different densities (ρ) and hence specific weights of the materials

All the GLARE types showed better crack growth resistance than AA2024-T3. However, it is clear that crack growth resistance equivalent to or better than that of AA2524-T351 depends on the type of GLARE: a better crack growth resistance is certainly achievable with GLARE.

An important practical aspect is fulfilment of the civil transport fuselage Fail-Safe crack criterion. This requires that a *complete* through-crack in two adjacent fuselage bays must be arrested within those bays under Limit Load conditions (see Fig. 18.3 in Chap. 18 of Volume 2 of these Source Books also). For GLARE this can be achieved by incorporating extra ‘crack stopping’ fibre layers in the fuselage skin laminate [1, 13].

13.4.4 DT Certification of GLARE

Laboratory tests and the MLB test have consistently shown that fatigue cracks initiate more readily in the aluminium alloy layers of GLARE than in monolithic aluminium alloy sheets. This negative aspect represents a potential issue for the Damage Tolerance certification of GLARE, despite the excellent resistance to fatigue crack growth. This issue, its resolution, and many other considerations are addressed in the book Flying GLARE® [15].

13.4.5 Impact Resistance

Impacts can occur from various sources, at both high and low velocities. Examples are runway and tyre debris, maintenance damage (dropped tools), collision with service vehicles and cargo, hail, bird and lightning strikes, and debris from uncontained engine failures (which fortunately rarely occur).

Figure 13.10 shows some impact results for aluminium alloy AA2024-T3, a Glare 3 laminate and a quasi-isotropic carbon fibre reinforced plastic (CFRP) laminate [1]. The CFRP impact resistance was low, as would be expected, since this is a major disadvantage of these materials. However, the GLARE laminate had better impact resistance than AA2024-T3, especially against high velocity impacts. This is attributed to high-strain-rate strengthening and a relatively high failure strain of the glass fibres [1, 16].

GLARE responds to impacts in a similar way as monolithic aluminium alloys, in that the damage is visually detectable and can be covered by the Code of Federal Regulations Section 25.571 [17, 18].

As mentioned in Sect. 13.3, the excellent impact resistance of GLARE, notably GLARE 5, has been exploited for cargo floors and liners, and the leading edges of the A380 horizontal and vertical stabilisers. GLARE 5 has been ‘tailored’ for high impact resistance by providing it with more prepreg layers than the other types, see Table 13.1.

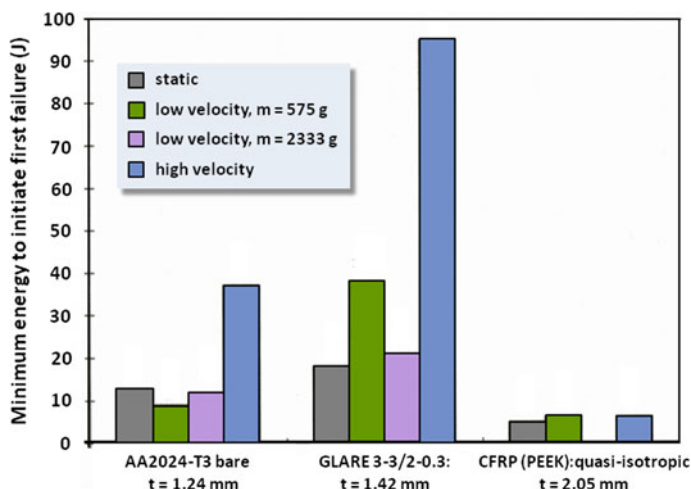


Fig. 13.10 Comparison of impact properties for AA2024-T3 aluminium alloy, a GLARE 3 laminate and a quasi-isotropic CFRP [1]; *PEEK* polyetherether ketone, a thermoplastic polymer; *m* the mass of the impactor (unspecified for the high velocity impacts)

Lightning strikes damage only the outer aluminium alloy layer, with local melting and a small disbonded area around the impact point [1, 19]. The damage is less extensive than that in a monolithic aluminium alloy panel [19].

13.4.6 Flame Resistance

The flame resistance of GLARE is extremely good [19]. Similarly to lightning strike damage, only the outer aluminium alloy layer melts. The exposed glass fibres withstand the flame temperature, while carbonisation of the epoxy matrix and delamination insulate the remaining laminate layers.

As an example, when aluminium alloy sheets 1.5–2 mm thick were exposed under standard test conditions [20] to an 1100 °C flame, the burn-through time was about 90 s. However, similar thickness GLARE 3 and 4 laminates resisted flame penetration for more than 15 min [19]. These tests showed that GLARE can be qualified as fireproof and used for firewalls [19].

13.4.7 Corrosion Resistance

The aluminium alloy sheets used for GLARE are anodised and coated with a corrosion-inhibiting primer before laminate assembly and bonding. Furthermore, to

avoid *bondline corrosion* only the outside surfaces of GLARE laminates are clad, if required [21].

Under severe accelerated corrosion testing conditions GLARE performs as well as, or better than, monolithic aluminium, see Fig. 13.11. Through-thickness corrosion in GLARE is prevented by the fibre-epoxy layers. It is worth noting here that the glass fibres are not electrically conducting, so there is no risk of galvanic corrosion of the aluminium layers.

13.4.8 Inspections and Repairs

Inspections: C-scan ultrasonic inspection is used for quality assurance of as-produced GLARE laminates [1]. Eddy current techniques may be used to detect fatigue cracking from fastener holes [22] (cracks only in the aluminium layers).

GLARE self-repairs: Damaged GLARE laminates may be repaired with GLARE patches using riveted [23] or bonded [24] repair techniques already developed for aluminium alloy structures [1].

GLARE repairs on other structures: GLARE bonded patches on aluminium alloy structures behave better than CFRP patches and also boron fibre composite patches [24]. The main reason for GLARE's better performance compared to CFRP patches is the closer match of the aluminium and GLARE thermal expansion coefficients [24].

As mentioned in Sect. 13.3, GLARE 2A/2B patch repairs have been applied to the fuselage crowns of Lockheed C-5A aircraft. The design and manufacture of these patches is discussed in detail by Guijt et al. [8]. Figure 13.12 shows a patch in situ before fastener re-installation.

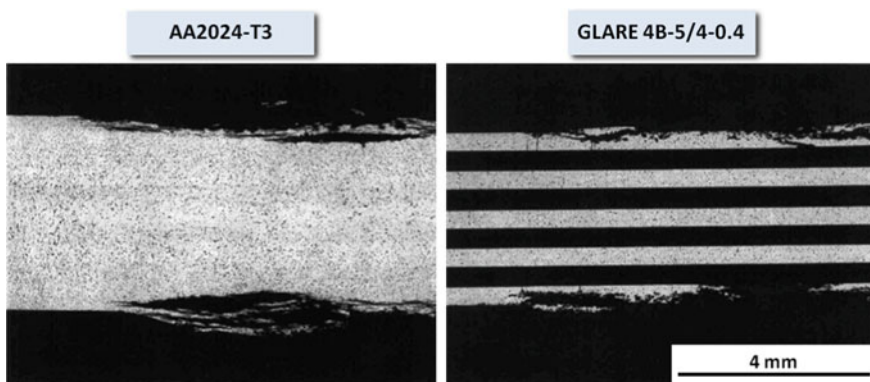
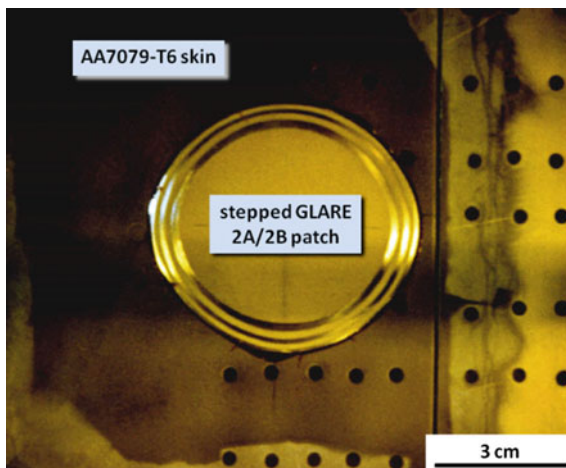


Fig. 13.11 Extent of corrosion in AA2024-T3 sheet and a GLARE 4 laminate after 175 h of EXCO testing [21]: EXCO EXfoliation COrrusion testing, ASTM Standard G34-01

Fig. 13.12 GLARE patch bonded to the fuselage crown skin of a Lockheed C-5A aircraft [8]



Glare may also be used to repair CFRP structures, since the stiffnesses are better matched than if using aluminium or titanium alloy patches. The external aluminium layers of GLARE are then omitted to avoid galvanic corrosion.

13.5 GLARE and Other Candidates for Primary Aircraft Structures

In practice, the selection of materials for aircraft structures is a complex process [25]. Table 13.2 lists many factors that may be considered as advantages and disadvantages of conventional (legacy) aluminium alloys, the latest (3rd generation) Al–Li alloys, CFRPs and GLARE [6]. The importance of these factors differs greatly, but some broad indications can be given:

Engineering properties: These must meet the aircraft load requirements, which vary for different structural areas.

Improved properties: The importance of these depends on both the load requirements and the weight savings potential. The greatest weight savings potentials come from low-density materials, which favours CFRPs and also Al–Li alloys as replacements for legacy alloys.

Other properties, especially strength and stiffness, also contribute to weight savings. For example, GLARE's excellent DT and impact properties have been combined with efficient design and manufacturing (see below) to enable competitive weight savings and actual deployment in the Airbus A380 upper fuselage and horizontal and vertical stabiliser leading edges, see Sect. 13.3 and Fig. 13.3.

Table 13.2 Relative advantages and disadvantages of conventional aerospace aluminium alloys, third generation Al–Li alloys, CFRPs and GLARE FMLs for aircraft structures [6]: information from various sources, including Mouritz [26]

Conventional Al alloys	Third generation Al–Li alloys	CFRPs	GLARE
<p><i>Advantages</i></p> <ul style="list-style-type: none"> • Moderate material, labour and manufacturing costs • Moderate specific stiffness • Isotropic mechanical properties • Good damage tolerance and property control by thermo-mechanical processing • Generally recyclable 	<ul style="list-style-type: none"> • Moderate labour and manufacturing costs • 8–15 % higher specific stiffness than conventional aluminium alloys and weldable: i.e. weight savings and reduced part count • Isotropic and improved mechanical properties • Good damage tolerance and property control by thermo-mechanical processing • Good/excellent corrosion and stress corrosion resistance: sheet cladding may be unnecessary • Recyclable: <i>but see below</i> 	<ul style="list-style-type: none"> • Higher and much higher specific stiffness, depending on percentages of aligned fibres • 10–20 % weight savings in actual components • (Greatly) reduced part count • High fatigue and corrosion resistance: reduced maintenance costs • Greater flexibility in designing structurally efficient components 	<ul style="list-style-type: none"> • Fabricability generally similar to aluminium alloys: <i>but see below</i> • High strength: weight savings in tension-loaded structures • Excellent damage tolerance (fatigue crack growth, impact) • Burn-through (firewall) resistance
<p><i>Disadvantages</i></p> <ul style="list-style-type: none"> • Poor corrosion resistance • Stress corrosion susceptibilities • Most alloys difficult or unsuitable to weld except with non-fusion techniques, e.g. friction stir welding (FSW) and linear friction welding (LFW) 	<ul style="list-style-type: none"> • Higher material costs compared to conventional aluminium alloys • Property dependences on multi-stage thermo-mechanical treatments • Separate recycling 	<ul style="list-style-type: none"> • High material, labour and manufacturing costs • Possible delaminations and other flaws during fabrication • Intrinsically anisotropic: complex components difficult to analyse, sometimes giving poor failure predictions • Higher notch sensitivity, e.g. fastener holes • Non-destructive inspection difficult • Conservative design and safety factors owing to: (a) high susceptibility to damage from impacts (bird strikes and ground operation vehicles), (b) damage growth difficult to control and predict, (c) difficult validation of repairs • Low electrical conductivity requires metal (Cu) mesh in external surface layers to protect from lightning strikes • Flammable • Non-recyclable 	<ul style="list-style-type: none"> • High material costs • Difficult to form • Only sheet products (skins, stringers, butt straps) at present • Lower buckling resistance: unsuitable for compression-loaded structures

Costs and weight savings: Material and manufacturing costs are relatively high for GLARE and CFRPs, but can be at least partially offset by their weight savings potentials. (CFRP material costs are particularly high—a significant disadvantage.)

GLARE is some 5–10 times more expensive per kg than conventional aluminium alloys [27], and this difference cannot be offset by weight savings alone. Additional savings must come from cost reductions during manufacturing, and these are best achieved by producing components directly from GLARE rather than half-product GLARE sheets [27].

Design principles and safety: Not only must aircraft have lightweight and highly efficient structures, but they must also be safe, see Chaps. 16 and 18 in Volume 2 of these Source Books. The design principles developed for the aircraft industry are based on mature engineering experience and well-established safety factors for metallic aircraft structures. This is an important advantage for aluminium and Al–Li alloys and also GLARE, which can be treated basically like a metallic material [15].

CFRPs, however, cannot use the design principles for metallic aircraft structures. In addition to problems in analysing complex components and predicting the onset of failure, even in nominally undamaged components, CFRPs are susceptible to impact damage and subsequent fatigue cracking and delamination.

The damage growth is difficult to predict, and this also makes it difficult to validate repairs. The overall result of these issues is that safety must be ensured by over-designing CFRPs according to the ‘No Growth’ damage tolerance principle [28, 29]. This increases their weight and manufacturing costs.

13.6 Summary

GLARE is a versatile FML concept that has been successful in important and diverse aerospace applications that exploit its excellent Damage Tolerance (DT) properties and impact and flame resistances. GLARE is also eminently suitable for repair patches on cracked and damaged aluminium alloy and CFRP aircraft structures.

GLARE has the advantage that well-established design methods for metallic structures can be used. However, the high material costs in comparison to aluminium alloys necessitate highly cost-effective manufacturing, whereby components are made directly as GLARE assemblies rather than from half-products.

The expertise in designing, manufacturing and using GLARE is primarily accessible via the Fibre Metal Laminates Centre of Competence (FMLC), founded in 2001 and based at the Delft University of Technology in the Netherlands. GLARE production currently takes place at Fokker Papendrecht (Netherlands) and Premium Aerotec Nordenhamm (Germany).

Acknowledgments The advice and assistance of Dr. René Alderliesten and Professor Jaap Schijve, Faculty of Aerospace Engineering, Delft University of Technology, the Netherlands, is much appreciated.

References

1. Vogelesang LB (2004) Fibre metal laminates, the development of a new family of hybrid materials. In: Guillaume G (ed) 'ICAF 2003: fatigue of aeronautical structures as an engineering challenge, vol I. Engineering Materials Advisory Services, Warrington, UK, pp 3–27
2. Vlot A, Gunnink JW (eds) (2001) Fibre metal laminates: an introduction. Kluwer Academic Publishers, Dordrecht, the Netherlands
3. Wit GP (2001) Fuselage barrel design and design for manufacturing (Chapter 15). In: Vlot A, Gunnink JW (eds) Fibre metal laminates: an introduction. Kluwer Academic Publishers, Dordrecht, the Netherlands, pp 237–254
4. Wanhill RJH, Platenkamp DJ, Hattenberg T, Bosch AF, De Haan PH (2009) GLARE tear-downs from the MegaLiner Barrel (MLB) fatigue test. In: Bos MJ (ed) ICAF 2009, Bridging the gap between theory and operational practice. Springer Science + Business Media, Dordrecht, the Netherlands, pp 145–167
5. Rendigs K-H, Knüwer M (2010) Metal materials in Airbus 380. In: 2nd Izmir Global Aerospace and Offset Conference, 6–8 Oct 2010, Izmir, Turkey
6. Wanhill RJH (2013) Aerospace applications of aluminum-lithium alloys. In: Prasad NE, Gokhale AA, Wanhill RJH (eds) Aluminum-lithium alloys, processing, properties and applications. Butterworth-Heinemann, Elsevier Inc., Oxford, UK, pp 503–535
7. Evancho JW (2001) Secondary applications (Chapter 20). In: Vlot A, Gunnink JW (eds) Fibre metal laminates: an introduction. Kluwer Academic Publishers, Dordrecht, the Netherlands, pp 309–324
8. Guijt CB, Verhoeven S, Greer JM (2001) Bonded repairs for C-5A fuselage crown cracking (Chapter 31). In: Vlot A, Gunnink JW (eds) Fibre metal laminates: an introduction. Kluwer Academic Publishers, Dordrecht, the Netherlands, pp 477–497
9. Roebroeks GHJJ (2001) Glare features (Chapter 2). In: Vlot A, Gunnink JW (eds) Fibre metal laminates: an introduction. Kluwer Academic Publishers, Dordrecht, the Netherlands, pp 23–37
10. Findley SJ, Harrison ND (2002) Why aircraft fail. *Mater Today* 5(11):18–25
11. Tiffany CF, Gallagher JP, Babish IV, CA (2010) Threats to structural safety, including a compendium of selected structural accidents/incidents. USAF Technical Report ASC-TR-2010-5002, Aeronautical Systems Center Engineering Directorate, Wright-Patterson Air Force Base, Ohio 454-33-7101, USA
12. Alderliesten RC (2001) Fatigue (Chapter 11). In: Vlot A, Gunnink JW (eds) Fibre metal laminates: an introduction. Kluwer Academic Publishers, Dordrecht, the Netherlands, pp 155–171
13. De Vries TJ (2001) Residual strength (Chapter 13). In: Vlot A, Gunnink JW (eds) Fibre metal laminates: an introduction. Kluwer Academic Publishers, Dordrecht, the Netherlands, pp 197–217
14. Wagner M (2001) Fatigue loads program for MegaLiner Barrel. Airbus Deutschland GmbH, Hamburg, Germany
15. Beumler T (2004) "Flying GLARE[®], a contribution to aircraft certification issues in non-damaged and fatigue damaged GLARE[®] structures. Doctor's Thesis, Delft University of Technology, Delft, the Netherlands
16. Hagenbeek M (2001) Impact properties (Chapter 27). In: Vlot A, Gunnink JW (eds) Fibre metal laminates: an introduction. Kluwer Academic Publishers, Dordrecht, the Netherlands, pp 409–426

17. Beumler T (2001) Damage tolerance aspects (Chapter 14). In: Vlot A, Gunnink JW (eds) Fibre metal laminates: an introduction. Kluwer Academic Publishers, Dordrecht, the Netherlands, pp 219–233
18. Code of Federal Regulations (annual edition), Section 25.571, Damage-tolerance and fatigue evaluation of structure. Federal Aviation Administration, U.S. Department of Transportation, Washington, DC, USA
19. Hooijmeijer PA (2001) Burn-through and lightning strike (Chapter 26). In: Vlot A, Gunnink JW (eds) Fibre metal laminates: an introduction. Kluwer Academic Publishers, Dordrecht, the Netherlands, pp 399–408
20. Federal Aviation Administration (1990) Powerplant installation and propulsion system component fire protection methods, standards, and criteria. Advisory Circular FAA AC 20-135, U.S. Department of Transportation, Washington, DC, USA
21. Borgonje B, Ijpma MS, 't Hart WGJ (2001) Corrosion (Chapter 28). In: Vlot A, Gunnink JW (eds) Fibre metal laminates: an introduction. Kluwer Academic Publishers, Dordrecht, the Netherlands, pp 427–439
22. Borsboom C (2001) Eddy current inspection (Chapter 32). In: Vlot A, Gunnink JW (eds) Fibre metal laminates: an introduction. Kluwer Academic Publishers, Dordrecht, the Netherlands, pp 499–512
23. Hooijmeijer PA (2001) Riveted repairs (Chapter 29). In: Vlot A, Gunnink JW (eds) Fibre metal laminates: an introduction. Kluwer Academic Publishers, Dordrecht, the Netherlands, pp 441–449
24. Woerden HJM, Mortier WJ, Guijt CB, Verhoeven S (2001) Bonded repair patches (Chapter 30). In: Vlot A, Gunnink JW (eds) Fibre metal laminates: an introduction. Kluwer Academic Publishers, Dordrecht, the Netherlands, pp 451–475
25. Hinrichsen J (2003) Praxis-Seminar Luftfahrt, Hochschule für Angewandte Wissenschaften Hamburg, DGLR, VDI. Airbus A380: Vertical Tailplane, 10th Apr 2003, Hamburg, Germany (in German)
26. Mouritz AP (2012) Introduction to aerospace materials. Woodhead Publishing Limited, Cambridge, UK
27. Vlot A (2001) Historical overview (Chapter 1). In: Vlot A, Gunnink JW (eds) Fibre metal laminates: an introduction. Kluwer Academic Publishers, Dordrecht, the Netherlands, pp 3–21
28. Federal Aviation Administration (2009) Composite aircraft structure, Advisory Circular FAA AC-20-107B. U.S. Department of Transportation, Washington, DC, USA
29. U.S. Department of Defense (2013) Military composite materials handbook, volume 3. Polymer matrix composites materials usage, design, and analysis. MIL-HDBK-17-3F, U.S. Department of Defense, The Pentagon, Arlington, Virginia 20301-1400, USA

Chapter 14

Carbon Fibre Polymer Matrix Structural Composites

R.J.H. Wanhill

Abstract This chapter concisely surveys the applications and properties of polymer matrix structural composites (PMCs), concentrating on carbon fibre reinforced composites. These are the most widely used composite materials, notably in aerospace, and are commonly called carbon fibre reinforced plastics (CFRP). A major source for this chapter is Baker et al. (Composite materials for aerospace structures. American Institute of Aeronautics and Astronautics, Inc., Reston, Virginia, USA, 2nd edn, 2004).

Keywords Polymer matrix composites · CFRP · Processing · Properties · Damage Tolerance · Applications

14.1 Introduction

Aircraft structural materials must have outstanding combinations of engineering properties and also enable the manufacturing of lightweight and durable structures (i.e. the airframe). Aluminium alloys have predominated in aircraft manufacturing since introduction of the Boeing 247 (1933) and Douglas DC-2 (1934), but composites (mainly carbon fibre reinforced plastics, CFRP) increasingly provide competition, Fig. 14.1.

There are two more points to note with reference to Fig. 14.1:

1. Tactical aircraft tend to use higher percentages of composites than transport aircraft.
2. Military aircraft with special qualities (VTOL, stealth) have higher percentages of composites than their more conventional contemporaries. (The Northrop Grumman B2 has a high-cost composite airframe mainly because of the radar-absorbing properties.)

R.J.H. Wanhill (✉)
Emmeloord, Flevoland, The Netherlands
e-mail: rjhwanhill@gmail.com

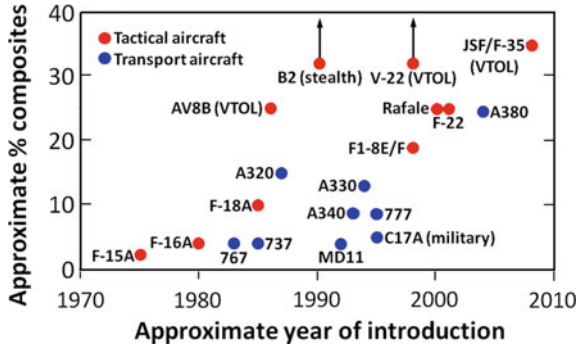


Fig. 14.1 Increasing use of CFRP composites in aircraft: main source Ref. [1]

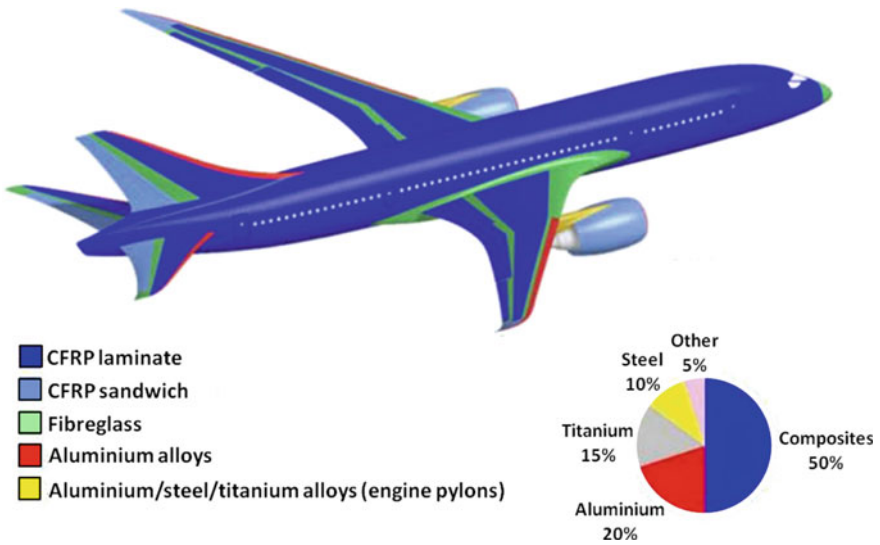


Fig. 14.2 Airframe materials distributions and percentages for the Boeing 787: The Boeing Company

For civil transport aircraft the introduction of the Boeing 787 (2011) and Airbus A350 (2015) represents a potential ‘game changer’. The airframes are about 50 and 52 % composites, respectively, e.g. Figure 14.2. However, some authorities doubt whether future aircraft in the Boeing 737 and Airbus A320 size category will have such high percentages of composite structures, since they are more expensive than comparable aluminium alloy structures. There are also other disadvantages, as well as advantages, in using composites, as will be discussed in Sect. 14.4.

What is more evident is an increasing trend to design and build hybrid airframe structures for both civil and military aircraft. An illustration of this trend is provided by Fig. 14.3, which points out the various types of materials in major structural locations of the Airbus A380. The amount of composite structure in the A380 is about 22–24 %, which is significantly higher than in previous transport aircraft, see Fig. 14.1.

N.B: Information on conventional aluminium alloys and aluminium-lithium (Al–Li) alloys is given in Chaps. 2 and 3 of this Volume of the Source Books. Al–Li alloys are also the subject of a recent book [2]: they can provide structural efficiencies that rival those of composites. GLARE (GLASS REinforced aluminium laminates) is discussed in Chap. 13 of this Volume.

14.2 Types of Composites

Composites are materials composed of two or more physically distinct components whose combination results in enhanced properties. The primary component is a continuous matrix. The secondary (but no less important) component is the filler material or materials. Composites may be classified into several categories, based on the materials used and also the fabrication methods. An overview concentrating on carbon fibre polymer matrix composites (PMCs) is given in Fig. 14.4.



Fig. 14.3 Airframe materials distributions for the Airbus A380 [2]: AA 2XXX, 6XXX and 7XXX = conventional aluminium alloys; Al–Li aluminium–lithium alloys; LBW Laser Beam Welding [3]

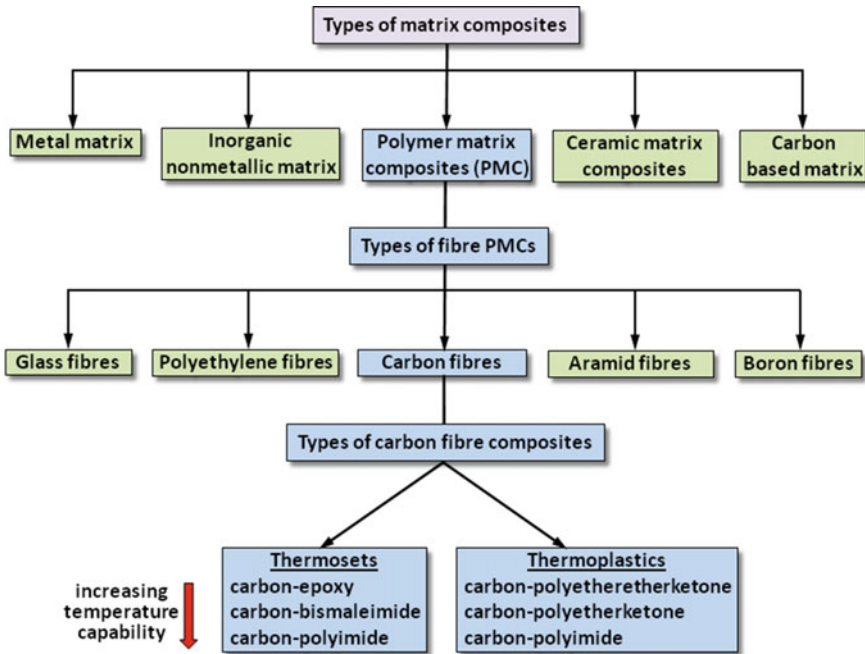


Fig. 14.4 Composites progressively classified according to the types of (i) matrix, (ii) fibre PMCs, (iii) carbon fibre—PMC (CFRP) thermosets and thermoplastics: main source Ref. [1]

14.3 CFRP Composites

14.3.1 CFRP Composite Matrices

As Fig. 14.4 shows, there are two categories of CFRPs, thermosets and thermoplastics, depending on the type of matrix:

Thermosets: The most widely used thermosets for aircraft structures are epoxy resins, since they are readily processed and have good chemical and mechanical properties. They also undergo a low-viscosity stage during cure, thereby enabling liquid resin-forming techniques like resin transfer moulding (RTM) [1], see Sect. 14.3.3.

Bismaleimide resins (BMIs) have similar processability and mechanical properties compared to epoxies. However, the higher resin costs limit their use to operating temperatures (up to about 180 °C) that are beyond those of epoxies (100–130 °C).

For higher operating temperatures polyimides could be used. These allow operating temperatures up to 300 °C, but they are more expensive than BMIs and much more difficult to process [1].

Thermoplastics: The matrices for thermoplastic CFRPs include polyetheretherketone (PEEK), used up to 120 °C; polyetherketone (PEK), up to 145 °C; and thermoplastic-type polyimide, up to 270 °C [1]. These three matrix types are the most suitable for aerospace applications.

Thermoplastics are fully polymerised before they are used to make composites. Hence they are unsuitable for RTM. Fabrication by resin-film infusion (RFI) or hot pressing of pre-coated fibres (prepregs) is more suitable [1].

Comparisons of the properties of thermosets and thermoplastics are presented in Table 14.1. Important points in comparing and considering thermosets and thermoplastics are:

1. Thermosets have relatively low fracture strains and fracture toughness, which result in poor fracture resistance in CFRPs. Thermosets also absorb moisture, which reduces the matrix-dominated properties like elevated temperature shear and compressive strengths [1].
2. Thermoplastics are generally more expensive and require high processing temperatures and pressures, which increase the cost differentials.
3. Overall, thermoset CFRPs are more extensively used, with thermoplastic CFRPs favoured when the need for high resistance to impacts and edge damage justifies the higher costs [1].

Table 14.1 Properties and comparisons for thermosets and thermoplastics [1]

Thermosets	Thermoplastics
Main characteristics	
<ul style="list-style-type: none"> • Undergo chemical change when cured • Low strain to failure • Low fracture energy • Irreversible processing • Very low-viscosity possible • Absorbs moisture • Highly resistant to solvents 	<ul style="list-style-type: none"> • Non-reacting, no cure required • High strain to failure • High fracture energy • Very high viscosity • Processing is reversible • Absorbs little moisture • Limited resistance to organic solvents, in some cases
Advantages	
<ul style="list-style-type: none"> • Relatively low processing temperature • Good fibre wetting • Formable into complex shapes • Liquid-resin manufacturing feasible • Resistant to creep 	<ul style="list-style-type: none"> • Short processing times possible • Reusable scrap • Post-formable: can be reprocessed • Unlimited shelf life without refrigeration • High delamination resistance
Disadvantages	
<ul style="list-style-type: none"> • Long processing time • Long cure (~ 1–2 h) • Restricted storage life (requires refrigeration) 	<ul style="list-style-type: none"> • Lower resistance to solvents • Requires high temperature (300–400°C) and pressure • Can be prone to creep • Very poor drapability^a and tack^b

^aAbility of a fabric to form pleating folds when deformed under pressure

^bAdhesive quality

14.3.2 CFRP Composite Fibres

There are three categories of carbon fibres used in aerospace CFRPs. These are high modulus (HM, Type I), high strength (HS, Type II) and intermediate modulus (IM, Type III). Examples of their properties are given in Table 14.2, which shows the considerably different mechanical properties of the three types of fibres. Although the strength properties of HM and HS fibres overlap somewhat, it is evident that there is a trade-off between modulus and strength: high modulus (HM) is traded for high strength (HS).

N.B: Fibre manufacturers present a bewilderingly wide range of tensile moduli and strength values within the three fibre categories. Furthermore, there are two other categories, referred to as ‘standard’ and ‘ultrahigh modulus’ (UHM). The trade-off for the UHM category is fracture resistance: the higher the modulus, the more brittle the fibres.

Carbon fibre production: The fibres are made from organic precursors by carbonisation. Most are made from polyacrylonitrile (PAN) fibres, which give the best carbon fibre properties. However, they can also be made from pitch. Details of the PAN and pitch-based fibre carbonising process are given by Baker et al. [1]. The final properties of the fibres depend on the processing details and also whether the fibres undergo a final graphitisation heat treatment.

Carbon fibre filaments: The finished PAN fibres have diameters between 5 and 10 μm . Examples are shown in Fig. 14.5. The surface finish is reminiscent of tree bark. Additional processing can strip off the ‘bark’, leaving smoother and smaller diameter fibres that can be packed into smaller spaces in the matrix, and hence provide higher stiffness per cross-sectional area. However, these fibres are more expensive owing to the additional processing.

Dry carbon fibre products: The PAN fibre process is set up to produce continuous fibre bundles called tows, which are used for weaving into fabrics with various weave patterns. These undergo subsequent processing into PMCs using pre-impregnation (prepreg), resin films or liquid resin injection.

Table 14.2 Typical properties of commercial carbon fibres [1]

Property	HM type I	HS type II	IM type III
Density (g/cm^3)	1.9	1.8	1.8
Tensile modulus (GPa)	276–380	228–241	296
Tensile strength (MPa)	2415–2555	2105–4555	4800
Ultimate strain (%)	0.6–0.7	1.3–1.8	2.0
Thermal expansion ($\times 10^{-6} \text{ mm}^{-1} \text{ K}^{-1}$)	–0.7	–0.5	N/A
Thermal conductivity ($\text{Wm}^{-1} \text{ K}^{-1}$)	64–70	8.1–9.3	N/A
Resistivity ($\mu\Omega \text{ m}$)	9–10	15–18	N/A

Prepreg products: These are made by infusing fibre tows and fabrics with epoxy resin. The prepregs are subsequently processed into PMCs. Most prepregs are unidirectional tapes and are made by spreading and collimating many fibre tows into a sheet of parallel fibres that is then prepregged.

14.3.3 CFRP Aerospace Components Production

The manufacturing of aerospace components and structures from CFRPs is discussed in detail in Chap. 5 of Ref. [1]. An overview is given here.

The main method of making CFRP aerospace components is (i) the lamination of woven fabrics or aligned-fibre sheets and tapes. The other methods are (ii) resin transfer moulding (RTM); (iii) filament winding and (iv) braiding onto rotating mandrels; (v) tow placement; and (vi) pultrusion [1]. Table 14.3 lists typical CFRP aerospace composite forms that can be made by these techniques.

However, there is much more to manufacturing CFRPs than the choice of forming technique: Fig. 14.6 is an example of the several steps involved from producing carbon fibres to obtaining a finished component. In this schematic the 'Intermediates' represent some of the above-mentioned forming techniques, notably laminating (lay-ups) and filament winding.

Figure 14.6 also helps to explain an important point mentioned in Sect. 14.1: composite structures are more expensive to manufacture than comparable aluminium alloy structures.

Laminating procedures: Aircraft manufacturers prefer epoxy prepreg as the starting material for laminates [1]. As mentioned in subsection 14.3.2, the prepregs can be tows and fabrics, and most are unidirectional, notably tapes. The lay-up of large laminated components (wing and empennage covers, fuselage shells) uses

Fig. 14.5 Carbon fibres viewed in the scanning electron microscope (SEM). The fibre ends are fracture surfaces

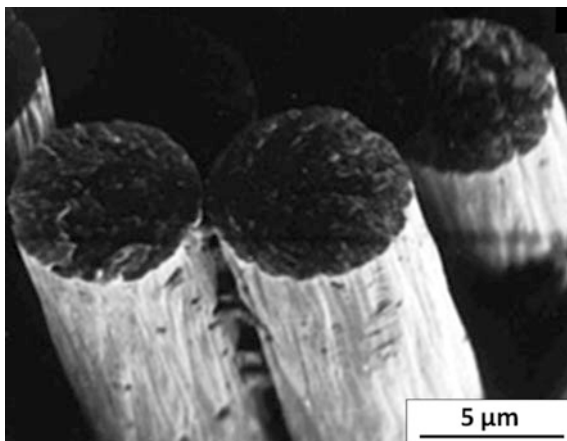


Table 14.3 Typical CFRP aerospace components formed by several techniques [1]

Techniques	Types of structures	Applications
Laminating	• Sheets, thick monolithic	• Wing skins
	• Sheets, integrally stiffened	• Empennage skins
	• Sandwich panels	• Control surfaces; floor sections
	• Shells	• Fuselage sections
	• Beams	• Spars; ribs
	• Complex forms	• Aerofoils
RTM	• Small complex forms	• Doors; door pillars; flaps; spoilers
Filament winding	• Closed shells	• Pressure vessels
	• Open shells	• Radomes; rocket motors
	• Tubes	• Drive shafts
	• Secondary formed tubes	• Helicopter blades
Braiding	• Tubes	• Drive shafts
	• Complex tubes	• Curved pipes; truss joints; ducts
	• Closed shells	• Pressure vessels
	• Secondary formed	• Fuselage frames; propellers; helicopter blades
Tow placement	• See laminating	• See laminating
	• Complex wraps	• Grips; shafts; ducts
Pultrusion	• Beams	• Floor beams; stringers; spars; ribs; longerons

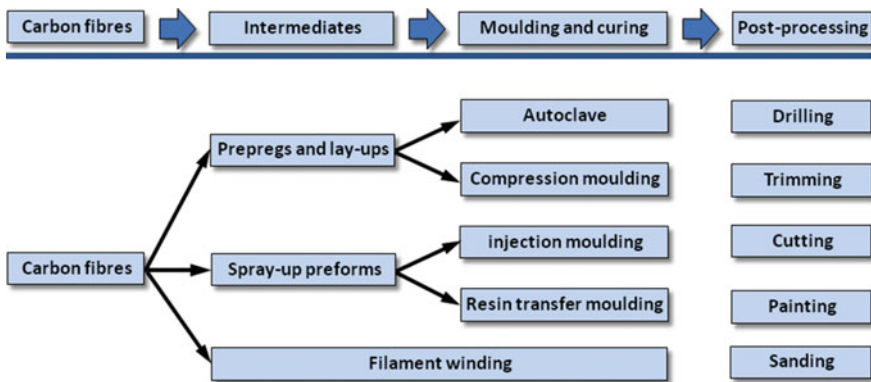


Fig. 14.6 Some methods for manufacturing CFRP components: Lux Research, Inc., Boston, USA

automated tape layer (ATL) and automated tow placement (ATP) equipment, for example Fig. 14.7.

An ATL tape laying head is multi-functional. Thus it (i) removes backing paper from the prepreg tape, (ii) delivers the tape to the lay-up tool with application of



Fig. 14.7 Automated tape laying: CFRP tape layers being placed on the lay-up tool for an Airbus A350 upper shell fuselage skin section: Premium AEROTEC, Nordenham, Germany

pressure, (iii) lays the tape in a programmed path (course), (iv) cuts the material at the precise location and angle, (v) lifts away from the tool, (vi) retracts to the start position, and (vii) begins laying the next course [4].

The tape laying head also has an optical flaw detection system that signals to stop laying tape when a flaw is detected, and a heating system that heats the prepreg to increase tack for tape-to-tape adhesion [4].

Resin transfer Moulding (RTM): This technique uses the epoxy thermoset characteristic of a low-viscosity stage during cure in an autoclave. Dry fabric preforms are put into matched-cavity moulds, preheated in the autoclave, and then filled with preheated injected resin under pressure: a vacuum is usually applied at an exit port in the preform/mould assembly to remove air and moisture before injection. After injection the mould temperature is increased to cure the component under autoclave pressure.

A variant, referred to as vacuum-assisted RTM (VARTM) involves placing a permeable membrane on top of the preform, vacuum bagging the mould/preform assembly, preheating it in an oven, and then applying a vacuum at the assembly exit port to enable the resin to infuse the preform via the permeable membrane. The advantage is lower costs, using an oven instead of an autoclave. However, the absence of autoclave pressure, relying on vacuum-compaction only, results in fibre volume-fractions about 5 % less than from RTM [1].

Resin-film infusion (RFI): In this process a film of resin is placed onto a mould either beneath or above the dry fabric preform. The assembly is then vacuum bagged and loaded into an autoclave. The temperature is raised to the resin's low-viscosity stage and a low-level pressure forces the resin into the preform. When infusion is complete the temperature and pressure are increased to compact and cure the component [1].

Filament winding: This involves laying down resin-impregnated continuous fibres on a stationary or rotating mandrel. The mandrel is removed *after* cure. This technique is best suited to components with simple surfaces of revolution, e.g. shells and tubes, see Table 14.3.

The fibres may be (i) wet wound, whereby dry fibres are impregnated with a low-viscosity resin during winding, (ii) dry wound and subsequently impregnated with resin under pressure or (iii) prepregged before winding. Thermoset resins are most commonly used, requiring curing after winding. Thermoplastics can be used in prepregs that are consolidated during winding [1]. This is more or less implied by the extended 'Filament winding' box in Fig. 14.6, although thermoplastics are not consolidated by curing, i.e. chemical conversion, see Table 14.1.

Pultrusion: This is an automated process for manufacturing constant cross-sectional profiles [1]. Continuous unidirectional fibre tows are impregnated with a thermosetting epoxy resin and pulled through a heated die to shape and cure the composite product. However, full cure is not normally achieved before the component exits the die, so post-curing needs to be considered.

Although pultrusion can be used for several types of aerospace components, see Table 14.3 and Fig. 14.10 in Sect. 14.4.1, the limited production runs are usually too short for pultrusion to be economically viable. There may also be quality issues compared with other manufacturing techniques unless special resins are used that enable relatively high fibre volume-fractions [1].

14.3.4 Reference Guidelines for CFRP Materials and Processing

Aerospace manufacturers have in-house and therefore proprietary guidelines and specifications for the characterisation and processing of CFRPs. In particular, the determination and evaluation of fibre and matrix properties are essential to selecting optimum combinations for particular applications.

However, Besides Ref. [1], open-source *guidelines* are available from the U.S. Department of Defence Composite Materials Handbook, Volumes 1–3 [5–7], which may be downloaded from the Internet.

14.4 CFRP Properties

The main incentive for developing CFRPs has been to obtain high structural efficiency owing to a combination of their relatively low densities, $\rho = 1.52\text{--}1.63 \text{ g/cm}^3$ [7] and high strength and stiffness.

In particular, the specific stiffnesses are basic design parameters for aircraft:

1. The specific stiffness E/ρ is important for lower wing surfaces, upper tailplane surfaces and spars, ribs and frames.
2. The specific buckling resistance $E^{1/3}/\rho$ is important for upper wing surfaces, lower tailplane surfaces and the fuselage.

However, as mentioned in Sect. 14.1, CFRP components and structures are more expensive than comparable aluminium alloy ones. Other properties and factors are of course important: see Table 14.4, which lists the advantages and disadvantages of CFRPs with respect to aluminium alloys.

Sections 14.4.1–14.4.3 focus on the following major topics: (i) specific mechanical properties and weight savings and costs, (ii) impact damage and inspections, and (iii) structural repairs.

14.4.1 *Specific Mechanical Properties and Practical Weight Savings and Costs*

The mechanical properties of CFRPs depend on the fibre volume-fractions, the orientations of the fibres with respect to the applied loads and—*most importantly*—on the component lay-ups and geometries. The fibres carry almost all the loads and are therefore responsible for the strengths and stiffnesses of CFRP components and structures.

Figures 14.8 and 14.9 present some data for the specific strengths and stiffnesses of CFRPs compared to those for aluminium alloys:

Specific strengths: Figure 14.8 shows that 100 % aligned-fibre CFRP laminates have intrinsically very high specific strengths, well beyond the capabilities of aluminium alloys. However, reduction factors accounting for property variabilities and environmental and notch effects greatly decrease the CFRP ‘allowables’, especially in compression: also see the remark about compression failures in Table 14.4.

Furthermore, when the dependence of CFRP strengths on the degree of fibre alignment is considered, Fig. 14.8 shows that the reduction factors can eliminate the CFRP-specific strength advantages compared to aluminium alloys.

Table 14.4 Relative advantages and disadvantages of CFRPs compared to aluminium alloys: information from various sources, including Refs. [3, 8–11]

Advantages	Disadvantages
<ul style="list-style-type: none"> • Higher and much higher specific stiffnesses, depending on percentages of aligned fibres • Greater flexibility in designing structurally efficient components: tailored directional properties • 10–20 % weight savings in actual components^a • Dimensional stability • (Greatly) reduced part count owing to largely integral assemblies with limited mechanical fastening • High fatigue strength • Corrosion resistant: reduced maintenance costs • Radar-absorbing properties (stealth) • Vibration damping (sometimes) • Possible self-healing (under development) 	<ul style="list-style-type: none"> • High material, labour and manufacturing costs • Possible delaminations and other flaws during fabrication, e.g. from drilling fastener holes • Intrinsically anisotropic: complex components difficult to analyse, sometimes resulting in poor predictions; complex failure modes and processes in compression make it difficult to develop failure criteria for compression loading • Higher notch sensitivity under static loading (e.g. fastener holes) • Conservative design and safety factors owing to <ul style="list-style-type: none"> – high susceptibility to impact damage – damage growth difficult to control and predict – difficult validation and certification of repairs – susceptibility to moisture pick-up (thermosets) and fuel absorption • Non-destructive inspection (NDI) difficulties • Low electrical conductivity requiring metal (copper) mesh in external surface layers to protect against lightning strikes • Flammable and non-recyclable

^aSee Sect. 14.4.1 for discussion of this very important point

These examples may be thought of as extreme cases, but they illustrate the points that (i) CFRP mechanical properties are much more complex to assess than those of aluminium alloys or, indeed, other metallic materials; and (ii) it is by no means a foregone conclusion that CFRPs will provide large specific strength benefits in actual structures.

Specific stiffnesses: Figure 14.9 compares the specific stiffnesses of conventional aerospace aluminium alloys and third generation Al–Li alloys with some examples for high-fibre-density CFRPs *without reduction factors*.

The overall advantages of CFRPs are much less than in the case of specific strengths. Even so, the aluminium alloys match only the 25 % aligned-fibre composites in terms of specific stiffness E/ρ .

Practical weight savings: Actual CFRP components are assembled from layers with different fibre orientations. Also, most aircraft structures are subjected to multidirectional loads, and this means that mechanical property isotropy will often be important. **N.B:** This is discussed further, and in detail, after Figs. 14.8 and 14.9.

For CFRP components a requirement of mechanical isotropy means that the amount of fibres aligned in the principal loading direction will be about 25 % [8], which is the *lowest* value in Fig. 14.9.

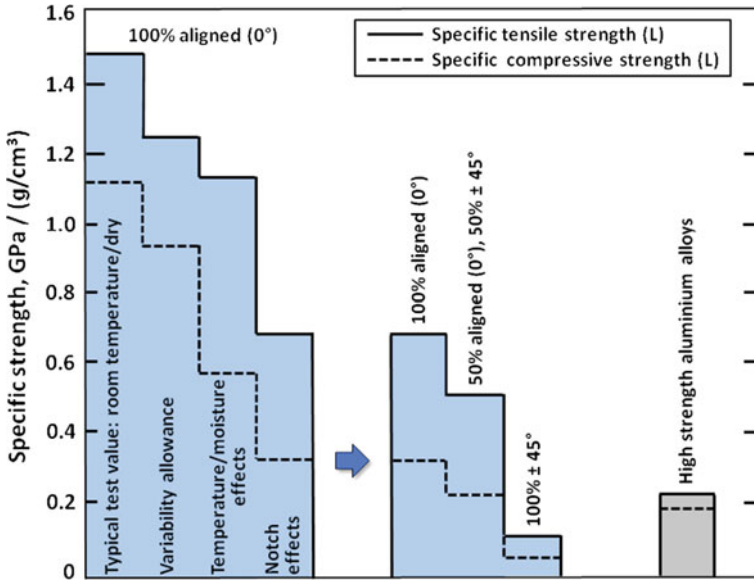


Fig. 14.8 Reduction factor effects on CFRP specific strengths, and comparison with high strength aluminium alloy specific strengths. The CFRP properties are for intermediate modulus fibres and a toughened resin system [12]

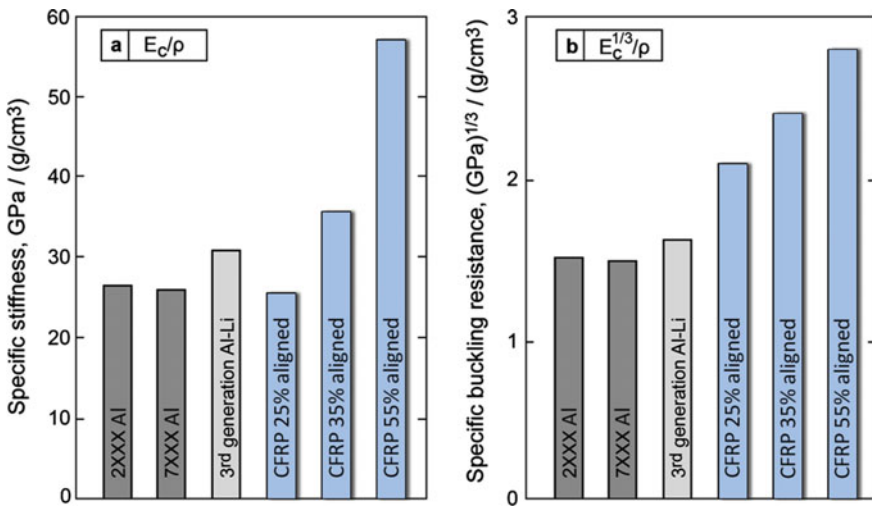


Fig. 14.9 Specific stiffnesses (average values) for high-fibre-density (60 % volume) CFRP composites tested in the aligned-fibre direction [10], conventional aerospace aluminium alloys and third generation Al-Li alloys [3]

On the other hand, if property isotropy is not necessary, the CFRP layers of a component can be ‘tailored’ to preferentially align some or most of the fibres in the principal loading direction, thereby increasing the structural efficiency: see Table 14.4.

The foregoing discussion is most important. It shows that although CFRPs with high percentages of aligned fibres have (very) high specific strengths and stiffnesses compared to aluminium alloys, a direct translation to high weight savings in actual components is not possible. This is the case even in the absence of reduction factors.

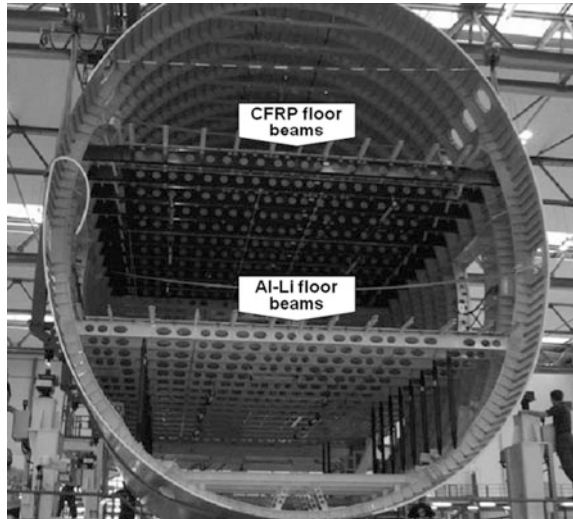
Mouritz [8] suggests 10–20 % weight savings from using CFRPs instead of aluminium alloys. This weight savings range is only slightly higher than the 8–15 % achievable by substituting third generation Al–Li alloys for conventional aluminium alloys [3]. Thus despite the increasing use of CFRPs in aircraft structures, Fig. 14.1, there is still potential competition from aluminium alloys. And, as also mentioned, there is an increasing trend to design and build hybrid structures.

Trade-off between stiffness, weight savings and costs: An instructive example of a trade-off between specific stiffness, weight savings and costs is given in Fig. 14.10. This shows different material choices, CFRP pultrusions [13] and Al–Li AA2196-T8511 alloy extrusions [14], for nominally identical applications in the Airbus A380.

The reasons for these differing choices are:

1. To maximise usable space the upper deck floor must span the entire fuselage without the intermediate supports commonly used for lower/main deck flooring.

Fig. 14.10 A380 CFRP and Al–Li alloy floor beams [3]: see Fig. 14.3 also



This puts great demands on the floor beam stiffness, favouring the use of CFRPs, see Fig. 14.9.

- On the other hand, the main/lower deck beams can be supported, as seen in Fig. 14.10. This enabled the Al–Li alloy extrusions to successfully compete for the beams, in a trade-off between the engineering properties, the resulting component weights, and the manufacturing costs.

14.4.2 Impact Damage and Inspections

Table 14.4 indicates that CFRPs have high fatigue strengths compared to aluminium alloys. However, CFRPs are highly susceptible to impact damage, which can grow during service, but not necessarily *or at all* by fatigue [1: p. 371].

In fact, CFRPs have the least impact resistance of any composites [1]. As an example, Fig. 14.11 compares a *thermoplastic* CFRP (i.e. a CFRP with better fracture resistance than thermoset CFRPs) with a standard damage tolerant aerospace aluminium alloy, AA2024-T3, and a damage tolerant version of GLARE. Note the especially high impact resistances of GLARE: this has led to its use as

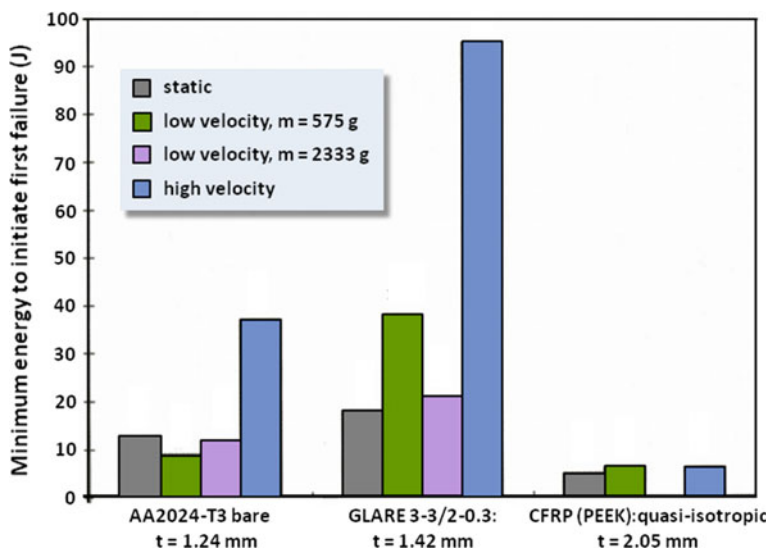


Fig. 14.11 Impact properties for a quasi-isotropic thermoplastic (PEEK) CFRP, aluminium alloy AA2024-T3, and a GLARE laminate [15]; m the mass of the impactor (unspecified for the high velocity impacts)

leading edge protection for the CFRP empennage on the Airbus A380: see Fig. 13.2 in Chap. 13 of this Volume.

Types of impact damage: These are various and varied, including hailstones (in-flight and on the ground), bird and lightning strikes, runway debris, tyre rupture, incidental contact with ground vehicles and installations, tool drop during maintenance, and engine blade loss or even rotor burst. The damage can be classified as shown in Table 14.5.

Several types of damage are obvious. However, there is a very important category of damage that is defined by the assumption that most in-service inspections are visual [19]. This damage is called ‘barely visible impact damage’ (BVID).

The importance of BVID lies in its threat to the structural integrity. BVID is difficult to detect by in-service inspections, and it could lead to visually undetectable damage growth (by whatever mechanisms) within the composite, followed by sudden failure at loads below the design allowables for nominally undamaged structures.

The reason why BVID can be so damaging is that impact effects are not confined to the composite surface [20]. A particularly severe example is shown in Fig. 14.12. The dominant type of damage is extensive delamination between the fibre layers; and in general it is delamination growth during service that is of most concern.

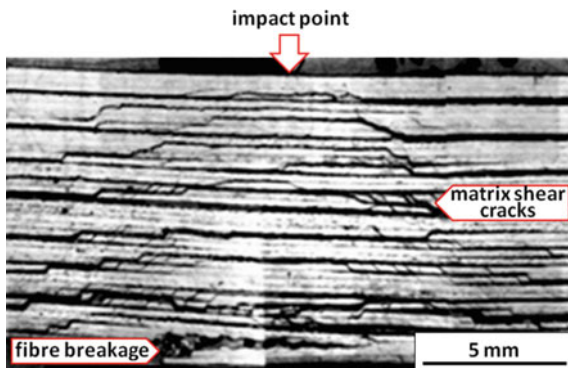
There are strength (and inspection) requirements to deal with all types of impact damage, including BVID, see Sect. 14.5, specifically 14.5.4.

N.B: Besides impact damage there are many types of manufacturing damage, including delaminations, voids, disbanded areas in skin/stringer interfaces, inclusions, scratches and fibre and matrix damage at drilled-hole locations [1]. These are accounted for by quality control inspections during manufacturing, see below, and a ‘Building Block’ (BB) test and analysis approach of validating composite structures for service [7, 18, 22–25]. This approach is also discussed in Section 14.5.

Table 14.5 Classification of specific types of impact damage [16–18]

Impact type	Self-evident	Impact location
Hail	Yes	Yes
Bird strike	Yes	Yes
Runway debris	Sometimes	Usually
Tyre rupture	Yes	Sometimes
Panels lost in-flight	Yes	Sometimes
Contact on ground	Sometimes	Yes
Tool drop	Sometimes	Yes
Engine blade/rotor	Yes	Yes
Lightning strike	–	–

Fig. 14.12 BVID ‘hidden’ damage in a CFRP laminate cross-section: modified photomontage from [21]



Inspections: NDI methods for BVID and quality control of production processes can be summarised as follows:

1. BVID may be assessed visually at two levels, namely general and detailed visual inspections [22]. General visual inspection (GVI) includes service-induced impact damage and screening of impact test results. Detailed visual inspection is more appropriate to test results.

The impact dent depth is widely used as a BVID criterion [22]. For GVI a typical detectable dent depth is about 0.25–0.5 mm [18]. For service components and structures the BVID dent depth is taken to be the minimum that can be reliably detected by scheduled inspections.

2. The majority of CFRP production defects are internal, so visual inspections, though necessary, are not sufficient. NDI techniques that establish internal defect acceptance and rejection limits are required [7].

The most used NDI techniques are ultrasonics [7, 26], usually through-transmission C-scan inspections [7] and sometimes pulse-echo A-scans. X-ray inspection is often used to check the bonding of inserts in laminate panels and honeycomb/facesheet bonds in sandwich panels [7].

The extent of this production-oriented NDI depends on whether the components are for (i) primary (safety-of-flight) structures, (ii) secondary structures, whose failure would affect aircraft operation but not the safety, and (iii) tertiary structures, whose failure would not significantly affect aircraft operation.

More information on CFRP NDI techniques may be obtained from Ref. [7] and specialist publications. As noted in Table 14.4, this is a difficult topic. The reasons are the variety of possible manufacturing defects and the ways in which CFRP structures can be built up. Another important point is that this subject area is continually evolving as the technique capabilities improve and new methods are developed.

14.4.3 Repairs of CFRP Structures

The previous topic, *Inspections*, is directly related to repairs. And like inspections, repairs of CFRP structures have difficult aspects, particularly validation, which is discussed in Sect. 14.5.5.

Repair options depend on several factors [1]:

- Types of damage
- Component and/or structural build-up and requirements
- Field or depot level repair possibilities
- Criticality with respect to flight safety and operation.

Figure 14.13 classifies repairs into non-patching techniques for minor damage (surface and potting repairs), and patching for more serious damage that affects the load-carrying capability.

A detailed discussion of the types of repairs, with supporting literature, is given by Baker et al. [1]. Similar and additional information is present in the U.S. Department of Defence Composite Materials Handbook, Volume 3 (MIL-HDBK-17-3F) [7], which, as stated earlier, may be downloaded from the Internet.

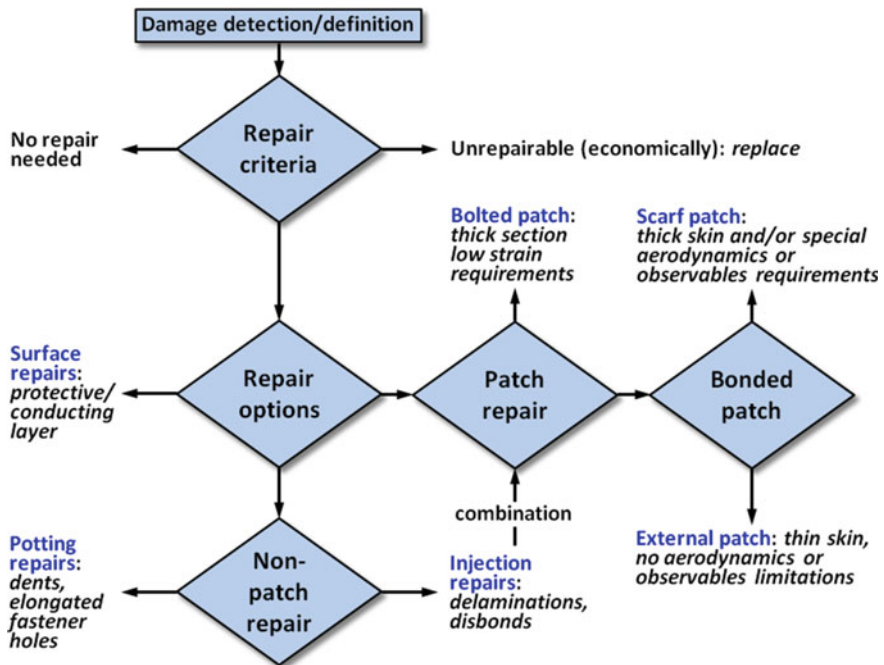


Fig. 14.13 Classification of CFRP repairs into non-patching and patching techniques: after [1]

Also, the Federal Aviation Administration (FAA) and European Aviation Safety Agency (EASA) sponsor CFRP composite research in several key areas, including structural substantiation; damage tolerance; maintenance and repair practices; materials control and standardisation; and advanced material forms and processes [16–19, 21–24, 27]. These activities, in which major companies (Airbus, Boeing) participate, provide continuing updates to the guidelines [7] and requirements for composite structures [25].

14.5 Safety and Damage Tolerance of CFRP Components and Structures

This Section summarises the Damage Tolerance (DT) and fatigue requirements for CFRP composite aircraft structures. A full discussion is beyond the scope of this Source Book Volume, and could also be misleading, since the subject area is continually evolving as part of the activities mentioned at the end of Sect. 14.4.3.

14.5.1 Strength and Safety Definitions

There are two essential basic strength requirements for ensuring aircraft safety. These are the airframe structural limit load (LL) and ultimate load (UL) definitions:

Limit Load (LL): Maximum load to be expected in service.

Ultimate Load (UL): Limit Load multiplied by a historically-based safety factor, $LL \times 1.5$ [28].

The limit load (LL) and ultimate load (UL) definitions apply to all possible types of external flight and ground loads on the airframe structure. The 1.5 safety factor on LL covers inadvertent service flight and ground loads greater than LL, structural deflections above LL that could compromise structural integrity, and as-built part thicknesses within tolerance but less than those assumed in the stress analyses. However, the safety factor *does not* cover:

- analysis or modelling errors
- poor design practice
- material property variations
- process escapes (e.g. different materials used than those specified, improperly drilled holes, etc.).
- damage and repairs
- environmental effects on composite properties.

14.5.2 Reduction Factors on Allowables

From Fig. 14.8 it was already pointed out that reduction factors greatly decrease the CFRP ‘allowables’ from those theoretically possible. A more general illustration is given in Fig. 14.14. This shows how manufacturing anomalies, service-induced damage, environmental effects and the 1.5 safety factor must be taken into account when designing CFRP structures. The reduction on allowable strain can be as much as two-thirds [29].

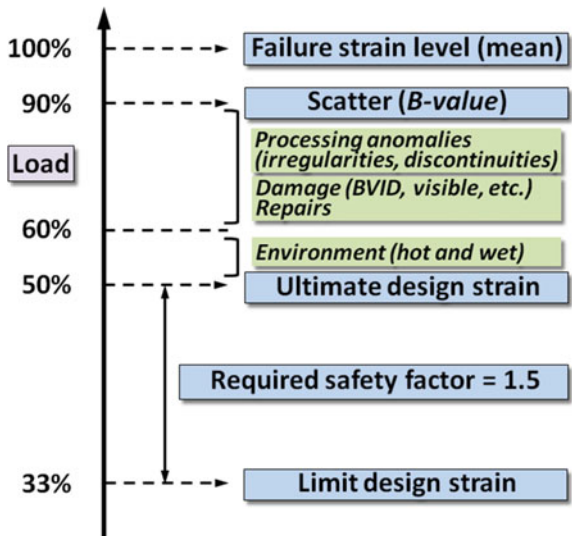
14.5.3 Testing to Determine Allowables

Accurate and reliable estimates of the design allowables for CFRP aircraft structures present many challenges, since together with the design details, all the factors shown in Fig. 14.14 must be considered. The general consensus is that a so-called ‘Building Block’ (BB) test and analysis approach should be used, see Fig. 14.15.

The BB approach may be viewed as a pyramid consisting of four levels of testing and analysis: (i) specimens, (ii) components, (iii) structural units, and (iv) full-scale units. Each level of the pyramid is the foundation for the next, and the complexity and costs increase with each upward level.

The overall purpose of the tests, and the supporting analyses, is to validate the structures for service. The final phase, leading to certification of the aircraft, is ground and flight testing.

Fig. 14.14 Reduction of strain allowables for CFRP structures: after [18, 29]



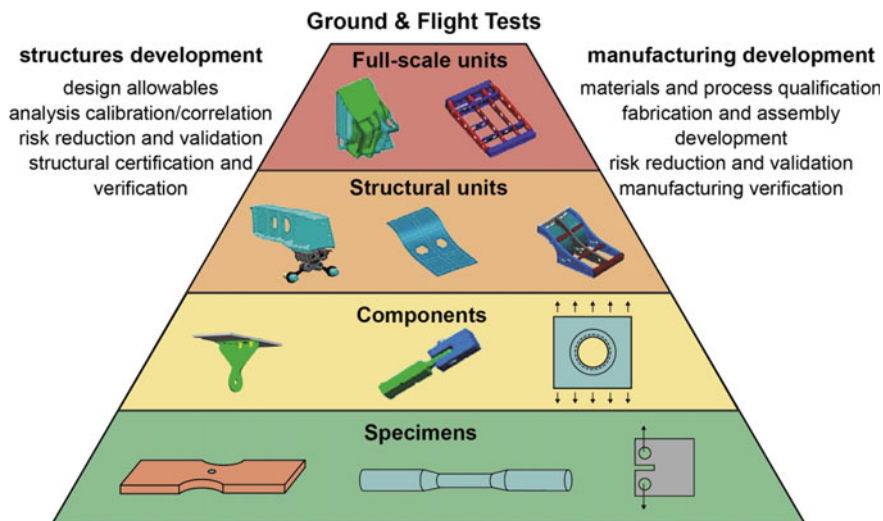


Fig. 14.15 ‘Building block’ test approach for materials, components and structures: after [30]

Important

Levels (i)–(iii): Up to the level of full-scale testing the BB approach for composite structures is broadly analogous to the BB approach for metallic airframe structures, see Chap. 16 in Volume 2 of these Source Books. However, there are major differences. Metallic airframe materials have better defined and consistent material and mechanical properties; considerably fewer types of manufacturing anomalies (especially in built-up structures); much less susceptibility to impact damage; and mechanical properties insensitive to environmental effects. (Another difference, this time an advantage of CFRPs, is that they are not susceptible to corrosion, unlike, for example, most aerospace aluminium alloys.)

Level (iv): There are also major differences at the full-scale test level. For CFRP composite structures there is *emphasis* on static proof tests and separate fatigue tests on impact- and discontinuity-damaged structures to demonstrate ‘no-growth’ damage behaviour [7, 25]. On the other hand, metallic aircraft structures are subjected to full-scale fatigue testing to demonstrate (a) adequate fatigue life and crack growth characteristics, and (b) adequate residual static strength after fatigue testing.

The word ‘*emphasis*’ in the previous paragraph is used because the MIL-HDBK-17-3F [7] and FAA AC-20-107B [25] guidelines do not exclude full-scale fatigue testing of CFRP aircraft structures, whereby the objective is to account for limited growth of impact (BVID) damage and/or manufacturing discontinuities during service.

For more, and more detailed, information on the testing of CFRP composite structures the reader should consult both of these guidelines, which have been

developed with joint consultation, but differ in scope and extent. For example, the MIL-HDBK-17-3F guidelines have been developed for military aircraft (although there is much information relevant to civil aircraft), while the FAA AC-20-107B guidelines are primarily concerned with civil transport aircraft.

N.B: The MIL-HDBK-17-3F and FAA AC-20-107B guidelines are continually evolving, and they are updated at appropriate intervals.

14.5.4 Damage Tolerance (DT) Allowables

MIL-HDBK-17-3F [7] and FAA AC-20-107B [25] provide extensive information on assessing the effects of various types of impact damage (see Table 14.5) and other damage on the integrity of CFRP airframe structures.

An outline of the FAA AC-20-107B guidelines for DT evaluation of damage is given in Table 14.6. This outline is derived from the guidelines for *all* types of damage, i.e. including manufacturing anomalies as well as service-induced damage.

Again following FAA AC-20-107B, completion of the first step in Table 14.6 allows the various types of damage to be classified into five categories, as shown in Fig. 14.16. In more detail these are:

Category 1: Allowable damage that may go undetected (BVID) in service and also allowable manufacturing defects. Structural substantiation includes a reliable service life while maintaining UL capability.

Category 2: Damage reliably detectable by field inspections. Structural substantiation includes demonstration of reliable inspection and the retention of LL capability. Examples of category 2 include visible impact damage (VID), deep

Table 14.6 Outline of guidelines for DT evaluation of damage in CFRP composite aircraft structures

1.	Identification of structure whose failure would reduce the structural integrity, and a damage threat assessment to determine possible locations, types and sizes of damage that may occur during manufacture, operation or maintenance
2.	Realistic testing (i.e. including service loads and environmental simulations) according to the BB approach to define the sensitivity of the structure to damage growth
3.	Establish the extent of initially detectable damage consistent with the inspection techniques used during manufacturing and service
4.	Establish the extent of damage for residual strength assessments, including considerations about the probability of detection using field inspection techniques
5.	Develop an in-service inspection programme for inclusion in a maintenance plan. Establish inspection intervals for reliable detection of damage between the time it initially becomes detectable and the time at which the extent of damage reaches the limits for the required residual strength
6.	For continued airworthiness the maintenance and repair should meet all the appropriate considerations covered in FAA AC-20-107B

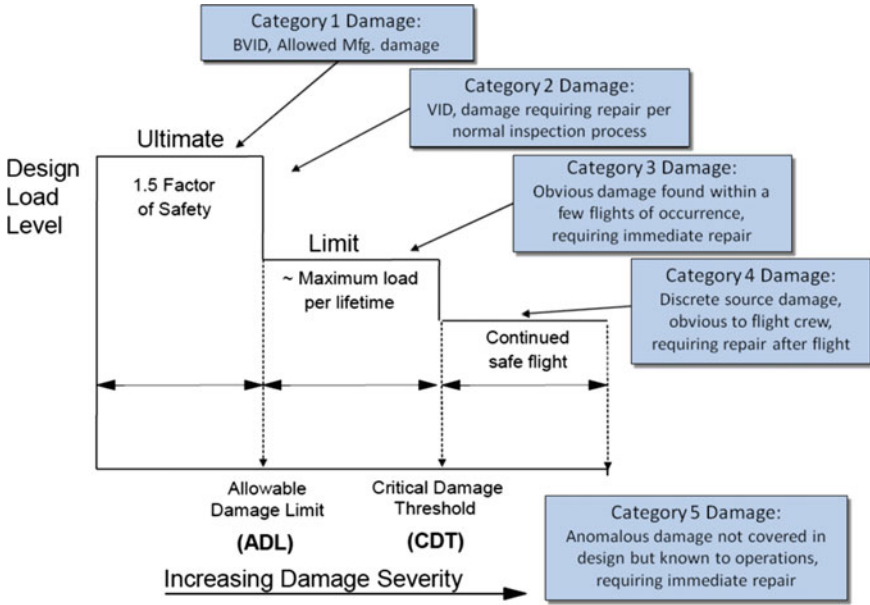


Fig. 14.16 Schematic diagram of design load levels versus categories of damage severity [25]

gouges or scratches, detectable delamination or disbonding, and local major heat or environmental degradation.

Category 3: Damage reliably detected within a few flights of occurrence by operations or maintenance personnel with no special skills. Structural substantiation includes demonstration of reliable quick detection and the retention of LL or near-LL capability. An example of Category 3 is large VID.

Category 4: Discrete source damage from a known incident such that flight manoeuvres are limited. Structural substantiation includes a demonstration of residual strength. Examples of Category 4 include severe in-flight hail, bird strikes, and tyre and rotor bursts.

Category 5: Severe damage from anomalous ground or flight events, and not covered by design criteria or structural substantiation procedures. This category is included in FAA AC-20-107B to make all concerned (design engineers, operations and maintenance personnel) aware of possible damage from Category 5 events, which need immediate reporting. Examples of Category 5 include severe collisions with ground vehicles, anomalous flight load conditions, abnormally hard landings, and loss of parts in flight with possible subsequent high-energy impacts on adjacent structures.

14.5.5 Repair Issues: Validation

Validation of repairs relies on strict attention to repair design and analysis, appropriate design values supported by tests, damage removal and site preparation,

appropriate choice of the repair materials and fabrication processes, and inspection (quality control) [7, 25]. Some damage types may need special instructions for field repair and the associated quality control [25]. In addition, the service inspectability and durability of the repairs must be verified: this is a difficult task.

Thus although the schematic in Fig. 14.13 appears straightforward, the actual repair procedures can be complex. For example, bonded repairs require more in-process quality control than bolted repairs [7]:

Bonded repairs: The composite materials and adhesives must be compatible with the original structure, and so must the repair process, which involves patch and parent surface preparation, adhesive application, bagging (enclosing the repair for curing) and the cure thermal cycle [1, 7]. Each of these activities may be different for the type of bonded repair and the component being repaired.

Bolted repairs: These are simpler, since a pre-processed patch is mechanically fastened to the damaged structure. Even so, drilling and reaming holes in both the patch and parent material require much care to avoid damaging the hole vicinities and prevent splitting of parent skin material.

14.6 Developments Old and New

The title of this Section may seem unusual, but it reflects the fact that development and introduction of aerospace materials is a long-term process, often taking 10 years or more. For example, although high-modulus carbon fibres were developed in the mid-1960s [31], the first CFRP applications were in tactical aircraft in the mid-1970s, see Fig. 14.1. Transport aircraft applications followed in the 1980s.

More recent developments, though not deserving the designation ‘new’, are so-called smart structures, three-dimensional (3D) fibre reinforcements, and self-healing matrices.

Smart structure technology uses the layered configuration of composite laminates to insert interlayer optical fibres and sensors for structural health monitoring (SHM). SHM is the subject of Chap. 22 of Volume 2 of these Source Books, and is also discussed specifically for CFRPs in Ref. [1]. Hence smart structures will not be considered here.

The incentive to develop 3D and self-healing CFRPs stems from trying to improve the damage resistance of conventional CFRP composite structures. These topics, 3D and self-healing CFRPs, are briefly discussed in Sects. 14.6.1 and 14.6.2.

14.6.1 3D CFRP Components and Structures

Laminated two-dimensionally (2D) reinforced CFRP composites have poor impact resistance, see Sects. 14.4 and 14.5 and also low through-thickness strength. It was realised more than 25 years ago [32] that these properties could be improved by

fabricating 3D composites. This is partly why NASA set up an Advanced Composites Technology (ACT) programme in 1989, followed by the first ACT conference in 1990 [33]. Thus the development of 3D CFRPs already has a respectably long history.

In 3D reinforcement some of the fibres are oriented in the through-thickness (z) direction. This can be obtained from 3D weaving or braiding, or by stitching-in fibres in the z -direction [1]. This z -stitching is much simpler than weaving, but it does not provide all the benefits of fully 3D fibre configurations [1].

Whichever type of reinforcement is used, a dry preform is made and then converted into a composite part using one of the liquid resin moulding techniques (RTM or RFI, see Sect. 14.3.3). Besides enabling 3D configurations, the RTM and RFI techniques have the additional advantage of relatively low cost compared with conventional laminating procedures [1].

The ACT programme initially concentrated on developing large composite wing structures for commercial aircraft. Several types of composite fabrics were evaluated, and it was found that stitching combined with RFI showed the greatest potential for overcoming the cost and damage tolerance restrictions [34].

The stitched/RFI CFRP wing manufacturing process used three textile processes, knitting, braiding and stitching, as follows [34]:

1. The wing covers were made from knitted tow preforms stacked in layers as few as two stacks in low-stress areas and up to twenty stacks in high-stress areas. Then the stacks were stitched to make solid wing cover preforms.
2. The stiffeners and rib clips were made from braided tubes, which were collapsed and stitched to make blade-shaped profiles. The braiding process made it easier for the components to conform to the wing contours.
3. The stiffening elements were stitched to the wing cover preforms, ready for the RFI process.

This manufacturing process required a very large Advanced Stitching Machine (ASM), which is also discussed in Ref. [34].

More recently, NASA and Boeing set up a demonstrator programme for a large CFRP multi-bay pressure box [35–38], whose configuration is derived from a Blended Wing Body design concept [39]. The box consists of stitched/RFI sub-assemblies that form the exterior shell and floor members and 4 interior sandwich rib panels. The stitched/RFI sub-assemblies were designed, manufactured and evaluated using the Building Block (BB) approach, whereby the stitching is intended to suppress interlaminar failures, arrest damage and turn cracks [37].

An illustration of the sub-assemblies, the sandwich panels and the box is given in Fig. 14.17. The box itself was assembled at Boeing's C-17 assembly site in Long Beach, California, by mechanically fastening the sub-assemblies [38]. After final assembly the box was transferred to the NASA Langley Research Center, to be statically tested under combined pressure and bending loads, firstly in the pristine condition and subsequently with interior and exterior BVID [38].

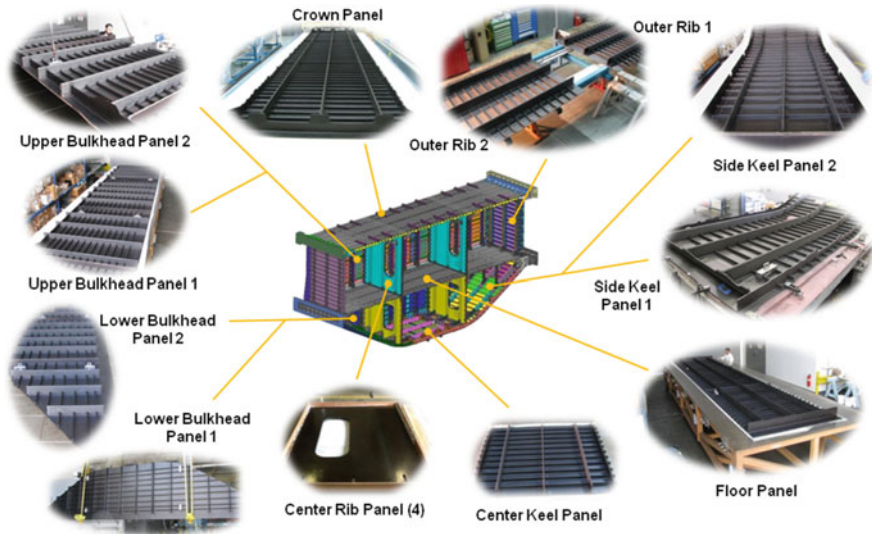


Fig. 14.17 CFRP Stitched/RFI sub-assemblies, sandwich panels and a schematic of the large multi-bay pressure box [38]: reproduced by permission from NASA/Boeing

This demonstrator programme has already been extensively reported in the open literature [35–38], and there will undoubtedly be much more follow-on information in the next few years.

14.6.2 Self-healing CFRPs

Over the past 20 years, and especially in the last decade, there has been much interest in developing self-healing polymer resins and, by extension, self-healing PMCs. Two recent and extensive reviews [40, 41] are available via the Internet.

The basic self-healing idea is shown in Fig. 14.18, progressing from (a) to (c). A growing crack breaks microcapsules that contain either a liquid resin (healing agent) or a catalyst (cure agent). The contents of these capsules react to polymerise the resin within the crack and heal it. Another possibility is to use hollow glass fibres as the encapsulating vessels [41].

Recovery of more than 90 % of the pristine resin fracture toughness properties is possible for capsule-based healing of epoxy resins [40, 41]. However, limited data show that CFRP fracture toughness recovery does not exceed 80 %, and can be much less [41]. This adverse result, which appears to be generally true for PMCs, has been attributed to insufficient amounts of self-healing resin to close cracks and delaminations, and thermal loss of the healing reaction to the fibres [41].

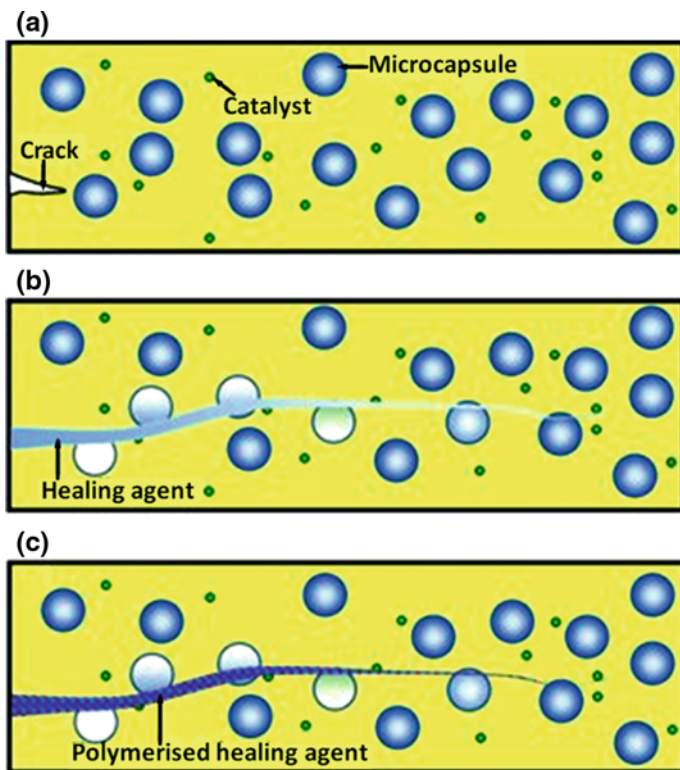


Fig. 14.18 Schematic of microcapsule self-healing of a resin

Disadvantages of incorporating microcapsules in PMCs were demonstrated for C-glass/epoxy composites [42]. Increasing amounts of microcapsules decreased the tensile strength and modulus, and increased the porosity [41, 42].

Much more research is needed. For CFRPs this includes developing more appropriate self-healing resins and survival of the encapsulated resins and catalysts during component manufacture.

14.7 Current Indian Scenario (*Contribution Partly by K. Vijaya Raju*)

Indian efforts in the development of CFRP products and components are summarised in this Section. Over the past three decades or so, a number of aerospace platforms have been developed in India. These include the Advanced Light Helicopter (ALH-Dhruv) from Hindustan Aeronautics Limited (HAL); the Light Combat Aircraft (LCA-TEJAS) developed by the Aeronautical Development

Agency with HAL as the principal partner; the Light Transport Aircraft (LTA-SARAS) and two-seater trainer aircraft (HANSA) developed by the National Aerospace Laboratories (NAL-CSIR); and a number of launch vehicles and satellites for the Indian Space Research Organisation (ISRO-DoS).

All these developments have employed composite materials for the realisation of efficient lightweight structures—mostly CFRP and glass fibre reinforced composites, and to a limited extent aramid (Kevlar) fibre reinforced composites.

14.7.1 Light Combat Aircraft TEJAS

The LCA-TEJAS is a multi-role combat aircraft and is the smallest aircraft in its class amongst contemporary aircraft. TEJAS has an unstable configuration and is controlled at all times by a fly-by-wire control system via on-board computers.

Among the important requirements for the airframe of such an aircraft are the lightweight construction, high degree of reliability over a long period, and the need to have aerodynamic shapes providing high aerodynamic efficiency under operating (flexed) conditions. It was realised that in order to meet these demands, it was necessary to have materials with high specific strength and stiffness that can take complex shapes easily and provide adequate fatigue and corrosion resistance.

Large-scale use of composites in TEJAS has provided effective solutions for such considerations. The TEJAS airframe consists of about 45 % CFRP that includes 90 % of the skin material. Illustrations of some of the CFRP components are given in the upper photomontage of Fig. 14.19. These include complex parts like the fin, rudder, centre fuselage and main landing gear doors, which are fabricated using co-curing and co-bonding.

The CFRP materials are mainly thermosets using epoxy resins. A high temperature CFRP is used for the engine bay door. Currently, carbon fibre prepreps are available both as unidirectional tapes (continuous carbon fibre tows embedded in partially cured matrix polymeric resin) and as bidirectionally woven fabrics embedded in partially cured matrix polymeric resin.

14.7.2 Light Transport Aircraft SARAS

The LTA-SARAS is a 14-seat twin-turboprop civilian light transport aircraft for general use. The airframe is about 35 % composites, mainly CFRP. Illustrations of some of the CFRP components are given in the lower photomontage of Fig. 14.19. These include the wing, horizontal and vertical stabilisers, the rear pressure bulkhead, front top skin, engine nacelles and flooring.

The CFRP wing is fabricated using a patented cost-effective manufacturing technology called VERITY (Vacuum Enhanced Resin Infusion Technology).

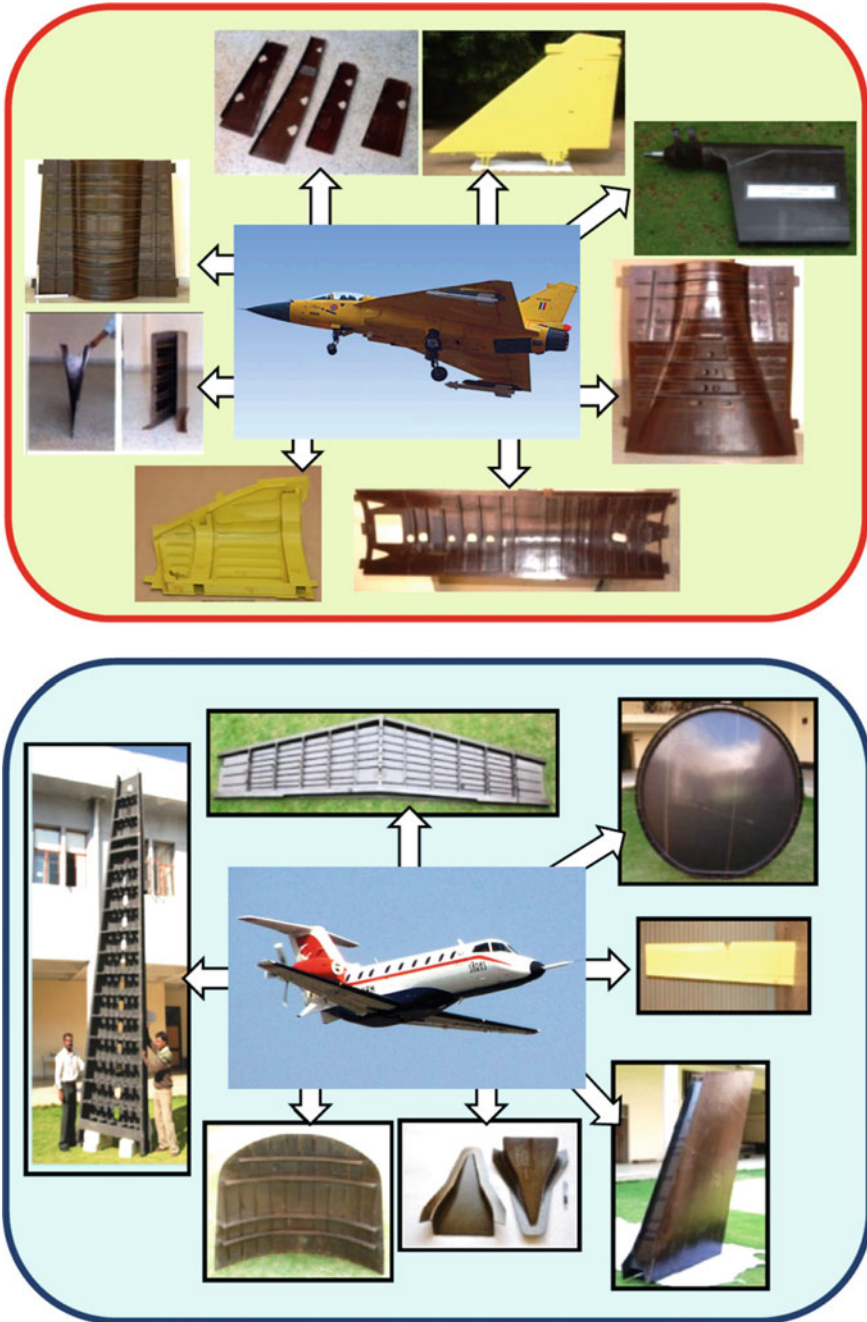


Fig. 14.19 Photomontages of CFRP composite parts in the Light Combat Aircraft TEJAS (*top*) and the Light Transport Aircraft SARAS (*bottom*). Source: Advanced Composites Division, CSIR-NAL, Bangalore, India

14.8 Summary

This chapter surveys the applications and properties of polymer matrix structural composites (PMCs), concentrating on carbon fibre reinforced composites (CFRPs), which are widely used in modern aerospace structures.

The discussion of CFRPs begins with considering the matrices and fibres and the production methods for aerospace components. Then some important CFRP properties and considerations are reviewed, namely the specific mechanical properties and their influences on practical weight savings and costs; and impact damage (to which CFRPS are very susceptible) and inspections and repairs of damage.

A complete Section is devoted to Safety and Damage Tolerance of CFRP components and structures. This is a complex topic and still very much an evolving discipline. The following Section mentions some 'old' but still current developments (high-modulus fibres and smart structures), and then discusses the newer developments of 3D fibre reinforcements and self-healing matrices. Especial attention is given to a NASA/Boeing demonstrator programme for a large 3D CFRP multi-bay pressure box simulating a centrally-located structure for an advanced Blended Wing Body aircraft.

The chapter ends with a contribution about the current CFRP scenario in India, highlighting the Light Combat Aircraft TEJAS and the Light Transport Aircraft SARAS, whose airframes consist of about 45 % and 35 % CFRPs, respectively.

References

1. Baker A, Dutton S, Kelly D (2004) Composite materials for aerospace structures, 2nd edn. American Institute of Aeronautics and Astronautics Inc., Reston, VA 20191, USA
2. Prasad NE, Gokhale AA, Wanhill RJH (eds) (2014) Aluminum–lithium alloys: processing, properties and applications. Butterworth-Heinemann, Elsevier Inc., Oxford, UK
3. Wanhill RJH (2013) Aerospace applications of aluminum-lithium alloys. In: Prasad NE, Gokhale AA, Wanhill RJH (eds) Aluminum-lithium alloys, processing, properties and applications. Butterworth-Heinemann, Elsevier Inc., Oxford, UK, pp 503–535
4. Grimshaw MN, Grant CG, Diaz JML (2001) Advanced technology tape laying for affordable manufacturing of large composite structures. In: Repecka L, Garemi FF (eds) 2001: a materials and processes odyssey. Society for the Advancement of Material and Process Engineering, Covina, CA 91724-3759, USA, pp 2484–2494
5. Department of Defense Handbook (2002) Composite materials handbook. Volume 1, polymer matrix composites guidelines for characterization of structural materials, MIL-HDBK-17-1F. Document Automation and Production Service (DAPS), Philadelphia, PA 19111-5094, USA
6. Department of Defense Handbook (2002) Composite materials handbook. Volume 2: polymer matrix composites materials properties, MIL-HDBK-17-2F. Document Automation and Production Service (DAPS), Philadelphia, PA 19111-5094, USA

7. Department of Defense Handbook (2002) Composite materials handbook. Volume 3: polymer matrix composites materials usage, design, and analysis, MIL-HDBK-17-3F. Document Automation and Production Service (DAPS), Philadelphia, PA 19111-5094, USA
8. Mouritz AP (2012) Introduction to aerospace materials. Woodhead Publishing Limited, Cambridge, UK
9. AGARD Report 785 (1992) The utilization of advanced composites in military aircraft. Advisory Group for Aerospace Research and Development, Neuilly-sur-Seine, France
10. Peel CJ (1990) The development of aluminium lithium alloys: an overview. In: New light alloys. AGARD Lecture Series No. 174, Advisory Group for Aerospace Research and Development, Neuilly-sur-Seine, France, pp 1-1-1-55
11. Campbell FC (2010) Structural composite materials. ASM International, Materials Park, OH 44073-0002, USA
12. Wright GA (1992) An overview of concerns relating to fluid effects on composites. In: The utilization of advanced composites in military aircraft. AGARD Report 785, Advisory Group for Aerospace Research and Development, Neuilly-sur-Seine, France, pp 13-1-13.6
13. Brosius D (2003) Advanced pultrusion takes off in commercial aircraft structures. Gardner Business Media, Inc., Cincinnati, OH 45244, USA. www.compositesworld.com
14. Lequeu P, Lassince P, Warner T (2007) Aluminium alloy development for the Airbus A380—Part 2. *Adv Mater Processes* 165(7):41-44
15. Voegesang LB (2004) Fibre metal laminates, the development of a new family of hybrid materials. In: Guillaume G (ed) 'ICAF 2003: fatigue of aeronautical structures as an engineering challenge, vol I, pp 3-27. Engineering Materials Advisory Services, Warrington, UK
16. Halpin JC, Kim H (2007) Managing impact risk for composite structures: unifying durability and damage tolerance perspective. FAA/EASA/Industry composite damage tolerance and maintenance workshop, 7-11 May 2007, Amsterdam, the Netherlands
17. Halpin JC, Kim H (2009) Managing damage threats for composite structures: unifying durability and damage tolerance perspective. In: 3rd FAA/EASA/Industry composite damage tolerance and maintenance workshop, 1-5 June 2009, Tokyo, Japan
18. Fawcett AJ Jr, Oakes GD (2006) Boeing composite airframe damage tolerance and service experience. In: FAA/Wichita State University composite damage tolerance & maintenance workshop, 19-21 July 2006, Chicago, Illinois, USA
19. Waite S (2006) Damage/defect types and inspection—some regulatory concerns. FAA/Wichita State University composite damage tolerance & maintenance workshop, 19-21 July 2006, Chicago, Illinois, USA
20. Clark G, Saunders DS (1991) Morphology of impact damage growth by fatigue in carbon fibre composite laminates. *Mater Forum* 15:333-342
21. Icewicz L (2006) Composite damage tolerance and maintenance safety issues. In: FAA/Wichita State University composite damage tolerance & maintenance workshop, 19-21 July 2006, Chicago, Illinois, USA
22. Fualdes C, Thévenin R (2006) Composites @ airbus damage tolerance methodology. FAA/Wichita State University composite damage tolerance & maintenance workshop, 19-21 July 2006, Chicago, Illinois, USA
23. Icewicz L (2009) Updates to AC 20-107B 'Composite Aircraft Structure'. In: 3rd FAA/EASA/Industry composite damage tolerance and maintenance workshop, 1-5 June 2009, Tokyo, Japan
24. Waite S (2014) Composite materials: developing continued airworthiness issues. In: SIASA (Support to the Improvement of Aviation Safety in Africa) workshop on technology evolution—impact on airworthiness, 23-24 Sept 2014, Windhoek, Namibia
25. Federal Aviation Administration (2010) Composite aircraft structure. Advisory Circular FAA AC-20-107B, Change 1, 24 Aug 2010. U.S. Department of Transportation, Washington, DC 20590, USA

26. Smith RA (2009) Composite defects and their detection. In: Rawlings RD (ed) *Materials science and engineering*, vol III. Encyclopedia of Life Support Systems, UNESCO, Paris, France, pp 103–143
27. Ilcewicz LB (2004) Composite technology development for commercial airframe structures. In: Kelly A, Zweben C, Bader MG, Kedward KT, Sawada Y (eds) *Comprehensive composite materials*, volume 6: design and applications. Elsevier Science Ltd., Oxford, UK, pp 121–163
28. Modlin CT, Zipay JJ (2014) The 1.5 & 1.4 ultimate factors of safety for aircraft and spacecraft—history, definition and applications. ntrs.nasa.gov/archive/nasa/casi.ntrs.nasa.gov/2140011147
29. Calomfirescu M, Hickethier H (2010) Damage tolerance of composite structures in aircraft industry. *Composites Europe 2010*, 14–16 Sept 2010, Essen, Germany
30. Ball DL, Norwood DS, TerMaath SC (2006) Joint Strike Fighter airframe durability and damage tolerance certification. AIAA paper 2006-1867, In: 47th AIAA/ASME/ASCE/AHS/ASC Structures, Structural Dynamics, and Materials Conference, 1–4 May 2006, Newport, Rhode Island, USA
31. Gorss J (2003) High performance carbon fibers. American Chemical Society Commemorative Booklet, 17 Sept 2003, Washington, DC 20036, USA
32. Dow MB, Smith DL (1989) Damage tolerant composite materials produced by stitching carbon fabrics. In: *Proceedings of the 21st International SAMPE Technical Conference 25–28 Sept 1989*, Atlantic City, New Jersey. Society for the Advancement of Materials and Process Engineering, Covina, CA 91724-3759, USA, pp 595–605
33. Davis JG Jr, Bohon HL (eds) (1991) First NASA advanced composites technology conference. NASA Conference Publication 3104, Parts 1 and 2, NASA Scientific and Technical Information Program STI Support Services, NASA Langley Research Center, Hampton, VA 23681-2199, USA
34. NASA Facts (1997) The advanced stitching machine: making composite wing structures of the future. National Aeronautics and Space Administration FS-1997-08-31-LaRC, Aug 1997, Langley Research Center, Hampton, VA 23681, USA
35. Velicki A, Thrash P, Jegley D (2009) Airframe development for the Hybrid Wing Body aircraft. Paper AIAA 2009-932, 47th AIAA Aerospace Sciences Meeting Including the New Horizons Forum and Aerospace Exposition, 5–8 Jan 2009, Orlando, Florida, USA
36. Velicki A, Jegley D (2011) PRSEUS development for the Hybrid Wing Body aircraft. Paper AIAA 2011-7025, AIAA centennial of naval aviation forum “100 years of achievement and progress”. 21–22 Sept 2011, Virginia Beach, Virginia, USA
37. Velicki A, Jegley D (2014) PRSEUS structural concept development. Paper AIAA-2014-0259, 55th AIAA/ASME/ASCE/AHS/SC Structures, Structural Dynamics, and Materials Conference, 13–17 Jan 2014, National Harbor, MD 20745, USA
38. Jegley DC, Velicki A (2015) Development of the PRSEUS multi-bay pressure box for a Hybrid Wing Body vehicle. Paper in: *AIAA 2015 Science and Technology Forum and Exposition*, 5–9 Jan 2015, Kissimmee, Florida, USA
39. Liebeck RH (2004) Design of the blended wing body subsonic transport. *J Aircr* 41(1):10–25
40. Blaiszik BJ, Kramer SLB, Olugebefola SC, Moore JS, Sottos NR, White SR (2010) Self-healing polymers and composites. *Annu Rev Mater Res* 40:179–211
41. Smith JG Jr (2012) An assessment of self-healing fiber reinforced composites. NASA Technical Memorandum NASA/TM-2012-217325, NASA Center for Aerospace Information, Hanover, MD 21076-1320, USA
42. Yin T, Zhou L, Rong MZ, Zhang MQ (2008) Self-healing woven glass fabric/epoxy composites with the healant consisting of micro-encapsulated epoxy and latent curing agent. *Smart Mater Struct* 17(1), 15019 (8 pp)

Bibliography

1. Tong L, Mouritz AP, Bannister MK (2002) 3D fibre reinforced polymer composites. Elsevier Science Ltd., Oxford, UK

Chapter 15

C/C and C/SiC Composites for Aerospace Applications

Suresh Kumar, K. Chandra Shekar, B. Jana, L.M. Manocha
and N. Eswara Prasad

Abstract This chapter deals with different aspects of the carbon fibre-reinforced carbon composites (C/C) and carbon fibre-reinforced silicon carbide composites (C/SiC), especially for aerospace applications. The reinforcement and matrix materials and the process technologies developed for these composites are discussed. Typical mechanical and thermal properties at room and high temperatures are also presented, together with some actual and potential aerospace applications. Some products developed in India are also included.

Keywords Carbon matrix composites · Processing · Properties · Applications

15.1 Introduction

Carbon fibre reinforced carbon matrix (C/C) composites and carbon fibre reinforced ceramic matrix composites (C_rCMC) offer some significant advantages over conventional high temperature materials for aerospace applications [1–7]. The development of C/C composites started in 1958, with US Air Force sponsored work, which later received significant impetus from the Space Shuttle programme. The C/C composite technology remained as guarded secret technology for the USA and European countries until other industrial applications were explored. Currently,

S. Kumar (✉) · L.M. Manocha · N. Eswara Prasad
DMSRDE, DRDO, Kanpur, India
e-mail: skumar@dmsrde.drdo.in

N. Eswara Prasad
e-mail: nep@dmsrde.drdo.in

K.C. Shekar
VITS, Hyderabad, India
e-mail: kcschandra2003@gmail.com

B. Jana
RCMA, Hyderabad, India
e-mail: biswanathjana@gmail.com

many countries, including India, have their own technologies with manufacturing units in civilian and military sectors.

The C/C composites possess high thermal stability, high specific strength, high stiffness, high thermal conductivity, low coefficient of thermal expansion, high fracture toughness and good fatigue and creep resistance. Also, these composites maintain good mechanical properties, including frictional properties, over the entire operational temperature range [1, 3, 4, 7]. The combination of these properties makes them the preferred materials for different aerospace structural components like ailerons, flaps, landing-gear doors and other structural parts. However, they have a major drawback, the lack of stability above 500 °C in oxidizing environments. This limits their application in such environments to short durations [4, 8, 9]. On the other hand, these composites can withstand very high heat fluxes for short durations, making them suitable for re-entry nose tips and leading edges of ballistic hypersonic missiles [2, 9].

In order to make C/C composites suitable for extended durations and repeated use, the oxidation resistance is improved by (i) oxidation-resistant coatings, or (ii) modifying the composite matrix by adding third phase oxidation-resistant ceramic fillers or (iii) converting the carbon matrix to carbides like SiC. The latter type of composite, carbon fibre reinforced SiC matrix composites, are called C/SiC composites.

The C/SiC composites possess most of the good properties of the C/C composites and in addition have better oxidation and erosion resistance. Moreover, the density of the carbon is lower than the density of many metallic and non-metallic materials, and this makes them ideal for lightweight applications.

15.2 Carbon Reinforcements

The reinforcements (usually fibres) are the mainstay of any composite product. The constituents in C/C (and C/SiC) composites have distinctly different structures. In C/C composites each constituent can range from non-crystalline carbon to semi-crystalline, or highly crystalline graphite. Thus by varying the starting materials and processing, composites can be made with a wide range of structures and properties.

15.2.1 Carbon Fibre Reinforcements

Since the processing temperature of C/C and C/SiC composites is very high, the fibres must not degrade during processing. This means that the fibres should be initially produced at a higher temperature than the subsequent composite processing temperature.

Carbon fibres can be produced from different precursors and are in this respect classified into the following categories [3, 4]:

- Rayon-based carbon fibres
- PAN-based carbon fibres
- Pitch-based carbon fibres
 - Mesophase pitch-based carbon fibres
 - Isotropic pitch-based carbon fibres
- Gas-phase-grown carbon fibres.

However, on the basis of the final heat treatment temperature, the fibres can be broadly categorized in the following three categories:

1. **Type-I.** These fibres are called high-heat-treatment carbon fibres (HTT), where the final heat treatment temperature should be above 2000 °C. These fibres have a high elastic modulus.
2. **Type-II.** These fibres are called intermediate-heat-treatment carbon fibres (IHT), where the final heat treatment temperature should be around 1500 °C. These fibres have high strengths.
3. **Type-III.** These fibres are called low-heat-treatment carbon fibres, where the final heat treatment temperature is around 1000 °C. These fibres have low modulus and strength.

The properties of the different fibre grades depend upon the precursor, the processing technology and the final heat treatment temperature.

Table 15.1 lists representative properties of the commercially available carbon fibre grades taken from the website of M/s Troyaca and M/s Toray. These data are shown only to illustrate the wide property ranges of the fibres, and consequently may vary slightly from the actual values. **N.B:** It is always necessary to obtain certified properties from the manufacturers for design use.

Table 15.1 Properties of carbon fibres (extracted from the website of M/s Troyaca and M/s Toray)

Trade name	Density (g/cm ³)	Tensile strength (MPa)	Tensile modulus (GPa)	Elongation (%)	CTE (m/m°C)	Thermal conductivity (Cal/cm s°C)
T300	1.76	3530	230	1.5	-0.41×10^{-6}	0.0250
T700S	1.80	4900	230	2.1	-0.30×10^{-6}	0.0224
T800S	1.80	5880	294	2.0	-0.56×10^{-6}	0.0839
T1000G	1.80	6370	294	2.2	-0.55×10^{-6}	0.0765
M40 J	1.77	4410	377	1.2	-0.83×10^{-6}	0.1640
M50 J	1.88	4120	475	0.8	-1.10×10^{-6}	0.3720
M60 J	1.93	3920	588	0.7	–	–

CTE coefficient of thermal expansion

15.2.2 Other Carbon Reinforcing Materials

Although most of the high performance composites use carbon fibres, other forms of carbon are also used as secondary reinforcements:

Graphite whiskers: These are pure graphite single crystals having a high degree of crystal perfection and possessing very high strength [10]. The whiskers can be used as a secondary reinforcement in combination with the primary reinforcement of carbon fibres. However, handling and uniform dispersion of the graphite whiskers may require additional precautions and skill.

Carbon Black: Carbon black is available in the form of spheres with fused aggregates below 1 μm size. It is produced by the combustion of hydrocarbons under oxygen-deficient conditions. Carbon black can be used as filler in the C/C composite matrix [4] to reduce the number of coal tar infiltration cycles (discussed in subsection 15.4.2). However, its use is mainly dictated by the desired properties of the final composite.

Carbon nanotubes: Owing to their unique properties, carbon nanotubes (CNTs) are potentially an ideal reinforcement candidate. Theoretical and experimental results have shown some unusual mechanical properties of CNTs, with Young's modulus as high as 1.2 TPa and tensile strength 50–200 GPa [11]. These features make CNTs an attractive option for secondary reinforcing materials in C/C or C/SiC composites. However, CNTs have been used mostly as fillers in experimental nanocomposite materials to enhance their properties [12, 13].

Carbon nanofibres: Carbon nanofibres are non-continuous filaments that differ from conventional carbon fibres with respect to both their dimensions and mechanical properties. Carbon nanofibres are produced using catalytic chemical vapour deposition (CVD) as well as by a combination of electrospinning of an organic polymer and thermal treatment [14, 15]. The diameter of these fibres is reported to be in the range of 100 nm and their aspect ratio is reported to exceed 100. They could become of great practical—as well as scientific—importance, owing to their combination of high specific area, flexibility and mechanical strength.

15.3 Carbon Fibre Preforms

Development of fibre scaffolding with carbon fibres orientated in specific amounts and directions is called the preforming process. The preform enables the subsequent composite product to have the desired strength in different directions. Since carbon fibres are also thermally anisotropic, the preforms should be designed such that the composite will absorb all the thermal stresses during processing and result in a delamination-free product. Also, multidirectional preform fabrication technology provides the means to produce a tailored and near-net shape composite that meets

the directional thermomechanical property requirements of the final composite product.

The preforming technology employs multidisciplinary approaches of structural engineering, mechanical engineering and textile technology to develop preforms. The preforms can be simple blocks, cylinders, conical contours, surfaces of revolution and complex geometries and shapes. They can be made using layers of conventional fabrics with dry yarns pierced through them in the third direction, or assembling semi-cured/pre-cured yarns (pre-pregs), using manual, semi-automated or automatic machines. An illustration of some complex preform schemes [1, 4, 16, 17] is given in Fig. 15.1. Some of these, and others, are briefly described in the following paragraphs.

UD preforms: These are the simplest preforms and are obtained by arranging either dry or resin-impregnated fibre tows (bundles of fibres) parallel to each other and employing pultrusion or filament winding in combination with a polymeric binder to obtain the required shape and volume fraction of fibres. The polymeric binder can be converted into the carbon matrix by heating the preform under inert atmosphere above 1000 °C.

These initial products are porous and can be densified using the standard C/C composite processing techniques described in Sect. 15.4.

2-D preforms: These are fabricated by stacking carbon fibre cloth in a suitable fixture, mostly in the dry condition. The stack is subjected to further processing along with the fixture till the preform acquires a stable shape and rigidity suitable for handling. The 2-D preforms can have different stacking arrangements where

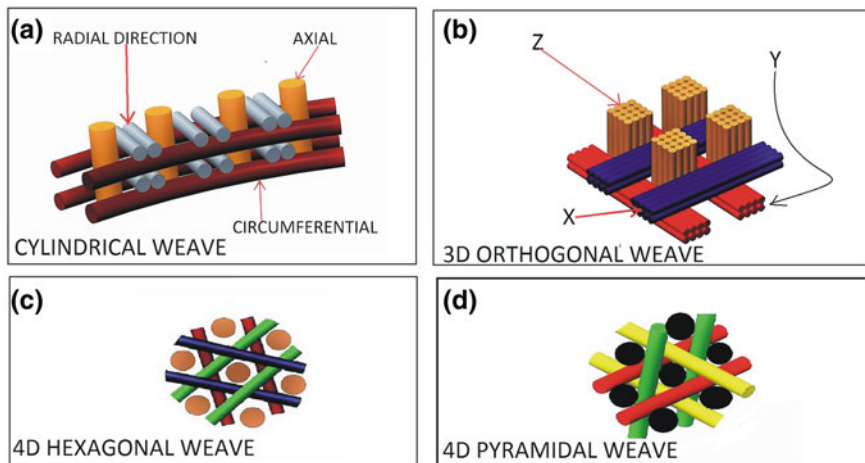


Fig. 15.1 Some typical schemes for developing multi-directional carbon fibre preforms

fibre tows are arranged in a regular fashion with different combinations of fibre orientations.

This type of preform provides good mechanical and thermal properties in two directions parallel to the fibre axes, but the composite properties are poor in the through-thickness direction. Also, 2-D preforms are somewhat susceptible to delamination during pyrolysis. However, the delamination problem can be overcome by using an optimum resin system and optimum heating cycle for the given fibre volume fraction, V_f or by making 2.5-D preforms.

2.5-D preforms: The delamination problem in 2-D preforms can be eliminated by stitching the carbon fabric stack with carbon fibre tows. Since the V_f of the stitching fibres is relatively low compared to the other main direction fibres, such preforms are called 2.5-D. Stitched preforms are suitable for many C/C and C/SiC composite products. These preforms are used for general applications owing to their straightforward fabrication process [18].

3-D preforms: 3-D orthogonal preforms are fabricated using multiple fibre tow bundles that are appropriately located within the structure in three mutually perpendicular directions. In each direction the fibre bundles are straight in order to obtain their maximum structural capability. This type of preform obviously can provide greater isotropy compared to UD, 2-D and 2.5-D preforms. However, the strengths of 3-D preforms are relatively low. 3-D preforms of different shapes and sizes can be made using automated machines.

3-D preforms are used for applications like rocket nozzles and hypersonic vehicle leading edges. 3-D cylindrical weave pattern based preforms are used for some near net conical or cylindrical shapes, but they have the disadvantage of non-uniform V_f across the thickness, and this affects the mechanical and thermal properties.

4-D preforms: These are modified versions of 3-D preforms that achieve even better isotropy, but at the cost of lower V_f and properties. 4-D preforms are made by introducing diagonal yarns between the main fibre planes.

In addition to 4-D preforms, 5-D and 7-D can also be developed. 4-D and 5-D preforms are mostly used when greater isotropy is required for re-entry missile nose tips and for throat inserts in rocket nozzles.

15.4 C/C Composites Processing

Carbon has a high melting temperature (above 3000 °C), and so the fabrication techniques used for polymer matrix or metal matrix composites cannot be used for C/C composites. Many research articles have been published on the processing of C/C composites, but the actual knowledge of fabrication—for both C/C and C/SiC composites products—remains proprietary and exclusive to a few research institutions.

A general flow diagram of C/C composite processing is shown in Fig. 15.2 [3, 19]. The processing is based either on vapour phase pyrolysis of some selected

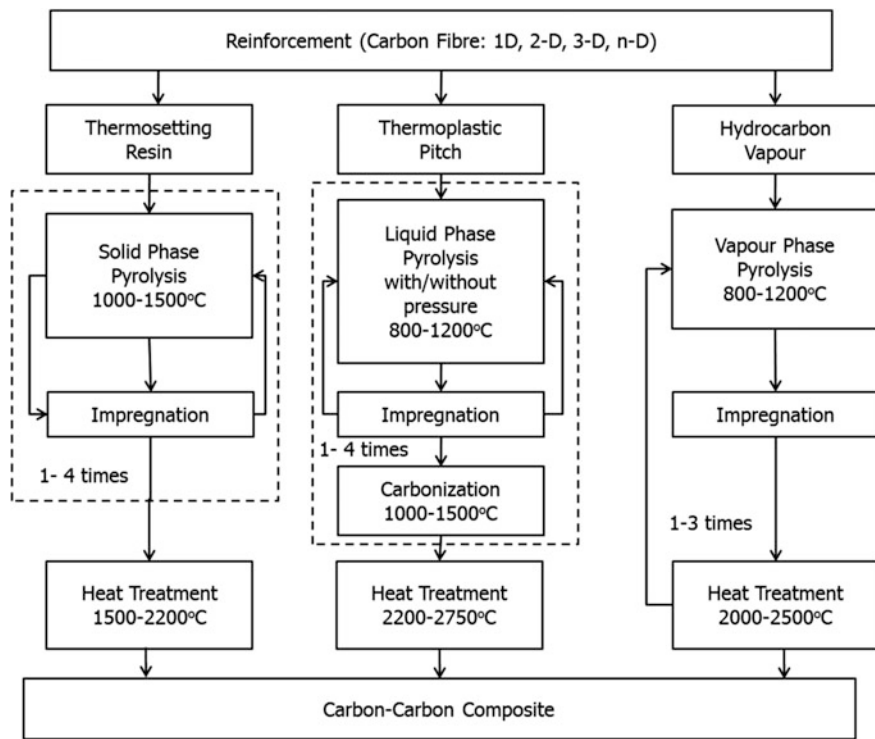


Fig. 15.2 Schematic layout of typical methods used to fabricate C/C composites from different reinforcement materials

hydrocarbons, or pyrolysis of solid/liquid carbonaceous precursors. The selection of the processing route and suitable precursor for the matrix development are the most important parameters [1, 4, 19]. The carbon matrix precursor materials can be divided into two categories:

1. Gaseous precursors, usually hydrocarbons such as methane and propane.
2. Liquid precursors (carbonaceous resins). The liquid route can be further categorized as
 - Aromatic thermosetting resins like phenolics and furfural.
 - Thermoplastic resins, including pitch material obtained from coal or petroleum.

The process route selection depends mostly on the availability of the processing equipment and types of preforms. For example, UD and 2-D based preforms are generally processed using thermosetting resin systems. 2.5-D and 3-D preforms of limited thickness are processed using chemical vapour deposition or infiltration processes (CVD/CVI), while thicker products of 3-D, 4-D and 5-D composites are processed using pitch impregnation.

The following factors should be taken into account while selecting the matrix precursor:

- The solid carbon yield of the precursor must be high. This minimizes the number of densification (infiltration and pyrolysis) cycles. It also helps in controlling delamination particularly in 2-D composites.
- The liquid or molten matrix precursor must readily wet the carbon fibres.
- The molten precursor should have a low viscosity to aid penetration into the preforms.
- On pyrolysis, the resulting matrix should (obviously) acquire a favourable microstructure for optimum mechanical and thermal properties.

15.4.1 Chemical Vapour Impregnation (CVD/CVI)

This processing route has been widely used by Western countries for the production of C/C composite thinner parts like aircraft brake discs and extendable rocket nozzle cones. The chemical vapour impregnation (CVI) technique evolved from chemical vapour deposition (CVD), which was generally used to obtain uniform coatings or films with tailored composition by decomposition of gaseous compounds. In this chapter the CVD/CVI term has been used for the process where entire matrices are developed by infiltrating fibre preforms with volatile hydrocarbon matrix precursors such as methane, propane, benzene and other similar low molecular weight hydrocarbons. Thermal decomposition of the hydrocarbons takes place on the heated surfaces of the carbon fibre preforms, resulting in deposition of pyrolytic carbon. This technique can be used to deposit carbon onto dry fibre preforms or on partially densified C/C composite structures produced by the liquid impregnation route [3, 4].

There are several variants of the CVD/CVI processes. These are summarized in the following paragraphs.

Isothermal CVD/CVI: This process is the most widely used for fabricating C/C composite products. The carbon fibre preform is positioned in a vacuum furnace having a gas management system. The temperature of the preform is raised to within the range of 700–1000 °C, and the precursor gases are passed through the preform. For CVD the pressure in the furnace is maintained in the range 10–100 mbar, while for CVI the pressure should be lower.

The gases decompose and solid carbon is deposited over the fibre surfaces and between the fibre bundles. In general, the deposition is higher at the surface of the preform than in the core, since surface deposition hinders diffusion of the gaseous precursors into the core. The result is non-uniform through-thickness deposition and an overall low density composite with closed porosity.

To achieve uniformly dense composites, the pores at the surface need to be opened up by intermittent surface machining, i.e. the CVD/CVI process is discontinuous. The final density is usually in the range 1.5–1.7 g/cm³. Even so, a

density gradient usually remains when using *isothermal* CVD/CVI. For thin sections this type of the process is acceptable, but for somewhat thicker sections thermal gradient CVD/CVI is recommended.

Thermal gradient CVD/CVI: For this process a known temperature gradient is maintained from one side of the preform to the other. The side where the precursor gases enter the preform is maintained at a lower temperature, while at the other side the temperature is maintained high enough to allow deposition, see Fig. 15.3.

As deposition continues the temperature front shifts towards the entry-point of the precursor gases, such that the whole preform is uniformly densified. The densification rate is improved by applying (i) a pressure gradient to the preform, i.e. by replacing slow diffusion mass transfer by the much faster convection mass transfer within the pore network, or (ii) an inverse temperature gradient [20, 21]. Another efficient way to increase the densification rate is to immerse the heated fibre preform in a boiling liquid precursor under reflux (calegation process) [21, 22]. However, design of the equipment and precise temperature control is a challenging task which needs to be carefully considered while selecting this process.

For still thicker C/C composites, the liquid impregnation process is recommended.

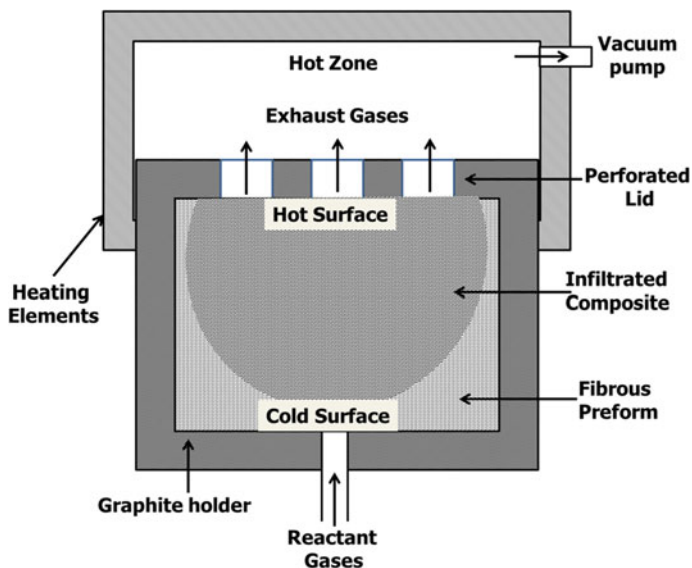


Fig. 15.3 Schematic of the thermal gradient CVI process

15.4.2 *Liquid-Phase Impregnation Process*

This process is based on impregnation with coal tar/petroleum pitches or high-char-yielding thermosetting resins into the fibre preforms, followed by pyrolysis. Figure 15.2 shows the schematic of the C/C composite manufacturing process using multiple impregnation; carbonization (1000 °C); high pressure (about 1000 bars) carbonization (HIP); and graphitization (up to 2750 °C).

Although it is possible to densify the C/C composite even by atmospheric pressure carbonization, the process requires several cycles of impregnation and carbonization because the carbon yield of the pitch is only around 50 % if pyrolysed at atmospheric pressure.

To reduce the total processing time, high pressure carbonization is recommended since the yield of the coal tar pitches is reported to be 80–90 % if pyrolysed at 750–1000 bars. Not only is the process time reduced, but high pressure helps in lowering the temperature of the mesophase formation in the pitch, resulting in a highly oriented crystalline structure of the matrix. The higher pressure carbonization also results in a coarser and isotropic microstructure, since it suppresses gas formation and prevents its escape, and therefore results in a higher char yield. In fact, the HIP process is the only practical route to lower the production costs of C/C composites.

15.5 Properties of C/C Composites

C/C composites for aerospace applications need to be characterized for general properties like strength and stiffness, fracture toughness, thermal conductivity and CTE, and for specific functional properties depending on the service requirements. For example, the composite needs to be characterized for frictional properties if it is intended to be used for brake pads, and ablation and erosion resistance if it is used for propulsion applications.

A large data base is available in the literature covering mechanical, thermal, electrical, frictional and fatigue properties of C/C composites. The effects of fibre type, V_f , preform type and the process route have also been reported. The mechanical properties of C/C composites are controlled by the properties of the constituents and their volume fraction bonding, and crack propagation mechanisms, whereas the thermal properties are governed by thermal transport phenomena. Moreover, both the fibres and matrix are likely to undergo a change in properties during processing, depending on the final heat treatment temperature, preform type and the resulting thermal stresses. It is therefore very difficult to compare the properties reported in different studies. However, characteristic and more or less representative properties are discussed in Sects. 15.5.1. and 15.5.2.

15.5.1 Mechanical Properties of C/C Composites

Extensive work has been done to enhance the fibre properties in these composites. The strength and stiffness of C/C composites are dominated by the type of fibre and preform. These composites are complex owing to many changes (physical and chemical interactions) that occur during processing. Broadly speaking, the properties change with the combined effect of the following factors:

- Fibre types: precursor, heat treatment temperature limit.
- Matrix precursors: resin, pitch, CVD/CVI or hybrid.
- Preforms: type of weave, and number of fibre directions, etc.
- Fibre volume fraction in a particular direction.
- Final density of the composite.

In general, C/C composites having strong fibre/matrix bonding fail catastrophically without fibre pull-out, while those having a desired interface fail in a mixed tensile and shear mode, resulting in high strength [1, 4, 19, 23].

Differences in the interfacial bonding, owing to residual stresses, are considered to be the prime factor for the different tensile strengths of 2-D and 3-D C/C composites. The residual stresses are induced mainly due to the following reasons:

1. Carbon fibres have different CTEs along the axis and in transverse directions. Along the axis the CTE is close to $0.1 \times 10^{-6}/^{\circ}\text{C}$, while in the transverse directions it is about eight times higher. The difference between these two CTEs varies slightly, depending on the fibre type and its thermal history.
2. Shrinkage of the matrix during the carbonization and graphitization stages. The as-infiltrated polymeric resin or pitch precursor has a density of the order of 1.0 g/cm^3 which converts to a higher density (about 2.0 g/cm^3) carbon matrix during pyrolysis. If the fibre preform does not allow uniform shrinkage during pyrolysis, then microcracks and residual thermal stresses occur. Also, the amount of microcracks and residual stresses will depend on the fibre and preform types.

Owing to the above factors, even composites having the same raw materials and processing route yield different properties depending on the preform types.

Thermal residual stresses in 3-D composites are reported to be much higher than those in 2-D composites [24]. Thus for 3-D composites, the cracks would be expected to be much larger and more numerous, and the interfacial strength much weaker, than in 2-D composites. Hence 3-D composites have lower strength than 2-D composites. Also, the properties of UD C/C composites are reported to be higher than those of 2-D and 3-D composites. A typical set of properties for UD C/C composites made with high strength and high modulus fibres is shown in Table 15.2 [25].

Table 15.2 Typical properties of UD C/C composites [25]

C/C properties	Parallel to the fibre axis		Perpendicular to the fibre axis	
	High strength	High modulus	High strength	High modulus
Flexural strength (MPa)	1250–1600	825–1000	20	30
Tensile strength (MPa)	600	572	4	5
Tensile modulus (GPa)	125	220	–	–
Compressive strength (MPa)	285	380	25	50
Shear strength (MPa)	20	28	–	–
Work of fracture (kJ/m ²)	70	20	0.4	0.8

15.5.2 Thermal Properties of C/C Composites

The complexity of C/C composites makes estimation of their thermal properties difficult. The thermal conductivity depends more on the crystalline nature of the fibres than the type of fibres. The thermal conductivity dependence of C/C composites on temperature is shown in Fig. 15.4. This shows that the thermal conductivity of C/C composites made with UHM (highly crystalline high modulus fibres) is higher than that of those made with HM (high modulus) fibres.

15.6 Example Applications of Aerospace C/C Composites

15.6.1 C/C Composite Brake Pads

Carbon in the form of graphite is a well-known solid lubricant. It is perhaps surprising that such a material can also be a promising friction material for a

Fig. 15.4 Thermal conductivity of UD carbon-carbon composites made with different pitch based carbon fibres

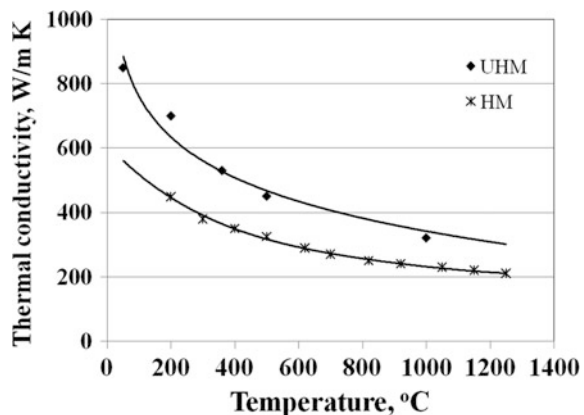


Fig. 15.5 Typical assembly of C/C brake discs



braking system. A typical C/C composite brake disc assembly is shown in Fig. 15.5.

The fact is that many of the characteristics that make carbon an attractive anti-friction material are equally required to make it an attractive friction material. Carbon, when rubbed against itself, exhibits a wide range of coefficient of friction (~ 0.1 to over 0.5) depending on the material type, load, speed and temperature [19, 26]. In comparison to steel, a carbon brake pad has low density ($1/4$ of steel density), high heat capacity (2.5 times that of steel), and a thermal conductivity almost equivalent to those of metals.

C/C composite brake pads rapidly conduct heat away from the rubbing surface and help in forming a smooth and stable wear controlling friction film: this is desirable to facilitate smooth braking and reduce the wear rate, which in turn increases the service life. In addition, carbon has a high thermal shock resistance owing to its high thermal conductivity and low coefficient of thermal expansion, and also does not soften at high temperatures. These properties make C/C composites ideal friction materials for brake design. Over 70% by volume of C/C composites are used as aircraft brake discs. M/s Dunlop, UK, provided the first major breakthrough for C/C composite brakes: these were introduced in the 1970s for the Concorde undercarriage. The Dunlop design with C/C composite brake discs saved more than 600 kg (\sim equivalent to seven passengers) as compared to steel brakes [27]. Many advanced tactical and commercial transport aircraft also use C/C composite brake materials [4, 26], as does the Indian Light Combat Aircraft (LCA).

15.6.2 C/C Nozzle and Throat

M/s SNECMA Propulsion Solide has developed C/C composite throat and lightweight exit cones for rocket nozzles [28]. The C/C composite exit cone concept significantly simplified the whole nozzle design. Lightweight C/C composite nozzles have significantly reduced the overall weight compared to phenolic nozzle

systems [28], which must be much thicker because they ablate and erode much more. Typical C/C composite nozzle and exit cone are shown in Figs. 15.6 and 15.7 respectively.

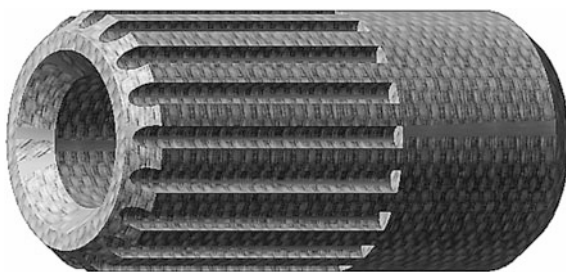
Fig. 15.6 Typical C/C composite exit cone



Fig. 15.7 A typical C/C composite nozzle test article



Fig. 15.8 A typical model showing transpiration cooled article



15.6.3 C/C Combustion Chamber

Transpiration-cooled C/C composite combustion chamber test article has been demonstrated [6, 29]. This cooling method is used for high heat fluxes and long times. A typical model showing transpiration cooling is shown in Fig. 15.8.

In a transpiration cooling system the coolant is injected into the hot gas flow through a porous structure like a semi-densified C/C composite, as opposed to a discrete structure with film cooling. Transpiration cooling also decreases the heat flux to the structure, and this could benefit its useful life.

15.7 C/SiC Composites

C/SiC composites exhibit excellent thermo-erosive properties up to 2000 °C [17, 18, 30]. Their high strength-to-weight ratio and oxidation resistance make them ideal candidates for highly demanding engineering applications such as high performance heat shields, structural re-entry components, ultrahigh temperature heat exchanger tubes, rocket nozzles and brake discs.

The choice of silicon carbide as a matrix is based on its high melting point (~ 2500 °C), excellent mechanical properties at high temperatures related to its covalent character, relatively good oxidation resistance up to about 1500 °C, and stability in fast neutron environments [22, 31]. Also, silicon carbide can be easily inserted into a fibre preform by a variety of techniques, discussed in Sect. 15.8.

However, when used in C/SiC composites, the SiC matrix undergoes multiple microcracking when loaded in tension beyond stress levels of only 100–200 MPa [22]. The density and widths of the microcracks depend on the fibre architecture, the fibre/matrix bonding and the applied load. The role of the fibre/matrix interface becomes very important for C/SiC and other ceramic matrix composites, since the matrix tends to react with the carbon fibres. The interface and its usefulness in C/SiC composites are described next.

15.7.1 C/SiC Fibre/Matrix Interface/Interphase

Fibre/matrix interfaces have a strong influence on the mechanical properties and lifetime of the ceramic composites. The interfacial domain remains a critical area because load is transferred from the matrix to fibres (and vice versa) through the interface. The fibre/matrix interface is the key to tolerating stress-induced damage and enhancing the toughness in brittle matrix composites.

The essential property of a composite interface where the matrix has a lower failure strain than the fibres, is the ability to disbond in the presence of matrix microcracks. The concept of weak interfaces has been widely used to increase the fracture toughness of the composite. However, the weak interface may be detrimental to the composite strength: a high strength requires efficient load transfer from fibre to matrix, which requires a strong interface. Hence the requirements of tough composites and strong composites are opposite in nature, and this must be considered when choosing a composite for the desired properties.

The interface is a thin film (about 500 nm) of a compatible material having low shear strength, and which is coated onto the fibre surfaces before composite processing, whereby the matrix is either deposited by a gaseous route or infiltrated by a liquid route. The main function of the interface is to arrest and/or deflect matrix microcracks, hence protecting the fibres from premature failure. The interface should also help in transferring the loads, when necessary.

All intended requirements of the fibre/matrix interface may not be met by a thin single layer. In such cases multiple thin layers of the same or different materials have been used. Thus the interface in actual composites is better described as an interface zone of finite dimensions called an interphase. Within the interphase the mechanical properties differ from the fibre and matrix.

Different kinds of interphase concepts have been suggested and are shown in Fig. 15.9 [32–34]:

- (a) Single layer pyrocarbon (PyC) or hexagonal boron nitride (BN) interphases.
- (b) Porous SiC single layer interphase.
- (c) Multi-layered $(X/Y)_n$ interphase, with $X = \text{PyC}$ or BN , and $Y = \text{SiC}$ (schematic).
- (d) Crack deflection in a multi-layered (PyC–SiC) interphase.

Layered crystal structures like PyC–BN or a layered microstructure, e.g. $(\text{PyC}–\text{SiC})_n$ or $(\text{BN}–\text{SiC})_n$, have been proposed as the best interphase materials, with the layers deposited parallel to the fibre surface via CVD. On the one hand, these layers are weakly bonded to one another, but on the other hand the interphase bonds strongly to the fibre surface [32–34]. Crack deflection occurs within the interphase, preferably parallel to the fibre surface. However, as Fig. 15.9 suggests, this ideal crack deflection is not always achieved. Even so, the load transfer capacity is improved compared to simple fibre/matrix bonding when this bonding is weak.

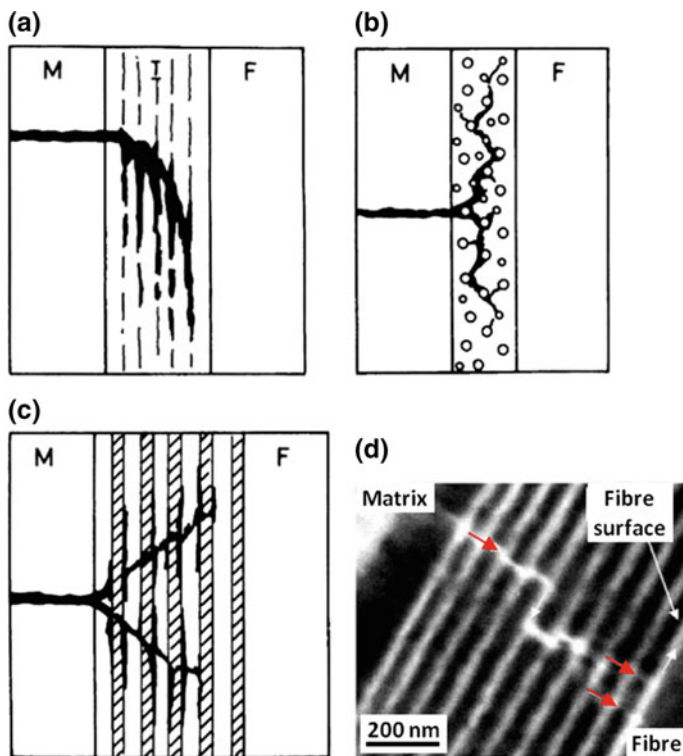


Fig. 15.9 Typical interphase schemes as described in [33, 34]

15.7.2 Oxidation

When C/SiC composites are exposed to an oxidizing atmosphere at medium or high temperatures, the matrix microcracks facilitate the depth-diffusion of oxygen towards the oxidation-prone interphases and fibres. Therefore the SiC matrix *and* the fibre/matrix interphase should be designed to hinder oxygen diffusion. The general guidelines are:

1. Introduction of boron-like elements in the SiC matrix. These form molten oxide phases over a wide temperature range, filling the cracks and acting as self-healing materials.
2. Proper design of the interphase to reduce the crack openings.

With respect to (1), boron oxide phases are efficient at relatively low temperatures (500–1000 °C) whereas silica-rich phases are more appropriate at high temperatures (1000–1500 °C). However, these solutions work only when the

environmental oxygen partial pressure is high enough to support passive oxidation. Then the molten oxide phases cover the surface of the composite and prevent further oxygen diffusion into the structure.

15.8 C/SiC Composite Processing

15.8.1 Chemical Vapour Impregnation (CVD/CVI)

As stated earlier, the solid matrix deposits on the preform fibre surfaces owing to a vapour phase reaction of the precursor gases under appropriate conditions. For CVI of C/SiC composites, methyltrichlorosilane (MTS) is generally used as precursor for SiC. The deposition of SiC takes place between 850–1200 °C in vacuum. The process requires several weeks of continuous deposition in order to obtain a dense C/SiC composite. There are several advantages of the CVD/CVI process:

1. The process temperature is lower than that of other processes, e.g. CVI can be accomplished at 800–1000 °C, whereas the process temperatures of liquid silicon infiltration (LSI) and polymer infiltration and pyrolysis (PIP) are in the range 1400–1600 °C.
2. Multi-directional preforms can be infiltrated, since gas can diffuse into any shape and size preform.
3. CVI results in better thermal and mechanical properties of the composites.

The CVD/CVI process yields mostly β -SiC deposits with controlled composition and microstructure. There are also some disadvantages: long process cycles; through-thickness density gradients; and requirements for accurate control of the precursor gas flow, temperature, pressure and handling of hazardous byproduct gases. It typically takes 40–60 h to infiltrate a 4–5 mm thick carbon preform to obtain residual porosity of the order of 15 %.

15.8.2 Polymer Infiltration and Pyrolysis (PIP)

The PIP process uses polycarbosilane (PCS), which is a ceramic precursor that converts into SiC if heated under an inert atmosphere or in vacuum above 1200 °C [35–39]. Polycarbosilane has also been used to fabricate continuous SiC fibres by melt spinning, followed by cross-linking and pyrolysis [40].

The PIP process has several advantages, including good matrix composition control, low densification temperature, and the possibility to join different parts of a complex-shaped component. There are a few disadvantages: multiple infiltration/pyrolysis/densification cycles (typically 10 cycles to achieve a density of 2.0 g/cm³) are required; local non-availability of the ceramic precursor in large

quantities; and large shrinkage of the matrix during pyrolysis, leading to matrix cracking. Also, interior cracks are difficult to fill during subsequent infiltration cycles.

The composites obtained by PIP have superior interfacial bonding, and this process has been proposed for making large C/SiC composite rocket nozzles. Such large products can be made by employing a variety of techniques, including filament winding, vacuum assisted resin transfer moulding, autoclave moulding, hydraulic press moulding or matched die moulding. Symmetrical as well as non-symmetrical composite components can be made.

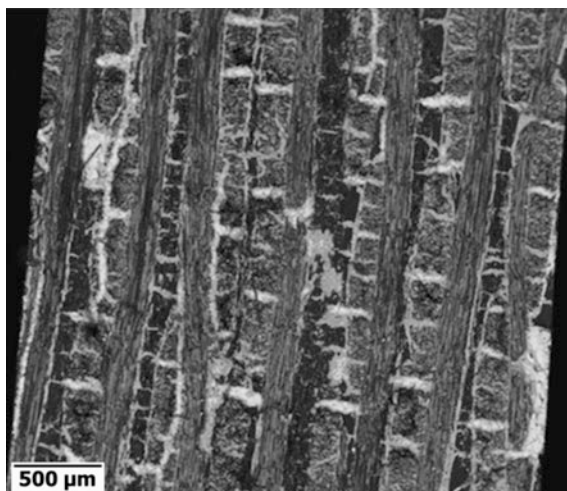
15.8.3 Liquid Silicon Infiltration (LSI)

Liquid silicon infiltration has been used to fabricate C/SiC composites for different applications. LSI is the most common and economical method to fabricate C/SiC composites of reasonable quality, especially for short-life components and thicker and complex shapes. Investigations of the LSI process have been carried out by many researchers [17, 18, 30, 41].

The processing by LSI consists of the infiltration of a porous C/C composite preform with molten silicon using a vacuum or inert gas furnace. Carbon and silicon react to form SiC at temperatures in the range of 1450–1650 °C. This process leads to the development of C/SiC composites with lower component fabrication time and therefore reduced component costs.

LSI-based, 3-D stitched, 3-D woven and 4-D C/SiC composite technology and product development work has been carried out extensively in India by Suresh Kumar et al. [17, 18, 42]. Several products have been realized using the process: of these, Jet-vanes for thrust vector control of rocket motors and a throat insert for a

Fig. 15.10 Typical microstructure of an LSI-based C/SiC composite



liquid propulsion based rocket motor have been included in the C/SiC composite application Section, see Sects. 15.10.2 and 15.10.4.

A typical microstructure of an LSI-based C/SiC composite is shown in Fig. 15.10.

15.9 Properties of C/SiC Composites

Much work has been done in achieving the highest possible use of the fibre properties in C/SiC composites. Nevertheless the properties vary widely, depending on the manufacturing process and the test results from different R&D laboratories. This should not be surprising, since C/SiC composites are obviously heterogeneous, consisting of fibres, matrix and pores. Also, the fibres and matrix can have a variety of microstructures.

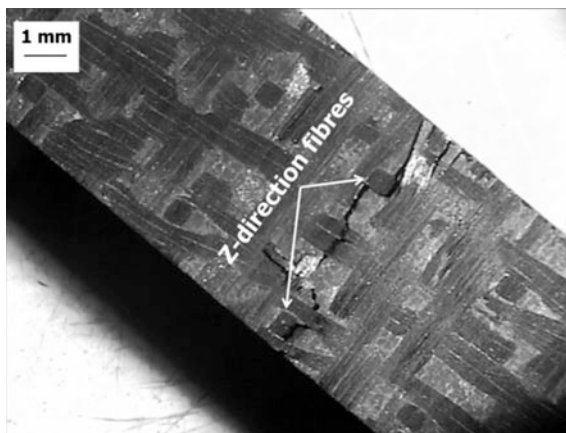
Typical properties for 2-D C/SiC composites are given in Table 15.3. Note that the thermal properties are experimental values, since calculations of these properties are difficult owing to the complex microstructures. It is seen from Table 15.3 that the CVD/CVI process gives superior mechanical properties compared to the LSI process: this is generally the case. Even so, different researchers have reported different ranges of properties even for the same processing technique. A typical image of a 3-D stitched C/SiC composite sample tested under three-point bending is shown in Fig. 15.11. It can be seen that the crack initiated from the stitching points.

Table 15.3 Properties of bi-directional (2-D) carbon fibre reinforced C/SiC composites [17, 18, 42, 43]

Composite configurations		With carbon fibres (2-D composites)			3-D stitched C/SiC
Property	Units	PIP -based C/SiC	CVD-based C/SiC	LSI-based C/SiC	LSI -based C/SiC
Fibre content (V_f)	vol.%	42–44	42–47		40–45
Density	g/cm^3	1.7–1.8	2.1–2.2	2.4	2.1–2.2
Flexural strength	MPa	250–330	450–500	180–200	140–180
Tensile strength	MPa	200–250	300–380	80–190	70–90
Young's modulus	GPa	60–80	90–100	60	–
Strain to failure	%	0.3–1.1	0.6–0.9	0.15–0.35	0.10–0.15
Compressive strength	MPa	590	–	–	–
Thermal conductivity	W/m K	11.53 (100 °C)	–	30–35	50–15 ^a
Specific heat	J/kg K	900 (100 °C)	–	800 (RT)	750–900
CTE					
Parallel ($\times 10^{-6}$)	$\text{m/m}^\circ\text{C}$	2–3	3	1.0–1.5	–0.5–1.5
Perpendicular ($\times 10^{-6}$)	$\text{m/m}^\circ\text{C}$	4–7	5	5.5–6.0	3.0–4.5

^aDerived from the thermal diffusivity value (25–1200 °C) in the through-thickness direction

Fig. 15.11 A typical image of 3-D-stitched C/SiC composite failure under 3-point bend testing



Thus on the one hand, stitching the fabric stack improves the integrity of the resulting composite and also the through-thickness thermal and mechanical properties; but on the other hand, stitching limits the in-plane strength. This means that it is important to optimize the preform to achieve the required thermal and mechanical properties.

15.10 Applications of Aerospace C/SiC Composites

C/SiC composites are used primarily for hot structures in aerospace systems. The applications correspond to very severe service conditions, namely high temperatures and corrosive environments, in which they must often demonstrate long service lives. However, for some space and missile systems the required life may be short, and the erosion resistance is paramount. C/SiC composites have also been proposed for high performance braking systems.

Some examples of C/SiC composite aerospace applications are given in the following subsections.

15.10.1 Thermal Protection Systems (TPS) and Hot Structures for Space Vehicles

The temperature during orbiter vehicle re-entry reaches up to 1800 °C. C/SiC composite thermal protection systems (TPS) have performed over more than two decades in spacecraft structures and numerous technology-driven projects in Europe, the USA and Japan. The hot structure of the cancelled X-38 (NASA's experimental space vehicle) was to be made from C/SiC composites. A nose cap, nose skirt, two leading edges segments and two body flaps for steering the vehicle

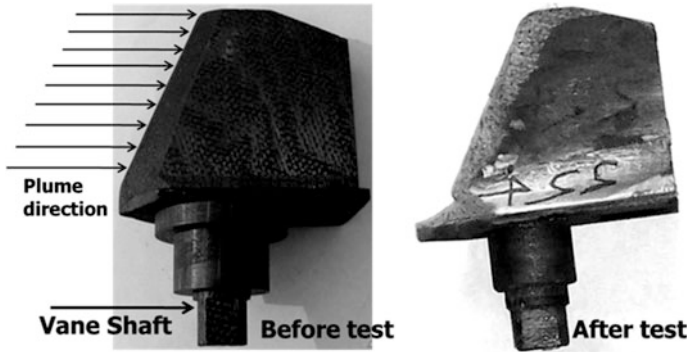


Fig. 15.12 C/SiC Jet-vanes for a thrust vectoring system [18]

were manufactured and qualified by a German consortium [44–46]. Similarly, the thermal structure of the cancelled Hermes (European Space Plane), which would have experienced high mechanical loading and surface temperatures as high as 1300 °C, was intended to be made from a C/SiC composite [47].

15.10.2 Jet-Vanes for Rocket Motors

Jet-vane materials must have good erosion resistance to particulate flow in addition to high thermal shock resistance (i.e. high thermal conductivity, low CTE and good strength). Erosion of the Jet-vanes depends on the fibre architecture, the ratio (V_f) of fibres to matrix, and testing/operation conditions. The formulation of the composite microstructure requires optimizing the conflicting demands for high fracture toughness (high carbon content) and high resistance to abrasion/erosion (high SiC content) [18].

A leading Indian laboratory has developed Jet-vanes made from LSI-based 3-D stitched C/SiC composites with excellent thermal and mechanical properties [17, 18, 42] and good resistance to erosion by solid rocket motor (SRM) plumes. A typical Jet-vane before and after testing is shown in Fig. 15.12. A CVD-applied SiC coating could further protect the Jet-vanes from oxidation and the blast of alumina particles deriving from the burnt solid fuel.

15.10.3 C/SiC Nozzles and Components for Rocket and Jet Engines

C/SiC composites have been developed as materials for combustion chambers and nozzles. The main advantages are an increased maximum combustion temperature

Fig. 15.13 Typical C/SiC thruster test articles



(up to 1500 °C) without requiring anti-oxidation coatings, and improved resistance to thermal cycles. C/SiC composite rocket engine for a bipropellant propulsion system has been used elsewhere [48]. Typical C/SiC thruster test articles are shown in Fig. 15.13. Such nozzles can be easily fabricated using the PIP process. A nozzle design demonstrator for the upper stage engine of the Ariane 5 has also been manufactured (by filament winding) using the PIP process.

Flame-holders, exhaust cones and engine flaps for military jet engines made of C/SiC composites have been reported [30, 43]. Outer flaps of the SNECMA M 88-2 engine have been made from C/SiC composites using the CVI process. These have provided 50 % weight savings over corresponding nickel-base superalloy flaps (Inconel 718).

15.10.4 C/SiC Composite Nozzle Throats

Especially for liquid propulsion systems, the exhaust gases contain huge amounts of H₂O molecules that would attack and oxidize C/C composites unless they were coated. The alternative for short-life components is to use LSI C/SiC composites. A variety of thrusters made from C/SiC composites for a liquid rocket engine and a solid rocket motor were qualified as an effort to develop the AESTUS C/SiC expansion nozzle [49]. LSI-based 4-D C/SiC nozzle throats and inserts with uniform thermomechanical properties have been developed in a leading Indian laboratory and tested satisfactorily for 30 s with a mixed hydrazine/nitrogen tetroxide fuel propulsion system [49]. The throat insert and nozzle configurations are shown in Figs. 15.14 and 15.15. The 4-D C/SiC composite nozzle throat performed much better than conventionally used high density graphite or C/C composites under similar testing conditions. It is envisaged that in future the largest sales volume of the fibre ceramic production, besides brake discs and in ballistic protection systems will be based on C/SiC and C/C-SiC composites.

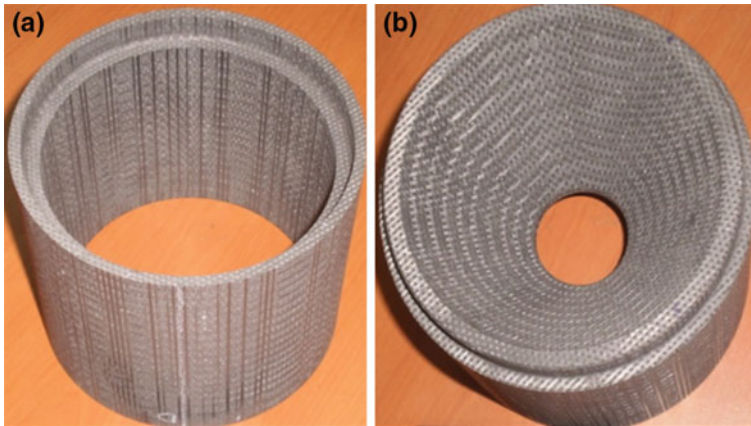


Fig. 15.14 A typical 4-D C/SiC composite thruster chamber (a) and throat insert (b) [17]

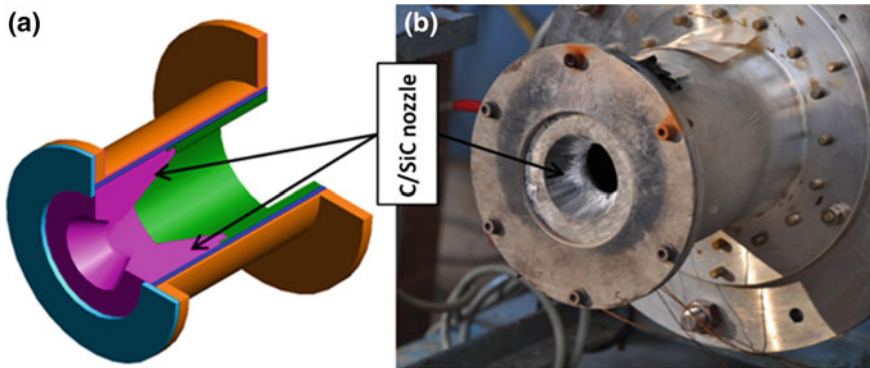


Fig. 15.15 4-D C/SiC composite nozzle tested under liquid propulsion [17]

15.11 Indian Scenario for C/C and C/SiC Development

C/C and C/SiC composites have been under investigation for a long time. Several leading agencies around the world have developed state-of-the-art facilities for the reinforcements, preforming, processing and characterization of these composites. Several products have been realized for defence and aerospace applications under the aegis of NASA, Russia and the European Union. With reference to India, a significant amount of work has been done in the last two decades. C/C composite brake discs and reentry ballistic missile nose tips have been fabricated and qualified for different defence programmes. C/SiC composite Jet-vanes and throat inserts have been made using the LSI process. The PIP and CVD/CVI processes have also been employed to obtain C/SiC composite specimens and test articles. Research

continues to develop a reliable design methodology, automation of the preforming process, non-destructive testing (NDT), life estimations, and the joining of C/C and C/SiC composites with other materials.

15.12 Summary

Carbon fibre-reinforced composites occupy an important position in aerospace. This chapter provides a brief description of the processing, properties and applications of C/C and C/SiC composites. It also provides some basic information on the raw materials used for the matrix and fibre reinforcements. Some aerospace applications of these composites are given as well.

Acknowledgments The authors wish to acknowledge the contribution of the colleague scientists at DMSRDE, ASL and DMRL who have given their valuable time for discussion about the chapter.

References

1. Rohini G, Rama Rao K (1993) Carbon-carbon composites—an overview. *Defence Sci J* 43 (4):369–383
2. Masataka Y, Motohiro A, Masayuki Y, Itsuro I, Satoshi M (1996) Development of C/C composites for OREX (orbital reentry experimental vehicle) nose cap. *Adv Compo Mater* 5 (3):241–247
3. Buckley JD, Eddie DD (1992) Carbon/carbon materials and composites. Noyes Publications, Park Ridge, NJ, USA
4. Fitzer E, Manocha LM (1998) Carbon fibers and carbon/carbon composites. Springer, Heidelberg, Germany
5. Torsten W, Gordon B (1997) Carbon-carbon composites: a summary of recent developments and applications. *Mater Des* 18(1):11–15
6. Glass DE (2008) Ceramic matrix composite (CMC) thermal protection systems (TPS) and hot structures for hypersonic vehicles. Paper AIAA-2008-2682 in: 15th AIAA Space planes and hypersonic systems and technologies conference, Dayton, Ohio, USA
7. Windhorst T, Blount G (1997) Carbon–carbon composites; a summary of recent developments and applications. *J Mater Des* 18:11–15
8. Li KZ, Shen XT, Li HJ, Zhang SY, Feng T, Zhang LL (2011) Ablation of the carbon/carbon composite nozzle-throats in a small solid rocket motor. *Carbon* 49:1208–1215
9. Auweter-Kurtz M, Hilfer G, Habiger H et al (1999) Investigation of oxidation protected C/C heat Shield material in different plasma wind Tunnels. *Acta Astronaut* 45(2):93–108
10. Bacon RG (1960) Structure and properties of graphite whiskers. *J Appl Phys* 31:283–290
11. Valentin N, Popov (2004) Carbon nanotubes: properties and application. *Mater Sci Eng* 43:61–102
12. Li, Y-L, Shen, M-Y, Su, H-S, Chiang, C-L, Yip, M-C (2012) A study on mechanical properties of CNT-reinforced carbon/carbon composites. *J Nanomaterials*, Article ID 262694, 6 p

13. Zhang Hai, Guo Lingjun, Song Qiang, Fu Qiangang, Li Hejun, Li Kezhi (2013) Microstructure and flexural properties of carbon/carbon composite with in-situ grown carbon nanotube as secondary reinforcement. *Prog Nat Sci Mater Int* 23(2):157–163
14. Baker RTK (1989) Catalytic growth of carbon filaments. *Carbon* 27:315–323
15. Rodriguez NM (1993) A review of catalytically grown carbon nanofibres. *J Mater Res* 8:3233–3250
16. Kumar Suresh, Kumar Anil, Rohini Devi G, Gupta AK (2011) Preparation of 3D orthogonal woven C-SiC composite and its characterization for thermo-mechanical properties. *Mater Sci Eng, A* 528:6210–6216
17. Kumar Suresh, Kumar Anil, Ramesh Babu M, Raghvendra Rao M (2015) Fabrication and ablation studies of 4D C/SiC composite nozzle under liquid propulsion. *Int J Appl Ceram Tech* 12(S3):E176–E190
18. Kumar S, Kumar A, Sampath K, Bhanu Prasad VV, Chaudhary JC, Gupta AK, Rohini Devi G (2011) Fabrication and erosion studies of C-SiC composite jet vanes in solid rocket motor exhaust. *J Euro Ceram Soc* 31(13):2425–2431
19. Manocha LM (2003) High performance carbon-carbon composites. *Sadhana* 28(1–2):349–358 (Printed in India)
20. Goleki I, Morris RC, Narasimhan D, Clements N (1995) Rapid densification of carbon-carbon composites by thermal-gradient chemical vapor infiltration. In: Evans AG, Naslain R (eds) High temperature ceramic matrix composites II. *Ceram Trans* 58:231–236
21. Besmann TM (1995) CVI processing of ceramic matrix composites. In: Evans AG, Naslain R (eds) High temperature ceramic matrix composites II. *Ceram Trans* 58:1–12
22. Naslain R (2004) Design, preparation and properties of non-oxide CMCs for application in engines and nuclear reactors: an overview. *Compo Sci Tech* 64:155–170
23. Kumar Suresh, Kushwaha Juhi, Mondal Samar, Kumar Anil, Jain RK, Rohini Devi G (2013) Fabrication and ablation testing of 4D C/C composite at 10 MW/m² heat flux under a plasma arc heater. *Mater Sci Eng A* 56:102–111
24. Hatta H, Takei T, Taya M (2000) Effect of dispersed microvoids on thermal expansion behavior of composite materials. *Mater Sci Eng A* 285:99–110
25. Kelly A, Zweben C, Warren R (2000) Comprehensive composite materials, C/C, cement, and ceramic matrix composites, vol 4. Pergamon Press (Elsevier), New York, USA, p 413
26. Chen JD et al (1995) Low energy tribological behavior of carbon-carbon composites. *Carbon* 33:57–62
27. Birch S (1996) A light touch on the brakes. *Aerospace engineering*, 24–25 Dec 1996
28. Berdoyes M (2006) Snecma propulsion solide advanced technology SRM Nozzles. History and future, Paper AIAA 2006-4596 in: 42nd AIAA/ASME/SAE/ASEE Joint propulsion conference & exhibit, Sacramento, California, USA
29. Hald H, Ortelt E, Fischer I, Greuel D, Haidn (2005) Effusion cooled cmc rocket combustion chamber. AIAA/CIRA 13th international space planes and hypersonics systems and technologies, CIRA, Italy. AIAA-2005-3229
30. Krenkel W (2004) Carbon fiber reinforced CMC for high performance structures. *Int J Appl Ceram Tech* 1(2):188–200
31. Jones, R.H., Steiner, D., Heinisch, H.L., Newsome, G.A., Kerch, H.M., 1997, “Radiation resistant ceramic matrix composites”, *J Nuclear Mater.*, 245, Pp.87–107
32. Kerans RJ, Hay RS (2002) Parthasarathy TA, Cinibulk MK (2002) Interface design for oxidation-resistant ceramic composites. *J Am Ceram Soc* 85(11):2599–632
33. Naslain R (1998) The design of the fibre-matrix interfacial zone in ceramic matrix composites. *Compos Part A* 29A:1145–55
34. Naslain R, Dugne O, Guette A, Sévely J, Robin-Brosse C, Rocher JP, Cotteret J (1991) Boron nitride interphase in ceramic matrix composites. *J Am Ceram Soc* 74:2482–2488
35. Richard ML (1993) Pre-ceramic polymer routes to silicon carbide. *Chem Mater* 5:260–279
36. Jian K, Chen ZH, Ma QS et al (2005) Effects of pyrolysis processes on the microstructures and mechanical properties of Cf/SiC composites using polycarbosilane. *Mater Sci Eng A* 390:154–158

37. Rak ZS (2001) A process for Cf/SiC composites using liquid polymer infiltration. *J Am Ceram Soc* 84:2235–2239
38. Berbon M, Calabrese M (2002) “Effect of 1600 °C heat treatment on C/SiC composites fabricated by polymer infiltration and pyrolysis with allylhydridopolycarbosilane. *J Am Ceram Soc* 85:1891–1893
39. Kumar S, Misra MK, Mondal S, Gupta RK, Mishra R, Ranjan A., Saxena AK (2015) Polycarbosilane based UD C/SiC composites: effect of in-situ grown SiC nano-pins on mechanical properties. *Ceram Trans* 41(10) Part A:12849–12860
40. Interrante LV, Whitmarsh CW, Sherwood W (1995) Fabrication of SiC matrix composites using a liquid polycarbosilane as the matrix source. In: Evans AG, Naslain R (eds) *High temperature ceramic matrix composites II*. *Ceram Trans*, 58:111–118
41. Hillig WB (1994) Making ceramic composites by melt infiltration. *Am Ceram Soc Bull* 73(4):56–62
42. Suresh K, Sweetey K, Anil K, Anupam S, Gupta AK, Rohini Devi G (2008) Mechanical properties of LSI based 3D-stitched-C–SiC composites prepared by coal–tar pitch as carbon precursor. *Scripta Mater* 58:826–9
43. Bansal NP (2005) “Hand book of ceramic composites. Kluwer Academic Publishers, Dordrecht, The Netherlands
44. Hald H, Weihs H, Benitsch B, Fischer I, Reimer T, Winkelmann P, Gulhan A (1999) Development of a nose cap system for X-38, In: *Proceedings of international symposium atmospheric re-entry vehicles and systems*, Arcachon, France
45. Muhlatzer A, Leuchs M (2001) Application of non-oxide CMCs, High temperature ceramics matrix composites. In: Krenkel, W., Naslain R, Scheider H (eds) *Wiley-VCH, Weinheim, Germany*, pp 288–298
46. Trabandt U, Fischer W (2001) Paper 01-ICES-184 in: *Proceedings of the international congress on environmental systems*, Orlando, FL, USA
47. Chawla KK (2003) *Ceramic Matrix Composites*, 2nd edn. Kluwer Academic Publishers, Dordrecht, The Netherlands
48. Liu CJ, Chen HH, Wang Y, Zhang Z (2004) A long duration and high reliability liquid apogee engine for satellites. *Acta Astronaut* 55:401–408
49. Schmidt Stephan, Beyer Steffen, Immich Hans (2005) Ceramic matrix composites: a challenge in space-propulsion technology applications. *Int J Appl Ceram Technol* 2(2):85–96

Chapter 16

Ceramic Matrix Composites (CMCs) for Aerospace Applications

N. Eswara Prasad, Anil Kumar and J. Subramanyam

Abstract Ceramic materials have excellent properties, but are brittle and the strengths are highly variable. Particulate reinforcements give isotropic properties, but only marginal improvement in toughness. Continuous reinforcements improve the ceramic materials both in terms of fracture toughness as well as strength variability. The processing of ceramic matrix composites and improving the required properties with the available reinforcements is an emerging technology that is finding new critical applications.

Keywords Ceramic matrix composites • Processing • Properties • Applications

16.1 Introduction

Ceramic materials, by virtue of their inherently high melting points, low density, good chemical inertness, good stiffness and high hardness, are considered to be candidates for extending performance limits beyond those offered by metallic materials. However, their inherent brittleness and poor strength reliability have inhibited the widespread use of ceramic materials for structural applications. In an effort to overcome these basic problems, considerable progress has been made during the past four decades in both compositional and microstructural design of ceramics, and this is well-summarized in the monograph edited by Professor Walter Krenkel [1].

N. Eswara Prasad (✉)
DMSRDE, DRDO, Kanpur, India
e-mail: nep@dmsrde.drdo.in

Anil Kumar
ASL, Hyderabad, India
e-mail: anil_drld43@hotmail.com

J. Subramanyam
DMRL, Hyderabad, India
e-mail: js_vij@yahoo.co.in

The deployment of composite technology is the principal methodology to achieve vastly improved mechanical properties and structural integrity, as is unequivocally advocated by several handbooks/monographs/edited volumes [1–17] as well as overviews [18–38] and comprehensive technical papers [39–59]. All of these data sources point to the fundamental fact that three major entities, namely the matrix, reinforcement and the interface are responsible for determining the characteristics and properties of a particular composite material.

The matrix is the major continuous phase in which the reinforcement is uniformly distributed. Depending upon the type of matrix, composite materials can generally be classified into four different categories, namely polymer matrix composites (PMCs), ceramic matrix composites (CMCs), metal matrix composites (MMCs) and intermetallic matrix composites (IMCs). This chapter discusses the second category, CMC materials.

16.2 CMC Constituents

16.2.1 Ceramic Matrices

Major advantages of ceramic matrices over polymer and metal matrices are their higher melting points, higher hardness, lower coefficient of thermal expansion (CTE) and better chemical inertness. The range of ceramic matrices is vast. Oxides like Al_2O_3 , MgO , ZrO_2 , Mullite, and Spinel, and non-oxides like SiC , Si_3N_4 , TiC , B_4C and TiB_2 belong to this category. High temperature structural silicides like MoSi_2 , WSi_2 and TiSi_3 are also being considered as potential matrix materials.

Even though the major emphasis in CMCs centres on the comparatively cheaper and abundant oxide matrices (Al_2O_3 in particular), other potential matrix systems, e.g. Mullite, SiC , SiAlON and MoSi_2 are also being examined for their potential as structural materials. Table 16.1 provides comparative thermal stability data for some common oxides and non-oxides [4], since such data primarily decide the choice of CMCs for high temperature applications in different environments.

Discontinuously reinforced ceramic matrix (DRCM) composites are CMCs reinforced by ceramic particulates, platelets, whiskers or short fibres. The reasons for success of these composites as structural ultrahigh temperature (UHT) materials are their remarkable isotropic properties, amenability to conventional ceramic powder processing techniques, and the availability of comparatively low-cost and high-volume production. The physical and mechanical properties of various common ceramic matrix materials are compiled and presented in Table 16.2 [7].

A series of early investigations indicated that continuous fibre reinforcements in alumina can impart high stiffness and better tensile properties as compared to most other CMCs [2, 6, 9, 22–24, 30, 34, 48, 54]. However, this approach has several limitations: expensive and complicated processing techniques; problems related to oxidation and reaction of fibres with the matrix material at elevated temperatures;

Table 16.1 Comparative thermal stability data for some of the most common ceramic materials [4]

Properties/materials	Melting point (°C)	Short term maximum use temperature (°C)	Maximum use temperature (°C) in air for no significant creep or loss of properties
Oxides		(In air)	
Alumina	2060	1950	1500
Zirconia (stabilized)	2680	2300	1500
Mullite	1810	1700	1400
Spinel (MgAl ₂ O ₄)	2135	1800	1400
Magnesia	2800	2000	1400
Non-oxides		(In inert atmosphere)	
Silicon carbide	2400 (dissociates)	2000	1450
Boron carbide	2420	1300	800
Titanium carbide	3050	1400	750
Silicon nitride	1800 (dissociates)	1500	1200
Titanium diboride	2880	2400	1000

Table 16.2 Comparative properties of various ceramic matrix materials [7]

Material	Density (g/cm ³)	Melting point (°C)	Hardness (GPa)	Fracture toughness (MPa√m)	Thermal conductivity (W/m°K) at 1273°K	Coefficient of thermal expansion ×10 ⁻⁶ (°K) at 1273°K	Electrical resistivity Ωm at 298°K
Al ₂ O ₃	3.97	2050	18	3.2	6	8	>10 ¹⁵
MgO	3.24	2800	12	2.6	7	9	10 ¹²
ZrO ₂	6.10	2720	12	8.0	3	13	10 ¹²
Mullite	2.80	1810	13	2.1	5	6	10 ¹³
SiC	3.21	2400 ^a	21	4.2	40	5	≈1
Si ₃ N ₄	3.20	1900 ^a	16	5.1	15	3	10 ⁴
TiB ₂	4.50	2800	22	5.2	25	6	10 ⁻⁵
MoSi ₂	6.25	2100	12	4.1	20	8	2 × 10 ⁻⁵
TiC	4.90	3050	25	4.2	30	9	10 ⁻⁴
AlN	3.26	2300	13	2.7	50	6	2
TiN	5.40	3090	18	4.1	30	9	5 × 10 ⁻⁵
BN	3.50	3000 ^a	32	3.1	35	6	10 ¹⁰
B ₄ C	2.50	2420	25	3.2	15	6	0.5

^aDissociates

poor resistance of polycrystalline fibres to creep deformation; considerable degradation of the continuous polycrystalline fibres due to grain growth at temperatures above 1250 °C; and fragmentation behaviour of the polycrystalline fibres during

high pressure—high temperature consolidation processing, such as hot pressing. Because of these inherent problems, and also because discontinuous reinforcements are easier to process and more available, discontinuous reinforcements are preferred to continuous reinforcements for toughening brittle ceramic matrices.

Although various alumina matrix composites have been developed over the past few years, major attention has been focussed on discontinuously reinforced alumina matrix (DRAM) composites using SiC fibres. Because of the potential of this $\text{Al}_2\text{O}_3\text{-SiC}_w$ system, it has become one of the most important members of the DRAM composite family. Some others are $\text{Al}_2\text{O}_3\text{-SiC}_p$ (particulate), $\text{Al}_2\text{O}_3\text{-TiB}$, $\text{Al}_2\text{O}_3\text{-TiC}$, $\text{Al}_2\text{O}_3\text{-TiN}$, $\text{Al}_2\text{O}_3\text{-SiC}_{p1}$ (platelet), $\text{Al}_2\text{O}_3\text{-B}_4\text{C}$ and $\text{Al}_2\text{O}_3\text{-Graphite}$ systems.

16.2.2 Ceramic Reinforcements

Most of the ceramic reinforcements based on oxides, carbides, nitrides and borides have already been found to be suitable reinforcements for incorporation into brittle ceramic matrices. Amongst these reinforcements, SiC is of the highest interest as a reinforcement material because of its relatively high modulus, low coefficient of thermal expansion (CTE), low density, good hardness, and availability in various forms ranging from different sizes of particulates to fine single crystal whiskers, multi-filament tows and relatively coarse monofilaments.

Reinforcements are generally available in the form of continuous fibres, short fibres, whiskers, platelets and particulates, see Fig. 16.1. Continuous fibres are

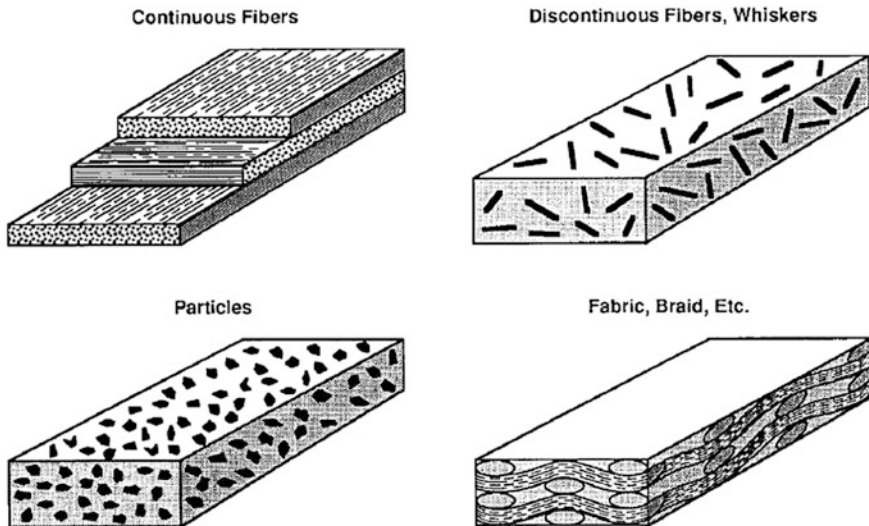


Fig. 16.1 Schematic diagram showing different types of CMCs—namely, particulate, discontinuous and continuous fibre-reinforced CMCs

unidirectionally oriented polycrystalline material and are available in the form of monofilaments or multifilaments. Monofilaments, such as Boron, Borsic and SiC, with diameters of about 100–150 μm , are made by the chemical vapour deposition (CVD) technique. Multifilaments such as Nicalon (SiC), Sumitomo (Al_2O_3) and Carbon fibres are made by pyrolysis of organometallic compounds in the form of tows (bundles of a few thousand 3–10 μm diameter fibres) or two/three-dimensional weaves of the tows. Short fibres such as Saffil and Kaowool are physically similar to multifilaments except for the shorter length.

Whisker-reinforced CMCs employ SiC and Si_3N_4 defect-free single crystals with lengths of the order of 0.2–250 μm and aspect ratio (length to diameter ratio) in the range of 2–250. Among the commercially available types, SiC whiskers have the greatest potential for improving the properties of brittle ceramic matrices, owing to their better reinforcing properties. Secondly, commercial grade SiC whiskers of high purity have been successfully produced by various routes, e.g. (i) thermal decomposition or hydrogen reduction of organic silicon compounds, (ii) hydrogen reduction of a gaseous mixture of silicon halides and hydrocarbons, (iii) recrystallisation of sublimed silicon carbide, (iv) supersaturation technique in the molten phase of silicon alloys, and (v) reaction between SiO_2 and C with a catalyst and reaction between Si and a hydrocarbon in the presence of H_2S .

Continuous fibre-reinforcement possesses the advantage of superior properties like stiffness and strength as compared to the discontinuous reinforcements (particulates, short fibres, etc.), but cannot impart isotropic properties and is unamenable to near-net-shape forming techniques. On the other hand, discontinuous reinforcements offer isotropic properties and the amenability to be processed by conventional ceramic powder processing techniques.

Chawla [9] has recently reviewed the major commercially available continuous fibre reinforcements and their suitability for different matrix systems. Effects of various reinforcements such as SiC, SiC_{pl} (platelet), SiC_{w} (whisker), TiC, B_4C , TiB_2 , $\text{B}_4\text{C}_{2\text{pl}}$ (platelet), $\text{B}_4\text{C}_{\text{w}}$ (whisker), $\text{Al}_2\text{O}_{3\text{pl}}$ (platelet), Graphite, TiN, $\text{ZrB}_{2\text{pl}}$ (platelet), SiAlON and Diamond on different ceramic matrix systems have been studied extensively. For the majority of such CMC systems, improvements in mechanical properties have been achieved as compared to their unreinforced counterparts. The properties of some of the commonly available ceramic reinforcements are summarized in Table 16.3 [3].

16.2.3 Interfaces

Performance of a composite material depends critically on the nature of the matrix/reinforcement interface, as well as the interfaces between the matrix grains and the reinforcement particles. The interfaces play a crucial role in the load transfer between the matrix and the reinforcement as well as in interactions between cracks and reinforcements. Moreover, physical properties like thermal conductivity, coefficient of thermal expansion (CTE) and dimensional stability depend on the

Table 16.3 Properties of some of the common ceramic reinforcements used in CMCs [3]

Properties/reinforcements	Density (g/cm ³)	Elastic modulus (GPa)	Tensile strength (GPa)	Fracture toughness (MPa√m)	Coefficient of thermal expansion $\times 10^{-6}$ (/°K)	Thermal conductivity (W/m °K)
Fibres						
SiO ₂	2.60	73.5	15.2	3.6	5.4	13
SiC (Nicalon)	3.15	616	8.3	11	2.5	25
Al ₂ O (Saffil)	3.90	265	1.5	6.2	8.8	14
C (Graphite)	1.90	256	5.5	3.8	1.9	38
Boron (on W Core)	2.60	385	7.0	2.2	5.0	38
Whiskers						
Al ₂ O ₃	3.96	450	20	8.7	8.8	16
Si ₃ N ₄	3.18	385	14	9.4	2.4	20
SiC (β)	3.18	490	21	9.7	4.1	60
B ₄ C	2.52	490	14	6.2	5.1	20
Graphite	2.00	700	19	4.2	1.8	328
Potassium-Titanate	3.30	280	7.0	2.1	9.6	10
Beryllia	2.85	350	13	2.4	5.6	12
Particulates						
AlN	3.26	350	-	2.7	6.1	50
B ₄ C	2.50	480	-	3.2	6.2	15
TiC	4.90	320	-	4.2	9.2	30
SiC	3.21	480	-	4.2	5.1	40
TiB ₂	4.50	532	-	5.2	6.1	25
Al ₂ O ₃	3.97	375	-	3.2	8.1	6.2

nature of the interface. It is thus desirable to have a clear understanding of the interfacial characteristics of different types of ceramic matrix composites and consequently to be able to tailor these for optimum performance of CMCs.

Although the primary role of the interface in CMCs is to transfer load from the matrix to the reinforcement, its nature primarily depends on the chemical reaction, wetting, and bonding between the matrix and reinforcement. Interfacial bonding can be categorized as mechanical and chemical. Mechanical bonding could arise due to mismatch of CTE or elastic modulus between the matrix and the reinforcement. It is comparatively a weaker bonding, but it is efficient in load transfer when the applied force is parallel to the interface. Interfacial bonding of this type can give rise to substantial toughening effects for brittle ceramic matrices via fibre pull-out/bridging mechanisms. On the other hand, chemical bonding due to one or more chemical reactions yields a much stronger interface between the matrix and the reinforcement. However, if a brittle reaction product is formed in the process, this may be a serious detrimental factor for the performance of a composite. It must be noted that although several studies of the influence of interface characteristics have been reported with many promising applications [14, 42, 45], these effects are not yet fully understood; hence this topic is being further researched.

16.3 Toughening by Fibre Reinforcement/Crack Bridging

The toughening of ceramics (which is also more generally discussed in Chap. 18 of this Volume) by fibre reinforcement is most effective in CMCs, and is discussed in detail here. First we note that even the toughening of monolithic ceramics can be a complex process, with several mechanisms contributing simultaneously, see Fig. 16.2. Bearing these comments in mind, the fracture process of a CMC adds additional complexities, which are illustrated schematically in Fig. 16.3.

Different micromechanisms of fracture take place in three fracture regions: (i) the process zone ahead of the crack tip; (ii) at the crack tip itself; and (iii) in the crack wake. For CMCs the most important result is crack tip shielding owing to crack bridging. These mechanisms include some or most of the following [30, 32, 40], *which by themselves might seem to be detrimental, but in combination with others become beneficial*:

1. Local increase in the stress level with the application of external loading.
2. Development of compressive residual stresses at the crack tip.
3. Crack extension in the compressive stress zone.
4. Relative displacement of matrix/ interface elements.
5. Matrix microcracking, leading to matrix failure (with or without significant crack path meandering, i.e. crack deflection and/or branching).
6. Disbonding of matrix/fibre interface (with or without significant frictional forces).
7. Fibre pull-out and fibre breakage in the crack tip process zone.

Fig. 16.2 Schematic of important toughening mechanisms in monolithic ceramics. After [33]

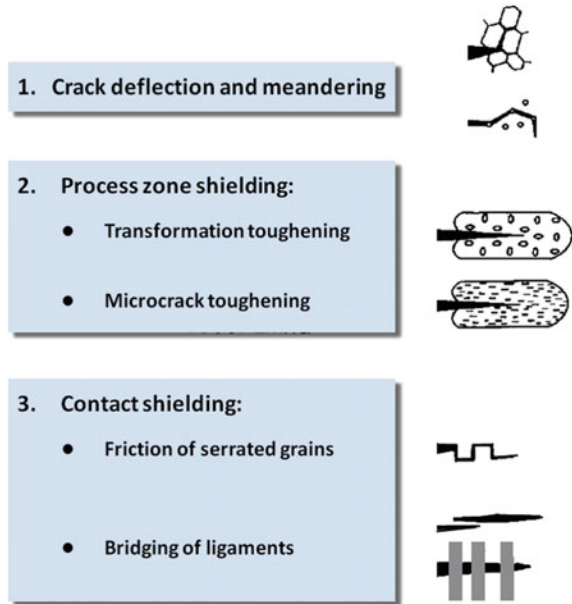
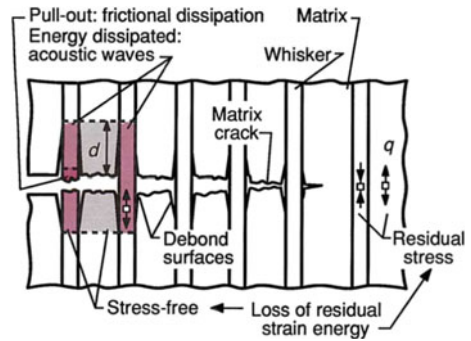


Fig. 16.3 Schematic showing various micromechanisms and processes of crack bridging in fibre-reinforced composites [30]; d disbond (debond) length; q residual stress normal to fibre interface [30]



8. Frictional sliding of the fibres along the matrix/fibre interfaces.
9. Loss of residual strain energy.

The overall result is significant energy dissipation through frictional events in the wake and process zones, acoustic emission and fibre disbonding, pull-out and breakage. Contributions from these stages of crack tip and fibre-reinforcement interactions, with or without the contributions from matrix fracture events, have led to significant increases in the fracture resistance [40].

Several constitutive laws and quantitative treatments of the fracture toughness enhancements by crack bridging are available in the literature and are summarized by Anthony G. Evans [30]. A closer look at these studies suggests that the mode I fracture toughness of any particular material that exhibits crack bridging, measured

in terms of the critical fracture energy (G_{Ic}), varies considerably with (i) interface disbond toughness (τ_i/τ_f the ratio of initial and final fibre sliding stresses), (ii) fibre characteristics, namely the length ($2d$, where d is defined in Fig. 16.3), radius (R) and volume fraction (f), (iii) misfit strain between the matrix and the fibre (ε_{ii}^T), (iv) frictional coefficient at the disbonding interface (μ), (v) fibre strength (S) and matrix toughness (significant for strongly bonded interfaces), and (vi) fibre sliding stress (τ) and pull-out length (h_p), where the value of τ usually varies inversely with h_p . This large number of variables and parameters makes predictions of CMC fracture toughnesses very difficult.

CMCs toughened by fibre reinforcement are also called “Inverse Composites”, since in these materials the brittle matrices fail before the fibres. Since the governing principle is that the failure strain for the matrix is less than that of the reinforcing fibres, matrix cracks have to be arrested and/or deflected at the fibre/matrix interfaces to avoid premature failure of the fibres. This is the only possibility for effective fibre-reinforced toughening.

16.4 Processing of CMCs

Processing of particulate and short fibre composites is carried out by a conventional powder metallurgy (P/M) process, since the reinforcements are essentially small-dimensional. The ceramic and reinforcement powders are blended with suitable additives. The powder can be cold pressed in a die followed by sintering or hot pressing. Another method involves mixing the blend of ceramic and reinforcement powders with a binder and shaping the mix by extrusion or injection moulding, followed by debonding and sintering. A general schematic is shown in Fig. 16.4.

CMCs reinforced with continuous fibres use a reinforcement skeleton or a preform woven into a porous solid block of fibres that has to be filled with a ceramic matrix. The preform can be woven/arranged in a solid block in a variety of forms, the most common being 3-D and 4-D (D-dimension) configurations. The pores are micron-sized and only a liquid or vapour can infiltrate and deposit the ceramic matrix within the preform.

There are four common methods adopted for the densification of the composite: reactive liquid infiltration (RLI), chemical vapour infiltration (CVI), polymer impregnation pyrolysis (PIP) and the Sol-Gel process. The processing methods are specific to certain composite systems:

1. RLI is used to process carbon fibre-reinforced silicon carbide composites (C-SiC). This process takes advantage of the high reactivity of carbon and liquid silicon. The preform is partially densified with carbon and infiltrated with molten silicon by capillary action under controlled conditions in a furnace. As the silicon infiltrates, it reacts to form silicon carbide. Figure 16.5 gives a schematic of the RLI process.

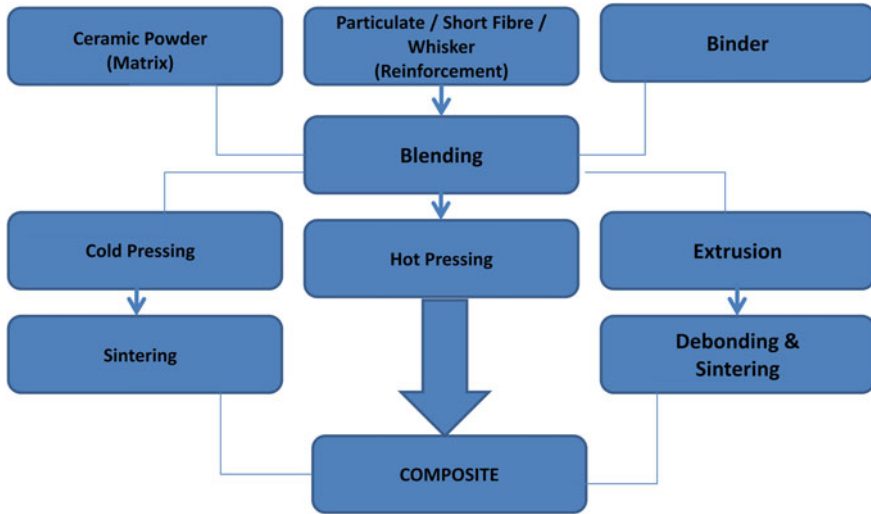


Fig. 16.4 Flow chart for the processing of ceramic matrix composites

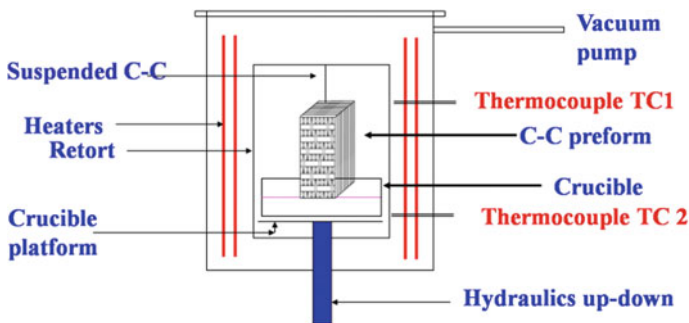


Fig. 16.5 Schematic of silicon melt infiltration in a reactive liquid infiltration (RLI) process. The crucible shown here contains liquid silicon, and the preform is essentially a carbon long fibre structure that is gradually infiltrated by silicon, which after reaction transforms to SiC

- CVI involves the infiltration and reaction of two or more chemical species in the vapour state to form the desired ceramic matrix in the preform. The process is carried out in highly controlled temperature gradient conditions in a furnace. This method may yield any type of ceramic and is most popularly used for the processing of C–SiC or SiC–SiC composites. The chemical used is methyl trichlorosilane, which yields SiC. The CVI process is very slow and takes several months of continuous operation to yield a product. However, the composite properties are excellent. Figure 16.6 shows a schematic of the CVI process.

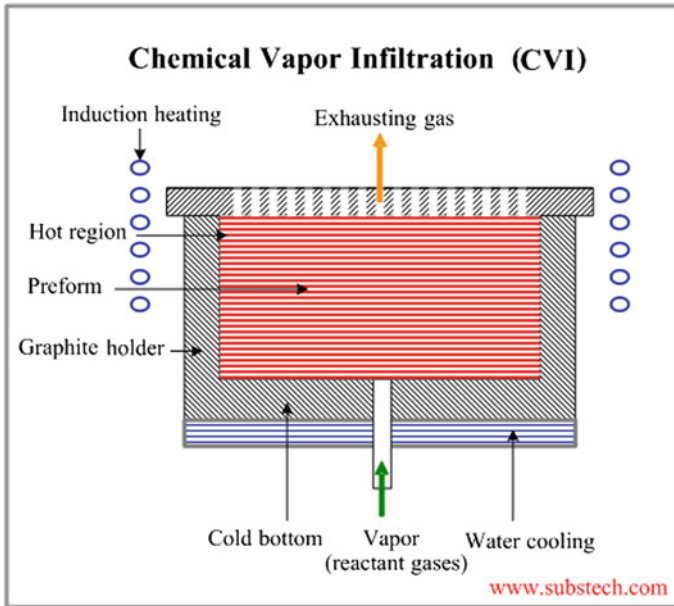


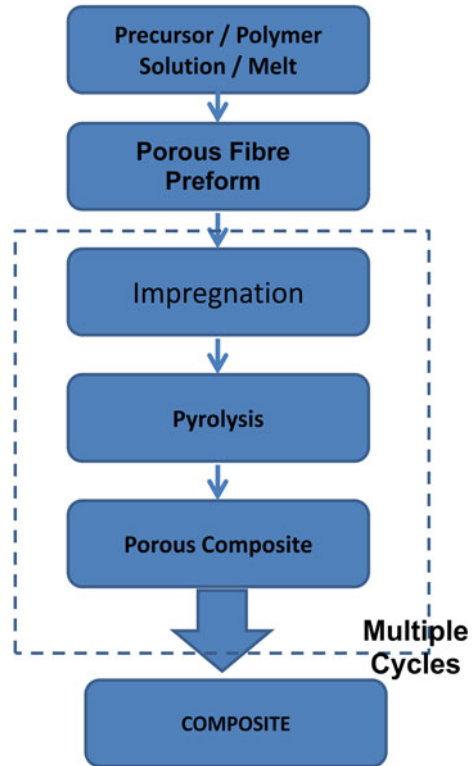
Fig. 16.6 Schematic figure of thermal gradient CVI processing

3. PIP involves the use of a ceramic precursor polymer to first impregnate the porous fibre preform, followed by pyrolysis to form the ceramic. As the polymer pyrolyses, it leaves porosity and the impregnation process has to be repeated many times until the required density of the composite is achieved. This process uses pyrolysis of a polycarbosilane polymer to form a SiC matrix. A schematic of the process is shown in Fig. 16.7.
4. Aqueous sols of oxide ceramics like alumina and silica can be used to infiltrate porous fibre preforms, followed by gelling and removal of the aqueous medium by drying. This process can be repeated many times until the required composite density is achieved.

16.5 CMCs Properties

The material behaviour of fibre-reinforced CMCs is more similar to that of metals than monolithic ceramics, in that the strength does not depend on the volume of the part or structure (size effect). Hence reliable large CMC structures can be realized without increasing the failure risk. However, the availability of reliable data for material properties is limited. Additionally, the published values cannot be

Fig. 16.7 Schematic of the polymer infiltration pyrolysis (PIP) process



compared directly, owing to different evaluation methods and a lack of information about material composition and manufacturing details. These caveats should be borne in mind when consulting Tables 16.4 and 16.5, which provide a rough guide to the properties of some CMCs: these data cannot be used as design data without consulting the material manufacturer.

The mechanical properties are investigated on samples loaded parallel to the fabric or fibre layers. High temperature properties are determined in an inert gas atmosphere for carbon fibre based CMCs, and in ambient air for SiC/SiC material. The variations of the values in Tables 16.4 and 16.5 originate from the standard material variants, based on different fibre types, fibre volume contents and matrix composition.

The mechanical properties of CMCs are strongly influenced by the fibre/ matrix bonding. Therefore these materials tend to show similar ultimate strengths and failure strains when highly compatible fibre coatings are used. However, for melt infiltrated C/C—SiC materials where the carbon fibres are processed as supplied (i.e. no costly fibre coatings), the tensile and flexural strengths are significantly lower.

Table 16.4 Typical material properties of fabric and UD crossply (0°/90°; EADS) based C/SiC and C/C—SiC materials, depending on the manufacturing method—chemical vapour impregnation (CVI), liquid polymer impregnation (LPI) or liquid silicon impregnation (LSI)

	CVI		LPI		LSI		
	C/SiC	C/SiC	C/SiC	C/C-SiC	C/C-SiC	C/SiC	
Manufacturer	SNECMA (SPS)	MT Aerospace	EADS	DLR	SKT	SGL	
Density (g/cm ³)	2.1	2.1–2.2	1.8	1.9–2.0	>1.8	2	
Porosity (%)	10	10–15	10	2–5	–	2	
Tensile strength (MPa)	350	300–320	250	80–190	–	110	
Strain to failure (%)	0.9	0.6–0.9	0.5	0.15–0.35	0.23–0.3	0.3	
Young's modulus (GPa)	90–100	90–100	65	50–70	–	65	
Compression strength (MPa)	580–700	450–550	590	210–320	–	470	
Flexural strength (MPa)	500–700	450–500	500	160–300	130–240	190	
ILSS (MPa)	35	45–48	10	28–33	14–20	–	
Fibre content (vol.%)	45	42–47	46	55–65	–	–	
Coefficient of thermal expansion (10 ⁻⁶ K ⁻¹)	∥	3 ^a	3	1.16 ^d	–1–2.5 ^b	0.8–1.5 ^d	–0.3
	⊥	5 ^a	5	4.06 ^d	2.5–7 ^b	5.5–6.5 ^d	–0.03–1.36 ^e
Thermal conductivity (W/mK)	∥	14.3–20.6 ^a	14	11.3–12.6 ^b	17.0–22.6 ^c	12–22	23–12 ^f
	⊥	6.5–5.9 ^a	7	5.3–5.5 ^b	7.5–10.3 ^c	28–35	–
Specific heat (J/kgK)	620–1400	–	900–1600 ^b	690–1550	–	–	

∥ and ⊥ = fibre orientation; ^aRT–1000 °C; ^bRT–1500 °C; ^c200–1650 °C; ^dRT–700 °C; ^e200–1200 °C; ^f20–1200 °C

At temperatures up to 1200 °C, and in an inert gas atmosphere, the mechanical properties of C/C—SiC are slightly higher than at room temperature, similar to the behaviour of C/C materials. However, at temperatures above 1350 °C in a vacuum, a certain decrease of tensile strength was observed.

N.B: The lifetimes of carbon fibre based CMCs in air is limited above 450 °C, owing to oxidation of exposed fibre ends and exposure of fibres owing to matrix cracking. Thus despite the fact that a SiC matrix and surface coatings significantly increase oxidation stability, C/SiC and C/C-SiC materials are not usable for long-term applications, e.g. in gas turbines.

Table 16.5 Typical material properties of SiC/SiC materials, depending on the manufacturing method

	Gas phase infiltration			Melt infiltration		
	SiC/SiC	Hypercomp PP-HN	Hypercomp SC-HN	Hypercomp PP-HN	Hypercomp SC-HN	N-24 B
Manufacturing method	CVI	CVI ^a		MI-Prepreg	MI-Slurry cast	MI-Slurry cast
Manufacturer	SNECMA (SPS)			NASA		
Fibre type	Nicalon	Hi-Nicalon	Hi-Nicalon	Hi-Nicalon	Hi-Nicalon	Sylramic-IBN ^b
Fibre content (vol.%)	40			20-25	35	36
Temperature (°C)	23	1400	1200	25	1200	23
Density (g/cm ³)	2.5	2.5	2.3	2.8	2.7	2.85
Porosity (%)	10	10	13	< 2	6	2
Tensile strength (UTS) (MPa)	200	150	315	321	224 ^c	450
Proportional limit stress (MPa)	—	—	—	167	165	170
Strain to failure (%)	0.3	0.5	0.5	0.89	0.31	0.5
Young's modulus (GPa)	230	170	220	285	243	210
ILSS (MPa)	40	25	31	135	124	—
CTE I (10 ⁻⁶ K ⁻¹)	I	3	3 ^f	—	3.73	3.74
	⊥	1.7	3.4 ^f	—	4.15	3.12
Thermal conductivity (W/mK)	I	19	15.2 ^f	—	33.8	30.8 ^g
	⊥	9.5	5.7 ^f	—	24.7	11.8
Specific heat (J/kgK)	620	1200 ^f	—	710	1140	700

I and ⊥ = fibre orientation; ^aSi-B-C self healing matrix; ^bCOI Ceramics—NASA; ^cStrain rate = $3 \times 10^{-5} - 10^{-4}$; higher values are obtained at higher strain rates; ^d204 °C; ^e1204 °C; ^f1000 °C; ^gEngineering estimates

16.6 Aerospace Applications

There are numerous actual and potential applications of CMCs in the aerospace arena. Most are for high temperature oxidizing environments pertaining to aero-engines and re-entry space vehicles.

Because of the sensitivity of carbon to oxidation, ceramic matrices have been developed since the middle of the 1970s to replace carbon in order to obtain materials capable of long-term resistance to high thermal fluxes and mechanical loads in oxidizing environments. C-SiC or SiC-SiC composite materials are preferred for these applications. These materials offer good strength (about 300 MPa) at room temperature, and a non-brittle behaviour, with an enhanced failure strain of about 0.5 %.

The feasibility of different aeroengine parts, hot gas valve parts, thermal structures and thermal protection systems (TPS) of re-entry vehicles based on carbon—ceramic or ceramic—ceramic materials, has already been demonstrated, see Figs. 16.8, 16.9 and 16.10.

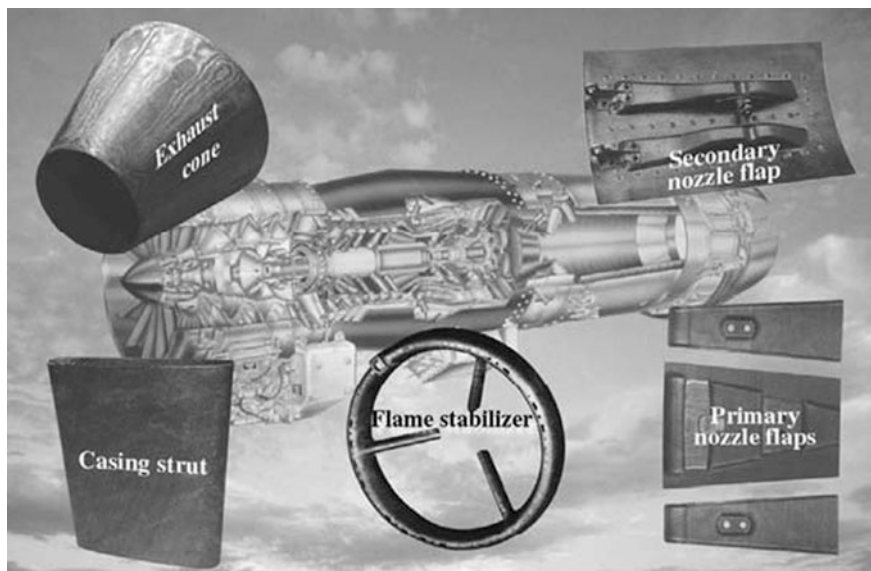


Fig. 16.8 SiC-SiC and C-SiC composites for aeronautical applications

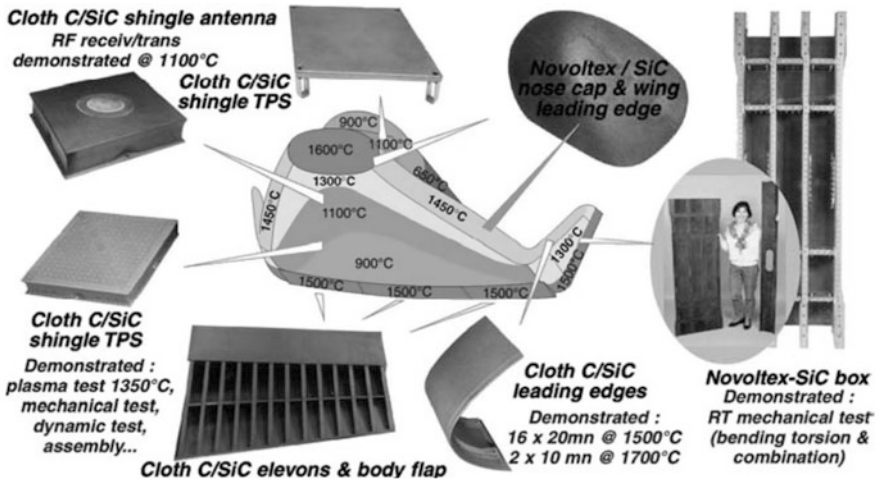


Fig. 16.9 C-SiC composites for thermal protection systems (TPS)

Fig. 16.10 SEPCARBINOX flaps for Rafale M88-2 engine



16.7 Summary

In designing ceramic matrix composites, due consideration is to be given for selecting the matrix, ceramic reinforcement and the interface. Each of them plays a vital role in deciding the final properties of the composite. Processing of discontinuously reinforced composites is relatively easy and has already found a number of applications. Complicated processing like chemical vapour infiltration is currently required to make SiC fibre reinforced SiC composites with excellent high temperature properties. Also, this process is slow and takes several days to months to make components. Alternative processing techniques as well as improved fibres need to be developed. At present the new fibre reinforced composites like C–SiC and SiC–SiC are replacing earlier materials in critical aerospace applications. With further developments and innovation in processing, they should find wider application.

Acknowledgments The authors sincerely acknowledge the support and information they received from several colleagues at DMRL and ASL (two DRDO laboratories in Hyderabad, India) as well as from colleagues elsewhere in India and abroad. They feel particularly indebted to Professor KS Ravi Chandran, Professor Rahul Mitra, Dr. SV Kamat, Dr. A Chakraborty, Mrs. Sweety Kumari, Dr. G Malakondaiah and Dr. D Banerjee. Funding from DRDO and INAE is gratefully acknowledged.

References

1. Krenkel W (ed) (2008) Ceramic matrix composites. Wiley-Vch Verlag GmbH & Co, KGaA, Weinheim, Germany, p 418
2. Rice RW (1981) Mechanisms of toughening in ceramic matrix composites. In: Proceedings of ceramic engineering science, vol 2, pp 661–701
3. Kelly A, MacMillan NH (1986) Strong solids. Oxford University Press, Oxford, UK, p 445
4. Morrel R (1987) Hand book of properties of technical and engineering ceramics: part—1: an introduction for engineers and designers and part—2: data reviews. HMSO, London, UK
5. Wu R (1988) In: Ishida H (ed) Interfaces in polymer, ceramic and metal matrix composites. Elsevier, New York, USA, p 425
6. Chawla KK (1991) Ceramic matrix composites. Chapman and Hall, New York, USA
7. Schneider DJR, Davidson GM, Lampman SR, Woods MS, Zorc TB, Uhl RC (1991) Ceramics and glasses: engineering materials handbook, vol 4. ASM International, Materials Park, OH, USA
8. Jessen JL, Bender BA, Lewis D (1993) Mechanical properties of layered and laminated ceramic matrix composite systems. Proc Ceram Eng Sci 13:796
9. Chawla KK (1993) Ceramic matrix composites. Chapman and Hall, New York, USA
10. Danial IM, Ishai O (1994) Engineering mechanics of composite materials. Oxford University Press, London, UK, pp 129–148
11. Watchman JB (1996) Mechanical properties of ceramics. Wiley, New York, USA, pp 391–408
12. Munz D, Fett T (1999) “Ceramics: mechanical properties”, ‘failure behaviour and materials selection’. Springer, Berlin, Germany
13. Somiya S, Aldinger F, Claussen N, Springs RM, Uchino K, Koumoto K, Kaneno M (2006) Vol II: processing and applications. Elsevier India Pvt. Ltd, New Delhi, India

14. Wu R (1988) In: Ishida H (ed) *Interfaces in polymer ceramic and metal matrix composites*. Elsevier, New York, USA
15. Warren R (1991) *Ceramic matrix composites*. Springer, New York, USA
16. Peters ST (1998) *Handbook of composites*. Springer, New York, USA
17. Low IM (ed) (2014) *Advances in ceramics composites and matrixes*. Woodhead Publishing Limited, Cambridge, UK
18. Garvie RC, Hannink RH, Pascoe RT (1975) Ceramic steel. *Nature* 258:703–704
19. Subba Rao EC (1981) Zirconia—an overview. *Advanced Ceramics*, vol 3, pp 1–24
20. McMeeking R, Evans AG (1982) Mechanics of transformation toughening in brittle materials. *J Am Ceram Soc* 65:242–246
21. Wiederhorn SM (1984) Brittle fracture and toughening mechanisms in ceramics. *Annu Rev Mater Sci* 14:374–403
22. Evans AG (1984) Toughening mechanisms in zirconia alloys. *Adv Ceram* 12:193–212
23. Classen N (1984) Microstructural design of zirconia—toughened ceramics (ZTC). *Adv Ceram* 1:325
24. Rice RW (1984) Mechanically reliable ceramics. *J Phys Chem Solids* 45:1033–1050
25. Ruhle M, Calussen N, Heuer AH (1986) Transformation and microcrack toughening as complementary process in ZrO_2 —toughened Al_2O_3 . *J Am Ceram Soc* 69:195
26. Chawla KK (1987) In: Ilschner B, Grant NJ (eds) *Composite materials: science and engineering, materials research and engineering (MSE) series*. Springer, New York, USA
27. Lange FF (1989) Powder processing: science and technology for increased reliability. *J Am Ceram Soc* 71:3–10
28. Evans AG, Marshall DB (1989) The mechanical behaviour of ceramic matrix composites. *Acta Metall* 37:2567–2583
29. Clegg WJ, Kendall K, Alford NM, Button TW, Birchall TW (1990) A simple way to make tough ceramics. *Nature London* 347:455–457
30. Evans AG (1990) Perspective On The Development Of High Toughness Ceramics. *J Am Ceram Soc* 73:187–206
31. Mahajan YR, Kuruvilla AK, Bhanu Prasad VV, Chakraborty A (1990) Polymer, metal and ceramic composites (PMC/MMC/CMC): a review. *Indian J Technol* 28:354–367
32. Becher PF (1991) Microstructural design of toughened ceramics. *J Am Ceram Soc* 74:255–269
33. Steinbrech RW (1992) Toughening mechanisms for ceramic materials. *J Euro Ceram Soc* 10:131–142
34. Faber, K.T., 1997, “Ceramic Composite Interfaces: Properties and Design”, *Annual Reviews on Materials Science*, Vol. 27, Pp.499–524
35. Ravi Chandran KS, Panda KB, Sahay SS (2004) TiBw-reinforced Ti composites: processing, properties, application prospects and research needs, in overview: Ti–B alloys and composites. *J Met* 56:42
36. Singh M, Levine SR (2004) Low cost fabrication of silicon carbide based ceramics fiber reinforced composites. NASA technical memorandum No. 107001, Washington DC, USA
37. Akira K, Hirotsu K (2013) SiC/SiC composite materials for nuclear applications. *Nucl Saf Simul* 4:72–79
38. Senthil Kumar A, Baruch LJ, King MFL, Oliver DG (2014) Experimental studies on mechanical properties of glass fiber reinforced ceramic matrix composites. *Int J Emerg Technol Adv Eng* 4:677–681
39. Wei GC, Becher PF (1985) Development of SiC-Whisker-reinforced ceramics. *Am Ceram Soc Bull* 64:298–304
40. Campbell GH, Ruhle M, Dagleish BJ, Evans AG (1990) Whisker toughening: a comparison between aluminium oxide and silicon nitride toughened with silicon carbide. *J Am Ceram Soc* 73:521
41. Zok F, Sbaizero O, Hom CL, Evans AG (1991) Mode I fracture resistance of a laminated fiber-reinforced ceramic. *J Am Ceram Soc* 74:187

42. Venkert A, Brandon DG (1991) HREM interface characterisation of sic whisker reinforced alumina composites in advanced structural inorganic composites. Montecatini Terme, Italy
43. Clegg WJ (1992) The fabrication and failure of laminar ceramic composites. *Acta Metall Mater* 40:3085–3093
44. Mitra R, Mahajan YR, Eswara Prasad N, Chiou WA, Ganguly C (1995) Reaction hot pressing and characterisation of $\text{MoSi}_2/\text{SiCp}$ composites. *Key Eng Mater* 108–110:11
45. Mitra R, Mahajan YR (1995) Interfaces in discontinuously reinforced metal matrix composites: an overview. *Bull Mater Sci* 18:405–434
46. Droillard C, Lamon J (1996) Fracture toughness of 2-D Woven SiC/SiC CVI composites with multilayered interfaces. *J Am Ceram Soc* 79:849–858
47. Mitra R, Mahajan YR, Eswara Prasad N, Chiou WA (1997) Processing—microstructure—property relationships in reaction hot pressed MoSi_2 and $\text{MoSi}_2/\text{SiCp}$ composites. *Mater Sci Eng A* 225:105
48. Nair SV, Wang YL (1998) Toughening behaviour of a two-dimensional SiC/SiC woven composite at ambient temperature I damage initiation and R-Curve behaviour II. Stress displacement relationship in the crack process zone. *J Am Ceram Soc* 81:1149–1157
49. Jessen TL, Greenhut VA, Lewis D, Friel JJ (1999) Effect of microstructure on the mechanical behaviour of continuous fiber reinforced ceramic matrix composites. *J Am Ceram Soc* 82:2753–2761
50. Cheong DS, Hwang KT, Kim CS (1999) Fabrication, mechanical properties and microstructure analysis of $\text{Si}_3\text{N}_4/\text{SiC}$ nanocomposite. *Compos A Appl Sci Manuf* 30:425–427
51. Ohnabe H, Masaki S, Onozuka M, Miyahara K, Sasa T (1999) Potential application of ceramic matrix composites to aeroengine components. *Compos A Appl Sci Manuf* 30:489–496
52. Mitra R, Eswara Prasad N, Kumari S, Venugopal Rao A (2003) High temperature deformation behaviour of coarse and fine grained MoSi_2 with different silica contents. *Metall Mater Trans A* 34A:1069–1088
53. Kumari S, Eswara Prasad N, Ravichandran KS, Malakondaiah G (2004) High temperature deformation behaviour of Ti-TiBw In-situ metal matrix composites, in research summary: Ti-B alloys and composite. *J Met* 56:51–56
54. Eswara Prasad N, Kumari S, Kamat SV, Vijayakumar M, Malakondaiah G (2004) Fracture behaviour of 2D-woven, silica—silica continuous fibre-reinforced, ceramic-matrix composites (CFCCs). *Eng Fract Mech* 71:2589–2605
55. Awaad M, Zawrah MF, Khaili NM (2008) In-situ formation of zirconia-alumina-spinel-mullite ceramic composites. *Ceram Int* 34:429–434
56. Heuer AG, Classen N, Kriven WM, Ruehle M (1982) Stability of tetragonal zirconia particles in ceramic matrices. *J Am Ceram Soc* 65:60–69
57. Budiansky B, Hutchinson J, Lambropoulos J (1983) *Int J Solid Struct* 19:325–337
58. Evans AG, Faber KT (1981) Toughening of ceramics by circumferential microcracking. *J Am Ceram Soc* 64:394–398
59. Evans AG, Faber KT (1984) Crack growth resistance of microcracking brittle materials. *J Am Ceram Soc* 67:255–260

Chapter 17

Nanocomposites Potential for Aero Applications

Naveen K. Mahenderkar, T. Ram Prabhu and Anil Kumar

Abstract This chapter briefly summarizes the types of nanocomposites, their fabrication and properties. Emphasis is placed on the strengthening mechanisms for metal, polymer and ceramic matrix nanocomposites. A brief introduction to the types of reinforcement and matrix materials is given, and finally the current developments and future trends of nanocomposites are discussed.

Keywords Nanocomposites · Metal matrix · Polymer matrix · Ceramic matrix · Processing · Applications

17.1 Introduction

Nanocomposites are materials similar to conventional composites with a matrix phase and a reinforcement phase, although unlike conventional composites the dimensions of reinforcement materials are typically on the order of 100 nm or less. The reinforcement are usually 1-D, 2-D or 3-D nanomaterials.

Nanocomposites are a fast growing area of research and application owing to their unique properties that are usually not seen in conventional composite materials. The properties of nanocomposites depend on both the matrix and reinforcement phases and are also influenced by the morphology and interfacial characteristics. Research so far showed that virtually all types of nanocomposites

N.K. Mahenderkar (✉)

Department of Materials Science and Engineering, Missouri University of Science and Technology, Rolla, MO, USA
e-mail: nm53f@mst.edu

T. Ram Prabhu (✉)

RCMA (F&F-FOL), CEMILAC, Hyderabad, India
e-mail: ramprabhu.t@gmail.com

A. Kumar

ASL, DRDO, Hyderabad, India
e-mail: anil_drld43@hotmail.com

show improved properties compared to their conventional counterparts. Therefore nanocomposites with mechanically reinforced lightweight materials show promising applications in the field of aerospace materials.

Nanocomposites are typically classified based on the type of materials used as the matrix. Other types of classifications include the shape and material of reinforcement, such as particle reinforced, lamellar reinforced and organic/inorganic reinforced. This chapter briefly summarizes the synthesis and properties of metal matrix nanocomposites (MMNCs), polymer matrix nanocomposites (PMNCs) and ceramic matrix nanocomposites (CMNCs).

17.2 Metal Matrix Nanocomposites (MMNCs)

Recently, the Inter-governmental Panel on Climate Change (IPCC) reported that aviation would account for 15 % of total greenhouse gas emissions by 2050. This emphasizes the need for developing ultra-lightweight airframe and engine materials to minimize the fuel consumption and operational cost, and to increase the payload and engine thrust. Among different materials, lightweight metal matrix composites (MMCs) are most promising because of the availability of mature processing techniques and the ability to tailor attractive properties such as specific strength, specific modulus, high thermal stability and wear resistance.

MMCs have typically micron-scale particles or whiskers, or long or short fibres in the metal matrix. When the size scale of reinforcements is selected to be in the nanometer range (typically less than 100 nm), the MMCs become MMNCs. The main advantage of using nanoscale reinforcements is that the required volume fraction of reinforcement is relatively much less (1–5 %) than that required for MMCs to obtain similar strength properties. The low volume fraction of nanoscale reinforcements in MMNCs has the benefit of retaining metallic matrix characteristics such as electrical and thermal conductivities, toughness, machinability and damping capacity.

17.2.1 Strengthening Mechanisms

Many mechanisms contribute to the strengthening of MMNCs. However, they are not additive since there is an interdependence of different mechanisms and also the dominance of one or more mechanisms over others. The brief description of each strengthening mechanism is presented below:

Grain size strengthening The grain size of the matrix in MMNCs is determined mainly by the size and volume fraction of the reinforcement. Increasing volume fractions and/or decreasing the size of the particles restrict grain growth by grain boundary pinning effects. The combined equation using the Zener and Hall–Petch

relations explains the effects of particle size (d_p) and volume fraction (v_p) on the yield strength (σ_y) of MMNCs, which is as follows: [1–3]

$$\sigma_y = \sigma_o + \frac{k_y}{\sqrt{\frac{4\alpha d_p}{3v_p}}} \quad (17.1)$$

where σ_o is the original strength of the matrix material (MPa) and k_y and α are constants. The square root term in the equation, as proposed by Zener, is related to the matrix grain size refinement.

Orowan and dislocation strengthening The strengthening effect from the Orowan mechanism (particle cutting or looping around particles by dislocations) depends on the particle geometrical characteristics and inter-particle spacing, and is generally expressed as [2, 3]

$$\sigma_{\text{orowan}} = \frac{(kMGb) \ln \frac{d_p}{b}}{\lambda \sqrt{1 - \nu}} \quad (17.2)$$

where k is a constant, M is the mean orientation factor, G is the shear modulus of the matrix, b is the Burgers vector, d_p is the particle size, ν is Poisson's ratio and λ is the interparticle spacing.

The above equation shows the significance of small particle size in improving the strength of the composites. It is also reported that the same mechanism helps in improving the creep strength of Mg (AS41/Al₂O₃) nanocomposites despite grain refinement by nanoparticles, which is undesirable with respect to creep failure [4].

On the other hand, the Orowan strengthening effect does not improve the strength linearly with decreasing particle size in the nanoscale range: there exists a critical size below which Orowan strengthening effects become insignificant because of the fact of easier particle shearing by dislocations; and this critical (nano) size is independent of the volume fraction of particles. For instance, the contribution of Orowan strengthening decreased abruptly below the critical particle size of 1.74 nm in Mg/Al₂O₃ composites [5].

Dislocation strengthening is facilitated in MMNCs by the formation of geometrically necessary dislocations (GNDs). The mismatches in the coefficient of thermal expansion and elastic modulus between the matrix and particles are mainly responsible for the formation of GNDs during processing. The dislocation forest around the particle/matrix interfaces causes severe work hardening during deformation, resulting in significant strengthening. The individual contributions of thermal mismatch (σ_{CTE}) [6, 7], elastic mismatch (EM) [8] and work hardening (σ_w) [9] on the strength of MMNCs are expressed as follows

$$\sigma_{\text{CTE}} = M\beta Gb \sqrt{\frac{A \Delta\alpha \Delta T v_p}{b d_p (1 - v_p)}} \quad (17.3)$$

$$\sigma_{EM} = C\alpha Gb \frac{1.9 v_p \varepsilon}{d_p^3} \quad (17.4)$$

$$\sigma_w = CGb \sqrt{\frac{\varepsilon}{b\dot{x}}} \quad (17.5)$$

where M is the Taylor factor, α , β , C and A are constants, G is the shear modulus of the matrix, b is the Burger's vector, $\Delta\alpha$ is the difference between the coefficient of thermal expansion between the matrix and reinforcements, ΔT is the difference between the processing and ambient temperatures, d_p is the particle size, v_p is the volume fraction, ε is the strain caused by work hardening, and \dot{x} is the average distance that dislocations move during deformation.

Load bearing effect The load bearing effect of very stiff particles contributes to the strengthening of MMNCs when the interfaces between the matrix and particles are sufficiently strong. The particle volume fraction (v_p) and the particle aspect ratio (l/t) are the critical factors deciding the load bearing efficiency of the particles. The contribution of load bearing ability of particles to the strengthening of MMNCs is expressed as [10]

$$\sigma_w = v_p \sigma_m \frac{(l+t)}{4t} \quad (17.6)$$

where l , t and σ_m are respectively the length and thickness of the particles and the matrix yield strength.

17.2.2 Synthesis and Processing

Conventional MMC processing methods are inappropriate for fabricating MMNCs because of the size scale of the reinforcements. Nanoscale sizes provide high surface areas of the reinforcements, increasing their reactivity and a tendency for agglomeration during processing. These result in an inhomogeneous reinforcement distribution in the matrix and undesirable brittle phases when conventional processing techniques are used. Therefore special processing techniques have been developed to synthesize and process MMNCs. We briefly discuss the state-of-the-art of these technologies in the following subsections.

Spark plasma sintering Conventional consolidation processes (cold compaction and sintering, pressure sintering, die casting) cannot be used to make MMNCs, owing to many problems such as coarse microstructure, poor densification, porosity defects, prolonged processing time and high sintering temperature requirements, low strength properties, and poor interface integrity between the matrix and particles.

These problems can be easily overcome by a novel sintering technique, such as pressure assisted spark plasma sintering (SPS). SPS has many unique features such as short processing time, low sintering temperature, no prior compaction step requirements, and high heating rate that help in retaining nanostructures with better particle and matrix interface characteristics, less shrinkage and near theoretical density consolidation in MMNCs [11].

The proper selections of DC pulse voltage, current, duration, ramp rate and holding time are important to generate heat (by spark plasma, Joule heating, spark impact pressure) in the shortest possible time. SPS has typically four stages, starting with the removal of gases and then application of vacuum, followed by the application of pressure coupled with the generation of heat by resistance pulse heating, and finally ending with cooling [11].

Solidification In this process, melt spinning and/or spray or gas atomization techniques are used to produce nanosize ceramic particles by rapid solidification. The nanosize particles and wetting agents are added to the molten metal by stirring or ultrasonic mixing. Then the melt is solidified under pressure or pressure-less conditions to obtain the MMNCs.

An example produced by this method is an Al/10 vol% Al₂O₃ (50 nm) nanocomposite, which showed high wear resistance and strength properties (yield strength ~515 MPa), owing to matrix grain refinement, dislocation strengthening and grain boundary pinning effects by the nanoparticles. Compared to an Al/46 vol % Al₂O₃ (29 μm) MMC or AISI 304 stainless steel, the strength is 6 or 1.5 times higher, respectively [12, 13].

Liquid metal infiltration In this process, the reinforcement particles are bonded using binders and additives to make a preform consisting of a network of interconnected pore structures. The preform is then infiltrated with molten metal under very high pressure (>1 GPa) to produce an MMNC. For example, Al/CNT nanocomposites are prepared by infiltrating liquid aluminium into a carbon nanotube (CNT) preform at 800 °C under a nitrogen atmosphere [14].

Severe plastic deformation (SPD) processing SPD processes such as equal channel angular pressing (ECAP), accumulative roll bonding (ARB) and high-pressure torsion (HPT) are very popular in the field of ultra-fine grain size materials development [15]. The same processes can also be employed to fabricate MMNCs.

In SPD processing of MMNCs the matrix grains and particles are continuously fragmented. On the one hand the fragmented particles refine the matrix grains by pinning the grain boundaries, increasing the dislocation density and forming a dislocation cell structure and subgrains; while on the other hand the grain fragmentation itself helps grain refinement by forming high angle grain boundaries [15]. For example, Al/Al₂O₃/B₄C nanocomposite processed by ARB resulted in a nanograin structure with mean matrix grain size of 230 nm [15].

Friction stir processing Friction stir processing (FSP) is an advanced thermomechanical process to develop surface nanocomposites [16]. In FSP the substrate matrix material is usually given a composite coating. The coating typically consists of nanoscale particles dispersed in the same substrate matrix.

A specially designed FSP tool pin is placed on the surface of the composite layer and moved along the designated path at a predetermined tool angle and speed. The forward rotation of the pin generates heat through friction, making the matrix melt and flow behind the pin, where it gets refined by severe plastic deformation. Subsequently, the melt is rapidly cooled under hydrostatic pressure to yield the composite with nanosize matrix grains containing nanosize particles [17]. The number of passes, the tool rotation speed, the penetration depth and the forward motion speed are the most important parameters deciding the matrix grain size and particle distribution in the nanocomposites.

Other methods Techniques such as electro-codeposition, disintegrated melt deposition, selective melting, microwave sintering, in situ composite formation by liquid metallurgical processes, melt stirring high-pressure die casting, arc discharge plasma method, high intensity ultrasound cavitation-based casting, hot extrusion, rheocasting and squeeze casting, are reported to be used either alone or in combination to prepare MMNCs [18].

17.2.3 Current Developments in Lightweight MMNCs

The combinations of lightweight matrixes such as Al, Mg and Ti with nanoscale particles of oxides (Al_2O_3 , Y_2O_3 , ZrO_2 , SiO_2), carbides (SiC , B_4C , TiC), nitrides (Si_3N_4 , AlN), borides (TiB_2) and carbon nanotubes (CNT) are promising in aerospace applications because of very high specific strength, specific stiffness and thermal stability.

Typical properties of potential Al, Mg and Ti matrix nanocomposites are presented in Table 17.1. CNT-based lightweight MMNCs are given much attention because of the extraordinarily high strength and elastic modulus of CNTs (~ 10 GPa and ~ 1 TPa respectively), very high thermal and electrical conductivity, low density (1.3 g/cm^3) and low cost.

17.3 Polymer Matrix Nanocomposites (PMNCs)

High performance polymer nanocomposites are fabricated using nanosize organic and/or inorganic additives in a polymer matrix, and show superior properties compared to traditional PMCs. The enhanced properties of polymer nanocomposites can be mainly attributed to the high surface-area/volume ratio of the

Table 17.1 Aluminium and magnesium matrix MMNCs for aerospace applications [19–28]

Composite type	Process	Particle size (nm)	Proof stress (MPa)	Ultimate tensile strength (MPa)	Elongation (%)	Hardness	Compressive strength (MPa)	Flexural strength (MPa)
Al-20 wt% TiB ₂	High energy ball milling followed by spark plasma sintering, hot extrusion	–	480	540	1.4	180 Hv	–	–
Al(5356)–B ₄ C	Cryo-milling followed by spark plasma sintering	–	–	–	–	244 Hv	–	707
Al(5083)–10 wt% SiC (Bathula)	High energy ball milling followed by spark plasma sintering	–	–	–	–	250 Hv	–	824
Al (A356)–3.5 vol % SiC	Vortex stir casting	50	145	283	3.6	75 BHN	–	–
Al-5 vol% Al ₂ O ₃	Mechanical milling followed by hot isostatic pressing and vacuum hot pressing	50	515	–	–	–	628	–
Al-5 wt% Si-4 vol % multiwall CNT	Attritor milling followed by hot rolling	70	520	–	5	–	–	–
Al-2.5 wt% CNT	Spark plasma extrusion	–	–	–	–	99 Hv	415	–
Al(2024)-2 vol% MWCNT	Mechanical alloying followed by hot pressing	–	770	–	–	245 Hv	810	–
Mg-2 wt% Al ₂ O ₃	Gravity die casting followed by hot rolling	–	200	218	–	–	–	–
AZ31 Mg alloy-2 wt% Al ₂ O ₃	Gravity die casting followed by hot rolling	–	290	306	–	–	–	–
Mg-0.66 wt% B ₄ C	Compaction followed by microwave sintering, hot extrusion	50	120	164	10	–	335	–

(continued)

Table 17.1 (continued)

Composite type	Process	Particle size (nm)	Proof stress (MPa)	Ultimate tensile strength (MPa)	Elongation (%)	Hardness	Compressive strength (MPa)	Flexural strength (MPa)
Mg-0.92 wt% Al 0.66 wt% B ₄ C	Compaction followed by microwave sintering, hot extrusion	50	130	238	7	–	356	–
Mg-1.11 vol% Al ₂ O ₃	Powder metallurgy followed by hot extrusion	50	194	250	7	–	–	–
Mg-0.66 vol% Y ₂ O ₃	Disintegrated melt deposition followed by hot extrusion	29	312	318	6.9	–	–	–
Mg-0.66 vol% ZrO ₂	Disintegrated melt deposition	29–68	221	271	4.8	–	–	–
Mg-0.54 vol% SiC	Ultrasonic cavitation casting	50	127	212	8	–	–	–
Mg-28 vol% Zn- 5 vol% Ca-1.5 vol % Al ₂ O ₃	Disintegrated melt deposition	50	750	780	2.6	–	–	–
AZ31 Mg alloy- 1.5 vol% Al ₂ O ₃	Disintegrated melt deposition followed by hot extrusion	50	219	308	14.5	–	–	–
AZ61 Mg alloy- 0.8 vol% SiO ₂	Powder metallurgy followed by hot extrusion	20	330	379	7	–	–	–
AZ91D Mg alloy- 15 vol% SiO ₂	Rheocasting followed by extrusion	150	257	289	0.7	–	–	–
ZK60A Mg alloy- 1 vol% Al ₂ O ₃	Disintegrated melt deposition followed by hot extrusion	50	158	266	19.4	–	577	–
AZ31/AZ91 alloy- 1.5 vol% Si ₃ N ₄	Disintegrated melt deposition followed by hot extrusion	50	232	331	13.1	–	517	–
Ti-0.35 mass% CNT	Spark plasma sintering followed by hot extrusion	10	592	742	26	–	–	–

reinforcement phase obtained from nanoparticles, which show a dramatic change in both physical and chemical properties [29].

The properties that show substantial improvements in a nanocomposite over the traditional filler polymers include mechanical strength, electrical conductivity, thermal stability, flame resistance, moisture resistance and chemical stability.

The aspect ratio of the nano-reinforcement and the degree of mixing between two phases are the two major factors crucial for controlling the overall properties of the composite [30]. Uniform dispersion of the nanoparticles in the polymer matrix enables homogeneity of properties and interaction of nanoparticles for superior mechanical strength. A high aspect ratio of the nanoparticles aids in improved adhesion at the nanoparticle–polymer interface [31].

17.3.1 Reinforced Strengthening

Nanomaterial reinforcements enhance the structural strength of a PMNC composite by allowing a transfer of load between them while closely bonded to the relatively soft polymer. Depending on the morphology and aspect ratio of nanomaterials, overall or directional strengthening can be achieved. Some of the nanomaterial morphologies currently being studied include nanoparticles, nanofibres, fullerenes, nanotubes and nanowires. The type of reinforcement used is broadly classified as fibrous, layered, and particles [32, 33].

Carbon and glass nanofibres are some of the most commonly used fibrous reinforcements which impart directional strength to the nanocomposites. Aramid fibres, which are commonly known as Kevlar, are also being used extensively for high-performance applications [32]. Graphite and organosilicates are some of the layered structures used as reinforcement due to their high aspect ratio. Nanoparticles of silica, carbon, metals and hard ceramics are used as particle reinforcements.

Carbon nanotube reinforcement Carbon nanotubes (CNTs) are cylindrical nanostructures of carbon with very high aspect ratios. They consist of tubes of graphene with nanometre-scale thickness and centimetre scale lengths. Typically, CNTs have one-atom-thick walls, but depending on the type of CNT used there may be multiple layers. Therefore CNTs can be classified as single-walled or multi-walled structures. CNTs are traditionally fabricated using chemical vapour deposition, arc discharge and laser ablation [34].

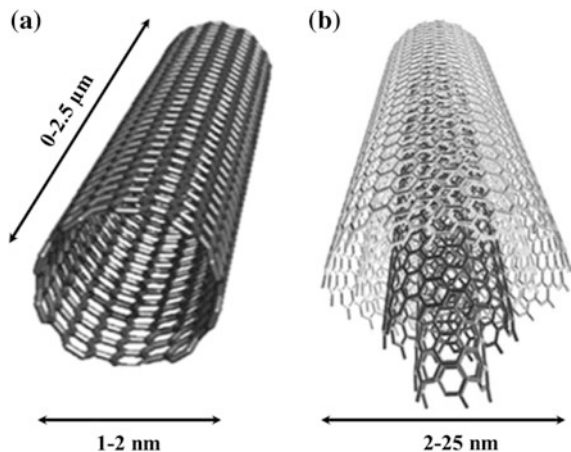
During the process of reinforcement a uniform dispersion of CNTs in the polymer matrix is essential [35–37]. Owing to van der Waals interactions, CNTs tend to aggregate during the mixing process, which could lead to an inhomogeneous strength distribution. Inefficient transfer of load through the material could lead to crack sites in the nanocomposite. Uniform dispersion of CNTs is also essential for electrical and thermal conductivity of the nanocomposites. CNTs are inherently hydrophobic in nature, but recent progress on chemical attachment to reduce the hydrophobicity has helped improve the adhesion to polymers [38–40].

Single-walled and multi-walled CNT reinforcements show different properties in a composite. Single-walled CNTs are graphene wrapped in a hollow cylindrical geometry, whereas multi-walled CNTs can be multiple concentric tubes or a scroll of graphene. CNTs tend to grow in a multi-walled geometry and therefore it is challenging to grow only single-walled nanotubes (Fig. 17.1). Due to the relatively smaller size, single-walled CNTs have a higher tendency to aggregate during the mixing process. Although multi-walled CNTs show a relatively lower agglomeration during the mixing process, they tend to show lower mechanical strength compared to single-walled CNTs. Double-walled CNTs have properties similar to those of a single-walled CNT but also have improved surface chemical resistance, which helps in chemical modification to improve the adhesion with the polymer.

Cadek et al. have shown an increase in Young's modulus by a factor of 1.8 and hardness by a factor of 1.6 in a multi-walled CNT/polyvinyl alcohol nanocomposite with 1 wt% of CNTs. It was also observed that the presence of nanotubes acts as a nucleation site for the crystallization of polyvinyl alcohol. Increased crystallinity of the polymer matrix has been shown to improve the mechanical strength of the nanocomposite [41]. Gojny et al. studied the enhancement of stiffness and fracture toughness of low carbon content CNT-reinforced epoxy. It was observed that compared to carbon black-reinforced epoxy, a relatively small amount (0.1 wt%) of CNTs resulted in a higher tensile strength and Young's modulus [42]. Kearns et al. showed that single-walled CNTs at 1 wt% content had 40 % higher tensile strength and 55 % higher Young's modulus compared to neat polypropylene fibres [43].

Carbon nanofibre reinforcement Carbon nanofibres (CNF) are cylindrical nanostructures of stacked cones of graphite. CNFs have a diameter typically ranging from 10 to 50 nm and can be few hundred microns long. CNFs have higher surface-area/volume ratios compared to a traditional carbon fibre. Higher surface area aids in better adhesion to the polymer and efficient load transfer characteristics. The ultimate tensile strength of a nanocomposite with CNFs is higher than that

Fig. 17.1 Schematic of **a** single-walled CNT with nanometer-scale width and high aspect ratio and **b** multi-walled CNT with relatively higher width showing concentric tubes



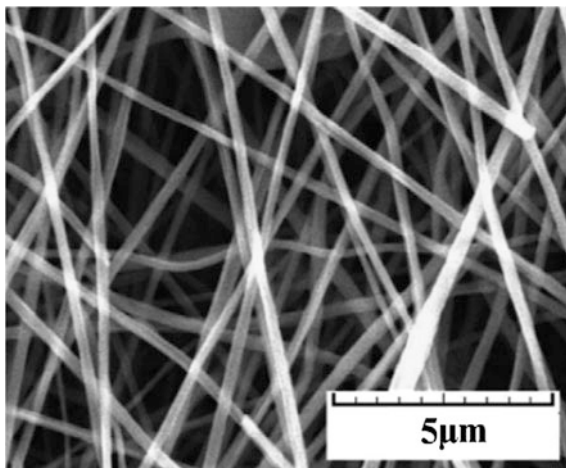
obtained from PMCs using traditional carbon fibres. This has been attributed to lower defects in the nanofibres and higher contact area with the polymer. CNFs also show higher flexibility due to the higher aspect ratio, which leads to superior mechanical properties.

Carbon nanofibres are typically fabricated from poly-acrylonitrile or pitch polymers. The polymer precursors are initially spun or drawn into filaments. This process aligns the polymer chains in one direction to have enhanced mechanical properties along the longitudinal direction. The filaments are then heated to a temperature of 1700 °C in a process known as carbonization or graphitization. This process evaporates or sublimates all the non-carbon atoms from the polymer, thereby producing the carbon fibre. Figure 17.2 shows a scanning electron micrograph of CNFs produced using a poly-acrylonitrile precursor.

CNFs can also be fabricated using pyrolysis of methane at 900 °C in the presence of a metal catalyst. Pyrolysis of hydrocarbons is one of the most studied methods to grow carbon fibres and could possibly be used for mass production at relatively low cost. Some of the other techniques for producing CNFs are template synthesis, electrospinning, phase separation, etc. [44, 45].

CNFs have superior mechanical and electrical properties compared to traditional carbon fibres. Vapour-grown CNFs by Endo et al. have shown that the tensile strength of a nanocomposite is inversely proportional to the diameter of the nanofibres. A tensile strength of 2 GPa and a tensile modulus of 200 GPa was observed [46]. Also, in contrast to CNT-reinforced nanocomposites, nanofibres have lower probability of aggregation and thus produce a homogeneous composite.

Fig. 17.2 SEM micrograph of poly-acrylonitrile-based carbon nanofibres



CNF-reinforced nanocomposites typically are also reinforced with CNTs for tandem properties and smoother surface finish.

Other reinforcements There are other materials such as exfoliated graphite, nano-structured titanium oxide, aluminium oxide, silica, polyhedral oligomeric silsesquioxane (POSS), montmorillonite nanoclays and silicon carbide (SiC) that have been used to form polymer nanocomposites with enhanced material properties.

17.3.2 Fabrication of PMNCs

Fabrication of PMNCs can be done using conventional composite methods. Some of the most widely used fabrication processes include wet lay-up, resin transfer moulding (RTM), vacuum assisted RTM, filament winding, resin film infusion, prepreg moulding, and autoclave processing [47].

Wet lay-up and pultrusion process This involves positioning layers of reinforcement material in or against a mould. These layers are then impregnated with a liquid resin system, either with a brush or roller, to ensure a good wet-out of the reinforcement material. Layering and impregnation are repeated until the required thickness is achieved.

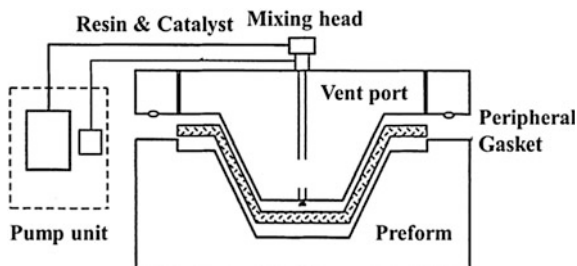
Curing can be performed at room temperature or under heat, depending on the resin system. This can be accomplished with or without the use of a vacuum bagging process. The mechanical properties of products are, however, usually poor due to the presence of voids and non-uniformity.

Pultrusion is similar to the wet lay-up process in terms of applying liquid resin and impregnation, but it is a process of producing a continuous length of reinforced polymer nanocomposites with constant cross-section. Mass production at relatively low cost can be achieved using this method. The amounts of voids and defects in this process are similar to those from the wet lay-up process. The fibre alignment in the composite can be optimized by varying the rate at which the fibres are pulled, the temperature, and the curing time.

Resin transfer moulding and vacuum assisted RTM Resin transfer moulding is a closed-mould process that yields high reinforcement-to-resin ratio, increased laminate compression and excellent strength-to-weight characteristics [48]. In this process a nanofibre preform or dry fibre reinforcement is packed into a mould cavity with the desired shape and the mould is then closed. Low viscosity resin with catalysts for hardening is then pumped into the mould under pressure, displacing the air at the edges until the mould is filled. The nanocomposites are then cured by heating to polymerize the resin into a rigid plastic. The shape and preparation methods of nanofibre preforms can also have a significant influence on the final properties of the nanocomposite. CNFs weaved into a fabric shows higher toughness than unidirectional fibres.

Vacuum-assisted RTM is also a closed-mould process using a partial vacuum to assist the resin flow. Vacuum assists in allowing air bubbles to escape and in

Fig. 17.3 Schematic of the vacuum-assisted resin transfer moulding process



eliminating voids in the final composite. It also helps a homogeneous resin flow through the nanofibre preform. Figure 17.3 shows a schematic of the vacuum-assisted RTM process.

Resin film infusion consists of a catalyzed semi-solid resin layered with the nanofibre preform in a vacuum mould. Vacuum eliminates any air in the mould to avoid air bubbles in the composite, and then the mould is heated in an autoclave. The resin is melted and impregnated into the preform and then polymerized to form a rigid plastic.

Filament winding and prepreg moulding Filament winding is typically used to fabricate hollow structures. A steel mandrel is rotated along its axis and carbon fibre impregnated with resin is wound on the mandrel. Carbon fibre is wound at different angles and orientations on the mandrel to achieve complex patterns for higher strength and toughness. The mandrel plus the desired thickness of nanocomposite is then cured, and the hollow structure is separated from the mandrel. Various process parameters like tension on the fibres, rate of mandrel rotation, resin concentration, nanoparticle reinforcement in the resin, and curing temperature can be used to optimize the final properties. Mass production of hollow nanocomposite structures is feasible using this process.

Prepreg composites consist of nanofibre reinforcements that have been pre-impregnated with a resin. The resins are usually pre-catalyzed and semi-cured for ease of handling at ambient temperatures. High-temperature annealing is usually required to achieve complete polymerization. The prepregs are placed in vacuum moulds having the desired configuration and are heated to allow the resin to soften. This helps the resin to reflow into the prepreg structure, and then the temperature is increased to completely cure the structure.

17.3.3 Current Challenges in PMNCs

PMNCs show promising improvements in material properties in contrast to the conventional counterparts. Relatively lower cost, and significant improvements in strength, toughness and electrical conductivity, are only a few among many properties that can be obtained using polymer nanocomposites.

Homogeneous dispersion and wettability of the nanoparticles and large-scale production of nanostructures is still being intensively researched [49]. The control of porosity during polymer pouring and densification affects the final properties. Formation of agglomerates could cause splitting of the nanocomposite when subjected to force. The (mis)orientation of carbon nanofibres in a unidirectional composite could also lead to crack initiation.

17.4 Ceramic Matrix Nanocomposites (CMNCs)

Ceramic matrix nanocomposites (CMNCs) are nanostructured metal, metal oxides and ceramics reinforced in a ceramic matrix. CMNCs exhibit improved fracture toughness, thermal stability, resistance to corrosion and show lower brittleness in contrast to conventional ceramics.

CMNCs can be classified into two groups based on grain size of the matrix phase: (i) the micro-nano type, where the matrix is composed of micrometre-sized grains with a nanometre reinforcement [50] and (ii) the nano-nano type, also referred to as nanoceramics. This second group contains nano-sized (<100 nm) constituents of both the matrix and reinforcement. A dramatic difference in properties is observed for these two groups of composites.

17.4.1 Types of Reinforcement/Strengthening Mechanisms

Conventional ceramic matrix composites use SiC, Si₃N₄, TiC, etc., as reinforcement. Although the reinforcements are hard and brittle, sufficient improvement in the strength and fracture toughness of the composite is observed. Soft reinforcements like graphite and metal nanoparticles also have shown improved overall properties [51–53]. Current research interest focusses on both hard and soft reinforcements on the nanometre scale and nanostructures with high aspect ratios.

Metal nanoparticle-reinforced CMNCs Enhanced mechanical and structural properties are obtained by reinforcing the ceramic matrix with nano-sized metal particles. Typically ceramics such as silica, silicon carbide, alumina, zirconia, mullite, etc., are used as ceramic matrix phase materials. Nanoparticles of tungsten, molybdenum, nickel, chromium, iron, etc., are used as reinforcement.

Powder processing techniques such as hot pressing or cold pressing and high-temperature sintering are used to fabricate CMNCs. Precursors for both matrix and reinforcement phases start as nanopowders; the desired proportions of metal and ceramic powders are mixed and hot pressed, allowing consolidation and sintering [54–60]. Besides simple powder mixing, the nanocomposites can also be made using oxide reduction, sol–gel, gel casting and salt infiltration.

Niihara et al. fabricated $\text{Al}_2\text{O}_3/\text{Mo}$ nanocomposites using α and γ alumina. It was observed that in a 5 vol% Mo system, elongated grains of Mo surrounded alumina grains, resulting in improved fracture toughness, hardness and strength of the nanocomposite. Ceramic nanocomposites containing lower melting point metals also show exceptional mechanical properties [54, 60]. Along with the mechanical properties, the magnetic properties are also expected to improve by simply incorporating nano-sized Ni, Co and Fe into an Al_2O_3 matrix.

Soft nanoparticle-reinforced CMNCs Besides the mechanical properties, the most important improvement using soft nanoparticles in CMNCs is the machinability [61–64]. One of the most studied soft reinforcements is hexagonal boron nitride (h-BN), which has excellent corrosion resistance, thermal shock resistance and machinability. Kusunose et al. [61] obtained a $\text{Si}_3\text{N}_4/\text{h-BN}$ nanocomposite with significant improvements in machinability, strength and dispersion. Also, hexagonal boron nitride nanocomposites with silicon nitride, silicon carbide and zirconia all showed property improvements over their monolithic ceramic counterparts.

It was observed that hexagonal boron nitride in the matrix inhibits grain growth during the sintering process. This yields in a finer microstructure of the nanocomposite. Although in most of these nanocomposites a decrease in toughness was observed, it was still higher than that of conventional ceramic composites. Hexagonal boron nitride also showed improvements of the thermal resistance in the silicon nitride system up to temperatures as high as 1500 °C.

Hard nanoparticle-reinforced CMNCs Hard materials such as SiC, Si_3N_4 , ZrO_2 and TiO_2 are used as reinforcements in oxide ceramic matrices like Al_2O_3 and MgO. These nanocomposites have higher sintering temperatures than the monolithic matrix materials. For example, in the $\text{Al}_2\text{O}_3/\text{SiC}$ system a dramatic increase in sintering temperatures was observed with the incorporation of 5 vol% SiC [50]. Similar to hexagonal boron nitride reinforcement, SiC promoted a fine grained microstructure. Nanoparticles of SiC with small grain size appeared to disperse in the matrix: however, large grains were dispersed along the grain boundary. SiC incorporation led to higher toughness and strength and this could be mainly because of the residual stress generated due to the difference in thermal expansion coefficients of Al_2O_3 and SiC [50].

Carbon nanotube (CNT)-reinforced CMNCs Carbon nanotube reinforced CMNCs are known to impart very high toughness to nanocomposites. CNTs are lightweight, hollow and high aspect ratio materials, see Sect. 17.3.1 for an introduction on CNTs. CNT reinforcement gives improved high temperature strength, toughness and electrical properties.

Ceramic matrices are brittle and stiff and the main purpose of reinforcement is to impart toughness. CNTs enhance the fracture toughness and also enable electrical conductivity in ceramics. However, significant improvements in the properties of ceramic nanocomposites have not been observed using CNTs. Only a limited amount of the CNTs' potential has been exploited, and more research is needed.

The critical parameters that affect the properties of CNT-reinforced CMNCs are the type of CNT, the sintering process, and the homogeneous dispersion and bonding of CNTs to the matrix material for an efficient load transfer.

17.4.2 Fabrication of CMNCs

CMNCs are fabricated using a wide range of techniques such as sol–gel, hot pressing, hot isostatic pressing, cold pressing and sintering, oxide reduction, salt infiltration, SPS, micro emulsion, auto ignition, codeposition, microwave sintering, etc. Dense CMNCs can be obtained using hot pressing; however, consolidation to high densities and the high sintering temperatures are still major difficulties.

Sol–gel and gel casting The sol–gel technique uses an innovative approach towards processing of ceramic structures. Suitable precursors are polymerized to form a colloidal solution known as a sol. Typically the precursors for preparation of sols include metal oxides or alkoxides which are subject to hydrolysis polymerization to form the sols. The liquid state then goes through hydrolysis or condensation at relatively high temperatures to form gels. Sintering of these gels at relatively high temperatures (lower than powder processing) yields dense ceramic composites. This sintering process and temperatures of the gels can be used to alter the structure and properties of the nanocomposites. Thin films of ceramics can also be produced by spray pyrolysis of gels. Relatively low processing temperatures and better control over homogeneity and particle distribution are some of the advantages of using this process. However, coarsening of the microstructure occurs during the sintering process, and this could lower the overall strength.

Hot pressing Powder mixing and consolidation is one of the simplest ways to fabricate CMNCs. This involves conventional mixing and/or milling processes, followed by compaction or consolidation and then densification (sintering and/or pressing). These powder processing techniques include hot pressing and hot isostatic pressing, where the compaction and sintering occur simultaneously. Similar to the sol–gel process, coarsening of grains during sintering could lower the overall strength of the nanocomposite. Depending on the size and shape of powder and the process used for compaction, complete densification is difficult to achieve. Metal powders during sintering at high temperatures have the tendency to oxidize and may also cause differences in the strength of the nanocomposite.

Other methods Some of the techniques such as oxide reduction, salt infiltration and SPS are also used in fabricating CMNCs. Similar to conventional powder processing, the oxide reduction process utilizes metal oxide powders in a ceramic matrix phase. During sintering the metal oxide particles are reduced to the metallic state in the presence of a reducing agent.

Salt infiltration utilizes the reduction of metal salts to metal nanostructures in the porous ceramic matrix. The ceramic matrix phase is produced using conventional powder compaction and sintering processes. The powder processing conditions are optimized to

achieve a network of pores without complete densification. The pores are infiltrated using a water-based metal salt solution and then dried to eliminate any water, leaving the dispersed metal salts in the pores of the nanocomposite. Annealing in a reducing atmosphere causes the metal salts to change the oxidation state to the metallic form.

17.5 Characterization of Nanocomposites

High resolution characterization tools such as the scanning electron microscope (SEM), transmission electron microscope (TEM), scanning tunnelling microscope (STM), atomic force microscope (AFM), X-ray diffraction (XRD), energy dispersive X-ray spectroscopy (EDAX), and focussed ion beam (FIB) techniques are generally used to assess the phases, morphologies and microstructures of nano-scale particle reinforced composites [17].

AFMs are widely used in developing MMNCs. An AFM is usually operated in three modes: (1) contact mode, (2) non-contact mode and (3) phase mode to analyze MMNCs. Both the contact and non-contact modes are used to obtain high resolution topographic images of the surfaces of MMNCs, whereas the phase mode provides the surface mapping of material composition [17].

An STM is generally used to obtain the atomic arrangements of the surfaces of MMNCs [17]. Electron microscopes (SEM with EDS, TEM) are also used to obtain surface topographies, phase identifications, composition maps, crystallographic orientations, electronic structure and phase shift. The grain sizes are commonly determined from XRD patterns.

Most of the characterization tools mentioned for MMNCs are the same for PMNCs and CMNCs. However, some of the techniques such as STM and conductive AFM require the material to be electrically conductive and thus could cause limitations due the lack of conductivity in CMNCs and PMNCs.

Various other techniques for characterization of PMNCs include wide-angle X-ray diffraction (WAXD), small-angle X-ray scattering (SAXS), scanning probe microscopy (SPM), differential scanning calorimetry (DSC), thermo gravimetric analysis (TGA), Fourier transform infrared spectroscopy (FTIR), and dynamic modulus analysis (DMA). Using these techniques enables obtaining a comprehensive understanding of the basic, physical, chemical and structural properties of PMNCs [65–70].

Some of the most commonly used characterization measurements for CMNCs include Vickers hardness (micro and nano hardness), impact fracture toughness, residual and fracture strength, and compressive and tensile strength.

17.6 Future Aerospace Applications

The use of MMNCs in aircraft or aero engine applications is still in the future. However, their potential has been noted by many recent researches.

MMNCs using Al, Mg or Ti matrices may find use in the next generation of aircraft, based on property improvements and weight savings. For instance, the substitution of Ti MMNCs for currently used Ni-base superalloys in the high pressure compressors of jet engines is one potential application where weight savings of more than 50 % are expected [71]. Other possible applications include helicopter rotor blades, vertical fins, fan guide exit vanes, turbine fan blades and discs, engine spacers and shafts, brake pads and brake discs, compressor rotor blisks and blings.

In recent years, PMNCs for aerospace applications have shown significant improvements in mechanical properties. PMNCs are being used by Boeing as high temperature materials in aerospace applications [72]. Researchers have developed lightweight and durable transparent nanocomposites for the aerospace industry [73].

CMNCs are being used in space applications owing to lower weight and high thermal stability. They are also being used in gas turbine components, brake pads and thrust control pads in jet engines. SiC/C CMNCs were proposed for steering flaps for the NASA space vehicle X-38 [74] which, however, was cancelled in 2002.

17.7 Conclusions

Although nanocomposites have the potential to provide exceptionally high strength, stiffness, wear resistance, thermal conductivity and significant weight savings, the major challenges such as aerospace product quality standard, reproducibility, machining, immature processing techniques, high capital investment for fabrication, and poor ductility and fracture characteristics should be addressed to obtain a wide commercial acceptance in aerospace applications. Research in the field on nanocomposites is very broad and in the early stages of development: more research and in-depth understanding of every process is required to optimize the conditions for fabrication of nanocomposites.

Acknowledgments One of this chapter's authors, Naveen Mahenderkar, would like to thank Dr. N. Eswara Prasad, Director, DMSRDE, Kanpur, India for giving the opportunity to contribute to this book series, and also for his valuable guidance and encouragement. T. Ram Prabhu would like to thank Dr. K. Tamilmani, DG (Aero), DRDO and Shri P. Jayapal, Chief Executive (A), CEMILAC, DRDO for their constant encouragement and support.

References

1. Witkin D, Lee Z, Rodríguez R, Nutt S, Lavernia E (2003) Al–Mg alloy engineered with bimodal grain size for high strength and increased ductility. *Scr Mater* 49:297–302
2. Ye J, Han BQ, Lee Z, Ahn B, Nutt SR, Schoenung JM (2005) A tri-modal aluminum based composite with super-high strength. *Scr Mater* 53:481–486
3. Sanaty-Zadeh A (2012) Comparison between current models for the strength of particulate-reinforced metal matrix nanocomposites with emphasis on consideration of Hall-Petch effect. *Mat Sci Eng A* 531:112–118

4. Kumar H, Chaudhari GP (2014) Creep behaviour of AS41 alloy matrix nano-composites. *Mater Sci Eng A* 607:435–444
5. Zhang Z, Chen DL (2008) Contribution of orowan strengthening effect in particulate-reinforced metal matrix nanocomposites. *Mater Sci Eng A* 483–484:148–152
6. Hassan SF, Tan MJ, Gupta M (2008) High-temperature tensile properties of Mg/Al₂O₃ nanocomposite. *Mater Sci Eng A* 486:56–62
7. Kapoor R, Kumar N, Mishra RS, Huskamp CS, Sankaran KK (2010) Influence of fraction of high angle boundaries on the mechanical behaviour of an ultrafine grained Al–Mg alloy. *Mater Sci Eng A* 527:5246–5254
8. Tun KS, Gupta M (2007) Improving mechanical properties of magnesium using nano-yttria reinforcement and microwave assisted powder metallurgy method. *Compos Sci Technol* 67:2657–2664
9. Li Y, Zhao YH, Ortalan V, Liu W, Zhang ZH, Vogt RG, Browning ND, Lavernia EJ, Schoenung JM (2009) Investigation of aluminum-based nanocomposites with ultra-high strength. *Mater Sci Eng A* 527:305–316
10. Nguyen QB, Gupta M (2010) Enhancing compressive response of AZ31B using nano-Al₂O₃ and copper additions. *J Alloys Compd* 490:382–387
11. Saheb N, Iqbal Z, Khalil A, Hakeem AS, Aqeeli N, Laoui T, Al-Qutub A, Kirchner R (2012) Spark plasma sintering of metals and metal matrix nanocomposites: a review. *J Nano Mater* 2012:1–13
12. Jun Q, Linan A, Blau PJ (2006) Sliding friction and wear characteristics of Al₂O₃–Alnanocomposites. Paper No. IJTC2006-12326 in: Proceedings of STLE/ASME International Joint Tribology Conference, IJTC 2006, 23–25 October 2006, San Antonio, TX, USA, pp 59–60
13. Rohatgi PK, Schultz B (2007) Lightweight metal matrix nanocomposites—stretching the boundaries of metals. *Mater Matters* 2:16
14. Zhou S, Zhang X, Ding Z, Min C, Xu G, Zhu W (2007) Fabrication and tribological properties of carbon nanotubes reinforced Al composites prepared by pressureless infiltration technique. *Compos A* 38:301–306
15. Beni HA, Alizadeh M, Ghaffari M, Amini R (2014) Investigation of grain refinement in Al/Al₂O₃/B₄C nano-composite produced by ARB. *Compos B* 58:438–442
16. Mazahery A, Shabani OS (2013) Plasticity and microstructure of A356 matrix nano composites. *J. King Saud Univ. – Eng. Sci.* 25:41–48
17. Gan YX (2012) Structural assessment of nanocomposites. *Micron* 43:782–817
18. Casati R, Vedani M (2014) Metal matrix composites reinforced by nano-particles—a review. *Metals* 4:65–83
19. Sadeghian Z, Lotfi B, Enayati MH, Beiss P (2011) Microstructural and mechanical evaluation of Al-TiB₂ nanostructure composite fabricated by mechanical alloying. *J Alloys Compd* 509:7758–7763
20. Vintila R, Charest A, Drew RAL, Brochu M (2011) Synthesis and consolidation via spark plasma sintering of nanostructured al-5356/B₄C composite. *Mater Sci Eng A* 528:4395–4407
21. Mazaheri Y, Karimzadeh F, Enayati MH (2011) A novel technique for development of A356/Al₂O₃ surface nanocomposite by friction stir processing. *J Mater Process Technol* 211:1614–1619
22. Prabhu B (2005) Microstructural and mechanical characterization of Al–Al₂O₃ nanocomposites synthesized by high-energy milling. M.S. Thesis, University of Central Florida, Orlando, FL, USA
23. Choi HJ, Shin JH, Min BH, Bae DH (2010) Deformation behaviour of Al–Si alloy based nanocomposites reinforced with carbon nanotubes. *Compos A* 41:327–329
24. Morsi K, Esawi AMK, Lanka S, Sayed A, Taher M (2010) Sparkplasma extrusion (SPE) of ball-milled aluminium and carbon nanotube reinforced aluminium composite powders. *Compos A* 41:322–326
25. Jafari M, Abbasi MH, Enayati MH, Karimzadeh F (2012) Mechanical properties of nanostructured Al₂O₃–MWCNT composite prepared by optimized mechanical milling and hot pressing methods. *Adv Powder Technol.* 23:205–210

26. Korayem MH, Mahmudi R, Poole WJ (2013) Work hardening behaviour of Mg-based nano-composites strengthened by Al₂O₃ nano-particles. *Mater Sci Eng A* 567:89–94
27. Kondoh K, Threrujirapong T, Imai H, Umeda J, Fugetsu B (2008) CNTs/TiC reinforced titanium matrix nanocomposites via powder metallurgy and its microstructural and mechanical properties. *J Nanomater* (doi:10.1155/2008/127538)
28. Goh CS, Wei J, Lee LC, Gupta M (2007) Properties and deformation behaviour of Mg–Y₂O₃ nanocomposites. *Acta Mater* 55:5115–5121
29. Luo JJ, Daniel IM (2003) Characterization and modeling of mechanical behaviour of polymer/clay nanocomposites. *Compos Sci Technol* 63:1607–1616
30. Park C, Park O, Lim J, Kim H (2001) The fabrication of syndiotactic polystyrene/organophilic clay nanocomposites and their properties. *Polymer* 42:7465–7475
31. Gorga RE, Cohen RE (2004) Toughness enhancements in poly (methyl methacrylate) by addition of oriented multiwall carbon nanotube. *J Polym Sci Part B Polym Phys* 42:2690–2702
32. Schmidt D, Shah D, Giannelis EP (2002) New advances in polymer/layered silicate nanocomposites. *Curr Opin Solid State Mater Sci* 6:205–212
33. Thostenson E, Li C, Chou T (2005) Review—nanocomposites in context. *J Compos Sci Tech* 65:491–516
34. Liu, J., Fan, S. and Dai, H., 2004, “Recent advances in methods of forming carbon nanotubes”, *MRS Bulletin*, Pp. 244–250
35. Shaffer MSP, Windle AH (1999) Analogies between polymer solutions and carbon nanotube dispersions. *Macromolecules* 32:6864–6866
36. Gong X, Liu J, Baskaran S (2000) Surfactant assisted processing of carbon nanotube/polymer composites. *Chem Mater* 12:1049–1052
37. Jin L, Bower C (1998) Alignment of carbon nanotubes in a polymer matrix by mechanical stretching. *Appl Phys Lett* 73:1197–1199
38. Karousis N, Tagmatarchis N, Tasis D (2010) Current progress on the chemical modification of carbon nanotubes. *Chem Rev* 110:5366–5397
39. Ajayan PM, Stephan O, Colliex C, Trauth D (1994) Aligned carbon nanotube arrays formed by cutting a polymer resin nanotube composite. *Science* 265:1212–1214
40. Thostenson ET, Ren Z, Chou TW (2001) Advances in the science and technology of carbon nanotubes and their composites: a review. *Compos Sci Tech* 61:1899–1912
41. Cadek M, Coleman JN, Barron V, Hedicke K, Blau WJ (2002) Morphological and mechanical properties of carbon-nanotube-reinforced semicrystalline and amorphous polymer composites. *Appl Phys Lett* 81:5123–5125
42. Gobjny FH, Wichmann MHG, Kopke U, Fiedler B, Schulte K (2004) Carbon nanotube-reinforced epoxy-composites: enhanced stiffness and fracture toughness at low nanotube content. *Compos Sci Technol* 64:2363–2371
43. Kearns JC, Shambaugh RL (2002) Polypropylene fibers reinforced with carbon nanotubes. *J Appl Polym Sci* 86:2079–2084
44. Larrondo L, Manley R, St J (1981) Electrostatic fiber spinning from polymer melts. I. Experimental observations on fiber formation and properties. *J Polym Sci Polym Phys* 19:909–920
45. Tibbetts GG, Finegan JC, McHugh JJ, Ting J-M, Glasgow DG, Lake ML (2000) Applications research on vapor-grown carbon fibers. In: Tomanek E, Enbody RJ (eds) *Science and application of nanotubes*, Kluwer Academic/Plenum Publishers, New York, USA, pp 35–51
46. Endo M, Kim YA, Hayashi T, Nishimura K, Matusita T, Miyashita K et al (2000) Vapor-grown carbon fibers (VGCFs)—basic properties and their battery applications. *Carbon* 39:1287–1297
47. Mazumder SK (ed) (2002) *Composites manufacturing: materials, product, and process engineering*. CRC Press LLC, Boca Raton, FL, USA
48. Ornaghi HJ Jr, Bolner AS, Fiorio R, Zattera AJ, Amico SC (2010) Mechanical and dynamic mechanical analysis of hybrid composites molded by resin transfer molding. *J Appl Polym Sci* 118:887–896

49. Jancar J, Douglas JF, Starr FW, Kumar SK, Cassagnau P, Lesser AJ, Sternstein SS, Buehler MJ (2010) Current issues in research on structure-property relationships in polymer nanocomposites. *Polymer* 51:3321–3343
50. Niihara K (1991) New design concept of structural ceramics: ceramic nanocomposites. *J Ceram Soc Jpn* 99:974
51. Gao L, Jin XH, Zheng S (2004) *Ceramic nanocomposites*. Chemical Engineering Publishers, Beijing, China
52. Sukanuma K, Sasaki G, Fujita T et al (1993) Mechanical properties and microstructures of Machinable silicon carbide. *J Mater Sci* 28:1175
53. Mizutani T, Kusunose T, Sando M et al (1997) Fabrication and properties of nano-sized BN-particulate dispersed sialon ceramics. *Ceram Eng Sci Proc* 18:669
54. Oh ST, Lee JS, Sekino T et al (2001) Fabrication of Cu dispersed Al₂O₃ nanocomposites using Al₂O₃/CuO and Al₂O₃/Cu-nitrate mixtures. *Scr Mater* 44:2117
55. Nawa M, Sekino T, Niihara K (1994) Fabrication and mechanical behaviour of Al₂O₃/Mo nanocomposites. *J Mater Sci* 29:3185
56. Nawa M, Yamazaki K, Sekino T et al (1994) A new type of nanocomposite in tetragonal zirconia polycrystal-molybdenum system. *Mater Lett* 20:299
57. Sekino T, Niihara K (1995) Microstructural characteristics and mechanical properties for Al₂O₃/metal nanocomposite. *Nanostruc Mater* 6:663
58. Sekino T, Niihara K (1997) Fabrication and mechanical properties of fine-tungsten-dispersed alumina-based composites. *J Mater Sci* 32:3943
59. Ji Y, Yeomans JA (2002) Processing and mechanical properties of Al₂O₃-5 vol% Cr nanocomposites. *J Eur Ceram Soc* 22:1927
60. Sekino T, Nakajima T, Satoru U et al (1997) Reduction and sintering of nickel-dispersed-alumina composite and its properties. *J Am Ceram Soc* 80:1139
61. Kusunose T, Sekino T, Chao YH et al (2002) Fabrication and microstructure of silicon nitride/boron nitride nanocomposite and its properties. *J Am Ceram Soc* 85:2678
62. Li YL, Qiao GJ, Jin ZH (2002) Machinable, Al₂O₃/BN composite ceramics with strong mechanical properties. *Mater Res Bull* 38:1401
63. Li YL, Zhang JX, Qiao GJ et al (2005) Fabrication and properties of machinable 3Y–ZrO₂/BN nanocomposites. *Mater Sci Eng A* 397:35
64. Wang XD, Qiao GJ, Jin ZH (2004) Fabrication of machinable silicon carbide-boron nitride ceramic nanocomposites. *J Am Ceram Soc* 87:565
65. Meyyappan M (ed) (2004) *Carbon nanotubes: science and application*. CRC Press LLC, Boca Raton, FL, USA
66. Giannelis EP (1996) Polymer layered silicates nanocomposites. *Adv Mater* 8:29–35
67. Reichert P, Kressler J, Thomann R, Mulhaupt R, Stoppelmann G (1998) Nanocomposites based on a synthetic layer silicate and polyamide-12. *Acta Polym* 49:116–123
68. Yano K, Usuki A (1993) Synthesis and properties of polyimide-clay hybrid. *J Polym Sci Part A Polym Chem* 31:2493–2498
69. Yano K, Usuki A, Okada A, Kurauchi T (1991) Synthesis and properties of polyimide-clay hybrid. *Polymer Prep* 32:65
70. Park JH, Jana S (2003) Mechanism of exfoliation of nanoclay particles in epoxy-clay nanocomposites. *Macromolecules* 36:2758–2768
71. Singerman SA, Jackson JJ (1996) Super alloys. In: Kissinger RD, Deye DJ, Anton DL, Cetel AD, Nathal MV, Pollock TM, Woodford DA (eds) *The Minerals, Metals and Materials Society*, Warrendale, PA, USA, pp 579–586
72. Koo J, Pilato L (2005) Polymer nanostructured materials for high temperature applications. *SAMPE Journal* 41(2):7–19
73. Transparent nanocomposites for aerospace applications. *Adv Compos Bullet*, Feb 2004
74. Pfeiffer K-H, Peetz K (2002) All-ceramic body flap qualified for space flight on the X-38. In: 53rd International Astronautical Congress. 10–19 October, 2002, Houston, TX, USA

Part III
Special Materials

Chapter 18

Monolithic Ceramics for Aerospace Applications

N. Eswara Prasad and S.B. Bhaduri

Abstract Following a brief introduction to monolithic structural ceramics and their mechanical properties and micromechanisms of toughening, the materials development and salient features of various high- and ultrahigh-temperature (UHT) ceramics are discussed. The discussion includes alumina, zirconia, silicon nitride, silicon carbide, molybdenum disilicide and carbon-based ceramics. Subsequently, emerging ceramics such as the titanium- and zirconium-boride ceramics are introduced and discussed. Finally, the Indian scenario on the development and production of these materials is described.

Keywords Ceramics · Mechanical properties · Creep · Thermal shock · Fracture · Applications

18.1 Introduction

The class of modern and advanced ceramics represents enabling materials, which in certain cases represent the only choices for numerous twenty-first century applications, such as in advanced electronics, telecommunications, optical, functional, sensor, heat engine, turbine, defence and aerospace applications.

This chapter on ceramics will focus on the materials that are both established and potentially important for ultrahigh-temperature (UHT) service (≥ 1200 °C). The motivation here is to review their applications in defence and aerospace where UHT conditions are frequently encountered. Ceramic-based materials are both attractive and viable UHT structural materials of the present era, thanks to several decades of dedicated global efforts in the areas of:

N. Eswara Prasad (✉)
DMSRDE, DRDO, Kanpur, India
e-mail: nep@dmsrde.drdo.in

S.B. Bhaduri
Department of MIME and Surgery, University of Toledo, Toledo, OH, USA
e-mail: sarit.bhaduri@utoledo.edu

- Innovative materials design (leading to newer toughening mechanisms).
- Advanced materials research (leading to newer materials including composites and coatings).
- Development of novel processing methods (establishing close control over atomic-scale, nano-scale and micro-scale structures).
- Sophisticated and well-established characterization techniques (covering a wide range of structure and physical and mechanical properties).
- Applications of several unconventional yet effective design methodologies (including advanced statistical analyses and computer simulated methods).

To describe the targeted applications, this chapter will begin with a discussion on important mechanical properties and strategies to improve them. Subsequently, the chapter will focus on specific materials. Since it is beyond the scope of the present review to cover the materials that are on the horizon for other applications, the reader is advised to refer to the literature [1–19] (especially the overviews and Ref. [15]).

18.2 Mechanical Properties

18.2.1 Strength Properties

The strength in ceramics is commonly defined as the materials' resistance to tensile stresses. Other modes used are 3- and 4-point bending and compression; although these are still used by materials developers, they are only of minor importance with respect to design and materials selection.

A tensile test enables a homogeneous stress distribution and a pure uniaxial stress state. This provides the clearest procedure to determine the tensile strength. However, tensile testing at ambient and ultrahigh temperatures is not only tedious but also very difficult due to complicated specimen clamping, which is necessary to avoid superimposed bending moments. Several standard test procedures are being established [8] to provide details of tensile strength determination. On the other hand, the procedures to determine the bend and compressive strengths are well established [20–22], and these properties are in fact much easier to determine. However, as mentioned earlier, they are of little or no practical use for design.

18.2.2 Fracture Toughness

Most ceramic components and structures fail from inherent discontinuities (natural flaws) when growing cracks attain a critical size. Owing to the inherent low fracture toughness of ceramics, the critical flaw sizes are often in the size range of the discontinuities. This is *the* major limitation for structural ceramics.

The critical crack size depends on the fracture toughness (expected to be lowest for mode-I or tensile loading); the distribution of flaws and flaw sizes ahead of the crack tip; crack wake zone effects; and finally the state of stress and environment. The methods of fracture toughness evaluation and methodologies of data analyses, including statistical treatments, are discussed in numerous publications [13–38].

18.2.3 Thermal Shock Resistance

Most ceramic materials are sensitive to thermal shock and thermal fatigue. High thermal stresses due to inhomogeneous temperature distributions during processing and/or service are responsible for extending pre-existing discontinuities and final fracture. If only one single severe thermal cycle occurs, it is called ‘thermal shock’. However, in service several thermal shocks of moderate stresses cause incremental damage leading to final fracture. This latter phenomenon is called ‘Thermal Fatigue’.

Fracture mechanics and non-fracture mechanics tests of the thermal shock resistance of ceramic materials are based on either time-independent stationary thermal stresses and their distributions, or non-stationary thermal stresses which are usually encountered during rapid heating or cooling [39–45]. Some of the important thermal shock parameters, namely the critical temperature difference ($R_s = \sigma_c (1 - \nu)/\alpha E$), thermal shock sensitivities ($R_s' = \lambda R_s$, $R_s'' = R_s'/\rho C_p$; and $R_s''' = K_{Ic}^2/\sigma_c^2$) and the related physical (α , E , ν , λ , ρ and C) and mechanical (σ_c and K_{Ic}) properties, can be obtained from the literature [39–41]

18.2.4 Creep and Creep Crack Growth

Deformation and failure of ceramics at ultrahigh temperatures are governed by creep and creep crack growth effects, respectively. Creep failure, otherwise known as ‘creep rupture’, is caused by the formation, extension and coalescence of creep cracks. The damage phenomena leading to this rupture process are in general (i) the formation of grain boundary cavities, (ii) growth of these cavities leading to microcrack formation, and (iii) growth of the microcracks [46, 47]. Langdon and co-workers [44, 48, 49] have done pioneering work on modelling the creep and creep damage process.

Property characterization in the fields of creep and creep rupture/creep crack growth include tensile, compression, flexure (3- or 4-point bend); indentation; tension/compression under variable stresses; crack growth with determination of the

stress intensity factor (K); and creep crack growth parameters C_h^* (primary creep region), C^* (secondary creep region) and crack growth for the entire regime (da/dt as a function of C^*) [44–52].

18.2.5 Mechanical Property Improvements via Toughening Micro Mechanisms

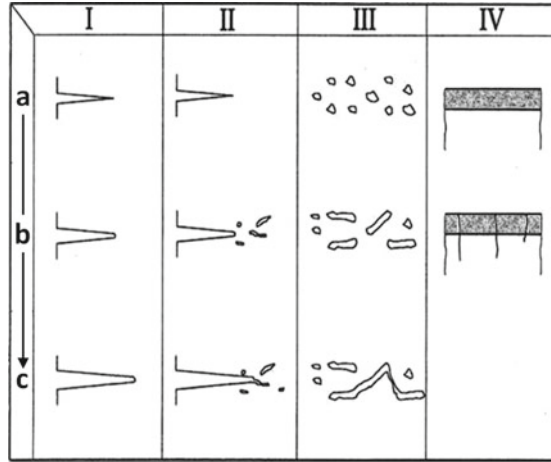
Toughening in ceramics [as well as in ceramic matrix composites (CMCs)] controls most structural and mechanical properties. This may be understood from the basic equation of linear elastic fracture mechanics (LEFM) that relates the fracture strength (σ_f) with the flaw bearing capability (in terms of the maximum flaw size (c) and the linear elastic (plane-strain) fracture toughness (K_{Ic}):

$$\sigma_f = \{K_{Ic}/Yc^{1/2}\} \quad (18.1)$$

where Y is a geometrical factor, which depends on the crack morphology and alignment with respect to the stress axis.

From Eq. (18.1) one can see that the fracture stress of a material can be enhanced if the flaw size is minimized. Several researchers [22, 32, 36] have shown that the fracture toughnesses of glasses and ceramic single crystals lie in the range 0.5–2 MPa \sqrt{m} . And Becher [17] states that most ceramic polycrystals that do not employ any toughening mechanisms will never exceed a fracture toughness of 5 MPa \sqrt{m} .

To achieve a fracture strength of 1000 MPa in a material with a fracture toughness (K_{Ic}) of 5 MPa \sqrt{m} , one needs to control the flaw size within 20 μm (assuming a disc-shaped flaw with $Y = 1.128$). Process control in current ceramic material technologies aims to contain initial inherent discontinuities (flaws) that are much less than this limiting flaw size by developing ultrafine powders, special forming and sintering techniques, and controlled final finish forming and machining [13, 14]. However, there is a limit to minimizing the inherent discontinuity size, since processing with extremely fine powders poses several problems [14]. Furthermore, a ceramic material containing an accidentally large ‘rogue’ flaw can have very dangerous implications because the material may fail catastrophically at stresses much below the design stress. Hence newer design methodologies simultaneously attempt to improve the fracture toughness by invoking one or more of the toughening mechanisms listed in Fig. 18.1.



General Mechanism	Detailed Micromechanism(s)
Crack Deflection [56-59]	Tilt and twist of crack plane around the grains and second phase particles.
Crack Bowing [60,61]	Bowing of the crack plane between two second phase crack pinning points.
Crack Branching [62,63]	Cracks may subdivide into two or more branches, which ultimately result in parallel cracks.
Crack Tip Shielding by Process zones	<ol style="list-style-type: none"> 1. Microcracking [64,65]. 2. Transformation toughening [18,66-69]. 3. Ductile yielding in the process zone (occurs essentially in ductile reinforcements [69]).
Crack Tip Shielding by Crack Bridging [18,19,69-78]	<ol style="list-style-type: none"> 1. Fibre reinforcements and their partial disbonding. 2. Frictional and ligamentary grain bridging. 3. Second phase ductile ligament bridging.

Fig. 18.1 Failure mechanisms under high temperature conditions: *I–IV*: various modes of failure (*I* From existing crack; *II* Crack tip pore formation and coalescence with the main crack; *III* Pores due to creep deformation without the requirement of any pre-existing crack; and *IV* Oxidation) [35]. The subdivisions *a* → *c* indicate damage evolution with time

18.3 Ultrahigh-Temperature Ceramics for Aerospace Applications

The focus of this section will be on structural ceramics for high and ultrahigh temperature applications, describing some of the candidate materials. Modern high-performance ceramics are the ‘enabling’ materials for many advanced technologies. With the recent interest in developing hypersonic aerospace vehicles and re-usable atmospheric re-entry vehicles, interest in such materials has increased significantly in the last few years.

Most high-performance ceramics under development today are based on silicon nitride, silicon carbide, zirconia, dispersion toughened alumina or CMCs [76–83]. Zirconia and Cr₂O₃ based coatings have proven successful in many gas turbine and diesel applications [76, 83]. Analogously, SiC, Al₂O₃ and mullite fibres are finding applications as reinforcements in ceramic composites.

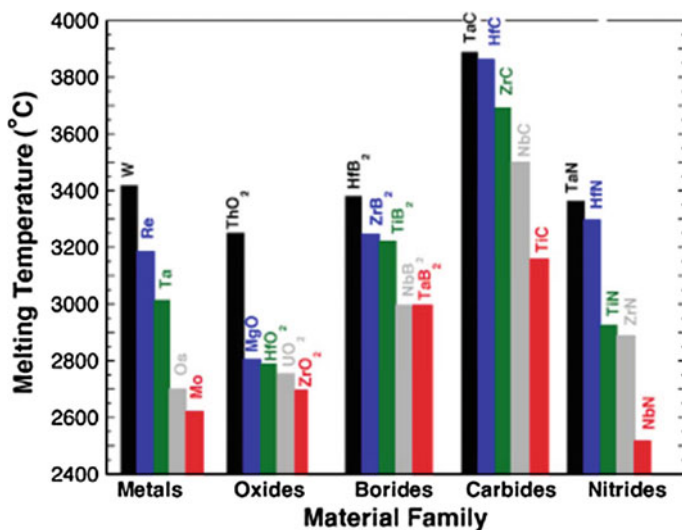


Fig. 18.2 Melting points of transition metals and their binary compounds, showing the superior high temperature capability (in terms of higher melting temperatures) of some ceramic materials, particularly carbides [84]

Last but not least, binary compounds of transition metals have generated considerable attention. Figure 18.2 presents a comparative summary of the melting points of transition metals and their compounds [84]. It is seen that carbides have the highest melting points. However, by the same token, it is difficult to process them into monolithic shapes. As opposed to carbides, borides have somewhat lower melting points and therefore are easier to work with. Table 18.1 lists some important transition metal borides with their melting points and density values.

Table 18.1 Properties of transition metal borides [84]

Metal boride	Density (gm/cm ³)	Melting point (°C)
TiB ₂	4.38	3225
ZrB ₂	6.17	3246
HfB ₂	11.2	3650
VB ₂	5.10	2450
NbB ₂	7.5	3050
NbB ₂	6.97	3050
TaB ₂	14.2	2040
TaB ₂	11.2	3100
CrB ₂	5.20	2170
Mo ₂ B ₅	7.48	2370
W ₂ B ₅	14.8	2370

18.3.1 Alumina Ceramics

Pure aluminium oxide, Al_2O_3 , has only one thermodynamically stable phase, the hexagonal α -phase (corundum). Ceramics based on alumina have been used for many years. These traditional ceramics are, however, unsuitable for high temperature structural applications, but within the last three to four decades a family of toughened aluminas has been developed. Alumina has been toughened by the addition of ZrO_2 dispersoids (zirconia toughened alumina, ZTA), and by the incorporation of SiC-whiskers.

ZTA consists of a polycrystalline α - Al_2O_3 matrix with a dispersion of ZrO_2 particles. The ZrO_2 can be either tetragonal and/or monoclinic, and is almost without exception located in the alumina grain boundaries. However, a ZTA containing intragranular *t*- ZrO_2 particles and intergranular *m*- ZrO_2 particles has been produced by sol-gel methods.

ZTAs are toughened by transformation toughening when *t*- ZrO_2 particles are present. These materials also exhibit a great deal of toughening due to microcracking (which hinders the growth of the main crack) when *m*- ZrO_2 is present. There appears to be a critical size associated with microcrack toughening just as there is with transformation toughening [76, 77]. If the zirconia particles are too small, the stresses produced upon transformation will be insufficient to nucleate microcracks. If the particles are too large, the stress field caused by transformation will, in addition to nucleating microcracks, also spontaneously extend them, thereby weakening the material. When both phases of zirconia are present, both transformation and microcrack toughening are active.

Further, the reinforcement of alumina by short, discontinuous SiC-whiskers ($\sim 0.5 \mu\text{m}$ diameter and $\sim 30 \mu\text{m}$ length) greatly improves the strength and fracture toughness [77–79]. Both the strength and fracture toughness increase with increasing whisker content. These properties are maintained up to temperatures in the 1000°C range. The primary toughening mechanism appears to be crack deflection by the SiC-whiskers, although there is some contribution by whisker pull-out.

18.3.2 Zirconia Ceramics

Zirconia (ZrO_2) has three allotropes—monoclinic (room temperature to 950°C), tetragonal (950 – 2370°C) and cubic (above 2370°C). The tetragonal to monoclinic transformation is martensitic, and so the tetragonal phase cannot be quenched to room temperature in the form of pure ZrO_2 . Uncontrolled transitions are undesirable because they are accompanied by a shear strain of ~ 0.16 and a volume expansion of $\sim 4\%$.

The addition of certain stabilizing oxides (MgO , CaO , Y_2O_3 , etc.) suppresses the uncontrolled phase transformations. These additions in small amounts result in a

two-phase material referred to as partially stabilized zirconia (PSZ), consisting of a cubic (*c*) matrix and tetragonal (*t*) and/or monoclinic (*m*) precipitates, depending on the thermal history.

It was in PSZ that Garvie et al. [88] first noted the importance of t-ZrO₂ precipitates in enhancing toughness. When a crack is present in PSZ (and in related ZrO₂ toughened materials such as TZP) the stress field near the crack tip causes the metastable t-ZrO₂ to transform to the monoclinic symmetry.

The transformation absorbs energy which would otherwise assist in advancing the crack, thereby increasing the resistance to crack growth, hence the use of the term ‘Transformation Toughening’. This ability makes zirconia ceramics unique among structural ceramics and prompted Garvie et al. [88] to label them ‘ceramic steels’ in their initial report, drawing the analogy with phase transformations in iron.

PSZ is classified by microstructure: conventional PSZ, fine-grained PSZ, polycrystalline tetragonal zirconia, fine-grained monoclinic, overaged conventional and single crystal PSZ.

Conventional PSZ ceramics are stabilized by the addition of MgO, CaO, Y₂O₃ or rare earth oxides such as CeO₂. They are usually sintered in the cubic solid solution field (1600–1900 °C). Appropriate cooling produces microstructures containing 50–100 μm c-ZrO₂ grains with coherent t-ZrO₂ precipitates dispersed within the cubic grains. The t-precipitates are then coarsened in the 1300–1500 °C range to optimize their ability to undergo the stress-induced transformations to m-ZrO₂ [63, 88–92].

The above process can be simplified by combining sintering and ageing into a single step heat treatment in the two-phase cubic/tetragonal field. This produces similar microstructures and properties.

Tetragonal zirconia polycrystals (TZP) are fine-grained, single-phase materials stabilized by Y₂O₃ (Y-TZP) or rare earth oxides CeO₂ (Ce-TZP). The constraints imposed by grains on each other allow the retention of the tetragonal phase. While the grain size is usually between 0.1 and 1.0 μm depending on the Y₂O₃ solute content (usually 1.5–5.0 wt%) and the density of the material, in the case of Ce-TZP a larger grain size is allowable (~10 μm).

Sintering takes place in the tetragonal field of the respective binary phase diagrams. The detrimental problem of Y-TZP ceramics is the *t* → *m* transformation at intermediate temperatures (200–400 °C) in humid atmospheres [92]. Ce-TZP does not have this problem.

18.3.3 Silicon Nitride Ceramics

Silicon nitride exists in two phases, α and β, both of which have hexagonal crystal structures. The α phase has a unit cell approximately twice as large as that of the β phase. The silicon nitride based ceramics include hot-pressed, reaction-bonded,

sintered and hot isostatic pressing (HIP) materials and also the β' -SiAlONs (a solid solution of Al_2O_3 and/or other metal oxides in the β - Si_3N_4 lattice).

Hot-pressed Si_3N_4 is produced by either conventional uniaxial or hot isostatic pressing (HIP). In these processes [95] one starts with α - Si_3N_4 powder and adds a densification aid such as MgO, Y_2O_3 , or SiBeN₂. Almost all hot-pressed silicon nitrides have room temperature flexural strengths of 690 MPa or higher, and retain these strengths to at least 1000–1200 °C, as well as exhibiting excellent resistances to thermal shock, erosion and corrosion.

Depending on the purity and phase composition of the starting Si_3N_4 powder, the type and percentage of additive, the milling and mixing procedures, and the hot-pressing parameters (temperature, time and pressure), one can obtain a wide variety of strength versus temperature, creep, or oxidation behaviours.

Of all the available high temperature structural ceramics, hot-pressed Si_3N_4 with MgO as a densification aid (typified by the Norton Company's NC-132 material) most nearly possesses the reproducible mechanical properties expected of a true engineering material. However, the presence of a magnesium silicate grain boundary phase causes a rapid decline in strength, creep and oxidation resistance between 1200 and 1350 °C.

Since it was apparent that the limitations of hot-pressed silicon nitride were due to the nature of the grain boundary phase and not intrinsic to the Si_3N_4 itself, Tsuge and his co-workers at Toshiba [93] and others [94, 95] have focussed their attention on controlled modification of the grain boundaries.

Sintered silicon nitrides are a more recent development [95]. The balance between dissociation of the Si_3N_4 and densification during sintering is such that material of only about 90 % theoretical density is obtainable with normal sintering processes. However, near full density sintered Si_3N_4 has been achieved using a nitrogen overpressure and other techniques to suppress the density-limiting dissociation of Si_3N_4 at the sintering temperatures.

In addition, high density preforms of Si_3N_4 can also be produced by conventional HIPping. These are more uniformly dense with higher Weibull moduli, and generally have lower component rejection rates than other silicon nitrides. HIPped Si_3N_4 also allows for more precise shape-definition. This eliminates most post-consolidation machining.

SiAlONs are an important new class of ceramic materials that are solid solutions of metal oxides in the β - Si_3N_4 crystal structure [94]. These solid solutions produce a distorted β - Si_3N_4 lattice; hence they are referred to as β' -SiAlONs.

SiAlONs were originally developed with Al_2O_3 , but MgO, BeO, Y_2O_3 and others have all been found to yield β' solid solutions, as well as a variety of other phases. Although SiAlONs were intended for applications in heat engines, they have not yet been extensively used in engine demonstration programmes, though this is likely to change.

Since SiAlON phases are present in the grain boundaries of most hot-pressed or sintered Si_3N_4 , they control the high-temperature behaviour of these materials.

Therefore understanding the phase relationships in these systems is of major importance.

18.3.4 Silicon Carbide Ceramics

Silicon carbide can be produced with either cubic (β) or hexagonal (α) crystal structure. The silicon carbide-based ceramics include hot-pressed, sintered, reaction-sintered, and chemically vapour-deposited (CVD) SiCs; and composites of SiC fibres in a silicon matrix [78, 96, 97].

Hot-pressed SiC can be fabricated to full density and high strength by using additions of boron and carbon or Al_2O_3 to either α or β SiC starting powder [87]. Hot-pressing is typically accomplished at temperatures of 1900–2000 °C with pressures of 35 MPa. This product is surpassed in strength only by hot-pressed silicon nitrides at low to moderate temperatures, and has a higher strength than any of the silicon nitride based ceramics in the range 1300–1400 °C.

However, hot-pressed SiC has the major drawback of requiring expensive diamond-machining to form shaped components. This has tended to focus industrial development on developing a sinterable SiC, which can be shaped into components in the ‘green’ (unfired) soft and relatively easily shaped state.

Sintered silicon carbide is a major accomplishment in ceramic science and technology. Until 1978 it was widely believed that SiC could not be conventionally sintered to full density because its highly covalent bonds precluded the volume- or grain boundary-diffusion required for densification.

However, in 1978 Prochazka [78] demonstrated that a very fine (sub-micrometre) β -SiC powder with a low oxygen content (< 0.2 wt% oxygen) and small additions of boron and carbon (about 0.5 and 1 wt%, respectively) could be sintered to nearly full density at temperatures of 1950–2100 °C under an inert gas or in vacuo, and without applying pressure. There are three reasons for this achievement:

- (1) The ultrafine powder provides a high thermodynamic driving force for densification as well as short diffusion distances.
- (2) Boron appears to accelerate both volume and grain boundary diffusion.
- (3) Carbon removes the SiO_2 layer from the SiC powders.

Prochazka also demonstrated that sintered β -SiC could be formed into useful shapes by slip casting, die pressing and extrusion. However, non-uniform distribution of the carbon additive and exaggerated grain growth of α -SiC were found to interfere with densification. This problem might be solved using α -SiC for the starting powder rather than β -SiC.

Reaction-sintered silicon carbides cover a wide range of compositions and manufacturing processes, in which a plastic body is formed from SiC powder, graphite

and a plasticizer. In some variants of the process SiC powder plus a char-forming binder are also used.

The plastic body is pressed, extruded, injection-moulded, or otherwise formed into a green body. The plasticizers are burned off or converted to a porous char by pyrolysis. Silicon ‘metal’ as a liquid or vapour is infiltrated into the body and reacts with the graphite powder or char to form SiC in situ, thereby reaction-sintering the components. Excess silicon (typically 2–12 wt%) is usually left to fill any voids, thus yielding a nonporous body.

Such materials exhibit quite reasonable strengths up to the melting point of silicon (1400 °C) or beyond, depending on the amount of retained free silicon: this free silicon is a problem in applications where temperatures above 1300 °C are likely to be encountered. The major advantage of these materials is that they maintain the geometry of the green preform after conversion to SiC. Thus little machining is required and the component cost is relatively low. A variety of successful experimental gas turbine components like combustors or stators have been made by this material-processing route.

Reaction-formed SiC fibre/Si composites have been developed by Prochazka [78]; and also Prasad and co-workers [97]. These are among the first engineered ceramic composite structural materials. The process consists of (i) starting with a graphite cloth, tow, felt, chopped fibre array or any other possible precursor; (ii) making a preform by any one of a variety of routes, and (iii) infiltrating the preform with liquid Si. The molten Si reacts with the filamentary graphite materials to form polycrystalline SiC fibres in a silicon matrix.

The result is a fully dense oxidation-resistant body with about 30–50 % Si fibres. This material is quite distinct from reaction-sintered SiC, and it permits the design of a composite component optimized for mechanical and thermal requirements.

The presence of free silicon would be expected to limit usage temperatures to 1400 °C. Despite this, the material has been used in an experimental combustion liner at temperatures above 1425 °C and also for ceramic vanes.

Chemically vapour-deposited (CVD) SiC is a fully dense material with no additives. However, the strength of CVD SiC, which on occasion can be very high, is variable. The large scatter in strength is due to the occurrence of large columnar grains and residual deposition stresses. Although CVD SiC has been produced in complex shapes, the technique may be too costly for production.

18.3.5 Molybdenum Disilicide ($MoSi_2$) Ceramics

$MoSi_2$ has a tetragonal (non-cubic) crystal structure, a high melting point (2030 °C), moderate density (6.31 g/cm³) and excellent oxidation resistance at temperatures above 600 °C. It is an abundant material, which is non-toxic and

environmentally benign [98, 99]. It can be electro-discharge machined due to its low electrical resistivity.

The strength of MoSi_2 compares favourably with that of SiC/SiC composite up to at least 1250 °C. The strength is strain rate sensitive, i.e. the strength increases with increasing strain rate. Recent work with single crystal MoSi_2 indicates that although it has a sufficient number of independent slip systems, the critical resolved shear stress necessary to activate the hardest orientations is extremely high at temperatures below 1300 °C [100–102].

MoSi_2 is inherently brittle at low temperatures: the ductile to brittle transition temperature (DBTT) is approximately 1000 °C. Dislocations and stacking faults were reported to be active during elevated temperature deformation, thus rendering the deformation to be relatively ductile in nature, in contrast to that exhibited by most ceramic materials [100, 101].

MoSi_2 is also known to exhibit excellent high temperature oxidation behaviour up to 1600 °C. The material forms glassy silica layers at high temperatures, and these are excellent diffusion barriers against oxidation. However, MoSi_2 can disintegrate rapidly during oxidation at temperatures around 500 °C, a phenomenon called PESTING. Qualitatively, the pest effect may be correlated with the tetragonal crystal structure and hence a highly anisotropic coefficient of thermal expansion (CTE) and the high DBTT: residual microstresses at grain boundaries can occur and result in microcracks, followed by brittle failure.

PESTING does not occur in materials of density greater than 98 %, crack- or pore-free samples and in stress-free single crystals. PESTING can also be minimized by the addition of MoGe_2 , which alters the viscosity and CTE of the SiO_2 layer.

Solid solution alloying of MoSi_2 has been attempted in order to improve its high temperature mechanical properties. Specifically, WSi_2 has been added owing to the similarity in crystal structure and lattice parameters with MoSi_2 , and this leads to significant improvements in high temperature strength and creep resistance. However, the effects of WSi_2 on room temperature ductility are very limited.

In view of their attractive properties, MoSi_2 and its composites are considered to be one of the most promising classes of candidate materials to be used in gas turbine engines expected to operate at temperatures up to 1600 °C [98–103]. More details of this class of materials are given in Chap. 10 of this Volume.

18.3.6 Carbon Ceramics

Carbon is a unique element with two allotropic forms, diamond and graphite, exhibiting very different properties. Diamond is extremely hard and abrasive, but graphite is extremely soft and a lubricant. Diamond consists of a regular three-dimensional network of strong covalent bonded carbon atoms, whereas in graphite the carbon atoms are held together by strong covalent bonds in *layers* of

two-dimensional hexagonal networks, with the layers held together by weak Van der Waals forces.

Apart from these defined allotropic forms, carbon can take any number of quasi-crystalline forms ranging from amorphous or glassy carbon to highly crystalline graphite. The latest developments are fullerenes (C60) and carbon nanotubes (CNTs).

Carbon and graphite are attractive materials for use at elevated temperatures in inert atmospheres and ablative environments. However, the use of monolithic carbon or particulate carbon composites is greatly limited by their brittle mechanical behaviour, low failure strains, thermal shock sensitivity, anisotropy, and processing difficulties associated with large and complex shapes.

Carbon-carbon (C-C) composites have been developed [43] to overcome the limitations of monolithic carbon. A detailed account of these UHT C-C composites, which have been developed based on 'Crack Bridging' toughening, is given in Chap. 16 of this Volume.

18.4 Emerging Monolithic Ceramics for Aerospace Applications

The focus of this section will be on borides, especially those of titanium and zirconium. The most important compounds in these systems are TiB₂ and ZrB₂. Table 18.2 summarizes the properties of these two materials. Their unique combination of properties makes them eminently suitable for aerospace applications.

18.4.1 Titanium Boride Ceramics

Ti-B System The phase diagram of the Ti-B binary system is shown in Fig. 18.3 [105]. Three compounds are known to exist: orthorhombic TiB, orthorhombic

Table 18.2 Comparison of properties between TiB₂ and ZrB₂ [104]

Properties	TiB ₂	ZrB ₂
Melting point (°C)	3225	3245
Density (gm/cm ³)	4.52	6.12
Thermal expansion (10 ⁻⁶ K ⁻¹)	$\alpha_c = 6.6$; $\alpha_c = 8.6$	5.9 (avg.)
Thermal conductivity (W m ⁻¹ K ⁻¹)	60-120	60
Electrical resistivity (10 ⁻⁶ Ω cm)	10-30	10
Elastic modulus (GPa)	530	489
Hardness (GPa)	25-30	21-23
Fracture toughness (MPa√m)	5-7	3.5-4.2

Ti_3B_4 and hexagonal TiB_2 . Their respective melting points and homogeneity ranges are evident from the phase diagram. Of the three compounds, TiB_2 has been researched over a long time, while research on TiB is more recent. In the following, these two materials are discussed in some detail.

Titanium diboride TiB_2 powder can be synthesized via reduction processes, chemical routes and reactive processes [104]. In a typical reduction technique, titanium oxide may be reduced with boron and carbon [106]. Alternatively, nanocrystalline TiB_2 has been synthesized using solution/gas phase reactions [107, 108].

Mechanical alloying of Ti and B can also result in TiB_2 nanoparticulates, although there may be some possibility of contamination from the grinding media [109]. Finally, combustion processes (also known as self-propagating high temperature synthesis reactions (SHS), especially in the former Soviet Union) have been successfully used to synthesize TiB_2 [110, 111].

After synthesis, the powders can be densified by sintering. There are two major problems associated with sintering TiB_2 to high density [112–114]:

- (1) A thin oxygen rich layer (mainly TiO_2 and B_2O_3) is present on the surface of TiB_2 powders, irrespective of the synthesis route [112]. Sintering additives to counteract this can be metallic or non-metallic. Metallic additives include Ni, Fe, Fe/Cr [113]. Addition of nitrides such as AlN and TiN, along with the application of pressure, has also been reported to enable very high density [114].

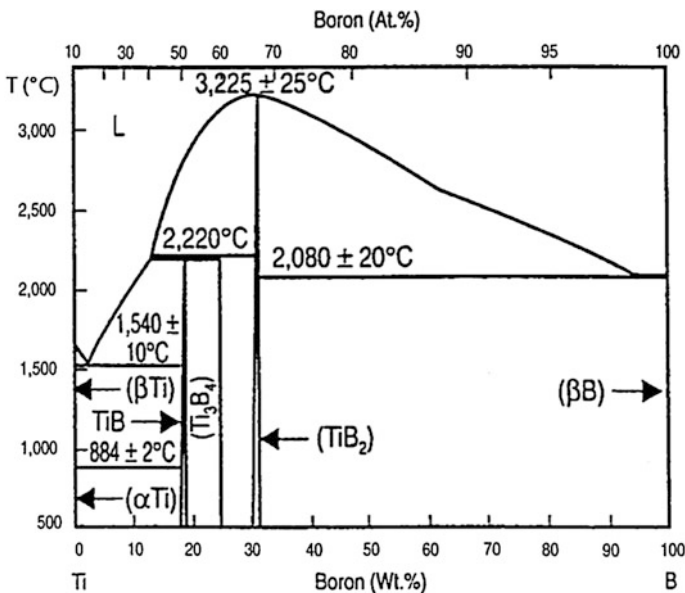


Fig. 18.3 The Ti-B phase diagram [108]

- (2) The second problem is the anisotropic thermal expansion coefficient, which eventually results in microcracks and loss in strength [113]. This happens if the grain size is greater than 15 μm . Thus densification at very high temperatures that results in grain sizes beyond 15 μm should be avoided.

Titanium monoboride Study of TiB and the rest of the Ti–B system is relevant to understanding and using these compounds as opposed to titanium diboride. As noted before, research on TiB is of recent origin. Until recently, synthesis of 100 % TiB was not possible. Since the 1990s Ti–TiB cermet compounds have been synthesized and studied. Ti–TiB composites have gained interest for their unique properties such as high elastic modulus (approximately 370 GPa) [115] and increased strength and deformation resistance owing to TiB whisker-induced strengthening [116].

TiB possesses important and useful properties including high hardness [117] and stiffness [118], high melting point and good chemical stability and thermal conductivity. Furthermore, the strong Ti–B covalent bonding makes Ti–B composites attractive ceramic materials. TiB has been widely used as reinforcement for titanium metal matrix composites [119–121].

Titanium and TiB have very similar densities of 4.50 and 4.56 g/cm^3 , respectively. This makes it possible to increase the TiB volume fraction in a Ti–TiB cermet without significantly increasing the density of the overall composite [120]. In 2006, Cao et al. [121] took advantage of this and developed a Ti–TiB composite with a 95 % volume fraction of TiB. This material has a very high Young's Modulus of about 450 GPa [121]. This value was later given support by Madtha et al. [122] after they synthesized and tested 100 % TiB and found E to be 425 GPa. Synthesis of 100 % TiB was done by reaction-sintering of Ti and TiB_2 [122]. Another method, spark plasma sintering (SPS), has been used by Zhang et al. [123], again using Ti and TiB_2 as reactants.

18.4.2 Zirconium Boride Ceramics

Zr–B System Okamoto initially described the zirconium-boron phase diagram as shown in Fig. 18.4 [124]. There are seven phases in the Zr–B system: liquid, hcp Zr, bcc Zr, $\beta\text{-B}$, ZrB, ZrB_2 and ZrB_{12} [125]. The melting points and the homogeneity ranges of the three compounds are evident from the diagram. Of the three compounds, only ZrB_2 is stable and has gained substantial attention. ZrB is believed to be unstable [126, 127]. The following paragraphs discuss these materials, especially ZrB_2 .

Zirconium diboride Research on ZrB_2 is well documented. Its unique combination of properties has made it an important member of the ultrahigh-temperature ceramics (UTHC) family. ZrB_2 is a grey refractory solid and is considered to have the best oxidation resistance of all refractory materials [128]. It also has excellent

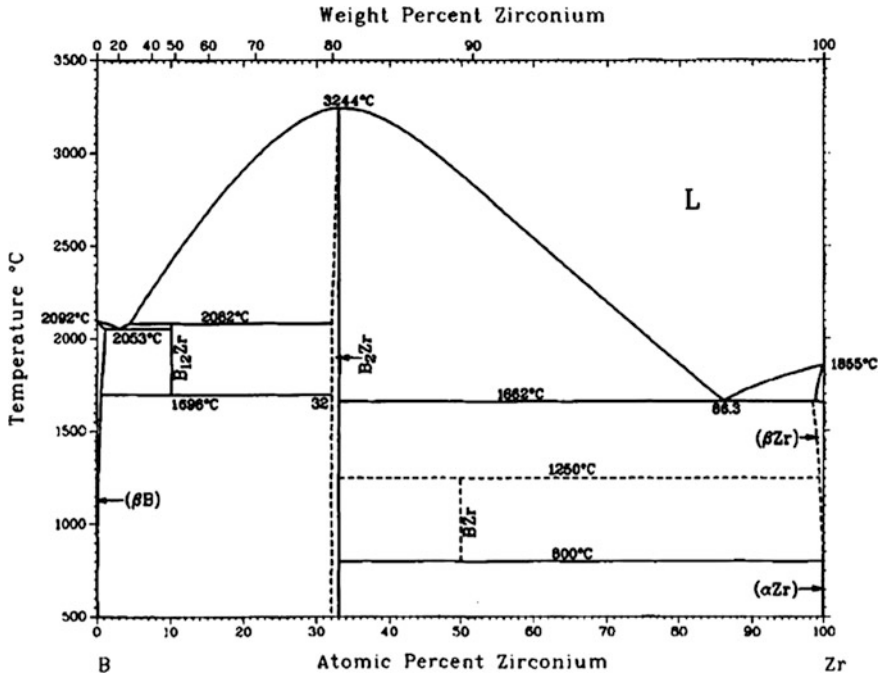


Fig. 18.4 Zr-B phase diagram (after Okamoto [124])

thermal shock resistance and thermal conductivity. However, the density of ZrB_2 is higher than that of TiB_2 [129].

Notable uses of ZrB_2 include a diffusion barrier in semiconductors, a container for molten metals, a burnable absorber in nuclear reactor cores, and perhaps most popularly, a thermal protective layer in aerospace systems that involve hypersonic flight and atmospheric re-entry.

Like its Ti-counterpart, technical-grade ZrB_2 powder can be produced in several ways. The three main synthesis routes are: (i) reduction processes; (ii) chemical routes and (iii) reactive processes. The reduction processes use zirconia as the source with either boron or carbon as reducing agents [130, 131]. Combustion (SHS) processes have also been used.

The powders are densified conventionally (e.g. hot pressing and pressure-less sintering) and non-conventionally, e.g. by reactive densification and SPS. Conventional hot pressing at temperatures $\geq 1800^\circ\text{C}$ with the simultaneous application of pressure has resulted in 99 % theoretical density.

Conventional pressing is useful for making simple shapes; and pressure-less sintering is useful in densifying green powder compacts into complex shapes. Like Ti-borides, sintering aids such as C, and BN, AlN, and SiC have been used [132].

Reactive hot-pressing using Zr, Si and B_4C has been reported in the fabrication of dense ZrB_2 -SiC composites [133]. Finally, SPS using the simultaneous

application of pressure and pulsed electric current has been reported for the fabrication of ZrB_2 based [134].

Zirconium monoboride While ZrB_2 has been well studied, very little attention is now been paid to ZrB . Because of this, it is now gaining importance in fields that require ultrahigh thermal protection, such as re-entry space vehicles. It is hypothesized that ZrB possesses interesting and useful properties that will be applicable in numerous scientific fields. However, (much) more research will be necessary.

18.5 Indian Scenario

The use of monolithic and composite ceramic materials in India has increased steadily in the last 2–3 decades owing to emerging aircraft, missile and space systems. However, there is a serious gap in the technology development and production of these materials in India because of the lack of production facilities for high-quality powders. At present most of the materials are imported, and this includes carbon fibres and structural graphite. It is expected that over the next decade a large number of small- to medium-scale industries will become operative for basic materials production.

Ultrahigh-temperature sintering and hot-pressing facilities are just becoming available in Indian industries. Also, fabrication facilities for components of varied configurations are being built at the system centers in India—mostly in the national units of ISRO, CSIR (especially NAL, Bangalore and CGCRI, Kolkata), DST (ARCI) and DRDO (DMRL, DMSRDE, ASL and DRDL).

18.6 Summary

The use of established and emerging structural monolithic ceramics is increasing in India owing to the evolution of several ongoing and new systems (aircraft, missiles and space). This chapter has discussed some of the known physical and mechanical properties of several monolithic ceramics, and also mentioned their actual and potential applications.

Acknowledgments The authors sincerely acknowledge the support and information they received from several colleagues at DMRL, Hyderabad, and RCMA (Materials), CEMILAC, as well as from other colleagues in India and abroad. They feel particularly indebted to Professor KS Ravi Chandran, Dr. YR Mahajan, Dr. J Subrahmanyam, Dr. VV Bhanu Prasad, Professor Rahul Mitra, Dr. J Janardhan Reddy, Dr. A Chakraborty, Dr. AR James and Mrs. Sweety Kumari. Funding from DRDO and INAE is gratefully acknowledged.

References

1. Bengisu M (ed) (1963) Engineering ceramics. Springer, Berlin, Germany
2. Bailey AE (2001) Electronic ceramics, handbook of ceramics, glasses and diamonds. Harper CA (ed) McGraw Hill, New York, USA, p 3.1
3. Jansen M (ed) (2003) High performance non-oxide ceramics. Springer-Verlag, Berlin, Germany
4. Somiya S et.al. (2003) Handbook of advanced ceramics: processing and their applications. Elsevier, Waltham, MA, USA
5. Handbook of advanced ceramics (2006). Somiya S, Aldinger F, Claussen N, Springs RM, Uchino K, Koumoto K Kaneno M (eds) Processing and applications, vol II. Elsevier India Pvt. Ltd., New Delhi, India, p 1
6. Balasubramanyam R (ed) (2007) Callister's materials science and engineering, Wiley India Pvt. Ltd., New Delhi, India, p 18
7. Riedel R, Chen I-W (ed) (2010) Ceramic Science and Technology, vols 1–3. Wiley-VCH, Verlag, Weinheim, Germany
8. Barry Carter C, Grante Norton M (2013) Ceramic materials: science and engineering. Springer, New York, USA
9. Muralt P (2008) Recent progress in materials issues for piezoelectric MEMS. J Am Ceram Soc 91:1385
10. Haertling GH (1999) Ferroelectric ceramics: history and technology. J Am Ceram Soc 82:797
11. Damjanovic D (1998) Ferroelectric, dielectric and piezoelectric properties of ferroelastic thin films and ceramics. Prog Phys 61:1267
12. Schlom DG, Chen LQ, Pan X, Schmehl A, Zurbuchen MA (2008) A thin film approach to engineering functionality into oxides. J Am Ceram Soc 91:2429
13. Lange FF (1989) Powder processing: science and technology for increased reliability. J Am Ceram Soc 71:3
14. Clegg WJ, Kendall K, Alford NM, Button TW, Birchall JD (1990) A simple way to make tough ceramics. Nature 347:455
15. Evans AG (1990) Perspective on the development of high toughness ceramics. J Am Ceram Soc 73:187
16. Campbell GH, Ruehle M, Dagleish BJ, Evans AG (1990) Whisker toughening: a comparison between aluminium oxide and silicon nitride toughened with silicon carbide. J Am Ceram Soc 73:521
17. Becher PF (1991) Microstructural design of toughened ceramics. J Am Ceram Soc 74:255
18. Munz D, Fett T (1999) Ceramics: mechanical properties, failure behaviour and materials selection. Springer, Berlin, Germany
19. Wang EZ, Shrive NG (1995) Brittle fracture in compression: mechanisms, models and criteria. Eng Fract Mech 52:1107
20. ASTM Standard C 1161-02 (2000) Standard test method for flexural strength of advanced ceramics at ambient temperature, vol 15.01, ASTM International, West Conshohocken, PA, USA, p 220
21. ASTM Standard C 1211-02 (2000) Standard Test Method for Flexural Strength of Advanced Ceramics at Elevated Temperatures, Vol. 15.01, ASTM International, West Conshohocken, PA, USA, p. 266
22. Quinn GD, Morrell R (1991) Design of data for engineering ceramics: a review of the flexure test. J Am Ceram Soc 74:2037
23. Sakai M, Bradt RC (1993) Fracture toughness testing of brittle materials. Int Mater Rev 38:53
24. Fett T, Munz D, Thun G, Hahr HA (1995) Evaluation of bridging parameters in aluminas from R-curves by use of the fracture mechanical weight function. J Am Ceram Soc 78:949

25. Malakondaiah G, Saxena VK, Prasad NE (1996) Fracture toughness evaluation. *Trans Indian Inst Met* 49:697–723
26. Nishida T, Pezzotti G, Mangialardi T, Paolini AE (1996) Fracture mechanics evaluation of ceramics by stable crack propagation in bend bar specimens. *Fract Mech Ceram* 11:107
27. Sakai M, Ishikawa H (1992) Work-of-fracture of brittle materials with microcracking and crack bridging. *Int J Fract* 55:65
28. Nair SV, Wang YL (1998) Toughening behaviour of a two-dimensional SiC/SiC woven composite at ambient temperature: I. Damage initiation and R-curve behaviour; II. Stress—displacement relationship in the crack process zone. *J Am Ceram Soc* 81:1149–1157
29. Esvara Prasad N, Kumari Sweety, Kamat SV, Vijayakumar M, Malakondaiah G (2004) Fracture behaviour of 2d-woven, silica–silica continuous fibre-reinforced, ceramic-matrix composites (CFCCs). *Eng Fract Mech* 71:2589
30. ASTM Standard C 1421 (2002), Standard test methods for determination of fracture toughness of advanced ceramics at ambient temperature, vol 14. ASTM International, West Conshohocken, PA, USA
31. Evans AG, Charles EA (1976) Fracture toughness determination by indentation. *J Am Ceram Soc* 59:371
32. Binner JGP, Stevens R (1984) The measurement of toughness by indentation. *Br Ceram* 83:168
33. Ponton CB, Rawlings RD (1989) Vickers indentation fracture toughness test—Part I: review of literature and formulation of standard indentation toughness equations. *Mater Sci Technol* 5:865–961
34. Antis GR, Chantikul P, Lawn BR, Marshall DB (1981) Elastic/plastic indentation damage in ceramics: the median/radial crack system. *J Am Ceram Soc* 64:533
35. Rice RW (1981) Mechanisms of toughening in ceramic matrix composites. *Proc Ceram Eng Sci* 2:661
36. Rice RW (1984) Mechanically reliable ceramics. *J Phys Chem Solids* 45:1033
37. Rice RW (1985) Ceramic matrix composite toughening mechanisms: an update, In: *Proceedings of ceramic engineering science* 6:589
38. Evans AG, Marshall DB (1989) The mechanical behaviour of ceramic matrix composites. *Acta Metall* 37:2567
39. Kingery WD (1955) Factors affecting thermal shock resistance of ceramic materials. *J Am Ceram Soc* 38:3
40. Hasselman DPH (1969) Unified theory of thermal shock. *J Am Ceram Soc* 52:600
41. Evans AG, Charles EA (1977) Structural integrity in severe thermal environments. *J Am Ceram Soc* 60:22
42. Keller K, Munz D, Fett T (1989) Investigation of the thermal fatigue behaviour of HPSN, SiC and glass, in *Euro ceramics*. Terpstra RA, Metselaar R, (eds) vol. 3. Elsevier Applied Science, London, UK
43. Davidge RW (1986) Perspectives of engineering ceramics in heat engines. In: *Conference proceedings of high temperature alloys for gas turbines and other applications*. Liege, Belgium
44. Cannon WR, Langdon TG (1983) Creep of ceramics. *J Mater Sci* 18:1
45. Riedel H (1987) *Fracture at high temperatures*. Springer, Berlin, Germany
46. Jelwan J, Zarrabi K, Karpour A, Pearce G (2011) High-temperature fracture mechanics: a comprehensive examination with a critical review. *Composites: Mechanics, Computations, Applications* 2:59–81
47. Radovic M, Barsoum MW, El-Raghy T, Wiederhorn SM (2003) Tensile creep of coarse grained Ti_3SiC_2 in the 1000–1200 °C temperature range. *J Alloys Compd* 361:299
48. Yawari P, Langdon TG (1981) In: *Surfaces and interfaces in ceramics and ceramic-metal systems*. Pask JA and Evans AG (eds) Plenum Press, New York, USA p 295
49. Langdon TG (1988) Creep of ceramics. *J Mater Sci* 23:1–20
50. Saxena A (1998) *Nonlinear fracture mechanics for engineers*. CRC Press, Boca Raton, Florida, USA

51. Satyanarayana DVV, Omprakash CM, Sridhar T, Kumar V (2010) Effect of microstructure on creep crack growth behaviour in a near a titanium alloy IMI-834. *Metall Mater Trans A*
52. Kumari S, Eswara Prasad N, Vijayakumar M, Subrahmanyam J (In Preparation) Evaluation of mechanical properties of ceramics and CMCs. DMRL Technical Report, DMRL, Hyderabad, India
53. Faber KT, Evans AG (1983) Crack deflection processes: I theory. *Acta Metall* 31:565
54. Faber KT, Evans AG (1983) Crack deflection processes: II. experiment. *Acta Metall* 31:577
55. Wiederhorn SM (1984) Brittle fracture and toughening mechanisms in ceramics. *Ann Rev Mater Sci* 14:374
56. Eswara Prasad N, Bhaduri SB (1988) Subcritical growth of long cracks in heterogeneous ceramics. *J Mater Sci* 23:3106–3112
57. Lange FF (1970) The interaction of a crack front with a second—phase dispersion. *Phil Mag* 22:983
58. Green DJ, Nicholson PS, Embury GH (1979) Fracture of a brittle particulate composite—part 2: Theoretical aspects. *J Mater Sci* 14:1657
59. Evans AG, Faber KT (1981) Toughening of ceramics by circumferential microcracking. *J Am Ceram Soc* 64:394
60. Huebner H, Jilek W (1977) Sub-critical crack extension and crack resistance in polycrystalline alumina. *J Mater Sci* 12:117
61. Evans AG, Faber KT (1984) Crack growth resistance of microcracking brittle materials. *J Am Ceram Soc* 67:255
62. Rice RW, Freiman SW, Becher PF (1981) Grain-size dependence of fracture energy in ceramics: I. Experiment. *J Am Ceram Soc* 64:345
63. Subba Rao EC (1981) Zirconia—An overview. *Adv Ceram* 3:1
64. Evans AG (1984) Toughening mechanisms in zirconia alloys. *Adv Ceram* 12:193
65. Claussen N (1984) Microstructural design of zirconia-Toughened Ceramics (ZTC). *Adv Ceram* 12:325
66. Watchman JB (1996) *Mechanical properties of ceramics*. Wiley, New York, USA
67. Lutz EH, Claussen N, Swain MV (1991) KR-curve behaviour of duplex ceramics. *J Am Ceram Soc* 74:11
68. Steinbrech RW (1992) Toughening mechanisms for ceramic materials. *J Eur Ceram Soc* 10:131
69. Danial IM, Ishai O (1994) *Engineering mechanics of composite materials*. Oxford University Press, London, UK
70. Faber KT (1997) Ceramic composite interfaces: Properties and design. *Ann Rev Mater Sci* 27:499
71. Zok F, Sbaizero O, Hom CL, Evans AG (1991) Mode—I fracture resistance of a laminated fiber-reinforced ceramic. *J Am Ceram Soc* 74:187
72. Clegg WJ (1992) The fabrication and failure of laminar ceramic composites. *Acta Metall Mater* 40:3085
73. Jessen JL, Bender BA, Lewis D (1993) Mechanical properties of layered and laminated ceramic matrix composite systems. *Proc Ceram Eng Sci* 13:796
74. Droillard C, Lamon J (1996) Fracture toughness of 2-D woven SiC/SiC CVI composites with multilayered interfaces. *J Am Ceram Soc* 79:849
75. Jessen TL, Greenhut VA, Lewis D, Friel JJ (1999) Effect of microstructure on the mechanical behaviour of continuous-fiber-reinforced ceramic-matrix composites. *J Am Ceram Soc* 82:2753
76. Leatherman GL, Katz RN (1989) Structural ceramics: processing and properties. In: *Superalloys, supercomposites and superceramics*, Ti₄n JK, Caufield T (eds). Academic Press, London, UK, p 671
77. Evans AG, Dalgleish BJ (2008) Some aspects of high temperature performance of ceramics and ceramic composites, p 697

78. Prochazka S (1974) Sintering of SiC. In: Ceramics for high performance applications, Burke JJ, Lenoe EN, Katz RN, Brook Hill Publishing Company, Chestnut Hill, MA, USA, p 239
79. Choksi A, Porter JR (1985) Creep deformation of an alumina matrix composite reinforced with silicon carbide whiskers. *J Am Ceram Soc* 68:144
80. Claussen N, Weisskopf KL, Ruhle M (1986) Tetragonal zirconia polycrystals reinforced with SiC whiskers. *J Am Ceram Soc* 69:288
81. Chawla KK (1987) Composite materials: science and engineering, Materials research and engineering (MSE) series. Ilshner B, Grant NJ (eds). Springer, New York, USA
82. Mahajan YR, Kuruvilla AK, Bhanu Prasad VV, Chakraborty A (1990) Polymer, metal and ceramic composites (PMC/MMC/CMC): a review. *Indian J Technol* 28:354
83. Warren R (ed) (1992) Ceramic matrix composites. Chapman and Hall, New York, USA
84. Fahrenholtz WG, Hilmas IG, Talmy, Zyakoski JA (2007) Refractory diborides of zirconium and hafnium. *J Am Ceram Soc* 90:1347
85. Ruhle M, Calussen N, Heuer AH (1986) Transformation and microcrack toughening as complementary process in ZrO₂—toughened Al₂O₃. *J Am Ceram Soc* 69:195
86. Becher PF, Wei GC (1984) Toughening behavior in SiC-whisker reinforced alumina. *J Am Ceram Soc* 67:C267
87. Wei GC, Becher PF (1985) Development of SiC-whisker reinforced ceramics. *Am Ceram Soc Bullet* 64:298
88. Garvie RC, Hannink RH, Pascoe RT (1975) Ceramic steel. *Nature* 258:703
89. Heuer AG, Claussen N, Kriven WM, Rühle M (1982) Stability of tetragonal zirconia particles in ceramic matrices. *J Am Ceram Soc* 65:60
90. McMeeking R, Evans AG (1982) Mechanics of transformation toughening in brittle materials. *J Am Ceram Soc* 65:242
91. Bhaduri SB, Chakraborty A, Rao RM (1988) Method of fabricating ceria-stabilized tetragonal zirconia polycrystal. *J Am Ceram Soc* 71:C410
92. Yoshimura M, Noma T, Kawabata T (1987) Role of H₂O on the degradation of Y-TZP. *J Mater Sci Lett* 6:465
93. Tsuge A, Nishida K, Komatsu M (1975) Effect of crystallising the grain boundary glassy phase on the high temperature strength of hot pressed Si₃N₄ containing Y₂O₃. *J Am Ceram Soc* 58:323
94. Jakh KH (1977) In: Riley F, Noordhoff L, Katz RN, Gazza GE (eds) Progress in nitrogen ceramics, p 417
95. Terwiliger GR, Lange FF (1975) Pressureless sintering of Si₃N₄. *J Mater Sci* 10:1169
96. Weaver GQ, Olsen BA (1974) Silicon carbide—1973. In: Marshall RC, Faust JW, Ryan CE (eds) University of South Carolina Press, Columbia, USA, pp 367–391
97. Bhanu Prasad VV, Kumari S, Eswara Prasad N, Subrahmanayam J (in preparation) Development of C–C–SiC composites for defence applications: part—I: processing and part—II: characterisation. DMRL technical report, DMRL, Hyderabad, India
98. Petrovic JJ (1993) MoSi₂—based high temperature structural silicides. *MRS Bullet* 18:35
99. Petrovic JJ, Vasudevan AK (1994) Overview of high temperature structural silicides. In: *Mater Res Soc Symp* 322:p 3
100. Mitra R, Mahajan YR, Eswara Prasad N, Chiou WA, Ganguly C (1995) Reaction hot pressing and characterisation of MoSi₂/SiC_p composites. *Key Eng Mater* 108–110:p 11
101. Mitra R, Mahajan YR, Eswara Prasad N, Chiou WA (1997) Processing—microstructure—property relationships in reaction hot pressed MoSi₂ and MoSi₂/SiC_p composites. *Mater Sci Eng A* 225:105
102. Mitra R, Eswara Prasad N, Kumari S, Venugopal Rao A (2003) High temperature deformation behaviour of coarse and fine grained MoSi₂ with different silica contents. *Metall Mater Trans A* 34A:1069
103. Srivastava AK, Eswara Prasad N, Kumari Sweety, Mitra R (2006) Microstructure and mechanical behaviour of reaction hot pressed multiphase Mo–Si–B and Mo–Si–B–Al intermetallic alloys. *Intermetallics* 14:1461

104. Basu B, Raju GB, Suri AK (2006) Processing and properties of monolithic TiB₂ based materials. *Int Mater Rev* 51:351
105. Baker H (1992) Binary alloy phase diagrams. In: ASM Handbook, vol 3. ASM International, Metals Park, OH, USA, p 285
106. Rao L, Gillan EG, Kaner RB (1995) Rapid synthesis of transition metal borides by solid state metathesis. *J Mater Res* 10:33
107. Bates SE, Buhro WE, Frey CA, Sashtry SML, Kelton KF (1995) Synthesis of titanium boride (TiB₂) nano crystallites by solution phase processing. *J Mater Res* 10:333
108. Axelbaum RL, DuFaux DP, Frey CA, Kelton KF (1996) Gas-phase combustion synthesis of titanium boride (TiB) nanocrystallites. *J Mater Res* 11:948
109. Hwang AY, Lee JK (2002) Preparation of TiB₂ powders by mechanical alloying. *Mater Lett* 54:1
110. Holt JB, Kingsman DD, Bianchini GM (1985) Kinetics of combustion synthesis of TiB₂. *Mater Sci Eng* 71:321
111. Cirakoglu M, Bhaduri S, Bhaduri SB (2000) Controlled combustion synthesis in the Ti–B system with ZrO₂ addition. *Mater Sci Eng* 282:223
112. Baik S, Becher PF (1987) Effect of oxygen contamination on densification of TiB₂. *J Am Ceram Soc* 70:527–530
113. Ferber MK, Becher PF, Finch CB (1983) Effect of microstructures on the properties of TiB₂ ceramics. *Commun Am Soc*, 64(1):2–4
114. Li LH, Kim HE, Kang ES (2002) Sintering and mechanical properties of titanium diboride with aluminum nitride as a sintering Aid. *J Eur Ceram Soc* 22:973
115. Atri R, Ravi Chandran KS, Jha SK (1999) Elastic Properties of in-situ processed Ti–TiB composites measured by impulse excitation of vibration. *Mater Sci Eng A* 271:150
116. Sahay SS, Ravi Chandran KS, Atri R, Hen RB, Rubin J (1999) Evolution of microstructure and phases, in situ processed Ti–TiB composites contacting high volume fractions of TiB whiskers. *J Mater* 14:4214
117. Panda KB, Ravi Chandran KS (2003) Ti–TiB functionally graded materials through reaction sintering: synthesis, microstructure and properties. *Metall Mater Trans*, vol 34A
118. Ravi Chandran KS, Panda KB, Sahay SS (2004) TiB_w-reinforced Ti composites: processing, properties, application prospects and research needs, an overview: Ti–B alloys and composites. *J Met* 56:42
119. Kumari S, Eswara Prasad N, Ravi Chandran KS, Malakondaiah G (2004) High temperature deformation behaviour of Ti–TiB_w in-situ metal matrix composites, Ti–B alloys and composite. *J Met* 56:51
120. DeGraef M, Lofvander JPA, Levi CG (1991) The structure of complex monoborides in γ -TiAl alloys with Ta and B additions. *Acta Metall Mater* 39:2381–2391
121. Cao G, Geng L, Naka M (2006) Elastic properties of titanium monoboride measured by nano indentation. *Am Ceram Soc*, vol 89
122. Madtha S, Lee C, Ravi Chandran KS (2008) Physical and Mechanical properties of nano structural titanium boride (TiB) ceramic. *J Am Ceram Soc* 91:1319
123. Zhang ZH, Shen XB, Wang FC, Lee SK (2011) A new rapid route for in situ synthesizing monolithic TiB ceramic. *J Am Ceram Soc* 94:2754
124. Okamoto H (1993) *J Phase Equilib* 14:261
125. Chen HM, Zheng F, Liu HS et al (2009) Thermodynamic assessment of B–Zr and Si–Zr binary systems. *J Alloys Compd* 468:209
126. Rudy E, Windisch S (1966) Techn. Rept. AFML-TR-65-2, vol VIII. Wright Patterson AFB, Dayton, Ohio, USA, pp 1–33
127. Callmer B, Rudy L, Windisch S, Tergenius L, Thomas JO (1978) *J Solid State Chem* 26:275
128. Guo SQ (2009) Densification of ZrB₂-based composites and their mechanical and physical properties: A review. *J Eur Ceram Soc* 29:995
129. Fahrenholtz WG, Hilmas GE, Chamberlain AL, Zimmermann JW, Fahrenholtz (2004) Processing and characterization of ZrB₂-based ultra-high temperature monolithic and fibrous monolithic ceramics. *J Mater Sci* 39:5951

130. Thomson R (1990) Production, fabrication, and uses of borides. In: Freer R (ed) *The physics and chemistry of carbides, nitrides and borides*. Kluwer Academic Publishers, Dordrecht, The Netherlands, pp 113–120
131. Schwarzkopf P, Kieffer R (1953) *Refractory hard metals*. Macmillan Co., New York, USA
132. Chamberlain AL, Fahrenholtz WG, Hilmas GE (2006) Low temperature densification of zirconium diboride by reactive hot pressing. *J Am Ceram Soc* 89:36–38
133. Zhang GJ, Deng ZY, Kondo N, Yang JF, Ohji T (2000) Reactive hot pressing of ZrB_2 -SiC composites. *J Am Ceram Soc* 83:23–30
134. Guo SQ, Nishimura T, Kagawa Y et al (2008) Spark plasma sintering of zirconium diboride. *J Am Ceram Soc* 91:28–48

Chapter 19

Nano-enabled Multifunctional Materials for Aerospace Applications

K. Balasubramanian, Manoj Tirumali, Yutika Badhe
and Y.R. Mahajan

Abstract This chapter discusses the significance of nano-enabled multifunctional materials for aerospace applications. Several studies of these materials report research breakthroughs on the in situ formation of nanostructures and hierarchical structures, and their effects on the improvement of both functional and structural properties for space and aircraft applications such as the EMI shielding, thermal, electrical and opto-magnetic properties, fracture toughness and strength. The materials discussed here relate mostly to polymers.

Keywords Nano-enabled materials · Functional materials · Structural applications · Sensors

19.1 New Challenges for High Performance Aerospace Materials

On February 1st 2003 the Space Shuttle Columbia disintegrated during re-entry over Texas, thereby killing all crew members on board. The catastrophe was attributed to the breaking-off of a piece of foam insulation from the propellant tank soon after take-off, leading to structural damage to the edge of the left wing of the Shuttle and its reinforced carbon-carbon (RCC) panel. This disaster stimulated research to explore high performance materials for aerospace vehicles with improved functional and structural properties such as the thermal resistance, impact tolerance and fracture toughness [1]. The exploration of these high performance materials is highly challenging and interesting.

K. Balasubramanian (✉) · M. Tirumali · Y. Badhe
Defence Institute of Advanced Technology (DU), DRDO,
Ministry of Defence, Girinagar, Pune 411025, India
e-mail: meetkbs@gmail.com

Y.R. Mahajan
Centre for Knowledge Management of Nanoscience
and Technology (CKMNT), Secunderabad 500 017, AP, India

This chapter discusses the ongoing research studies of nanostructural materials and their associated nanofunctional effects applicable for aerospace vehicles.

19.2 Definitions

Nano: The term “nano” represents any one dimension of a particle to be of nano size (10^{-9} m) [2].

Nanofunctional: The term “nanofunctional” denotes the combination of size and properties of a material and their effects when formed as a composite (Shape Memory Alloys/Shape Memory Polymers, Metal Matrix Composite, Polymer Matrix Composite, Polymer Composite, Ceramic Matrix Composite, Functionally Graded Materials, SMART materials) especially for aerospace [3–6].

Functional Materials: These include materials with both structural and non-structural or functional properties that vary with the size of particles over the macro–micro–nano-scales.

The structural properties are the basic mechanical properties: for instance stiffness, strength, fracture toughness, creep and toughness. Non-structural or functional properties are function-related, such as electrical/thermal conductivity, optical, magnetic, electromagnetic interference shielding, energy harvesting/storage, structural health monitoring, super hydrophobicity, thermal barriers and ablation resistance [7]. Therefore some authors refer to functional materials as “Structure+” materials [8, 9]. These materials can be ceramics, metals, polymers and organic molecules.

In conventional aerospace structures the load-bearing function is performed separately by the aerospace structure, while the non-structural or functional activities are performed by additional added equipment or devices which necessarily add weight. However, there are R&D efforts to develop integrated structures that perform both load-bearing and non-load-bearing functions [10–12].

SMART Materials: These are multifunctional [13]. Potential aerospace applications include morphing of aircraft wings, and optically transparent impact absorbing structures [2, 13, 14].

19.3 Examples of Functional Materials

Some examples of functional materials are shape memory metals and polymers; micro-electromechanical systems (MEMS) and nano-electromechanical systems (NEMS), which promise to have many applications in electronic equipment [7, 15, 16]; piezoelectric sensors; and self-healing agents in composites [13], which are widely researched for future aerospace usage.

Piezoelectric materials: Materials like lead zirconate titanate (PZT), polyvinylidene fluoride (PVDF) and aluminium nitrides have the required electromechanical

couplings suitable for both actuation and sensing. Piezoelectric materials are used as thin films and thin wafers embedded in a composite structure.

A piezoelectric fibre composite (PFC) is a classical example of a functional material composite structure. The piezoelectric material is embedded between the carbon fibre/epoxy layers, and interlayer electrodes apply the electric field required for actuation [8, 13]. The piezoelectric coupling coefficient, K_s , defines the electromechanical coupling efficiency given by the conversion efficiency of mechanical energy into electrical energy, and is given by the following relation:

$$K_s = \text{SQRT}(U_e/W_m)$$

where U_e is the electrical (dielectric) energy density, and W_m is the mechanical (strain) energy density.

Figure 19.1 shows the construction of a PFC consisting of a hollow carbon fibre coated with a piezoelectric middle layer and an external electrode layer. The principle of sensing and actuation is achieved by converting the longitudinal deformation of the fibre into radial electric output; and in reverse, the radial poling into longitudinal deformation. The electromechanical coupling efficiency of such a composite structure is 65–70 %.

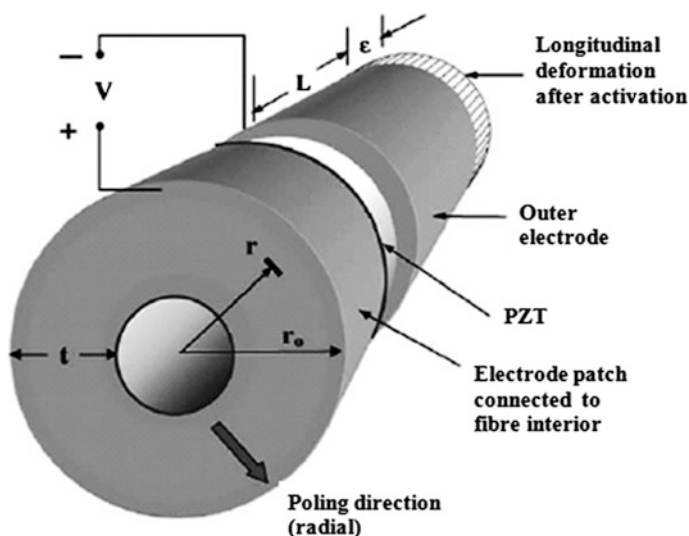


Fig. 19.1 Hollow piezoelectric fibre with radial poling and longitudinal deformation: reprinted with permission from [13]

Uses of PFCs include energy harvesting, structural health monitoring, vibration control and damping. Further improvement may be achieved using a PFC for actuation and a Fibre Bragg Grating (FBG) for sensing, since this will rule out the possibility of cross-interference ‘talk’ between the sensing and actuation functions in a PFC when operating as both sensor and actuator.

Self-healing Agents: The other classical examples for nanofunctional materials are resin-containing nanoporous glass capsules and nanoporous silica capsules as self-healing agents. When a crack in a structure pierces the micro-encapsulations, the resin flows out by capillary action and mixes with a catalyst which polymerises the resin in the crack, see Fig. 19.2.

However, as mentioned in Chap. 14 of this Volume, limited data (up till 2012) show that the fracture toughness recovery in carbon fibre-reinforced plastic (CFRP) composites does not exceed 80 % and can be as low as 41 %. This adverse result appears to be generally true for polymer matrix composites, and has been attributed to insufficient amounts of self-healing resin to close cracks and delaminations, and thermal loss of the healing reaction to the fibres.

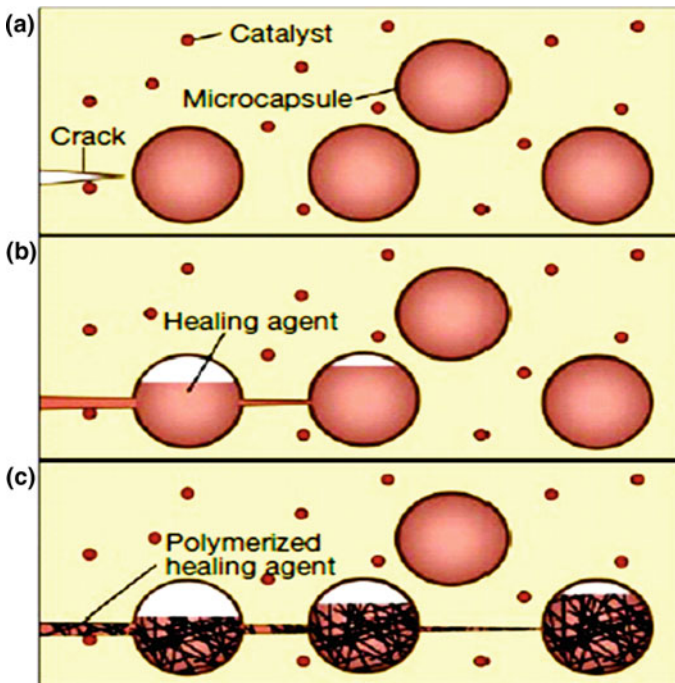


Fig. 19.2 Illustration of self-healing agent. Reprinted with permission from [13]

19.4 Studies of Functional Materials and Potential Aerospace Applications

In recent years there have been numerous studies especially of micro/nanofunctional materials and structures. Many of these studies and their topics are listed here:

- Various opportunities and challenges in multifunctional nanocomposites (MFC) [17].
- Carbon nanotubes (CNTs) and their composites as sensors and actuators [18].
- Vibrations of CNTs and their composites [19].
- A range of kinds of energy absorption in composites [20].
- Electrical percolations in CNT polymer composites [21].
- Vibration-based structural health monitoring (SHM) of composite materials [22, 23].
- Self-healing polymeric materials [24].
- Energy harvesting and storage for sensor networks in SHM [25, 26].

Many of the studies in the above list are relevant to advanced aerospace applications, particularly for composite structures and also for SHM in general.

19.5 Nanomaterials and Structures for Aerospace: An Overview

Nanomaterials and nanostructures are basically small-sized materials and structures. The dimensions range between 100 nm and 1 nm. Nanostructures have been synthesised as one dimensional (nanoplates), e.g. nanoclay silicates; two dimensional (nanofibres); and three dimensional (nanoparticles), see Fig. 19.3. These particles can be used as fillers in the synthesis of nanocomposites.

A more complex and very important class of nanostructures is carbon nanotubes (CNTs). A CNT is graphene rolled up into a tubular structure. If rolled up with one

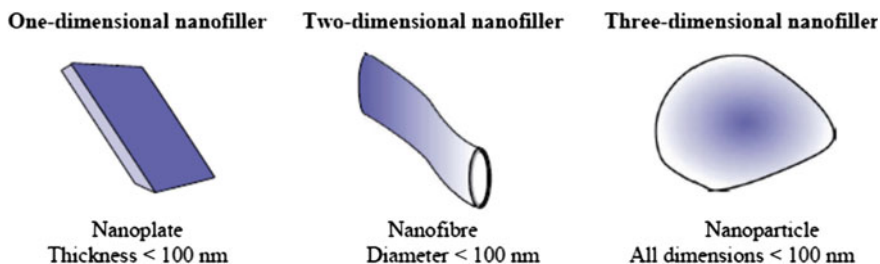


Fig. 19.3 Nanostructures. Reprinted from [32]

wall, it is called a single-walled CNT (SWCNT) and has a diameter of 1–2 nm. If there is a concentric set of cylinders, a CNT is called multi-walled (MWCNT). MWCNTs can have diameters of 4–150 nm. Figure 19.4 illustrates the two types.

Some of the specific applications being researched and proposed for nanoparticles and nanocomposites are high performance fabrics, sensor devices for sensing and actuation, armour plating for military aircraft, microwave absorbers, fire retardation, electrostatic discharge (ESD) dissipation, corrosion protection, stealth, and control valves in rheological fluids [2, 7, 9, 10, 13, 27–31].

For CFRPs the use of nanoparticles and CNTs offers the prospect of improved strength and stiffness along with enhanced thermal conductivity of the resin [9, 32] and electromagnetic interference (EMI) shielding. The main difficulty in synthesising such composites is to obtain a homogeneous distribution of CNTs in the resin [9].

19.6 Specific Assessments of Some Nanostructural Materials

This section discusses the following topics:

- Carbon compounds: CNTs and nanofibres.
- Ablative applications: nanostructural fillers and in situ developed nanostructures.
- Sensor films (spacecraft).
- Superhydrophobic coatings.

19.6.1 Carbon Compounds

Carbon Nanotubes (CNTs): CNTs are potential reinforcement fillers since they contribute remarkable stiffness and specific strength properties in a polymer composite. This is achieved with minimal increase in weight. The other added values

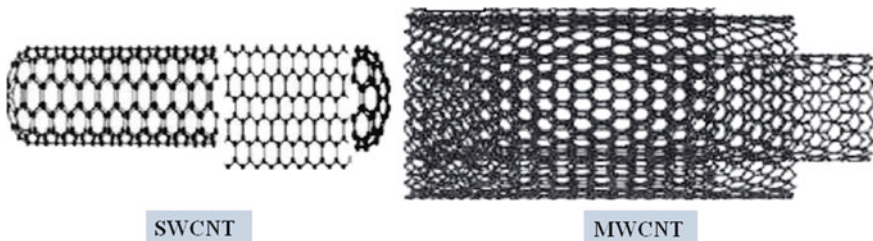


Fig. 19.4 Examples of a SWCNT, reprinted with permission from [9], and MWCNT, reprinted from [32]

are that they enable increases in vibration and flame resistances [33, 34]. Nevertheless, there are several obstacles to commercialization of CNT-reinforced polymer composites,

First, high-quality CNTs can cost up to 1000/g USD. However, with several efforts undertaken for mass production the cost is falling rapidly, enabling economic feasibility. This trend is complemented by refined synthesis and setting up many manufacturing plants.

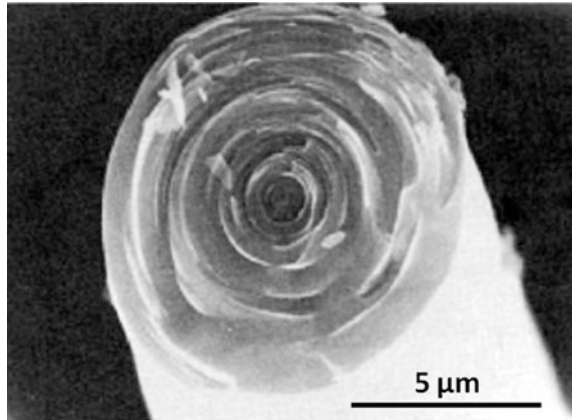
Second, for effective reinforcement there are four processing needs to be satisfied [35]:

- (1) *High aspect ratio*: CNTs have considerable aspect ratios, but their lengths are small, only of the order of microns. This makes them difficult to handle and process. Methods to synthesise longer tubes are under development.
- (2) *Interfacial stress transfer*: Due to their unique structural and electrical properties CNTs do not adhere well to their host matrix or each other. This has an adverse influence on the mechanical properties owing to limited load transfer. Much research has focussed on increasing the reinforcement strength via chemical functionalization and surface modification of the CNTs [36–38].
- (3) *CNT dispersion*: It is important to obtain a fine dispersion of CNTs within the matrix to attain positive load transfer to the nanotubes. This enables a homogeneous stress distribution and minimises the consequences of stress concentrations. The two main dispersion problems are debundling (separation) from each other and fine mixing in the matrix. To overcome these problems, processes such as the homogeneous dispersion (sonication) of CNTs within a solvent may be used (this is one of the most common methods [35]) and shear mixing and magnetic stirring are also used.
- (4) *Alignment for tailored properties*: The alignment of CNTs within a matrix should be controlled in order to ‘tailor’ the composite properties for specific applications. Unidirectional fibres provide strength along the direction of the fibre, and little or no improvement in the transverse direction. On the other hand, randomly directionalised fibres result in isotropic mechanical properties, but with much lower levels of property enhancements [35–39]. This problem remains to be solved.

Vapour Grown Carbon Nanofibres (VGNF): VGCFs possess superior thermal insulation, low thermal conductivity (0.45–0.58 W/mK) and high thermal shock resistance, which make them suitable candidates for thermal shielding systems [40]. VGCNFs are graphene layers cylindrical in form and arrayed in a stacked coned shape, see Fig. 19.5.

VGCNF synthesis is carried out by catalytically decomposing hydrocarbon gas-phase molecules at high temperature, resulting in fibre depositions on a substrate. Fibres with diameters from 7–30 μm have been grown, and it was established that the tensile strength and Young’s modulus decrease with increasing diameter [41], which is disadvantageous.

Fig. 19.5 Transverse section of a VGCNF showing a tree ring morphology. Reprinted with permission from [40]



Nitric acid or plasma oxidative surface treatments of the fibres improve their adhesion to a polymer (phenolic) matrix without altering their morphology. The VGCNF–phenolic matrix combination has use as an ablative material for solid rocket motors [40]. NASA currently uses the MX-49 grade of VGCNFs, composed of two types of reinforcements: woven ex-rayon carbon fibres (AvtexFibres, Inc) and carbon black fillers with a phenolic resin matrix.

As in the case of CNTs, the fibre orientations of VGCNF composites are very important.

19.6.2 Ablative Applications

Ablation occurring in all re-entry vehicles is the thermal degradation of a material due to frictional forces that causes high temperatures of the order of 2000–3000 °C. “Char” is an ablative carbonaceous material that insulates the substrate from superheated gases and hyper-thermal environments. Successful ablative materials expend thermal energy by enduring sacrificial loss of material owing to a self-regulating heat and mass transfer process [42].

Popular ablative materials are phenolic resins, which have excellent char retention capability [43]. These resins can be intrinsically improved by molecular changes [44, 45], and they may be used as the matrix for ablation-resistant composites.

Nanostructural fillers: A wide range of reinforcements such as fibres made up of carbon, refractory oxides, mineral asbestos, or glasses and elements with high bond energies (B, P, Mo, Ti) may be added to the resin matrix [46–51] to assist the retention of char.

Another possibility is nanofillers: the nanoparticles have remarkable surface to volume ratio, making them effective as filler reinforcement for ablative composites.

The reinforcing effects depend on the particle crystalline microstructures and the effective interfacial bonding with the parent matrix [31, 52].

Nanofillers with high thermal stability, low thermal conductivity and high adhesive bonding with the matrix enhance the ablative material's resistance to thermal degradation and high temperature erosive aerodynamic shear forces [53].

Some of the nanofillers can be listed under the category of nanoclays, including clays like bentonite and montmorillonite. Besides clays, a prominent filler is nano-sized silicon carbide (SiC). SiC nanoparticles take the form of a greyish white powder with a cubic morphology. Several studies [54–57] have investigated the thermal properties of silicon carbide, concluding it to be an excellent thermal insulator.

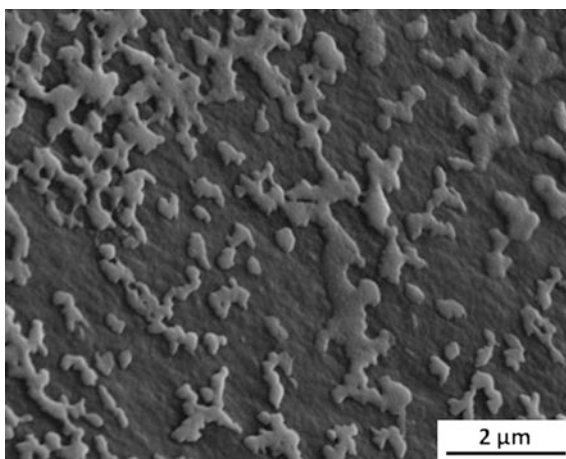
In situ developed nanostructures: Some materials like silicon carbide and boron carbide (B_4C) form *in situ* nanostructures at the very high temperatures that occur on ablating surfaces.

SiC nanostructures having a low coefficient of thermal expansion ($4.0 \times 10^{-6}/K$) are stable up to very high temperatures (Melting Point, 2730 °C). This property derives from the absence of phase transitions, thereby avoiding abrupt changes in thermal expansion [58]. During ablation, SiC forms a fused mass of silica glass (silicon dioxide) that acts a barrier inhibiting oxygen attacking the underlying polymer layer, see Fig. 19.6.

B_4C yields nanospheres and nanoagglomerations during ablation. These are made of borate glass, and like silica glass act as oxygen scavengers, thereby protecting the underlying polymer [59].

The formation of *in situ* developed glassy nanostructures is an important development in nanostructures for ablative applications.

Fig. 19.6 Ablated surface with fused mass of silicon dioxide. Reprinted from [58]



Another aspect is that C–SiC composites have a high resistance to aerodynamic shear forces under high temperature erosive environments. These composites also enhance the ablation resistance [60].

19.6.3 *Sensor Films (Spacecraft)*

Aerospace systems depend on highly developed sensors for various defence and security applications, such as reconnaissance, fire control and imaging (infrared and hyper spectral) [58].

Launch vehicles and spacecraft require large quantities of explosive and/or toxic chemicals. The hazard to civilians from contact to deadly plumes during launches could constrain access to space. The launch opportunities are enhanced with the confidence gained by taking real-time data to improve the accuracy of exhaust plume dispersion models. The protection of the personnel working in the region of the aerospace craft and payloads is ensured by having better chemical sensors for dangerous propellants.

Nowadays, progress in miniaturised chemical sensors of low power permits the instrumentation of aerospace vehicles and tank regions to detect contact with dangerous gases. These kinds of sensors allows rapid detection of leaks, enabling operators to quickly measure the level and penalty of a small leak and minimise the time and effort needed for fault and failure analysis.

Infrared sensor coatings: Multi-metallic oxides and perovskites like barium titanate (BaTiO_3) and barium strontium titanate (BaSrTiO_3) are synthesised with a fairly simple catalytic process [61]. This was developed at the Institute for Collaborative Biotechnologies at UC Santa Barbara. The prefabricated infrared sensor circuitry has a refined high-quality thin film of uniformly distributed nanocrystals. The films are mechanically tough, and have rapid response times and excellent spatial resolution. This responsiveness and better resolution is due to the large surface to volume ratio of the nanoscale particles, resulting in high sensitivity and fast heating/cooling [61].

Chemical Sensors: Polyaniline nanofibres in nanostructured sensor layers enable much improved diffusion. This is due to the fact that these materials have a remarkable surface area that allows easier diffusion of gas molecules than in the bulk material. Fibres surpass even ultrathin films of similar diameter owing to the large surface to volume area. Thus sensors with nanofibres (less than 100 nm) are likely to have superior performance [62–66].

19.6.4 *Superhydrophobic coatings*

Ice build-up on aircraft wing leading edges is a serious potential (and actual) hazard affecting flight performance. Under exceptional circumstances the internal de-icing

systems do not always cope with this problem. There is thus the potential for applying hydrophobic and superhydrophobic coatings to selected areas of the external surfaces. Other applications are to reduce corrosion and fouling of the aircraft surfaces.

Hydrophobic coatings, and their limitations, are discussed in Chap. 25 in this Volume. Here we shall mention superhydrophobic coating developments. Such coatings have contact angles between water droplets and the surface that exceed 170° [67–70]. Recent developments are as follows:

- (1) Optical photolithography + reactive ion etching to obtain nanoscale pillar-like structures on polymethylmethacrylate (PMMA) sheet surfaces. Micro- as well as nano-patterned structures were observed on the PMMA sheet surfaces, and a contact angle of around 168° was achieved [71].
- (2) Immersion of copper foil in hydrochloric acid and then a wax solution, resulting in nanoscale ‘cabbage-like’ copper oxide (CuO) structures with superhydrophobic properties [72].
- (3) Carbon soot fillers in various polymers applied to a variety of substrates [73, 74].

19.7 Update of Nanofunctional Materials Research

An exhaustive review of the overall status update of nanofunctional materials research is given in the recent book by Banerjee and Tyagi [75]. This book is not restricted to aerospace. Some specific topics will be mentioned here (see Sect. 19.4 also):

- Ongoing research in the fields of ferroelectricity, piezoelectricity, magnetism, EMI shielding, ESD dissipation and energy harvesting and storage, involving nanostructured materials and coatings [17–26].
- Functional oxides are receiving much attention in the study of ferroelectricity and piezoelectricity [8, 13].
- Nanostructured materials for electronics and optoelectronics [7].
- SWCNT sensors for piezoelectric actuators or sensing devices [6, 13, 15, 18, 37, 42, 76].
- Polymer–clay nanocomposites for flame-retardant and gas barrier materials [14, 32].
- Polymer–clay–CNT (or some other filler) nanocomposites for further enhancement of thermal, electrical and mechanical properties [14, 32].

Overall, there is a trend to study nanofunctional materials and structures for multifunctional applications in aerospace, and to determine how nanoscale properties and functions relate to and affect the macroscopic functionality.

Also studied are the constraints imposed on the design of nanofunctional materials by practical considerations such as fabrication and inspection.

19.8 Summary

This chapter has reviewed current and ongoing research on nanofunctional materials and structures that have potential applications in aerospace. Innovative materials and processing techniques need thorough assessment studies to substantiate their appropriateness for aerospace usage. Therefore these innovative and challenging concepts will need more time in order to become practical realities.

Acknowledgments The authors thank the Vice Chancellor, DIAT (DU) and Director, MILIT, Pune, Dr. N. Eswara Prasad, Dr. R.J.H Wanhill and the “DIAT: NANO project EPIPR/ER/1003883/M/01/908/2012/D (R&D)/1416” for encouragement and support. They also thank the Defence Institute of Advanced Technology, Pune, for financial support.

References

1. Mouritz AP, Feih S, Kandare SE, Kandare Z, Mathys Z, Gibson AG, Des Jardin PE, Case SW, Lattimer BY (2009) Review of fire structural modelling of polymer composites. *Compos Part* 40(12):1800–1814
2. Kurahatti Singh RV, Surendranathan AO, Kori Nirbhay SA (2010) Defence applications of polymer nanocomposites. *Defence Sci J* 60(5):551–563
3. Koussios A, Buckers H, Berkee S (2011) Composite materials, a vision for the future. Book Chapter I pp 1–50. doi:[10.1007/978-0-85729-166-0_1](https://doi.org/10.1007/978-0-85729-166-0_1)
4. Halpin JC, Luigi N, Michele M, Eva M (2011) Composite materials, a vision for the future. Book Chapter II 51–68 doi:[10.1007/978-0-85729-166-0](https://doi.org/10.1007/978-0-85729-166-0)
5. Wee WH, Zong RG, Maguire SS, Sangari PH, Lucas, Durand P (2008) Major trends in polymeric composites technology composite materials research progress. Nova Science Publishers Inc., New York, USA, pp 107–127
6. Tao X (2011) Recent advances in shape memory alloy. *Polymers* 52(22):4985–5000
7. Zhang Y, Wenyi L (2011) Structure analysis and choosing materials for the aerospace multi-functional structure of electronic equipment. In: Proceedings of international conference on computer engineering and applications (IPCSIT), vol 2:240–243
8. Defense Committee on Materials Research for Structural and Multifunctional Materials (2003) Materials research to meet 21st century defense needs. In: Proceedings of committee on materials research for defense, Washington DC, USA, pp 27–53
9. Meyyappan M (2005) Nanotechnology in aerospace applications. RTO-EN-AVT-129, Paper 7. Neuilly-sur-Seine, France, pp 7.1–7.37
10. Suresh Kumar KVVS, Reddy M, Kumar A, Rohini Devi G (2013) Development and characterization of polymer–ceramic continuous fiber reinforced functionally graded composites for aerospace application. *Aerosp Sci Technol* 26(1):185–191
11. Koizumi M (1997) FGM activities in Japan. *Compos Part B* 28:1–4
12. Cooley WG (2005) Application of functionally graded materials in aircraft structures. M.Sc. thesis, Department of Aeronautics and Astronautics, M.SC thesis, Air Institute of Technology, Wright-Patterson Air Force Base, Ohio, USA

13. Gibson R (2010) A review of recent research on mechanics of multifunctional composite materials and structures. *Compos Struct* 92(12):2793–2810
14. Dr Morgan AB (2011) Design and application of multi-functional materials. *Mater Matters* 2 (1):1–6
15. Atkinson HV (2001) Structural and functional materials. *Mater Sci Eng II*:1–13
16. Schottner G (2001) Hybrid sol-gel-derived polymers: applications of multifunctional materials. *Chem Mater* 13(10):3422–3435
17. Baur J, Silverman E (2007) Challenges and opportunities in multifunctional nanocomposite structures for aerospace applications. *Mater Res Soc* 32(4):328–334
18. Li C, Thostenson ET, Chou TW (2008) Sensors and actuators based on carbon nanotubes and their composites: a review. *Compos Sci Technol* 68(6):1227–1249
19. Gibson RF, Ayorinde EO, Wen YF (2007) Vibrations of carbon nanotubes and their composites: a review. *Compos Sci Technol* 67(1):1–28
20. Sun L, Gibson RF, Gordaninejad F, Suhr J (2009) Energy absorption capability of nanocomposites: a review. *Compos Sci Technol* 69(14):2392–2409
21. Bauhofer W, Kovacs JZ (2009) A review and analysis of electrical percolation in carbon nanotube polymer composites. *Compos Sci Technol* 69(10):1486–1498
22. Montalvao D, Maia NMM, Ribeiro AMR (2006) A review of vibration-based structural health monitoring with special emphasis on composite materials. *Shock Vib Digest* 38(4):295–324
23. Zou Y, Tong L, Steven GP (2000) Vibration-based model dependent damage identification and health monitoring for composite structures—a review. *J Sound Vib* 230(2):357–378
24. Wu DY, Meure S, Solomon D (2008) Self-healing polymeric materials: a review of recent developments. *Prog Polym Sci* 33(5):479–522
25. Sodano HA, Inman DJ, Park G (2004) Review of power harvesting from vibration using piezoelectric materials. *Shock Vib Digest* 36(3):197–205
26. Park G, Rosing T, Todd MD, Farrar CR, Hodgkiss W (2008) Energy harvesting for structural health monitoring sensor networks. *J Infrastruct Syst* 14(1):64–79
27. RyszardPilawka SP, Rosłaniec Z (2012) Epoxy composites with carbon nanotubes. *Adv Manuf Sci Tech* 36(3):67–79
28. Yasmin A, Daniel IM (2004) Mechanical and thermal properties of graphite platelet/epoxycomposites. *Polymer* 45(24):8211–8219
29. Nigrawal A, Chand N (2010) Electrical and thermal investigations on exfoliated graphite filled epoxy gradient composites. *Malays Polym J* 5(2):130–139
30. Huda Z, Edi P (2013) Selection in design of structures and engines of supersonic aircrafts: a review. *Mater Des* 46(2013):552–560
31. Balasubramanian K, Tirumalai M (2013) High Temperature Polymer Nanocomposites. In: *Structural Nanocomposites: Perspectives for Future Applications (Engineering Materials)*, James N (ed), Springer, Berlin, pp. 165–186
32. Marquis DM, Guillaume É, Chivas-Joly C (2011) Properties of nanofillers in polymer. www.intechopen.com, Chapter 11, pp 261–284
33. Jonghwan S, Wei Z, Ajayan PM, Koratkar NA (2006) Temperature-activated interfacial friction damping in carbon nanotube polymer composites. *Nano Lett* 6(2):219–223
34. Kashiwagi T, Fangming DU, Douglas JF, Winey KL, Harris RH Jr, Shields JR (2005) Nanoparticle networks reduce the flammability of polymer nanocomposites. *Nat Mater* 4 (12):928–933
35. Coleman JN, Khan H, Gun'Ko YK (2006) Mechanical reinforcement of polymers using carbon nanotubes. *Adv Mater* 18(6):689–706
36. Dalton AB, Collins S, Muñoz E, Razal JM, Ebron VH, Ferraris JP, Coleman JN, Kim BG, Baughman RH (2003) Super-tough carbon-nanotube fibres. *Nature* 423(6941):703–704
37. Zhang M, Fang S, Zakhidov AA, Lee SB, Aliev AE, Williams CD, Atkinson KR, Baughman RH (2005) Strong, transparent, multifunctional, carbon nanotube sheets. *Science* 309(5738):1215–1219

38. Velasco-Santos C, Martínez-Herná AL, Ndez FT, Castañ VM (2003) Improvement of thermal and mechanical properties of carbon nanotube composites through chemical functionalization. *Chem Mater* 15(23):4470–4475
39. Kis AC, Salvétat G, Lee JP, Couteau T, Kulik E, Benoit A, Brugger W, Forro JL (2004) Reinforcement of single-walled carbon nanotube bundles by intertube bridging. *Nat Mater* 3 (2004):53–157
40. Patton RD Jr, Wang C, Hill L, Day JR (2002) Ablation, mechanical and thermal conductivity properties of vapor grown carbon fiber / phenolic matrix composites. *Compos Part A-Appl S* 33(2):243–251
41. Tibbetts GG, Lake ML, Strong KL, Rice BP (2007) A review of the fabrication and properties of vapor-grown carbon nanofiber/polymer composites. *Compos Sci Technol* 67(7–8):1709–1718
42. Kimberly AT, Saliba TE (1995) Mechanism of the pyrolysis of phenolic resin in carbon/phenolic composite. *Carbon* 33(11):1509–1515
43. Srikanth I, Padmavathi N, Suresh Kumar P, Anil Kumar G, Subrahmanyam Ch (2013) Mechanical, thermal and ablative properties of zirconia, CNT modified carbon/phenolic composites. *Compos Sci Tech* 80:1–7
44. Mouritz AP, Gibson AG (2006) Fire properties of polymer composite materials. 1st ed. solid mechanics and its applications. (pbk), 14:163–213
45. Balasubramanian K, Yutika B (2014) Indian patent, cost effective processing of defect/ blister free ablative composites of functionally tailored resins of ultra high temperature ceramics for layered composite. Patent number: 641/MUM/2014
46. Abdalla MO, Ludwick A, Mitchell T (2003) Boron-modified phenolic resins for high performance applications. *Polymer* 44(24):7353–7359
47. Kawamoto AM, Pardini LC, Diniz MF, Lourenco VL, Takahashi MFK (2010) Synthesis of a boron modified phenolic resin. *J Aerosp Technol Manage* 2(2):169–182
48. Yu H, Liu J, Wen X, Jiang Z, Wang Y, Wang L, Zheng J (2011) Charring polymer wrapped carbon nanotubes for simultaneously improving the flame retardancy and mechanical properties of epoxy resin. *Polymer* 52(21):4891–4898
49. Zhang Y, Shen S, Liu Y (2013) The effect of titanium incorporation on the thermal stability of phenol-formaldehyde resin and its carbonization microstructure. *Polym Degrad Stab* 98 (2):514–518
50. Cho Donghwan (1996) Phenolic composites fabricated using h_3po_4 -coated carbon fibres. *J Mater Sci Lett* 15(20):1786–1788
51. Dhani TL, Bahl OP, Awasthy BR (1995) Oxidation-resistant carbon-carbon composites up to 1700 °C. *Carbon* 33(4):479–490
52. Tirumalai M, Balasubramanian K, Kumaraswamy A (2013) Epoxy composites of graphene oxide (GO): a review. In: Proceedings of IEEE-International Conference on Research and Development Prospectus on Engineering and Technology (ICRDPET), EGS Pillay Engineering College, 29–30 March, 2013 Nagapattinam, India, pp. 94–98
53. Sanoj P, Balasubramanian K (2014) Hybrid carbon-carbon ablative composites for thermal protection in aerospace. *J Compos* 2014:1–15
54. Kovalcikova A, Dusza J, Sajgalik P (2009) Thermal shock resistance and fracture toughness of liquid-phase-sintered SiC-based ceramics. *J Eur Ceramic Soc* 29(11):2387–2394
55. Yamada K, Kamiya N (1999) High temperature mechanical properties of Si_3N_4 - MoSi_2 and Si_3N_4 -SiC composites with network structures of second phases. *Mater Sci Eng A* 261 (1999):270–277
56. Zhang XH, Wang Z, Hu P, Han W, Hong CQ (2009) Mechanical properties and thermal shock resistance of ZrB_2 -SiC ceramic toughened with graphite flake and SiC whiskers. *Scripta Materialia* 61(8):809–812
57. Buchheit AA, Hilmas GE, Fahrenholtz WG, Deason DM (2009) Thermal shock resistance of an AlN-BN-SiC ceramic. *J Am Ceramic Soc* 92(6):1358–1361
58. Badhe Y, Balasubramanian K (2014) Novel Novel hybrid ablative composites of resorcinol formaldehyde as thermal protection systems for entry vehicles. *RSC Adv* 4:28956–28963

59. Wang J, Jiang N, Jiang H (2010) Micro-structural evolution of phenol-formaldehyde resin modified by boron carbide at elevated temperatures. *Mater Chem Phys* 120(1):187–192
60. Konstantinov AO (1995) Sublimation growth of SiC. In: *Properties of Silicon Carbide*. Harris GL (ed), INSPEC, the Institution of Electrical Engineers, London, UK, pp. 170–203
61. Livingston F, Sarney W, Niesz K, Ould-Ely T, Tao A, Morse D (2009) Bio-inspired synthesis and laser processing of nanostructured barium titanate thin-films: implications for uncooled IR sensor development *SPIE Proc* 7321:1–13
62. Huang J, Virji S, Weiller B, Kaner R (2003) Polyanilinenanofibers: facile synthesis and chemical sensors. *J Am Chem Soc* 125(2):314–315
63. Virji S, Huang J, Kaner R, Weiller B (2005) Polyanilinenanofiber composites with metal salts: chemical sensors for hydrogen sulphide. *Small* 1(6):624–627
64. Virji S, Huang J, Kaner R, Weiller B (2004) Polyanilinenanofiber gas sensors: examination of response mechanisms. *Nano Lett* 4(3):491–496
65. Virji S, Huang J, Kaner RB, Weiller BH (2004) Polyaniline nanofiber gas sensors: Examination of response mechanisms. *Nano Lett* 4:491–496
66. Virji S, Kaner R, Weiller B (2007) Hydrogen sensors based on conductivity changes in polyanilinenanofibers. *J Phys Chem B* 110(44):22266–22270
67. Kulinich A, Farzaneh M (2009) How wetting hysteresis influences ice adhesion strength on superhydrophobic surfaces. *Langmuir* 25(16):8854–8856
68. Zhang G, Wang D, Gu Z, Mchwald H (2005) Facile fabrication of super-hydrophobic surfaces from binary colloidal assembly. *Langmuir* 21(20):9143–9148
69. Liu B, He Y, Fan Y, Wang X (2006) Fabricating super-hydrophobic lotus-leaf-like surfaces through soft-lithographic imprinting. *Macromol Rapid Commun* 27(21):1859–1864
70. Jiang L, Zhao Y, Zhai J (2004) Alotus-leaf-like super hydrophobic surface: a porous microsphere/nanofiber composite film prepared by electro hydrodynamics. *Angew Chem Int Ed* 43(33):4338–4341
71. Sahoo BN, Balasubramanian K, Sabarish B (2014) Controlled fabrication of non-fluoropolymer composite film on glass surfaces with hierarchically nano structured fibers. *Prog Org Coat* 77(4):904–907
72. Sahoo BN, Balasubramanian K (2014) Facile synthesis of nano cauliflower and nano broccoli like hierarchical super hydrophobic composite coating using pvdf/carbon soot particles via gelation technique. *J Colloid Interface Sci* 436:111–121
73. Sahoo BN, Balasubramanian K (2014) An experimental design for the investigation of water repellent property of candle soot particles. *Mater Chem Phys* 148(1–2):134–142
74. Sahoo BN, Balasubramanian K (2014) Photoluminescent carbon soot particles derived from controlled combustion of camphor for superhydrophobic application. *RSC Adv* 4(22):11331–11342
75. Banerjee S, Tyagi AK (eds) (2012) *Functional materials: preparation, processing and applications*. Elsevier, New York, USA
76. Guozhong G (2003) *Nanostructures and Nanomaterials*. Imperial College Press, London, UK, pp 51–269

Chapter 20

MAX Phases: New Class of Carbides and Nitrides for Aerospace Structural Applications

Sai Priya Munagala

Abstract This chapter summarizes the new class of carbides and nitrides discovered in recent decades. These materials serve as a bridge between metals and ceramics, having advantages from both classes of materials. Due to this reason, MAX phases fit into a wide range of applications from electronic to structural materials. The synthesis methods have been discussed, with the scope for improvement, in order to discover newer phases as well.

Keywords MAX phases · Carbides · Nitrides · Physical metallurgy · Processing · Properties · Applications

20.1 Introduction

In the late 1960s a new class of materials called ‘MAX’ phases was discovered [1]. However, it was not until 1996 that Barsoum [2] successfully synthesized MAX phases in bulk form using hot pressing (HP). Later the parameters were optimized and synthesis took place by hot isostatic pressing (HIP).

$M_{n+1}AX_n$ (or MAX in short) are nanolayered carbides or nitrides where $n = 1, 2, 3$, M is an early transition metal, A is from group A (mostly IIIa or IVa) and X is either carbon or nitrogen. With well-defined stoichiometry and chemistry, these phases usually consist of hexagonal structures with densities ranging from 4 to 14 g/cm³ (most have densities in the range 4–7 g/cm³). There are around 60 known MAX phases at present. The important (most-researched) ones are Ti₂AlC, Ti₃SiC₂ and Ti₄AlN₃, which have densities in the range 4.1–4.7 g/cm³. Figure 20.1 indicates the elements involved or expected to be involved in MAX phase formation.

S.P. Munagala (✉)

Department of Materials Science, TU Darmstadt, Darmstadt, Germany
e-mail: priya.munagala@gmail.com

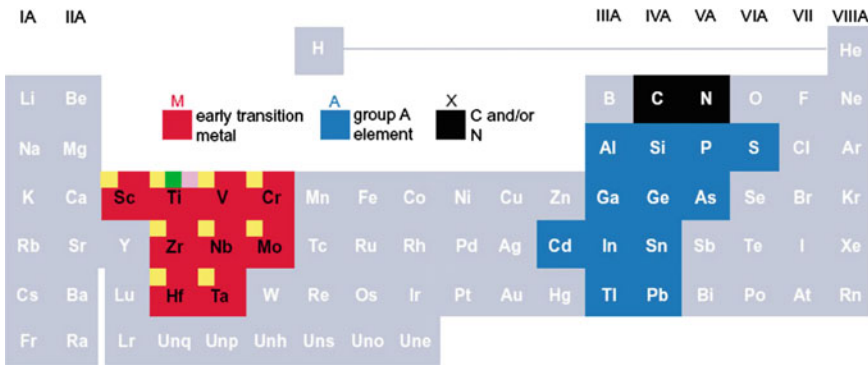


Fig. 20.1 Elements involved in actual and probable MAX phase formation [25]

These materials combine properties of metals and ceramics, and can be ‘tailored’ for certain applications. They exhibit high rigidity and good machinability along with good electrical and thermal conductivity [1].

This unique combination of properties is due to the hexagonal-layered structure consisting of $M_{n+1}X_n$ with intercalated pure element A layers. Because of the stoichiometry, ‘A’ layers intercalated between MX and MAX phases can be referred to as 211, 312 and 413 for $n = 1, 2$ and 3 respectively. The number of M layers being separated by A is equal to ‘ n ’. The crystal structures are shown in Fig. 20.2.

20.2 Physical Metallurgy of MAX Phases

MAX phases collectively come under the category of “*layered ternary ceramics*”. The transmission electron microscopy (TEM) investigations made by Jiang et al. [3] have shown that there is a wide variety of these ceramics.

20.2.1 Polymorphism of MAX Phases

Till now, only two types of polymorphism have been discovered, one for the 312 type of phases, and the other for the 413 type of phases. The former one involves the shearing of A layers, which was assumed to occur during TEM sample preparations. However, a specimen of Ti_3GeC_2 , showed an α - β transformation occurring at very high pressures (~ 90 GPa).

The second type of polymorphism was discovered in the 413 type of phases (high pressure sintered Ta_4AlC_3 and Ti_4AlN_3). Separate characterization techniques finally concluded that Ta_4AlC_3 has two polymorphs, α (same as Ti_4AlN_3) and β . The differences in these polymorphs compared to the 312 type lie in the positions of Ta and C. Density functional theory (DFT) investigations have suggested that the α phase is more stable when compared to β at room temperature and ambient pressure.

Intergrown hybrid structures: A new set of hybrid structures has been discovered, and these phases are called 523 and 725 phases. They are referred to as hybrid due to their irregular stacking and the combination of half unit cells from the original set of MAX phases. For example, the unit cell of 725 hybrid phase consists of unit cells of 312 and 413 phases. Similarly, the 523 hybrid phase has 211 and 312 unit cells.

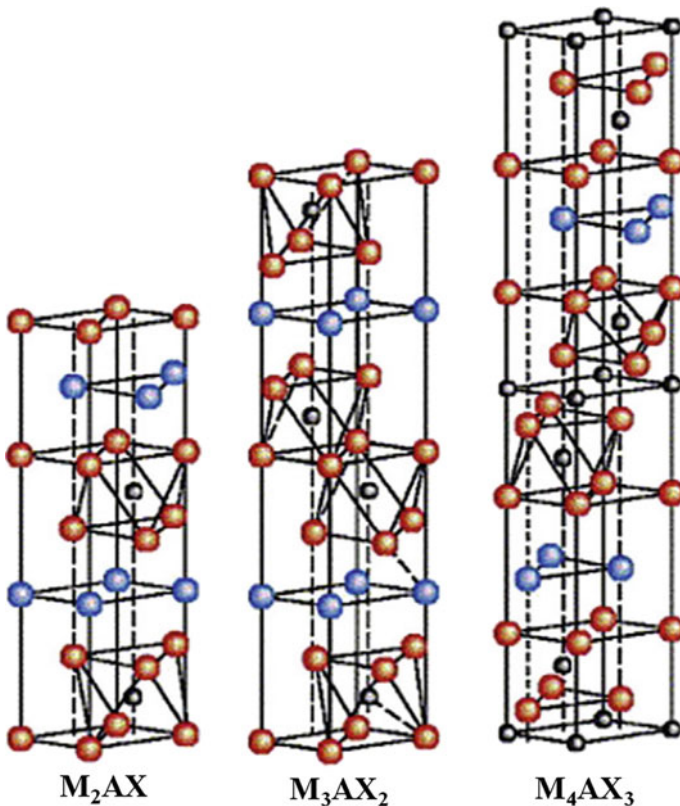


Fig. 20.2 Crystal structures of the 211, 312 and 413 MAX phases [26]

20.3 Synthesis Procedures

The synthesis procedures can be broadly categorized into (a) thin phase films and (b) bulk processing. Any synthesis procedure resulting in a film or coating $\geq 100 \mu\text{m}$ thick can be conveniently categorized as bulk processing. Of all the current MAX phases, Ti_3SiC_2 has attracted much attention, and synthesis of this material is discussed in detail in order to compare the different techniques.

Chemical vapour deposition (CVD) processes were initially favoured for thin films. These processes were later improved by conversion of CVD into plasma vapour deposition (PVD) processes.

Hot pressing has been the most popular procedure in the bulk category. An alternative is combustion reaction, but this results in less purity of the MAX phase and many undesirable secondary phases. The advantage of combustion reaction synthesis is its speed, sometimes taking only a few seconds [4].

Progress in synthesizing has called attention to pressureless sintering [5] as a commercially viable procedure for bulk forms. Spark plasma sintering (SPS) and pulse discharge sintering (PDS) are some of the popular techniques being much studied as well.

20.3.1 Synthesis of Thin MAX Phases

The initial concept of producing thin films by CVD was successful, but later it was proven to be not so beneficial in terms of assay value and process control. This led to less interest in the CVD technique. The procedure evolved to the PVD process, which gave more favourable results. For this process Ti_3SiC_2 has been produced successfully by magnetron sputtering [1] and spark plasma sintering (SPS) [6], both of which have become popular.

Figure 20.3 gives a schematic of PVD magnetron sputtering. Plasma is created, and the positively charged ions from the plasma are accelerated by an electrical field superimposed on the negatively charged electrode or target. The same PVD process has been used for more systems like the Ti–Ge–C, Ti–Al–N and Ti–Al–C systems, but impurities were obtained. Besides PVD, techniques like pulsed cathodic arc, plasma spray coating, and high velocity oxy-fuel spraying are also used.

The thin film microstructures depend on the formation temperature. For example, when formed at higher temperatures, textured or single crystals are possible. When formed at lower temperature ($<300 \text{ }^\circ\text{C}$) the result is nanocomposite films, which find applications in coating electrical friction contacts, since these films combine metallic conductivity and resistance to wear and corrosion [5].

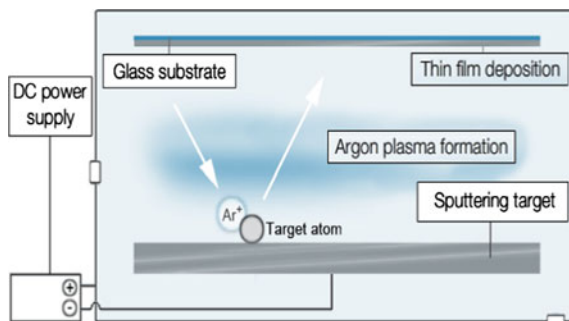


Fig. 20.3 PVD magnetron sputtering for thin film formation of MAX phases

20.3.2 *Synthesis of Bulk MAX Phases*

MAX phases were initially produced in bulk using hot pressing (HP) or hot isostatic pressing (HIP). This technique overcame the drawbacks of combustion synthesis, which resulted in less purity and unwanted secondary phases. To avoid any inadvertent reactions, an inert gas is used during HIP.

Zhou and Gu [7] performed in situ HP solid–liquid synthesis of dense Ti_3SiC_2 and successfully obtained 92 wt% purity. The solid–liquid reaction was also modified by adding small amounts of metallic Sn to improve the purity. This process was extended to other systems like Ti_3GeC_2 , Ta_2AlC and Nb_2AlC , and good results were obtained.

MAX production via powder synthesis has served as an alternative to HIP bulk production. Studies have also suggested that high purity (up to 99.3 wt%) Ti_3SiC_2 was obtained by isothermal heating of stoichiometric proportions of Ti–Si–Ti–C powder mixtures [5]. However, a similar process when applied to Ti_3AlC showed that the elemental powder mixture could be explosive: metallic Sn was seen to be a remedy to suppress the explosion.

Pressureless sintering seems a viable synthesis procedure for bulk production, being both economical and scalable. This technique consists of sintering a green powder compact without mechanical pressure. Initial attempts were made from mechanical alloying of powders and a traditional sintering technique, which gave samples that lacked purity. Promising advancements include tape casting or cold pressing, which are expected to retain the purity levels.

20.3.3 *Synthesis of MAX Phases in Commercially Viable Bulk Forms*

Since the early 2000s spark plasma sintering (SPS) has been noted as a novel technique with the advantages of high efficiency and energy saving characteristics [8–10]. This process can also be referred to as pulsed electric current sintering

(PECS) or the field-assisted sintering technique (FAST) or pulsed discharge sintering (PDS). SPS does not require external heating equipment, since heat is generated internally (http://en.wikipedia.org/wiki/Spark_plasma_sintering). A schematic of the SPS process is shown in Fig. 20.4.

The SPS energy saving, higher heating and cooling rates, and shorter holding times when comparing to other bulk procedures, make it one of the better techniques for economical industrial scale production [11]. The end product has higher density and enhanced properties, including mechanical strength, fracture toughness, wear and corrosion resistance, flexural strength, and conductivity.

This synthesis was initially attempted for producing bulk Ti_3AlC_2 - and Ti_3SiC_2 -based composites. Al was found to be a very good sintering aid in order to produce Ti_3SiC_2 of high purity in this technique. Also, production of Ti_3SiC_2 was possible in situ. However, the complete mechanism underlying the formation of this phase is still under study, and efforts are being made to reduce the costs further.

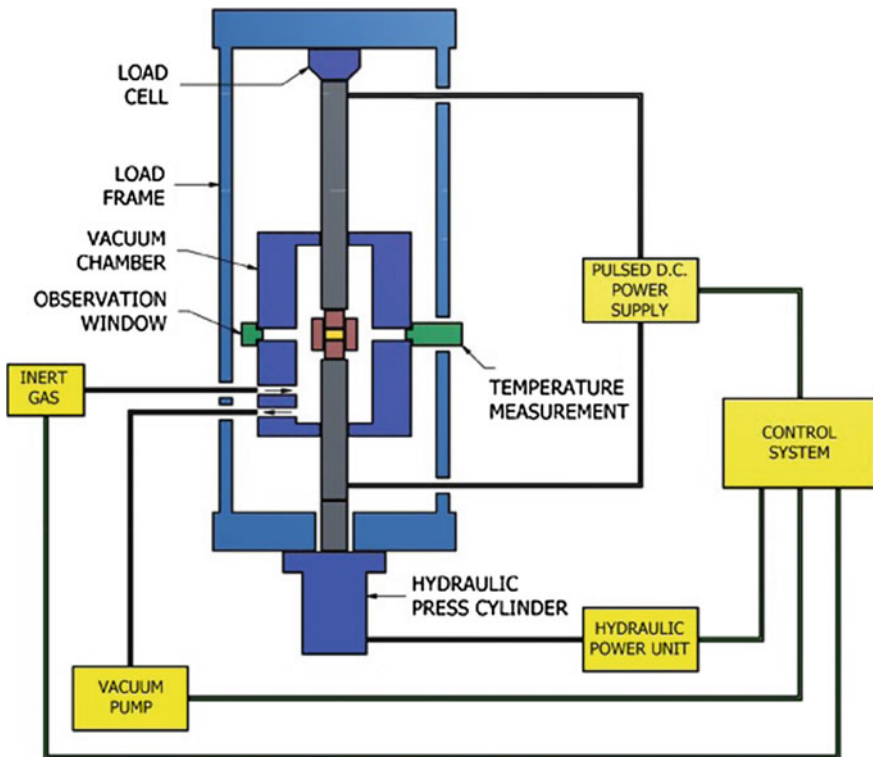


Fig. 20.4 Schematic of spark plasma sintering (SPS) equipment [27]

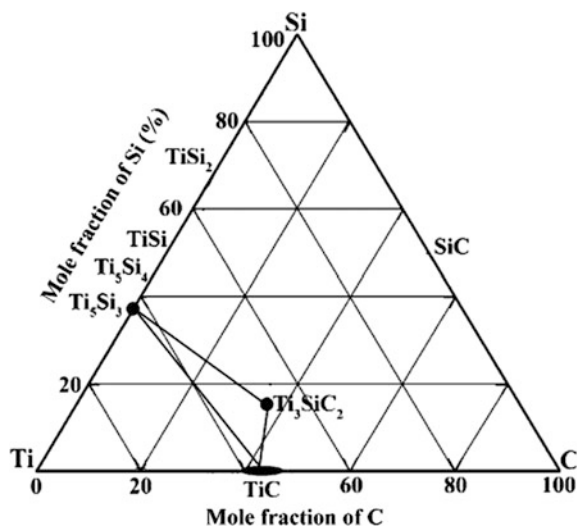


Fig. 20.5 Isothermal tertiary phase diagram of Ti–Si–C at 1200 °C [12]

There are several factors that affect the purity levels of the Ti_3SiC_2 phase. These will be discussed with the aid of the 1200 °C section of the tertiary Ti–Si–C phase diagram in Fig. 20.5. This diagram shows that the Ti_3SiC_2 phase region is very small, such that it is difficult to obtain a thermodynamically stable single-phase product [12, 13]. Hence the synthesis inevitably results in impurities like TiC, SiC and TiSiC_2 . However, Barsoum and El-Raghy [14] managed to synthesize 98 wt% pure Ti_3SiC_2 from Ti, graphite and SiC powders at 1600 °C, under 40 MPa pressure for 4 h.

Furthermore, the impurity levels can be altered by varying parameters like holding time, sintering temperature and pressure, and by sintering aids. The main factor affecting the purity of Ti_3SiC_2 is the powder proportion being used. Of the various powder mixtures used, a mixture of Ti/Si/TiC with addition of Al gave the highest purity Ti_3SiC_2 (≥ 99 wt%) [15, 16].

SPS without Al: Zhang et al. [17] produced Ti_3SiC_2 without using Al as a sintering aid. This was also an attempt to investigate the effect of Si content on the purity of the end product. SPS was conducted in the range of 1250–1300 °C for 15–30 min, resulting in a TiC impurity content ~ 2.5 wt%. The Si content had no effect on the purity of Ti_3SiC_2 .

Gao et al. [18] also synthesized Ti_3SiC_2 using a mixture system of Ti/Si/2TiC. This was successful in decreasing the content of TiC by 0.5 wt% when compared to earlier work.

Effect of Al: Zhou et al. [19] synthesized Ti_3SiC_2 by SPS and HP, and with Al as a sintering aid. Their work showed that Al decreased the reaction temperature and improved the density of the end product. The powder system used for SPS was

3Ti/Si/2C/0.2Al, heated at 1150–1250 °C; and for HP the powder system was 2TiC/Ti/Si/0.2Al, heated at 1300–1400 °C.

Further studies conducted using other powder systems resulted in increased diffusion of Ti and Si atoms and a decrease of TiC content. An increased holding time at temperature also resulted in lower TiC content.

20.4 Properties of MAX Phases

Many investigators have already reviewed the properties of MAX phases in detail. Here we give an overview of the main properties.

20.4.1 Physical Properties

The main physical properties, like the electrical conductivity and optical properties, arise from the impurities present in the MAX phases. Optical properties are due to delocalization of the electrons and are not temperature dependent [14]. Electrical resistivities for these materials are observed to be in the range of 0.2–0.7 $\mu\Omega\text{m}$ [20]. The materials are called “compensated conductors” due to the fact that the conductivity is contributed by both holes and electrons (though some exceptions exist). This is confirmed by measurement of the Hall and Seebeck coefficients, which tend to fluctuate near zero and give slightly positive or negative values. More information can be obtained from Refs. [14, 20, 21].

The thermal conductivity of these materials is good, similar to that of their MX counterparts, since they are also good electrical conductors. The thermal conductivities of MAX phases range between 12 and 60 W/m.k [21]. They also have quite low thermal expansion coefficients, with the exception of Cr-containing phases: sputter-deposited Cr_2AlC has a high thermal expansion coefficient, making it suitable as an oxidation-resistant coating for steels and turbine materials [4].

20.4.2 Chemical Properties

Al-containing MAX phases show exceptional stability up to 1500 °C in inert atmospheres. The behaviour at high temperatures mainly depends on the type of environment. MAX phases form oxide scales in oxidizing atmospheres owing to their stability and chemistry. The main oxidation resistance comes from an Al_2O_3 layer that forms in these environments.

Ti_2AlC is the most oxidant-resistant material, and can survive 10,000 thermal cycles up to 1350 °C without spalling or physical damage [20].

Cr_2AlC is also considered to have good oxidation resistance: however, it is observed to fail by spalling during thermal cycling [22]. Therefore the environmental temperature conditions are considered to be the biggest factor deciding the oxidation stability of any MAX phase.

While many studies of oxidation have been done on bulk MAX phases, thin films show different oxidation resistances. For example, epitaxial Ti_3SiC_2 thin films are stable only until 1000–1100 °C, and not up to 1800 °C as in the case of bulk material. It has been observed that the presence of an interphase reduces the chemical potentials of the elements, leading to less oxidation resistance; whereas for the bulk material the surface oxides act as diffusion barriers leading to better oxidation resistance [1, 5].

20.4.3 Mechanical Properties

MAX phases show much similarity to their MX counterparts with respect to physical properties, but the mechanical properties are vastly different. MAX phases are relatively softer (1–5 GPa) [22], have good machinability, and are more resistant to thermal shock. They also possess very high compression strengths. Some exhibit brittle-to-ductile transitions at high temperatures, together with better fatigue, creep and oxidation resistance as compared with their MX counterparts.

The better mechanical properties of MAX phases are mainly due to their hexagonal and layered crystal structure, which helps in generating mobile dislocations. Their better machinability, enabling electric discharge machining (EDM), is due to their being good electrical conductors [23].

Limited fatigue data are available, and only Ti_3SiC_2 has been studied in some detail. Fatigue crack growth progresses in a cyclic manner similar to that in structural ceramics. This behaviour is attributed to the heterogeneous and laminated crystal structure [5, 24].

20.5 Applications

MAX phases have become a popular topic in the field of advanced materials, and they have potential to replace traditional metals for several applications. MAX phases in bulk are found widely in temperature-resistant structural applications, notably

- Rotating electrical contacts and bearings
- Heating elements
- Nozzles
- Heat exchangers
- Tools for die pressing

- Impact-resistant materials.

Thin films of Ti_3SiC_2 could possibly be used as radiation-resistant cladding material in the aerospace and nuclear industries. Other applications include sensors, low friction surfaces and electrical contacts. Special applications have been found for exceptional MAX phases like Cr_2AlC , as coatings on turbine blades.

Semiconductor devices or sensor applications are the next potential fields. Phases such as Ti_4AlN_3 and V_4AlC_3 have the potential to be coated on spacecraft to avoid solar heating and increase the cooling capacity.

20.6 Summary and Conclusions

After only a few decades of investigation, researchers have discovered a new class of materials called MAX phases. These have the potential for numerous applications in the electronic and structural fields. The main focus of this chapter is on the synthesis processes used in producing this special class of materials.

MAX phases are advanced materials with unique combinations of properties, since they are intermediate between metals and ceramics. Efforts are being made to achieve economic industrial-scale manufacturing of these materials. Investigators are now working on some of the issues such as microstructural control and thermal shock resistance, and also exploring the possibilities for combining MAX phases with other composites and ceramics.

Acknowledgments The author is grateful to Dr. N. Eswara Prasad for his encouragement and kind support. She also would like to thank the editors for their numerous inputs in finalization of this chapter.

References

1. Eklund P, Beckers M, Jansson U, Högberg H, Hultman L (2010) The $\text{M}_{n+1}\text{AX}_n$ phases: materials science and thin film processing. *Thin Solid Films* 518(8):1851–1878
2. Barsoum M (2013) MAX phases: properties of machinable ternary carbides and nitrides. Wiley-VCH, Weinheim, Germany, p 436
3. Jiang L, Shil L, Zhang J, Wang L (2011) Fabrication, microstructure and mechanical properties of $\text{TiC}/\text{Ti}_2\text{AlC}/\text{TiAl}_3$ in situ composite. *J Mater Sci Technol* 27:239–244
4. Eklund P, Beckeres M, Jansson U, Hoegberg H (2010) The $\text{M}_{n+1}\text{AX}_n$ phases: materials science and thin-film processing. *Thin Solid Films* 8:1851–1878
5. Sun ZM (2011) Progress in research and development on MAX phases: a family of layered ternary compounds. *Int Mater Rev* 56:143–166
6. Low IM, Hu CF, Sakka Y (2013) MAX phases and ultra-high temperature ceramics for extreme environments. *Eng Sci Ref* (an imprint of IGI global), p 679
7. Zhou YC, Gu WL (2004) Chemical reaction and stability of Ti_3SiC_2 in Cu during high temperature processing of $\text{Cu}/\text{Ti}_3\text{SiC}_2$ composites. *Metallkd* 95:50–56

8. Omori M (2000) Sintering, consolidation, reaction and crystal growth by the spark plasma system (SPS). *Mat Sci Eng A* 287:183–188
9. Orru R, Licheri R, Locci AM, Cincotti A, Cao G (2009) Consolidation/synthesis of materials by electric current activated/assisted sintering. *Mater Sci Eng* 63:127–287
10. Sairam k, Sonber JK, Murthy TSR, Subramanian C, Fotedar RK, Hubli RC (2014) Reaction spark plasma sintering of niobium diboride. *Int J Refract Metal Hard Mater* 43:259–262
11. Wang YC, Leu IC, Hon MH (2004) Dielectric property and structure of anodic alumina template and their effects on the electrophoretic deposition characteristics of ZnO nanowire arrays. *J Appl Phys* 95:1444–1449
12. Lin ZJ, Zhuo MJ, Zhou YC, Li MS, Wang JY (2006) Microstructural relationships between compounds in the Ti–Si–C system. *Scripta Materiala* 55:445–448
13. Wakelkamp WJJ, Van Loo FJJ, Metselaar R (1991) Phase relations in the Ti–Si–C system. *J Eur Ceram Soc* 8:135–139
14. Barsoum M, El-Raghy T (1996) Synthesis and the characterization of the remarkable Ti_3SiC_2 . *J Am Ceram Soc* 79:1953–1956
15. Li JT, Zhang D, Miyamoto Y (2002) Rapid synthesis of dense Ti_3SiC_2 by spark plasma sintering. *J Eur Ceram Soc* 22:2365–2370
16. Zhang J, Wang I, Jiang W, Chen L (2007) Fabrication of high purity Ti_3SiC_2 from Ti/Si/C with the aids of Al by spark plasma sintering. *J Alloy Compd* 437:203–207
17. Zhang ZF, Sun ZM, Hashimoto H, Abe T (2003) Effects of sintering temperature and Si content on the purity of Ti_3SiC_2 synthesized from Ti/Si/TiC powders. *J Alloy Compd* 352:283–289
18. Gao NF, Li JT, Zhang D, Miyamoto Y (2002) Rapid synthesis of dense Ti_3SiC_2 by spark plasma sintering. *J Eur Ceram Soc* 82:2855–2860
19. Zhou A, Wang CA, Huang Y (2003) A possible mechanism on synthesis of Ti_3AlC_2 . *Mater Sci Eng A* 352:333–339
20. Radovic M, Barsoum M (2013) MAX phases: Bridging the gap between metals and ceramics. *Am Ceram Soc Bull* 92:20–27
21. Barsoum MW, Radovic M (2011) Elastic and mechanical properties of the MAX phases. *Annu Rev Mater Res* 195–227
22. Barsoum (2010) The $M_{n+1}AX_n$ phases and their properties. In: Riedel R, Chen I-W (eds) *Ceramics Science and Technology*, vol.2: materials and properties, Wiley Online Library. doi: [10.1002/9783527631735](https://doi.org/10.1002/9783527631735)
23. Scabarozzi TH, Amini S, Finkel P, Leaffer OD, Spanier JE, Barsoum M, Drulis H, Tambussi WM, Hettinger JD, Lofland SE (2008) Electrical, thermal, and elastic properties of the MAX-phase Ti_2SC . *J Appl Phys* 104
24. Barsoum M (2000) The $M_{N+1}AX_N$ phases: a new class of solids: Thermodynamically stable nanolaminates. *Prog Solid State Chem* 28:201–281
25. <http://max.materials.drexel.edu/research-areas/max-phases/>
26. Högberg H, Hultman L, Emmerlich J, Joelsson T, Eklund P, Molina-Aldareguia JM, Palmquist J-P, Wilhelmsson O, Jansson U (2005) Growth and characterization of MAX-phase thin films. *Surf Coat Technol* 193:6–10
27. Thermal Technology LLC, Elgin, Ill. <http://www.technoinfo.ru/technoinfo/products/56/138/files/1256553143306.pdf>

Chapter 21

Shape Memory Alloys (SMAs) for Aerospace Applications

R.J.H. Wanhill and B. Ashok

Abstract Shape memory alloys (SMAs) have the ability to ‘memorise’ or recover their previous form when subjected to thermal, thermomechanical or magnetic variations. This ability has resulted in a new class of materials for engineering applications in the aerospace, medical, automotive and home appliance sectors. This chapter surveys SMAs and the developments for aerospace applications.

Keywords Shape memory alloys · Properties · Applications

21.1 Introduction

The first shape memory alloys (SMAs) and the shape memory effect (SME) were discovered in the early 1930s by Ölander [1], who found that gold–cadmium (Au–Cd) alloys could be plastically deformed when cool, and restored to their original form when heated. In 1938 Greninger and Mooradian [2] observed the SME for copper–zinc (Cu–Zn) and copper–tin (Cu–Sn) alloys. Similar effects in other alloys such as In–Tl and Cu–Al–Ni were found in the 1950s.

The origin of the shape memory effect, which is governed by the thermoelastic behaviour of a reversible martensitic transition, was reported already in 1949 by Kurdjumov and Khandros [3], and by Chang and Read [4] in 1951.

In 1959 the important Ni–Ti alloy was discovered by Buehler [5]. The commercial potential of Ni–Ti was soon appreciated [5], and the first use was in 1969 for CryoFit™ “shrink-to-fit” hydraulic tube couplings in the Grumman Aerospace Corporation F-14 tactical aircraft. This success was followed by the alloy’s use for

R.J.H. Wanhill
Aerospace Vehicles Division, Netherlands Aerospace Centre NLR,
Emmeloord, The Netherlands
e-mail: rjhwanhill@gmail.com

B. Ashok (✉)
Aeronautical Development Agency, Bangalore, India
e-mail: ashoktwinn@yahoo.com

orthodontic bridge wires in 1971 [5]. Since the 1980s many non-aerospace applications of Ni–Ti alloys have been developed owing to their unique capabilities.

Some useful books on SMAs are as follows:

- Shape Memory Alloys: Manufacture, Properties and Applications, 2010, Ed. Chen, H.R., Nova Science Publishers, Inc., Hauppauge, NY 11788-3619, USA.
- Shape Memory Alloys, Modelling and Engineering Applications, 2008, Ed. Lagoudas, D.C., Springer Science+Business Media, LLC, New York, NY 10013, USA.
- Shape Memory Materials, 1998, Eds. Otsuka, K. and Wayman, C.M., Cambridge University Press, Cambridge, UK.
- Engineering Aspects of Shape Memory Alloys, 1990, Eds. Duerig, T.W., Melton, K.N., Stöckel, D. and Wayman, C.M., Butterworth Heinemann Ltd., London, UK.

21.2 SME Mechanisms

Shape memory alloys undergo temperature-dependent phase changes, or upon application of stress or (less commonly) a magnetic field. The basic changes due to temperature and stress are illustrated in Figs. 21.1, 21.2 and 21.3, and are discussed as follows:

1. Figure 21.1 shows the temperature-induced changes in crystal structure that are common to SMAs. The high temperature austenite structure (named after W.C.

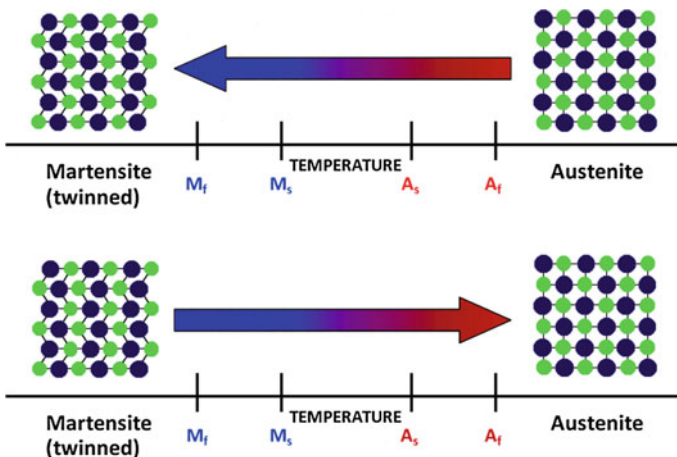


Fig. 21.1 Temperature-induced phase transformations in SMAs: after [6]. M_s and M_f are the martensitic transformation start and finish temperatures; A_s and A_f are the austenitic transformation start and finish temperatures

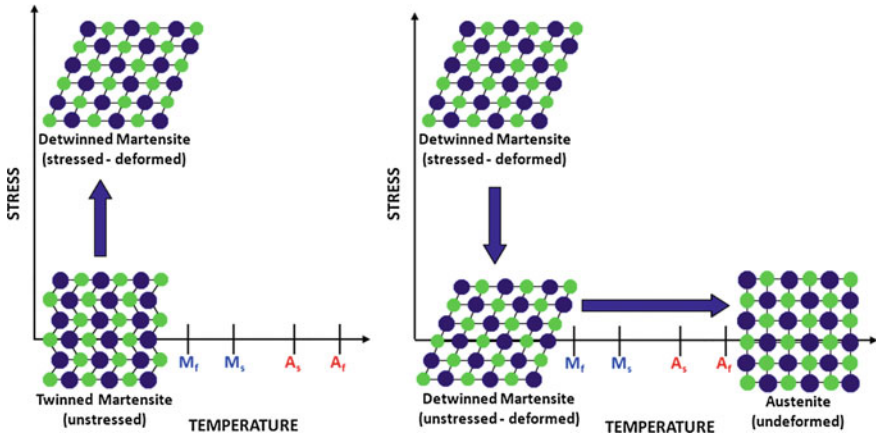


Fig. 21.2 Two-dimensional illustration of the SME: stress-free shape recovery on heating: after [6]

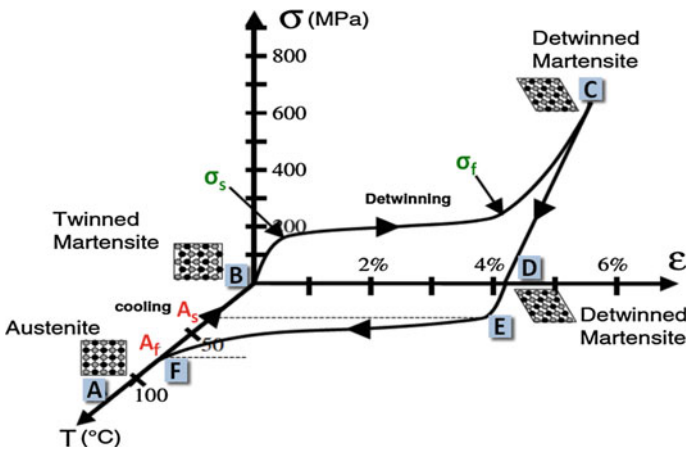


Fig. 21.3 Illustration of the shape memory effect (SME) on stress–strain–temperature axes: after [6]. Note that besides start and finish temperatures (A_s and A_f on the temperature axis) there are also stress–strain start (σ_s) and finish (σ_f) points in the σ – ϵ plane

Roberts-Austen) transforms to twinned martensite (named after A. Martens) on cooling, and changes back to austenite on reheating. Note that the transformations occur over temperature ranges.

- Figure 21.2 is a two-dimensional simplified representation of the SME. In the first instance, an unstressed twinned martensite undergoes a stress-induced isothermal change to detwinned martensite. Secondly, when the stress is removed the crystal structure remains unchanged until the material is heated. Then it transforms to austenite, as would undeformed martensite, see Fig. 21.1.

- 3 Figure 21.3 gives a fuller illustration of the SME, following the circuit ABCDEFA. Note that there are stress–strain start (σ_s) and finish (σ_f) points in the σ – ε plane; and that for clarity the M_s and M_f points between A_s and B have been omitted.

21.2.1 SMA Behaviour

Only a brief survey is given here. Much more is available from the bibliography, e.g. Ref. [6].

SMA transformations These are *thermoelastic martensitic transformations*. They involve small volume changes, a generally *relatively small* temperature hysteresis (tens of degrees °C) and good reversibility.

The temperature hysteresis means that the reverse transformation occurs at higher temperatures than the original transformation. Although it is described above as *relatively small*, the temperature hysteresis is important for practical applications (actuators), see Sect. 21.3.2.

Formation of the twinned martensite structure takes place by deformation (mainly shear) of the crystal lattice. This is illustrated schematically by the atom displacements in Fig. 21.1. The shear deformation is almost completely elastically accommodated, but this elastic energy accommodation nevertheless requires continuous cooling of the alloy to complete the transformation.

During transformation from the parent (austenite) phase, each martensite crystal can have a different orientation direction (variant). The assembly of variants can exist in two forms: (i) twinned and (ii) detwinned, see Figs. 21.2 and 21.3.

Transformation temperatures There are two basic aspects, which to some extent are related. First, the transformation temperatures for different alloys cover a wide range from near absolute zero to about 320 °C, and mainly depend on alloy composition. The alloys exhibiting these transitions include Au–Cd, In–Ti, Ni–Ti and some Cu-based alloys.

Secondly, the transformation temperatures are *stress-dependent*. Thus not only do the forward and reverse transformations occur over a range of temperatures (M_s to M_f ; A_s to A_f) for a particular alloy, but these ranges also depend on the applied stress level [6].

Pseudoelasticity This behaviour is associated with isothermal or thermomechanical stress-induced transformation, which results in strains during loading and subsequent strain recovery upon unloading at temperatures above A_f . More details are given in Ref. [6]. However, this property is also important for practical applications, e.g. in springs and vibration dampers. In commercial brochures and some archival literature the pseudoelastic effect is also referred to as *superelasticity*.

One- and two-way memory effects : The SME can be classified as either a one-way shape memory effect or a two-way effect:

1. A one-way SME is a reverse transformation where a mechanically worked detwinned martensitic material reverts during heating to its original austenitic shape, and in doing so all memory of the low temperature mechanical working is lost.
2. A two-way SME is where memory of the low temperature mechanical working is retained. In other words, renewed mechanical working is not necessary when the material again undergoes a transformation from the austenitic structure to the detwinned martensitic structure.

Both of these memory effects are important for practical applications of SMAs. But it must be noted that the two-way memory effect is not an inherent property, and it requires repeated specific thermomechanical processing before a satisfactorily reproducible response is obtained [7].

21.3 SME Alloys

Table 21.1 lists some alloy systems that have shape memory characteristics. The bold typeface rows indicate the commercially important alloy systems. These are the only alloys which can recover substantial amounts of strain or generate significant force upon changing shape.

Table 21.1 Some shape memory effect (SME) alloys: after [8–10]

Alloy	Composition	M_s temperature range (°C)	Approximate hysteresis temperature range $M_s - A_f$ and/or $M_f - A_s$ (°C)
Ag–Cd	44–49 at.% Cd	–190 to –50	15
Au–Cd	46.5–50 at.% Cd	30 to 100	15
Cu–Al–Ni	14–14.5 wt% Al; 3–4.5 wt% Ni	–140 to 100	35
Cu–Sn	~ 15 at.% Sn	–120 to 30	large
Cu–Zn	38.5–41.5 wt% Zn	–180 to –10	10
Cu–Zn–X (X = Si, Al, Sn)	a few wt% of X	–200 to 200	10
In–Ti	18–23 at.% Ti	60 to 100	4
Ni–Al	36–38 at.% Al	–180 to 100	10
Ni–Ti	49–51 at.% Ni	–100 to 110	30
Fe–Pt	~ 25 at.% Pt	~ –130	4
Mn–Cu	5–35 at.% Cu	–250 to 180	25
Fe–Mn–Si	32 wt% Mn; 6 wt% Si	–200 to 150	100

The Ni–Ti alloys are especially important, since compared to Cu–Al–Ni and Cu–Zn–Al alloys they have greater SME strain (up to 8 % vs. 4–5 %), much higher ductility and thermal stability, and better corrosion resistance [8]. On the other hand, the Cu-based alloys are much less expensive, they can be melted in air (unlike Ni–Ti alloys, which require vacuum or inert environments) and they have a wider range of transformation temperatures [8, 9].

More information on the alloy properties is given in Sects. 21.3.1 and 21.3.2.

21.3.1 Properties of Commercial SMAs

A comparative overview of the properties of Ni–Ti, Cu–Ni–Al and Cu–Zn–Al alloys is given in Table 21.2, concentrating on the engineering aspects. There are several points to note:

1. The strengths and E-moduli of the three alloy classes are similar, but the Ni–Ti alloys are much more ductile and can tolerate greater strains (as mentioned earlier).
2. The Ni–Ti alloys have higher working stress capabilities and can tolerate much larger numbers of thermal cycles (if necessary). They also have good fatigue strengths, and better corrosion resistance, also mentioned earlier.
3. The Cu-based alloys have wider ranges of transformation temperature ranges, which can be advantageous, and the Cu–Zn–Al alloys have a much higher damping capacity.

Table 21.2 Some important properties of Ni–Ti, Cu–Ni–Al and Cu–Zn–Al alloys manufactured by Advanced Materials Technologies Pte Ltd. [10]

Property	Ni–Ti	Cu–Zn–Al	Cu–Al–Ni
Melting point (°C)	1250	1020	1050
Density (g/cm ³)	6.45	7.9	7.15
Thermal expansion coefficient (10 ⁻⁶ /K)	6.6–10	17	17
E-modulus (GPa)	95	70–100	80–100
UTS, martensite (MPa)	800–1000	800–900	1000
Elongation to fracture, martensite (%)	30–50	15	8–10
Fatigue strength at 10 ⁶ cycles (MPa)	350	270	
Transformation temperature range (°C)	–100 to +110	–200 to +110	–150 to +200
Maximum one-way memory strain (%)	7	4	6
Normal two-way memory strain (%)	3.2	0.8	1
Normal working stress (MPa)	100–130	40	70
Normal number of thermal cycles	+100,000	+10,000	+5000
Maximum overheating temperature (°C)	400	150	300
Damping capacity (%)	20	85	20
Corrosion resistance	Excellent	Fair	Good

4. The lower density and thermal expansion coefficient of Ni–Ti alloys are potential advantages for applications where weight savings and dimensional tolerances are critical, e.g. in spacecraft and some medical devices.

21.3.2 Ni–Ti Alloy Variants

Ni–Ti alloys are highly sensitive to changes in the binary alloy composition, and the addition of other elements also significantly affects the properties [11]:

1. Binary alloys. The common composition range for commercial alloys is 49.0–50.7 at.% Ti (see Table 21.1 also):
 - superelastic alloys: 49.0–49.4 at.% Ni
 - SME alloys: 49.7–50.7 at.% Ni.

The alloys usually have M_s temperatures between -50 and $+100$ °C, although a wider range is given in Tables 21.1 and 21.2.

2. Ternary alloys. The most important are Ni–Ti–Cu and Ni–Ti–Nb alloys:
 - Ni–Ti–Cu alloys cover a range of compositions whereby copper substitutes for nickel. More than 15 at.% Cu embrittles the alloys [12], making conventional casting unsuitable (such high-Cu alloys can be made via melt spinning [13], but the aerospace industry generally avoids low-ductility alloys).
The most useful practical effect of Cu substituting for Ni is a *narrowing* of the temperature hysteresis [14]. This makes these alloys better suited to applications like actuators, which usually need rapid response times (narrow hysteresis loops) during thermal cycling.
 - Ni–Ti–Nb alloys cover a wide range, up to at least 30 at.% niobium, substituting for nickel *and* titanium [15]. These alloys have increased yield strength, but more importantly a *wider* temperature hysteresis [11, 15]. This makes these alloys better suited for couplings and fasteners.
3. Other alloying additions. Fe, Al, Cr, Co and V are added to binary Ni–Ti alloys to lower the M_s temperature while maintaining the basic stability and ductility [11]. The main practical result is creation of a cryogenic SMA.
Pd and Pt additions first decrease the M_s temperature and then increase it up to as high as 350 °C [16]. This gives possibilities for using SMAs as actuators in aerospace gas turbines [17, 18], e.g. in valves for switching or moderating fluid flows.

Note

There are numerous companies advertising Ni–Ti alloy variants. The exact chemical compositions are proprietary, but it is interesting that several variants are offered. For example, the following alloys are advertised by Memry Corporation:

- superelastic, high-strength superelastic, Cr-doped superelastic, high temperature and body temperature Ni–Ti alloys
- narrow hysteresis Ni–Ti–Cu alloy
- high-strength superelastic Ni–Ti–Fe alloy
- high-stiffness Ni–Ti–Co alloy.

21.4 Aerospace Applications of SMAs

21.4.1 Overview

Figure 21.4 shows compilations of the percentages of US patents and world-wide published articles on SMAs over the time period January 1990 to September 2013 [18]. These are discussed in detail in Ref. [18], and only a summary is given here:

1. Biomedical patent applications predominate, but this is not reflected in the number of published articles.
2. The ‘Others’ percentage for published articles reflects the great scientific interest in these materials.
3. The aerospace sector percentages reflect ‘niche’ applications or potential applications.

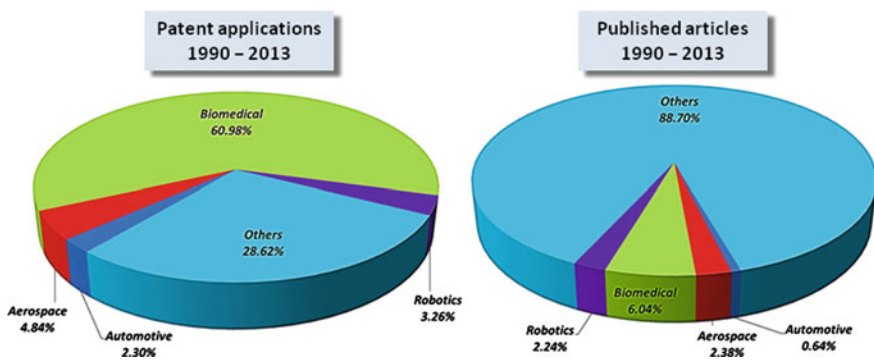


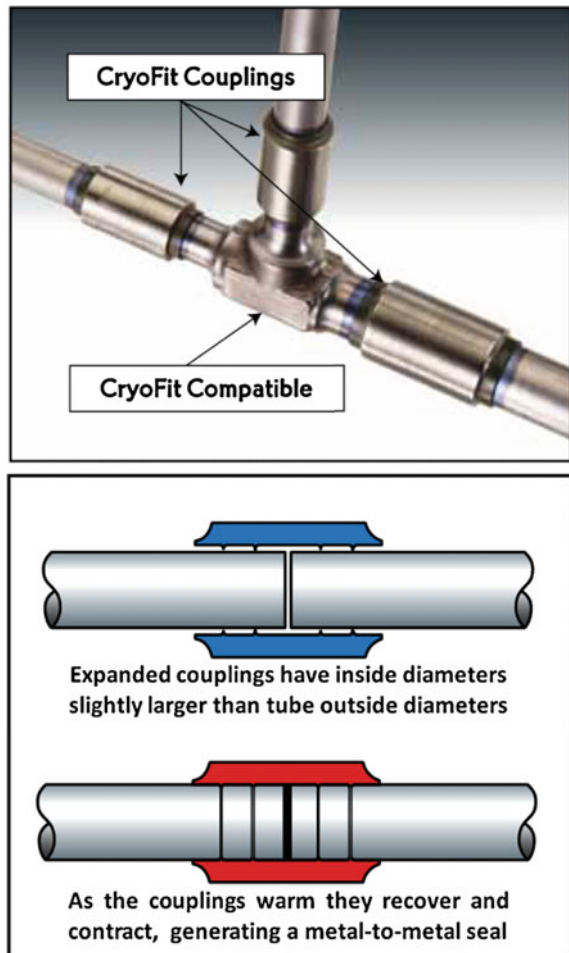
Fig. 21.4 Relative numbers of patents (US) and publications per application sector from January 1990 to September 2013 [18]

21.4.2 Actual and Potential Applications in Aircraft

Background: As part of a 1996 NATO–AGARD Lecture Series on Smart Structures and Materials, a lecture on SMAs stated that their application in aircraft was limited to shrink fit hydraulic tube couplings, and that this was understandable because the application does not require precise temperature control or taking full advantage of the potential of SMAs [19]. The authors also remarked upon the complexity of SMAs and SMA-activated structures.

The foregoing observations were made 27 years after the first use of SMAs for the CryoFit™ couplings in F-14 tactical aircraft, e.g. Fig. 21.5. Now, another two decades on, the situation with respect to *in-service* SMA applications in aircraft is virtually unchanged. In fact, Hartl et al. recently emphasized that there are no certified SMA-based actuators for use in commercial aircraft [20].

Fig. 21.5 Examples of CryoFit™ couplings



SMA actuators current situation There are several reasons why SMA actuators are not presently used in aircraft:

1. Incorporating these actuators into engineering structures and systems is a complex and multi-disciplinary process.
2. Although much metallurgical knowledge has been gained in the last 25 years, as may be found in the Bibliography, there are still many engineering issues. For actuators, which employ the two-way memory effect, these include the following [18, 21]:
 - relatively small usable strains (less than half the maximum strains in Table 21.2)
 - low actuation frequencies and narrow frequency bandwidths
 - low activation (energy) efficiencies
 - ‘training’, i.e. repeated thermomechanical processing, to obtain reproducible responses.
 - long-term durability and reliability under repeated thermomechanical loading, i.e. the in-service fatigue performance.
3. The transformation-based properties and testing methods for SMAs to be used in actuators are not (yet) standardized [20]. Also, it appears from the fatigue data surveyed and obtained in Ref. [22] that actuator requirements and specifications would benefit from a comprehensive data bank on thermomechanical transformation fatigue.

Perhaps the most important engineering issue is the low actuation frequency and narrow bandwidth [18, 21], which are related since they depend on the achievable heating and cooling rates of the SMA actuators. The narrow frequency bandwidth is a particular issue for vibration control. More information on these and the other issues is obtainable from Refs. [18, 21, 22].

SMA actuator prospects Fig. 21.6 shows an overview of the potential applications of SMA actuators in aircraft. These are discussed in detail in Refs. [18, 21, 23, 24], whereby Refs. [23, 24] are devoted exclusively to ‘morphing’, i.e. changing the shapes of aerodynamic surfaces, especially the wings. The authors of Ref. [23] realistically quote NASA in concluding that aircraft with morphing control surfaces are decades into the future.

Advantages of SMAs The primary advantages of SMAs are significant reductions in mechanical complexity and size [18, 21] owing to the following:

1. Direct reaction to environmental stimuli.
2. High energy densities. Substantial forces and displacements can be generated in small components. Besides saving space this is beneficial for weight savings and hence structural efficiency.
3. Three-dimensional actuation. SMAs with the usual polycrystalline microstructures can be produced in a variety of shapes.

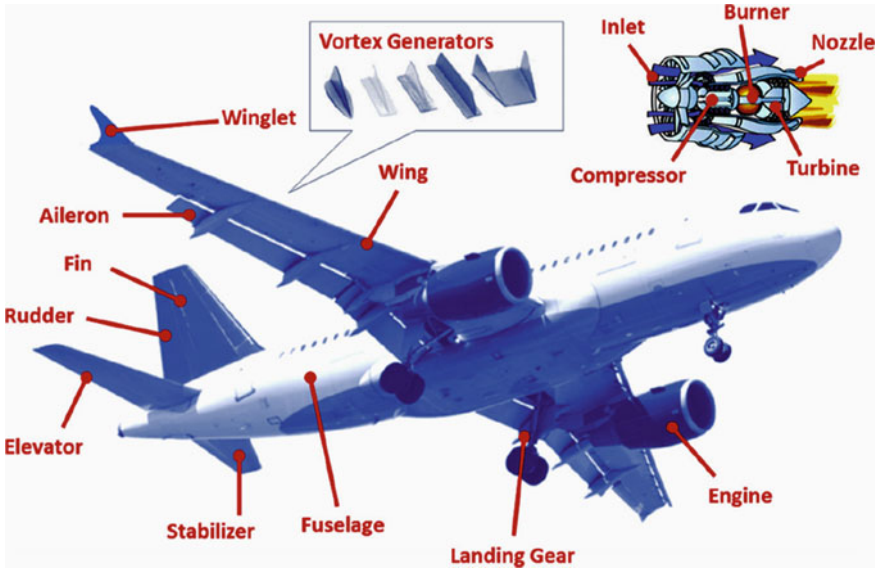


Fig. 21.6 Overview of potential applications of SMA actuators in aircraft [18]

Note

Huang [25] has compiled a series of charts to assist in selecting SMAs for use in actuators.

21.4.3 Applications in Spacecraft

SMAs have been, and continue to be, used in spacecraft for several types of applications [18, 21]:

1. Low-shock release. Unlike pyrotechnic release mechanisms, SMA release devices can be actuated slowly, avoiding shock failures in satellites. This type of application is very important for satellites, and can also be used for ‘microsatellites’, since compact separation devices with very small SMA release triggers can be made. Examples including the popular Starsys Qwknut system are given in Refs. [26–28]. These are all testable and re-settable on the spacecraft. A particularly simple *concept* is the Frangibolt release mechanism, Fig. 21.7: a compressed (deformed) SMA cylinder recovers and lengthens by heating, and exerts sufficient force on the notched bolt retaining nut to break the bolt. (N.B: this is obviously not re-settable.)

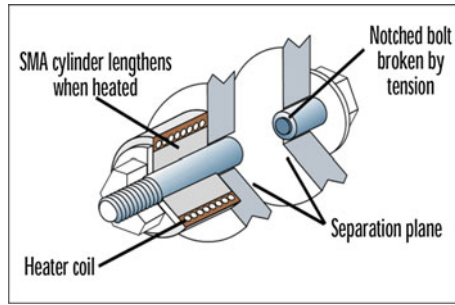


Fig. 21.7 Illustration of the Frangibolt[®] low-shock release mechanism

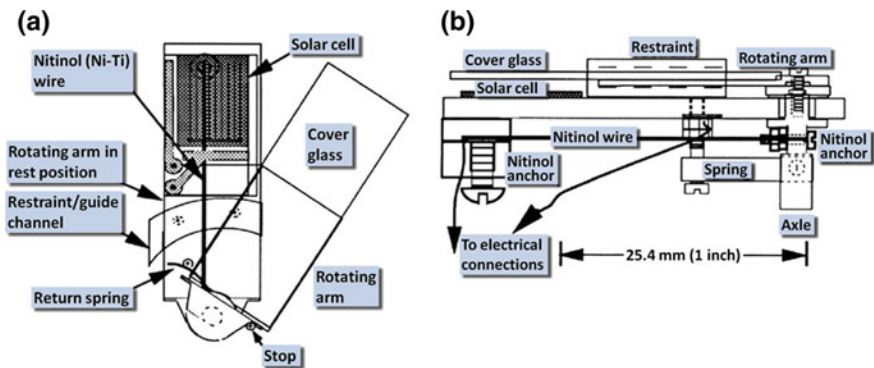


Fig. 21.8 SMA actuator assembly for the Mars Pathfinder lander [30]: see text for explanation

2. Low-shock deployment. SMA actuators can also be used in deploying satellite antennae, solar arrays [29] and other devices. A well-known and early use was for the Mars Pathfinder Lander [30]. The SMA actuator assembly is shown schematically in Fig. 21.8. Heating the Ni–Ti wire caused it to contract, turning the axle and rotating the cover glass arm to the right. A spring ensured that the arm returned to its rest position when the Ni–Ti wire was allowed to cool. The procedure was repeatable, and this was the first multi-cycle SMA actuator used in a space application [30].

Note

The Pathfinder and Frangibolt devices use(d) SMA behaviour in opposite ways: heating *lengthens* the Frangibolt SMA but *shortened* the Pathfinder wire.

3. **Sensors.** Since SMAs are thermally activated, they can also be used as sensors. In this capacity SMAs acquire information from a thermomechanical system (i.e. they are heated or cooled), and transformation-induced material property changes, e.g. resistivity [21], are monitored.
4. **Vibration damping.** An additional exploitable benefit of using SMAs in spacecraft is that the pseudoelastic effect makes them suitable for absorbing vibrations. However, the use of SMAs specifically for vibration dampers appears to be still largely in the R&D and patent application stages [18, 21, 31].

Special considerations Spacecraft mechanisms and devices are often custom-built: the Pathfinder lander SMA assembly shown in Fig. 21.8 is a prime example. However, space agencies like NASA and ESA have stringent requirements, and all mechanisms and devices must undergo rigorous qualification programmes.

21.5 Concluding Remarks

Aerospace applications of shape memory alloys (SMAs) are limited, especially for aircraft, less so for spacecraft. The alloys have unique properties and capabilities, and there are numerous potential applications. However, their usage is hindered by several inherent issues and the complexity of incorporating their behaviour into engineering structures and systems. For example, even an apparently simple system like that for the Mars Pathfinder Lander had to account for many factors in order to guarantee its reliability [30].

Multi-disciplinary R&D, including reliability engineering, will be needed to change this situation. Even so, widespread application of SMA mechanisms and devices in aircraft appears to be many years in the future. Space applications—although different—could provide greater familiarity with some of the design issues.

Any consideration of SMA applications should involve the alloy manufacturing companies, who obviously have much proprietary knowledge at their disposal: see the note in Sect. 21.3.2.

References

1. Ölander A (1932) An electrochemical investigation of solid cadmium-gold alloys. *J Am Electrochem Soc* 54:3819–3833
2. Greninger AB, Mooradian VG (1938) Strain transformation in metastable beta copper–zinc and beta copper–tin alloys. *Trans AIME* 128:337–368
3. Kurdjumov GV, Khandros LG (1949) First reports of the thermoelastic behaviour of the martensitic phase of Au–Cd alloys. *Dokl Akad Nauk SSSR* 66:211–213
4. Chang LC, Read TA (1951) Plastic deformation and diffusionless phase changes in metals: the gold-cadmium beta phase. *Trans AIME* 191:47–52

5. Kauffman G, Mayo I (1996) The story of Nitinol: the serendipitous discovery of the memory metal and its applications. *Chem Educ* 2(2):1–21; *Electronic Journal* (S 1430–4171 (97) 02111-0)
6. Kumar PK, Lagoudas DC (2008) Introduction to shape memory alloys. In: Lagoudas DC (ed) Chapter 1 in ‘Shape Memory Alloys, Modeling and Engineering Applications’. Springer Science+Business Media, LLC, New York, NY 10013, USA, pp 1–52
7. Taha OMA, Bahrom MB, Taha OY, Aris MS (2015) Experimental study on two way shape memory effect training procedure for NiTiNOL shape memory alloys. *ARPN J Eng Appl Sci* 10(17):7847–7851
8. Hodgson DE, Wu MH, Biermann RJ (1990) Shape memory alloys. In: *ASM Handbook: Volume 2: Properties and selection: nonferrous alloys and special-purpose materials*. ASM International, Materials Park, OH 44073-0002, USA, pp 897–902
9. Novotny M, Kilpi J (2001) Shape memory alloys. Referenced in Gök MO, Bilir MZ, Gürcüm BH (2015) Shape-memory applications in textile design. *Procedia—Social and behavioural Sciences*, vol 195, pp 2160–2169
10. Melton KN (1990) Ni-Ti based shape memory alloys. In: Duerig TW, Melton KN, Stöckel D, Wayman CM (eds) *Engineering aspects of shape memory alloys*. Butterworth Heinemann Ltd., London, UK, pp 21–35
11. Duerig TW, Pelton AR (1994) Ti–Ni shape memory alloys. In: Boyer R, Welsch G, Collings EW (eds) *Materials Properties Handbook: Titanium alloys*. ASM International, Materials Park, OH 44073-0002, USA, pp 1035–1048
12. Nam TH, Saburi T, Nakata Y, Shimizu K (1990) Shape memory characteristics and lattice deformation in Ti–Ni–Cu alloys. *Mater Trans Jpn Inst Met* 31(12):1050–1056
13. He W, Min G, Yin Y, Tolochko O (2009) Martensitic transformation and mechanical properties of Ti-rich Ti–Ni–Cu melt-spun ribbon. *Trans Nonferrous Met Soc China* 19: 1464–1469
14. Moberly WJ, Melton KN (1990) Ni-Ti-Cu shape memory alloys. In: Duerig TW, Melton KN, Stöckel D, Wayman CM (eds) *Engineering aspects of shape memory alloys*. Butterworth Heinemann Ltd., London, UK, pp 46–57
15. Simpson JA, Melton K, Duerig T (1988) Nickel/titanium/niobium shape memory alloy and article. *United States Patent* 4,770,725, 13 Sept 1988
16. Lindquist PG, Wayman CM (1990) Shape memory and transformation behavior of martensitic Ti-Pd-Ni and Ti-Pt-Ni alloys. In: Duerig TW, Melton KN, Stöckel D, Wayman CM (eds) *Engineering aspects of shape memory alloys*. Butterworth Heinemann Ltd., London, UK, pp 58–68
17. Bigelow G, Noebe R, Padula II S, Garg A, Olson D (2006) Development and characterization of improved NiTiPd high-temperature shape-memory alloys by solid solution strengthening and thermomechanical processing. In: Berg B, Mitchell MR, Proft J (eds) *SMST-2006, Shape memory and superelastic technologies*. ASM International, Materials Park, OH 44073-0002, USA, pp 113–132
18. Jani JM, Leary M, Subic A, Gibson MA (2014) A review of shape memory alloy research, applications and opportunities. *Mater Des* 56:1078–1113
19. Boller C, Brand W, Brinson LC, Huang M (1996) Shape memory alloys and their applications. In: *Smart structures and materials: implications for military aircraft of new generation*. AGARD Lecture Series 205, Advisory Group for Aerospace Research and Development, Neuilly-sur-Seine, France, pp 2-1–2-13
20. Hartl DJ, Mabe JH, Benafan O, Coda A, Conduit B, Padan R, Van Doren B (2015) Standardization of shape memory alloy test methods toward certification of aerospace applications. *Smart Mater Struct* 24:082001 (6 p)
21. Hartl D, Lagoudas DC (2007) Aerospace applications of shape memory alloys. *Proc Inst Mech Eng Part G, J Aerosp Eng* 221(4):535–552
22. Lagoudas DC, Miller DA, Rong L, Kumar PK (2009) Thermomechanical fatigue of shape memory alloys. *Smart Mater Struct* 18:085021 (12 p)

23. Barbarino S, Bilgen O, Ajaj RM, Friswell MI, Inman DJ (2011) A review of morphing aircraft. *J Intell Mater Syst Struct* 22:823–877
24. Barbarino S, Saavedra Flores EI, Ajaj RM, Dayyani I, Friswell MI (2014) A review on shape memory alloys with applications to morphing aircraft. *Smart Mater Struct* 23:063001 (19 p)
25. Huang W (2002) On the selection of shape memory alloys for actuators. *Mater Des* 23(1): 11–19
26. Smith SH, Downen D, Fossness E, Peffer A (1999) Development of shape memory alloy (SMA) actuated mechanisms for spacecraft release mechanisms. Paper SSC99-XI-7. In: Proceedings of the 13th AIAA/USU Conference on Small Satellites, Cheaper by the Dozen: The Move to Small Satellite Constellations. <http://digitalcommons.usu.edu/smallsat/1999/all1999/6/>
27. Lazansky C, Christiansen S (2006) Problems and product improvements in a qualified, flight heritage product. In: 38th Aerospace Mechanisms Symposium. Compiled by Boesiger EA, NASA Conference Proceedings NASA/CP-2006-214290, NASA Center for Aerospace Information (CASI), Hanover, MD 21076-1320, USA, pp 75–88
28. Willey CE, Huettl B, Hill SW (2001) Design and development of a miniature mechanisms tool-kit for micro spacecraft. In: 35th Aerospace Mechanisms Symposium. Compiled by Boesiger EA, NASA Conference Proceedings NASA/CP-2001-209626, NASA Center for Aerospace Information (CASI), Hanover, MD 21076-1320, USA, pp 287–300
29. Huang W, Pellegrino S, Bashford DP (1996) Shape memory alloy actuators for deployable structures. In: Burke WR (ed) Proceedings of an International Conference on Spacecraft Structures, Materials and Mechanical Testing. ESA SP-386, European Space Agency, Paris, France, pp 53–61
30. Jenkins PP, Landis GA (1995) A rotating arm using shape-memory alloy. In: Schneider WC (ed) 29th Aerospace Mechanisms Symposium. NASA Conference Publication 3293, NASA Center for Aerospace Information (CASI), Hanover, MD 21076-1320 (formerly Linthicum Heights, MD 21090-2934), USA, pp 167–171
31. Lagoudas DC, Kalmár-Nagy T, Lagoudas MZ (2010) Shape memory alloys for vibration isolation damping of large-scale space structures. Annual Report AFRL-OSR-VA-TR-2912-0440, Air Force Office of Scientific Research, Arlington, VA 22203, USA

Bibliography

1. Chen HR (ed) (2010) Shape memory alloys: manufacture, properties and applications. Nova Science Publishers, Inc., Hauppauge, NY 11788-3619, USA
2. Lagoudas DC (ed) (2008) Shape memory alloys, modeling and engineering applications. Springer Science+Business Media, LLC, New York, NY 10013, USA
3. Otsuka K, Wayman CM (eds) (1998) Shape memory materials. Cambridge University Press, Cambridge, UK
4. Duerig TW, Melton KN, Stöckel D, Wayman CM (eds) (1990) Engineering aspects of shape memory alloys. Butterworth Heinemann Ltd., London, UK

Chapter 22

Detonation Sprayed Coatings for Aerospace Applications

D. Srinivasa Rao, L. Rama Krishna and G. Sundararajan

Abstract This chapter presents a concise overview of detonation spray technology and the associated principles and applications for the aerospace industry. The most popular feedstock powders for obtaining a wide variety of coatings with varying composition and properties are emphasized. The strategies for obtaining improved structure–property combinations via spray process optimization are discussed, and also the utilization of novel powders for enhanced protection. The typical microstructural features as a key to achieving the required mechanical, tribological and corrosion properties are briefly illustrated with specific examples.

Keywords Detonation sprayed coatings · Processing · Wear resistance · Thermal barriers

22.1 Introduction

In the modern world many materials are expected to deliver multi-functional properties and performances. The available choice window often becomes narrow and therefore encourages non-conventional materials processing routes.

An important example is the development of thermal spray coatings. This technology has expanded especially over the last few decades in such a way as to significantly broaden the otherwise narrow material selection window. In fact, thermal spray technologies have become essential for enhancing the service life of various engineering components, and have therefore become an integral part of the manufacturing process. For example, almost all aircraft landing gear manufacturers have one or more thermal spray systems as part of the regular manufacturing line.

D.S. Rao (✉) · L. Rama Krishna · G. Sundararajan
International Advanced Research Centre for Powder Metallurgy
and New Materials (ARCI), Balapur PO, Hyderabad 500005, India
e-mail: raods@arci.res.in

In view of the large number of thermal spray technologies employed for various industrial applications, including aerospace, this chapter focusses mainly on one of the most important thermal spray technologies known as detonation spraying.

The detonation spray coating (DSC) technology (also known with popular trade names such as D-Gun, Super D-Gun) primarily depends upon the kinetic energy of particles-in-flight, rather than the thermal energy transferred to the particles (e.g. unlike plasma spraying). In view of the lower thermal energy input the feedstock undergoes skin melting or plasticizing. Therefore the oxidation tendency and solidification stresses (tensile) are minimal. The detonation causes the particles to bombard the substrate with high kinetic energy, leading to formation of a coating with uniformly dense microstructure (porosity < 0.5 %) and excellent inter-splat bonding and adhesion to the substrate.

In the aerospace industry detonation sprayed coatings are used mainly on aircraft gas turbine components. Some of these are illustrated in this chapter and are from the authors' institute.

22.2 Detonation Spraying

22.2.1 The Spraying Process

While most thermal spray techniques deposit coatings continuously, DSC is a 'pulsed' process in which oxygen and acetylene are injected in pre-measured quantities into the combustion chamber of a long water-cooled stainless steel barrel. This is shown schematically in Fig. 22.1. The oxy-fuel mixture is ignited explosively using a spark plug, and the combustion products expand rapidly owing to their high specific volume and the high temperature generated by the explosion.

Upstream of the combustion process, and assisted by a nitrogen carrier gas, metered quantities of powder (usually 5–45 μm size) are fed into the zone of reduced barrel inner diameter where detonation waves are generated, as shown in

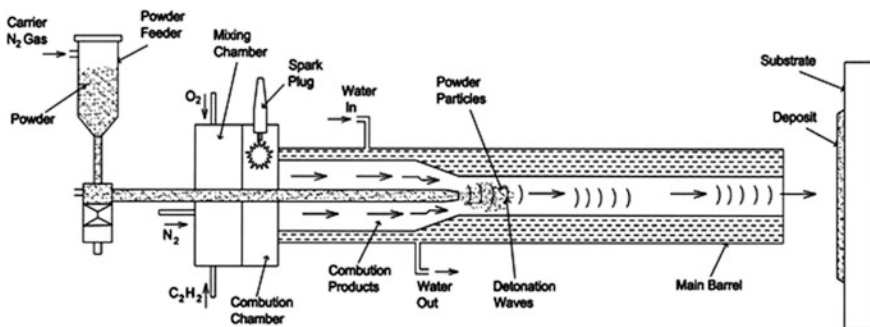


Fig. 22.1 Schematic representation of the detonation spray coating process

Fig. 22.1. The powder particles interact with the surrounding combustion products and undergo physico-chemical changes while travelling towards the open end of the barrel.

The thermal and kinetic energy transport rate primarily depends upon the relative ratio of oxygen to fuel (acetylene) and the total volume of the gas mixture. The particles are accelerated to supersonic velocities that can be as high as 1200 m/s. The temperature and velocity of the particles exiting the barrel depend upon the size, density and thermo-physical properties of the particles.

The particles ejected in each detonation cycle impact the substrate to form layer-by-layer coatings. By manipulating the movement of the barrel (and the part being coated), a uniformly thick coating can be deposited. More details about the process fundamentals and coating formation mechanisms are described in Refs. [1–3].

One interesting feature which distinguishes the DSC process from most other thermal spray methods is its ability to spray metals, ceramics and cermets very effectively by way of creating neutral, oxidizing or reducing environments, simply by altering the relative oxygen/fuel ratio.

22.2.2 Equipment Characteristics

The DSC technology was proprietary until the last decade. However, commercial systems based on the original design from the former Soviet Union are now available. The typical water-cooled stainless steel barrel illustrated in Fig. 22.1 is 1350 mm long and has a 22 mm internal diameter, see Fig. 22.2 also.

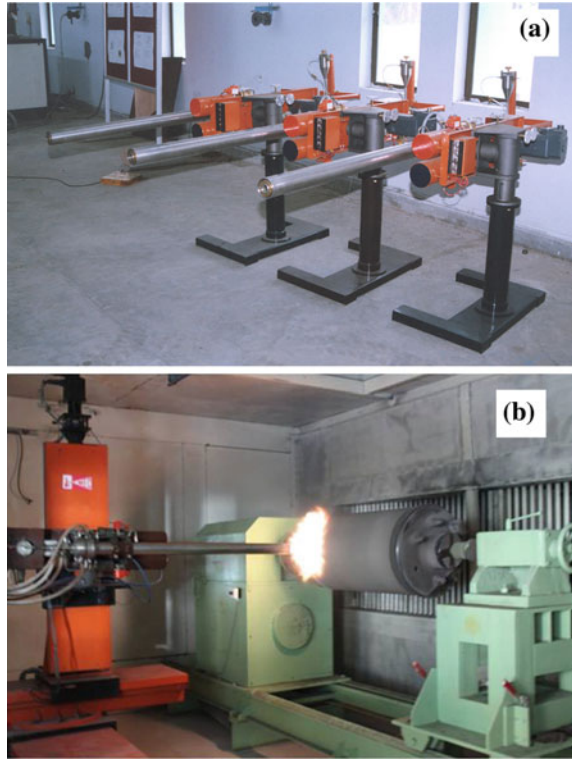
A variety of powder feeder designs are available, based on the application needs. For instance, multiple powder feeder systems may be used to allow spraying different powders; or sequential spraying that permits formation of coating layer gradients with varied composition in each layer.

The spray process is usually controlled and monitored remotely via a panel located outside the spray booth, which is sound- and dust-proof. A typical spray booth is shown in Fig. 22.2b.

22.3 DSC Technology Compared with Other Thermal Spray Techniques

Although DSC was initially meant for depositing wear-resistant carbide coatings, its ability to deposit dense ceramic coatings has enabled it to secure an equivalent position with respect to high velocity oxy-fuel spray coating (HVOF). Also, the thermo-kinetic energy transport of powder particles is better controlled in the DSC

Fig. 22.2 a Typical configuration of DSC systems and b spraying in progress



process than in the well-established thermal spray technologies APS and VPS (air and vacuum plasma spraying).

HVOF is the chief alternative to DSC. The HVOF combustion gases are discharged through a confined cooled nozzle at high gas flow (up to Mach 3 velocity), and the resultant particle velocities, especially for carbide powders, are similar to those of DSC (up to 1200 m/s). The HVOF coatings also have similar densities to those produced by DSC: both types of coating are much denser than plasma sprayed coatings.

In fact, most wear-resistant carbide coatings are sprayed using either the HVOF or DSC systems with identical aerospace quality specifications. This demonstrates wide acceptance of these techniques as being equivalent. (However, since DSC is only recently commercially available, HVOF has been the only option for depositing dense, wear-resistant carbide coatings on a large variety of aircraft and helicopter components.)

DSC is very versatile: it can accommodate a wide variety of spray grade powders including metals, alloys, ceramics, cermets and composites with low melting point binders [4–9]. Also, the number of spray grade powders being formulated and manufactured has steadily increased, such that a wide variety of DSC coatings is potentially available.

Although DSC can deposit almost any material that melts without decomposition, the size of the gun prevents complete internal coatings. Internal cavities connected to the outer surface can be coated only via line-of-sight. Therefore, utilizing the 45° angle of deposition, it is possible to provide internal coating of a cylindrical object to a length equal to its diameter.

Other competing technologies are powder flame spraying, wire flame spraying and wire arc spraying. These find limited use at present, although they have the advantages of moderate equipment costs and are portable for on-site repairs and refurbishments. Recent developments such as the introduction of solid ceramic rods as feed in wire arc spraying systems have increased their potential for relatively non-critical and corrosion-resistant aerospace applications.

22.4 DSC Coating Applications in Aerospace

22.4.1 Tungsten Carbide/Cobalt (WC–Co) Coatings

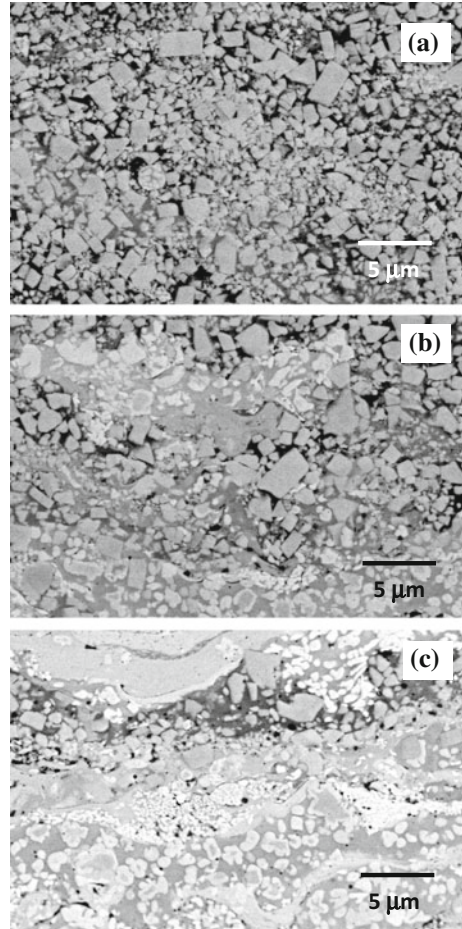
Tungsten carbide/cobalt (WC–Co) coatings are the main thermal spray coatings used in aerospace. These coatings possess a unique combination of extreme hardness (12–14 GPa), high modulus (350–400 MPa), high indentation toughness (5–7 MPa \sqrt{m}) and low porosity (0.5 %), and have excellent resistance to fretting wear, corrosion and rolling contact fatigue. Such wide-ranging properties are attributed mainly to a uniform distribution of extremely hard (24 GPa) WC cuboids in the softer (2.5 GPa) cobalt matrix, which typically constitutes 20 vol% of the coating [10]. The cuboids have a typical size range of 0.5–6 μm .

Unlike plasma spraying, both the HVOF and DSC processes can maintain reducing atmospheres within the combustion gas stream, making these techniques particularly suited to depositing carbide-based coatings. The DSC process has some advantages over HVOF in (i) its flexibility to employ a wide range of oxy-fuel ratios while maintaining a reducing atmosphere, and (ii) the use of a much longer barrel that enables better thermo-kinetic energy transfer to the particles. Thus DSC coatings are often preferred to HVOF coatings, especially when close control over the final coating microstructure is essential.

An illustration of the DSC flexibility is given in Fig. 22.3: using the same WC–12Co feedstock powder, the DSC technique can significantly alter the coating microstructure simply by varying the oxy-fuel ratio [10].

Decarburization: Whichever technique is used, a common issue is the decarburization of WC cuboids during spray deposition. On the one hand, the powder particle temperature during spraying needs to be sufficiently high to attain cobalt melting and therefore achieve higher inter-splat cohesion. But on the other hand, higher particle temperatures lead to decomposition or decarburization of WC, whereby W and C dissolve into the cobalt matrix [11]. Therefore the temperature and oxidation potential of the gas stream needs to be balanced to achieve a practical

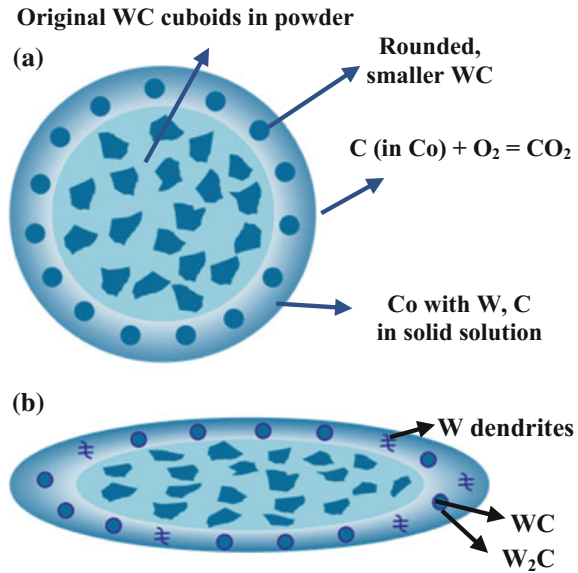
Fig. 22.3 WC–12Co coatings deposited by DSC at various oxy-fuel ratios. **a** 1.16 **b** 1.5, **c** 2.0



balance of these opposing phenomena. Also, the finer the WC-cuboid size in the WC–Co powder, the greater is the extent of decarburization during the coating process, while too-large cuboids lead to relatively poor cohesion with the cobalt matrix [12].

Particle changes during deposition: It is noteworthy that decarburization cannot be completely eliminated, since the Co matrix has to melt to impart sufficient inter-splat bonding. At the same time, formation of the harder W_2C phase (30 GPa—harder than WC itself) should be minimal because W_2C embrittles the coating, see Ref. [10]. The presence of W_2C can be easily identified in the coating microstructure by the formation of typical W_2C shells around the WC cuboids [10, 11]. Since the solid solubility of both W and C in the Co matrix decreases rapidly as the splat cools down, precipitation of W_2C around the WC cuboids and

Fig. 22.4 Schematic illustration of physico-chemical changes in WC–Co powder particle **a** during spraying, **b** during splat solidification: Refs. [12, 13]



W in dendritic form can be observed in the coating microstructure, as schematically illustrated in Fig. 22.4b.

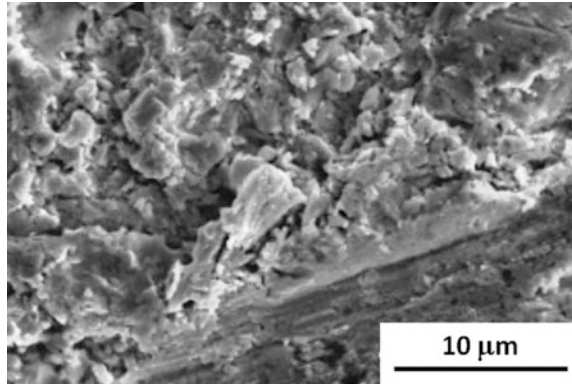
Also, while the primary goal is to retain the typical composite structure of WC cuboids distributed in the Co matrix, the cuboids will eventually reduce in size, and the shape changes to non-cuboidal (with rounded edges) due to WC loss from the sharp edges, as also indicated in Fig. 22.4.

It should be noted that the extent of retention of dissolved C in Co is determined by the rate at which C is lost from the Co matrix owing to the formation of CO_2/CO during the rapid solidification when the particles impact the substrate [14].

In view of the above-mentioned physico-chemical changes that are likely to happen during spray deposition of WC–Co coatings, it is very important to understand the influence of all possible interacting factors to arrive at the optimum process parameters, including the inter-splat cohesion. Any compromise in inter-splat cohesion will have a deleterious effect on the fracture toughness and wear resistance of the coatings. Experience has shown that an oxy-fuel ratio of 1.3–1.5 is the optimum for obtaining the best property combinations.

Wear resistance: As already mentioned, WC–Co coatings have excellent resistance to wear and rolling contact fatigue. They also have a high erosion resistance: erosive media, e.g. sand, usually have grain sizes much larger than the WC cuboids, and so the WC–Co composite modulus provides a high resistance to erosion damage. This can be explained with the aid of Fig. 22.5 [15]. This shows the formation of lips on the WC–Co coating surface, implying a ploughing mechanism, which is a common feature of ductile materials undergoing and resisting erosion.

Fig. 22.5 Eroded surface of WC–Co coating showing lip formation [15]



WC–Co coatings also provide excellent protection under abrasive and sliding wear modes [16–19]. In addition, these coatings significantly enhance service life by resisting fretting wear, erosion–corrosion and rolling contact fatigue [20, 21], as was also mentioned earlier.

Gas turbine applications: The exceptional combination of properties obtainable from WC–Co coatings has resulted in numerous applications in aircraft gas turbines. In the turbine section these include actuator piston rods and fuel pump impellers in the afterburner; combustion chamber positioning pins; gear box support pins, bushings and lugs; labyrinth seal fins and seal teeth; gears; oil pump scavenge and breather tubes; bearing housings and seal assemblies; and exhaust fairing pins and bushings.

In addition, WC–Co coatings are used to meet the functional requirements of numerous parts in the compressor section, e.g. bevel gears; gear box drives; bleed manifold expansion joint liners and sleeves; fan and compressor blades; case flanges; hubs; discs; rotor tubes and sleeves; diffusers; impellers and vane sectors; and variable vanes.

Figure 22.6 depicts some aircraft parts that have been coated with the two most popularly employed coatings, viz., WC–12Co and WC–17Co.

Helicopter applications: WC–Co coatings to combat wear, corrosion, fretting and sliding wear damage are applied to a wide selection of helicopter components including main rotor shafts, rotor blade extension sleeves, blade bolts, transmission gears, damper housings, swash plates, tail rotor hubs, pinion gears, blade radius rings, cylinder assembly plungers, inner race bearings, spur gears, bearing retaining nuts, bevel drive gears, and conical and input gears.



Fig. 22.6 a WC-17Co coated compressor disc and b-c WC-12Co coated nozzle parts

22.4.2 *Modified Tungsten Carbide/Cobalt (WC-Co-Cr) Coatings*

A slightly modified WC-Co coating chemistry is the WC-10Co-4Cr composition, which is recognized as an actual and potential replacement for hard chrome electroplating [22], thereby avoiding the environmentally hazardous chemicals used in the plating process.

Although WC-Ni and WC-Ni-Cr coatings have also been extensively studied, the WC-Co-Cr coatings demonstrate superior corrosion and erosion resistance. Also, these coatings are superior to hard chrome electroplate with respect to pitting, spalling and cracking under stress [23, 24]. Further, it should be noted that these coatings are more rapidly deposited via DSC/HVOF routes as compared to the electroplating process.

Owing to their superior erosion and corrosion resistance, the WC-Co-Cr coatings are now used to effectively provide functional property enhancement of numerous landing gear components; piston rods and swash plate sliders; low- and

high-pressure turbine shafts; pinch locks; bearing housings; and front- and rear-compressor hubs of aircraft and helicopter gas turbines.

22.4.3 Cr_3C_2 -NiCr Coatings

Besides WC-based coatings, DSC-deposited Cr_3C_2 -NiCr coatings are widely used to provide high thermal stability, excellent resistance to wear [25], oxidation, fretting, corrosion and high temperature wear, especially in the harsh operating conditions of an aircraft engine. Also, the solid particle erosion resistance at low angles of impingement is better than that of special grade stainless steels, and the coatings are well-bonded to the substrate (bond strength ~ 70 MPa [26]).

The relative proportion of NiCr ranges from 20–40 at.%, although Cr_3C_2 -25NiCr (50:50 at.% Ni-Cr solid solution) is the most popular spray grade powder [27]. The Cr_3C_2 -NiCr coating exhibits a typical plate-like lamellar structure oriented roughly parallel to the substrate, as shown in Fig. 22.7. The microstructure is characterized by a dense skeletal network of fine chromium carbide (Cr_3C_2) and chromium oxide (Cr_2O_3) bound within the NiCr ductile matrix [28]. With such a microstructure and a coating hardness in the range of 750–950 HV, the high temperature wear resistance up to 980 °C is excellent, especially under moderate load, dry frictional conditions [25, 29].

Owing to the above-mentioned specific properties, the Cr_3C_2 -NiCr coatings are being used for seals, flaps, nozzle segments and spray bars of afterburner sections; sealing rings, spacers, air seals, shrouds, blades and vanes in turbine sections; clamps, liners, nozzle nuts and fuel swirlers in combustion sections; and seal seats and spacers of bearings. As an illustration, a Cr_3C_2 -NiCr coated turbine blade is shown in Fig. 22.8.

It should be noted that the Cr_3C_2 phase in Cr_3C_2 -NiCr powder undergoes decarburization during the spraying process. Hence a proper selection of the spraying parameters is essential. Decarburization of the Cr_3C_2 phase leads to

Fig. 22.7 Typical lamellar microstructure of a 325- μ m-thick Cr_3C_2 -NiCr coating deposited by the DSC process

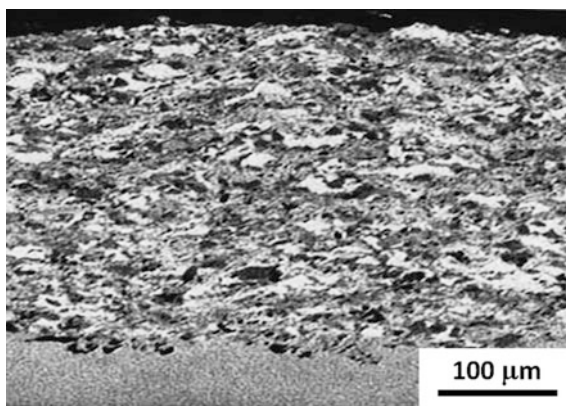
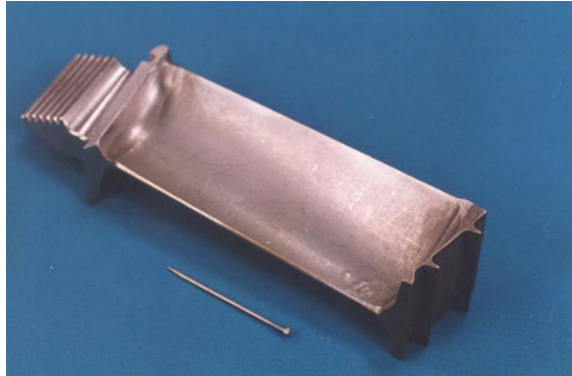


Fig. 22.8 Aircraft engine turbine blade coated with $\text{Cr}_3\text{C}_2\text{-NiCr}$ for corrosion, oxidation and fretting wear resistance



formation of lower carbides such as Cr_7C_3 and Cr_{23}C_6 phases, thereby negatively influencing the coating properties [25].

22.4.4 Abradable Coatings

Abradable coatings are mostly deposited by vacuum plasma spraying and HVOF processes. The DSC process is also capable of depositing abradable coatings, and owing to its better thermal management during spraying it is used for specialized abradable applications on various aeroengine components.

Unlike wear-resistant coatings, abradable coatings should preferentially wear away, and the debris should not damage the mating surfaces. Besides good abrasability these coatings should have high resistance to gas and particulate erosion, good thermal properties, be self-lubricating, and have minimum affinities with the substrate materials. In view of these requirements, abradable coatings are mostly combinations of metals (e.g. Al-Si and MCrAlYs, where M=Ni, Co, Fe or a combination of these elements) with polyester and solid lubricants such as hexagonal boron nitride (h-BN), bentonite or graphite [30].

Al-Si-polyester, Ni-graphite and Ni-Cr-Al-bentonite can withstand engine operating temperatures up to 325, 450 and 815 °C, respectively [31]. The abrasability requirements are met by introducing controlled porosity in the coating microstructure, thereby reducing the overall cohesive strength; while the substrate-coating bond strength is designed to be higher than the inter-splat cohesive strength.

22.4.5 Thermal Barrier Coatings (TBCs)

Components such as blades, vanes, combustion chambers, liners and domes in the hottest parts of gas turbines are usually provided with thermal barrier coatings

(TBCs) to better resist corrosion, oxidation or excessive heat loads [32]. The most used TBC, yttria-stabilized zirconia (YSZ) containing 7–8 wt% Y_2O_3 , serves as a functional topcoat, and is usually deposited by plasma spray or electron beam physical vapour deposition (EB-PVD) [33].

EB-PVD provides the most sophisticated TBC, since it builds up a columnar YSZ microstructure that has better strain tolerance and resistance to cracking and spalling. However, the success of TBCs also relies on a good bond coat between the YSZ and the substrate. The bond coat provides the main resistance to high temperature oxidation and corrosion.

Bond coats are MCrAlYs, and are deposited by thermal spray variants such as vacuum plasma spray (VPS), low pressure plasma spray (LPPS), air plasma spray (APS), HVOF or DSC [34]. Sufficient aluminium content in the MCrAlY bond coat allows formation of a thin Al_2O_3 layer (thermally grown oxide, TGO) between the bond coat and YSZ topcoat: the TGO hinders further oxidation of the bond coat.

A NiCoCrAlY TGO-forming bond coat is the most generally used, since it provides the best cyclic oxidation resistance. Recent research has shown that a DSC-deposited NiCoCrAlY bond coat outperforms a similar HVOF-sprayed bond coat under cyclic oxidation testing [35].

22.4.6 Coating Refurbishments

Refurbishment of previously coated and damaged or worn components by thermal spraying is most important, since it extends the service lives of many expensive parts and assemblies, notably in aircraft gas turbines. Refurbishing usually entails completely stripping away the original coating by mechanical or electrochemical means (or both), followed by surface preparation (e.g. grit blasting) and recoating.

The versatility of DSC technology enables it to be used for refurbishing various parts. For example, Fig. 22.9 shows a refurbished blade and the entire assembly of a low pressure compressor module, where the faces of the snubber abutments (interlocking mid-span supports) have been DSC sprayed with a WC–17Co coating.

Other examples are given in Fig. 22.10, which shows high-pressure compressor spacers after refurbishing with a *plasma sprayed* NiCr bond coat and DSC Al_2O_3 top coat as abradable coating.

22.5 Other Coating Processes

Combustion flame spray: This process, with its flame temperature of 3000 °C and relatively lower particle velocity (90–180 m/s), is used for depositing metallic coatings (molybdenum) and self-fluxing coatings.

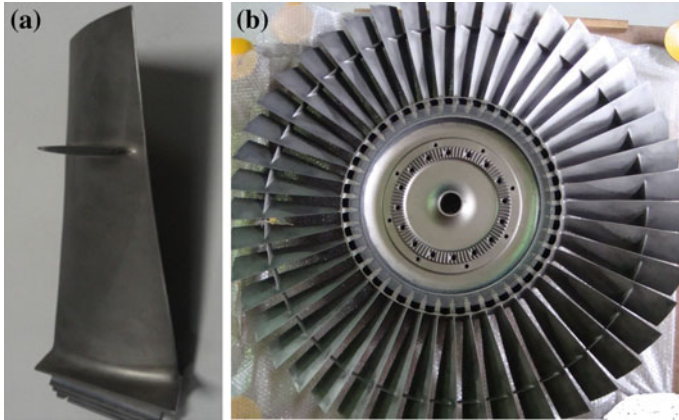


Fig. 22.9 Refurbished compressor module. **a** individual blade with snubber abutment face coated with DSC-sprayed WC-17Co coating, and **b** the assembled module

Plasma spraying: This is performed via three principal techniques: air plasma spraying (APS); argon-shrouded plasma spraying (ASPS); and vacuum plasma spraying (VPS) or low pressure plasma spraying (LPPS).

The principal limitation of the APS technique is the incorporation of air in the plasma jet, thereby slowing it and simultaneously causing some oxidation of metallic or alloy powders, resulting in higher oxide contamination in the coating. The particle velocities are higher in the VPS technique (400–600 m/s), leading to formation of relatively denser coatings with good adhesion and significantly reduced oxide content.

Typical uses of VPS–LPPS in aeroengines include M–Cr–Al–Y systems (overlays and thermal barrier bond coats), hot gas path seal systems, TBC coatings on afterburner liners, seals, flaps, nozzle segments and numerous combustion chamber parts [31]. Apart from these applications, TBCs are also employed on a wide variety of high pressure turbine blades and vanes, whereby both the bond coat and the TBC YSZ topcoat are applied via plasma spray.

EB-PVD: With the advent of EB-PVD technology, many of the critical applications have been shifted from plasma coating to EB-PVD bond coat + EB-PVD topcoat, while the bond coat market is also popularly shared with platinum–aluminide coating by chemical vapour deposition (CVD) [36, 37]. Figure 22.11 shows a high-pressure turbine vane with a CVD platinum–aluminide bond coat and EB-PVD topcoat.

Ion vapour deposition: Another popular process in the aerospace industry is ion vapour deposition (IVD) of aluminium as a replacement for cadmium plating [38–40]. The largest use of IVD aluminium is for corrosion protection of low-alloy steel parts such as cylinders, retainers, caps, retainer rings, spacers, strikers, springs, bolts, brackets, standoffs, links, flap tracks, rings, outboard actuators, strut

Fig. 22.10 High-pressure compressor spacers pertaining to **a** stage-1, **b** stage-2 and **c** 7 spacer stages in an assembled module

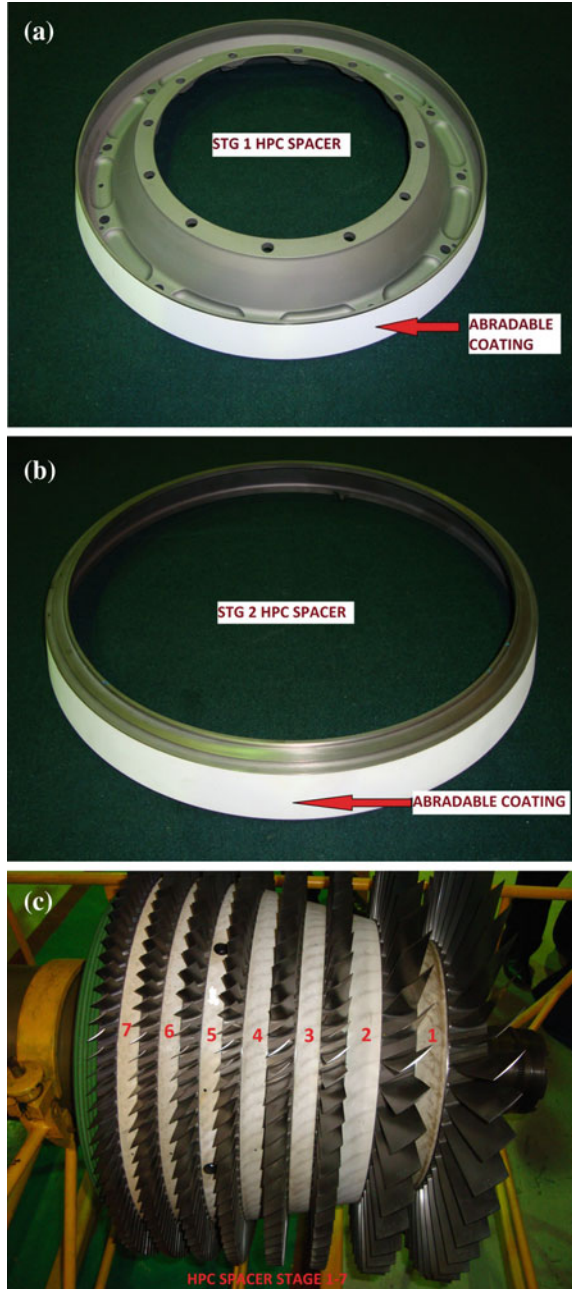
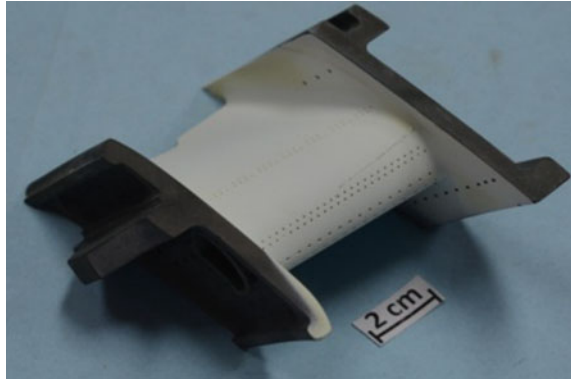


Fig. 22.11 High pressure turbine vane with platinum–aluminide bond coat and EB-PVD TBC YSZ topcoat



terminals, blower impellers, stops, screw assembly ball nuts, plates, housings leg bolts, fasteners, nuts, covers, housings, etc.

Selected aluminium alloys are also IVD aluminium-coated for corrosion protection and to eliminate a fatigue debit associated with anodizing aluminium parts: anodizing high-strength aluminium alloy parts can cause surface pits that nucleate fatigue cracks.

22.6 Summary and Concluding Remarks

Engine design concepts are moving towards greater thermal and propulsive efficiency. Materials and especially coatings will continue to play an important role in advancing performance, efficiency and reliability. Future engines are expected to operate at much higher temperatures and speeds; hence the need for extended component lives as well as reduced costs will grow [41]. With respect to coatings, reduced costs need to be realized via a compatibility and commonality of coating processes and compositions, and also the ease of coating repair and refurbishment.

Processing methodologies will be essential in creating new generation coating systems. For a given coating system it will be necessary to have more rigorous optimization schemes, such that even minor improvements in coating properties should be seen as an important opportunity. Sub-systems should also be developed to incorporate new and modified coatings with minimal alterations in existing production facilities.

As an example, Fig. 22.12 shows that Cr_3C_2 –NiCr powders of almost identical median size ($20 \pm 5 \mu\text{m}$) but manufactured via different routes give DSC coatings with widely differing porosity levels and hardness [25]. Although Fig. 22.12 shows that the blend (B) powder delivers the best combination of porosity and hardness, further refining or re-optimizing the process parameters may enable higher coating hardness from pre-alloyed and blended powders. In any event, the data in

Fig. 22.12 Variation in **a** hardness and **b** porosity of $\text{Cr}_3\text{C}_2\text{-NiCr}$ coatings deposited using powders manufactured via different routes *B* blended; *A&S* agglomerated and sintered; *S&C* sintered and crushed; *PA&B* pre-alloyed and blended

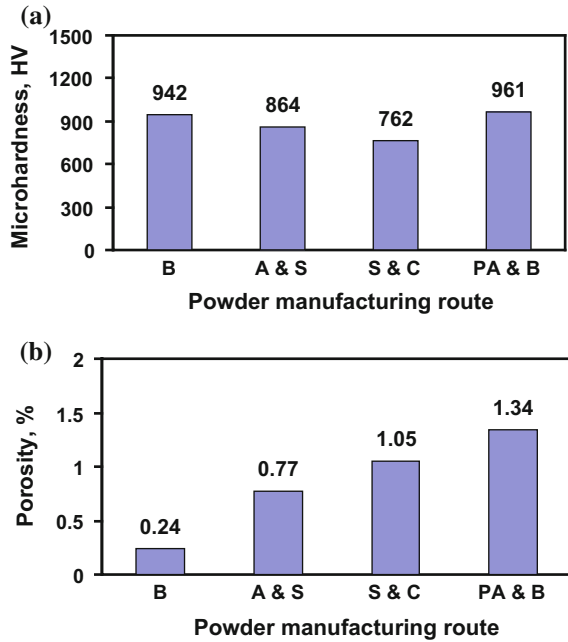


Fig. 22.12 highlight the need to optimize the process parameters separately for each powder.

An altogether new set of properties is achieved from composite coating structures, see Ref. [2]. Thermal spray systems and in particular the DSC and HVOF technologies should be evaluated with respect to achieving through-thickness graded or layered coating architectures. Recent world-wide R&D activities in developing multiple powder feeding systems indicate the interest in such coatings.

Finally, spray system automation to enhance the robustness of the processes needs to be increased. For example, the present authors have recently taken the initiative to completely replace all the mechanically moving parts of earlier designed DSC systems by using advanced flow metres and process controls. This is being done to improve the deposition efficiency, deposition rate, coating integrity and overall process reliability [42].

Acknowledgments The authors would like to thank Dr. P. Suresh Babu, Scientist, ARCI, for the technical discussions and help during preparation of this chapter, and also Dr. R.J.H. Wanhill for his detailed reviewing and suggestions.

References

1. Sundararajan G, Srinivasa RD, Sivakumar G, Joshi SV (2013) Detonation spray coatings. In: Wang J, Chung W (eds) Encyclopedia of tribology. Springer Science + Business Media, Berlin, Germany, pp 736–742
2. Rao DS, Sivakumar G, Sen D, Joshi SV (2015) Detonation sprayed coatings and their tribological performances. In Roy M, Davim J (eds) Thermal sprayed coatings and their tribological performances, IGI Global, Hershey, PA, USA, pp 294–327. doi:[10.4018/978-1-4666-7489-9.ch010](https://doi.org/10.4018/978-1-4666-7489-9.ch010)
3. Kadyrov V, Margarita Y, Sen D, Rao DS, Rao KP, Saibaba AV (1993) Detonation coating process. *Trans PMAI* 20:1–5
4. Fauchais PL, Heberlein JV, Boulos MI (2014) *Thermal spray fundamentals* Springer, New York, USA
5. Pawlowski L (1995) *The science and engineering of thermal spray coatings*. John Wiley & Sons Ltd, Chichester, UK
6. Wang J, Chung W (eds) (2013) *Encyclopedia of tribology*. Springer Science+Business Media, Berlin, Germany
7. Roy M, Davim J (eds) (2015) *Thermal sprayed coatings and their tribological performances*. IGI Global, Hershey, PA, USA: doi:[10.4018/978-1-4666-7489-9](https://doi.org/10.4018/978-1-4666-7489-9)
8. The basic principles of detonation coating (1974) In: Chapman BN (ed) *Science and technology of surface coating*. Academic Press, London, UK
9. Tucker RC Jr (1994) Thermal spray coatings. In: Cotell CM, Sprague JA, Smidt FA Jr (eds) *ASM Handbook*, vol. 5: Surface engineering, ASM International, Materials Park, OH, USA, pp 497–509
10. Suresh Babu P, Basu B, Sundararajan G (2008) Processing-structure-property correlation and decarburization phenomenon in detonation sprayed WC-12Co coatings. *56:5012–5026*
11. Verdon C, Karimi A, Martin JL (1998) A Study of high velocity oxy-fuel thermally sprayed tungsten carbide based coatings. Part 1: Microstructures. *Mater Sci Eng* 246:11–24
12. Stewart DA, Shipway PH, McCartney DG (2000) Microstructural evolution in thermally sprayed WC-Co coatings: comparison between nanocomposite and conventional starting powders. *Acta Mater* 48:1593–1604
13. Du H, Hua W, Liu J, Gong J, Sun C, Wen L (2005) Influence of process variables on the qualities of detonation gun sprayed WC-Co coatings. *Mater Sci Eng A* 408:202–210
14. Suresh Babu P, Basu B, Sundararajan G (2013) A comparison of mechanical and tribological behavior of nanostructured and conventional WC-12Co detonation-sprayed coatings. *J Therm Spray Technol* 22:478–490
15. Suresh Babu P, Basu B, Sundararajan G (2011) The influence of erodent hardness on the erosion behavior of detonation sprayed WC-12Co coatings. *Wear* 270:903–913
16. Sundararajan G, Rao DS, Prasad KUM, Joshi SV (1998) A comparative study of tribological behavior of plasma and D-gun sprayed coatings under different wear modes. *J Mater Eng Perform* 7:343–351
17. Suresh Babu P, Rao DS, Rao GVN, Sundararajan G (2007) Effect of feedstock size and its distribution on properties of detonation sprayed coatings. *J Therm Spray Technol* 16:281–290
18. Suresh Babu P, Basu B, Sundararajan G (2010) Abrasive wear behavior of detonations sprayed WC-12Co coatings: Influence of decarburization and abrasive characteristics. *Wear* 268:1387–1399
19. Sundararajan G, Suresh Babu P (2009) Detonation sprayed WC-Co coatings: unique aspects of their structure and mechanical behavior. *Trans Indian Inst Met* 62:95–103
20. Ahmed R, Hadfield M (1997) Rolling contact fatigue performance of detonation gun coated elements. *Tribol Int* 30:129–137
21. Souza VAD, Neville A (2007) Aspects of microstructure on the synergy and overall material loss of thermal spray coatings in erosion-corrosion environments. *Wear* 263:339–346
22. Murthy JKN, Rao DS, Venkataraman B (2001) Effect of grinding on the erosion behaviour of WC-Co-Cr coatings deposited by HVOF and detonation gun spray process. *Wear* 249:592–600

23. Karimi A, Verdon C (1993) Microstructure and hydroabrasive wear behaviour of high velocity oxy-fuel thermally sprayed WC-Co Cr coatings. *Surf Coat Technol* 57:81–89
24. Berget J, Rogne T, Bardal E (2007) Erosion–corrosion properties of different WC–Co–Cr coatings deposited by the HVOF process—influence of metallic matrix composition and spray powder size distribution. *Surf Coat Technol* 201:7619–7625
25. Somaraju KRC, Sivakumar G, Rao DS, Sundararajan G (2000) The influence of powder characteristics on the properties of detonation sprayed Cr_3C_2 –25NiCr coatings. In: *Thermal Spray 2000: Proceedings of the 1st international thermal spraying conference*, Berndt CC (ed), ASM International, Materials Park, OH, USA, pp 309–316
26. Quets JM, Walsh PN, Srinivasan V, Tucker RC Jr (1994) The high temperature fatigue characteristics of an erosion-resistant detonation gun chromium carbide coating. *Surf Coat Technol* 68(69):99–105
27. Rao DS, Sen D, Somaraju KRC, Kumar SR, Ravi N, Sundararajan G (1998) The influence of powder particle velocity and temperature on the properties of Cr_3C_2 –25NiCr coating obtained by detonation-gun. In: *Thermal spray 1998: Meeting the challenges of the 21st century*, ASM International, Materials Park, OH, USA, pp 385–393
28. Wang J, Zhang L, Sun B, Zhou Y (2000) Study of the Cr_3C_2 –NiCr detonation spray coating. *Surf Coat Technol* 130:69–73
29. Lindgren JR, Johnson WR (1987) Friction and wear behavior of chromium carbide coatings. *Surf Coat Technol* 32:249–260
30. Talib RJ, Saad S, Toff MRM, Hashim H (2003) Thermal spray coating technology—a review. *Solid State Sci Technol* 11:109–117
31. Jones TNR (1990) Thermally sprayed coating systems for surface protection and clearance control applications in aero engines. *Surf Coat Technol* 43(44):402–415
32. Altun O, Boke YE (2009) Effect of the microstructure of EB-PVD thermal barrier coatings on the thermal conductivity and the methods to reduce the thermal conductivity. *Arch Mater Sci Eng* 40:47–52
33. Yuan FH, Chen ZX, Huang ZW, Wang ZG, Zhu SJ (2008) Oxidation behavior of thermal barrier coatings with HVOF and detonation-sprayed NiCrAlY bondcoats. *Corros Sci* 50:1608–1617
34. Miramontes JAC, Tiburcio CG, Calderon A, Lopez FHE, Basulto GKP, Salas CAP (2014) Parameter studies on high-velocity oxy-fuel spraying of CoNiCrAlY coatings used in the aeronautical industry. *Int J Corros*. doi:10.1155/2014/703806
35. Rao DS, Janardhan GR, Krishna V, Joshi SV (2011) Processing–structure–property relationships in EB-PVD yttria stabilized zirconia (YSZ) coatings. *J Vacuum Sci Technol A* 29:031501–031508
36. Das DK, Laxmi SG, Rao DS, Bhanumathi S, Singh AK (2011) Microstructure, texture and thermal cycling performance of EB-PVD TBCs deposited under different processing conditions. *J High Temp Mater Processes* 30:539–548
37. Jie S, Dan Z, Lili Z, Yong T (2011) Thermal corrosion behavior of NiCoCrAlY coatings prepared by different thermal spraying methods. *Mater Sci Forum* 686:686–691
38. MacDonald D, Jodoin B, Gaydos S, Pollack M, Falkowski J, (2013) Study on the restoration of aluminum aerospace IVD coatings using cold gas dynamic spray. In: *Proceedings of international thermal spray conference and exposition: innovative coating solutions for the global economy*, ITSC, 13–15 May 2013, Busan, South Korea, Code 107529
39. Alanazi NM, Leyland A, Yerokhin AL, Matthews A (2010) Substitution of hexavalent chromate conversion treatment with a plasma electrolytic oxidation process to improve the corrosion properties of ion vapour deposited AlMg coatings. *Surf Coat Technol* 205:1750–1756
40. Voorwald HJC, Peres MP, Costa MYP, Cioffi MOH, Evaluation on fatigue strength of AISI 4340 steel aluminum coated by electroplating and IVD processes. *J Mater Sci* 45:6094–6100
41. De MJT, Gupta DK (1994) Protective coatings in the gas turbine engine. *Surf Coat Technol* 68(69):1–9
42. Nirmala S, Sivakumar G, Joshi AS, Aruna N, Rao DS, Sundararajan G (2013) A Computer—based approach for developing functionally graded and layered coatings with detonation spray coating process. *J Sci Ind Res* 72:477–480

Chapter 23

Piezoceramic Materials and Devices for Aerospace Applications

P.K. Panda

Abstract Piezoelectric materials produce electric charges on application of mechanical stress, or change their dimensions when subjected to an electric field. Lead zirconate titanate (PZT) is a synthetic piezoceramic material with high piezoelectric properties. In aerospace PZT is used widely as sensors and actuators for vibration control of structures, health monitoring, development of smart aeroplane wings/morphing structures, energy harvesting and self-powering applications in micro aerial vehicles (MAVs), unmanned aerial vehicles (UAVs), as precision fuel injectors in propulsion systems, etc. This chapter reviews the preparation of piezoceramic materials, e.g. PZT, PZT–PMN and PMN–PT, and the fabrication and characterization of multilayer (ML) stacked devices and their applications in aerospace.

Keywords Piezoceramics · Mechanisms · Processing · Structural health monitoring · Fuel injectors

23.1 Introduction

Piezoelectric materials generate electric charges on application of mechanical stress (direct piezoelectric effect) and also a mechanical stress or strain on application of an electric field (converse piezoelectric effect). Piezoelectricity was discovered by Pierre and Jacques Curie in 1880, while studying the effect of pressure on natural minerals such as quartz and tourmaline. Since then there has been tremendous development of new piezo materials, fabrication of devices and their uses. This development was stimulated by the discovery of synthetic piezo materials such as barium titanate (BaTiO_3) and lead zirconate titanate (PZT) with improved piezoelectric properties. Also, fabrication of piezo devices in multilayered form has

P.K. Panda (✉)

Materials Science Division, CSIR-National Aerospace Laboratories,
Kodihalli, Bangalore 560017, India
e-mail: pkpanda@nal.res.in

reduced the driving voltage from a few kilovolts (kV) to only a few volts and millivolts for very thin films and micro-electrical-mechanical devices (MEMs).

Owing to their advantages, piezoelectric materials are currently used for many aerospace applications, including sensors and actuators for vibration control of structures, health monitoring, development of smart aeroplane wings/morphing structures, energy harvesting and self-powering applications in micro aerial vehicles (MAVs), unmanned aerial vehicles (UAVs), and as precision fuel injectors in propulsion systems [1–4]. In this chapter we review the preparation of piezoceramic materials, e.g. PZT, PZT–lead magnesium niobate (PMN), PMN–lead titanate (PT), and the fabrication and characterization of multilayer (ML) stacked devices and their applications in aerospace.

23.1.1 Origin of Piezoelectricity

The piezoelectric effect arises due to an asymmetry in the crystallographic unit cell and the electric dipoles generated due to mechanical stress. For a crystal to possess a piezoelectric effect, it must be non-centrosymmetric, i.e. it does not have a centre of symmetry. However, not all non-centrosymmetric crystalline substances are piezoelectric. The relationship between piezoelectric properties and crystallographic subgroups on the basis of symmetry is given in Fig. 23.1.

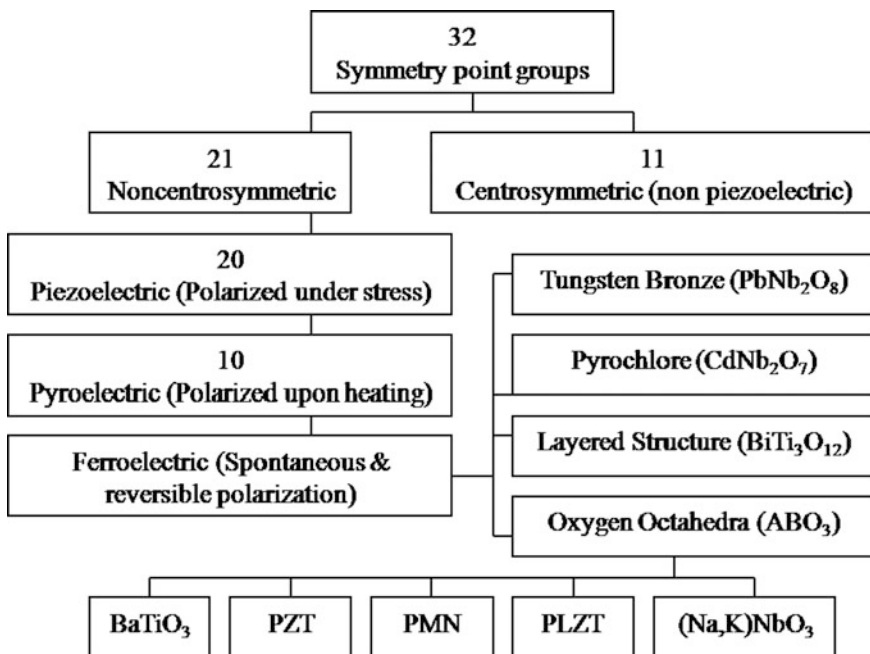


Fig. 23.1 Interrelationship of piezoelectrics and subgroups on the basis of symmetry

23.1.2 Piezoelectric Charge Coefficient (D)

On application of a mechanical stress, the charges (Q) developed in a piezoelectric material are proportional to the applied force (F), i.e. $Q \propto F$

Now $Q = d \times F$, where d is the piezoelectric charge constant expressed in Coulombs/Newton. Therefore,

$$d = Q/F = Q/(A \times T) = D/T \tag{23.1}$$

where T is the mechanical stress and D is the dielectric displacement (equal to the total charge Q per unit area A). The sign is positive for compression and negative for tension.

In the converse effect, the strain produced is directly proportional to the applied field (E). Thus $S \propto E$ or $S = d \times E$, where d is expressed in metres/Volt. Now

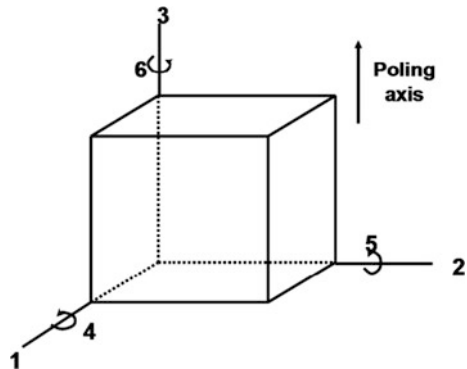
$$d = S/E = D/T \tag{23.2}$$

For both the direct and converse effects the piezoelectric constant d is numerically identical and is usually expressed as $10^{-12}C/N$ for the direct effect and $10^{-12}m/V$ for the converse effect. High “ d ” coefficients are desirable for materials used for motional or vibration producing devices, such as actuators/sensors and ultrasonic transducers.

23.1.3 Notation of Axes

The piezoelectric properties are directional quantities. Hence they are usually specified with subscripts to identify the orientation directions as described in Fig. 23.2. The direction “3” is usually taken as the poling axis and the directions

Fig. 23.2 Notation of axes for poled PZT ceramics



“1” and “2” are the two other orthogonal axes. Shear effects are indicated by the subscripts 4, 5 and 6.

The charge coefficients d are generally expressed by two subscripts: the first refers to the electrical direction (electric field or dielectric displacement) and the second refers to the mechanical direction (stress or strain). For example, the first subscript (3) of d_{33} indicates the direction of polarization and the second subscript (3) is the direction of the applied stress causing this polarization. Similarly, for d_{31} the polarization direction is “3” when the stress is applied in the direction “1”. Equations 28.1 and 28.2 can be written with directional properties as

$$D_3 = d_{33}T_3(\text{direct effect}) \quad (23.3)$$

$$S_3 = d_{33}E_3(\text{converse effect}) \quad (23.4)$$

23.1.4 Structure of PZT

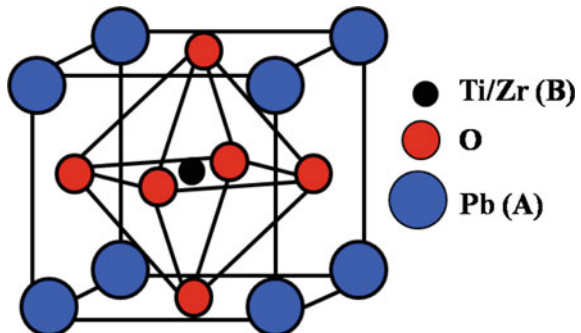
PZT has a cubic unit cell and the general formula ABO_3 , where “A” is a divalent cation (Pb^{2+}) at the corners of the cube, “B” is a tetravalent cation (Zr^{4+} or Ti^{4+}) in the body centred position and “O” is the oxygen at the face-centred positions of the cubic structure (Fig. 23.3).

The ionic radii of both lead and oxygen ions are about 1.2 Å and 1.4 Å, respectively, and together they make a face-centred cubic array having a lattice parameter of nearly 4.0 Å. When an electric field is applied to the PZT unit cell, the Ti^{4+} or Zr^{4+} ion moves to a new position (up or down, or to one side or the other) along the direction of the applied field.

23.1.5 Piezoelectric Effect—Importance of Poling

Naturally occurring single crystals, such as quartz, tourmaline, etc., are examples of natural piezoelectric materials. However, the synthetic ceramic materials such as

Fig. 23.3 Cubic (perovskite) structure of PZT



PZT, barium titanate, etc., are polycrystalline and not piezoelectric by themselves, since the piezoelectric effects from individual crystals cancel each other. A strong DC electric field is required to align the randomly oriented dipoles of the crystals in the direction of the applied field and develop piezoelectricity. This process is known as poling. After poling, the ceramic develops a net dipole moment and responds linearly to an applied electric field or mechanical stress.

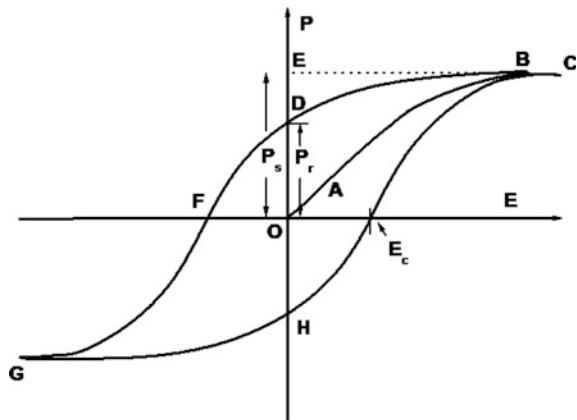
Complete alignment of dipoles in the direction of the electric field (domain switching) is not possible owing to internal friction among the domains, resulting in hysteresis. This is an important characteristic of ferroelectric materials and is called the ‘fingerprint’ of ferroelectric ceramics. A typical ferroelectric hysteresis loop is shown in Fig. 23.4.

When a small electric field is applied, only a linear relationship between polarization (P) and the electric field (E) is observed because the field is not sufficient enough to align any domain and the crystal behaves as a normal dielectric material. This corresponds to the segment OA of the curves in Fig. 23.4. As the electric field is increased a number of negative domains, which have a polarization opposite to the direction of the field, are switched over to the positive direction along the field, and domain orientation occurs. This results in a sharply rising ‘ P ’ with increasing field ‘ E ’, and the polarization increases rapidly (segment AB) until all the domains are aligned in the positive direction (segment BC). This is the state of saturation in which the crystal is composed of just a single domain.

As the field strength decreases, the polarization generally decreases but returns to point D rather than zero. This is because some of the domains remain aligned in the positive direction and the crystal exhibits a remanent polarization (P_r). Extrapolation of the linear segment BC of the curve back to point E on the polarization axis gives the value of the saturation polarization (P_s).

The remanent polarization (P_r) in a crystal cannot be removed until an applied field in the opposite direction reaches a certain value, at the point F. The strength of the field required to reduce the remanent polarization (P_r) to zero is called the

Fig. 23.4 A typical hysteresis graph for PZT



“coercive field” (E_c). Further increase of the field in the negative direction causes a complete alignment of the dipoles in this direction, at point G. Then the cycle can be completed by reversing the field into the positive direction.

23.2 Preparation of Piezoelectric Powders

23.2.1 PZT Materials

PZT is a solid solution of (i) ferroelectric lead titanate (PbTiO_3) and (ii) anti-ferroelectric lead zirconate (PbZrO_3) phases [9]. PZT is rhombohedral in Zr-rich compositions ($\text{ZrO}_2 > 54\%$) and tetragonal for TiO₂-rich compositions ($\text{ZrO}_2 < 48\%$). In the intermediate compositions both rhombohedral and tetragonal phases coexist, see Fig. 23.5. This intermediate region is known as the morphotropic phase boundary (MPB).

PZT compositions in the MPB region produce maximum piezoelectric properties owing to the coexistence of tetragonal and rhombohedral phases totalling 14 possible polarization directions (6 from tetragonal and 8 from rhombohedral) and a low energy barrier available for dipole orientation [5].

The properties of PZTs are modified by addition of different dopants in the “A” or “B” sites [6–8], see Fig. 23.3. These dopants are mainly of two types: (i) “donor” dopants which are higher valence cations such as La^{3+} and Nd^{3+} for substitution in A sites, and Nb^{5+} , Ta^{5+} , etc. for B sites; these dopants induce cation vacancies, thereby facilitating easy domain wall motion during poling, resulting in “soft” PZTs; and (ii) “acceptor” dopants which are of lower valence cations such as K^+ and Na^+ for A sites and Sc^{3+} , Mg^{2+} and Fe^{3+} for B sites. These dopants induce

Fig. 23.5 XRD traces for PZT near the MPB

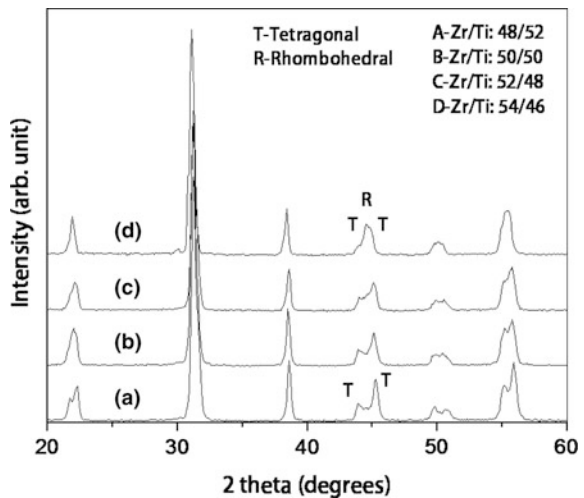


Table 23.1 Typical piezo properties of PZT-5H powders prepared by the wet-chemical route

Piezo properties of PZT-5H powders	
Particle size (μm)	0.91
Density (% theoretical)	98.0
Piezoelectric charge constant (d_{33}) pC/N	590
Relative dielectric constant (K)	1700
Dissipation factor ($\tan \delta$) at 100 Hz	0.025

oxygen vacancies, making the domain wall motion difficult and thereby developing “hard” PZTs.

The conventional method of PZT preparation is by the “mixed-oxide” route, although there are other methods such as co-precipitation, sol-gel, spray pyrolysis, hydrothermal synthesis and molten salt synthesis. In the “mixed-oxide” route the oxide powders are mixed in a ball mill and calcined for PZT phase formation. This process is very simple and cost effective. The main drawbacks are (i) inhomogeneity at the micro-level; (ii) high reaction temperature, therefore high lead loss; and (iii) difficulty in maintaining the stoichiometry, leading to variations in the piezo properties.

The above drawbacks could be overcome by following a wet-chemical route [9–11]. In this process an aqueous solution of precursors (generally in the form of nitrates) is converted into a homogeneous hydroxide precipitate that is converted into PZT after calcination. The calcined powders are generally de-agglomerated in an attrition mill. Test samples/pellets are prepared by hydraulic pressing, sintered in the temperature range of 1100–1250 °C, poled, and the properties measured. Typical properties of PZT powders prepared by the wet-chemical route are presented in Table 23.1.

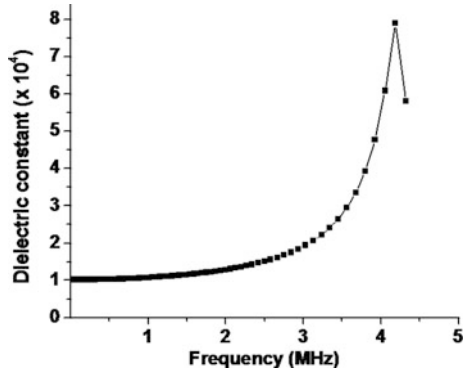
23.2.2 PMN Materials

PMN [$\text{Pb}(\text{Mg}_{1/3}\text{Nb}_{2/3})\text{O}_3$] is a relaxor ferroelectric material with high dielectric constant ($K \sim 20,000$) and used as a capacitor. It produces a large electric-field-induced strain, and is therefore used as an electrostrictive actuator [12, 13].

It is very difficult to prepare the pure PMN phase, owing to formation of a low dielectric constant ($K \sim 200$) lead niobate “pyrochlore” phase. PMN is usually synthesized by various chemical processing routes such as sol-gel, combustion synthesis, EDTA gel, citrate gel, co-precipitation, molten salt synthesis, partial oxalate method and also by polymeric precursor methods [14–19]. These chemical routes have the potential to form pyrochlore-free PMN powders owing to better homogeneity, compositional control, and lower processing temperature, and are therefore preferred over solid-state reaction processes.

Figure 23.6 shows the dependence of the room temperature dielectric constant of a PMN sample on frequency, ranging from 100 Hz to 4.5 MHz. The dielectric

Fig. 23.6 Dielectric constant versus frequency for a PMN sample at room temperature



constant is 10,335 at 100 Hz, and reaches a maximum value of 79,098 at a frequency of 4.18 MHz [18].

23.2.3 PZT–PMN Materials

PZT powders possess a very high charge coefficient, while PMN is generally a high dielectric material. Combining PZT and PMN powders in suitable ratios is therefore expected to produce materials with the required/desired piezoelectric and dielectric properties [20]. Typical hysteresis loops of pure PZT, PZT + PMN (40 %) and pure PMN are presented in Figs. 23.7a–c.

23.2.4 PMN–PT Materials

$\text{Pb}(\text{Mg}_{1/3}\text{Nb}_{2/3})\text{O}_3\text{--PbTiO}_3$ materials have high electrostrictive, piezoelectric and dielectric properties and are used for various applications such as multilayer capacitor and electromechanical systems [21]. This material is generally prepared similarly to PMN. A typical SEM picture, dielectric constant and ferroelectric loop of PMN–PT are presented in Figs. 23.8a–c.

23.3 Fabrication of PZT Devices

23.3.1 Fabrication of Multilayered Stacks

A multilayer (ML) stack consists of a large number of PZT electrode layers stacked in an alternate manner as shown in Fig. 23.9. On application of the voltage, the ML stack expands or contracts depending on the polarity of the applied voltage. The dimensional change is about 0.1 % of the total height of the stack.

Fig. 23.7 Typical hysteresis loops of **a** pure PZT, **b** PZT + PMN (40 %) and **c** pure PMN

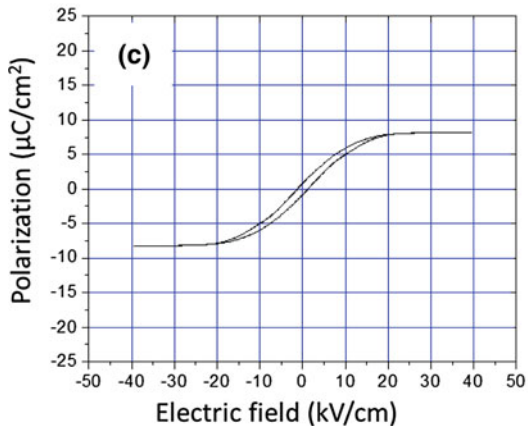
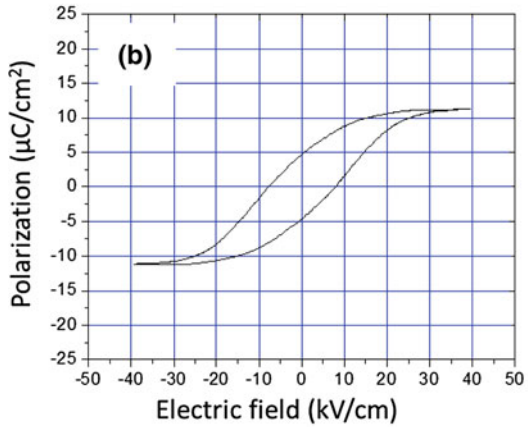
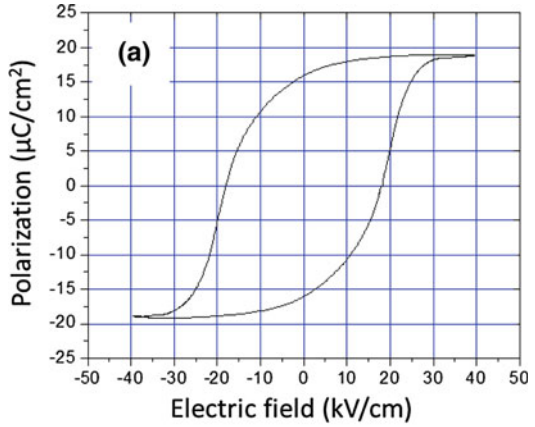


Fig. 23.8 Typical **a** SEM picture, **b** dielectric constant and **c** ferroelectric loop of PMN-PT samples

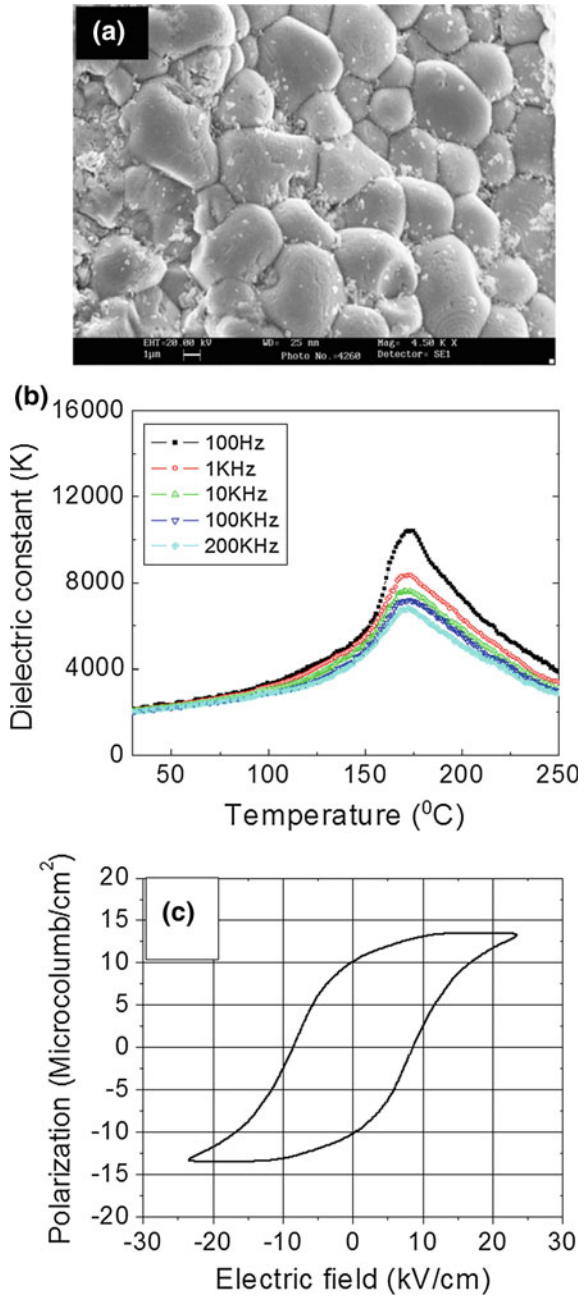


Fig. 23.9 Schematic of a multilayer stack of PZT electrode layers

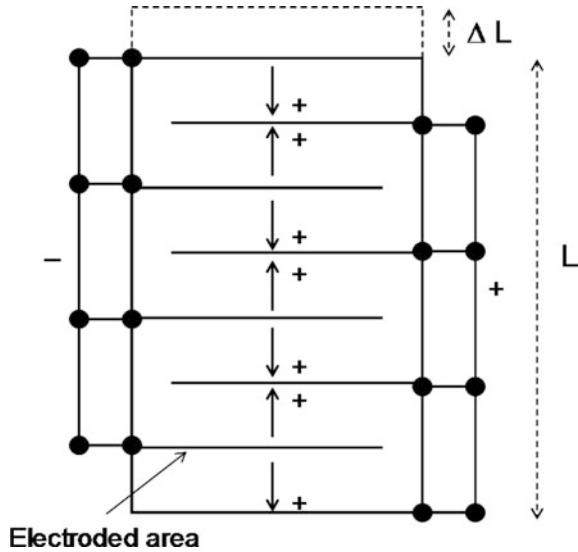
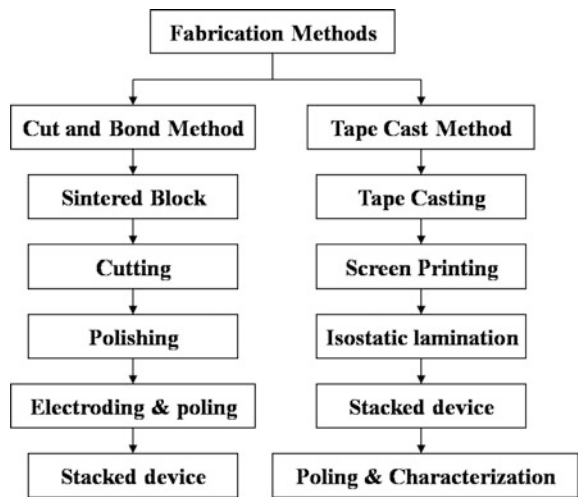


Fig. 23.10 Flow chart of ML stack fabrication by the “Cut and Bond” and “Tapecasting” methods



Stacks are generally fabricated by two methods: (i) “Cut and Bond” and (ii) “Tapecasting”. A typical flow chart of ML stack fabrication by both methods is presented in Fig. 23.10.

Cut and Bond method: In the ‘cut and bond’ method the individual layers are cut from pre-sintered PZT blocks. Each layer is supplied with an electrode, and they are poled and bonded together properly. This method is suitable only for thick-layered (few mm) ML stacks which can be operated at higher voltage (in kV). Typical PZT sintered blocks, strips and fabricated stacks are shown in Fig. 23.11.

Fig. 23.11 a-d Photographs of PZT sintered blocks, strips, and fabricated stacks made by the cut and bond method

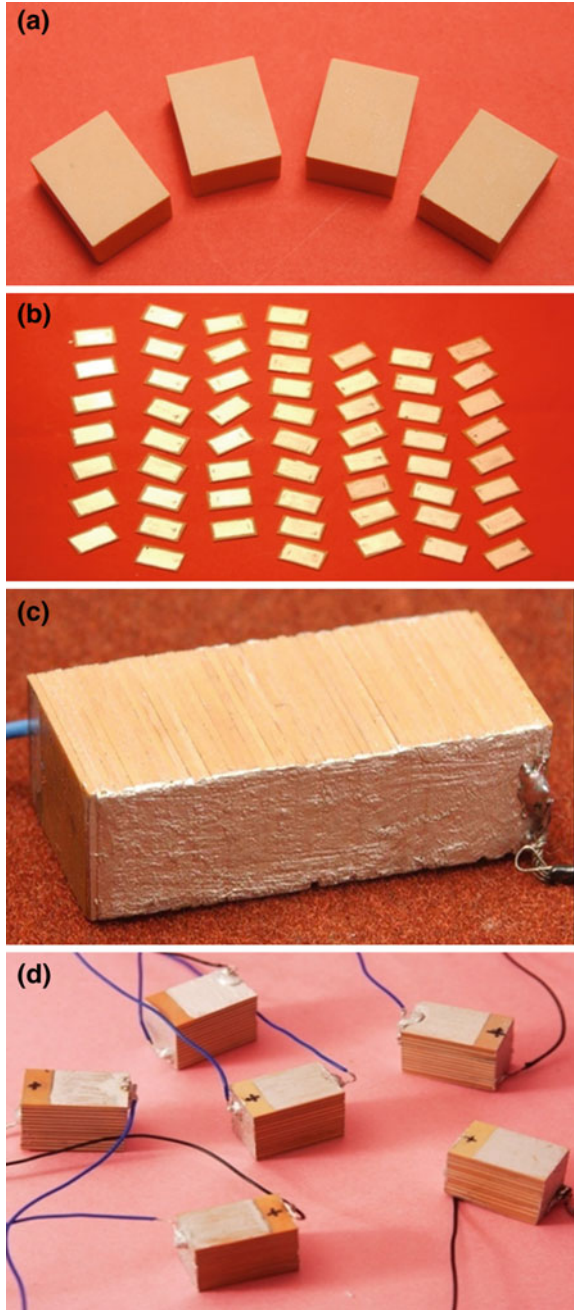
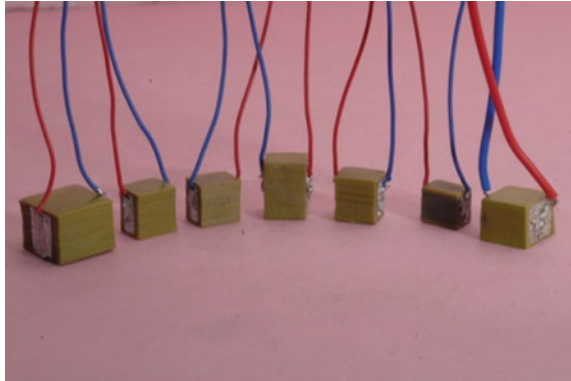


Fig. 23.12 Photograph of ML stacks fabricated by the tape casting method



Tapecasting method: This method is used to build stacks consisting of very thin layers $\sim 100 \mu\text{m}$. Such stacks then have the advantage of working at low driving voltages. ML PZT actuators consisting of 100–120 layers, each $\sim 100 \mu\text{m}$ thick, are generally fabricated using a tape casting unit, screen printer, laminator, etc. The process consists of preparation of a homogeneous PZT slurry containing the required amounts of PZT powder, solvent, dispersant, binder and plasticizers. This slurry is poured into a tape caster to make PZT tapes of the required thickness. The dried PZT tapes are screen printed with Pt electrode paste, stacked and laminated. The green stacks are co-fired at $1250 \text{ }^\circ\text{C}/2 \text{ h}$. The co-fired stacks are then given electrodes and poled at 2 kV/mm . Examples are shown in Fig. 23.12.

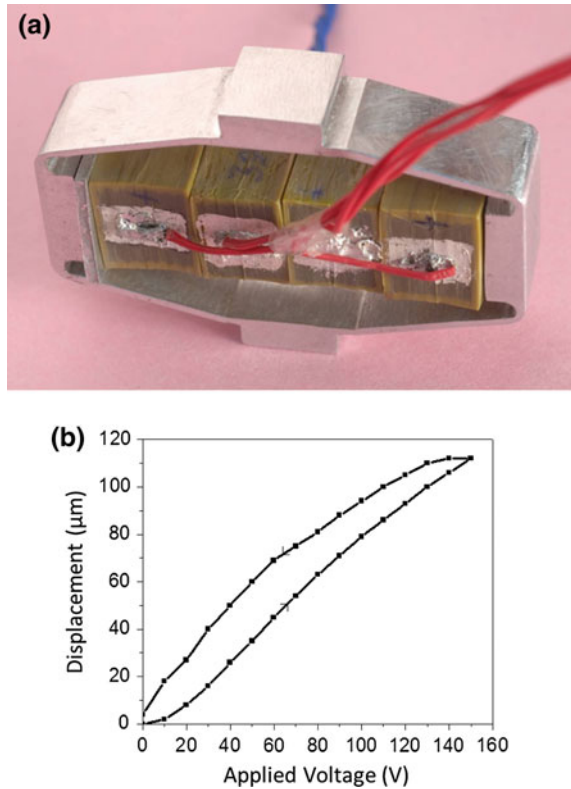
23.3.2 Amplified PZT Actuators

The displacement of a simple ML PZT actuator is very small, typically $1 \mu\text{m}$ per 1 mm height of the stack. To amplify the displacement a simple diamond-shaped metal casing is used. The PZT stacks are placed inside the casing horizontally in a pre-stressed condition. On application of the voltage, the stacks expand horizontally with a simultaneous contraction along the vertical direction. The ratio of contraction to the horizontal expansion is called the amplification factor [5]. A typical amplified piezo actuator and its displacement profiles are presented in Fig. 23.13. Such an actuator using six multilayered piezo stacks produces a maximum displacement of $173 \mu\text{m}$ at 175 V , with an amplification factor of 4.3 [22].

23.3.3 Ring Actuators

Ring-type actuators are mainly used for fluid flow control. An example is shown in Fig. 23.14. The ring portion of the actuator is glued to a substrate in an inverted

Fig. 23.13 **a** Photograph of an amplified piezo actuator, and **b** its displacement profile



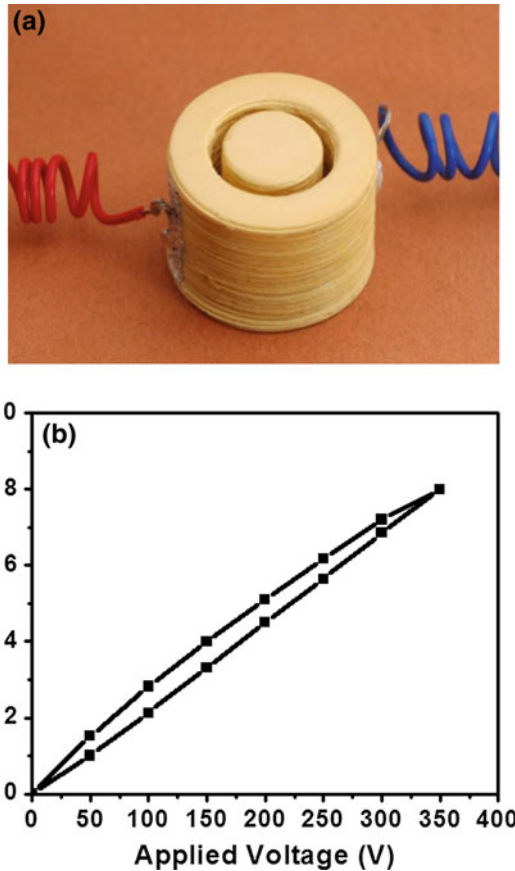
position. On application of a DC voltage the active ring part expands in the upward direction, and the central inactive rod attached to the actuator cap remains as such, thereby producing a gap in-between the substrate and the central rod, facilitating the flow of fluid [23].

23.4 Aerospace Applications of PZT ML Stacks

23.4.1 Shape and Vibration Control

Shape control of flexible aero structures has been carried out to improve the performance of aerodynamic lifting surfaces and to reduce drag on components. Piezo actuators are mostly used for this purpose. These actuators operate linearly, using only tensile and compressive forces to correct the structural deformations produced by air pressure.

Fig. 23.14 Photograph of **a** a ring actuator and **b** its displacement profile



The same principle is used in active vibration control, where piezo elements are utilized both to detect vibrations that are disrupting the structure and to cancel out these vibrations by imparting counter-vibrations into the structure [24].

23.4.2 Structural Health Monitoring (SHM)

Structural health monitoring (SHM) is a very important aspect of aircraft operations: see Chapter 22 in Volume 2 of these Source Books. Piezoelectric devices can be used for this purpose. For example, piezoelectric ceramics have been bonded to the outsides of structures to monitor delamination and damage in composites via changes in the natural vibration frequencies. If the composite begins to delaminate, its vibrational frequency will be affected and the piezoelectric sensor will be able to detect the changes. This can aid in timely structural maintenance and repair, avoiding failures in service [25].

23.5 Other Applications

23.5.1 Piezo Energy Harvesting

The process of acquiring energy from surrounding systems and converting it into usable electrical energy is called power or energy harvesting. The research on power harvesting has rapidly increased in recent years. Piezoelectric materials are used as mechanisms to transfer ambient vibrations into electrical energy that can be stored and used to power other devices. With the recent surge of interest in micro-scale devices, piezoelectric power generation can provide an alternative to traditional power sources used to operate certain types of sensors/actuators [26–29].

23.5.2 Piezo Fuel Injection Systems

High-pressure direct injection (HPDI) technology is used to reduce the emissions produced by diesel engines. The technology uses multilayer PZT actuators for injector-needle opening, replacing conventional solenoid technology. In the late 1990s fuel injection systems were developed using piezoelectric actuators. These have better performance than conventional actuators. In a fuel injector, PZT stack actuators control the injection process via an applied electric field: the stroke of the actuator is used to activate a valve needle, allowing the pressurized fuel to be injected. The response time of the needle nozzle is typically less than 0.1 ms. The short response time reduces the fuel delivery rate and the energy required from the high-pressure fuel pump. Also, since the valve is actuated more quickly, very precise injection intervals are possible between pre- and main injections, which significantly reduce emissions and reduce fuel consumption by up to 15 % [30]. Overall, the advantages of piezoelectric injectors over conventional solenoid technology are that they provide an optimized injection system, i.e. more economical, more powerful and with reduced emissions [31].

23.6 Conclusions

Piezoelectric materials are increasingly used in the aerospace industry as sensors and actuators for vibration control of structures, health monitoring, development of smart aeroplane wings/morphing structures, energy harvesting and self-powering applications in micro aerial vehicles (MAVs), unmanned aerial vehicles (UAVs) and as precision fuel injectors in propulsion systems. This chapter has described the development of piezoceramic materials, the fabrication and characterization methodology for piezoelectric devices, and their applications.

Acknowledgments The author thanks Dr. B. Sahoo for the R&D support. The author also thanks the XRD and SEM groups of the Materials Science Division, TGA for CSMST Division, and Dr. S. Raja and Mr. V. Shankar of the STTD Division, for dynamic characterization of the amplified actuator. The author sincerely thanks NPSM, NPMAS, CSIR FYPs for the financial support.

References

1. Uchino K (1995) Advances in ceramic actuator materials. *Mater Lett* 22:1–4
2. Newnham RE, Ruschau GR (1991) Smart electroceramics. *J Am Ceram Soc* 74:463–480
3. Cattafesta LN, Garg S, Shukla D (2001) Development of piezoelectric actuators for active flow control. *AIAA J* 39:1562–1568
4. Giurgiutiu V, Zagrai A, Bao JJ (2002) Piezoelectric wafer embedded active sensors for aging aircraft structural health monitoring. *Struct Health Monit* 1:41–61
5. Jaffe B, Jaffe H, Cook WR (1971) *Piezoelectric ceramics*. Academic Press, London, UK
6. Sahoo B, Panda PK (2013) Effect of lanthanum, neodymium on piezoelectric, dielectric and ferroelectric properties of PZT. *J Adv Ceram* 2:37–41
7. Donnelly NJ, Shrout TR, Randall CA (2007) Addition of a Sr, K, Nb (SKN) combination to PZT(53/47) for high strain applications. *J Am Ceram Soc* 90:490–495
8. Sahoo B, Panda PK (2007) Ferroelectric, dielectric and piezoelectric properties of $\text{Pb}_{1-x}\text{Cex}(\text{Zr}_{0.60}\text{Ti}_{0.40})\text{O}_3$, $0 \leq x \leq 0.08$. *J Mater Sci* 42:9684–9688
9. Linardos S, Zhang Q, Alcock JR (2007) An investigation of the parameters affecting the agglomerate size of a PZT ceramic powder prepared with a sol–gel technique. *J Eur Ceram Soc* 27:231–235
10. Lee BW (2004) Synthesis and characterization of compositionally modified PZT by wet chemical preparation from aqueous solution. *J Eur Ceram Soc* 24:925–929
11. Sahoo B, Jaleel VA, Panda PK (2006) Development of PZT powders by wet chemical method and fabrication of multilayered stacks/actuators. *Mater Sci Eng, B* 126:80–85
12. Swartz SL, Shrout TR, Schulze WA, Cross LE (1984) Dielectric properties of lead magnesium niobate ceramics. *J Am Ceram Soc* 67:311–315
13. Uchino K (1986) Electrostrictive actuators: materials and applications. *Am Ceram Soc Bull* 65:647–652
14. Narendar Y, Messing GL (1999) Seeding of perovskite lead magnesium niobate crystallization from Pb-Mg-Nb-EDTA gels. *J Am Ceram Soc* 82:1659–1664
15. Carvalho JC, Santos COP, Zaghete MA, Oliveria CF, Varela JA (1996) Phase analysis of seeded and doped $\text{Pb}(\text{Mg}_{1/3}\text{Nb}_{2/3})\text{O}_3$ prepared by organic solution of citrates. *J Mater Res* 11:1795–1799
16. Cavalheiro AA, Foschini CR, Zaghete MA, Santos COP, Cilense M, Varela JA, Longo E (2001) Seeding of PMN powders made by the pechini method. *Ceram Int* 27:509–515
17. Camargo ER, Kakhana M, Longo E, Leite ER (2001) Pyrochlore free PMN prepared by a combination of partial oxalate methods. *J Alloy Compd* 314:140–146
18. Panda PK, Sahoo B (2005) Preparation of pyrochlore free PMN powder by semi-wet chemical route. *Mater Chem Phys* 93:231–236
19. Swartz SL, Shrout TR (1982) Fabrication of perovskite lead magnesium niobate. *Mater Res Bull* 17:1245–1250
20. Sahoo B, Panda PK (2007) Dielectric, ferroelectric and piezoelectric properties of $(1-x)[\text{Pb}_{0.91}\text{La}_{0.09}(\text{Zr}_{0.60}\text{Ti}_{0.40})\text{O}_3]_x[\text{Pb}(\text{Mg}_{1/3}\text{Nb}_{2/3})\text{O}_3]$, $0 \leq x \leq 1$. *J Mater Sci* 42:4270–4275
21. Sahoo B, Panda PK (2007) Effect of CeO_2 concentration on dielectric, ferroelectric and piezoelectric properties of PMN-PT (67/33) composition. *J Mater Sci* 42:4745–4752

22. Panda PK, Sahoo B, Raja S, Vijaya Kumar MP, Shankar V (2012) Electromechanical and dynamic characterization of in-house-fabricated amplified piezo actuator. *Smart Mater Res* 2012:203625
23. Sahoo B, Panda PK (2012) Fabrication of simple and ring-type piezo actuators and their characterization. *Smart Mater Res* 2012:821847
24. Prasad SE, Waechter DF, Blacow RG, King HW, Yaman Y (2005) Application of piezoelectrics to smart structures. In: *Proceedings of II conference on smart structures and materials*, 18-21 July 2005, Portugal, Ecomas Thematic Conference, Ecomas, Barcelona, Spain, pp 1–16
25. Boller C (1999) Monitoring the integrity of aircraft structures—current procedures and smart sensing options. In: *Proceedings of the international conference on smart materials, structures and systems*, 7–10 July 1999, Bangalore, India, Mangalgi PD, Upadhyaya AR, Selvarajan A (eds) Allied Publishers Limited, New Delhi, India, pp 31–43
26. Sodano HA, Inman DJ (2004) A Review of power harvesting from vibration using piezoelectric materials. *Shock Vib Dig* 36:197–205
27. Starner T (1996) Human-Powered wearable computing. *IBM Systems Journal* 35:618
28. Kymissis J, Kendall C, Paradiso J, Gershenfeld N (1998) Parasitic power harvesting in shoes. In: *Proceedings of second IEEE international conference on wearable computing*, pp 132–139
29. Priya S, Chen CT, Fye D, Zhand J (2005) Piezoelectric windmill—a novel solution to remote sensing. *Jpn J Appl Phys* 44:L104–L107
30. Randall CA, Kelnberger A, Yang GY, Eitel RE, Shrout TR (2005) High strain piezoelectric multilayer actuators: a material science and engineering challenge. *J Electroceram* 14:177–191
31. Boecking F, Sugg B (2006) Piezo actuators: a technology prevails with injection valves for combustion engines. In: *Actuator 2006: 10th international conference on new actuators*, 14–16 June 2006, Bremen, Germany, Borgmann H (ed), HVG Hanseatische Veranstaltungs-GmbH, Bremen, Germany, pp 171–176

Chapter 24

Stealth Materials and Technology for Airborne Systems

N. Kumar and S.R. Vadera

Abstract “Stealth” normally signifies “radar stealth”, but it actually means suppression of all the following signatures: visual, radar, infrared, electromagnetic and sound. After a brief historical introduction, this chapter summarizes the basic stealth requirements for military assets, particularly airborne systems. Special sections are devoted to radar-absorbing materials and structures, plasma stealth (a means of active stealth), acoustic stealth and counter stealth.

Keywords Stealth technology · Stealth materials and coatings · Sensors · Radar absorption · Applications

24.1 Introduction

The dictionary meaning of **stealth** is the act or action of proceeding secretly or imperceptibly. In military circles the so-called stealth technology, also termed “low-observable” technology or signature management, is a sub-discipline of camouflage or other countermeasures that make combat military systems such as aircraft difficult to detect by CCDs, infrared, radar, and other detection methods.

The concept of stealth is not new. Being able to operate without the knowledge of the enemy has always been a goal of military technology and tactics. Initially, stealth technology mainly referred to invisibility of an aircraft from radar. However, rapid advancements in detection and interception technologies extending from visible to infrared (IR) to microwave regimes, and acoustic, seismic or magnetic signatures have increased the necessity of stealth technology to be multispectral [1]. The implementation of stealth technology therefore requires the use of special materials and techniques that reduce the optical, thermal, acoustic, IR and radar signatures of a target while blending it into its background.

N. Kumar (✉) · S.R. Vadera
Defence Laboratory, Jodhpur, India
e-mail: nkjainjd@yahoo.com

The importance of stealth is second only to lethal military combat systems, and any significant development in this area is a closely guarded secret. Successful stealth technologies make use of functional materials and design aspects, and are deployed today on several types of aircraft and naval vessels, especially submarines. Developments in the area of counter-stealth technologies are also important [2].

The importance of stealth technology is judged from the fact that in any war scenario it serves not only to counter threats from guided weapons and surveillance, but also acts as a force multiplier. Also, stealth is a cost-effective measure and therefore an inescapable military requirement in its own right.

24.2 History of Stealth Technology

The beginning of stealth technology may be traced back even to before 1912, when German scientists reported the concept of a monoplane with its wings and fuselage made from cellulose-based materials, although it was never put into operation [3]. Since radar had not been invented at that time, optical visibility was the sole concern, and the goal was to create aircraft that were hard to see. Taking clues from these developments, Russian scientists attempted to design a transparent aircraft in the 1930s [4].

Historically, the first attempt towards the construction of an aircraft with low observable (LO) characteristics is considered to be the German Horten Ho-229, Fig. 24.1, which was built just before the end of WWII and flew in 1944, though it never became operational. It is said to have made use of graphite-based radar-absorbing paint together with special shape-deflecting radar waves. (The special “flying wing” shape is believed to have inspired Northrop to design the B-2 stealth bomber.)

The advent of RADAR during World War II and its threat perception to detect aircraft and surface naval vessels during the war led to the development of radar-absorbing materials (RAMs) both in Germany [5] and the USA in 1945: these materials were based on iron and charcoal to make an aircraft less visible to RADAR [6].

Fig. 24.1 Artist’s impression of the Horten Ho 229 ‘stealth’ aircraft: <https://creativecommons.org>



There have been slow but continuous efforts for development of stealth technology since WWII. Notable among them is the development of the SR-71 “Blackbird”, a high-altitude reconnaissance aircraft, by Lockheed in the USA in the mid-1960s, see Fig. 24.2. This aircraft was highly invisible to the radar of that period [7]. The aircraft was designed with only a few vertical surfaces that would directly reflect radar waves back towards a transmitter. Furthermore, the external surfaces were coated on the leading edges and tail fins with radar-absorbing materials consisting of carbonyl iron and carbon black. This unique aircraft was used for high-altitude surveillance in other countries.

In the 1970s the pace of development of stealth technology was accelerated, particularly in the USA, while employing every available method to avoid detection by visual, radar, infrared, electromagnetic and acoustic means, *and* keeping these methods highly secret. As an outcome, the existence of two U.S. stealth combat aircraft, the F-117 fighter and B-2 bomber, has become publicly known in the 1980s, though the technical details are still classified.

24.3 Threat Perception and Analysis

Over the past three decades there have been tremendous advancements in sensor technology, so much so that sensors with high degrees of precision are available now for detection and acquisition of military targets over a broad range of the electromagnetic spectrum (i.e. optical, infrared, microwave) or acoustic regions, see Table 24.1.

Amalgamation of these sensor technologies, aided with advances in computer technologies and the operational platforms using them, make it very difficult to hide any target [8]. It is now even possible to obtain real-time information about enemy deployments in battlefields. Development of stealth technology to counter these detection measures is therefore a real challenge.

Fig. 24.2 Lockheed SR-71 “Blackbird”, designed to have basic stealth characteristics:
<https://pixabay.com>



Table 24.1 Threat sensors available for surveillance reconnaissance and guided weapon systems [8]

Wavelength/frequencies	Threat sensors	Platforms	Remarks
Visual to near-infrared $\lambda = 0.4\text{--}1.0 \mu\text{m}$	<ul style="list-style-type: none"> • Aided/unaided human eye, telescopes • TV cameras, photography (true and false colour) • Spectral imagers • Charge coupled devices (CCD) • Low light devices (Lidar) 	<ul style="list-style-type: none"> • Surface • Subsurface • Airborne • Satellites 	<ul style="list-style-type: none"> • Passive • High resolution (cm to metres) • Identification and classification of military objects • Short and long range
Thermal infrared (IR) $\lambda = 3\text{--}5 \mu\text{m}$ and $8\text{--}14 \mu\text{m}$	Imaging and non-imaging: <ul style="list-style-type: none"> • IR films, SWIR, FLIR • Thermal imagers (InSb and HgCdTe chips) 	<ul style="list-style-type: none"> • Surface • Subsurface • Airborne and guided weapon systems 	<ul style="list-style-type: none"> • Passive • High accuracy • Weather/atmosphere dependent • Short range detection (up to 10 km)
Microwave $f = 2\text{--}18 \text{GHz}$	<ul style="list-style-type: none"> • Synthetic aperture radar (SAR) • Side-looking airborne radar (SLAR) • Moving target indication (MTI) radar 	<ul style="list-style-type: none"> • Surface (land and sea) • Airborne • Satellites 	<ul style="list-style-type: none"> • Active • All weather • Day and night • Short and long range detection
Acoustics	<ul style="list-style-type: none"> • Sonars, torpedoes 	<ul style="list-style-type: none"> • Subsurface 	<ul style="list-style-type: none"> • Detection of submarines

24.4 Multispectral Stealth

Stealth technology is very much a multidisciplinary, complex, and challenging subject. It involves integration of many materials, techniques and strategies to address the need for avoiding detection. For better understanding, stealth technology can be categorized based on the wavelengths and/or frequencies listed in Table 24.1. Multispectral stealth may be achieved with the aid of carefully selected materials that have different electromagnetic properties, e.g. refractive index, permittivity and permeability. Table 24.2 lists the physical principles and materials for each spectral range and type.

Table 24.2 Physical principles and materials for multispectral stealth applications

Wavelength/frequencies	Physical principles	Coating materials
Visual to near-infrared $\lambda = 0.4\text{--}1.0 \mu\text{m}$	<ul style="list-style-type: none"> • Coating to adjust the reflectance of an object to resemble its immediate surroundings • Should match in colour and texture with that of surroundings • Low specular reflectance (gloss) 	<ul style="list-style-type: none"> • Paint pigments <u>Green</u>: Cr, Ni, Co, Fe oxides; phthalocyanin; soluble dyes <u>Earth Yellow</u>: (sand) TiO_2, C-black, Fe oxides <u>Brown</u>: TiO_2, ZnO, Fe oxides, organic dyes • Paint binders: resin dyes • Aqueous foams in different colours • Antireflective coatings on windscreens
Thermal IR $\lambda = 3\text{--}5 \mu\text{m}$ and $8\text{--}14 \mu\text{m}$	<ul style="list-style-type: none"> • Scattering and reflection of IR radiation • Low emissivity 	<ul style="list-style-type: none"> • Obscurants (smoke) • Surface coatings: metal flakes in low emissivity resins • Foam (liquid or solid)
Microwave $f = 2\text{--}18 \text{GHz}$	<ul style="list-style-type: none"> • High absorption and/or dispersion of radar waves • Impedance matching 	<ul style="list-style-type: none"> • Magnetic: ferrites, carbonyl iron • Dielectric: carbon, conducting polymers, complex Ba, Ti and Mn oxides • Chiral: organic and liquid crystalline materials
Acoustics	<ul style="list-style-type: none"> • Viscoelastic loss and local strain deformation • Vibration damping • Flow noise reduction 	<ul style="list-style-type: none"> • Polyurethane foam • Interpenetrating network polymers (IPN) • Ceramics

24.4.1 Visual Stealth

Visual stealth may be understood as minimization of the contrast in reflectance between a target and its surroundings. Visual stealth is realized in several ways such as by elimination of smoke contrails (improved engine combustion), blending the target with its surroundings through surface treatments, and low level flight.

An aircraft can be made stealthy in the optical region by camouflaging the aircraft, e.g. Fig. 24.1. Other examples are (i) black paint for high-altitude reconnaissance planes, see Fig. 24.2, (ii) painting the undersides grey to match with the sky during daytime, and (iii) black or dark grey for night operation. In addition, coatings need to be non-glossy, and cockpit glass or other smooth surfaces should be antireflective. An ideal solution for visibility stealth, however, lies in the development of smart materials capable of chameleon-like mimicking of backgrounds.

24.4.2 Infrared Stealth

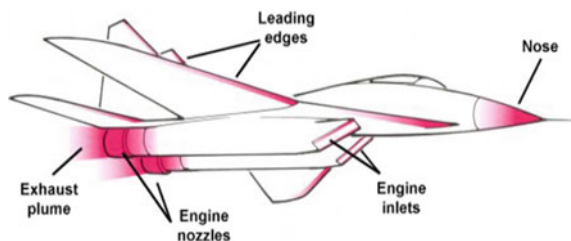
Temperature contrast of ± 25 °C between an object and its surroundings are not uncommon in the military operational theatre. Under ideal conditions, thermography and thermal imaging cameras can detect temperature differences as little as 0.1 °C, although the accuracy decreases with distance between the camera and object. Transmittance of radiation through the atmosphere can also be hindered by meteorological conditions like mist or airborne particles [9]. Nevertheless, thermography cameras generally give good contrast between warmer and cooler objects and surroundings.

Aircraft emit infrared radiation from several sources, see Fig. 24.3. Although the IR band is broad, covering electromagnetic radiation with wavelengths between 0.8 and 1000 μm , the region of most relevance for stealth is the near-infrared, i.e. shorter than 10 μm . This is because the principal source is the aircraft engine, which radiates waste energy as heat in two basic ways: (i) the tailpipe and (ii) the exhaust gas plume. Igniting the afterburner will dramatically increase the plume temperature, which will then dominate the aircraft's IR signature. More IR is emitted by hot engine parts, particularly the afterburner nozzle, and also probably from the aircraft surface, owing to both aerodynamic heating and reflected and re-emitted sunlight.

Passive stealth measures: IR signatures can only be reduced, not eliminated. However, there are several possible passive stealth measures. The main one is to cool aircraft engines. Other measures are embedding the engines inside the fuselage or wings, thereby screening them from the external surfaces; extra shielding of hot parts; mixing of cool air with hot exhausts before emission; baffling of exhaust gases; and application of special coatings to hot spots to absorb and diffuse heat over larger areas [10, 11].

Flying at lower speeds, and using surface paints is liable to reduce emissions from the aircraft's skin. For example, thermal infrared coatings which have a similar IR reflectance to the background help to disturb the thermal signature, making detection more difficult. It is noteworthy that the B-2 bomber uses special chemicals injected into the exhaust gases. These chemicals modify the IR signature as well as forcing water droplets in the exhaust plume to break up into much finer particles, thereby reducing or even eliminating contrails.

Fig. 24.3 Sources of infrared (IR) radiance from a tactical aircraft



Active infrared stealth: Similar to passive radar stealth, the use of active infrared stealth is quite prevalent. This basically involves infrared jamming and the launching of infrared decoy flares. This is particularly important for combat helicopters [12], which fly at low altitudes and relatively low speeds and have to avoid heat-seeking weapons.

24.4.3 Radar Stealth

Radar is a very powerful way to detect reflected electromagnetic energy in the microwave region. There are several types of radar, differing in their detection range depending on the radiation energy. The outstanding features of radar include round-the-clock operation irrespective of weather conditions. Effectively in use since WWII, there have been tremendous advancements in radar technology: so much so, that radar now finds applications in early detection of surface or airborne objects, and provides extremely accurate information on distance, direction, height and speed of the objects. Radars are also used to provide long-distance surveillance and navigation information [13], and in missiles to seek and attack targets.

24.4.3.1 Radar Cross-Section (RCS)

The signature of an object target is ascertained in term of its radar cross-section (RCS). The RCS is defined as the cross-sectional area of a perfect metal sphere that gives the same radar reflection as the object or target [14]. The larger the RCS the easier it is to detect an object and the greater the distance at which it is detected. Table 24.3 lists RCS values and the maximum detection range, R_{\max} , for several types of tactical aircraft. N.B: $R_{\max} \propto \sqrt{4\text{RCS}}$.

Table 24.3 shows that the RCS values differ enormously, but the $\sqrt{4\text{RCS}}$ dependence of R_{\max} means that the maximum detection range is much less changed. Nevertheless, the well-stealthed F-35A and F/A-22 aircraft are much less readily detectable than the others. These examples are, however, only for illustration. RCS values of most targets are rather complex and vary depending on their positions with respect to the tracking radar. Other factors influencing RCS include the target geometry, its surface composition, the radar frequency and the radar antenna polarization [14].

24.4.3.2 RCS Reduction

The principle of RCS reduction or radar stealth is straightforward, i.e. incoming waves should be absorbed or deflected away from the tracking radar. The stealth

Table 24.3 RCS and corresponding maximum detection range, R_{\max}

Aircraft types	RCS (m^2)	R_{\max} (km)
F-15C; Su-27	10–15	450–600
Tornado	8	420–500
MIG-29	5	370–450
F/A-18C	3	330–395
F-16C	1.2	260–310
JAS39	0.5	210–250
Su-47	0.3	185–220
Rafale X	0.1–0.2	140–200
F-18E	0.1	140–170
F-35A	0.0015	50–60
F/A-22	$\leq 0.0002\text{--}0.0005$	30–45

level of an aircraft depends on its shape and materials, particularly the special materials used to cover the external (metallic or composite) surfaces.

Shape: The shape of an aircraft—not its size—is the most important factor affecting the RCS. Many decades of research have evolved the Physical Theory of Diffraction (PTD) [15], which was successfully used to design the F-117 and B-2 aircraft [16]. This theory explains the reduction of RCS by specially designed surfaces and edges that *reflect/deflect* the incoming radar energy away from the tracking radar. Generally, flat vertical surfaces, corners and fasteners are avoided in low RCS aircraft. The Horten Ho 229 and B-2 bomber are examples of streamlined flying wings that avoid the use of empennage, see Figs. 24.1 and 24.4.

More specifically, stealth design includes shielded (coated) cockpits; no surface seams or gaps; no right angles on the empennage (if any); angled wings deflecting radar waves rather than reflecting them; screened engine ducts (the screens are similar to those used for microwave ovens); and internal fuel tanks, weapons and other stores. Finally, intake cavities must be minimized, since they make it impossible to reduce radar reflections from objects and surfaces inside the cavities. Obvious problem areas are engine intakes. These may be made stealthy by

Fig. 24.4 Northrop Grumman B-2: <https://pixabay.com>



incorporating S-shaped ducts instead of straight ones. All the foregoing design aspects are employed in the design of new stealth aircraft.

24.5 Radar-Absorbing Materials and Structures (RAMS and RAS)

Materials that are capable of attenuating the reflection of microwaves are known as radar-absorbing materials (RAMs). They can do this in two main ways:

- By being absorbed into a material that converts the microwave energy into another form of energy such as heat; and
- By destructive interference.

In the former, the electric or magnetic fields of the radiation react with the material such that energy is consumed and dissipated in the form of heat energy [1, 17]. In the second case, incident waves are cancelled out by antiphase reflections, with the necessary 180° phase shift being achieved by reflecting surfaces that are spaced a nominal quarter wavelength apart. Some RAMs, and also radar-absorbing structures (RAS), utilize both principles.

Apart from military applications of radar stealth, RAMs have several non-military applications in telecommunication and medical equipment and home appliances [18, 19]. The major requirements common to both RAMs and RAS include: (i) strong absorption over a broad microwave frequency range, (ii) low density, (iii) thin coatings and (iv) simple coating-layer structures requiring minimal processing.

24.5.1 Radar-Absorbing Materials (RAMs)

As mentioned above, one of the functions of RAMs is to attenuate the reflection of microwave radiation. RAMs must have high values of complex permittivity and permeability to allow incoming waves to be absorbed and dissipated as heat inside the materials. The dissipation mechanisms may be magnetic and/or dielectric, and physical, chemical or both. Impedance matching (see Table 24.2) is important, since impedance matching of materials with air ($Z = 377 \Omega$) allows radar waves first to penetrate the material (if permeable) and then be absorbed.

To optimize the attenuation of incident microwaves, RAMs need to adjust their electrical and magnetic properties in order to achieve good impedance matching. The combination of different materials results in different impedance values, and consequently different absorption characteristics. Besides absorption there is also a “skin-effect”. This confines the electrical and magnetic fields (voltages and currents) generated by the impinging radar waves to a thin surface layer, the “skin

depth”, within which all the radiation is absorbed. This skin depth parameter is relevant to the optimum design of thin lightweight coatings that still enable absorption [20].

Besides absorption over a broad range of microwave frequencies, other requirements for aircraft stealth RAMs include environmental compatibility (temperature, humidity, atmospheric pressure), erosion resistance, and conformity with the external aerodynamic surfaces.

24.5.2 Classification of RAMS

The types of RAMs used depend broadly on the applications [21]. RAMs are generally classified into two types, according to their interactions with radar waves: (i) magnetic absorbers and (ii) dielectric absorbers. The absorption in magnetic absorbers is due to the magnetic hysteresis effect, which is obtained when particles like ferrites are used as fillers in a polymeric (paint/coating) matrix [22]. On the other hand, absorption in dielectric materials depends on the ohmic loss of energy achieved by fillers like carbon, graphite, conducting polymers, or metal particles or powders in a polymeric matrix.

There is a wide range of polymers available for the production of radar-absorbing coatings/structures. However, the choice of a matrix material depends on the type of application. Polyurethanes, epoxy and thermoplastic polymers such as polyphenylene sulphide (PPS) are the preferred matrix materials because of their mechanical strength, erosion resistance and ability to withstand physical and chemical extremes.

Other ways of classifying RAMs are: (i) narrow band (resonant) or broad range absorbers; (ii) single- or multi-layered; (iii) specular or non-specular; and (iv) graded multi-layer dielectrics, whose dielectric constant varies within the layers.

24.5.2.1 Magnetic Absorbers

Magnetic absorbers are based on carbonyl iron, spinel ferrites, and hexaferrites. These materials absorb in the MHz to GHz ranges. The resonance frequency is related to particle size. These materials can be tuned to absorb at higher frequencies (5–20 GHz) based on particle size and sintering temperature. The bandwidth of standard ferrite absorbers could be improved via a two-layer absorber design, with a ferrite layer at the air/absorber interface and a layer containing ferrite and short metal fibres at the absorber/metal interface.

These materials are loaded as fillers in a flexible matrix consisting of elastomeric polymers such as polyisoprene, neoprene, nitrile rubber, silicone, urethanes and

fluoroelastomers. The thickness and magnetic properties of these materials are controlled in order to achieve the required permeability characteristics. This enables “tuning” to achieve the desired loss factor and impedance. In the case of magnetic materials, losses are produced by changes in the alignment and rotation of the magnetization spin.

Examples of magnetic materials having potential for stealth application on aircraft or other military targets include: (i) paints based on spinal ferrites, i.e. Ni–Zn ferrite with the formula $\text{Ni}_{1-x}\text{Zn}_x\text{Fe}_2\text{O}_4$ ($x \leq 0.5$); Mn–Zn ferrite with a surface-organized polyaniline coating; (iii) paints based M-type barium hexaferrites, $\text{Ba Fe}_{12}\text{O}_{19}$; (iv) paints based on carbonyl iron in polyurethane or epoxy resins [23, 24]. Generally, magnetic absorbers are thinner by a factor of about ten than dielectric absorbers for the same frequency range.

24.5.2.2 Dielectric Absorbers

Dielectric materials are characterized by the presence of permanent positive and negative charges on their atoms and molecules, which are kept in the same position by the atomic and molecular forces and are not free to dislocate. However, when an electric field is applied to such materials, several electric dipoles are formed and align themselves according to the orientation of the applied electric field.

Such materials are known as dielectric absorbers. The dominant mechanisms involved in microwave absorption by dielectric RAMs are the absorption of the incident energy and multiple reflections of the radiation [25]. These effects are due to physical phenomena such as ohmic losses, and the backscattering of the radiation in different directions by using proper geometric shapes.

Dielectric absorbers are obtained from combinations of (i) rigid or polymeric matrices such as epoxy, phenolic, bismaleimide, polyurethane, polyimide and silicone resins; and (ii) both inorganic (carbon, graphite, titanates, carbides, nitrides, etc.) and organic (conducting polymer) materials.

Artificial Dielectrics: These are fabricated electromagnetic materials consisting of synthetic substances, usually consisting of orderly arrangements, e.g. arrays. These arrays are usually evenly spaced on or within a substrate. Hence the dielectric inclusions are in a kind of periodic lattice, whereby the lattice spacing is designed to be smaller than the impinging electromagnetic wavelengths, and the effective permittivity and effective permeability are as required.

These structures are considered to find application particularly in radar-absorbing structures mimicking metamaterials. The materials used include radar-absorbent plastics, carbon-based materials and ceramics. Blends of these materials provide the desired specific electrical and magnetic properties.

24.5.2.3 Conducting Polymers

Organic polymers that conduct electricity were discovered in the late 1970s and are referred to as conducting polymers. These materials have the unique combination of the chemical and mechanical properties of polymers with the electrical properties of metals and semiconductors. Conducting polymers can be obtained from a variety of organic monomers such as acetylene, aniline, pyrrole, thiophene, etc. These monomers form conjugated bonded polymers that upon exposure to electron acceptor or donor species give rise to conducting polymers of varied electrical conductivities. Conducting polymers find numerous applications in electronics, catalysis and electromagnetic devices. The latter area also covers electromagnetic wave (radar) absorption.

The controllability of conductivity and the ease of manufacturing/coating of conducting polymers enable tailor-made dielectric loss components for radar-absorbing materials (RAMs). Conducting polymers derived from pyrrole (PPy) and aniline (PAn), and doped with electron accepting dopants, are among the most studied conducting polymers for radar-absorbing applications [26, 27]. Reflection loss strongly depends on the thickness and complex permittivity of the material. For a single layer material the optimum values of the real part (epsilon') and imaginary part (epsilon'') of the required complex permittivity are found from theoretical calculations.

24.5.2.4 Nanomaterials

An ideal RAM is required to have properties such as (i) strong microwave absorption properties over a broad frequency range; (ii) to be thin and lightweight, especially for aircraft; (iii) simple coating-layer structures and easy processing. Materials scientists are always in search of new microwave-absorbing materials with a high magnetic and electric loss. In recent years nanostructured RAMs have received growing interest because they absorb more microwave radiation compared with their bulk or micro-sized counterparts [28].

Nanostructured RAMs mainly consist of the following four types: nanocrystal RAMs; core-shell nanocomposite RAMs; nanocomposites of multi-walled carbon nanotubes (MWCNT) and inorganic material RAMs; and nanocomposites of carbon nanomaterials [29, 30]. Furthermore, core-shell type nanomaterials offer the possibility to design RAMs that combine suitable high-absorption dielectric and magnetic properties with light weight [31, 32].

It is noteworthy that core-shell FeCo(C) alloy nanoparticles with magnetic FeCo cores ~ 25 nm diameter and dielectric graphitic shells of thickness ~ 10 – 15 nm synthesized in the authors' laboratories [33] show good microwave absorption properties, since they have both dielectric as well as magnetic loss over a broad frequency range.

Carbon-based nanomaterials and their composites with metal, metal oxides and polymers (conducting or insulating) display outstanding physical properties such as high electrical conductivity, low density, and good stability that make them better candidates for microwave applications.

Carbon nanotubes (CNTs) and graphene are among the emerging carbon nanomaterials being investigated for radar-absorbing applications [34–37] as conductive fillers. There are several recent reports on microwave-absorbing materials based on graphene and used in combination with conducting polymers or metal oxides [38–40].

Metallic thin films: Metals are excellent reflectors of microwaves, since they tend to keep the electric field zero on their surfaces [41]. However, some metals behave as absorbers when brought to nanometre thickness. As an example, Kantal films with thicknesses varying from 10 to 200 nm perform effectively as RAMs when used as coatings on waveguide internal walls. In comparison to conventional RAMs, the nanometre films can present similar electromagnetic wave attenuation performance, but they are lighter.

24.5.3 Radar-Absorbing Structures (RAS)

Metallic surfaces of aircraft are good reflectors of radar waves and hence a primary source of detection. Stealth aircraft structures should therefore be coated either with RAMs or made out of them. The latter are called radar-absorbing structures (RAS). Composites come into greater focus when considering radar-absorbing structures (RAS). Reinforced plastic materials are known for their unique combination of low weight with high strength, stiffness and fatigue resistance, but their electromagnetic (EM) characteristics are also important.

RAS are preferable because no additional RAM coatings are needed. An actual RAS usually refers to a resin-based composite structure, typically made from carbon fibre reinforced plastics (CFRPs). The combination of structural composites with RAMs can also be used. For example, the matrix resin of a CFRP can be loaded with fillers or a lossy material [42], provided that the load-carrying requirements are met.

Low-weight RAS can be made from glass fibre reinforced plastics (GRPs) and carbon fibre composite lattices in which the voids are occupied by microwave absorbent foams. The absorption effectiveness is normally related to the volume fraction of the grid cell structure and the distance between elements. In radio/radar frequency (RF) absorbers, carbon composite can be used instead of metal for conductive backplanes, as can metallised fabrics and conductive polymers [43]. Further potential lies in combining the conductive properties of carbon fibre with low (dielectric) loss GRP in textile composites that then have tailored electromagnetic properties. In particular, frequency-selective fabric composites (FSFCs) can be produced by weaving glass and carbon fibres together in particular patterns.

Such fabrics can be both load-bearing and RF energy absorbing. Furthermore, they can be mass produced using existing fabrication processes. This means that their use to protect large assets such as ships and aircraft becomes feasible.

RAS can be single-layered or double-layered structures. Single skin absorbers have a metallic mesh as the back scattering surface [44]. A single layer RAS consisting of Kevlar/graphene/epoxy composite has been reported with a broad bandwidth in the 12–18 GHz range [45].

24.6 Plasma Stealth

A technology that uses ionized gas (plasma) to reduce an aircraft's RCS is known as plasma stealth [46]. Plasma stealth technology is an "Active stealth technology" and was first developed by the Russians. In plasma stealth a stream of plasma is ejected in front of the aircraft. The intention is to cover the entire body of the aircraft with plasma, such that this will absorb most of the electromagnetic energy of the radar waves and make the aircraft difficult to detect.

While it is theoretically possible to reduce an aircraft's RCS by wrapping the airframe in plasma, it may be very difficult to do so in practice. Various methods might plausibly be able to produce a layer or cloud of plasma around an airframe, from "simple" electrostatic or RF discharges to more exotic possibilities like laser-produced plasmas [46, 47]. The Russians have performed more than 100 h of testing of plasmas to reduce the RCS of a Sukhoi Su-35 aircraft.

24.7 Acoustic Stealth

All wings, either natural or engineered, create turbulent eddies as they cut through the air. When these eddies hit the trailing edge of the wings, they are amplified and scattered as sound. Conventional aircraft, which have hard trailing edges, are particularly noisy in this regard and are easily detected from a distance, even though sound moves slowly. Owls, however, possess no fewer than three distinct physical attributes that are thought to contribute to their silent flight capability: a comb of stiff feathers along the leading edge of the wing; a soft downy material on top of the wing; and a flexible fringe at the trailing edge of the wing. Considerable efforts have been made to understand the exact mechanism behind the silent flight of an owl and apply it to reduce the noise of an aircraft.

Using mathematical models, it has been demonstrated that elastic and porous properties of a trailing edge could be tuned so that the dominant noise source for conventional wings could be eliminated.

24.8 Counter Stealth

Especially for military aircraft, stealth technology has become ubiquitous. All new aircraft types are designed while taking into account “low observable” principles and techniques, and existing aircraft types are considered for modification in order to reduce their radar signature. However, irrespective of the degree of stealth of an aircraft, it still remains vulnerable, to detection using counter-stealth strategies and technologies that include the following:

1. Detecting trails of warm air by thermal cameras.
2. Imaging of swirls of air from a stealthy jet by using high resolution Doppler radar.
3. Detection of aircraft-caused disturbances in the Earth’s magnetic field (magnetic anomaly detection).
4. Use of specially shaped radar pulses that resist absorption.
5. Use of more than one receiver, and possibly more than one transmitter, in a network.

To defeat the counter-stealth capabilities is a real challenge for a stealth technologist.

24.9 Currently Available Stealth Aircraft

A number of stealth aircraft have been developed or are undergoing development [48–58]. These include:

1. Northrop Grumman B-2, see Fig. 24.4. These aircraft are designed to deflect most of the radar away from the source. They are also covered with a radar-absorbing skin or paint, which makes the radar echo much weaker. This makes a stealth aircraft seem so small that it easily gets lost among the countless random echoes (noise) that come back to the radar.
2. Lockheed F-117. The first stealth fighter known to have low RCS, using a combination of designed shape and radar-absorbing materials. The airframe uses only about 10 % metal.
3. Lockheed Martin F-22A. This employs a “stealthy” design; the ability to cruise over long ranges at supersonic speed without afterburning; a very high level of aerial agility and STOL capability with the aid of a two-dimensional thrust vectoring system; a fly-by-light control system for a relaxed stability airframe; and an advanced navy/attack system using artificial intelligence to filter data and reduce the pilot’s workload while improving his grasp of the tactical situation.
4. Lockheed Martin F-35. This is a multirole fifth generation fighter with stealth and other capabilities such as Short Take-Off and Vertical Landing, and Conventional Take-Off and Landing. The F-35 has been developed under the Joint Strike Fighter (JSF) programme between the USA and allied nations. It is believed to be the current front runner stealth fighter.

5. Sukhoi PAK FA (T-50). This is a fifth generation stealth fighter considered to be one of the best available combat fighters with super-cruise capabilities, i.e. its normal cruise speed is beyond Mach 1. Besides low RCS, the other salient features include a wide combat radius, supersonic cruise speed, superb low-speed manoeuvrability, and the ability to make short take-offs and landings with a normal take-off weight.
6. HAL AMCA. This is India's contribution to developing a fifth generation stealth multirole fighter, better known as the Advanced Medium Combat Aircraft (AMCA). It is an advanced version of the TEJAS aircraft and is being designed and developed by the Defence Research and Development Organization (DRDO) of India.
7. Chengdu J-20. This is a fifth generation stealth fighter prototype developed and demonstrated by China. It is considered to match the performance of the U.S. F-22. Its maiden flight was held in January 2011 and the aircraft is expected to be operational in 2017–2019.
8. Mitsubishi ATD-X Shinshin. This is a prototype fifth generation stealth fighter aircraft indigenously developed by Mitsubishi, Japan. The Shinshin uses advanced stealth technology.
9. Dassault nEUROn. This is an experimental Unmanned Combat Air Vehicle (UCAV) jointly developed by a consortium of European aerospace companies: Dassault (France), Alenia Aermacchi (Italy), SAAB (Sweden), EADS-CASA (Spain), Hellenic Aerospace Industry (Greece) and RUAG (Switzerland). It is essentially a technology demonstrator incorporating state-of-the-art stealth features.

24.10 Summary

Stealth materials and technology are of great significance for any type of military airborne system including fighter aircraft, helicopters and UAVs. The impact of stealthy airborne systems, mainly developed by the USA, has been well demonstrated during several recent wars and operations. This has been the primary reason to keep the technological aspects classified, and hence the advancements in stealth are not reported in the open literature.

Nevertheless, the two most fundamental aspects of stealth technology remain the shape design and radar-absorbing materials (RAMs). These form part of the structure (radar-absorbing structure, RAS) or are applied as surface coatings. The present chapter has given a brief description of important stealth materials, with special emphasis on advanced materials such as conducting polymers and nano-materials that are the subject of R&D in both developed and developing countries, including India. It is believed that some of these materials will play key roles in future stealth technologies, especially by providing lightweight and broadband MW-absorbing structures.

References

1. Rao JVR (1999) Introduction to camouflage and deception. Defence Research & Development Organisation, Ministry of Defence, New Delhi, India
2. Zhou X (2004) Anti-stealth radar techniques and electronic countermeasures. *Ship Electron Eng* 24:124–131
3. Sheffield R, The official F-19 stealth fighter. www.flightsimbook.com
4. Panait AM (2010) General principles of passive radar signature reducing—stealth technology and its applications. *INCAS Bulletin*, National Institute for Aerospace Research “Elie Carafoli”, vol 2(1): <http://bulletin.incas.ro>
5. Arndt, German Stealth Materials of WW2. <https://groups.google.com/forum/#!topic/rec.aviation.military/ReYpeoIg4II>
6. www.popsci.com/technology/article/2010-07/stealth-paint-turns-any-aircraft-radar-evading-stealth-plane
7. Creating The blackbird. <http://www.lockheedmartin.co.in/us/100years/stories/blackbird.html>
8. Vadera SR, Kumar N (2015, Jan 30) Nanotechnology and nanomaterials for camouflage and stealth applications. www.nanowerk.com/spotlight/spotid=38899_4.php
9. Mahulikar SP, Sonawane HR, Rao GA (2007) Infrared signature studies of aerospace vehicles. *Prog Aerosp Sci* 43(7–8):218–245
10. Gilman L (2003) Stealth technology. *Encyclopedia of Espionage, Intelligence, and Security*
11. Vass S (2003) Stealth technology deployed on the battlefield. *AARMS Inf Robot* 2(2): 257–269
12. Caplan WD (2014) Requirements for laser counter measures against imaging seekers. *Proc SPIE* 9251:952103. doi:10.1117/12.2067264
13. Peebles PZ (1998) Radar principles. Wiley, New York, USA
14. Knott EF, Shaeffer JF, Tuley M (2004) Radar cross section, 2nd edn. SciTech Publishing Inc, Raleigh, NC, USA
15. Ufimtsev PY (1962) Method of edge waves in the physical theory of diffraction. Soviet Radio Publishing, Moscow, Russia
16. Browne MW (1991) Lockheed credits soviet theory in design of F-117. *Aviation Week & Space Technology*, December 1991, p.27
17. Balaris CA (2012) Advanced engineering electromagnetics, 2nd edn. Wiley, Hoboken, NJ, USA
18. Padilla WJ, Basov DN, Smith DR (2006) Negative refractive index metamaterials. *Mater Today* 9(1):28–31
19. Hyper Stealth Biotechnology Corp/Canada (2011) Visual animal camouflage: mechanisms and function. In: Stevens M, Merilaita S (eds). Cambridge University Press, Cambridge, UK: <http://www.arkive.org/c/camouflage/>
20. Quéffelec P, Le Floc’h M, Gelin P (1998) Broad-band characterization of magnetic and dielectric thin films using a microstrip line. *IEEE Trans Instrum Measure* 47(4):956–963
21. Saville P (2005) Review of radar absorbing materials. Technical Memorandum TM 2005-003, Defence Research and Development Canada - Atlantic, Dartmouth, NS, Canada
22. Petrov VM, Gagulin VV (2001) Microwave absorbing materials. *Inorg Mater* 37(2):93–98
23. Kazantseva NE, Saha N, Sedlarik V, Saha P, Kar S (2006) Magnetic materials based on manganese–zinc ferrite with surface-organized polyaniline coating. *J Magn Magn Mater* 301(1):155–165
24. Folgueras LC, Alves MA, Rezende MC (2009) Electromagnetic radiation absorbing paints based on carbonyl iron and polyaniline. In: Proceedings of the international microwave and optoelectronics conference, vol 1. IEEE, pp 510–513
25. Folgueras LC, Luis Nohara EI, Faez R, Rezende MC (2007) Dielectric microwave absorbing material processed by impregnation of carbon fiber fabric with polyaniline. *Mat Res* 10(1)
26. Margolis J (ed) (1989) Conductive polymers and plastics. Chapman and Hall, p 33

27. Salaneck WR, Clark DT, Samuelsen EJ (1991) Science and application of conducting polymers. IOP Publishing, Bristol, UK
28. Wang Y, Li T (2011) Research progress on nanostructured radar absorbing materials. *Energy Power Eng* 3:580–584
29. Zhou K, Deng J, Yin L et al (2007) Microwave absorbing properties of $\text{La}_{0.8}\text{Ba}_{0.2}\text{MnO}_3$ nano-particles. *Trans Nonferrous Metals Soc China* 17(5):947–950. doi:10.1016/S1003-6326(07)60205-2
30. Sharma R, Agarwala RC, Agarwala V (2005) Development of radar absorbing nano crystals by microwave irradiation. *Mater Lett* 62(15):2233–2236
31. Sharma R, Agarwala RC, Agarwala V (2009) Development of electroless (Ni–P)/ $\text{BaNi}_{0.4}\text{Ti}_{0.4}\text{Fe}_{11.2}\text{O}_{19}$ nanocomposite powder for enhanced microwave absorption. *J Alloys Compd* 467(1–2):357–365
32. Xiao HM, Liu XM, Fu SY (2006) Synthesis, magnetic and microwave absorbing properties of core-shell structured $\text{MnFe}_2\text{O}_4/\text{TiO}_2$ Nanocomposites. *Compos Sci Technol* 66(13):2003–2008
33. Gupta V, Patra MK, Shukla A, Sain Songara S, Jani R, Vadera SR, Kumar N (2014) Synthesis and investigations on microwave absorption properties of core–shell FeCo(C) alloy nanoparticles. *Sci Adv Mater* 6:1–7
34. Sun X, Gao M, Li C, Wu Y, Microwave absorption characteristics of carbon nanotubes. www.intechopen.com
35. Shen ZM, Zhao DL (2001) Study on the microwave absorbing property of composite material containing carbon nanotubes with Ni coating. *New Carbon Mater* 16(1):1–3
36. Lin H, Zhu H, Guo H, Yu L (2008) Microwave-absorbing properties of Co-filled carbon nanotubes. *Mater Res Bull* 43:2697–2702
37. Zhan Y, Zhan R et al (2010) A novel carbon nanotubes/ Fe_3O_4 inorganic hybrid material, synthesis, characterization and microwave electromagnetic properties. *Magn Magn Mater* 1–5
38. Singh VK, Shukla A, Patra MK, Saini L, Jani RK, Vadera SR, Kumar N (2012) Microwave absorbing properties of a thermally reduced graphene oxide/nitrile butadiene rubber composite. *Carbon* 50(6):2202–2208
39. Zhao J, Lin J, Fan H (2015) Synthesis and electromagnetic, microwave absorbing properties of polyaniline/graphene oxide/ Fe_3O_4 nanocomposites. *RSC Adv* 5:19345–19352
40. Wang L, Jia X, Li Y (2014) Synthesis and microwave absorption property of flexible magnetic film based on graphene oxide/carbon nanotubes and Fe_3O_4 nanoparticles. *J Mater Chem A* 2:14940–14946
41. Wang Z, Luo J, Zhao G (2014) Dielectric and microwave attenuation properties of graphene nanoplatelet–epoxy composites. *AIP Adv* 4:017139
42. Chin WS, Lee DG (2007) Development of the composite RAS (radar absorbing structure) for the X-band frequency range. *Compos Struct* 77(4):265–457
43. Kim JB (2012) Broadband radar absorbing structures of carbon nanocomposites. *Adv Compos Mater* 21(4):333–344
44. Baron SE, Mbarek SB, Vairac P, Creti B (2009) Design of metallic mesh absorbers for high bandwidth electromagnetic waves. *Prog Electromagn Res C* 8:135–147
45. Shin JH, Jang HK, Choi WH et al (2009) Design and fabrication of RAS with graphene added kevlar fiber reinforced composites. In: ICCM-17, 17th international conference on composite materials, 27–31 July 2009, Edinburgh, Scotland: www.iccm-central.org/
46. http://en.wikipedia.org/wiki/Plasma_stealth
47. Nikolay N (1999) Russian scientists created revolutionary technologies for reducing radar visibility of aircraft. ITAR-TASS, January 1999
48. Fiszer M, Gruszczynski J (2002, June) Russia working on stealth plasma. *J Electr Defense*
49. <https://www.f35.com/>
50. Trimble S (2009) F-15 silent eagle media briefing, flight global blogs. <http://www.flightglobal.com/blogs/the-dewline/2009/03/f-15-silent-eagle-media-briefi.html>
51. Carey B (2013) Boeing flies ‘Advanced Super Hornet’ demonstrator AINonline: www.ainonline.com

52. Pelosi MJ, Kopp C (2012) A preliminary assessment of specular radar cross section performance in the sukhoi T-50 prototype. Air Power Australia Analysis <http://www.ausairpower.net/APA-2012-03.html>
53. Sukhoi PAK FA T-50 much more powerful than USA's F-22 Raptor, Pravda 18 Aug 11 http://english.pravda.ru/russia/economics/18-08-2011/118783-pak_fa_raptor-0/
54. Perrett B, Hewson R, Johnson, Sweetman B (2012) Avic promotes J-31 as an export fighter. AW&ST, 19 Nov 12 http://www.aviationweek.com/Article.aspx?id=/article-xml/AW_11_19_p26-517474.xml&p=1
55. Tellis AJ (2011) Dogfight! India's medium multi-role combat aircraft decision. Carnegie Endowment for International Peace, Washington DC, USA
56. Rafale International, "Fox Three" no. 15. http://www.dassault-aviation.com/wp-content/blogs.dir/1/files/2012/08/FoxThree_Fox15.pdf
57. de Larrinaga N: IDEF 2013, TAI reveals fifth generation fighter designs, IHS Jane's Defence Weekly, 08 May 13. <http://www.janes.com/article/12439/idef-2013-tai-reveals-fifth-generation-fighter-designs>
58. Turkey to replace F-16s with local jets, Instabul, Hürriyet 29 Mar 13 <http://www.hurriyetdailynews.com/turkey-to-replace-f-16s-with-local-jets.aspx?pageID=238&nID=43867&NewsCatID=374>

Chapter 25

Paints for Aerospace Applications

**K. Shunmugapriya, Shirish S. Kale, G. Gouda, P. Jayapal
and K. Tamilmani**

Abstract Paints are important for aerospace applications in view of appearance, surface protection, and as stealth coatings. Paints are generally applied as a scheme involving primer-coats and top-coats for achieving ultimate protection. The satisfactory performance of paint coatings throughout the service life of an aircraft depends on many aspects. The present chapter discusses these paint aspects under the following topics: importance for aerospace applications; selection for aerospace applications; application areas in military aircraft; special functional paints; the properties, testing and analysis of paints; ageing of paints; airworthiness certification of paints; volatile organic compounds regulations; and paint monitoring. Some important new developments of paints are also discussed.

Keywords Paints · Constituents · Functional paints · Properties · Testing · Applications

25.1 Importance of Paints for Aerospace Applications

Aircraft operate up to high altitudes and high speeds (subsonic and supersonic speeds for combat aircraft). This environment imposes temperature differentials and changing pressures on the aircraft structure, resulting in expansion and contraction, severe wing and empennage flexure, condensation of water on the aircraft surface

K. Shunmugapriya (✉) · S.S. Kale (✉)
Regional Centre for Military Airworthiness (Foundry & Forge),
CEMILAC, Bangalore, India
e-mail: k.shunmugapriya@cemilac.drdo.in

S.S. Kale
e-mail: shirish.kale@cemilac.drdo.in

G. Gouda · P. Jayapal
CEMILAC, DRDO, Bangalore, India

K. Tamilmani
Office of DG (AERO), DARE, DRDO, Bangalore, India

[1] and transpiration via externally connected structural joints, etc. Metallic aircraft structures and components deteriorate/corrode due to the presence of moisture, saline and polluted atmospheres, ultraviolet (UV) light and bacteria. Corrosion is most likely to occur at and within joints and attachment points, which provide entrapment areas for moisture accumulation and corrosive agents.

From the foregoing it follows that aircraft external surfaces and also the internal structures, sub-assemblies and components need to be protected from environmental degradation.

Paint coatings serve as barriers to environmental degradation. The paints need to have certain prime properties like flexibility, good adhesion with the substrate, and retention of film properties under extreme operating conditions. In addition they should resist:

- The effect of low air pressure at high altitudes in making residual liquid in the paint more volatile
- UV radiation, which is considerable at high altitudes
- High humidity and saline atmospheres, particularly for naval aircraft
- A variety of in-service aircraft fluids such as fuels, lubricating oils, and hydraulic fluids, which are especially aggressive.

Civil and military transport aircraft have broadly similar design and manufacturing criteria, operational limits and mission requirements [2]. However, the mission requirements of combat (tactical) aircraft are very critical and highly explicit.

Transport aircraft experience moderate loads, frequent pressurization and depressurization, both low (at altitude) and high (ground level) temperatures, and humidity changes. In contrast, tactical aircraft fly for fewer hours but experience frequent high flight loads due to manoeuvres and large throttle excursions. These flight conditions generally place more mechanical stresses on the aircraft coating systems than transport aircraft flight loads.

There are also differences in the requirements for the surface properties of paints. External paint systems for civil aircraft are primarily meant for aesthetic appearance and surface protection. However, external paints and coatings for military aircraft must meet advanced military needs, which include antistatic, thermal flash resistance, radar signal absorbing, and camouflage [3].

Paints for space vehicles form a special category. Space vehicles are exposed to varying forms of thermal energy, atomic oxygen, UV radiation, and thermal cycles [4, 5]. These extreme exposure conditions render most aircraft paint systems unsuitable for space applications. For this reason, the scope of the present chapter will be restricted to aircraft applications, especially military aircraft.

25.2 Selection of Paint Formulations for Aerospace Applications

A paint system is a combination of binder, pigment, solvent and additives. The properties of the paint largely depend on its constituents. These are discussed here.

Binders These determine the film forming mechanism, weathering ability and environmental resistance; and also the required surface preparation, application equipment and techniques. Common binders used for aerospace applications are epoxy resins, polyurethane (PU) resins, nitrocellulose (NC), acrylics, and modifications thereof.

The structure of an epoxy resin is shown in Fig. 25.1. Resins having n values (number of polymer repeat units) ranging from 1 to 2 are generally chosen for two-pack, ambient-cure coating applications. Epoxies possess attractive properties like good corrosion resistance, chemical resistance and adhesion. However, their major drawbacks are poor gloss retention and inferior durability.

PU resins have good gloss retention and durability. The ASTM classifies PUs in six general types [6]: Type IV, which are high-solid coatings are attractive for aircraft applications.

NC is developed from natural cellulose, primarily from wood and cotton fibres. In its normal state, cellulose is an insoluble material. However, the molecule contains a number of hydroxyl groups and can therefore be esterified to make it soluble to yield useful products. NC-based finish coats for aerospace applications consist of cellulose nitrate, glycol sebacate, glyceryl phthalate resin, pigment, and volatile spirits such as toluene, butyl acetate, butyl alcohol and ethyl acetate. NC-based paints are fast-drying and provide excellent recoatability, but have poor corrosion and erosion resistance, durability and gloss retention. They are used in locations where corrosion resistance is not required [7].

Acrylics belong to the family of synthetic resins formed by polymerizing esters of acrylic acids. Acrylics have excellent colour stability and resistance to hydrolysis and UV degradation. Acrylic urethanes are invaluable as high quality aerospace coatings. Another category are reduced solvent acrylics, which are made by modifying acrylic urethane with reactive diluents that act like solvents, but react with the resin to form part of a cross-linked network [8].

We note here that the properties of binders, especially the molecular weight, play a major role in deciding the film properties. For instance, the increase in molecular

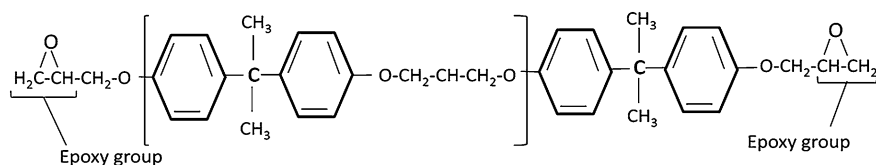


Fig. 25.1 Structure of an epoxy resin

weight of an epoxy resin increases the flexibility and flexibility retention, the film levelling properties, hiding power, appearance and pot life. However, increased molecular weight reduces the cross-link density, thereby resulting in reduced solvent and chemical resistance and increased non-volatile content of the paint at the application viscosity. Hence, an intermediate optimum molecular weight of binders is preferred for balanced properties.

Pigments Can be classified as corrosion inhibiting pigments and colouring pigments. They determine the corrosion-inhibitive properties, the colour, and flow control properties of the applied paint. The paint viscosity depends on pigment particle size and shape, ease of wettability by the binder, bulking property and specific gravity. The viscosity affects the application characteristics of the wet coating, and ultimately the properties of the dry protective coating.

Solvents These enable paint application, substrate wettability, and penetration to aid in sealing crevices, voids or depressed irregularities. Solvents must also volatilize fast enough to prevent runs and sags in the drying coating. However, a solvent that is too volatile can cause solvent pops, loss of gloss, dry spray; and poor surface wetting, penetration, and film flow.

Virtually all coating formulations use a blend of solvents to achieve optimum properties. Ultimately, all solvents should evaporate to allow the coating to achieve the required hardness, cure and final properties. Commonly used solvents are turpentines, hydrocarbons, ketones, esters, alcohols, and glycol ethers.

Additives A number of compounds are also required in the paint formulation for specialized purposes. These include driers, anti-skinning and anti-settling agents, fungicides or bactericides, and surface active agents used to assist pigment dispersion [9]. Extenders are constituents used to replace part of the pigment to reduce cost.

More information on aerospace paint formulations may be found in the published literature [10–12].

25.3 Paint Application Areas in Military Aircraft

Paints find applications in various parts of military aircraft, and a few of these applications are explained in the next subsections.

25.3.1 *Airframes*

Airframe structures have large external and internal surface areas, and more than one type of material may be used in their construction. Aluminium alloys form the major structural materials, but composites are also widely used, particularly in tactical aircraft.

Apart from surface protection, paints are applied to the external surface contours to promote a non-turbulent airflow that remains attached to the skin. Military aircraft also rely on paints for camouflage properties to minimize enemy detection and tracking during operations. A typical airframe paint scheme for a metal/composite substrate consists of BS X 33 epoxy primer coat (or) DEF STAN 80-216/1, followed by a PU finish coat to BS X 34 with content of volatile organic compounds (VOC) less than 420 g/l.

Epoxy primers Epoxy primers are applied at temperatures between 15.5 °C and ~37.7 °C. In service, epoxies can be used at both low and high temperatures, but should not be exposed to temperatures above 148.8 °C.

Primers inhibit corrosion of the substrate and enhance adhesion of subsequent topcoats. Anticorrosive primer formulations are based on epoxy resins that react at ambient temperature with amine adducts (amidoamine-based hardeners). The epoxide rings at the ends of epoxy resin molecules and a number of hydroxyl groups along the molecular chain make the resins polar and promote good adhesion to polar/metallic surfaces [13]. Good chemical and moisture resistances of epoxies are attributed to the stable C–C bond and ether linkages. The ether linkages also impart much better colour to the paint film. Coatings with low VOC (less than 300 g/l) are obtained by formulating with modified bisphenol A and modified polyamidoamine-based hardeners.

Strontium chromate is used as an anticorrosive pigment in epoxy primers, since it is electrolytically active and prevents filiform corrosion. When the paint film is permeated by water, the strontium chromate pigment slowly releases chromate ions. These accumulate at the sites of heightened humidity, in particular near exfoliations of the coating from the substrate, and act as a classical inhibitor for metal corrosion [14]. However, although chromate pigments are highly effective, there has been much research to replace them owing to the carcinogenic properties of chromates.

An additional function of pigments, and also extenders, is to allow the primers to react with Cl^- and SO_4^{2-} that diffuse into the primer film from the atmosphere.

Etch/wash primers These are referred to as metal conditioners, and are used as pretreatments before applying a yellow epoxy primer to non-ferrous metals that have not undergone other kinds of pretreatment. Etch primers eliminate the need for phosphating and chromate rinsing the metal surfaces.

Etch primers have a threefold action:

1. Firstly a zinc phosphate film, similar to that formed in the common phosphating process, is deposited on the metal.
2. Secondly, the primer also provides a continuous supply of chromate ions for the repair of any pinholes present in the phosphate film. Thus a special chromate rinse is eliminated.
3. Thirdly, a polyvinyl butyral (PVB) film is chemically bound in the organic layer via a chromium complex, thus providing additional mechanical protection to the metal surface (Source: *Tuff Coat Polymers Private Ltd., Pune, India*).

An etch primer based on PVB resin provides water resistance via its paraffin structure. Besides the film having excellent hardness and flexibility, good chemical resistance is achieved with the dioxin-link nucleus of six atoms. The film is also reported to have excellent resistance to seawater, oil and grease, and temperatures up to 400 °C.

Topcoats (epoxy, PU, acrylic, and new developments)

Epoxy topcoats are used only for interior applications, since they tend to fade, become matt and exhibit chalking under the influence of light and weather [15].

PU topcoats are used for exterior surfaces, since they possess the mandatory properties of low temperature cure, high flexibility, toughness, resistance to abrasion and chemicals, and excellent weatherability. These topcoats consist of an isocyanate cured polyester polyol/acrylic polyol resin, and are formed by the cross-linking reaction between an isocyanate-containing ($-N=C=O$) material and a material with a polyhydroxylate-containing ($-OH$) co-reactant. The structure of polyurethane is shown in Fig. 25.2. Cross-linking occurs due to the high reactivity and affinity of the isocyanate group for the active hydrogen of the polyhydroxyl group.

The isocyanate reactant can be strictly an aliphatic hydrocarbon because these do not fade or darken and have good light stability due to the absence of a benzene ring. A PU topcoat based on HDI (Hexamethylene di-isocyanate) imparts excellent resistance to discoloration, hydrolysis and heat degradation.

The light-fastness properties of PU coatings can be improved by the use of rutile titanium dioxide (TiO_2) and carbon black pigments. The TiO_2 absorbs UV radiation, transforming it into heat; and carbon black absorbs heat and renders the coating insensitive to degradation by light.

Before applying the paint, the two-pack isocyanate and polyol constituents are mixed, allowing the cross-linking to proceed. All PU coatings must be applied relatively thinly, $\sim 38\text{--}49\ \mu\text{m}$ (1.5–2.0 mils) per coat, to prevent the inclusion of bubbles and voids due to carbon dioxide gas formation during curing and hardening.

To obtain an optimum surface finish, filling in small indentations and smoothing uneven surfaces, an intermediate polyester putty coat is applied between the epoxy primer and PU topcoat. A military aircraft with such a paint scheme is illustrated in Fig. 25.3.

Acrylic topcoats DTD 5602 is an acrylic finish for general purpose use on aircraft; and DTD 5599 is a selectively strippable acrylic finish. MIL-L-81352 covers one grade of acrylic-nitrocellulose lacquer (gloss, camouflage shades) for general use as an exterior protective coating for metal surfaces: this is particularly formulated for resistance to di-ester lubricating oil.

Fig. 25.2 Structure of polyurethane

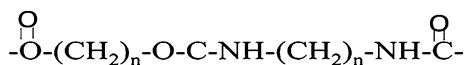


Fig. 25.3 A military aircraft showing an exterior paint scheme (LCA Tejas)



New developments On composite structures the paints should have excellent resistance to moisture permeability. Fluoropolymers suitable for composites have recently been introduced as finish coats to provide reduced permeability and better performance [16]. However, these coatings have yet to find applications for Indian military aircraft. Two military specifications for fluoropolymer-based aircraft coatings are Boeing BMS 10-125 and MIL-PRF-85285.

Self-priming topcoats, which perform as both primer and topcoat in a single coating, have also been introduced [17, 18]. If validated, these will save weight on the aircraft.

25.3.2 Radomes

The primary function of radome paints is protection from the harsh environments associated with extreme temperatures; high-speed impact by rain, snow and abrasive particles; sunlight; and high-voltage surface charges of static electricity. Aircraft grade primers and topcoats suitable for use on radomes include polyester, polyurethane, acrylic, and epoxy. Table 25.1 lists various paint types and their relative antistatic, erosion resistance and transmission properties required for radome applications [19].

Table 25.1 Paint types and their properties for radome application [19]

Paint type	Antistatic qualities	Erosion resistance	Transmission efficiency
Epoxy	Fair	Fair	Good
Acrylic	Fair	Fair	Good
Polyurethane	Fair	Fair/Good	Good
Polyester	Good	Fair/Good	Good
Polyurethane, black antistatic/anti-erosion	Excellent	Excellent	Fair
Neoprene, black antistatic/anti-erosion	Excellent	Good	Fair

Radomes on aircraft encounter rainstorms, resulting in a phenomenon known as “rain erosion”. The impact of rain on the high-speed surface destroys or diminishes the usefulness of the radome by eroding and deforming its surface. Special purpose protective neoprene (MIL-C-7439) and PU (SAE-AMS-C-83231) finishes are recommended for countering severe rain erosion. These are antistatic coatings, also known as electrostatic dissipation coatings. They contain graphite or carbon black particles to make them semi-conductive so that static charges do not build up on the radome. However, Neoprene is limited to a service temperature of 90 °C, and PU (SAE-AMS-C-83231) is used instead up to 150 °C.

Above 200 °C PU erosion coatings lose their elastomeric character and erosion occurs very rapidly. Hence fluorocarbon copolymers of vinylidene fluoride-hexafluoropropylene have been developed to retain erosion resistance and cater for long-term exposure up to 260 °C. Furthermore: these coatings can withstand rainfall conditions of 25 mm/hr at 223 m/s for an average of 100 min; they demonstrate one-way power transmission of 94 % at 9.275 GHz and have a surface resistivity of 0.5–15 ohm/square inch; and they last more than 3 years in outdoor exposure.

Antistatic protection and camouflage of the radome to the desired colour is achieved by incorporation of conductive fibres in fluorocarbon. (Leafing pigments like small slivers of aluminium or bronze metals should not be used in radome paint formulations, since they may have a significant negative effect on the radar signal.)

25.3.3 Gear Boxes

Aircraft gear boxes are generally made of magnesium alloys. Corrosion protection is accomplished by protective coatings developed to meet UK specification DTD 5562. These consist of a solution of epoxide resin, a modified epoxide or a mixture of epoxides in volatile solvents; a hardener, and chromate pigment for corrosion resistance.

Primers on magnesium alloys should be based on alkali-resistant binders (e.g. vinyl, epoxy, polyvinyl butyral (PVB), acrylic, polyurethane, and vinyl—epoxy). Zinc and strontium chromates are used as pigments.

The operating conditions of magnesium gear boxes may require paints with high thermal stability. The best resins for service from 260 to 315 °C are silicones, followed by silicone-modified epoxies or epoxy-phenolics.

25.3.4 Fuel Tanks

The microorganisms present in aviation turbine fuel (ATF) generate solid and acidic by-products in the presence of air and water, and this can accelerate metal corrosion. Hence all fuel storage tanks or fuel truck tanks should be protected by epoxy paint, as illustrated in Fig. 25.4 [20].

Fig. 25.4 Aircraft wing tank/ATF tank coated with epoxy (picture courtesy of WING, Canada.)



Table 25.2 Fungicide compositions and their modes of action

Fungicide composition	Proposed action
3-iodo-2-propynylbutyl carbamate	Chelation
2-(thiocyanomethylthio) benzothiazole	Reacts with thiols/inactivates metal-enzyme complexes
2-(thiocyanomethylthio) benzothiazole + Methylenebis (thiocyanate)	Uncouples oxidative phosphorylation, reacts with SH-groups

The hyphae from fungal growth in ATF can extend into the coating, releasing enzymes that lead to physical degradation. This deterioration results in an increase in the porosity of the surface coating and loss of adhesion to the substrate. Hence an anticorrosive epoxy paint complying with specification BS 2X 33 is fortified with a powerful fungicide that prevents microbial spoilage of the surface.

These fungicides are membrane-active compounds or electrophilic agents that interfere with the activity of organisms without necessarily killing them. Some sulphur- and/or nitrogen-containing fungicides and their modes of action are listed in Table 25.2.

In the past, compounds based on phenyl mercuric and tributyl tin were used as fungicides. However, owing to their high toxicity they have been replaced by complex organics such as carbamates, alkylisothiazolinone, benzothiazoles, chlorinated isophthalonitriles, and chlorinated adamantane complexes.

25.3.5 *Stored Aircraft Weapons*

Weapons stored on military aircraft must be protected from accidental fuel fires, which are associated with a high flux thermal environment. Intumescent (flame retardant) paints to specification MIL-C-81945B are applied to weapon stores as exterior insulating coats. These coatings consist of an epoxy modifier with curing

Fig. 25.5 Intumescent paint
(picture courtesy of
OMNOVA Solutions)



agent, thermally activated fillers, diluents and a thixotrope. The coatings must have a minimum thermal efficiency of ~ 0.079 s/ μm (i.e. 2 s/mil) to reach 260° C (500° F).

Upon exposure to flame or heat, an intumescent paint immediately foams and swells, forming a thick, dense, cellular matrix structure that deflects heat away from the surface, e.g. Fig. 25.5. The expansion of the paint film is many times the original thickness. More details about intumescent paints are given in subsection 25.4.7.

25.4 Special Functional Paints

Special paints include camouflage paint schemes, radar signal absorbing paints, fluorescent paints, anti-skid paints, hydrophobic paints, infrared (IR) paints, and intumescent paints (already mentioned, see Fig. 25.5).

25.4.1 Camouflage Paint Schemes

Camouflage may use two or three colour shades of paint on an aircraft. These paints are intended to blend well with the background and reduce the apparent visibility of the aircraft. Hence bright colours are not used, since they tend to attract attention and reflect sun flashes. Effective camouflage can be achieved with matt finish pastel grey, blue, tan, and green colours.

The specular gloss requirement of military aircraft paint coating is a maximum of 5 at 60° angle of incidence, tested as per ASTM D523. Glossiness can also be judged by the opacity/hiding power. To be opaque, the paint coating should have a high contrast ratio greater than 0.9 for a film thickness $\sim 48\text{--}53$ μm (i.e. 1.9–2.1 mils): the contrast ratio is obtained according to ASTM D2244.

Camouflage patterns can be obtained by applying a variety of paint shades in a pseudo-random manner (much like shadow cutting, straight lines or curves) across various parts of the aircraft to break up the recognizable shape. Examples are shown in Fig. 25.6.

Fig. 25.6 Helicopter and fighter aircraft with camouflage paint schemes



Concealment (low visibility) may also be assisted by light absorption or scattering by the paint coating. Paint binders are transparent and virtually colourless, so do not contribute to low visibility. This task depends entirely on the pigment. Black pigments strongly absorb over the entire visible spectrum, while white pigments scatter light strongly, i.e. both types can contribute to concealment.

The pigment properties that influence low visibility are the refractive index, particle size and pigment volume concentration:

- Pigments with a high refractive index provide the best concealment. Among white pigments TiO_2 is the best, especially the rutile mineral form.
- Particle size selection with suitable grit level and pigment volume concentration plays a vital role in obtaining the required type of finish (glossy, semi-glossy, matt) to facilitate concealment.
- Various shades of camouflage paints as per military terrain requirements can be achieved by selection of suitable pigments, their combinations, and extenders. The representative colour of the pigment is obtained by selective absorption and reflection of certain wavelengths of light by its chemical bonds. For example, grey in a PU-based topcoat is obtained by combining carbon black and titanium dioxide. Extenders are generally inert, and added to control gloss and impart a much better matt finish. Commonly used extenders for this purpose are barytes, calcite, and aluminium and magnesium silicates.

25.4.2 Radar Signal Absorbing Paints (RAPs)

Enemies track military targets by obtaining the radar cross-section (RCS), (see Fig. 25.7). Hence for defensive purposes it is required to reduce the RCS.

There are four methods of reducing the RCS: viz., shaping, active loading, passive loading and distributed loading. Distributed loading involves covering the surface with radar absorbing materials (RAMs [21]). RAMs reduce radar echo by soaking up the incident electromagnetic energy/signals, thereby reducing the net energy available for reflection: see also Chap. 24 in this Volume.

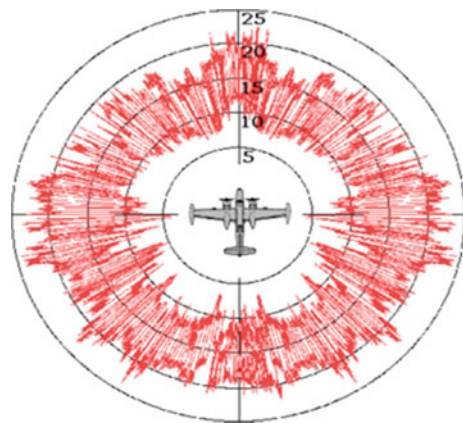
Radar signal absorbing paints (RAPs) are examples of RAMs. Established formulations of RAPs consist of a PU binder incorporating ferromagnetic particles of e.g. carbonyl iron and ferrite iron oxides. Coating the particles with a non-conductive coating (the binder) results in poor conductivity by the particles, giving them the ability to convert radar wave energy into heat, which is subsequently dissipated into the aircraft structure. A uniform particle size distribution (without agglomerates) also helps. The overall result is good radar absorbing characteristics [22]. However, a potential disadvantage of using carbonyl iron and ferrites is doubt about the coating's corrosion resistance.

Interesting new materials for RAPs include polypyrrole and carbon nanotubes [23]. Polypyrrole-paint [9] is formulated by mixing a PU-based paint with conducting polypyrrole (PPy) powder. The conducting PPy powder is made from polypyrrole doped with *p*-toluene sulphonic acid sodium salt, or 5-sulfosalicylic acid dehydrate [24].

25.4.3 Fluorescent Paints

Fluorescent paints react to long-wave UV radiation, commonly known as black light. Through the mechanism of fluorescence, UV-sensitive pigments present in the

Fig. 25.7 Typical RCS diagram



paint absorb black light and give off visible light in return. Visibly fluorescent paint can appear any bright colour, and glows brilliantly under black light.

These paints are formulated with hydrocarbon type powdered resins and fluorescent dyes soluble in solvents like ketones and alcohols. Stabilizers such as substituted dihydroxy benzophenones are added for protection from UV.

Uses of fluorescent paints include (i) illuminating aircraft instrument pointers and dials [25] (particularly important, indeed essential) and (ii) marking escape paths in transport aircraft. Also, these high-visibility coatings are essential for trainer aircraft.

Another use, *albeit undesirable*, is that when an aircraft crashes, there may be needle-slap against the black background. Some transfer of fluorescent paint may occur, and although this may not be directly discernible, it could show up under UV light. Thus readings at impact may be obtained, and these can aid determination of the cause of the accident.

25.4.4 *Anti-Skid Paints*

Skid in this context refers to loss of traction between footwear and its contact surface. This situation is worse on aircraft/helicopter surfaces that are smooth, damp or wet (due to humid weather, rain, spills and contaminants like sea spray, lubricating oil, grease and soil).

Anti-skid paints overcome skid by facilitating surface roughness. Initially, they were applied on aircraft wing walkways, facilitating routine base-level service and repair operations. Currently they are also recommended for military application on leading edge extensions of fighter aircraft, and in heavy traffic areas like helicopter cabins. Other (non-aircraft) applications of anti-skid paints include radar/machinery equipment, decking and truck beds.

The required properties of anti-skid paints include the use of grits with different particle sizes to obtain a rough, gritty texture/finish; effective lower profile (low surface roughness); low drag; resistance to wear, abrasion and chemicals; and low maintenance costs in terms of cleaning and repainting. Also, the surface should be safe without causing laceration injuries to personnel.

Traditional liquid-based anti-skid coatings consist of a volatile liquid component containing dispersed polymer droplets (epoxy, polyurethane or alkyd systems) in friction-contributing additives such as metal, ceramic or polymeric particulates [26] (i.e. graphite, alumina or polybeads). Epoxies are preferred in such formulations since they are tough and chemically resistant. An epoxy-based resin system cured by a polyamide hardener developed to MIL-W-5044C (superseded by A-A-59166) is used for the cabin floor and maintenance steps in military helicopters in India.

The surface roughness of anti-skid coatings can cause significant aerodynamic drag [27]. On the other hand, smooth surfaces will not provide the required coefficient of friction (COF). Therefore, to get an optimum roughness and desirable surface coverage, the total solids in the coating formulation have been restricted to

Table 25.3 COF requirements for anti-skid paint (Ref: MIL-W-5044C)

Test parameter	Specification requirements
<i>Factor of sliding friction (leather)</i>	
Dry	min. 0.5
Watered	min. 0.8
Oiled	min. 0.45
<i>Factor of sliding friction (rubber)</i>	
Dry	min. 0.9
Watered	min. 0.8
Oiled	min. 0.6

between 60 and 80 %. The COF is an important parameter for anti-skid properties, which depend very much on the natures of the two surfaces in contact with each other [28]. For example, Table 25.3 illustrates the COF requirements according to MIL-W-5044C.

25.4.5 Hydrophobic Paints

Water repellence (or hydrophobicity) of a solid surface is an important property that depends on the chemical composition and geometrical micro- and nano-structures of the surface. Self-cleaning is a key advantage, whereby rainwater beads up and rolls over the surface, entrapping dirt and particulates as illustrated in Fig. 25.8.

Hydrophobic coatings have potential use in reducing corrosion and fouling of aircraft surfaces, and also icing-up. A method of forming a hydrophobic coating and the materials involved are well described by Jones et al. [29, 30]. There are also so-called superhydrophobic coatings with a water contact angle $CA > 160^\circ$. These could be applied on aircraft surfaces by combining them with the usual paint coatings (Source: “*Super hydrophobic or icephobic coatings*”, SAE international). They are manufactured using certain patented techniques [31].

However, there are numerous challenges to realizing a hydrophobic coating for aircraft surfaces, including adherence of the coating to the substrate, mechanical and thermal stability, and long-term stability. Since hydrophobic coatings function on microscopic levels in terms of surface roughness, they are easily damaged. Also,

Fig. 25.8 Hydrophobicity (picture courtesy of Larkrise Coatings)



their elevated temperature capability is limited, since their wettability increases owing to a decrease in the surface tension of water.

The most suitable application methods for these coatings to large areas appear to be plasma treatment techniques, sol-gel methods and some spraying techniques.

25.4.6 Infrared (IR) Paints

Infrared (IR) paints are of interest as defensive methods of preventing IR detection and laser-induced damage. These paints are also of general interest in reflecting near-IR solar radiation, keeping the painted surface cooler. For reference, Fig. 25.9 shows the full IR spectrum.

Solar heat reflection can be further improved by applying a thin layer of white basecoat under a thin layer of a final semi-transparent colour in the near-IR region. Such coatings are being developed for glass and plastic aircraft transparencies to help reduce interior cockpit and cabin temperatures (and air-conditioning demands), and also for heat-sensitive electronic equipment.

Well known PU-based solar heat reflective paints to specification DTD 5618 [British Aerospace Material Specification DTD 5618, Exterior and Interior Finishing Schemes—Matt and Glossy—Solar Heat Reflecting (Cold Curing Polyurethane Type), HMSO, London, October, 1974] are available in both gloss and matt finishes.

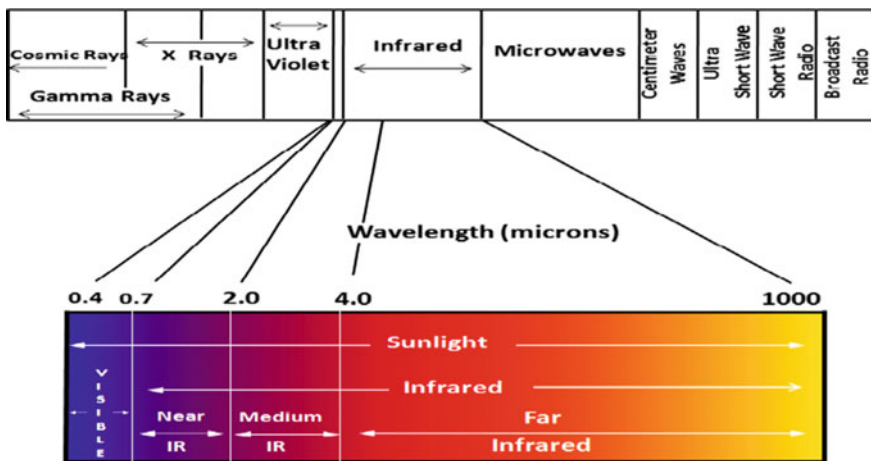


Fig. 25.9 Spectrum showing near-, far- and medium-infrared (IR): N.B. Sunlight extends into the UV region (picture courtesy of FINNLEO)

25.4.7 Intumescent Paints

Intumescent paints were already mentioned in subsection 25.3.4 with respect to stored weapons, and an example of their behaviour is illustrated in Fig. 25.5. These paints also have potential usage in fire-risk areas for aircraft fuel pumps, hydraulic landing gear parts, cabin interior parts, engine bays, engine firewalls, and carbon fibre reinforced plastic (CFRP) composites. In particular, CFRP aircraft structures have introduced potential fire threats and raised concerns about fire safety in both in-flight and post-crash environments [32, 33].

Intumescent paints for military aircraft need to be lightweight, preferably of low thickness combined with adequate protection, and having no adverse effects on existing coatings. A current specification (under review) for suitable intumescent paints is BS X 37:2004. There are also newly developed flame retardant coatings and a CFRP thermal protective system [34, 35].

25.4.8 Miscellaneous Paints

Several other types of paints are available for special applications. Examples are bituminous paint for the interiors of seaplane hulls, acid-resisting paint in the vicinity of storage batteries [36], and pressure and temperature sensitive paints for measurements of surface pressure and temperature in wind tunnel and flight tests [37].

25.5 Properties, Testing and Analysis of Paints

The performance of aircraft paints depends on a number of factors like the substrate material, surface preparation, the operational environment and flight conditions, besides their own properties. Military aircraft experience high structural loads and flight conditions placing mechanical and environmental stresses on the aircraft paint system. Therefore appropriate test and evaluation procedures are essential for determining acceptable paint coatings for aircraft applications.

Important paint properties relevant to aircraft applications are (i) viscosity, density, fineness of grind and coarse particles, solid content, VOC, storage stability, flash point, drying time, film thickness, colour, opacity, gloss and hardness; (ii) adhesion, flexibility, tensile and fatigue properties; (iii) resistance to low temperature impact, wear, corrosion, fluid immersion, weathering, and heat exposure. The significance of some of these properties and tests for them are discussed here:

- The rheological (flow and viscosity) characteristics affect paint application properties such as atomization, levelling, sagging and brushability. Viscosity determination by the Ford cup method as per ASTM D1200 is preferred to other

available methods like the Zahn cup and Brookfield and Stormer viscometers, since the Ford cup method has better accuracy and stability.

- The fineness of grinding (ASTM D1210-Hegman gauge) and coarse particles (ASTM D185) decides the pigment dispersion and paint coating finish.
- Drying properties are important for aerospace coatings, owing to the strict time and processing constraints placed on production and maintenance facilities.
- Fluid compatibility tests are carried out with in-service aircraft fluids like lubricating oils to MIL-PRF-23699F and DEF STAN 91-98/2, hydraulic oil to MIL-PRF-5606H, and Jet-A1 fuel.
- Water-borne coatings must be additionally evaluated for their freeze-thaw stability according to ASTM D2243.

25.5.1 Chemical Analysis

Chemical analysis of paints has been performed historically for deformation or re-engineering, quality control, safety and regulatory compliance, defect analysis, and forensics and restoration in art and archaeology [38]. Numerous analysis techniques are available. The most common ones are Fourier transform infrared (FTIR) spectroscopy, UV spectroscopy, scanning electron microscopy (SEM) along with energy dispersive X-ray analysis (SEM/EDS), and nuclear magnetic resonance (NMR). A list of applications follows:

- Paint binders: IR spectroscopy and NMR
- Paint solvents: Gas chromatography/mass spectrometry (GC/MS)
- Paint additives: IR, UV, visible spectroscopy and high performance liquid chromatography (HPLC)
- Inorganic pigments: Atomic absorption and X-ray spectroscopy; and micro-attenuated total reflectance Fourier transform infrared spectroscopy (ATR-FTIR) in the low wave number range ($500\text{--}230\text{ cm}^{-1}$) can be used to identify pigments in paint samples having no absorptions in the mid-IR region [39].
- Trace elements: Inductively coupled plasma and mass spectrometry (ICP-MS)
- Surface contamination: Time-of-flight secondary ion mass spectrometry (TOF-SIMS)

For clear interpretation and information about paint layers, it has been recommended to judiciously use combinations of light and UV-fluorescence microscopy, scanning electron microscopy combined with energy dispersive X-ray microanalysis, and X-ray micro-diffraction [40]. A recent edition of the “Paint and Coating testing manual” of the Gardner-Sward Handbook (edited by Joseph V. Koleske) may be referred to for extensive literature on this subject.

25.6 Ageing of Paints

Paint is one of the most important materials tested for its weathering resistance. The major atmospheric factors causing coating deterioration are sunlight, temperature, moisture, saline environments, pollution, and bio-deterioration.

Sunlight in particular leads to discoloration, premature loss of gloss, scaling, embrittlement and chalking; *moisture* may cause blistering, flaking, mildew and early loss of adhesion; *heat* may cause embrittlement, cracking and peeling; and *atmospheric oxygen* promotes oxidation on the coating surface that may eventually lead to oxidation of internal layers, causing embrittlement, softening, cracking or crazing.

The negative effects of weathering are seen as surface appearance changes, and these are primarily due to breakdown of the basic polymer structure.

Paints are tested for weathering resistance either in natural environments or under simulation test conditions in the laboratory, or both. To be acceptable, the paint film should retain its initial colour and finish after completion of the tests.

25.6.1 Outdoor Weathering

Outdoor weathering tests are important for aerospace coatings and are conducted for a minimum of two years to account for actual use in an uncontrolled environment. The test fixtures and mounting techniques are selected to create similar exposure conditions as in service. Aluminium racks are preferred as the test fixtures. The exposure angle will affect the amount of solar radiation on the sample, the time the sample remains wet from rainfall or dew, and the sample temperature. All three factors have an impact on the type and degree of degradation.

Besides exposure to the sun's energy, an important adjunct is testing for resistance to saline environments. For such tests the panels are sprayed three times per working day at intervals of three to four hours with a solution of artificial sea water, the composition of which has to be as per BS 3900 part F4 Clause 6.1/Def-1053 Method 24. Alternatively marine shoreline tests can be done, if suitable locations are available.

25.6.2 Accelerated Weathering

Accelerated, or artificial, weathering involves laboratory tests whereby the elements of radiation, temperature and humidity are more intensely applied compared to outdoor exposure. Obviously, the conditions are more controllable and reproducible, and the results are also available more quickly. However, these should be

used only for comparison purposes, since direct correlations between artificial and natural weathering data have not yet been developed.

The choice of exposure conditions for an accelerated weathering test is more challenging. For example, although sunlight is composed of light from the UV, visible and IR regions of the electromagnetic spectrum (see Fig. 25.9), the most harmful rays to paint films come from the UV region, especially the shorter wavelengths ranging down to 295 nm.

The UV region can be divided into three domains: UV-A, UV-B and UV-C. The UV-A domain is 315–400 nm, the UV-B domain is 280–315 nm, and the UV-C domain is 200–280 nm. Although UV-C is the most damaging, these wavelengths are filtered out by the atmosphere and hence not used in accelerated testing.

Considering UV-A and UV-B, the energy in the UV-B domain is higher, ranging from about 91–102 kcal/mol. These energy levels cause more severe and rapid deterioration of coatings, since they are high enough to break C–N, C–C, N–H, C–O and C–H bonds in the polymeric part of the coating. These bond-breakages result in pigment attack, causing fading, chalking and loss of gloss. Hence UV-B light is selected for testing aerospace paints.

Most of the paint test specifications require the use of “sunlight” carbon arcs, xenon arcs and fluorescent lamps for accelerated weathering. These light sources include UV-B and more closely simulate the degrading UV light range of sunlight, whereby they accelerate the photochemical ageing process in the coating. Other parameters such as temperature and moisture are also specified for artificial weathering, e.g. in BS 3900: Part F16:1997.

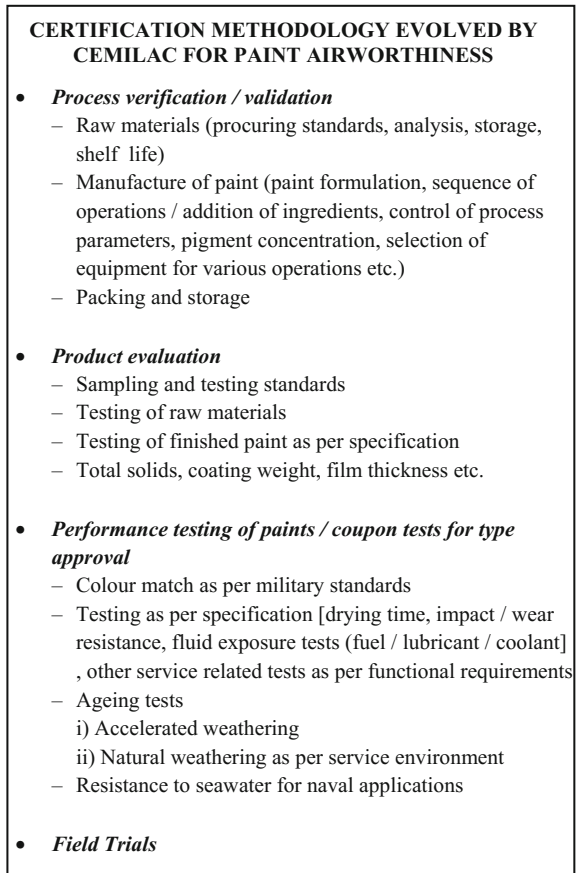
25.7 Airworthiness Certification of Paints

Paints fail prematurely during service owing to various reasons, e.g. improper coating formulations, inadequate surface preparation, wrong application methodology, poor drying, improper adhesion and ageing.

During formulation and subsequent storage of paints for a long period, defects such as thickening, skinning, settling and flocculation may occur. Application-related defects include pinholing, orange peeling, fish eyes, mottling and lifting. Some common defects that occur during curing are levelling, drying loss, sagging, bleeding, flooding, floating, blushing, and hazing. Internal stresses during organic coating film formation [41] result in coating degradation [42]: it is known that coating components play a role in generating stresses [43].

Paints are expected to withstand exposure to outdoor and chemical environments for their required service life. However, this is no easy task: (i) variations in temperature and relative humidity induce hygrothermal stress [41] in organic coatings, resulting in degradation; (ii) ageing may cause defects like blistering, chalking, alligatoring, erosion, embrittlement, fading, flaking, cracking, peeling, scaling, yellowing, darkening, and growth of mildew and algae.

Fig. 25.10 Paint certification methodology developed by CEMILAC, India



Various factors like raw material quality, paint formulation, manufacturing conditions, packing and storing affect the paint quality. The airworthiness agency for military aviation: CEMILAC, with which the present authors are affiliated, has evolved the certification methodology for paint airworthiness illustrated in Fig. 25.10.

The above four-step process is designed to validate and ensure the airworthiness of the selected paints.

25.8 Volatile Organic Compound (VOC) Regulations

According to the Environmental Protection Agency (EPA), VOC means any compound of carbon (excluding carbon monoxide, carbon dioxide, carbonic acid, metallic carbides or carbonates, and ammonium carbonate) that participates in atmospheric photochemical reactions. For example, VOCs react with oxides of

nitrogen (NO_x) in the presence of heat and sunlight to form ground level photochemical smog. Also, on January 6, 2010 the EPA proposed an increased protection by strengthening the national ambient air quality standards (NAAQS) for ozone, which is generated by several natural means as well as reactions involving VOCs.

The approach to reduce VOC emissions due to painting and repainting aircraft and aircraft components has been for the applicators to either adopt an alternative coating technology (VOC-exempt solvents, high solids content, water-borne, powder, UV cure) or install engineering controls (carbon adsorption, incineration, etc.).

25.9 Paint Monitoring

Monitoring the paints' performance and degradation is obviously an important aspect of evaluating their service life. Techniques involved in paint monitoring tasks are listed here [44]:

- Microwave techniques
- Thin film electrochemical sensors embedded under paint films
- Electrochemical sensors applied to the outer surfaces of paint films
- Thermography
- Colour and fluorescence changes (smart coatings)
- Fibre optic sensing
- Chemical sensors for detecting surface contamination at the surface preparation stage.

It is particularly important to monitor paints used for corrosion protection on naval aircraft, which experience high humidity and a saline environment. However, procedures for doing this have not yet been standardized.

25.10 Some Important New Developments

There are some other coatings intended for aerospace applications that are worth mentioning. Coatings based on nitrocellulose are used for aircraft markings. Fluoropolymer-based coatings are applied to the internal wiring insulation: this protects the wiring and reduces the risk of fire in the aircraft. Applications of silicone-based coatings include jet engine components, furnace parts, incinerators, high-temperature applications and missile coatings [45].

Technologies like chromate-free primers (e.g. MIL-PRF-23377 and MIL-PRF-85582), self-healing conversion coatings, and new coatings for CFRP substrates (Boeing BMS 10-103, BMS 10-125, BMS 10-126) are potential areas for future research. Moreover the '80 % solids rule' has provided the impetus for

companies to investigate new coating technologies like powder coating, radiation cure and high solids formulations.

Another innovative feature is incorporation of microspheres into paints, since they have many attractive aerospace applications (Source: Composites Technology, 2008). One important potential application is leaching of corrosion inhibitors from hollow microspheres to protect the substrate when the paint system is damaged.

25.11 Indian Scenario

In India the success of paint technology developments will require the involvement of overseas and indigenous business partners to effectively exploit local materials and resources. This would provide self-sufficiency and economic benefits to this country.

25.12 Conclusions

Modern and future generation fighter aircraft combine high speed and high altitude operations with novel material technologies, placing a great challenge to paint technologies and materials. The ultimate goal for military application is to provide a complete stealth aircraft whose performance is benefited or unaffected by paint application, without much gain in weight. Nanotechnology research on paint developments for specific applications needs to be initiated.

Acknowledgments The authors of this chapter wish to place on record their profound gratitude to the numerous researchers and technologists on whose work this manuscript is based. They are most grateful to Dr RJH Wanhill and Dr N Eswara Prasad for their detailed chapter review and guidance. They are most grateful to Dr Hegde, MD, Southfield Paints, Bangalore, for his advice and chapter review. The authors express their gratitude to Shri Veerappa for his support in presenting the chapter figures.

References

1. Blackford RW (1997) Aerospace coatings and the environment: some problems and constraints. *J Surf Coat Int Part B Coat Trans* 80(12):564–567
2. Improving the continued airworthiness of civil aircraft: a strategy for the FAA's aircraft certification service, Chapter 7. National Academy Press, Washington DC, USA, 1998
3. Robert Shives T, Marshall Peterson B (1984) Mechanical properties, performance, and failure modes of coatings", 1st edn. Cambridge University Press, Cambridge, UK, p 148
4. Anvari A, Farhani F, Niaki KS (2009) Comparative study on space qualified paints used for thermal control of a small satellite. *Iran J Chem Eng* 6(2):50–60

5. Berman ES et al (2004) Spacecraft materials development programs for thermal control coatings and space environment testing. *Amptiac Quarterly* 8(1):59–65
6. ASTM D16 (2003) Standard terminology for paint, related coatings, materials, and applications. In: Annual book of ASTM standards, vol 6.01. ASTM International, West Conshohocken, PA, USA
7. Titterton GF (1947) *Aircraft materials and processes*, 3rd edn. Pitman Publishing Corporation, New Delhi, India
8. Watson DM, Schall DC (1991) *Am Paint Coatings J.*, August 19, p 58
9. Morgans WM (1990) *Outlines of paint technology*, 3rd edn. Edward Arnold, London, UK, p 9
10. Chattopadhyay AK, Zentner MR (1990) *Aerospace and aircraft coatings*. Fed Soc Coat Technol, Philadelphia, PA, USA
11. Lewin JB (1975) *Aircraft finishes*. In: Meyers RR, Long SJ (eds) *Treatise on Coatings Volume 4, Formulation Part I*, Marcel Dekker, New York, USA, pp 1–84
12. Hegedus CR, Pulley DF, Spadafora SJ, Eng AT, Hirst DJ (1989) A review of organic coating technology for U.S. naval aircraft. *J Coat Technol* 61(778):31
13. Bentley J, Patrick G, Turner A (1998) *Introduction to paint chemistry and principles of paint technology*, 4th edn. Chapman & Hall, London, UK, p 203
14. Pokhmurs'kyi VI, Kwiatkowski L, Zin IM, Lyon SB, Bilyl LM, Ratushna MB (2006) Corrosion protection of Aluminium alloys by inhibiting pigments. *Mater Sci* 42(5):7–11
15. Stoye D, Freitag W (1998) *Paints, coatings and solvents*. 2nd edn. Wiley-VCH, Verlag, Weinheim, Germany, p 74
16. Teng Hongxiang (2012) Overview of the development of the fluoropolymer industry. *Appl Sci* 2:496–512
17. Hegedus CR, Eng ATM, Hirst DJ (1990) Program summary: uniconat development laboratory characterization and field evaluation. Naval Air Development Center, Warminster, PA, USA
18. Hegedus CR (1987) A combination primer/top coat for aluminium. In: *Finishing 87 conference paper FC87-625*, September 1987, Society for Manufacturing Engineers, Dearborn, MI, USA
19. Feeler RA (1992) Proper radome care is essential to peak performance. *Flight safety foundation-aviation mechanics bulletin*, Jan
20. Lombardo DA (1993) *Advanced aircraft systems*. 1st edn. TAB Books, New York, USA, p 194
21. Saville Paul (2005) Review of radar absorbing materials. Technical Memorandum TM 2005-003, Defence Research and Development Canada - Atlantic, Dartmouth, NS, Canada
22. Peterman DJ (2002) Chemically modified radar absorbing materials and an associated fabrication method. US Patent 6486822, p 3
23. Shi Haofei, Ok Jong G, Baac Hyoung Won, Jay Guo L (2011) Low density carbon nanotube forest as an index-matched and near perfect absorption coating. *Appl Phys Lett* 99:211103
24. Truong VT, Riddell SZ, Muscat RF (1998) In: Truong VT, Turner BD, Muscat RF, Russo MS (eds) *Proceedings of the SPIE the international society of optical engineering*, 1997, pp 3241,98 (*J. Mat. Sci. Lett.* 33,4971)
25. McCormick BW, Papadakis MP (2007) Aircraft accident reconstruction and litigation. *Lawyers & Judges Publishing Company Inc.*, Tucson, AZ, USA, p 201
26. Brogan JA, Jefferson P (2002) Non-skid coating and method of forming the same, US Patent Office 10/016, 458
27. TDA Research, Inc. (Undated) Low profile non-skid coatings for aircraft. TDA Research, Inc., Wheat Ridge, CO, USA
28. Melhuish D, Wegand J (2007) Coefficient of friction, the development of a standard portable device for the US Naval fleet. In: 2007 Tri-Service Corrosion Conference: <https://es.scribd.com>
29. Ashley J, Lamb N, Zhang H (2004) Hydrophobic coating, US Patent WO/2004/090064, p 22
30. Ashley J, Lamb N, Zhang H (2004) Hydrophobic material, US Patent 6,743,467 B1, p 8
31. Sun T, Feng L, Gao X, Jiang L (2005) *Accounts of chemical research*, vol 38, pp 644–652

32. Sikoutris DE, Vlachos DE, Kostopoulos V, Jagger S, Ledin S (2012) Fire burnthrough response of CFRP aerostructures. Numerical investigation and experimental verification. *Appl Compos Mater* 19(2):141–159
33. La Delfa G, Luinge JW, Gibson AG (2009) Integrity of composite aircraft fuselage materials under crash fire conditions. *Plast Rubber Compos* 38:111–117
34. Taylor EW, Feldman R, Rippe JA (2005) Composite thermal protective system and method, US Patent 6,855,401 B2, p 6
35. Weil ED (2011) Fire-protective and flame-retardant coatings—a state-of-the-art review. *J Fire Sci* 29:259–296 (May 2011)
36. Titterton George F (1947) *Aircraft materials and processes*, 3rd edn. Pitman Publishing Corporation, New York, USA
37. Liu T, Sullivan JP (2004) *Pressure and temperature sensitive paints*. Springer
38. Hutanu et al (2013) Recent applications of mass spectrometry in paint analysis, Review article. *Mod Chem Appl* 1:3, 1000109
39. Vahur Signe et al (2009) ATR-FTIR spectroscopy in the region of 500–230 cm^{-1} for identification of inorganic red pigments. *Spectrochim Acta Part A Mol Bimolecular Spectrosc* 73(4):764–771
40. Hochleitner B, Schreiner M, Drakopoulos I, Snigrev A et al (2003) Analysis of paint layers by light microscopy, scanning electron microscopy and synchrotron induced x-ray micro-diffraction. In: *Proceedings of Conference Art 2002*, Antwerp, Belgium, A.A. Balkema Publisher, Rotterdam, The Netherlands
41. Perara DY, Van den Eynde D (1987) Moisture and temperature induced stress (Hygrothermal stress) in organic coatings. *J Coat Technol* 59(748):55–63
42. Gusman (1963) Studies of the adhesion of organic coatings. *J Paint Technol* 27(1):17–26
43. Koleske JV (2012) *Paint and coating testing manual*. Fifteenth Edition of the Gardner-Sward Handbook, ASTM International, West Conshohocken, PA, USA
44. Veleva L (2012) Protective coatings and inorganic anti-corrosion pigments”, Chapter 28. In: Koleske JV (ed) *Paint and coating testing manual*. Fifteenth Edition of the Gardner-Sward Handbook, ASTM International, West Conshohocken, PA, USA
45. Petraitis DJ (2012) Silicone coatings, chapter 4. In: Koleske JV (ed) *Paint and coating testing manual*. Fifteenth Edition of the Gardner-Sward Handbook, ASTM International, West Conshohocken, PA, USA

Chapter 26

Elastomers and Adhesives for Aerospace Applications

C.M. Bhuvaneshwari, Shirish S. Kale, G. Gouda, P. Jayapal
and K. Tamilmani

Abstract This chapter deals with the varieties and characteristics of elastomers and adhesives used in the aerospace industry. The key terms, various grades, structure and properties of each elastomer are discussed. An outline of rubber compounding and vulcanisation is presented. Significant elastomer properties for aerospace applications are highlighted. Further, an adhesives section includes the varieties of adhesives, mechanism of adhesive bonding, surface preparation, and joint designs for some loading conditions. Applications of elastomers and adhesives in the aerospace field are also surveyed.

Keywords Elastomers · Adhesives · Mechanical properties · Fluid resistance · Adhesive bonding · Applications

26.1 Elastomers

26.1.1 Introduction

Elastomers are elastic materials that recover to almost their original shape after complete release of the applied force [1]. Elastomers are characterized by large deformability, low shape rigidity, large energy storage capacity, nonlinear stress-strain curves, high hysteresis and a large variation of stiffness with temperature and

C.M. Bhuvaneshwari (✉) · S.S. Kale (✉)
Regional Centre for Military Airworthiness (Foundry and Forge),
CEMILAC, Bangalore, India
e-mail: cm.bhuvaneshwari@cemilac.drdo.in

S.S. Kale
e-mail: shirish.kale@cemilac.drdo.in

G. Gouda · P. Jayapal
CEMILAC, DRDO, Bangalore, India

K. Tamilmani
Office of DG (AERO), DARE, DRDO, Bangalore, India

rate of loading [1]. Particular combinations of these properties make elastomers suitable for aerospace applications.

Many aircraft components use elastomers as O rings, gaskets, canopy window or door seals, firewall seals, lip seals and T seals. Elastomers can be compressed to make a tight seal owing to their excellent elasticity without damage or permanent deformation. Characteristics like superior tear strength and excellent resistance to heat build-up make elastomers well-suited for high-performance aircraft tyres. The high damping capacity of elastomers solves dynamic problems in many fields, including space applications. For example, elastomeric shock absorbers and passive dampers are mounted onboard launchers and satellites [2].

26.1.2 Varieties of Elastomers

Natural rubber was the only source of rubber until the advent of synthetic polymers in the early part of the twentieth century. The natural and synthetic rubbers are the two classes of commercial rubber products. The source of natural rubber is the latex obtained from rubber trees. The purified form of natural rubber is the chemical polyisoprene, which can also be produced synthetically. Synthetic rubbers are produced by two important stages: the primary step is the production of monomers, followed by polymerization of monomers. Some of the most important synthetic rubbers are acrylonitrile butadiene, polychloroprene, chlorosulphonated polyethylene, butyl, polybutadiene, silicone, ethylene propylene and fluoropolymers.

The basic chemical structure of each elastomer dictates most of the properties such as oil and fuel resistance, ozone, heat and weathering resistance. The fuel resistance of acrylonitrile butadiene rubber (NBR), weathering resistance of ethylene propylene diene monomer (EPDM), or the high resilience of natural rubber significantly determine the suitability of an elastomer for any given application.

26.1.3 Elastomer Compounding

Compounding is the process of mixing elastomers with various additives and curatives to enhance the properties. Compounding is carried out to tailor the properties of elastomers according to the functional requirements [3]. According to the nature of the additives, properties like increases of modulus, ozone resistance, flame resistance, and electrical conductivity can be achieved.

The processing method also plays a major role in the product performance. Manufacturing of rubber compounds involves mixing, forming and curing. The two main types of mixing machines are two-roll rubber mixing mills and internal mixers. The latter are extensively used for large quantity mixing. Internal mixers generate high shear forces that disperse and mix the fillers and raw materials into a uniform quality compound. After mixing, the compound is fed into a mill. The

two-roll rubber mixing mill disperses the reinforcing fillers within the polymer by repeated milling. The next manufacturing stage is forming the compound to the required shape by an extrusion process.

Compounding ingredients [4] may be categorized as:

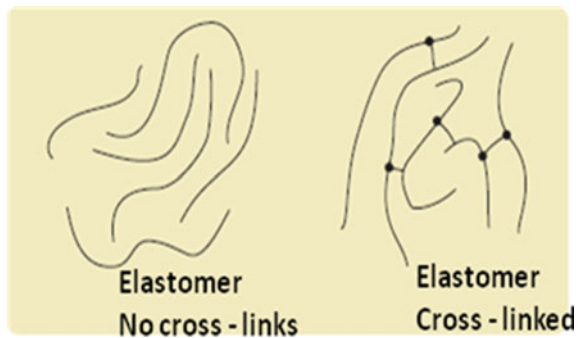
- Base polymer (natural or synthetic rubber)
- Curing or vulcanising agents
- Accelerators, accelerator activators and retarders
- Stabilizer systems (antioxidants and anti-ozonants)
- Processing aids (plasticizers, softeners, tackifiers, etc.)
- Reinforcing fillers (carbon black, silica, mineral fillers) and resins
- Inert fillers and diluents
- Special additives (abrasives, blowing agents, colours, pigments, deodorants, etc.).

26.1.4 Vulcanising

Vulcanising is the process of applying heat for specific temperatures and times. The selection of temperature and time depends on the type of elastomer. The properly mixed elastomer compounds can be vulcanised by one of many processes [5], such as moulding, autoclaving or oven curing, etc. The vulcanising process can be batch or continuous curing. During vulcanising the following changes occur:

- The vulcanising agent reacts with the long chains of the rubber molecules and forms cross-links to form three-dimensional structures as shown in Fig. 26.1. The cross-links resist the large molecular chains slipping past each other under the application of external forces.
- The cross-linked rubber becomes a solid elastomer with improved strength and resistance to degradation.

Fig. 26.1 Schematic representation of polymer chains before and after vulcanising [7]



The most common vulcanising agents are sulphur and peroxide [6]. Unsaturated elastomers (with double bonds in the backbones) are vulcanized by sulphur, forming carbon—sulphur—carbon bonds. Saturated elastomers cannot be vulcanised by sulphur and accelerators: organic peroxides are necessary. The peroxides give rise to carbon—carbon bonds, which are quite stable.

26.1.5 Elastomer Types and Properties [8–10]

Elastomers are classified according to chemical composition. ASTM D 1418 classifies elastomers and gives a set of abbreviations as shown in Table 26.1.

For example, elastomers with only carbon atoms in the main chain and no double bonds (reactive areas) are referred to as M-types. If the elastomer main chains contain double bonds, these elastomers are referred as R-types. These are also referred to as unsaturated or diene rubbers.

The main chains containing only alternating silicon and oxygen atoms are called Polysiloxanes. These elastomers are known as silicone rubbers and referred to as Q-types. Table 26.2 clearly illustrates the variety of elastomers and their chemical and trade names. The following paragraphs discuss the important elastomers [8–10] that are useful in the aerospace industry:

(i) Natural rubber (NR)

The chemical name of NR is cis-1,4 polyisoprene. The molecular structure is given in Fig. 26.2. NR is made by the coagulation and drying of aqueous milky sap from rubber trees (*Hevea brasiliensis*).

Due to the superior structural regularity and strain crystallization, NR acquires high strength. This property is exploited for applications requiring abrasion or wear resistance, and damping or shock-absorbing. Hence NR is used in large truck tyres, off-road giant tyres and aircraft tyres [11, 12]. It is resistant to acids, alkalis and alcohol, but has poor resistance to atmospheric oxygen, ozone and fuel.

Fig. 26.2 Molecular structure of NR

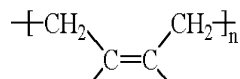


Table 26.1 Classification of elastomers [10]

Last letter in the abbreviation: meaning	Examples
M: saturated chains of carbon atoms, no double bonds	EPDM, FKM, FFKM
R: double bonds in the carbon chain (unsaturated)	NR, CR, SR, SBR, IIR, NBR, HNBR
O: oxygen in the polymer chain	Epichlorohydrin rubber
Q: silicon and oxygen in the polymer chain	VMO, FVMQ
T: sulphur in the polymer chain	Polysulphide elastomer
U: carbon, oxygen, and nitrogen in the polymer chain	Polyurethane rubber

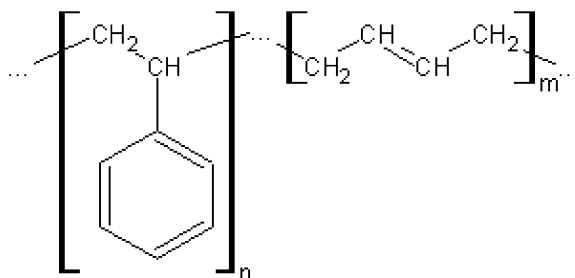
Table 26.2 Elastomer chemical and trade names [8]

ASTM D 1418 abbreviation	Chemical names	Trade names
CR	Chloroprene	Neoprene [®] , Skyprene [®] , Butclor [®] , Baypren [®] , Denka [®]
CSM	Chlorosulphonyl polyethylene (Chlorosulphonated polyethylene)	Hypalon [®] , Noralon [®]
EPD	Ethylene-propylene copolymer	Buna-AP [®] , Dutral [®]
EPDM	Ethylene propylene diene terpolymer	Epsyn [®] , Nordel [®] , Epcar [®] , Keltan [®] , Royalene [®] , Polysar-EDM [®]
FEPM	See TFE/P	Aflas [®] Epsyn [®]
FFKM/FFPM	Perfluoroelastomer	Perlast [®] , Kalrez [®] , Chemraz [®]
FKM/FPM	Fluoroelastomer	Viton [®] , Dai-el [®] , Fluorel [®] , Tecnoflon [®]
FVMQ	Fluorosilicone	Silastic LS [®] , FSE [®]
HNBR	Hydrogenated nitrile	Therban [®] , Tornac [®] , Zetpol [®]
IIR	Butyl rubber	Exxon Butyl [®] , Polysar Butyl [®] , Esso Butyl [®]
IR	Isoprene	Shell Isoprene Rubber [®]
NBR	Nitrile butadiene	Breon, Butakon [®] , Chemigum [®] , Hycar [®]
XNBR	Carboxylated nitrile	Buna-N [®] , Butacril [®] , Paracil [®] , Perbunan [®] , Krynac [®] , Europrene-N [®] , Nipol [®]
NR	Natural rubber	Nastsyn [®]
SBR	Styrene butadiene (Buna-S)	Cariflex S [®] , Plioflex [®] , Europrene [®] , Pliolite [®] , Buna Huls [®] , Carom [®] , Solprene [®]
TFE/P	Tetrafluoroethylene/propylene	Alfas [®] , Flourel [®] , Fluoraz [®]
VMQ PVMQ	Silicone	Silastic [®] , Siloprene [®] , Rhodorsil [®] , Silplus [®]

(ii) Synthetic Polyisoprene (IR)

IR is synthetic natural rubber with the same chemical composition of cis-1,4 polyisoprene. However, IR is inferior in green strength, cure rate, tear and ageing properties compared to natural rubber. IR is mostly used in tyre manufacture and as shock absorbers [13].

Fig. 26.3 Molecular structure of SBR



(iii) Styrene butadiene rubbers (SBR)

SBRs are copolymers of styrene and butadiene, with the regular grades containing nearly 23 % styrene. The molecular structure is shown in Fig. 26.3. This rubber was originally developed to replace natural rubber. Absence of strain crystallization in SBR makes it inferior in tensile strength, resilience and abrasion resistance. Owing to backbone unsaturation, SBRs have poor resistance to oxygen and ozone compared to other elastomers. Typical applications are seals for hydraulic braking systems and tyre treads [14].

(iv) Butyl rubbers (IIR)

Isobutene-isoprene rubbers (IIR), or butyl rubbers, are copolymers containing isobutene and isoprene. The molecular structure is shown in Fig. 26.4. These rubbers have an effective long-term temperature range of -50 to $+120$ °C.

A small percentage of isoprene is introduced to furnish the necessary sites for vulcanising. The densely packed structure of IIR elastomers promotes very low gas permeability and water absorption. Typical applications are in gas retentions such as tyre inner tubes, vacuum seals and membranes [15].

(v) Poly butadiene Rubbers (BR)

BR is a homopolymer of butadiene. The molecular structure is depicted in Fig. 26.5. This rubber contains approximately 97–98 % cis-1,4 Butadiene units, and is an NR substitute with properties generally inferior to those of NR. However, some polybutadienes exhibit better low temperature flexibility than NR.

Hydrogenated polybutadiene is chemically resistant to hydrazine, propyl nitrate and tricresyl phosphate, and is useful for missile applications [16]. Hydroxyl-terminated polybutadiene is used as the polymeric binder in solid rocket propellants [17].

(vi) Ethylene Propylene Diene Rubber (EPDM)

EPDM is a terpolymer of ethylene, propylene and a small percentage of non-conjugated diene, which provides unsaturation in side-chains pendent from the fully saturated backbone. The molecular structure is depicted in Fig. 26.6. EPDM's mechanical properties are inferior to those of NR but it has superior resistance to ageing, swelling and chemicals.

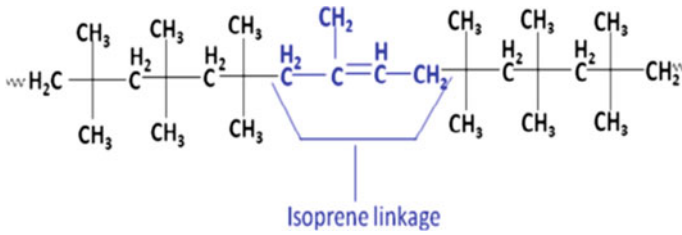


Fig. 26.4 Molecular structure of IIR

Fig. 26.5 Molecular structure of BR

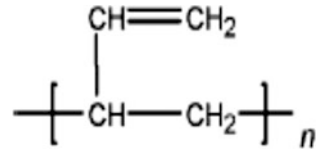
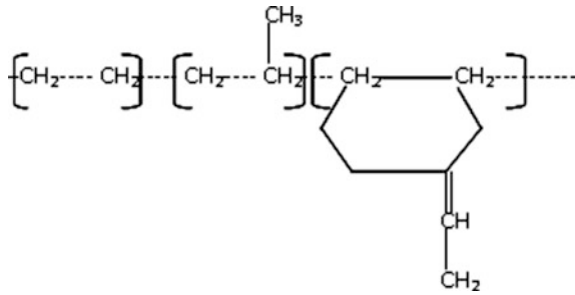


Fig. 26.6 Molecular structure of EPDM



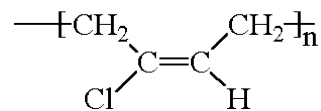
Owing to its low density, EPDM is used as the rocket motor insulator for rocket and missile applications [18, 19]. It is also used as elastomeric bushings in aircraft and helicopter applications [20].

(vii) Polychloroprenes (CR)

This type of rubber is a homopolymer of chloroprene (chlorobutadiene). These are also called Neoprene rubbers. The molecular structure is depicted in Fig. 26.7. The backbone chains are of the trans-1,4 configuration, which gives a high degree of stereo-regularity. This property enables CRs to crystallize on stretching.

Neoprene has inferior mechanical properties at room temperature and poorer low temperature flexibility compared to natural rubber. However, neoprene is ozone and

Fig. 26.7 Molecular structure of CR



flame resistant, and also has fair resistance to corrosive chemicals and moderate swelling resistance to oils, fuels and solvents.

Owing to its strain-induced crystallization, neoprene is used as rubber pads, elastomeric bushings, seals, O rings and shock mounts [21].

(viii) Nitrile rubbers (NBR)

NBR is a copolymer of acrylonitrile and butadiene rubber. The properties of this copolymer are governed by the ratio of the two monomers acrylonitrile and butadiene. The molecular structure is shown in Fig. 26.8.

Nitrile rubber can be classified as three types based on the acrylonitrile (ACN) content (low, medium and high) as follows:

- High nitrile: >45 % ACN content
- Medium nitrile: 30–45 % ACN content
- Low nitrile: <30 % ACN content

As the ACN content increases, NBRs show superior resistance to aromatic hydrocarbons. This can be attributed to the polarity nature of ACN. However, the lower the ACN content, the better will be the low temperature flexibility. Hence the medium nitrile NBR is widely used for the best overall balance.

NBRs show excellent resistance to aircraft fuel, and hydraulic and lubricating oils. But they are not suitable for strong polar liquids. They are widely used as seals, gaskets and hoses in fuel/hydraulic system of aircraft, helicopters, rockets and aero engines.

Nitrile rubbers are also available as carboxylated (XNBR) and Hydrogenated (HNBR) nitrile rubbers [22]. Compared to regular NBR, XNBR shows increased tensile strength, higher modulus and better abrasion and tear resistance. HNBR gives improved resistance to heat and ozone.

(ix) Chlorosulphonated polyethylene rubbers (CSM)

Polyethylene is converted into CSM by reacting with chlorine and sulphur dioxide. The molecular structure is depicted in Fig. 26.9. Hypalon is a trade name

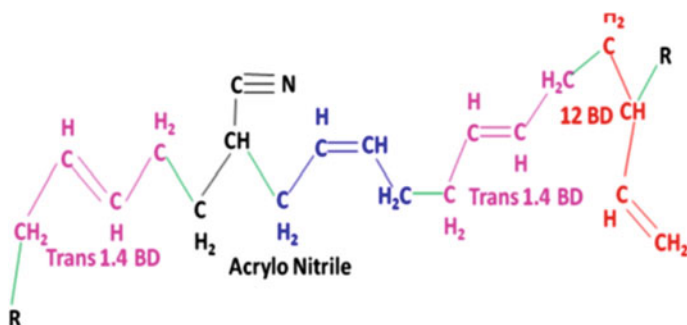


Fig. 26.8 Molecular structure of NBR

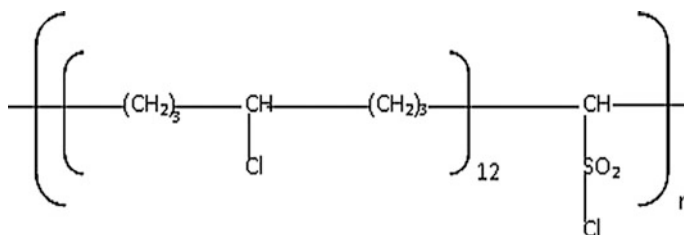


Fig. 26.9 Molecular structure of CSM

for a CSM. It is resistant to chemicals, temperature extremes and ultraviolet light. Hypalon also has fair mechanical properties and excellent resistance to heat, fatigue, chemicals, ozone and weather. Its major uses are to blend [23] with other elastomers, and for chemical barrier elements and static seals.

(x) Silicone elastomers (VMQ)

Silicone rubber is a polymer with a backbone of silicone-oxygen linkages as depicted in Fig. 26.10. While the backbone of silicone rubber is silicone-oxygen, the pendent groups can be methyl (MQ, most popular), Vinyl methyl (VMQ, higher peroxide cross-linking efficiency), phenyl vinyl methyl (PVMQ, crystallization inhibition, low temperature flexibility), and trifluoropropyl (FSR or FVMQ, solvent/fuel resistance).

According to ASTM D 1418 there are various classes of silicone rubbers [10], see Table 26.3. VMQs have excellent resistance to ozone and weathering, and good resistance to compression set at high temperatures. Due to the flexible backbone of Si–O–Si linkages, they have poor tensile strength, low tear and abrasion resistance, and high gas permeability.

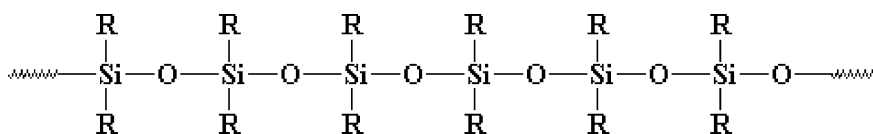


Fig. 26.10 Molecular structure of VMQ

Table 26.3 Classes of silicone elastomers [26]

Class	Substituent in polymer chain	Applications
MQ	Methyl	Not commonly used
VMQ	Vinyl	General purpose
PMQ	Phenyl	Extremely low temperature
PVMQ	Methyl, phenyl and vinyl	Extremely low temperature
FVMQ	Trifluoropropyl	Fuel, oil and solvent resistance

The saturated backbone and flexible chain find wide application in aircraft as weather resistant canopy seals. The properties like inertness and lack of toxicity make these elastomers suitable for pilots' oxygen masks. They are also widely used in the aerospace industry as pneumatic seals [24, 25].

(xi) Fluorosilicone elastomers (FVMQ)

The FVMQ elastomer is a modified silicone rubber. The molecular structure is as shown in Fig. 26.11. The trifluoropropyl substitution in the polymer chain induces the polarity in an FVMQ. This elastomer overcomes the disadvantages of silicone in terms of fuel resistance without compromising the weathering resistance and low temperature flexibility.

These rubbers have a very wide service temperature range and low chemical reactivity. However, they have low tensile strength, and poor tear and abrasion resistance compared to fluorocarbon rubbers. Typical uses include sealing systems [27, 28] requiring wide temperature exposure and resistance to aerospace fuels and oils.

(xii) Fluorocarbon elastomers (FKM or FPM)

Fluorocarbon gums are prepared by copolymerizing monomers such as vinylidene fluoride (VF) and hexafluoropropylene (HFP). The type of monomer determines the fluorine content, and there are three different types of FKM, see Table 26.4. The molecular structures of all three types are shown in Fig. 26.12.

The high strength of FKMs can be attributed to the C–F bond compared to the C–H bond. General properties of FKMs include excellent resistance to heat,

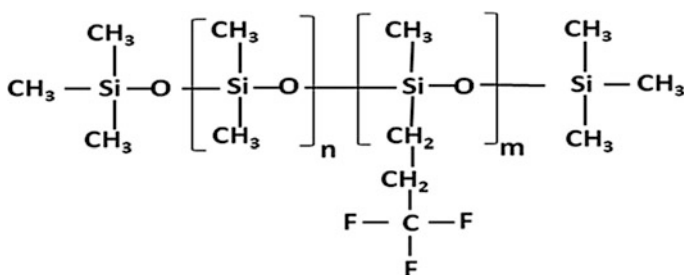
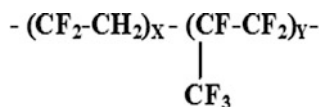
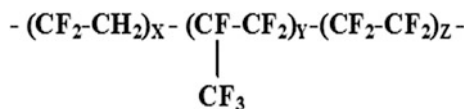


Fig. 26.11 Molecular structure of FVMQ

Table 26.4 Types of FKMS [10]

Class: fluorine content	Properties/applications
Copolymer of vinylidene fluoride (VF) and hexafluoropropylene (HFP): 65–65.5 %	Good fluid and best compression set
Terpolymer of VF, HFP and tetrafluoroethylene (TFE): 67 %	Better chemical resistance and inferior compression set
Tetrapolymer of VF, HFP, TFE and cure site monomer: 67–69 %	Improved chemical resistance and compression set compared to terpolymers

Fig. 26.12 Molecular structures of FKMs**VF-HFP COPOLYMERS****VF-HFP-TFE TERPOLYMERS**

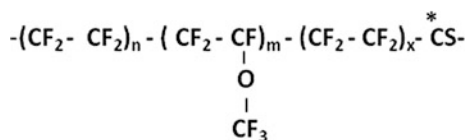
petroleum oils and hydrocarbon fuels, organic and silicate ester-based lubricants, and aromatic hydrocarbons. On the other hand, they have poor resistance to ethers, ketones, esters, amines, and hydraulic fluids based on phosphate esters. Superior tensile strengths make them suitable for dynamic sealing applications, with the lowest operating temperature between -15 and -18 °C, i.e. these elastomers are not suitable for low temperature applications. The excellent fluid resistance can be attributed to the fluorine content in the molecular structure. The fuel resistance of FKMs increases with the fluorine content at the expense of compression set.

Owing to their excellent fuel resistance and strength, FKMs are widely used in aircraft and spacecraft fuel systems as dynamic seals [29].

(xiii) Perfluoroelastomers (FFKM)

An FFKM is chemically a terpolymer of tetrafluoroethylene (TFE) and perfluoromethylvinylether (PMVE) with a small amount of cure-site monomer. The molecular structure is depicted in Fig. 26.13. The absence of hydrogen atoms in cured FFKM polymers increases the heat and chemical resistance as compared to FKMs. The unique property of FFKMs is the long-term resistance to exposure at high temperatures up to 260 °C and short-term resistance up to 310 °C.

FFKMs are the most chemically resistant elastomers available—effectively a rubber form of PTFE (polytetrafluoroethylene). They are extremely inert and have excellent resistance to the majority of chemicals that attack other elastomers. They have outstanding resistance to ketones, hot fuming nitric acid, oil field sour gases and high temperature steam; and they give low out-gassing under vacuum. Also, they have good long-term high temperature compression set resistance. The major disadvantage is the poor low temperature flexibility. The high strength and high

Fig. 26.13 Molecular structure of FFKM

temperature resistance properties make FFKMs suitable for static and dynamic seals in aerospace applications [30].

26.1.6 Elastomer Aerospace Requirements

The exceptionally high elasticity, with elongation values from one hundred to several thousand percent, makes elastomers suitable for aircraft tyres, seals and gaskets. Tyres must have many capabilities [31], including supporting vehicle loads, maintaining dimensional stability, giving adequate tread life, and having low energy consumption. To meet these requirements they must combine enough rigidity and flexibility to cope with obstacles without sustaining damage, and give long flexural fatigue lives. Moreover, aircraft tyres must cope with use at high speeds and high loads relative to their size.

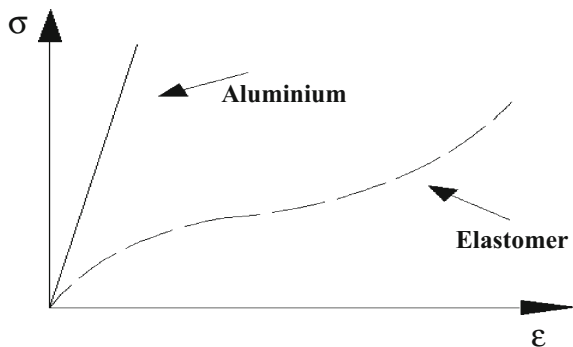
Their outstanding dynamic properties make elastomers suitable as shock absorbers and passive dampers in the space industry, where they are mounted onboard launchers and satellites. Historically, the damping properties of elastomers were first used for launchers to prevent damage due to shock loads generated by stage separations. Subsequently, they were mounted inside spacecraft as passive damping equipment. The intention is always to limit shock level effects on equipment and micro-vibrations generated by onboard reaction wheels and gyroscopes.

The following elastomeric properties play major roles in aerospace applications:

(i) Mechanical characteristics

The main mechanical characteristic of elastomers is extreme flexibility. They can be strongly extended (more than 400 % elongation) without damage, and return to their original positions when the stress is removed. The extreme flexibility can be

Fig. 26.14 Schematic tensile stress–strain curves for an elastomer and aluminium [31]



attributed to the long molecular chains made of monomer units rearranging themselves to dispense the applied stress. Moreover the network of cross-links formed between the molecular chain helps the elastomer to return to the original shape. Figure 26.14 compares the stress–strain behaviour of a metal and elastomer.

(ii) Thermophysical aspects

Owing to the high mobility of the macromolecular chains, the glass transition temperature (T_g) of elastomers is lower than room temperature, and it also depends on the chemical structure of the elastomer. Elastomers above T_g will be soft, flexible and exhibit a delayed elastic response (viscoelasticity), while those below their T_g will be hard and brittle. When the temperature is higher than T_g , thermal agitation of macromolecular chains is very high inside the material, making the elastomer very elastic around T_g . This is the relaxation area where the damping of the elastomer is maximum.

(iii) Viscoelasticity

Elastomers exhibit a viscoelastic behaviour intermediate between a perfectly elastic spring and a viscous fluid. This is why a first approximation to modelling a rubber damper is a spring connected to a dashpot, as shown schematically in Fig. 26.15.

This viscoelastic model is called the Voigt model. On loading, the spring tries to elongate instantaneously, but the piston in the dashpot moves rather slowly and delays the response of the spring. On releasing the load, the spring tries to pull the system back, but again the dashpot delays the motion. This is the phenomenon of delayed elasticity, which can be described by both the modulus and viscosity. The total stress (σ) is equal to the sum of the elastic and viscous stresses, as shown in Eq. (26.1). Here the modulus can be expressed as an in-phase component, the storage modulus (G'), which is the measure of the elastic behaviour. G'' is the measure of the viscous behaviour, and is known as the loss modulus. The ratio of the loss to the storage modulus, shown in Eq. (26.2), is called the damping (ϕ).

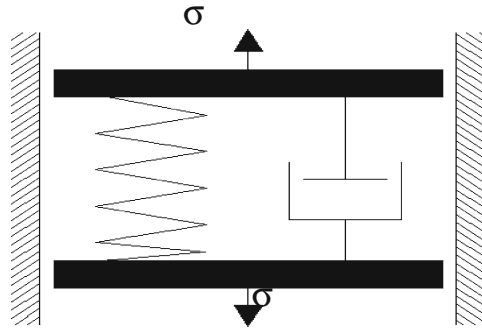
$$\sigma = \gamma_0[G'(\omega) \sin(\omega t) + G''(\omega) \cos(\omega t)] \quad (26.1)$$

and

$$\phi = \tan^{-1}(G''/G') \quad (26.2)$$

- *Frequency influence:* From Eq. (26.1), G' and G'' depend on the frequency, ω :
 - when ω is low the molecular chains have time to return to their original positions. Here the viscous or liquid-like flow predominates. Hence the material appears flexible.

Fig. 26.15 Viscoelastic model [31]



- when ω increases, the molecular chains lag behind the original positions and lead to unrecoverable deformation. Here the elasticity dominates and the material behaves in elastic fashion.
- finally, if ω continues to increase, the molecular chains cannot return to their original positions. The macromolecular chains are in permanent tension and the material appears rigid.
- *Temperature influence:* Temperature and frequency have opposite influences on elastomers:
 - at very low temperatures the elastic moduli are very high and the elastomer is rigid and brittle.
 - at high temperatures the elastic moduli are low and the elastomer is elastic.
 - at intermediate temperatures the elastomers are most viscous near the glass transition temperature T_g .

(iv) Fluid resistance [32]

Many aerospace products such as seals, gaskets and hoses encounter lubricating and hydraulic oils, greases, and fuels. Therefore it is important to select elastomers with resistance to these fluids.

Two relationships are of primary importance in the interaction of chemical compounds: solution and reaction. Many liquids are good solvents for particular elastomers but do not react with the material: these liquids cause reversible swelling and property changes in elastomers. Other liquids are not solvents but are highly reactive: these degrade elastomers by surface attack.

Liquids intermediate between these two extremes cause both swelling and irreversible changes in the properties. Swelling causes volume changes that alter the physical properties of elastomers. An immersion test under controlled conditions is the most reliable method for selecting an elastomer for use in the presence of specific fluids.

The fluid resistance of elastomers depends on the following factors:

- Elastomer grade
- Compounding ingredients
- Temperature and time of exposure
- Dimensions of the elastomer part
- Chemical composition of fluid medium.

26.1.7 Aerospace Applications of Elastomers

Elastomers are essential materials for the following aerospace systems:

- (i) Airframe systems
 - Structural system vibration damping elements
 - Pressurization system sealing parts
 - Control system power source, actuator, servo, and vibration damping parts
 - Chemical, thermal, and abrasion-resistant coatings and parts
 - Electrical system parts
 - Heating and cooling system parts.
- (ii) Instrument, weapon, indicator and guidance systems
 - Power source and transmission parts
 - Electrical insulation
 - Shock absorption and vibration damping parts
 - Chemical, thermal and abrasion resistant coatings and parts.
- (iii) Landing gear systems
 - Tyres
 - Shock absorption and vibration damping parts
 - Braking device parts
 - Retraction mechanism parts.
- (iv) Propulsion systems
 - Fuel containment and transfer element parts
 - Actuator and servo parts
 - Shock absorption and vibration damping parts
 - Electrical insulation
 - Solid propellant ingredients.

26.2 Adhesives

26.2.1 Introduction

Adhesive bonding is widely accepted as a valuable method for obtaining structural assemblies with very good strength-to-weight ratios. The aerospace industry uses adhesive bonding extensively, for both metallic and composite structures, and also hybrid metal/composite structures and components.

Adhesives for elevated temperature applications must operate in severe environments. Hence one of the mandatory capabilities is to maintain the mechanical properties and structural integrity at the designed service temperatures. Adhesive systems that meet some of these requirements include epoxies (high strength and temperature resistance), silicones (excellent sealants for low stress applications, high degree of flexibility and very high temperature capabilities), phenolics, polyimides, bismaleimides and ceramic adhesives.

In recent years, adhesive bonding has either been replacing or supplementing conventional joining methods such as riveting, welding and mechanical fastening in a variety of applications [33]. This type of bonding is preferable for thin structures with defined loads, and is being extensively used to repair cracked sheet structures in aircraft, using composite patches [34]. However, thicker structures with heavy loads are more suited to mechanical fastening [35].

26.2.2 Advantages of Adhesive Bonding

There are many potentially advantageous industrial applications [36, 37] of adhesives relevant to aerospace structures, for which the major concerns are structural efficiency (light weight), safety and reliability. In recent years the use of adhesive bonded aerostructures has increased tremendously due to the following advantages:

- Improvement of load carrying capability
- Excellent fatigue properties
- Attractive fracture mechanics properties
- Corrosion resistance
- Weight reduction.

However, there are also various disadvantages like the requirement of stringent process control and difficulties with various testing methods.

26.2.3 *Mechanisms of Adhesive Bonding*

26.2.3.1 Adhesion

The mechanisms [38, 39] and factors mainly responsible for developing strong and durable bonded joints are

- Molecular attraction, mechanical interlocking or electrostatic attraction of surfaces held together.
- Wetting of surfaces
- Contact angles
- Adherend surface quality
- Adhesive type and properties.

26.2.3.2 Adherend surface

The surface roughness of the adherend surface plays a major role. The rougher the surface, the more surface area is available for bonding. Good adhesion can be achieved with good wetting of the adherend surfaces and uniform spreading of the adhesives. In this respect the surface cleanliness is paramount for successful bonding.

26.2.4 *Surface Treatment of Substrates*

Surface preparation is a key factor for the satisfactory service life. There is a wide range of surface treatments available [40– 44]. All the substrates have to be chemically treated to remove impurities and promote good adhesion. Best practice is collected in ISO Standards 4588 (metals) and 13895 (plastics). The techniques can be classified into five groups, according to treatment type:

- (i) **Cleaning/Degreasing:** Grease, oil, wax and other organic contaminants can be removed by wiping, dipping or spraying with organic solvents or alkaline aqueous solutions. Dust can be removed by a clean brush or blast of air.
- (ii) **Surface Roughening:** An abrasion treatment increases the surface roughness and energy. Abrasive materials enhance the roughness and improve the chemical activity of the adhesives.
- (iii) **Chemical Treatments:** The type of chemical treatment depends on the variety of substrate. A chemically active surface can be achieved by immersion of the substrate in the chemical solution.
- (iv) **Physical Treatments:** The surface of the substrate is exposed to ionized or active gases, e.g. corona discharges, plasmas, flames and ozone. This method has wide scope for fine tuning the substrate surface properties.

Table 26.5 Surface pre-treatment methods [40, 41]

Mechanical	Chemical	Energetic
Alumina grit blast	Solvent cleaning	Plasma
Cryo-blast (Dry ice blast)	Detergent wash	Corona discharge
Soda-blast	Acid etch	Flame
Ply peeling	Anodizing	Excimer laser
Silicon carbide abrasion	Primer	

- (v) **Primers:** Primers provide protection and durability to the chemically or mechanically treated surface. These coatings prevent the surface from corrosion and are applied by dipping, brushing or spraying.

Each of the above categories can be further divided into a given technique or method of surface preparation, see Table 26.5.

Selection of a pre-treatment will be based on the type of substrate, durability, health and safety, and production costs. Pre-treatment facilities can include equipment, chemicals and consumables. Key surface features are wettability, roughness, soundness, stability, lack of contamination, uniformity and adhesive compatibility.

26.2.5 Adhesive Type and Properties

The selection of adhesives [45–47] for aerostructures is vital in achieving satisfactory performance. The following points list the factors involved in the selection of adhesives.

- Basic type of adhesive system
- Cure parameters of bonded structure
- Temperature range of exposure
- Durability
- Mechanical properties
- Environmental resistance
- Performance evaluation.

The key types of structural adhesives [48] may be summarized as follows:

- **Epoxies**—Epoxy adhesives consist of an epoxy resin plus a hardener. They are available in one-part, two-part and film form. There are many resins and different hardeners, providing a great variety in formulation and performance. Polyamines are generally used as the hardeners for epoxy adhesives. However, dicyanamide is used for high temperature curing. Epoxy adhesives form extremely strong durable bonds with most of the substrates. The adhesive joints show good resistance to fatigue, creep, heat, moisture and solvents. **Toughened epoxies** contain an epoxy resin toughened with an elastomer. In general, Nitrile

rubber is used for elastomer-modified epoxy resin systems. Elastomers improve the bond durability, fracture and impact resistance. They are extensively used in larger wing and honeycomb assemblies for aircraft structures.

- **Polyurethanes**—Polyurethane adhesives basically consist of polyisocyanates, polyols and chain extenders. They are produced by the reaction of polyisocyanates and polyols. This type of resin is usually two-part and fast curing. They have high impact resistance and durability. They are useful for bonding to glass-reinforced plastics. Fibre-reinforced plastic surfaces to be bonded are often treated with solvent based primers.
- **Cyanoacrylates**—These are very important adhesives because of rapid curing. They are produced by anionic polymerisation of cyanoacrylic acid ester. These adhesives are not suitable for high temperature applications. **Toughened acrylics** are elastomer-modified acrylics, which are fast curing and offer high impact resistance.
- **Modified phenolics**—The epoxy and nitrile modified phenolics find use in military and space applications for metal to metal joints. They have excellent short-time resistance to high temperatures. Epoxy phenolics have good resistance to high humidity environments.
- **Hot melts**—Hot melt adhesive systems include ethylene-vinyl acetate copolymers, polyolefins, polyamides, polyesters and thermoplastic elastomers. They remain solid up to a certain temperature. At this temperature they start melting and are applied to the surface. Cooling results in rapid setting. They are usually designed for light loads, and only polyamides and polyesters can withstand limited loads at elevated temperatures without creep. They are typically used in door panels, tail-light assemblies, electronic controls and window seals.
- **High temperature adhesives**—These are used for high service temperatures. Epoxy and phenolic resins weaken due to rapid thermal degradation at high temperatures. Thus for specialist applications where brittle ceramic adhesives are not appropriate, recourse must be made to more exotic, synthetic polymers. Polyimide and bismaleimide adhesives are the most established types in this class. They are available as liquids or films, but are relatively expensive and difficult to handle. However, they are superior to most other adhesive types with regard to long-term strength retention at elevated temperatures.
- **Rubber adhesives**—These are based on various elastomer solutions or latexes, and solidify through loss of solvent or water medium. They are not suitable for sustained load.

26.2.6 Adhesive Joint Design [47, 48]

The important motives to use adhesive joints are to avoid welding or mechanical fastening, which can introduce local damage. In aerospace applications the substrate may be a metallic or composite structure. Hence it is very important to have an

optimum joint design resistant to failure. The following points are key factors in designing bonded joints:

- Joint geometry
- Adhesive selection
- Mechanical properties of adhesive and substrate
- Stress in the joint
- Surface preparations of substrate
- Processing and curing conditions.

The bonded joints may be subjected either to the following types of load or combinations of loads [47].

- Tensile
- Compression
- Shear
- Cleavage
- Peel.

Adhesive joints show great resistance in shear, compression and tension, but become vulnerable under peel and cleavage loading. Hence the two main criteria of design are (i) uniform distribution of stresses over the bonded joints and (ii) the stress should be tensile, compression or shear: peel and cleavage loading should be avoided because they concentrate the applied forces into a single line of high stress. Thus for maximum strength the cleavage and peel stresses should be as much as possible designed out of the joints.

Generally in aeronautical structures two or more following basic type of bonded joints [48, 49] may be used in combination.

- Simple Lap Joint
- Tapered Lap Joint
- Scarf Joint
- Stepped Lap Joint
- Double Strap Joint
- Tapered Double Strap Joint.

The significance of tapering the ends of joints is a more uniform distribution of stresses and therefore reductions of stress concentrations.

26.2.7 Aerospace Applications of Adhesives

Adhesives are widely used for bonding applications [50–52] in the aerospace industry. Current applications are summarized here:

Aircraft:

- Aluminium alloy or composite skins, frames and stiffeners bonded to form major structural parts (fuselage, wings and empennage). Bonding is usually combined with some mechanical fastening (rivets and bolts).
- Aluminium alloy skins bonded to aluminium honeycomb for flight control surfaces.
- Composite structures such as honeycomb-based floor panels, engine and transmission decks, cabin work decks and tunnel covers.
- Nano-toughened epoxy paste adhesives with outstanding mechanical properties are currently used for aircraft structural metal and composite bonding.
- Radomes: Glass-fibre-reinforced plastic skins bonded to glass-fibre-reinforced plastic honeycomb. Cyanate ester formulations offer outstanding electrical properties, and are good candidates for both composite matrices and film adhesives for radome applications.
- Rotor blades: aluminium, titanium, or carbon fibre reinforced plastic skins bonded to metal ribs.

Spacecraft:

- Apollo command module: leak-tight aluminium alloy sheet and honeycomb core sandwich structures bonded with epoxy-phenolic adhesive.
- Apollo heat shield: this was an epoxy novolac resin with special additives in a fibreglass honeycomb matrix. Adhesives were used to bond the glass-reinforced honeycomb core to stainless steel to form a sandwich substructure.
- Apollo Service Module: aluminium alloy skins and composite honeycomb core sandwich bonded with epoxy-phenolic tape adhesive.
- Lunar Module: Seals for mechanical fasteners, and seams with epoxy-based adhesive for sandwich structure.
- Epoxy-glass skins co-bonded to aluminium honeycomb core for solar panels.
- Solar cells bonded onto polyimide film laminated with a thin glass-epoxy layer.
- Second surface mirrors: Thin fragile glass or quartz plates, metallised on the back faces, and bonded on the spacecraft.
- Reflective radiation surfaces: bonded on spacecraft exteriors.
- Multi-layer circuit boards, antenna reflectors, tabular truss configurations, mounting panels, re-entry heat shields.
- Space Shuttle: bonding of tiles for temperature protection. The adhesive used to bond the ceramic tiles was an RTV (room temperature vulcanising) silicone rubber [53, 54]. During re-entry to the atmosphere the adhesive strength was sufficient to hold the tiles in place at the extreme temperatures.

Tactical Missiles:

- Adhesive bonding technology is used for wings, bonding of insulators and bonding of liners to solid rocket propellant motors, and bonding nozzles to propellant engines.

26.3 Indian Scenario

Various *ab initio* projects in the Indian aerospace field of elastomer compounds and adhesives have resulted in much indigenous manufacture and use. At present an enormous number of elastomer compounds are indigenised as per the aeronautical elastomer specifications, and are being used in Indian aerospace organizations.

In a similar way, many adhesives such as rubber-based polychloroprene, nitrile, epoxy resin, and lanolin are indigenously available. Epoxy resin with the commercial designation Araldite is widely used as an adhesive in the Indian aeronautical field. Epoxy resins are used in electrical and electronic components, and also for bonding glass, carbon and aramid fibre in reinforced plastics, and for bonding metals to non-metals.

26.4 Conclusions

The types of elastomers used in the aerospace industry include Natural, Nitrile, Neoprene, Butyl, Silicone, Fluorocarbon, and Ethylene Propylene rubbers; and Hypalon and Fluorosilicones. Their exceptionally high elasticity and elongation characteristics make them especially suitable for aircraft tyres, vibration dampers and seals.

Adhesives are extensively used in the aerospace industry for bonding metal-to-metal, metal-to-composite and composite-to-composite parts. There are many types of structural adhesives. However, high-performance epoxies, nitrile phenolics and bismaleimides are the most prevalent.

Acknowledgments The authors are most grateful to Dr. N Eswara Prasad and Dr RJH Wanhill for their detailed chapter review and guidance. They would also like to thank Shri Verrapa for graphical support.

References

1. DeGarmo EP, Black JT, Kosher RA (1988) Materials and processes in manufacturing. Macmillan Publishing Company, New York, USA
2. Lancho M, Fernandez A, Kiryenko S (2005) Shock attenuation system for spacecraft and adaptor. In: European conference on spacecraft structures, materials & mechanical testing. ESA Publications Division, ESTEC, Noordwijk, The Netherlands
3. Barlow FW (1993) Rubber compounding: principles: materials and techniques. Marcel Dekker Inc., New York, USA
4. Franta I (2012) Elastomers and rubber compounding materials. Elsevier Science Publishers Company, New York, USA
5. Groover MP (2010) Fundamentals of modern manufacturing materials processes and systems. John Wiley & Sons, Hoboken, New Jersey, USA
6. Griskey R (1995) Polymer process engineering. Chapman & Hall, New York, USA

7. Parker Hannifin Corporation (2007) Parker O ring handbook ORD 5700. Parker Hannifin Corporation, Cleveland, Ohio, USA
8. White JR, De SK (eds) (2001) Raprarubber technology handbook. Rapra Technology, Billingham, UK
9. Morton M (ed) (1973) Rubber technology. Van Nostrand Reinhold Company, New York, USA
10. Nadgi K (1993) Rubber as an engineering material: guideline for users. Hanser Publishers, Munich, Germany
11. Ahmadi, HR, Muhr AH (1994) Damping of structural vibrations using rubbery materials. In: Third international congress on air- and structure-borne sound and vibration. June 13–15, 1994, Montreal, Canada, The International Institute of Acoustics and Vibration IIAV: www.iiav.org
12. Roland CM (2004) Naval applications of elastomers. *Rubber Chem Technol* 77:544–551
13. Mark HF, Kroschwitz JI (1987) Encyclopedia of polymer science and engineering. John Wiley & Sons, Hoboken, New Jersey, USA
14. Hodges P (2004) Hydraulic fluids. Elsevier Ltd., Oxford, UK
15. Simpson RB (2002) Rubber basics. Smithers Rapra Ltd., Shawbury, UK
16. Agrawal JP (2010) High energy materials: propellants, explosives and pyrotechnics. Wiley VCH Verlag GmbH & Co., Weinheim, Germany
17. Yang V, Brill TB, Ren W-Z (2000) Solid propellant chemistry, combustion and motor interior ballistics. In: Zarchan P (ed) Progress in astronautics and aeronautics, vol 185. American Institute of Aeronautics and Astronautics Inc., Reston, Virginia, USA
18. Bhuvanewari CM, Kakade SD, Deuskar VD, Dange AB, Gupta M (2008) Filled ethylene-propylene diene terpolymer elastomer as thermal insulator for case-bonded solid rocket motors. *Def Sci J* 58(1):94–102
19. Bhuvanewari CM, Sureshkumar MS, Kakade SD, Gupta M (2006) Ethylene-propylene diene rubber as a futuristic elastomer for insulation of solid rocket motors. *Def Sci J* 56(3):309–320
20. Wright WW (1990) Polymers in aerospace applications. Pergamon Press, Oxford, UK
21. Gent AN (2001) Engineering with rubber: how to design rubber components. Hanser Gardener Publications, Cleveland, Ohio, USA
22. Cheremisinoff NP (1997) Handbook of engineering polymeric materials. Marcel Dekker Inc., New York, USA
23. Sureshkumar MS, Bhuvanewari CM, Kakade SD, Gupta M (2008) Studies on the properties of EPDM-CSE blend containing HTPB for case bonded solid rocket motor insulation. *Polym Adv Technol* 19:144–150
24. Bielinski, DM, Pieczynska D, Jagielski J, Stomil (2007) Modification of elastomer friction by ion bombardment. In: High performance and speciality elastomers 2007: the fourth international conference, 5–6 December, 2007, Frankfurt, Germany, Rapra Technology Ltd., Shrewsbury, UK
25. Burkitt B, Burner S (2007) Incorporating functional fillers into silicone elastomer systems. In: Polymers in defence and aerospace applications, Smithers Rapra Technology Ltd., Shawbury, UK
26. Brydson JA (1999) Plastic materials. Butterworth-Heinemann, Oxford, UK
27. Franssen O, Bosshammer S (2008) Real fluorosilicones combined with LSR. Processing new product family FFSL. Smithers Rapra Technology Ltd., Shawbury, UK
28. Bhuvanewari, CM, Shanmugavel R, Kale SS, Gouda G (2011), Study and evaluation of fluorosilicone—silicone elastomer blend as aeroengine seal. In: National conference on advanced polymers, fibres & fabrics, Kanpur, India
29. Drobny JG (2009) Technology of fluoropolymers. CRC Press, London, UK
30. Ebnesajjad S (2013) Introduction to fluoropolymers: materials, technology and applications. Elsevier Inc., Oxford, UK
31. Demerville T, Rubber materials and dynamic space applications. SMAC group, Mont Blanc Technologies, Toulon Cedex, France

32. Shanks RA, Kong I (2013) General purpose elastomers: structure, chemistry, physics and performance. In: Visakh PM, Thomas S, Chandra AK, Mathew AP (eds) *Advances in elastomers: blends and interpenetrating networks*. Springer-Verlag, Berlin, Germany
33. Ferrandez P (2008) Fluoroelastomers, FKM, FEPDM. In: Klingender RC (ed) *Handbook of speciality elastomers*. CRC Press, London, UK
34. Cognard P (ed) (2005) *Handbook of adhesives and sealants; basic concepts and high tech bonding*. Elsevier Ltd., Oxford, UK
35. Madani K, Touzain S, Feaugas X, Benguediab M, Ratwani M (2009) Stress distribution in a 2024-T3 aluminum plate with a circular notch, repaired by a graphite epoxy composite patch. *Int J Adhes Adhes* 29:225–233
36. Campbell FC (2001) Secondary adhesive bonding of polymer matrix composites. In: *ASM handbook*, vol. 21, Composites, ASM International, Materials Park, Ohio, USA
37. Barnes TA, Pashby IR (2000) Joining techniques for aluminium spaceframes used in automobiles part II—adhesive bonding and mechanical fasteners. *J Mat Process Tech* 99:72–79
38. Dixon DG (2005) Aerospace applications of adhesives. In: Packham DE (ed) *Handbook of adhesion*. John Wiley & Sons Ltd., Chichester, UK
39. Crompton JS (1989) An examination of interfacial failure in adhesively bonded aluminum. *J Adhes* 28:135–143
40. Minford JD (1993) *Handbook of aluminum bonding technology and data*. Marcel Dekker Inc., New York, USA
41. Lee L-H (1991) *Adhesive bonding*. Plenum Press, New York, USA
42. Wernick S, Sheasby PG, Pinner R (1987) *Surface treatment and finishing of aluminium and its alloys*. Finishing Publications Ltd, Stevenage, UK
43. Dahm RH (2005) Recently developed surface treatment methods. In: Packham DE (ed) *Handbook of adhesion*. John Wiley & Sons Ltd., Chichester, UK
44. Briggs D (2005) Plasma treatment. In: Packham DE (ed) *Handbook of adhesion*. John Wiley & Sons Ltd., Chichester, UK
45. Cope BC (2005) Fibre orientation, fibre–matrix interface; surface treatment. In: Packham DE (ed) *Handbook of adhesion*. John Wiley & Sons Ltd., Chichester, UK
46. Dixon DG, Cope BC (2005) Silane adhesion promoters. In: Packham DE (ed) *Handbook of adhesion*. John Wiley & Sons Ltd., Chichester, UK
47. Dillard DA (2010) *Advances in structural adhesive bonding*. Woodhead Publishing Ltd., Cambridge, UK
48. Petrie EM (2000) *Handbook of adhesives and sealants*. McGraw-Hill, New York, USA
49. Corporation H (2007) *Users guide to adhesives*. Freeman Manufacturing and Supply & Co., Basel, Switzerland
50. Campbell FC (2006) *Manufacturing technology for aerospace structural materials*. Elsevier Ltd., Oxford, UK
51. Patrick RL (1976) *Structural adhesives with emphasis on aerospace applications*. Marcel Dekker Inc., New York, USA
52. Dunn DJ (2003) *Adhesives and sealants: technology, applications and markets*. Rapra Technology, Shawbury, UK
53. Zhang S, Zhao D (eds) (2012) *Aerospace materials handbook*. CRC Press, New York, USA
54. Da Silva LFM (2010) *Technology of mixed adhesive joints*. In: *Advanced structural materials*. Springer, Berlin, Germany